Advanced RFI Detection, RFI Excision, and Spectrum Sensing: Algorithms and Performance Analyses

by

Tilahun Melkamu GETU

MANUSCRIPT-BASED THESIS PRESENTED TO ÉCOLE DE TECHNOLOGIE SUPÉRIEURE IN PARTIAL FULFILLMENT FOR THE DEGREE OF DOCTOR OF PHILOSOPHY
Ph.D.

MONTREAL, MARCH 25, 2019

ÉCOLE DE TECHNOLOGIE SUPÉRIEURE
UNIVERSITÉ DU QUÉBEC

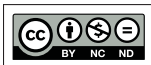

BOARD OF EXAMINERS

THIS THESIS HAS BEEN EVALUATED

BY THE FOLLOWING BOARD OF EXAMINERS

Prof. Dr. Wessam Ajib, Thesis Supervisor
Department of Computer Sciences, Université du Québec à Montréal, Montreal, Canada

Prof. Dr. René Jr. Landry, Co-supervisor
Department of Electrical Engineering, École de Technologie Supérieure, Montreal, Canada

Prof. Dr. Mohamed Cheriet, President of the Board of Examiners
Department of Systems Engineering, École de Technologie Supérieure, Montreal, Canada

Prof. Dr. Georges Kaddoum, Member of the Jury
Department of Electrical Engineering, École de Technologie Supérieure, Montreal, Canada

Prof. Dr. Benoit Champagne, External Independent Examiner
Department of Electrical & Computer Engineering, McGill University, Montreal, Canada

THIS THESIS WAS PRESENTED AND DEFENDED

IN THE PRESENCE OF A BOARD OF EXAMINERS AND THE PUBLIC

ON MARCH 7, 2019

AT ÉCOLE DE TECHNOLOGIE SUPÉRIEURE

DEDICATION

To my parents

Atsede Admassu and Melkamu Getu

for being my lifelong teachers and mentors;

my siblings

Hana, Muluwerk, Desalegn, Dawit, Solomon, and Bethelihem

for their unconditional love, support, and inspiring belief in me;

and my grandfather

Admassu Malede

for making me, first, crave for knowledge.

"We can do anything we want to if we stick to it long enough."—Helen Keller

ACKNOWLEDGMENTS

"Gratitude is a miracle of its own recognition. It brings out a sense of appreciation and sincerity of a being."—Auliq-Ice

The existence of this Ph.D. dissertation boils down to not only *hard-work* (and *persistence*) but also to the encouragement of several people whom I wish to convey my heartfelt gratitude for.

First and foremost, I am exceedingly grateful to my Ph.D. supervisor Prof. Wessam Ajib for offering me a Ph.D. position by the time I needed it dearly. As a manifestation of his unique supervision style, the research freedom Prof. Ajib bestowed upon me throughout this dissertation has made me enjoy research indefinitely not only as a *specialist* operating within the scope of this dissertation but also as a *generalist* curious about literally everything. Apart from directing this dissertation with his unforgettable fatherly care, kind encouragement, and gentle treatment, Prof. Ajib has taught me timeless lessons that are useful not only for a career but also for life. As one of my finest research experiences, working with Prof. Ajib has made me a better person not only as a researcher but also as a persistent learner.

Along with the supervision of Prof. Ajib, I have been fortunate enough to have Prof. René Jr. Landry as my Ph.D. co-supervisor. In particular, I am grateful to Prof. Landry for his catalytic leadership skills, dynamic engaging skills, a strong belief in me, and generous funding of all my conference trips. Recalling the initial years of this dissertation, I also thank Dr. Omar A. Yeste-Ojeda—who was serving as my Ph.D. co-supervisor—for his criticisms and leadership that have uplifted the quality of our joint papers. Recalling the comments and criticisms of my pre-doc oral exam that have also shaped the depth and breadth of this dissertation, I am grateful to the jury members of this dissertation: Prof. Mohamed Cheriet and Prof. Georges Kaddoum. I also thank Prof. Benoit Champagne, my external independent examiner, for his comments regarding the draft version of this dissertation.

With respect to the raised and shaped character that has finally disseminated this dissertation, I am immensely thankful to my parents Atsede Admassu and Melkamu Getu for being my life-

long mentors, for being my lifelong teachers, and for encouraging me—all the time—to be a *man of value*. Along with my parents', the unconditional love, support, and inspiring belief in me of my siblings have never waned throughout the research that has led to this dissertation. I, thus, convey my immense gratitude to all of them: Hana Melkamu, Muluwerk Melkamu, Desalegn Melkamu, Dawit Melkamu, Solomon Melkamu, and Bethelihem Melkamu. Meanwhile, I convey my heartfelt gratitude to my grandfather Admassu Malede for making me, since my childhood times, crave for knowledge. Moreover, I thank these close family members for their encouragement: Amha Admassu, Tadele Gonae, Kassahun Girma, and Fisseha Andualem.

While sailing toward this very dissertation, I had to—once upon a time—sail through a bad weather which was indeed a challenge. However, being fortunately surrounded by absolutely kind people, the challenge was transformed into an opportunity that has finally led to this dissertation. In this regard, I am indebted to Beyene Aleme, Dr. Inge Barten, Dr. Eva-Maria Rao, Prof. Franz Faupel, Prof. Axel Bangert, and Prof. Animesh Yadav. Along with these kind people, several friends encouraged me to maintain a scientific curiosity which has eventually rendered this dissertation. In this regard, I am thankful to Abebe Mengiste, Girma Gebo, Yonas Belete, Ezera Wubishet, Wubishet Yibabie, Natnael Teshome, Elsa Weiss, Wubishet Tekalign, Praveen Rego, Saikiran Telker, Supreeth Vasisht, Christian Frank, Dr. Marx Awasung, Dr. Iurii Motroniuk, and Dr. Yetsedaw Andargie.

Having been engaged in a Ph.D. research which was sometimes surprising, my North American vacations during the last four years cannot be better—thanks to the kind hosting, treatment, and encouragement of my family members and friends who reside in the USA. In this respect, I am grateful to Yismaw Zewdu, Muna Zewdu, Eden Zewdu, Yewunetu Dessalegn, Yewubmirt Dessalegn, Roman Mengiste, Banche Dessie, Senait Zewdu, Alemtsehay Zewdu, Meles Zewdu, Yetayesh Eshetu, Tigabu Wubie, Gashaw Wubie, Ephinos Teshome, Rodas Teshome, Yohannes Yimer, Wanaw Getahun, Asaye Birhanu, and Yigrem Israel.

Throughout my Ph.D. studies, I had always enjoyed gorgeous Canadian summers and truly peaceful Canada—a country of character. Recalling my first two years in Montreal as a

man who had grown up in a temperate climate, however, adapting to the freezing Canadian winters was a challenge as well as frustration. Having been well aware of such an environment and the newcomers' respective frustration, the Ethiopian community in Montreal had been a source of encouragement, life experience, and support. Generally, I thank every member of the aforementioned community, including the innocent kids whom I had missed whenever I was very busy with this dissertation. Specifically, I acknowledge the encouragement of Debebe Emissa, Kassu Demeke, Aster Abrham, Hailu Tafere, Esayas Kiros, Samuel Hailu, Getinet Wubet, Bossena Wubet, Girma Emissa, Eleni Takele, Woinshet Belay, Bethelihem Girma, Melaku Emissa, Mekdelawit Bekele, Mekdes Bekele, Zerihun Tesfaye, Addis Kebede, Tigest Abera, Amleset Araya, Asrat Ashine, Roman G/Selassie, Gelachew Bekele, Zufan Mehari, Azeb Assefa, Yeshihareg Ashenafi, Birtukan Tafesse, Hermela Bogale, Tsegemariam Negussie, Mekoya Sintayhu, Tsigeselassie Melese, Tadela Hailu, Zecharias Zelalem, Abel Bogale, Amanuel Etbarek, Hafiz Agraw, Behailu Tsegaye, and Theodros Girma.

As there could be infinite perspectives about anything, I have been entertaining and discussing numerous perspectives with several researchers throughout the years. In this respect, I thank Prof. Schahram Dustdar, Prof. Franz Faupel, Prof. Christian Fayomi, Prof. Animesh Yadav, Prof. Tadilo Bogale, Dr. Abebe Geletu, Dr. Haile Tekle, Dr. Tri Nguyen, Dr. Gulilat Diro, Dr. Mathew Goonewardena, Dr. Marx Awasung, Zakaria Ismaili, and Zoubir Milka.

Concerning the raised and shaped character that has eventually disseminated this dissertation, I also thank all my teachers, lecturers, and professors who have taught, nurtured, and shaped me from my childhood until the end of this dissertation. Specifically, for inspiring me with science and for teaching me how to do research during my master's study at the University of Kassel, I am thankful to—my former German professors—Prof. Dirk Dahlhaus, Prof. Axel Bangert, Prof. Hartmut Hillmer, Prof. Klaus David, and Dr. Thomas Hunziker.

The last but not the least, I wish to thank the IEEE ComSoc and the IEEE SPS anonymous technical reviewers for their comments and time that have contributed to the improvement of my manuscripts that, eventually, comprise this manuscript-based Ph.D. dissertation.

Détection avancée de RFI, excision de RFI et détection de spectre: algorithmes et analyses de performances

Tilahun Melkamu GETU

RÉSUMÉ

En raison d'interférence intentionnelle et non intentionnelle, l'interférence radiofréquence (RFI) entraîne une perte de performance dans divers systèmes tels que la radiométrie à hyperfréquences, la radioastronomie, les communications par satellite, les communications ultra-large bande, le radar et la radio cognitive. Pour surmonter l'impact de la RFI, une détection RFI robuste avec une excision RFI efficace est donc nécessaire. Parmi leurs limites, les techniques existantes tendent à être complexes en calcul et à rendre inefficace l'excision des RFI. D'un autre côté, plusieurs techniques de détection de spectre sont disponibles pour la radio cognitive (CR). Cependant, la plupart des techniques existantes reposent sur la disponibilité de l'information d'état de canal (CSI) ou sur les caractéristiques du signal d'intérêt. Motivé par les limitations soulignées, cette thèse présente les résultats de recherche en trois volets: détection avancée de RFI, excision avancé de RFI et détection avancée de spectre.

Concernant la détection avancée de RFI, cette thèse présente cinq détecteurs RFI: un détecteur de puissance (PD), un détecteur d'énergie (ED), un détecteur de valeurs propres (EvD), un détecteur à base de matrice et un détecteur à base de tenseur. Tout d'abord, un PD simple permettant de détecter une RFI large bande est étudiée. En supposant des canaux à atténuation Nakagami-*m*, des expressions analytiques exactes pour la probabilité de détection RFI et pour la fausse alarme sont dérivées et validées par simulations. Les simulations également démontrent que le PD surpasse le détecteur de kurtosis (KD). Deuxièmement, on étudie un ED pour la détection de RFI dans les systèmes de communication sans fil. Sa probabilité moyenne de détection est approximée, et des expressions analytiques asymptotiques sont dérivées. Aussi, une expression exacte pour la probabilité moyenne de fausse alarme est dérivée. Des simulations Monte-Carlo valident les expressions analytiques dérivées et corroborent le fait que le détecteur d'énergie étudié (ED) dépasse les performances de KD et d'un détecteur de test de rapport de vraisemblance généralisée (GLRT). La performance d'ED est également évaluée en utilisant de données réelles contaminées par RFI. Troisièmement, un EvD aveugle est proposé pour les systèmes SIMO (Single-Input Multiple-Output) pouvant être affectés par la RFI. Pour caractériser les performances d'EvD, des expressions de performance fermées valables pour des échantillons infiniment énormes sont dérivées et validées par le biais de simulations. Les simulations corroborent également le fait qu'EvD manifeste, même dans des paramètres de saturation d'échantillon, des performances de détection comparables avec un détecteur GLRT alimenté avec la connaissance du canal de signal d'intérêt (SOI) et un détecteur de sous-espace adapté alimenté avec les canaux SOI et RFI. Enfin, pour une détection robuste de RFI reçue via un canal à chemins multiples, cette thèse présente des détecteurs RFI multi-antennes à base de matrice et à base de tenseur, tout en introduisant une hypothèse de test à base de tenseur. Pour caractériser les performances de ces détecteurs, des analyses de performance ont été menées.

Les simulations évaluent les performances des détecteurs proposés et valident les caractérisations asymptotiques dérivées.

Concernant l'excision avancée de RFI, cette thèse introduit une méthode basée sur l'algèbre multi-linéaire pour une excision de multi-interféreurs (MI-RFI) en proposant un algorithme multi-linéaire d'estimation et de projection (MLSEP) pour les systèmes SIMO. Après avoir utilisé des fenêtres d'observation lissées, un algorithme MLSEP (s-MLSEP) lissé est également proposé. MLSEP et s-MLSEP nécessitent la connaissance du nombre d'interféreurs et de leur ordre de canal respectif. En conséquence, un nouveau énumérateur d'interféreurs à base de matrice lissée et un énumérateur d'ordre de canaux est proposé. Les analyses de performance confirment que MLSEP et s-MLSEP peuvent exciser tous les brouilleurs lorsque les perturbations deviennent infiniment petites. Pour de telles perturbations, les analyses confirment également que le s-MLSEP présente une convergence plus rapide vers une erreur d'excision nulle que le MLSEP, qui converge plus rapidement qu'un algorithme de projection de sous-espace. Malgré sa faible complexité, les simulations et l'évaluation des performances sur des données réelles démontrent que le MLSEP surpasse les algorithmes d'excision RFI basés sur la projection. Les simulations confirment également que s-MLSEP surpasse MLSEP à mesure que le facteur de lissage diminue.

En ce qui concerne la détection de spectre avancée, ayant été inspiré par un détecteur de F–test avec une expression de seuil de fausse alarme analytique considéré comme une alternative aux détecteurs aveugles existants, cette thèse présente et évalue la simple technique de détection du spectre F–test basée sur des tests ne nécessitant pas la connaissance des CSI pour les CR multi-antennes. Des expressions de performances analytiques exactes et asymptotiques sont dérivées. Les simulations évaluent les performances et valident les expressions analytiques. Pour un bruit additif présentant la même variance sur plusieurs antennes, les simulations montrent que les détecteurs présentés ont un taux de fausse alarme constant, et ils sont également robustes contre l'incertitude liée au bruit.

Mots-clés: détection de RFI, excision de RFI, détection de spectre, détection robuste, excision efficace, analyses de performance.

Advanced RFI Detection, RFI Excision, and Spectrum Sensing: Algorithms and Performance Analyses

Tilahun Melkamu GETU

ABSTRACT

Because of intentional and unintentional man-made interference, radio frequency interference (RFI) is causing performance loss in various radio frequency operating systems such as microwave radiometry, radio astronomy, satellite communications, ultra-wideband communications, radar, and cognitive radio. To overcome the impact of RFI, a robust RFI detection coupled with an efficient RFI excision are, thus, needed. Amongst their limitations, the existing techniques tend to be computationally complex and render inefficient RFI excision. On the other hand, the state-of-the-art on cognitive radio (CR) encompasses numerous spectrum sensing techniques. However, most of the existing techniques either rely on the availability of the channel state information (CSI) or the primary signal characteristics. Motivated by the highlighted limitations, this Ph.D. dissertation presents research investigations and results grouped into three themes: advanced RFI detection, advanced RFI excision, and advanced spectrum sensing.

Regarding advanced RFI detection, this dissertation presents five RFI detectors: a power detector (PD), an energy detector (ED), an eigenvalue detector (EvD), a matrix-based detector, and a tensor-based detector. First, a computationally simple PD is investigated to detect a broadband RFI. By assuming Nakagami-*m* fading channels, exact closed-form expressions for the probabilities of RFI detection and of false alarm are derived and validated via simulations. Simulations also demonstrate that PD outperforms kurtosis detector (KD). Second, an ED is investigated for RFI detection in wireless communication systems. Its average probability of RFI detection is studied and approximated, and asymptotic closed-form expressions are derived. Besides, an exact closed-form expression for its average probability of false alarm is derived. Monte-Carlo simulations validate the derived analytical expressions and corroborate that the investigated ED outperforms KD and a generalized likelihood ratio test (GLRT) detector. The performance of ED is also assessed using real-world RFI contaminated data. Third, a blind EvD is proposed for single-input multiple-output (SIMO) systems that may suffer from RFI. To characterize the performance of EvD, performance closed-form expressions valid for infinitely huge samples are derived and validated through simulations. Simulations also corroborate that EvD manifests, even under sample starved settings, a comparable detection performance with a GLRT detector fed with the knowledge of the signal of interest (SOI) channel and a matched subspace detector fed with the SOI and RFI channels. At last, for a robust detection of RFI received through a multi-path fading channel, this dissertation presents matrix-based and tensor-based multi-antenna RFI detectors while introducing a tensor-based hypothesis testing framework. To characterize the performance of these detectors, performance analyses have been pursued. Simulations assess the performance of the proposed detectors and validate the derived asymptotic characterizations.

Concerning advanced RFI excision, this dissertation introduces a multi-linear algebra framework to the multi-interferer RFI (MI-RFI) excision research by proposing a multi-linear subspace estimation and projection (MLSEP) algorithm for SIMO systems. Having employed smoothed observation windows, a smoothed MLSEP (s-MLSEP) algorithm is also proposed. MLSEP and s-MLSEP require the knowledge of the number of interferers and their respective channel order. Accordingly, a novel smoothed matrix-based joint number of interferers and channel order enumerator is proposed. Performance analyses corroborate that both MLSEP and s-MLSEP can excise all interferers when the perturbations get infinitesimally small. For such perturbations, the analyses also attest that s-MLSEP exhibits a faster convergence to a zero excision error than MLSEP which, in turn, converges faster than a subspace projection algorithm. Despite its slight complexity, simulations and performance assessment on real-world data demonstrate that MLSEP outperforms projection-based RFI excision algorithms. Simulations also corroborate that s-MLSEP outperforms MLSEP as the smoothing factor gets smaller.

With regard to advanced spectrum sensing, having been inspired by an F–test detector with a simple analytical false alarm threshold expression considered an alternative to the existing blind detectors, this dissertation presents and evaluates simple F–test based spectrum sensing techniques that do not require the knowledge of CSI for multi-antenna CRs. Exact and asymptotic analytical performance closed-form expressions are derived for the presented detectors. Simulations assess the performance of the presented detectors and validate the derived expressions. For an additive noise exhibiting the same variance across multiple-antenna frontends, simulations also corroborate that the presented detectors are constant false alarm rate detectors which are also robust against noise uncertainty.

Keywords: RFI detection, RFI excision, spectrum sensing, robust detection, efficient excision, performance analyses.

TABLE OF CONTENTS

Page

I Preliminaries

II Advanced RFI Detection

IV Advanced Spectrum Sensing

LIST OF TABLES

LIST OF FIGURES

LIST OF ALGORITHMS

LIST OF ABBREVIATIONS AND ACRONYMS

ADC	analog-to-digital converter
AGC	automatic gain control
APB	asynchronous pulse blanking
AWGN	additive white Gaussian noise
BAM-KLT	bordered autocorrelation method-KLT
BIC	Bayesian information criterion
BPSK	binary phase shift keying
CDF	cumulative distribution function
cf.	confer
CFAR	constant false alarm rate (constant FAR)
Ch. (Chs.)	Chapter (Chapters)
CON	convergence
CR	cognitive radio
CROC	complementary receiver operating characteristics (complementary ROC)
CSI	channel state information
CSP	cross subspace projection
2D	two-dimensional
DFT	discrete Fourier transform
DoA	direction-of-arrival

DoF	degrees of freedom
DWVD	discrete Wigner-Ville distribution
ECCM	electronic counter-countermeasures
ED	energy detection (detector)
EFA	extended factor analysis
EM	expectation-maximization
eq. (eqs.)	equation (equations)
EvD	eigenvalue detector
EVD	eigenvalue decomposition
EVM	error vector magnitude
EVs	eigenvalues
FAR	false alarm rate
FFT	fast Fourier transforms
Fig. (Figs.)	figure (figues)
FIR	finite-duration impulse response
FM	frequency modulation
FT	F–test
FT-v-SVD	F–test via singular value decomposition
4G	fourth generation
5G	fifth generation

GEO	geostationary earth orbit
g-FT-v-SVD	generalized F–test via singular value decomposition (generalized FT-v-SVD)
GLRT	generalized likelihood ratio test
GNSS	global navigation satellite system
GPS	global positioning system
HOSVD	higher-order singular value decomposition (higher-order SVD)
HRD	Hadamard ratio detector
IEE	interference error envelope
IF	intermediate frequency
iff	if and only if
i.i.d.	independent and identically distributed
IIR	infinite-duration impulse response
i.ni.d.	independent and non-identically distributed
INR	interference-to-noise ratio
IRG	Interference Reduction Group
I/Q	in-phase/quadrature
J-RMSE	joint root mean square error (joint RMSE)
KD	kurtosis detector
KLT	Karhunen−Loève transform
LMS	least mean squares

LoS	line-of-sight
LTI	long-term interval
MB	matrix-based
MB-MSE	matrix-based MI-RFI subspace estimator
MB-RD	matrix-based RFI detector
MCED	multi-channel energy detection (detector) or multi-channel ED
MCED-U	multi-channel energy detection with noise uncertainty
MIMO	multiple-input multiple-output
MIMO CR g-FT-v-SVD	multiple-input multiple-output cognitive radio g-FT-v-SVD
min	minimum
MI-RFI	multi-interferer RFI
MIS	maximal invariant statistic
MLSEP	multi-linear subspace estimation and projection
MME	maximum-minimum eigenvalue
MoG	mixture of Gaussian
MR	moment ratio
MSD	matched subspace detector
MSE	mean square error
MUSIC	multiple signal identification and classification
NCPs	noncentrality parameters

No.	number
non-LoS	non-line-of-sight
NRAO	National Radio Astronomy Observatory
NSERC	Natural Sciences and Engineering Research Council of Canada
OFDM	orthogonal frequency division multiplexing
OPB	oblique projection beamforming
OOC	order of convergence
PAM	pulse amplitude modulation
PCM	population covariance matrix
PCSI	perfect channel state information (perfect CSI)
PD	power detector
PDF	probability density function
PMF	probability mass function
PSK	phase shift keying
PSP	polynomial-augmented subspace projection
PU	primary user
QAM	quadrature amplitude modulation
QPSK	quadrature phase shift keying
RA	radio astronomy
RF	radio frequency

RFI	radio frequency interference
RHS	right-hand side
RMSEE	root mean square excision error
RMSE	root mean square error
ROC	receiver operating characteristics
RVs	random variables
SatCom	satellite communications
SCM	sample covariance matrix
SCT	sample covariance tensor
Sec.	Section
SIG	Satcoms Innovation Group
SIMO	single-input multiple-output
SINR	signal-to-interference-plus-noise ratio
SMB-JoNICOE	smoothed matrix-based joint number of interferers and channel order enumerator
SMB-MSE	smoothed matrix-based MI-RFI subspace estimator
s-MLSEP	smoothed multi-linear subspace estimation and projection
SNR	signal-to-noise ratio
SOI	signal of interest
SP	subspace projection
s-RMSEE	smoothed root mean square excision error

s-SCM	smoothed sample covariance matrix
STB-MSE	smoothed tensor-based MI-RFI subspace estimator
STIs	short-term intervals
SU	secondary user
SVD	singular value decomposition
TB	tensor-based
TB-MSE	tensor-based MI-RFI subspace estimator
TB-RD	tensor-based RFI detector
TDTs	transformed-domain techniques
TF	time-frequency
Thm.	Theorem
VHDL	VHSIC hardware description language
VHSIC	very high speed integrated circuit
VLA	Very Large Array
VSAT	very small aperture terminal
w.r.t.	with respect to

LIST OF SYMBOLS AND UNITS OF MEASUREMENTS

Common Symbols

$\triangleq$	equal by definition
$>>$	much greater than
$\in$	element of (belongs to)
$\rightarrow$	approaches to
$\leftarrow$	assignment
$\sim$	distributed as
$\approx$	approximated as
$\propto$	statistically equivalent
$\gtrless$	greater than, less than, or equal to
$\lceil \cdot \rceil$	the ceiling function
lim	limit
$\equiv$	equivalence
$*$	a discrete-time convolution
$[\cdot\,,\cdot]$	horizontal concatenation
$\frac{\partial}{\partial x}$ $\left(\frac{\partial}{\partial z}\right)$	partial differentiation w.r.t. x (w.r.t. z)
$\mathrm{Re}\{\cdot\}$	real part
$\mathrm{Im}\{\cdot\}$	imaginary part
$\vert$	conditioned on (under)

$n!$	n factorial
$\otimes$	Kronecker product
$(\cdot)^T$	transpose
$(\cdot)^H$	Hermitian
$(\cdot)^{-1}$	inverse
$(\cdot)^+$	the Moore-Penrose inverse
$(\cdot)^{+r}$	the r-mode pseudoinverse of a tensor
$\|\|\cdot\|\|$	the Euclidean norm
$\|\|\cdot\|\|^2$	norm squared
$\|\|\cdot\|\|_F$	Frobenius norm
$\mathbb{C}^{N_R}\left(\mathbb{C}^{N_R W}\right)$	the sets of $N_R(N_R W)$—dimensional vectors of complex numbers
$\mathbb{C}^{N_R W \times N}$	the sets of $N_R W \times N$ complex matrices
$\mathbb{H}^{N_R \times N_R}$	the sets of $N_R \times N_R$ Hermitian matrices
$\mathbb{H}^{N_R W \times N_R W}$	the sets of $N_R W \times N_R W$ Hermitian matrices
$\mathbb{C}^{N_R \times W \times N}$	the sets of $N_R \times W \times N$ three-way tensors
$\boldsymbol{A}(i,j)$	the (i,j)-th element of $\boldsymbol{A}$
$\boldsymbol{A}(:,j)$	the j-th column of $\boldsymbol{A}$
$\boldsymbol{A}(:,i:j)$	the columns of $\boldsymbol{A}$ between its i-th and j-th columns including its i-th and j-th columns
$\mathrm{tr}(\cdot)$	trace
$\mathrm{vec}(\cdot)$	vectorization

$\mathrm{unvec}(\cdot)$	unvectorization
$\mathrm{diag}(\cdot)$	diagonal (block diagonal) matrix
$\mathscr{O}(\cdot)$	the Landau notation
$\mathbb{E}\{\cdot\}$	expectation
$\Pr\{\cdot\}$	the probability of
$U(\cdot)$	the unit step function $\big($i.e., $U(y \geq 0) = 1\big)$
χ^2	chi-square
χ^2_ν	the central chi-square distribution with ν degrees of freedom
$\chi'^2_\nu(\lambda)$	the noncentral chi-square distribution with ν degrees of freedom and non-centrality parameter λ
$I_n(\cdot)$	the nth-order modified Bessel function of the first kind
$Q_u(\cdot,\cdot)$	the uth-order generalized Marcum Q-function
$\Gamma(\cdot)$	the gamma function
$\Gamma(\cdot,\cdot)$	the (upper) incomplete gamma function
$\mathscr{G}(\cdot,\cdot)$	the gamma distribution
$\mathscr{NA}(\cdot,\cdot)$	the Nakagami-m distribution
${}_1F_1(\cdot;\cdot;\cdot)$	the special case of the generalized hypergeometric function
F_{ν_1,ν_2}	the central F–distribution with (ν_1,ν_2) DoF
$F'_{\nu_1,\nu_2}(\lambda_1)$	the singly noncentral F–distribution with (ν_1,ν_2) DoF and an NCP of λ_1
$F''_{\nu_1,\nu_2}(\lambda_1,\lambda_2)$	the doubly noncentral F–distribution with (ν_1,ν_2) DoF and NCPs of (λ_1,λ_2)
$F(\lambda;\nu_1,\nu_2)$	the CDF of F_{ν_1,ν_2} evaluated at λ

$F^{-1}(\lambda;\nu_1,\nu_2)$	the inverse CDF of F_{ν_1,ν_2} evaluated at λ
$F'(\lambda;\nu_1,\nu_2\|\lambda_1)$	the CDF of $F'_{\nu_1,\nu_2}(\lambda_1)$ evaluated at λ
$F''(\lambda;\nu_1,\nu_2\|\lambda_1,\lambda_2)$	the CDF of $F''_{\nu_1,\nu_2}(\lambda_1,\lambda_2)$ evaluated at λ
$G^{\cdot,\cdot}_{\cdot,\cdot}(\cdot)$	the Meijer G-function
H_0	hypothesis on the absence of an RFI or Q RFIs (also on the absence of a primary user)
H_1	hypothesis on the presence of an RFI or Q RFIs (also on the presence of a primary user)
$P_d(P_D)$	the probability of RFI detection (also the probability of a primary user detection)
$P_f(P_{FA})$	the probability of false alarm in RFI detection (also the probability of false alarm in a primary user detection)
P_m	the probability of miss in RFI detection (the probability of miss in a primary user detection)
λ	a decision threshold
σ^2	the variance of the AWGN
$\mathrm{C/N_0}$	carrier-to-noise ratio
$\mathscr{G}$	a three-way RFI or MI-RFI filtering tensor
$\mathscr{H}$	a three-way SOI filtering tensor (a three-way secondary filtering tensor)
$\mathscr{Y}$	a three-way received signal tensor
$\mathscr{Z}$	a three-way noise tensor
$\mathscr{Z}^s$	the smoothed version of $\mathscr{Z}$

N_R, N_T	the number of receive antennas, the number of transmit antennas
γ_{snr}, γ_{inr}	the SNR, the INR
$\bar{\gamma}_{snr}$, $\bar{\gamma}_{inr}$, $\bar{\gamma}_{inr}^{j}$	the average SNR, the average INR, the average INR of the j-th RFI
$[\mathscr{G}]_{(3)}$, $[\mathscr{H}]_{(3)}$	the 3-mode unfolding of tensor $\mathscr{G}$, the 3-mode unfolding of tensor $\mathscr{H}$
$[\mathscr{Y}]_{(r)}$, $[\mathscr{X}]_{(r)}$	the r-mode unfolding of tensor $\mathscr{Y}$, the r-mode unfolding of tensor $\mathscr{X}$

Symbols Common to Chapter 2

$\mathscr{N}(\cdot,\cdot)$	the normal distribution
$r(t)$, $r[n]$	the received baseband signal, the n-th sample of $r(t)$—i.e., $r[n] = r(nT)$
$s(t)$, $v_j(t)$	the SOI, the j-th Gaussian RFI
$s[n]$, $v_j[n]$	the n-th sample of $s(t)$—i.e., $s[n] = s(nT)$, the n-th sample of $v_j(t)$—i.e., $v_j[n] = v_j(nT)$
Q, T	the number of RFIs, the sampling interval (symbol duration)
s_n, $v_{j,l}$	the n-th unknown and deterministic SOI, the l-th sample of the j-th Gaussian RFI
$p(t)$	a rectangular pulse shape of duration T
P, P_j	the power of the SOI, the power of the j-th RFI
h, $\bar{h}_s$	the flat fading SOI channel gain, the local mean received power of the SOI
g_j, $\bar{g}_{j,s}$	the channel gain of the j-th RFI, the local mean received power of the j-th RFI
m_1, m_{j+1}	the SOI fading severity parameter, the fading severity parameter of the j-th RFI

$\eta_1,\ \ \eta_j$	a scale parameter defined as $\frac{\bar{\gamma}_{snr}}{m_1}$, a scale parameter defined as $\frac{\bar{\gamma}_{inr}^{j}}{m_{j+1}}$
$z(t),\ \ z[n]$	a band-limited zero mean AWGN, the n-th sample of $z(t)$—i.e., $z[n]=z(nT)$
N	the number of intercepted samples
$Y,\ \ \tilde{Y}$	a decision variable, a decision variable defined as $\tilde{Y}=Y-\sigma^2$
$f_{\tilde{Y}\|H_0}(y),\ F_{\tilde{Y}\|H_0}(y)$	the PDF of $\tilde{Y}\|H_0$, the CDF of $\tilde{Y}\|H_0$
$f_{\tilde{Y}\|H_1}(y),\ F_{\tilde{Y}\|H_1}(y)$	the PDF of $\tilde{Y}\|H_1$, the CDF of $\tilde{Y}\|H_1$
$\Xi_{\eta_1\ldots\eta_{Q+1}}^{m_1\ldots m_{Q+1}}(i,k)$	a weight defined through (Karagiannidis *et al.*, 2006a, eqs. (7) and (8))
$\Xi_{\eta_1\eta_2}^{m_1 m_2}(i,k)$	a weight defined via (Karagiannidis *et al.*, 2006a, eq. (A-5))
$\kappa,\ \ \sigma_{R0}$	kurtosis, the standard deviation of the RFI-free kurtosis

Symbols Common to Chapter 3

$\mathscr{M}^-$	the set of all possible negative values
$\mathscr{M}^+$	the set of all possible positive values
$\mathscr{M}$	the set of all possible values, i.e., $\mathscr{M}=\mathscr{M}^-\cup\{0\}\cup\mathscr{M}^+$
$r\in\mathscr{M}\backslash\{0\}$	r takes all values in set $\mathscr{M}$ except 0
$r(t)$	a noise pre-filtered received baseband signal
$s(t)$	an SOI that is the baseband equivalent of a deterministic passband signal
$v(t)$	an RFI assumed unknown and deterministic
$T_s,\ \ p(t)$	the symbol duration, a rectangular pulse of duration T_s
$f_c,\ \ M$	carrier frequency, the modulation order
$h,\ \ g$	the SOI channel gain, the RFI channel gain

m_1, m_2	the SOI fading severity parameter, the RFI fading severity parameter
η_1, η_2	a scale parameter defined as $\frac{\bar{\gamma}_{snr}}{m_1}$, a scale parameter defined as $\frac{\bar{\gamma}_{inr}}{m_2}$
N_0	power spectral density
Y	the ED test statistic (decision variable)
E_s, E_v	the SOI energy, the RFI energy
$f_{Y\|H_0}(y)$, $f_{Y\|H_1}(y)$	the PDF of $Y\|H_0$, the PDF of $Y\|H_1$
$P_C(c_j)$, $P_{Y_4}(r)$	the PMF w.r.t. the RV C, the PMF w.r.t. the RV Y_4
$F_{Y\|H_0}(y)$, $F_{Y\|H_1}(y)$	the CDF of $Y\|H_0$, the CDF of $Y\|H_1$
T, W	the integration interval of ED, bandwidth
ρ, u	the noncentrality parameter, the time-bandwidth product
P_s, P_v	the SOI power, the RFI power
s_j, v_j	the j-th SOI symbol, the j-th RFI symbol
$\Xi_{\eta_1\eta_2}^{m_1m_2}(i,k)$	a weight defined in (Karagiannidis *et al.*, 2006a, eq. (A-5))
$f_P(\rho)$	the PDF of ρ
$\bar{P}_d$	the average probability of RFI detection
$\bar{P}_f$	the average probability of false alarm in RFI detection
$\bar{P}_m$	the average probability of miss in RFI detection
$f_Y(\gamma_{snr};m_1,\eta_1)$	the PDF of γ_{snr}
$f_Y(\gamma_{inr};m_2,\eta_2)$	the PDF of γ_{inr}
κ, $\boldsymbol{P}$	kurtosis, a projection matrix that projects orthogonal to the SOI subspace

N_t	the number of samples in the VLA data
φ	a constant used to adjust the power of the extracted RFI w.r.t. the desired INR
C	the number of mixture components required for an approximation using an MoG distribution
N	the number of independent and identically distributed Nakagami-m random samples
$\mathrm{sinc}(\cdot)$	the *sinc* function

Symbols Common to Chapter 4

N	the number of intercepted per-antenna samples
$\boldsymbol{I}_{N_R}$	an $N_R \times N_R$ identity matrix
$\mathbf{0}_{N\times M}$	an $N \times M$ zero matrix
$\mathbf{0}_{1\times(N_R-2)}$	a $1 \times (N_R - 2)$ zero vector
$\mathrm{Var}\{\cdot\}$	variance
$\mathrm{Cov}\{\cdot,\cdot\}$	covariance
$\mathscr{N}_1(\cdot,\cdot)$	the normal distribution
$\mathscr{N}_{N_R}(\cdot,\cdot)$	the multivariate normal distribution of dimension N_R ($N_R \geq 2$)
$\mathscr{CN}_1(\cdot,\cdot)$	the circularly symmetric complex normal distribution
$\mathscr{CN}_{N_R}(\boldsymbol{\mu},\boldsymbol{\Sigma})$	the circularly symmetric complex multivariate normal distribution with mean $\boldsymbol{\mu} \in \mathbb{C}^{N_R}$ and covariance matrix $\boldsymbol{\Sigma} \in \mathbb{H}^{N_R\times N_R}$ ($N_R \geq 2$)
$\mathscr{CN}_{N_R}(\mathbf{0},\boldsymbol{I}_{N_R})$	the circularly symmetric complex multivariate normal distribution with mean of a zero vector and covariance matrix of $\boldsymbol{I}_{N_R}$ ($N_R \geq 2$)

$\boldsymbol{h}$	the flat fading SOI channel gain vector
$\boldsymbol{g}$	the flat fading RFI channel gain vector
$\boldsymbol{H}$, $\boldsymbol{G}$	the SOI channel matrix, the RFI channel matrix
$s[k]$	the k-th unknown and deterministic symbol of the SOI
s_k^I, s_k^Q	the in-phase and quadrature components of a QPSK modulated SOI signal
$v[k]$	the k-th unknown and deterministic symbol of the RFI
v_k^I, v_k^Q	the in-phase and quadrature components of a QPSK modulated RFI signal
P_s, P_v	the transmitted SOI power, the transmitted RFI power
T	a test statistic
T_{eq}	an equivalent test statistic
$\boldsymbol{y}[k]$	the k-th sampled multi-antenna received baseband signal vector
$\boldsymbol{y}$	the received and stacked multi-antenna signal samples
$\boldsymbol{Y}$	a matrix made of the horizontal concatenation of N $\boldsymbol{y}[k]$s
$\boldsymbol{z}[k]$	a zero mean circularly symmetric complex AWGN vector
$\boldsymbol{z}$	a vector of vertically concatenated multi-antenna AWGN samples
$\hat{\boldsymbol{R}}_{yy}$	the sample covariance matrix
$\hat{\boldsymbol{U}}$, $\hat{\boldsymbol{V}}$	the left and right unitary matrices that comprise the SVD of $\hat{\boldsymbol{R}}_{yy}$
$\hat{\boldsymbol{\Sigma}}$	a diagonal matrix of the singular values that comprises the SVD of $\hat{\boldsymbol{R}}_{yy}$
$\{\hat{\sigma}_i\}_{i=1}^{N_R}$	the singular values—making the diagonal elements of $\hat{\boldsymbol{\Sigma}}$—sorted out in descending order

$\hat{\boldsymbol{P}}_2$	a projection matrix that projects toward the subspace spanned by the singular vector corresponding to the second largest singular value in $\hat{\boldsymbol{\Sigma}}$
$\hat{\boldsymbol{P}}_{2:N_R}$	a projection matrix that projects toward the joint subspace spanned by the singular vectors corresponding to the non-largest singular values in $\hat{\boldsymbol{\Sigma}}$
$\hat{\boldsymbol{P}}_{3:N_R}$	a projection matrix that projects toward the joint subspace spanned by the singular vectors corresponding to all singular values in $\hat{\boldsymbol{\Sigma}}$ except the first two largest singular values
$\hat{\boldsymbol{R}}_{yy}^{(p)}$	the projected sample covariance matrix
$\tilde{\boldsymbol{U}}$, $\tilde{\boldsymbol{V}}$	the left and right unitary matrices comprising the SVD of $\hat{\boldsymbol{R}}_{yy}^{(p)}$
$\tilde{\boldsymbol{\Sigma}}$	a diagonal matrix of the singular values that comprises the SVD of $\hat{\boldsymbol{R}}_{yy}^{(p)}$
$\boldsymbol{P}$	a projection matrix that projects orthogonal to the perfect SOI subspace, i.e., $\boldsymbol{P} = \boldsymbol{I}_{N_R} - \boldsymbol{h}(\boldsymbol{h}^H\boldsymbol{h})^{-1}\boldsymbol{h}^H$.
$\boldsymbol{P}'$	a projection matrix that projects orthogonal to the perfect RFI subspace, i.e., $\boldsymbol{P}' = \boldsymbol{I}_{N_R} - \boldsymbol{g}(\boldsymbol{g}^H\boldsymbol{g})^{-1}\boldsymbol{g}^H$
ν_1	the degrees of freedom of the numerator, i.e., $\mathrm{tr}(\hat{\boldsymbol{P}}_2\hat{\boldsymbol{R}}_{yy}^{(p)})$
ν_2	the degrees of freedom of the denominator, i.e., $\mathrm{tr}\big((\boldsymbol{I}_{N_R} - \hat{\boldsymbol{P}}_2)\hat{\boldsymbol{R}}_{yy}^{(p)}\big)$
η_{nu}	a factor regarding noise power uncertainty
ξ_{nu}	a constant noise power uncertainty factor in dB
$\hat{\sigma}^2$	the estimated noise power.
`fpdf`$(\cdot,\cdot,\cdot)$	the MATLAB® function scripted to compute the PDF of the central F–distribution analytically

Symbols Common to Chapter 5

$L+1$	the number of channel taps for the considered multi-path SOI channel
L_1+1	the number of channel taps for the considered multi-path RFI channel
W	the number of samples per STI
N	the number of intercepted STIs
T^{MB}	the MB-RD test statistic
T^{TB}	the TB-RD test statistic
$\min(\cdot,\cdot)$	minimum
$\max(\cdot,\cdot)$	maximum
$\mathbf{0}_{M\times N}$	an $M\times N$ zero matrix
$\boldsymbol{I}_W\left(\boldsymbol{I}_{N_RW}\right)$	a $W\times W$ $\left(N_RW\times N_RW\right)$ identity matrix
$\mathscr{CN}_{N_RW}(\boldsymbol{\mu},\boldsymbol{\Sigma})$	the circularly symmetric complex multivariate normal distribution with mean $\boldsymbol{\mu}\in\mathbb{C}^{N_RW\times 1}$ and covariance matrix $\boldsymbol{\Sigma}\in\mathbb{H}^{N_RW\times N_RW}$—$W\geq 1$ ($N_RW\geq 2$)
$\mathscr{CN}_{N_R}(\mathbf{0},\boldsymbol{I}_{N_R})$	the circularly symmetric complex multivariate normal distribution with mean of a zero vector and covariance matrix of $\boldsymbol{I}_{N_R}$ ($N_R\geq 2$)
$\mathscr{CN}_{N_RW}(\mathbf{0},\boldsymbol{I}_{N_RW})$	the circularly symmetric complex multivariate normal distribution with mean of a zero vector and covariance matrix of $\boldsymbol{I}_{N_RW}$ ($N_RW\geq 2$)
$s[k]$	the k-th symbol of the SOI
$s_k^I,\ \ s_k^Q$	the in-phase and quadrature components of a QPSK modulated SOI signal
$\boldsymbol{s}_m$	a vector of the SOI samples structured w.r.t. the m-th STI
$\boldsymbol{S}$	the horizontal concatenation of N $\boldsymbol{s}_m$s

L

$v[k]$	the k-th symbol of the RFI
$v_k^I,\ \ v_k^Q$	the in-phase and quadrature components of a QPSK modulated RFI signal
$P_s,\ \ P_v$	the transmitted SOI power, the transmitted RFI power
$\boldsymbol{v}_m$	a vector of the RFI samples structured w.r.t. the m-th STI
$\boldsymbol{V}$	the horizontal concatenation of N $\boldsymbol{v}_m$s
$\boldsymbol{h}_l$	the SOI channel gain vector for the l-th multi-path component
$\boldsymbol{H}$	the SOI filtering matrix
$\boldsymbol{g}_l$	the RFI channel gain vector for the l-th multi-path component
$\boldsymbol{G}$	the RFI filtering matrix
$\boldsymbol{y}[k]$	the k-th sampled multi-antenna received baseband signal vector
$\boldsymbol{y}_m$	the structured received signal vector of size $N_R W \times 1$ w.r.t. the m-th STI
$\boldsymbol{Y}$	the horizontal concatenation of N $\boldsymbol{y}_m$s
$\tilde{\boldsymbol{Y}}$	the noiseless version of $\boldsymbol{Y}$
$\hat{\boldsymbol{R}}_{yy}$	the sample covariance matrix computed using $\boldsymbol{y}_m$
$\boldsymbol{z}[k]$	the k-th zero mean circularly symmetric complex AWGN vector
$\boldsymbol{z}_m$	the sampled AWGN vector structured w.r.t. the m-th STI
$\boldsymbol{Z}$	the AWGN matrix of samples made of the horizontal concatenation of N $\boldsymbol{z}_m$s
$\tilde{\boldsymbol{U}},\ \tilde{\boldsymbol{V}}$	the left and right unitary matrices that comprise the SVD of $\boldsymbol{Y}$
$\tilde{\boldsymbol{\Sigma}}$	a diagonal matrix of the singular values that comprises the SVD of $\boldsymbol{Y}$
$\left\{\tilde{\sigma}_i\right\}_{i=1}^{N_R W}$	the singular values—comprising the diagonal elements of $\tilde{\boldsymbol{\Sigma}}$—sorted out in descending order

$\hat{\boldsymbol{U}},\ \hat{\boldsymbol{V}}$	the left and right unitary matrices that comprise the SVD of $\hat{\boldsymbol{R}}_{yy}$
$\boldsymbol{U},\ \boldsymbol{V}$	the true version of $\hat{\boldsymbol{U}}$, the true version of $\hat{\boldsymbol{V}}$
$\hat{\boldsymbol{U}}_{1:r}$	the estimated subspace spanned by the eigenvectors corresponding to the largest $r = W + L$ eigenvalues, i.e., $\hat{\boldsymbol{U}}_{1:r} = \hat{\boldsymbol{U}}(:, 1:r)$
$\boldsymbol{U}_{1:r}$	the true version of $\hat{\boldsymbol{U}}_{1:r}$
$\Delta\boldsymbol{U}_{1:r}$	the perturbations in $\hat{\boldsymbol{U}}_{1:r}$
$\hat{\boldsymbol{U}}_{r+1:N_RW}$	the estimated subspace spanned by the eigenvectors corresponding to the non-largest $N_RW - r$ eigenvalues, i.e., $\hat{\boldsymbol{U}}_{r+1:N_RW} = \hat{\boldsymbol{U}}(:, r+1:N_RW)$
$\boldsymbol{U}_{r+1:N_RW}$	the true version of $\hat{\boldsymbol{U}}_{r+1:N_RW}$
$\Delta\boldsymbol{U}_{r+1:N_RW}$	the perturbations in $\hat{\boldsymbol{U}}_{r+1:N_RW}$
$\hat{\boldsymbol{\Sigma}}$	a diagonal matrix of the singular values that comprises the SVD of $\hat{\boldsymbol{R}}_{yy}$
$\boldsymbol{\Sigma}$	the true version of $\hat{\boldsymbol{\Sigma}}$
$\left\{\hat{\sigma}_i\right\}_{i=1}^{N_RW}$	the singular values—comprising the diagonal elements of $\hat{\boldsymbol{\Sigma}}$—sorted out in descending order
$\hat{\boldsymbol{P}}_{nd}$	a projection matrix that projects toward the subspace spanned by $\hat{\boldsymbol{U}}_{r+1:N_RW}$
$\hat{\boldsymbol{R}}_{yy}^{(p)}$	the projected SCM computed using $\hat{\boldsymbol{P}}_{nd}$ and $\hat{\boldsymbol{R}}_{yy}$
$\tilde{\hat{\boldsymbol{U}}},\ \tilde{\hat{\boldsymbol{V}}}$	the left and right unitary matrices that comprise the SVD of $\hat{\boldsymbol{R}}_{yy}^{(p)}$
$\tilde{\hat{\boldsymbol{\Sigma}}}$	a diagonal matrix of the singular values that comprises the SVD of $\hat{\boldsymbol{R}}_{yy}^{(p)}$
$\tilde{\hat{\boldsymbol{U}}}_{1:r_1}$	the estimated subspace spanned by the eigenvectors corresponding to the largest $r_1 = W + L_1$ eigenvalues, i.e., $\tilde{\hat{\boldsymbol{U}}}_{1:r_1} = \tilde{\hat{\boldsymbol{U}}}(:, 1:r_1)$
$\tilde{\hat{\boldsymbol{U}}}_{r_1+1:N_RW}$	the estimated subspace spanned by the eigenvectors corresponding to the non-largest $N_RW - r_1$ eigenvalues, i.e., $\tilde{\hat{\boldsymbol{U}}}_{r_1+1:N_RW} = \tilde{\hat{\boldsymbol{U}}}(:, r_1+1:N_RW)$

$\hat{\boldsymbol{P}}_d$	a projection matrix that projects toward the subspace spanned by $\tilde{\tilde{\boldsymbol{U}}}_{1:r_1}$
ν_1	the degrees of freedom of the numerator, i.e., $\mathrm{tr}\big(\hat{\boldsymbol{P}}_d \hat{\boldsymbol{R}}_{yy}^{(p)}\big)$
ν_2	the degrees of freedom of the denominator, i.e., $\mathrm{tr}\big((\boldsymbol{I}_{N_R W} - \hat{\boldsymbol{P}}_d)\hat{\boldsymbol{R}}_{yy}^{(p)}\big)$
$\mathscr{Y} \times_{R+1} \mathscr{Y}^H$	the $(R+1)$-mode multiplication of tensor $\mathscr{Y}$ and its Hermitian
$\hat{\mathscr{P}}^{[nd]}$	a tensor defined through its 3-mode unfolding as $\left[\hat{\mathscr{P}}^{[nd]}\right]_{(3)}^{T} = \hat{\boldsymbol{P}}_{nd}$
$\mathscr{Y}_p$	a tensor defined through a 3-mode product as $\mathscr{Y}_p = \hat{\mathscr{P}}^{[nd]} \times_3 \mathscr{Y}$
$[\mathscr{Y}_p]_{(r)}$	the r-mode unfolding of $\mathscr{Y}_p$
$\hat{\mathscr{R}}_{yy}^{(p)}$	the sample covariance tensor
$\tilde{\tilde{\mathscr{S}}}^{[1:r_1]}$	the truncated core tensor
$\tilde{\tilde{\boldsymbol{U}}}_1^{[1:r_1]}$	the left unitary matrix of the singular vectors of $[\mathscr{Y}_p]_{(1)}$
$\tilde{\tilde{\boldsymbol{U}}}_2^{[1:r_1]}$	the left unitary matrix of the singular vectors of $[\mathscr{Y}_p]_{(2)}$
$\tilde{\tilde{\boldsymbol{U}}}_3^{[1:r_1]}$	the left unitary matrix of the singular vectors of $[\mathscr{Y}_p]_{(3)}$
$\tilde{\tilde{\boldsymbol{T}}}_1$	a projection matrix computed as $\tilde{\tilde{\boldsymbol{T}}}_1 = \tilde{\tilde{\boldsymbol{U}}}_1^{[1:r_1]} \tilde{\tilde{\boldsymbol{U}}}_1^{[1:r_1]^H}$
$\tilde{\tilde{\boldsymbol{T}}}_2$	a projection matrix computed as $\tilde{\tilde{\boldsymbol{T}}}_2 = \tilde{\tilde{\boldsymbol{U}}}_2^{[1:r_1]} \tilde{\tilde{\boldsymbol{U}}}_2^{[1:r_1]^H}$
$\hat{\tilde{\tilde{\mathscr{P}}}}_{1,2}$	a tensor defined through its 3-mode unfolding as $\left[\tilde{\tilde{\mathscr{P}}}_{1,2}\right]_{(3)}^{T} = \tilde{\tilde{\boldsymbol{T}}}_1 \otimes \tilde{\tilde{\boldsymbol{T}}}_2$
$\tilde{\tilde{\mathscr{U}}}^{[1:r_1]}$	a subspace estimating tensor
$\left[\tilde{\tilde{\mathscr{U}}}^{[1:r_1]}\right]_{(3)}$	the 3-mode unfolding of $\tilde{\tilde{\mathscr{U}}}^{[1:r_1]}$
P_d	the probability of RFI detection exhibited by TB-RD
P_d^{mat}	the probability of RFI detection manifested by MB-RD

Symbols Common to Chapter 6

α, β	high INR evoking factor, a roll-off factor
ξ, η	phase ambiguity compensation factor, smoothing factor
t_0	propagation delay
$\mathbf{0}_{M\times N}$	an $M \times N$ zero matrix
$\mathbf{0}$	a zero matrix whose dimension is deduced from the context
$\boldsymbol{I}_{N_R}$	an $N_R \times N_R$ identity matrix
$\boldsymbol{I}_W$, $\boldsymbol{I}_{N_R W}$	a $W \times W$ identity matrix, an $N_R W \times N_R W$ identity matrix
$\min(\cdot,\cdot)$	minimum
$\max(\cdot,\cdot)$	maximum
$\mathscr{CN}(\cdot,\cdot)$	complex (multivariate) normal distribution
`diag`$(\cdot)$	the MATLAB® function that returns the diagonal elements of a square matrix
`min`$(\cdot)$	the MATLAB® function that returns the minimum element of a vector or the minimum element of every column of a matrix
`length`$(\cdot)$	the MATLAB® function that returns the length of a vector or the size of a matrix
`zeros`(m,n)	the MATLAB® function that returns an $m \times n$ zero matrix
$\mathscr{O}_t$	a zero tensor
$\hat{\boldsymbol{\Sigma}}$	a diagonal matrix of the singular values comprising the SVD of $\boldsymbol{Y}_I$
$\hat{\boldsymbol{\Sigma}}_I$	a diagonal matrix made of the $r = \sum_{i=1}^{Q}(W + L_i)$ largest singular values in $\hat{\boldsymbol{\Sigma}}$

$\hat{\boldsymbol{\Sigma}}_n$	a diagonal matrix made of the $N_R W - r$ smallest singular values in $\hat{\boldsymbol{\Sigma}}$
$f_i(n)$	the symbol emitted by the i-th RFI transmitter at time n
$\boldsymbol{f}_{im}$	a vector of the i-th RFI samples structured w.r.t. the m-th STI
$\boldsymbol{f}_m$	a vector made of the vertical concatenation of Q $\boldsymbol{f}_{im}$s, $1 \leq i \leq Q$
$\boldsymbol{F}$	the sampled MI-RFI matrix
$\boldsymbol{F}^s$	the smoothed version of $\boldsymbol{F}$
$\boldsymbol{g}_i^{(l)}$	the array response of the N_R antennas corresponding to the i-th RFI's l-th channel tap
$\boldsymbol{G}$	the MI-RFI filtering matrix
$\boldsymbol{G}_{ij}$	a banded Toeplitz matrix associated with the i-th RFI and the j-th receive antenna's impulse response $\boldsymbol{g}_{ij} \stackrel{\triangle}{=} \left[g_{ij}^0, \ldots, g_{ij}^{L_i}\right]^T = \left[g_{ij}(t_0), \ldots, g_{ij}(t_0 + L_i T_s)\right]^T$
$\boldsymbol{h}_l$	the array response of the N_R antennas corresponding to the l-th SOI channel tap
$\boldsymbol{H}$	the SOI filtering matrix
$\mathscr{I}_3$	the 3-mode identity tensor
$L+1$	the number of channel taps of the SOI channel
L_i+1	the number of channel taps of the i-th RFI channel
$\left\{\hat{L}(\hat{Q}-i)\right\}_{i=0}^{\hat{Q}-1}$	the set of the estimated channel orders of the Q broadband interferers
n, N	time index, the number of STIs per LTI
N^s	the number of overlapping observation windows
N_{SOI}	the number of LTIs by which SOI transmission is conducted

N_R^a	the number of auxiliary antennas
$\boldsymbol{P}$	a projection matrix
$\gamma_{sinr}(\boldsymbol{P})$	SINR in dB computed after projecting with $\boldsymbol{P}$
$\mathscr{P}$	the estimated three-way projection tensor
$\left[\mathscr{P}\right]_{(3)}$	the 3-mode unfolding of $\mathscr{P}$
$\mathscr{P}^s$	the estimated three-way smoothed projection tensor
$\left[\mathscr{P}^s\right]_{(3)}$	the 3-mode unfolding of $\mathscr{P}^s$
$Q,\ \hat{Q}$	the number of interferers, the estimated number of interferers
$\boldsymbol{R}_{y^s y^s}$	the population covariance matrix w.r.t. $\boldsymbol{y}_m^s$s
$\boldsymbol{R}_{f^s f^s}$	the smoothed MI-RFI population covariance matrix
$\hat{\boldsymbol{R}}_{y^s y^s}$	the smoothed sample covariance matrix
$s(n)$	the symbol emitted by the SOI transmitter at time n
$\boldsymbol{s}_m$	a vector of the SOI samples structured w.r.t. the m-th STI
$\boldsymbol{S}$	the sampled SOI matrix (the horizontal concatenation of N $\boldsymbol{s}_m$s)
$\boldsymbol{S}^s$	the smoothed SOI matrix
t_0	the propagation delay (time-of-arrival)
T_s	the symbol duration of the SOI signal
$\hat{\mathscr{S}}^{[I]}$	a three-way core tensor which satisfies the all-orthogonality conditions
$\hat{\mathscr{S}}^{s[I]}$	the smoothed version of $\hat{\mathscr{S}}^{[I]}$
$\boldsymbol{U}_I$	the left unitary matrix corresponding to the SVD of the noiseless version of $\boldsymbol{Y}_I$

$\hat{\boldsymbol{U}}_I$	the estimated MI-RFI subspace
$\Delta\boldsymbol{U}_I$	the perturbations in $\hat{\boldsymbol{U}}_I$
$\hat{\boldsymbol{U}}_I^s$	the smoothed version of $\hat{\boldsymbol{U}}_I$
$\hat{\boldsymbol{U}}_1^{[I]}$	the left unitary matrix of the singular vectors of $[\mathscr{Y}_I]_{(1)}$
$\Delta\boldsymbol{U}_1^{[I]}$	the perturbations in $\hat{\boldsymbol{U}}_1^{[I]}$
$\hat{\boldsymbol{U}}_1^{s\,[I]}$	the smoothed version of $\hat{\boldsymbol{U}}_1^{[I]}$
$\hat{\boldsymbol{U}}_2^{[I]}$	the left unitary matrix of the singular vectors of $[\mathscr{Y}_I]_{(2)}$
$\hat{\boldsymbol{U}}_2^{s\,[I]}$	the smoothed version of $\hat{\boldsymbol{U}}_2^{[I]}$
$\hat{\boldsymbol{U}}_3^{[I]}$	the left unitary matrix of the singular vectors of $[\mathscr{Y}_I]_{(3)}$
$\hat{\boldsymbol{U}}_3^{s\,[I]}$	the smoothed version of $\hat{\boldsymbol{U}}_3^{[I]}$
$\hat{\mathscr{U}}^{[I]}$	the MI-RFI subspace estimating three-way tensor
$\hat{\mathscr{U}}^{s\,[I]}$	the smoothed version of $\hat{\mathscr{U}}^{[I]}$
$\left[\hat{\mathscr{U}}^{[I]}\right]_{(3)}$	the 3-mode unfolding of $\hat{\mathscr{U}}^{[I]}$
$\left[\hat{\mathscr{U}}^{s\,[I]}\right]_{(3)}$	the 3-mode unfolding of $\hat{\mathscr{U}}^{s\,[I]}$
$\hat{\boldsymbol{U}}_n$	the estimated noise subspace
$\boldsymbol{V}_I$	the right unitary matrix corresponding to the SVD of the noiseless version of $\bar{\boldsymbol{Y}}_I$
W	the number of samples per STI
$\boldsymbol{y}_m$	a structured received signal vector of size $N_R W \times 1$ w.r.t. the m-th STI
$\boldsymbol{Y}$	the horizontal concatenation of N $\boldsymbol{y}_m$s

$\boldsymbol{Y}_I$	the received signal matrix without the SOI
$\boldsymbol{Y}_I^s$	the smoothed version of $\boldsymbol{Y}_I$
$\mathscr{Y}_I$	a received three-way tensor in the absence of the SOI
$\mathscr{Y}_I^s$	a received smoothed three-way tensor in the absence of the SOI
$\left[\mathscr{Y}_I\right]_{(3)}$	the 3-mode unfolding of $\mathscr{Y}_I$
$\left[\mathscr{Y}_I^s\right]_{(3)}$	the 3-mode unfolding of $\mathscr{Y}_I^s$
$\boldsymbol{z}(n)$	the sampled AWGN with a distribution $\mathscr{CN}\left(\boldsymbol{0}, \sigma^2 \boldsymbol{I}_{N_R}\right)$
$\boldsymbol{z}_m$	the sampled AWGN vector structured w.r.t. the m-th STI
$\boldsymbol{Z}$	an AWGN matrix of samples made of the horizontal concatenation of N $\boldsymbol{z}_m$s
$\boldsymbol{Z}^s$	the smoothed version of $\boldsymbol{Z}$

Symbols Common to Chapter 7

$L+1$	the number of channel taps of the primary-to-secondary multi-path channel
M	oversampling factor
N	the number of intercepted per-antenna samples
$\tilde{N}$	the number of intercepted STIs w.r.t. the g-FT-v-SVD algorithm
$\tilde{\tilde{N}}$	the number of intercepted STIs w.r.t. the MIMO CR g-FT-v-SVD algorithm
T	the FT-v-SVD test statistic
$\tilde{T}$	the g-FT-v-SVD test statistic
$\tilde{\tilde{T}}$	the MIMO CR g-FT-v-SVD test statistic

$\tilde{\lambda}$	a decision threshold w.r.t. the g-FT-v-SVD algorithm
$\tilde{\tilde{\lambda}}$	a decision threshold w.r.t. the MIMO CR g-FT-v-SVD algorithm
W	the number of samples per STI
$\max\{\cdot,\cdot\}$	maximum
$\boldsymbol{I}_{N_R}\left(\boldsymbol{I}_{N_RW}\right)$	an $N_R \times N_R$ $\left(N_RW \times N_RW\right)$ identity matrix
$\mathbf{0}_{M\times N}$	an $M \times N$ zero matrix
$\mathbf{0}$	a zero matrix whose dimension is deduced from the context
$\mathscr{CN}_M(\boldsymbol{\mu},\boldsymbol{\Sigma})$	the circularly symmetric complex multivariate normal distribution with mean $\boldsymbol{\mu} \in \mathbb{C}^M$ and covariance matrix $\boldsymbol{\Sigma} \in \mathbb{H}^{M\times M}$ $(M \geq 2)$
$\mathscr{CN}_{N_R}(\mathbf{0},\boldsymbol{I}_{N_R})$	the circularly symmetric complex multivariate normal distribution with mean of a zero vector and covariance matrix of $\boldsymbol{I}_{N_R}$ $(N_R \geq 2)$
$\boldsymbol{y}[k]$	the k-th sample received multi-antenna signal vector
$\boldsymbol{y}_m$	the structured received multi-antenna signal vector of size $N_RW \times 1$ w.r.t. the m-th STI
$\tilde{\boldsymbol{y}}_m$	the structured MIMO received multi-antenna vector of size $N_RW \times 1$ w.r.t. the m-th STI
$\boldsymbol{Y}$	a matrix made of the horizontal concatenation of N $\boldsymbol{y}[k]$s
$\tilde{\boldsymbol{Y}}$	a matrix made of the horizontal concatenation of $\tilde{N}$ $\boldsymbol{y}_m$s
$\tilde{\tilde{\boldsymbol{Y}}}$	a matrix made of the horizontal concatenation of $\tilde{\tilde{N}}$ $\tilde{\boldsymbol{y}}_m$s
$\boldsymbol{h}_l$	the primary-to-secondary l-th multi-path fading component's CSI vector
$\boldsymbol{h}_0$ $(\boldsymbol{h})$	the primary-to-secondary flat fading CSI vector

$\boldsymbol{H}_l$	the MIMO channel impulse responses corresponding to the primary-to-secondary l-th multi-path fading component
$\boldsymbol{H}$	the secondary filtering matrix
$\boldsymbol{H}_T$	the MIMO filtering matrix made of banded Toeplitz matrices
$s[k]$	the k-th unknown and deterministic primary symbol
$s_k^I,\ \ s_k^Q$	the in-phase and quadrature components of a QPSK modulated primary signal (for the considered SIMO CR networks)
P_s	the transmitted primary power
$s_j[k]$	the k-th unknown and deterministic primary symbol transmitted through the j-th antenna
$s_{kj}^I,\ \ s_{kj}^Q$	the in-phase and quadrature components of a QPSK modulated primary signal transmitted through the j-th antenna (for the considered MIMO CR networks)
$\boldsymbol{s}[k]$	the k-th symbol vector transmitted through the N_T transmit antennas
$\boldsymbol{s}_m$	a vector of the primary samples structured w.r.t. the m-th STI
$\tilde{\boldsymbol{s}}_m$	a vector of the MIMO primary samples structured w.r.t. the m-th STI
$\boldsymbol{E}$	an error matrix accommodating the respective calibration uncertainties on the N_R antenna frontends
$\tilde{\boldsymbol{E}}$	an error matrix adjusted as per the adopted vertical stacking pre-processing of the g-FT-v-SVD algorithm
$\boldsymbol{z}[k]$	the k-th zero mean circularly symmetric AWGN vector
$\boldsymbol{z}_m$	a vector of the AWGN samples structured w.r.t. the m-th STI
$\hat{\boldsymbol{R}}_{yy}$	the sample covariance matrix computed using $\boldsymbol{y}[k]$

$\tilde{\hat{\boldsymbol{R}}}_{yy}$	the sample covariance matrix computed using $\boldsymbol{y}_m$
$\tilde{\boldsymbol{R}}_{yy}$	the population covariance matrix, under H_1, w.r.t. the MIMO CR g-FT-v-SVD algorithm
$\boldsymbol{R}_{\tilde{s}\tilde{s}}$	the primary data correlation matrix w.r.t. the MIMO CR g-FT-v-SVD algorithm
$\tilde{\hat{\boldsymbol{R}}}_{yy}$	the sample covariance matrix computed using $\tilde{\boldsymbol{y}}_m$
$\boldsymbol{R}_{yy}^{(n)}$	the noiseless sample covariance matrix
$\hat{\boldsymbol{U}}$, $\hat{\boldsymbol{V}}$	the left and right unitary matrices that comprise the SVD of $\hat{\boldsymbol{R}}_{yy}$
$\boldsymbol{U}$, $\boldsymbol{V}$	the true version of $\hat{\boldsymbol{U}}$, the true version of $\hat{\boldsymbol{V}}$
$\tilde{\hat{\boldsymbol{U}}}$, $\tilde{\hat{\boldsymbol{V}}}$	the left and right unitary matrices that comprise the SVD of $\tilde{\hat{\boldsymbol{R}}}_{yy}$
$\tilde{\tilde{\boldsymbol{U}}}$, $\tilde{\tilde{\boldsymbol{V}}}$	the left and right unitary matrices that comprise the SVD of $\tilde{\tilde{\boldsymbol{R}}}_{yy}$
$\hat{\boldsymbol{\Sigma}}$	a diagonal matrix of the singular values that comprises the SVD of $\hat{\boldsymbol{R}}_{yy}$
$\tilde{\hat{\boldsymbol{\Sigma}}}$	a diagonal matrix of the singular values that comprises the SVD of $\tilde{\hat{\boldsymbol{R}}}_{yy}$
$\tilde{\tilde{\boldsymbol{\Sigma}}}$	a diagonal matrix of the singular values that comprises the SVD of $\tilde{\tilde{\boldsymbol{R}}}_{yy}$
$\boldsymbol{\Sigma}$	the true version of $\hat{\boldsymbol{\Sigma}}$
$\left\{\hat{\sigma}_i\right\}_{i=1}^{N_R}$	the singular values—comprising the diagonal elements of $\hat{\boldsymbol{\Sigma}}$—sorted out in descending order
$\hat{\boldsymbol{U}}_s$	the estimated subspace spanned by the singular vector corresponding to the largest singular value, i.e., $\hat{\boldsymbol{U}}_s = \hat{\boldsymbol{U}}(:,1)$
$\Delta\boldsymbol{U}_s$	the perturbations in $\hat{\boldsymbol{U}}_s$
$\tilde{\hat{\boldsymbol{U}}}_s$	the estimated subspace spanned by the eigenvectors corresponding to the largest $r = W + L$ eigenvalues, i.e., $\tilde{\hat{\boldsymbol{U}}}_s = \tilde{\hat{\boldsymbol{U}}}(:,1:r)$

$\Delta\tilde{\boldsymbol{U}}_s$ the perturbations in $\tilde{\hat{\boldsymbol{U}}}_s$

$\tilde{\tilde{\boldsymbol{U}}}_s$ the estimated subspace spanned by the eigenvectors corresponding to the largest $\tilde{\tilde{r}} = N_T(W+L)$ eigenvalues, i.e., $\tilde{\tilde{\boldsymbol{U}}}_s = \tilde{\tilde{\boldsymbol{U}}}(:, 1:\tilde{\tilde{r}})$

$\hat{\boldsymbol{U}}_n$ the estimated subspace spanned by the singular vectors corresponding to the $N_R - 1$ non-largest singular values, i.e., $\hat{\boldsymbol{U}}_n = \hat{\boldsymbol{U}}(:, 2:N_R)$

$\Delta\boldsymbol{U}_n$ the perturbations in $\hat{\boldsymbol{U}}_n$

$\tilde{\hat{\boldsymbol{U}}}_n$ the estimated subspace spanned by the eigenvectors corresponding to the non-largest $N_R W - r$ eigenvalues, i.e., $\tilde{\hat{\boldsymbol{U}}}_n = \tilde{\hat{\boldsymbol{U}}}(:, r+1:N_R W)$

$\tilde{\tilde{\boldsymbol{U}}}_n$ the estimated subspace spanned by the eigenvectors corresponding to the non-largest $N_R W - \tilde{\tilde{r}}$ eigenvalues, i.e., $\tilde{\tilde{\boldsymbol{U}}}_n = \tilde{\tilde{\boldsymbol{U}}}(:, \tilde{\tilde{r}}+1:N_R W)$

$\hat{\boldsymbol{P}}_s$ a projection matrix that projects toward the subspace spanned by $\hat{\boldsymbol{U}}_s$

$\tilde{\hat{\boldsymbol{P}}}_s$ a projection matrix that projects toward the subspace spanned by $\tilde{\hat{\boldsymbol{U}}}_s$

$\tilde{\tilde{\boldsymbol{P}}}_s$ a projection matrix that projects toward the subspace spanned by $\tilde{\tilde{\boldsymbol{U}}}_s$

P_d^{iid} the probability of detection under i.i.d. noise samples

P_d^{inid} the probability of detection under i.ni.d. noise samples

ν_1 the degrees of freedom of the numerator, i.e., $\text{tr}(\hat{\boldsymbol{P}}_s \hat{\boldsymbol{R}}_{yy})$

ν_2 the degrees of freedom of the denominator, i.e., $\text{tr}\big((\boldsymbol{I}_{N_R} - \hat{\boldsymbol{P}}_s)\hat{\boldsymbol{R}}_{yy}\big)$

$\tilde{\nu}_1$ the degrees of freedom of the numerator, i.e., $\text{tr}(\tilde{\hat{\boldsymbol{P}}}_s \tilde{\hat{\boldsymbol{R}}}_{yy})$

$\tilde{\nu}_2$ the degrees of freedom of the denominator, i.e., $\text{tr}\big((\boldsymbol{I}_{N_R W} - \tilde{\hat{\boldsymbol{P}}}_s)\tilde{\hat{\boldsymbol{R}}}_{yy}\big)$

$\tilde{\tilde{\nu}}_1$ the degrees of freedom of the numerator, i.e., $\text{tr}(\tilde{\tilde{\boldsymbol{P}}}_s \tilde{\tilde{\boldsymbol{R}}}_{yy})$

$\tilde{\tilde{\nu}}_2$ the degrees of freedom of the denominator, i.e., $\text{tr}\big((\boldsymbol{I}_{N_R W} - \tilde{\tilde{\boldsymbol{P}}}_s)\tilde{\tilde{\boldsymbol{R}}}_{yy}\big)$

η_{nu} a factor of uncertainty regarding a noise power overestimation

ξ	a constant noise uncertainty factor related with η_{nu} as $\xi = 10\log_{10}\eta_{nu}$
$\hat{\sigma}^2$	the estimated noise power

Units of Measurements

W	Watt
Hz	Hertz
MHz	Megahertz
W/Hz	Watt per Hertz

Part I

Preliminaries

INTRODUCTION

"A thousand mile journey begins with one step."—Lao Tsu

Man-made interference, intentional or unintentional, manifested in terms of radio frequency interference (RFI) is causing system performance loss in various radio frequency (RF) operating systems. The main causes of RFI identified in (AVIO-601, 2018) include human error, improper installation, lack of training, poor or sub-standard equipment, equipment failure, lack of adherence to regulatory requirements and industry, poor system design, adjacent (nearby systems), terrestrial interferers, orbital interferers, RF jammers, malicious interference, and spoofing attacks. Because of these causes, RFI is becoming increasingly common in various RF operating systems as diverse as microwave radiometry (Guner *et al.*, 2007), radio astronomy (van der Tol & van der Veen, 2005), and satellite communications (SatCom) (Borio *et al.*, 2008; Newtec and IRG, Sep. 2013). RFI also occurs in ultra-wideband communications for wideband interferers (Shi *et al.*, 2007); radar because of wideband jammers (De Maio & Orlando, 2016; Orlando, 2017; Bandiera & Orlando, 2009); and cognitive radios as a result of an imperfect spectrum sensing (Getu *et al.*, 2015a)—neighboring primary users emitting such interference can constrain the energy detector's spectrum sensing capability, as analytically demonstrated in (Boulogeorgos *et al.*, 2016b).

If left unmitigated, such a widely occurring RFI can evoke severe system performance losses. Consequently, the state-of-the-art comprises several RFI detection and excision algorithms. Based on their signal processing schemes, these algorithms can be divided into six groups: spectral (Guner *et al.*, 2007), temporal (Johnson & Ellingson, 2005), spectral-temporal (Borio *et al.*, 2008), statistical (Ruf *et al.*, 2006; Arribas *et al.*, 2013a,b), spatial filtering-based (van der Tol & van der Veen, 2005; Jeffs *et al.*, 2005), and transformed domain-based (Dovis *et al.*, 2012) RFI detection and excision algorithms. Despite the several algorithms, the existing techniques exhibit huge computational complexity; provide unsatisfactory detection performance

and most of them are effective for huge sample settings; detect some type of RFIs only; render inefficient RFI excision; and/or have limited applicability.

On the other hand, spectrum sensing is crucial for cognitive radios (CRs), especially for the ones which employ a *spectrum overlay* access scheme. The state-of-the-art on spectrum sensing comprises numerous contributions and techniques. Based on the bandwidth of the primary signal to be detected, these techniques have been classified as *narrowband* and *wideband* sensing techniques (Ali & Hamouda, 2017; Sharma *et al.*, 2015; Yucek & Arslan, 2009). Upon the advent of *active sensing* techniques (Miridakis *et al.*, 2017; Heo *et al.*, 2014; Song *et al.*, 2010b), spectrum sensing techniques are classified as active sensing (Miridakis *et al.*, 2017; Heo *et al.*, 2014; Song *et al.*, 2010b) and *quiet sensing* (Ali & Hamouda, 2017; Sharma *et al.*, 2015; Wang & Liu, 2011; Axell *et al.*, 2012; Yucek & Arslan, 2009; Haykin *et al.*, 2009).

In spite of the numerous disseminated techniques, the state-of-the-art in spectrum sensing features several limitations. In particular, most of the existing techniques rely on assumptions regarding the primary signal; several conventional narrowband techniques are either computationally complex or rely on huge samples; most of the wideband techniques manifest high computational complexity and some require synchronization circuits; some of the active sensing techniques require more spectrum and extra power resources and the protocol they employ would keep on conducting a secondary transmission while emitting interference to a primary receiver whenever a *hidden terminal* problem occurs; the F–test based techniques (Huang & Chung, 2013a,b) rely on the knowledge of the channel state information between the primary transmitter and secondary receivers; and most of the existing techniques notably rely on the consideration of independent and identically distributed (i.i.d.) noise samples.

Motivated by the aforementioned limitations regarding the state-of-the-art RFI detection, RFI excision, and spectrum sensing, this Ph.D. dissertation has set out to realize these objectives: the investigation and development of robust RFI detection algorithms for satellite and terrestrial

communications; the investigation and development of efficient RFI excision algorithms for satellite and terrestrial communications; and the investigation and development of advanced low-complexity spectrum sensing techniques. Toward the realization of these objectives, in the meantime, this dissertation has contributed advanced RFI detection techniques, advanced RFI excision techniques, and advanced spectrum sensing techniques. It is to be noted that the proposed techniques can be widely applied in both terrestrial and satellite communications.

Along with this introduction, Part I presents the preliminaries of this dissertation. Part II presents contributions in advanced RFI detection. Part III continues with the presentation of contributions concerning advanced RFI excision. Part IV follows with contributions in advanced spectrum sensing. At last, Part V presents discussions on the reported results; the conclusion and recommendations of this dissertation; and the accompanying appendices of this dissertation.

CHAPTER 1

MOTIVATION AND RESEARCH PROBLEMS

"Scientific knowledge is a body of statements of varying degrees of certainty—some most unsure, some nearly sure, none absolutely certain."—Richard P. Feynman

As motivated in (AVIO-601, 2018), systems based on satellite communications (SatCom) are increasingly suffering from radio frequency interference (RFI) because of the near congestion of satellite communication bands (L/S/C/Ku) (Maral & Bousquet, 2009), scarcity of radio frequency (RF) spectrum, and an increase of interference events. This observation is also corroborated by an industrial survey conducted by Newtec (Newtec, 2018) and the Satcoms Innovation Group (SIG) (SIG, 2018)—formerly known as the Satellite Interference Reduction Group (IRG). According to this industrial survey (Newtec and IRG, Sep. 2013), 93% of satellite operators experience RFI; 24% of satellite operators experience RFI weekly; and 17% of satellite operators experience RFI daily. Accordingly, the research community has paid considerable attention to the detection and mitigation of RFI—mainly—in radio astronomy (van der Tol & van der Veen, 2005; Jeffs *et al.*, 2005), microwave radiometry (Ruf *et al.*, 2006; Misra *et al.*, 2009), and SatCom (Wildemeersch & Fortuny-Guasch, 2010; Nguyen *et al.*, 2015).

The state-of-the-art comprises various RFI detection and excision algorithms. Despite the rich literature, most of the state-of-the-art RFI detection and excision algorithms are either *non-robust* techniques and/or suffer from a considerable computational complexity induced by their inherent non-linearities. In addition, the state-of-the-art techniques have limited applicability. Consequently, RFI detection and excision have continued to be an active field of research, chiefly, in satellite communications, radio astronomy, and microwave radiometry. Meanwhile, it is worthwhile noting that the statistical signal processing problems of RFI detection and spectrum sensing are similar. As a matter of this fact, some of the contributions of this Ph.D. dissertation—with respect to RFI detection—have motivated new contributions regarding spectrum sensing pursued in the context of a cognitive radio (CR) that targets at the exploitation

of the vacant space-time-frequency voids (Goldsmith *et al.*, 2009) of a primary user (PU) by a secondary user (SU).

Following this brief introduction, the remainder of this chapter is organized as follows. Section 1.1 presents the literature on the state-of-the-art RFI detection, RFI excision, and spectrum sensing techniques. Section 1.2 presents the limitations of the respective state-of-the-art techniques. Section 1.3 highlights the motivation of this dissertation. Section 1.4 outlines the research objectives and methodologies. Section 1.5 then enumerates the contributions of this dissertation. Finally, Section 1.6 outlines the overall organization of this dissertation.

1.1 State-of-the-art

1.1.1 Literature on RFI Detection and Excision

The state-of-the-art on RFI detection and excision encompasses various algorithms. These algorithms have been proposed, mainly, for microwave radiometry, radio astronomy, and global navigation satellite systems (GNSS) applications. In line with the purpose of this chapter while being inspired by the classifications[1] of (Misra, 2011; Motella, 2008; Bauza, 2012), the state-of-the-art RFI detection and excision algorithms are presented via six groups: spectral, temporal, spectral-temporal, statistical, spatial filtering-based, and transformed domain-based algorithms. Subsequently, the main state-of-the-art techniques are summarized.

1.1.1.1 Spectral Algorithms

The existing spectral detection and excision algorithms, first, apply discrete Fourier transform (DFT) to the incoming signal. Thereafter, a comparison is performed between the spectrum of the received signal and a theoretical threshold that is determined according to the statistical model of the received signal. Meanwhile, some of the state-of-the-art spectral detection and excision algorithms are itemized beneath.

[1] Since some of the state-of-the-art techniques employ two or more signal processing schemes, it is worth noting that distinct classification of the existing techniques would be difficult.

- Cross frequency blanking is a frequency domain RFI mitigation technique which essentially consists of three thresholding operations versus frequency. This technique is successful in mitigating low-level RFI. Nonetheless, it is relatively efficient for a large number of channels (Johnson & Guner, 2007; Guner *et al.*, 2007).
- A non-parametric spectral estimation approach based on the Welch windowed *periodogram* (Proakis & Manolakis, 2006) is proposed in (Tani & Fantacci, 2008). This algorithm relies on a pre-correlation operation so as to detect RFI happening in GNSS.
- To detect RFI, the work in (Chen *et al.*, 2010) reconstructs interference using the estimated frequency, amplitude, and phase parameters of the signal spectrum. Then, it subtracts the artificial interference from the time domain complex input signal. However, the technique disseminated in (Chen *et al.*, 2010) is hardly helpful in wideband interference mitigation.

1.1.1.2 Temporal Algorithms

Amongst the existing temporal detection and excision algorithms, asynchronous pulse blanking (APB) is a popular one. As also implied by its name, APB blanks the portion of the received signal where the amplitude of the complex in-phase/quadrature (I/Q) signal exceeds a certain level of the threshold set with respect to the noise amplitude. Proposed in (Johnson & Ellingson, 2005), APB maintains a running estimate of the mean and variance of the sample magnitudes. Whenever a sample magnitude greater than a threshold number of standard deviations from the mean is detected, APB blanks a block of samples beginning from a predetermined period before the triggering sample. Furthermore, APB has been tested in several field trials and is convenient for pulsed RFI mitigation (Johnson & Ellingson, 2005).

1.1.1.3 Spectral-Temporal Algorithms

An interfering signal mostly appears for a limited time and present a variable behavior in frequency. In such cases, the presence of interference is limited to a region of the time-frequency

(TF) plane. Using a TF representation, it is possible to better monitor the interference contribution (Musumeci & Dovis, 2012).

In (Borio *et al.*, 2008), a general class of TF excision algorithm is represented by three functional blocks: the TF representation, the interference intermediate frequency (IF) estimation unit, and the excision filter. In this context, the use of *spectrogram* and of a simple interpolation technique for the IF estimation is proposed; statistical interference detection algorithm has been proposed; and an analytical expression for the interference detection threshold has been derived. Moreover, the use of infinite-duration impulse response (IIR) notch filters for interference excision in GNSS applications has also been introduced. It is to be highlighted that the introduced IIR filters render better performance than the FIR notch filters.

1.1.1.4 Statistical Algorithms

Statistical detection algorithms detect the presence of RFI by applying detection theory to the received signal (Kay, 1998; Schonhoff & Giordano, 2006). Concerning these algorithms, the statistics of the RFI are either known as a priori or unknown and evoking a variation in the covariance matrix of the noise—for instance, as in (Arribas *et al.*, 2013a,b).

The state-of-the-art comprises several statistical RFI detection algorithms and some of them are summarized beneath.

- In order to detect RFI happening in microwave radiometry, kurtosis detection is an algorithm proposed in (Ruf *et al.*, 2006) and comparatively detailed in (Misra *et al.*, 2009). Kurtosis detector (KD) evaluates the fourth central moment of a signal divided by the square of its second central moment. Thereafter, it considers those values which differ from the kurtosis of a Gaussian distributed signal as the ones caused by RFI(s) (Misra *et al.*, 2009). KD relies on the fact that the kurtosis of a Gaussian source is three and it deviates, in most cases, from three in the presence of a non-normal (typically man-made) interfering source. However, the algorithm manifests a considerable computational com-

plexity due to the intrinsic non-linearities evident in the kurtosis expression. Besides, it fails to discriminate Gaussian (near-Gaussian) distributed RFI.

- In (Arribas *et al.*, 2013a), the Neyman-Pearson detection framework and a generalized likelihood ratio test (GLRT) (Kay, 1998; Schonhoff & Giordano, 2006) are deployed to obtain a new GNSS detector. The proposed detector is able to mitigate temporally-uncorrelated point source interferences even if the array is unstructured and moderately uncalibrated. In the aforementioned work, an arbitrary and unknown covariance noise matrix which attempts to capture the statistical behavior of the RFI(s) and other nondesirable signals is assumed.
- In (Arribas *et al.*, 2013b), the GLRT-based detection algorithm of (Arribas *et al.*, 2013a) is extended to multiple antenna techniques.
- In the presence of continuous wave and wideband RFI signals, the authors of (Nguyen *et al.*, 2015) have developed analytical and simulation models so as to evaluate the carrier acquisition and tracking performances of practical unified S-band satellite operations command systems. The impacts of RFI on the carrier synchronizer were used in the detection of the RFI events. The same authors described an approach to predict the RFI interfering time duration using a carrier synchronizer. They also assessed the impacts of the carrier performance degradation of a synchronizer on the command bit error rate performance. Furthermore, advanced signal processing algorithms to estimate, predict, and characterize continuous wave and wideband RFI signals were described in detail along with the derived analytical expressions which characterize the estimators' performance.

1.1.1.5 Spatial Filtering-Based Algorithms

Having assumed that the signal of interest (SOI), RFI(s), and noise are located in some region[2]of a space-time field, spatial filtering-based techniques deploy arrays to filter signals (of interest to an application at hand) in a space-time field through the exploitation of their spatial

[2] Depending on the applications of interest, the regions pertaining to a space-time field of the SOI, RFI, and noise have some overlap (Van Trees, 2002, Ch. 2).

characteristics (Van Trees, 2002, Ch. 2). Referring to arrays, they can have linear, planar, or volumetric configuration (Van Trees, 2002, Ch. 1). Apart from their configuration, the spacing among arrays is an important design parameter: for instance, uniform spacing, non-uniform spacing, and random spacing are often considered in linear arrays (Van Trees, 2002, Ch. 1).

With respect to the aforementioned filtering, spatial filtering-based RFI detection and excision algorithms first estimate the RFI subspace. Thereafter, projection onto the orthogonal subspace of the estimated RFI subspace is executed so as to excise the RFI. To carry out the RFI subspace estimation, either the eigenvalue decomposition (EVD) of the received signal's space-time autocorrelation matrix (van der Tol & van der Veen, 2005) or the singular value decomposition (SVD) of the received signal's space-time cross-correlation matrix is, generally, deployed (Jeffs *et al.*, 2005). Beneath, the existing spatial filtering-based RFI detection and excision algorithms are briefly summarized.

- Subspace projection (SP): SP is a spatial filtering-based algorithm proposed and analyzed in (van der Tol & van der Veen, 2005). It relies on the EVD of the sampled autocorrelation matrix and forms an orthogonal projector out of the eigenvectors which correspond to the dominant eigenvalues. In order to ease the separation of the RFI and noise subspaces, however, it is assumed that the SOI autocorrelation matrix is approximately a zero matrix (van der Tol & van der Veen, 2005). Recently, SP was enhanced in (Sardarabadi *et al.*, 2016) which has proposed two reference-antenna based algorithms. The first algorithm deploys factor analysis to estimate an improved interference subspace. The second one estimates the RFI-free covariance matrices directly using extended factor analysis (EFA).
- Cross subspace projection (CSP): auxiliary-antenna assisted CSP is an RFI excision algorithm proposed in (Jeffs *et al.*, 2005). This algorithm relies on the SVD of the space-time cross-correlation matrix computed from the received signal vector. For its improved estimation of the RFI subspace, CSP constructs a projection matrix that utilizes the information regarding the strong interference received via the auxiliary-antennas. By cascad-

ing a zero matrix in its last columns, at the same time, the constructed projection matrix rejects the strong RFI received via the auxiliary antennas.

- Oblique projection beamforming (OPB): OPB is proposed in (Hellbourg *et al.*, 2012) for RFI mitigation in radio astronomy, especially for cyclostationary RFI. OPB is based on (Behrens & Scharf, 1994) and reported outperforming both classical beamforming and orthogonal projection with respect to relative error considered as a performance metric. Nevertheless, a practical implementation of OPB requires the knowledge of the RFI and the SOI spatial signatures.
- Polynomial-augmented subspace projection (PSP): PSP is proposed in (Landon *et al.*, 2012) to address low interference-to-noise ratio (INR), relatively rapid interference motion, and correlated noise across the receiving array. PSP is proposed for a wireless system suffering from interference, in general, and radio astronomy, in particular. A polynomial-based model is incorporated in the proposed algorithm to track changes, over time, in the array covariance matrix, mitigate interference subspace estimation errors, and improve canceler's performance (Landon *et al.*, 2012).

1.1.1.6 Transformed Domain-Based Algorithms

Transformed domain techniques (TDTs) are used to detect the interference waveform affecting the received signal whose presence could be masked in the time domain (Musumeci & Dovis, 2012; Dovis *et al.*, 2012). To detect the masked interference, TDTs, first, obtain the representation of the received signal in a different domain. Afterward, they detect interference by comparing the value of the statistic inferred from the obtained representation with a pre-determined threshold. Meanwhile, the existing TDTs are summarized beneath.

- **Techniques based on the TF representation**: in these techniques, first, the TF representation of the received signal is obtained by performing Gabor expansion on the samples at the output of the analog-to-digital converter (ADC). Second, a pre-determined mask on the previously obtained TF representation is applied to the received signal. Third, the interference coefficients are obtained by performing an inverse transformation and the

interfering signal is synthesized. Finally, so as to excise the interference, the synthesized interference is subtracted from the received signal (Musumeci & Dovis, 2012).

- **Techniques based on the Wavelet transform**: these mitigation techniques are based on the decomposition of a received signal through the use of local basis functions. These functions are obtained from a mother Wavelet through scaling and shifting as highlighted in (Dovis & Musumeci, 2011; Musumeci & Dovis, 2012). To continue, the proposed techniques start with the Wavelet decomposition of the received signal. The Wavelet decomposition is performed so as to isolate the interference frequency components. Once the received signal is decomposed, a detection strategy is needed in order to identify the presence of interference on each scale. A possible detection approach is based on the determination of a threshold according to the specified false alarm rate (FAR) or misdetection probability. Interference isolation is then achieved via the compact TF behavior of the Wavelet functions (Dovis & Musumeci, 2011). Once the interference frequency components are identified and isolated, a synthetic reconstruction of the interference signal, in the time domain, is provided through the inverse Wavelet transformation. At last, the reconstructed interference signal is subtracted from the received signal rendering interference excision (Dovis & Musumeci, 2011).
- **Techniques based on the Karhunen−Loève transform (KLT)**: in these techniques, KLT is used to detect, especially, feeble interference using eigenvalue sensitivity (Maccone, 2010). For a Gaussian signal contaminated with no RFI, its eigenvalues converge to one and are equal to one on average. On the contrary, since the eigenfunctions would correlate with a hidden RFI, the eigenvalues will be greater than one upon the reception of an RFI. Using this property of eigenvalues, techniques based on KLT detect RFI even if it is very weak. Nevertheless, the computational complexity required to extract a very large number of eigenvalues and eigenfunctions is a notable drawback. Consequently, bordered autocorrelation method-KLT (BAM-KLT) was proposed in (Maccone, 2010) as an efficient implementation of KLT—like fast Fourier transforms (FFT) being an efficient implementation of DFT. BAM-KLT is an alternative technique to evaluate the KLT of stationary processes that may run faster on computers than the traditional full-solving

KLT technique. Nonetheless, BAM-KLT is not yet capable of unambiguously detecting wideband signals such as a BPSK signal appearing as noise or interference in a GNSS-like signals (Szumski, 2010). Similar to the Wavelet-based techniques, the interference excision is performed by applying an inverse KLT and using only those eigenfunctions representing the useful signal. The threshold in the eigenvalues domain has been chosen such that about 90% are used for the GNSS signal reconstruction (Musumeci & Dovis, 2012). Even if KLT-based mitigation techniques are, in principle, one-dimensional methods, they showcase good performance in terms of isolating interference and preserving GNSS signal energy. Such a performance is due to the properties of the KLT basis functions—derived through the properties of an autocorrelation function—that can vary and adapt to the shape of the received signal (Musumeci & Dovis, 2012; Szumski, 2010).

1.1.2 RFI in Satellite Communications

For a satellite operator, the most common sources of interference are adjacent satellite interference, co-polarized interference, and cross-polarized interference (Oltrogge & Rashid, 2012). In addition, intentional interferers like in-car jammers (Bauernfeind *et al.*, 2011) can cause a denial of service in SatCom, in general, and in GNSS, in particular. Hence, attention has been paid to the detection and mitigation of RFI that might happen in GNSS and various detectors have been proposed. Henceforth, some of these techniques are itemized.

- Interference detection in GNSS receiver by monitoring the behavior of the automatic gain control (AGC) is highlighted in (Wildemeersch & Fortuny-Guasch, 2010). In GNSS receivers, where the signal power is below that of the thermal noise floor, the AGC is driven by the ambient noise environment rather than the signal power. With respect to this property, accordingly, AGC is employed to detect interference impinging in a GNSS receiver.
- After the received signal is digitized, it is also discussed in (Wildemeersch & Fortuny-Guasch, 2010) that interference can be detected via the acquisition and code tracking performance. Useful during the acquisition phase, different acquisition metrics have

been proposed in (Motella *et al.*, 2007). These metrics are used to investigate the effects of real out-of-band signals on GNSS receivers and to analyze the impact on the overall receiver chain. Mentioning the metrics, the first one is the ratio of the highest correlation peak to the second highest peak in the search space; the second one is the ratio of the highest correlation metric to the mean value of the correlation floor.

- The authors of (Balaei *et al.*, 2006) present a technique proposed to detect and characterize a continuous wave RF interference. In (Balaei *et al.*, 2006), the carrier-to-noise ratio (C/N_0) at the output of the correlator is used to estimate the frequency of the RFI. The comparison between a mathematical expression of C/N_0 and an estimation of the actual C/N_0 is used to determine the frequency of the interference. Yet, the power of the interference is estimated by the value of the AGC.
- (Ying *et al.*, 2012) presents a GNSS interference detection using a software defined radio. The proposed detection algorithms employ pre-correlation and post-correlation techniques. The pre-correlation techniques make use of digital signals, at an IF or baseband, that are available at a software receiver's sensor. Whereas the post-correlation techniques exploit standard measurements such as satellite orbit information and signal-to-noise ratio (SNR) measurements. However, the algorithms of (Ying *et al.*, 2012) require a network of distributed receivers for cooperative detection.
- The system proposed in (Bauernfeind *et al.*, 2011) attempts to mitigate GNSS interference by providing a reasonable warning and a localization system based on currently standardized vehicular communication architecture. By relying on a car-to-car communication and an existing infrastructure, it is reported that it is possible to simultaneously warn advancing vehicles and inform local authorities about the strength, location, and movement of the interference source.
- Unlike (Ying *et al.*, 2012) and (Bauernfeind *et al.*, 2011), the authors of (Kurz *et al.*, 2014) propose a self-contained camera integrated array-antenna GNSS receiver for spatial detection of RFI sources. The proposed receiver is capable of generating the RFI source-maps to be superimposed to real-world pictures obtained from the camera. Source-map generation is generally based on direction-of-arrival (DoA) estimation performed

using the multiple signal identification and classification (MUSIC) algorithm. Amplitudes in the spectrum indicate the DoA of RFI sources depending on azimuth and elevation angles in the hemisphere above the array-antenna. These coordinates are transferred into cartesian image coordinates and an overlay image is generated with colors reflecting the shape of the spectrum. Thereafter, the image is superimposed to a gray-scale picture obtained from the camera and the RFI sources can be visualized in the image.

- As highlighted in Section 1.1.1.1, a non-parametric spectral estimation approach based on the Welch windowed periodogram is proposed in (Tani & Fantacci, 2008). The spectral detection technique of (Tani & Fantacci, 2008) exploits a pre-correlation operation to detect RFI that might also occur in GNSS.
- Furthermore, (Wildemeersch & Fortuny-Guasch, 2010) highlights RFI detection algorithms which employ interference error envelope (IEE) and error vector magnitude (EVM). The concept of IEE is to express the distortion of the discriminator function as a function of several parameters of the interfering signal, i.e., the frequency shift and the continuous wave phase (Wildemeersch & Fortuny-Guasch, 2010). On the other hand, EVM describes the quality of the employed modulation by quantifying the distance between the constellation points and their corresponding ideal locations (Wildemeersch & Fortuny-Guasch, 2010).

Once RFI is properly detected, signal processing for its efficient excision should follow. In this respect, some of the state-of-the-art RFI mitigation techniques are summarized beneath.

- A TF excision algorithm employing a TF representation, an IF estimation unit, and an excision filter is proposed for GNSS applications in (Borio *et al.*, 2008). In this work, IIR filters which render better performance than FIR notch filters are also introduced.
- (Wildemeersch & Fortuny-Guasch, 2010) discusses a technique which consists of a pre-whitening linear filter mounted in front of a conventional receiver optimized for a white Gaussian noise. The filtering performed in the frequency domain yields to large computing load. In addition, it renders a significant correlation loss in the presence of wide-band interference such as frequency modulation (FM) or pulsed jammers. Meanwhile,

a structure made out of adaptive notch filters connected in series and controlled by the least mean squares (LMS) algorithm is proposed to track multiple jammers.

- In (Sgammini *et al.*, 2012), a two-step blind adaptive beamforming approach employing orthogonal projections is proposed for GNSS applications. A subspace-based approach is deployed by (Sgammini *et al.*, 2012) so as to propose a two-stage adaptive beamformer for interference suppression and line-of-sight (LoS) signal amplification. In the first stage, the covariance matrix is determined immediately from the digital antenna signals for interference mitigation. In the second stage, an *eigen-beamformer* which maximizes the ratio of the power of the desired LoS signal to the power of the undesired non-LoS signal is derived. Meanwhile, a fixed-point VHSIC hardware description language (VHDL) implementation of such an algorithm is presented in (Kurz *et al.*, 2012).

1.1.3 Literature on Spectrum Sensing

The state-of-the-art on spectrum sensing encompasses numerous techniques disseminated over the years (Ali & Hamouda, 2017; Sharma *et al.*, 2015; Yucek & Arslan, 2009). Upon the advent of active sensing techniques, the state-of-the-art spectrum sensing techniques can be classified as active sensing (Miridakis *et al.*, 2017; Heo *et al.*, 2014; Song *et al.*, 2010b) and quiet sensing (Ali & Hamouda, 2017; Sharma *et al.*, 2015; Wang & Liu, 2011; Axell *et al.*, 2012; Yucek & Arslan, 2009; Haykin *et al.*, 2009). To begin with, quiet sensing is performed by an SU which senses the channel for a fixed time-duration (Miridakis *et al.*, 2017) and transmits afterward provided that the primary channel is idle. To overcome the capacity reduction due to quiet periods which are usually short to provide adequate samples for an accurate spectrum sensing (Miridakis *et al.*, 2017; Heo *et al.*, 2014), and to surmount an extra burden of synchronization for the quiet periods (Song *et al.*, 2010b)—for instance, the one needed in IEEE 802.22 intra-frame sensing (Stevenson *et al.*, 2009), active sensing has emerged as a promising spectrum sensing paradigm. In particular, the authors of (Song *et al.*, 2010b) have proposed quiet-active sensing scheme by using inactive SUs which sense the primary channels in both quiet and active periods. At the cost of quiet-period synchronization (Song *et al.*, 2010b), the

advantage of this scheme over quiet sensing emanates from the additional samples obtained during the active period. To overcome the synchronization requirement of quiet-active sensing, the same authors have proposed an active sensing scheme—dubbed optimized active sensing—by placing quiet samples in the frequency domain so that selection diversity would be achieved (Song *et al.*, 2010b).

Capitalizing on the three-port antenna based spatial filtering technique of (Tsakalaki *et al.*, 2014), the authors of (Heo *et al.*, 2014) have introduced a simultaneous sensing and data transmission technique by deploying a spatial isolation technique on the antennas of each cognitive node. Relying on the self-interference cancellation technique, the proposed scheme divides the spatial resources so that some antennas are devoted to spectrum sensing while others for data transmission (Miridakis *et al.*, 2017). Nevertheless, this very technique suffers from a large self-interference produced during spectrum sensing and an appropriate physical distance should be maintained between the sensing and transmitting antennas (Miridakis *et al.*, 2017). To alleviate these issues, (Miridakis *et al.*, 2017) has investigated a distributed multiple-input multiple-output (MIMO) CR-based system operating in the presence of multiple PUs. In particular, the paper proposes a communication protocol made of training, data transmission, and spectrum sensing phases which alternate periodically. After the introductory training phase, the paper assumes a spectrum sensing per every symbol duration prior to a transmission by the secondary nodes, and a joint minimum mean squared error detection and an energy detection based spectrum sensing.

The wideband techniques can be Nyquist based or sub-Nyquist based depending on the adopted sampling rate (Ali & Hamouda, 2017; Sun *et al.*, 2013). Sub-Nyquist sampling techniques usually deploy either compressive sampling (Donoho, 2006) or multi-coset sampling (Venkataramani & Bresler, 2000). On the other hand, Nyquist based wideband sensing techniques are based on either fast Fourier transforms (Quan *et al.*, 2009), Wavelets (Tian & Giannakis, 2006), or filter-banks (Farhang-Boroujeny, 2008). Delving into narrowband sensing, several narrowband spectrum sensing techniques have been proposed (Wang & Liu, 2011; Axell *et al.*, 2012; Ali & Hamouda, 2017; Sharma *et al.*, 2015). The conventional ones are energy de-

tection (ED) (Sonnenschein & Fishman, 1992; Digham *et al.*, 2007; Sofotasios *et al.*, 2013), matched filtering (Poor, 1994), feature-based detection (Gardner, 1988), polarization detection (Guo *et al.*, 2016), sample covariance matrix (SCM) based algorithms (Kortun *et al.*, 2012; Zeng & Liang, 2009b,a; Bianchi *et al.*, 2011), moment ratio detection (Bogale & Vandendorpe, 2013a), and max-min detection (Bogale & Vandendorpe, 2014, 2013b). Apart from these conventional algorithms, some other algorithms such as Bartlett estimate-based energy detection (Gismalla & Alsusa, 2012), a frequency domain eigenvalue-based spectrum sensing algorithms (Yousif *et al.*, 2016), subband energy-based spectrum sensing algorithm (Dikmese *et al.*, 2016), energy detection spectrum sensing under RF imperfections and with multiple PUs (Boulogeorgos *et al.*, 2016a,b), and a robust estimator-correlator and a robust generalized likelihood detectors (Patel *et al.*, 2016) have been proposed.

On the other hand, unlike most of the aforementioned multi-antenna techniques which presume *independent and identically distributed* (i.i.d.) noise samples, calibration uncertainties in the different antenna frontends are inevitable rendering *independent and non-identically distributed* (i.ni.d.) noise samples. Such a scenario was considered in (Leshem & van der Veen, 2001; Tugnait, 2012; Ramírez *et al.*, 2011): by assuming a Gaussian distributed received signal, a Hadamard ratio detector (HRD) was derived in (Leshem & van der Veen, 2001); a spectrum sensing technique which deploys an asymptotic analysis of the DFT of the received multi-antenna signal—whose time domain version is an HRD—is proposed in (Tugnait, 2012); and (Ramírez *et al.*, 2011) devised a GLRT-based technique by proposing an efficient alternating minimization algorithm so as to compute its statistic. Recently, the F–test (FT) based spectrum sensing technique was proposed in (Huang & Chung, 2013a) and corroborated to be superior over an energy detector, a maximum-minimum eigenvalue (MME) detector (Zeng & Liang, 2009b), and a GLRT detector (Taherpour *et al.*, 2010; Wang *et al.*, 2010), especially at low SNR. While exhibiting a moderate computational complexity, this detector is also robust against noise uncertainty and doesn't require the knowledge of the noise power.

1.2 Limitations

1.2.1 Limitations of the Existing RFI Detection and Excision Techniques

The RFI detection and excision algorithms that have been proposed to date exhibit the following limitations.

- **Complexity**: most of the state-of-the-art techniques exhibit various non-linear operations that render a huge number of processing cycles.
- **Unsatisfactory detection performance**: most of the state-of-the-art techniques are effective for huge sample settings. Thus, the existing techniques are hardly useful for real-time implementation, as this would require only very few samples.
- **Detection for some type of RFIs only**: some of the state-of-the-art techniques fail to detect Gaussian (near-Gaussian) RFI(s); for instance, KD fails to detect Gaussian (near-Gaussian) RFI (Misra *et al.*, 2009; Ruf *et al.*, 2006). Nevertheless, detection should be made regardless of the type of the RFI(s).
- **Inefficient RFI excision**: the state-of-the-art RFI excision algorithms render, mostly, an inefficient RFI excision which is also aggravated when the impinging RFI traverses through a highly time-variant channel. However, an RFI excision technique should always have an efficient RFI excision capability irrespective of the time-variant channel(s) of the impinging RFI(s).
- **Limited applicability**: the majority of the state-of-the-art RFI detection and excision algorithms have been proposed, mainly, for microwave radiometry and radio astronomy applications. Some have also been proposed for GNSS applications. On the contrary, any RFI detection and excision technique shall have broad applicability to any RF operating systems, including—for instance—terrestrial communications and mobile satellite communications (Arapoglou *et al.*, 2011; Richharia, 2014) systems.

1.2.2 Limitations of the Existing Spectrum Sensing Techniques

In spite of a nearly mature research sub-field encompassing numerous contributions, the state-of-the-art spectrum sensing techniques manifest several limitations that are summarized below.

- **Assumptions regarding the primary signal(s)**: several of the state-of-the-art detection techniques rely on assumptions concerning the primary signal characteristics. For instance, Bartlett estimate-based energy detection (Gismalla & Alsusa, 2012), a frequency domain eigenvalue-based spectrum sensing algorithms (Yousif *et al.*, 2016), subband energy-based spectrum sensing algorithm (Dikmese *et al.*, 2016), energy detection spectrum sensing under RF imperfections and with multiple PUs (Boulogeorgos *et al.*, 2016a,b), and a robust estimator-correlator as well as a robust generalized likelihood detectors (Patel *et al.*, 2016) rely on the complex Gaussian distributed primary signal. Nonetheless, if a given spectrum sensing technique has to be attractive for practical CR applications, there shall not be any assumption on the characteristics of the primary signal, as the rendered detection will not be robust otherwise.
- **Limitations of the conventional narrowband techniques**: most of the conventional narrowband techniques exhibit their respective limitations. To mention, ED relies on the known power spectral density of the noise and exhibits a high sensitivity to noise uncertainty (Wang & Liu, 2011) leading to a poor performance at a low SNR regardless of the number of intercepted samples, as demonstrated via *SNR walls* (Tandra & Sahai, 2008); matched filters suffer from intrinsic computational complexity and hence are unattractive for practical spectrum sensing applications; particular features need to be introduced to deploy feature detectors in orthogonal frequency division multiplexing (OFDM) based communications (Wang & Liu, 2011); polarization detectors are computationally complex and sensitive to estimation errors (Guo *et al.*, 2016); SCM-based techniques suffer from performance loss under sample-starved settings and their asymptotic threshold differs considerably from the exact value for finite sensors and samples (Kortun *et al.*, 2012); a moment ratio detection (Bogale & Vandendorpe, 2013a) is computationally complex and relies on the asymptotic Gaussian distribution; and max-min

detector (Bogale & Vandendorpe, 2014, 2013b) suffers from a huge computational complexity.

- **Limitations of the wideband techniques**: as tabulated in (Ali & Hamouda, 2017, Table III), the various wideband techniques have also their own limitations. Highlighting these limitations, the FFT-based detectors require a high sampling rate; the Wavelet-based detectors and the filter-bank based detectors manifest high computational complexity; and the multi-coset sampling based detectors require synchronization circuits. Moreover, the compressive sampling based detectors exhibit high computational complexity; rely on the sparsity assumption; and manifest dynamic behaviors for sparsity level.
- **Limitations of the active sensing techniques**: the schemes of (Song *et al.*, 2010b) require more spectrum resources and extra power resources are required because of the signalling overhead, and sensing of the primary signal and transmission of the sensing information to the active SU; the technique proposed by (Heo *et al.*, 2014) suffers from large self-interference produced during spectrum sensing and an appropriate physical distance should be maintained between the sensing and transmitting antennas; and whenever a hidden terminal problem (Axell *et al.*, 2012; Yucek & Arslan, 2009) arises, the protocol deployed in (Miridakis *et al.*, 2017) will keep on conducting a secondary transmission and emitting interference to a primary receiver which may not be blocked, unlike the blocked primary transmitter.
- **Limitations of the FT-based technique**: it requires prior knowledge of the channel state information (CSI) between the primary transmitter and secondary receiver rendering it susceptible to CSI estimation errors. Moreover, the FT detector of (Huang & Chung, 2013a) assumes a single-antenna primary transmitter which is not the case for the transmitters of the fourth generation (4G) and the fifth generation (5G) era, as they are usually equipped with a number of antennas for the sake of array gain, spatial diversity gain, spatial multiplexing gain, and interference reduction (Biglieri *et al.*, 2007).
- **Reliance on i.i.d. noise samples**: unlike the numerous state-of-the-art techniques whose developments and analyses rely on i.i.d. noise samples, calibration uncertainties in the

different antenna frontends are evident—rendering i.ni.d. noise samples. In this respect, (Leshem & van der Veen, 2001; Tugnait, 2012; Ramírez *et al.*, 2011) consider i.ni.d. noise samples and devise the respective detectors, as highlighted in Section 1.1.3. Nevertheless, new spectrum sensing techniques that do not assume anything on the characteristics of the primary signal while considering i.ni.d. noise samples are needed.

1.3 Motivation

The limitations of the state-of-the-art techniques have motivated this Ph.D. dissertation. While underscoring the natural *performance versus complexity* trade-off, the limitations itemized in Section 1.2.1 have inspired less complex RFI detection techniques that have a satisfactory detection performance, broad applicability, and detection of any type of RFI. Besides, they have also inspired a widely applicable tensor-based RFI excision algorithms that render efficient RFI excision at the cost of computational complexity. Similarly, some of the limitations of the state-of-the-art spectrum sensing techniques summarized in Section 1.2.2 have inspired matrix-based FT spectrum sensing techniques that are blind and efficient, especially in terms of overcoming hidden terminal problems by rendering detection at very low SNRs. With respect to this motivation, Section 1.4 presents the research objectives and methodologies of this Ph.D. dissertation.

1.4 Research Objectives and Methodologies

1.4.1 Research Objectives

This Ph.D. dissertation has three objectives that are enumerated below.

1. The investigation and development of robust RFI detection algorithms for satellite and terrestrial communications.
2. The investigation and development of efficient RFI excision algorithms for satellite and terrestrial communications.

3. The investigation and development of advanced low-complexity spectrum sensing techniques.

Regarding the first objective, *robustness* in RFI detection can be inferred from:

- satisfactory detection performance for the desired FAR even in sample starved settings. It is to be noted that most of the existing RFI detection algorithms offer satisfactory detection performance, mainly, for a huge number of available samples.
- ability to detect the unknown RFI irrespective of its statistics or type, i.e., detection capability of narrowband, wideband (Gaussian or near-Gaussian), continuous wave, and pulsed RFI.
- ability to detect a feeble RFI.
- sufficient detection performance regardless of a noise power uncertainty.

Concerning the second objective, efficiency in RFI excision can be deduced from an RFI excision performance close to the average signal-to-interference-plus-noise ratio (SINR) gain performance of a *perfect excision algorithm*—an algorithm that relies on a perfect knowledge of the RFI channel.

With respect to the third objective, advanced low-complexity spectrum sensing techniques can be deduced from an efficient and robust spectrum sensing which is:

- blind;
- independent of any assumption regarding the noise power;
- independent of an assumption about any type of CSI;
- able to overcome hidden terminal problems by rendering excellent detection at very low SNRs; and
- computationally simple.

Moreover, advanced low-complexity spectrum sensing techniques shall exhibit:

- a minimum number of non-linear operations;
- a minimum number of multiplications; and
- a minimum number of processing cycles.

1.4.2 Research Methodologies

This Ph.D. dissertation commenced through a detailed research survey regarding the state-of-the-art. In this initial phase of the doctoral research:

- the state-of-the-art RFI detection and excision algorithms proposed for radio astronomy, microwave radiometry, and SatCom applications were identified and studied;
- the limitations of the state-of-the-art RFI detection and excision techniques were delineated;
- numerous the state-of-the-art spectrum sensing (narrowband versus wideband and active versus quiet) techniques were identified and studied; and
- the limitations of the state-of-the-art spectrum sensing techniques were also delineated.

After carrying out the above-mentioned initial phase of this doctoral research, we have shifted our attention toward the realization of the three objectives enumerated in Section 1.4.1. Toward this end, this dissertation has employed the underneath mathematical frameworks and performance analysis tools.

- In order to propose robust RFI detection algorithms, we have deployed detection and estimation theory (binary hypothesis testing as well as binary composite hypothesis testing), statistical signal processing, linear algebra, and tensor (multi-linear) algebra. As to performance analysis tools, we have exploited the first-order perturbation analysis, the estimation theory of a population covariance matrix (PCM), probability distributions, and theories regarding probability, random variables, and stochastic processes.
- To propose efficient RFI excision techniques, we have employed the tensor (multi-linear) algebra framework. To analyze the performance of these excision techniques, we have deployed a higher-order singular value decomposition (HOSVD) based parameter estimation, the first-order perturbation analysis, and the estimation theory of a PCM.
- To propose advanced low-complexity spectrum sensing techniques, we have deployed the FT, linear algebra, and multi-linear (tensor) algebra frameworks. To pursue the respective performance analyses, we have employed the first-order perturbation analysis,

tensor-based signal processing, the estimation theory of a PCM, and probability distributions.

For the performance assessment of the proposed algorithms and validation of the derived closed-form expressions, this dissertation has deployed the MATLAB® software. In order to assess the performance of the proposed techniques over real-world scenario, we have also deployed real-time RFI contaminated ADC data received by one of the antennas of the Very Large Array (VLA) (NRAO, 2017) of the National Radio Astronomy Observatory.

1.5 Thesis Contributions

This Ph.D. dissertation has made contributions in terms of the journal and conference papers itemized in Appendix 1 and Appendix 2 (under APPENDIX I), respectively. Meanwhile, the highlight of the respective contributions is noted in Appendix 3 (under APPENDIX I).

1.6 Thesis Organization

For the sake of the systematic reporting of the journal contributions—enumerated in Appendix 1 (under APPENDIX I)—and its coherent organization, this Ph.D. dissertation is organized into five parts. To highlight each:

- Part I covers the preliminaries, including an introduction to this dissertation as well as its motivation and research problems —detailed in Chapter 1—of this dissertation.
- Part II details the dissertation contributions to the research sub-field of RFI detection. In particular, Chapter 2 reports a power-based broadband RF interference detector; Chapter 3 presents the performance analysis of an energy-based RFI detector; Chapter 4 presents an eigenvalue-based RF interference detector; and Chapter 5 presents linear and multilinear RFI detectors.
- Part III introduces tensor-based advanced multi-antenna RFI(s) excision techniques detailed in Chapter 6.

- Part IV reports the dissertation contributions concerning the research sub-field of spectrum sensing. In this respect, Chapter 7 presents simple F–test based multi-antenna spectrum sensing techniques.
- For better readability of this dissertation, Part V encompasses the appendices of Chapters 1-7 preceded by the discussion of the results highlighted in Chapter 8 which, in turn, is followed by the conclusion and recommendations of this dissertation.

Part II

Advanced RFI Detection

CHAPTER 2

POWER-BASED BROADBAND RF INTERFERENCE DETECTOR FOR WIRELESS COMMUNICATION SYSTEMS

Tilahun M. Getu[1,2], Wessam Ajib[2], and René Jr. Landry[1]

[1] Department of Electrical Engineering, École de Technologie Supérieure,
1100 Notre-Dame West, Montréal, Québec, Canada H3C 1K3
[2] Department of Computer Sciences, Université du Québec à Montréal,
201 Av. President-Kennedy, Montréal, Québec, Canada H2X 3Y7

This article was published in *IEEE Wireless Communications Letters* as of December 2018 (Getu *et al.*, 2018c).

"You must have long-term goals to keep you from being frustrated by short-term failures."—Charles C. Noble

Abstract—As broadband radio frequency interference (RFI) affects various systems operating radio frequencies, it has to be detected and mitigated. Accordingly, a computationally simple power-based detector (PD) is investigated. By assuming reception over the Nakagami-*m* fading channels, exact closed-form expressions for the probabilities of RFI detection and of false alarm are derived and validated via simulations. Simulations also demonstrate that PD outperforms kurtosis detector.

Index Terms—RFI mitigation, RFI detection, power detection.

2.1 Introduction

Radio frequency interference (RFI) is mainly the result of out-of-band emissions by nearby transmitters and harmonics, jamming, spoofing, and meaconing. These interferences might be a broadband RFI which affects several systems operating radio frequencies over a large bandwidth such as microwave radiometry (Misra *et al.*, 2009), radio astronomy (van der Tol & van der Veen, 2005), and satellite communications (Newtec and IRG, Sep. 2013). Similarly, a global navigation satellite system (GNSS) and a very small aperture terminal (VSAT) suffer

from broadband RFI (Borio *et al.*, 2008). Broadband RFI can also happen in ultra-wideband communications for wideband interferers (Shi *et al.*, 2007); radar for wideband jammers (De Maio & Orlando, 2016; Orlando, 2017; Bandiera & Orlando, 2009); and cognitive radios for an imperfect spectrum sensing (Getu *et al.*, 2015a): neighboring primary users emitting such interference can constrain the spectrum sensing capability of an energy detector, as analytically demonstrated in (Boulogeorgos *et al.*, 2016b). To be mitigated efficiently, broadband RFI, thus, should be detected robustly.

For microwave radiometry and GNSS applications, the state-of-the-art encompasses various RFI detectors (Misra *et al.*, 2009; De Roo *et al.*, 2007; De Roo & Misra, 2010; Balaei & Dempster, 2009; Dovis *et al.*, 2012). However, these computationally complex detectors are not widely applicable in various systems operating radio frequencies and kurtosis detector (KD) fails to detect Gaussian (near-Gaussian) RFI (Misra *et al.*, 2009; Ruf *et al.*, 2006). Meanwhile, a power detector (PD) was employed for an RFI detection in microwave radiometry (Guner *et al.*, 2007). Similar detectors were deployed in a radiometer (Sonnenschein & Fishman, 1992), a multi-channel energy detector (Wang *et al.*, 2010), and the cooperative spectrum sensing of (Hussain & Fernando, 2014). Despite the several RFI detectors, their exact performance closed-form expressions have not been reported—to the best of our knowledge—to date. Moreover, due to the lack of a false alarm rate (FAR) expression that is often used to set a decision threshold, the PD of (Guner *et al.*, 2007) employed a heuristic decision threshold.

Capitalizing on the aforementioned power-based detectors, this paper investigates a power-based broadband RFI detector by modeling—like (Wildemeersch & Fortuny-Guasch, 2010)—broadband RFIs as Gaussian processes. Unlike the state-of-the-art literature on RFI detection, we derive exact closed-form performance expressions for this computationally simple and practically appealing PD. Having deployed an average power-based test statistic, we, specifically, derive exact expressions for the probabilities of RFI detection and of false alarm along with the analytical assessment of the impact of the number of RFIs. Following this introduction, Sec. 2.2 outlines the system model and the investigated detection. Sec. 2.3 presents the performance

analysis. Sec. 2.4 highlights the respective practical issues. Sec. 2.5 reports the simulation results followed by conclusions drawn in Sec. 2.6.

Notation: $\triangleq$, $\sim$, $|$, $n!$, $\mathbb{E}\{\cdot\}$, and $\Pr\{\cdot\}$ stand for equal by definition, distributed as, conditioned on, n factorial, expectation, and the probability of, respectively; $U(\cdot)$, $\Gamma(\cdot,\cdot)$, $\mathscr{G}(\cdot,\cdot)$, $\mathscr{N}(\cdot,\cdot)$, and $\mathscr{NA}(\cdot,\cdot)$ denote the unit step function $\big($i.e., $U(y \geq 0) = 1\big)$, the (upper) incomplete gamma function, the gamma distribution, the normal distribution, and the Nakagami-m distribution, respectively.

2.2 System Model and the Investigated Detection

2.2.1 System Model

Consider the detection of Q independent Gaussian RFIs that might be received along with the signal of interest (SOI) through Nakagami-m fading channels (Karagiannidis *et al.*, 2007). Employing the Rician shadowed model (Giunta *et al.*, 2018; Abdi *et al.*, 2003), such a problem can also be recast as the detection of Q Nakagami-m distributed non-line-of-sight (non-LoS) components received along with Nakagami-m distributed LoS component. For the received passband signal downconverted to its baseband equivalent denoted by $r(t)$, a binary hypothesis test is formulated regarding the detection of the Q RFIs as

$$r(t) = \begin{cases} hs(t) + \sum_{j=1}^{Q} g_j v_j(t) + z(t) & : H_1 \\ hs(t) + z(t) & : H_0, \end{cases} \tag{2.1}$$

where H_0 and H_1 are hypotheses on the absence and presence of the Q RFIs, respectively; $s(t) = \sqrt{P}\sum_{n=-\infty}^{\infty} s_n p(t - nT)$ is the SOI for s_n, $p(t)$, and P being the n-th unknown and deterministic SOI symbol, a rectangular pulse shape of duration T, and the power of the SOI, respectively; $h \sim \mathscr{NA}(m_1, \bar{h}_s)$ is the flat fading SOI channel gain for m_1 being the SOI fading severity parameter and $\bar{h}_s \triangleq \mathbb{E}\{h^2\}$; $v_j(t) = \sqrt{P_j}\sum_{l=-\infty}^{\infty} v_{j,l} p(t - lT)$ is the j-th Gaussian RFI for $v_{j,l} \sim \mathscr{N}(0,1)$ and P_j denoting the power of the j-th RFI; $g_j \sim \mathscr{NA}(m_{j+1}, \bar{g}_{j,s})$ is the

channel gain of the j-th RFI for m_{j+1} being the fading severity parameter of the j-th RFI and $\bar{g}_{j,s} \triangleq \mathbb{E}\{g_j^2\}$; and $z(t)$ is a band-limited zero mean additive white Gaussian noise (AWGN) process. We assume that $v_{j,l}$, $\{g_j\}_{j=1}^{Q}$, h, and the AWGN are statistically independent; $\{m_j\}_{j=1}^{Q+1}$ are integers; and an estimate of the noise power is available.

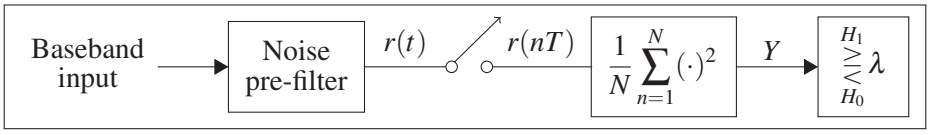

Figure 2.1 The investigated broadband RFI detector

2.2.2 The Investigated Detection

The PD that can be easily integrated into a baseband receiver is depicted in Fig. 2.1, where the baseband input is first filtered by a noise pre-filter that serves to limit the noise bandwidth (Urkowitz, 1967). Sampling in every T—as per the Nyquist rate (Oppenheim & Schafer, 2010)—and squaring then follow. Averaging N squared samples, the mean received power is approximated to render a decision variable Y.[1] If Y exceeds the decision threshold denoted by λ, H_1 is detected. Otherwise, H_0 is detected.

2.3 Performance Analysis

From Fig. 2.1 and (2.1), denoting $r(nT)$ by $r[n]$ leads to

$$r[n] = \begin{cases} hs[n] + \sum_{j=1}^{Q} g_j v_j[n] + z[n] & : H_1 \\ hs[n] + z[n] & : H_0, \end{cases} \tag{2.2}$$

[1] Having realized that average received power is the average received energy per unit time, it is to be noted that the investigated power detector can also be posed as an energy detector.

where $s[n] = s(nT)$, $v_j[n] = v_j(nT)$, and $z[n] = z(nT)$. The exact mean received power—$Y = \mathbb{E}\{r^2[n]\}$—is computed as

$$Y = \begin{cases} \mathbb{E}\left\{\left(hs[n] + \sum_{j=1}^{Q} g_j v_j[n] + z[n]\right)^2\right\} & : H_1 \\ \mathbb{E}\{(hs[n] + z[n])^2\} & : H_0. \end{cases} \tag{2.3}$$

Meanwhile, (2.3) is characterized via the following theorem.

Theorem 1. For $\sigma^2 = \mathbb{E}\{z^2[n]\}$, (2.3) simplifies to

$$Y = \begin{cases} \sigma^2\left(\bar{\gamma}_{snr} + \sum_{j=1}^{Q} \bar{\gamma}_{inr}^{j} + 1\right) & : H_1 \\ \sigma^2\left(\bar{\gamma}_{snr} + 1\right) & : H_0, \end{cases} \tag{2.4}$$

where $\bar{\gamma}_{snr}$ and $\bar{\gamma}_{inr}^{j}$ are, respectively, the average signal-to-noise ratio (SNR) and the j-th RFI's average interference-to-noise ratio (INR) defined via

$$(\bar{\gamma}_{snr}, \bar{\gamma}_{inr}^{j}) = \left(\bar{h}_s P \mathbb{E}\{s_n^2\}/\sigma^2, \bar{g}_{j,s} P_j/\sigma^2\right). \tag{2.5}$$

Proof. Please see Appendix 1 under APPENDIX II.

Under H_0, $\tilde{Y} = Y - \sigma^2 \sim \mathscr{G}(m_1, \Omega_1)$ for $h \sim \mathscr{NA}(m_1, \bar{h}_s)$. Hence, its probability density function (PDF)—$f_{\tilde{Y}|H_0}(y)$—is given by (Karagiannidis *et al.*, 2006a, eq. (2)) for $\Omega_1 = \mathbb{E}\{\tilde{Y}|H_0\} = \sigma^2\bar{\gamma}_{snr}$. Integrating $f_{\tilde{Y}|H_0}(y)$ results in the respective cumulative distribution function (CDF)—$F_{\tilde{Y}|H_0}(y)$—equated as (Karagiannidis *et al.*, 2006a, eq. (3))

$$F_{\tilde{Y}|H_0}(y) = \left[1 - \frac{\Gamma(m_1, \frac{m_1}{\Omega_1} y)}{(m_1 - 1)!}\right] U(y). \tag{2.6}$$

Under H_1, $\tilde{Y}$ is the sum of $Q+1$ mutually independent gamma distributed random variables—$Y_1 \sim \mathscr{G}(m_1, \Omega_1)$ and $\{Y_{j+1}\}_{j=1}^{Q} \sim \mathscr{G}(m_{j+1}, \Omega_{j+1})$, $\Omega_{j+1} = \sigma^2\bar{\gamma}_{inr}^{j}$—which admit the Erlang distribution (Karagiannidis *et al.*, 2006a) for the integerness of $\{m_j\}_{j=1}^{Q+1}$. Hence, the PDF—

$f_{\tilde{Y}|H_1}(y)$—given by (Karagiannidis *et al.*, 2006a, eqs. (2) and (6)) leads to a CDF of $\tilde{Y}$ under H_1—$F_{\tilde{Y}|H_1}(y)$—equated as (Karagiannidis *et al.*, 2006a, eqs. (3) and (9))

$$F_{\tilde{Y}|H_1}(y) = \sum_{i=1}^{Q+1} \sum_{k=1}^{m_i} \Xi_{\eta_1 \ldots \eta_{Q+1}}^{m_1 \ldots m_{Q+1}}(i,k) \left[1 - \frac{\Gamma(k, y/\eta_i)}{(k-1)!} \right] U(y), \tag{2.7}$$

where $\eta_i = \frac{\Omega_i}{m_i}$ and $\Xi_{\eta_1 \ldots \eta_{Q+1}}^{m_1 \ldots m_{Q+1}}(i,k)$ is a weight defined through (Karagiannidis *et al.*, 2006a, eqs. (7) and (8)). Hereinafter, the probability of RFI detection—denoted by P_d—and the probability of false alarm—denoted by P_f—exhibited by PD are derived.

2.3.1 The Probability of RFI Detection

Using Y in (2.4), the exact P_d is computed as $P_d = \Pr\{Y > \lambda | H_1\} = \Pr\{\tilde{Y} > (\lambda - \sigma^2) | H_1\} = \int_{\lambda-\sigma^2}^{\infty} f_{\tilde{Y}|H_1}(y)dy$. Thus,

$$P_d = 1 - \int_{-\infty}^{\lambda-\sigma^2} f_{\tilde{Y}|H_1}(y)dy = 1 - F_{\tilde{Y}|H_1}(\lambda - \sigma^2). \tag{2.8}$$

Subsequently, two cases are discussed.

2.3.1.1 The Case of a Single RFI

In this case, $\tilde{Y}$ becomes the sum of Y_1 and $Y_2 \sim \mathscr{G}(m_2, \Omega_2)$—$\Omega_2 = \sigma^2 \bar{\gamma}_{inr}^1$. Deploying (2.7) in (2.8) and using $\{\Omega_i\}_{i=1}^2 = U(1-i)\sigma^2 \bar{\gamma}_{snr} + U(i-2)\sigma^2 \bar{\gamma}_{inr}^1$,

$$P_d = \sum_{i=1}^{2} \sum_{k=1}^{m_i} \frac{\Xi_{\eta_1 \eta_2}^{m_1 m_2}(i,k) \Gamma\left(k, \frac{m_i(\lambda/\sigma^2 - 1)}{U(1-i)\bar{\gamma}_{snr} + U(i-2)\bar{\gamma}_{inr}^1}\right)}{(k-1)!}, \tag{2.9}$$

where $\Xi_{\eta_1 \eta_2}^{m_1 m_2}(i,k)$ is a weight defined via (Karagiannidis *et al.*, 2006a, eq. (A-5)).

2.3.1.2 The Case of Multiple RFIs

Substituting (2.7) and, in turn, $\{\Omega_i\}_{i=1}^{Q+1} = U(1-i)\sigma^2 \bar{\gamma}_{snr} + U(i-2)\sigma^2 \bar{\gamma}_{inr}^{i-1}$ into (2.8) gives

$$P_d = \sum_{i=1}^{Q+1} \sum_{k=1}^{m_i} \frac{\Xi_{\eta_1 \ldots \eta_{Q+1}}^{m_1 \ldots m_{Q+1}}(i,k)\Gamma\left(k, \frac{m_i(\lambda/\sigma^2-1)}{U(1-i)\bar{\gamma}_{snr}+U(i-2)\bar{\gamma}_{inr}^{i-1}}\right)}{(k-1)!}. \tag{2.10}$$

Furthermore, P_d is characterized via the following lemma.

Lemma 1. P_d improves with the number of RFIs.

Proof. Using (2.4), $P_d = \Pr\{\sigma^2(\bar{\gamma}_{snr} + \sum_{j=1}^{Q} \bar{\gamma}_{inr}^j) > \tilde{\lambda}\}$ for $\tilde{\lambda} = \lambda - \sigma^2$. For the same desired FAR, the P_d' in the presence of $Q' > Q$ RFIs can be equated as $P_d' = \Pr\{\sigma^2(\bar{\gamma}_{snr} + \sum_{j=1}^{Q} \bar{\gamma}_{inr}^j) > (\tilde{\lambda} - \sum_{j=Q+1}^{Q'} \bar{\gamma}_{inr}^j)\}$. As $\{\bar{\gamma}_{inr}^j\}_{j=Q+1}^{Q'} > 0$, $\tilde{\lambda} > (\tilde{\lambda} - \sum_{j=Q+1}^{Q'} \bar{\gamma}_{inr}^j)$ and hence $P_d' > P_d$. ■

2.3.2 The Probability of False Alarm

The exact P_f is obtained as $P_f = \Pr\{Y > \lambda | H_0\} = \Pr\{\tilde{Y} > (\lambda - \sigma^2) | H_0\} = \int_{(\lambda-\sigma^2)}^{\infty} f_{\tilde{Y}|H_0}(y)dy$. Accordingly,

$$P_f = 1 - \int_{-\infty}^{(\lambda-\sigma^2)} f_{\tilde{Y}|H_0}(y)dy = 1 - F_{\tilde{Y}|H_0}(\lambda - \sigma^2). \tag{2.11}$$

Deploying (2.6) in (2.11) and, in turn, employing $\Omega_1 = \sigma^2 \bar{\gamma}_{snr}$,

$$P_f = \frac{\Gamma\left(m_1, \frac{m_1(\lambda/\sigma^2-1)}{\bar{\gamma}_{snr}}\right)}{(m_1-1)!}. \tag{2.12}$$

Remark 1. The single RFI case can be inferred from the multiple RFIs case. Besides, (2.10) and (2.12) are the special cases of (Boulogeorgos *et al.*, 2016b, eq. (12)) and (Boulogeorgos *et al.*, 2016b, eq. (13)), respectively.

2.4 Practical Issues

As in Fig. 2.1, PD computes the mean received power to detect RFI. However, (2.12) should be solved for λ should it be set as per the desired FAR. To do so, first, the detector can be calibrated to estimate the actual noise power with high accuracy (Quan *et al.*, 2009). Thereafter, the average SNR should be estimated via (2.5). To carry out this estimation, the SOI channel estimator is required and such an estimator has to be broadband RFI-aware channel estimator,

as RFI(s) can impinge at any time. Accordingly, the broadband RFI-aware channel estimators of (Getu *et al.*, 2015a) can be deployed to obtain the estimate of the average SNR via (2.5). Having performed the aforementioned estimations, the λ rendering the desired FAR can finally be determined through (2.12). Moreover, the inevitable RF impairments such as phase noise, amplifier non-linearities, and in-phase and quadrature-phase imbalance (Boulogeorgos *et al.*, 2016a; Gokceoglu *et al.*, 2014) shall be compensated. As a preliminary step, the Gaussianity of the received signal samples might also be tested (Giannakis & Tsatsanis, 1994; Yuan, 1998; Sigut *et al.*, 2005).

2.5 Simulation Results

Unless otherwise mentioned, the reported results—generated using the MATLAB® codes in (Getu, Apr. 2018)—deploy the parameters of Table 2.1.

Table 2.1 Simulation parameters unless otherwise mentioned

Parameters	Assigned value
(m_1, m_2, m_3, Q)	$(2,2,2,1)$
(P, P_1, P_2, σ^2)	$(10,10,10,1)$ W
$\big($No. of realizations$, N\big)$	$(10^4, 10^4)$

Without loss of generality, the subsequent assessments are conducted in the context of a VSAT communication system under these settings: the LoS reception of a binary phase shift keying (BPSK) modulated SOI transmitted by a regenerative geostationary earth orbit (GEO) satellite; one or more independent Gaussian RFIs that might be emitted by a nearby regenerative GEO satellite(s); and perfectly estimated and identical propagation delays of the SOI and RFI(s).

Having computed λ—rendering the desired FAR of 0.1—using (2.12), PD is simulated as per Fig. 2.1. Approximating expectation via the average of N samples, KD is simulated via kurtosis (κ) computed via (Misra *et al.*, 2009, eqs. (1) and (2)) for a factor z determined via the KD's FAR expression (Misra *et al.*, 2009, eq. (5)). Thereafter, a no RFI detection interval of $3 - z\sigma_{R0} \leq \kappa \leq 3 + z\sigma_{R0}$ (Misra *et al.*, 2009; De Roo *et al.*, 2007) is deployed for $\sigma_{R0} = \sqrt{\frac{24}{N}}$—

$N > 5 \times 10^4$—being the standard deviation of the RFI-free kurtosis (De Roo *et al.*, 2007, Sec. III).

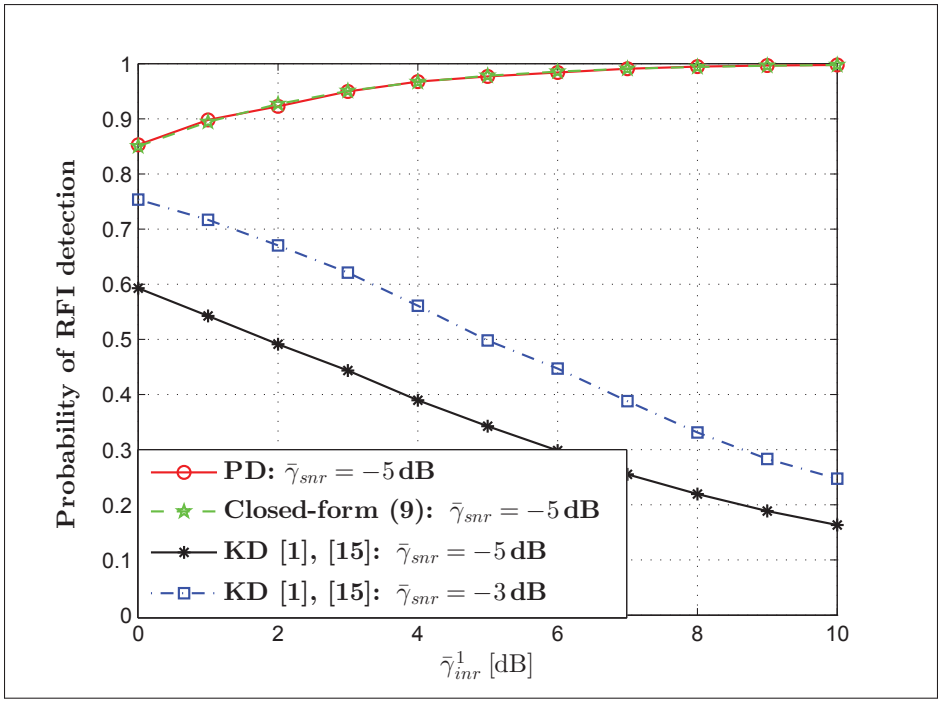

Figure 2.2 P_d versus $\bar{\gamma}^1_{inr}$: $P_f = 0.1$ and $N = 10^5$. Note that (9) stands for (2.9), [1] represents (Misra *et al.*, 2009), and [15] represents (De Roo *et al.*, 2007)

With regards to the desired FAR of 0.1, the P_d exhibited by PD and KD is depicted via Fig. 2.2 which showcases—for a broadband RFI—that the former outperforms the latter. The substantial performance gain is attributed to the fact that PD takes the mean received RFI power into account unlike KD that relies on kurtosis. Specifically, KD relies on the fact that the kurtosis of a Gaussian signal equals three (Misra *et al.*, 2009; Ruf *et al.*, 2006). If the kurtosis is different from three, an RFI would, thus, be detected. However, when a Gaussian RFI impinges, the respective kurtosis also becomes three which makes KD fail to detect a Gaussian RFI, as reported in (Misra *et al.*, 2009) and (Ruf *et al.*, 2006). Despite intercepting the received signal for a much longer duration, Fig. 2.2 demonstrates that KD fails to detect a Gaussian RFI, especially at high INRs. Remarkably, the Gaussian RFI superimposes on the AWGN indiscriminately rendering KD to be an SOI detector operating as per the signal-to-interference-plus-noise ratio (SINR).

As seen in Fig. 2.2 for higher INRs which result in small SINRs, KD suffers a performance loss in RFI detection which is the implicit result of a poor SOI detection at small SINRs. For small INRs leading to relatively larger SINRs, on the other hand, the performance of KD gets better—for the better detection of the SOI at relatively larger SINRs—though it is still inferior to PD's. Furthermore, Fig. 2.2 validates (2.9).

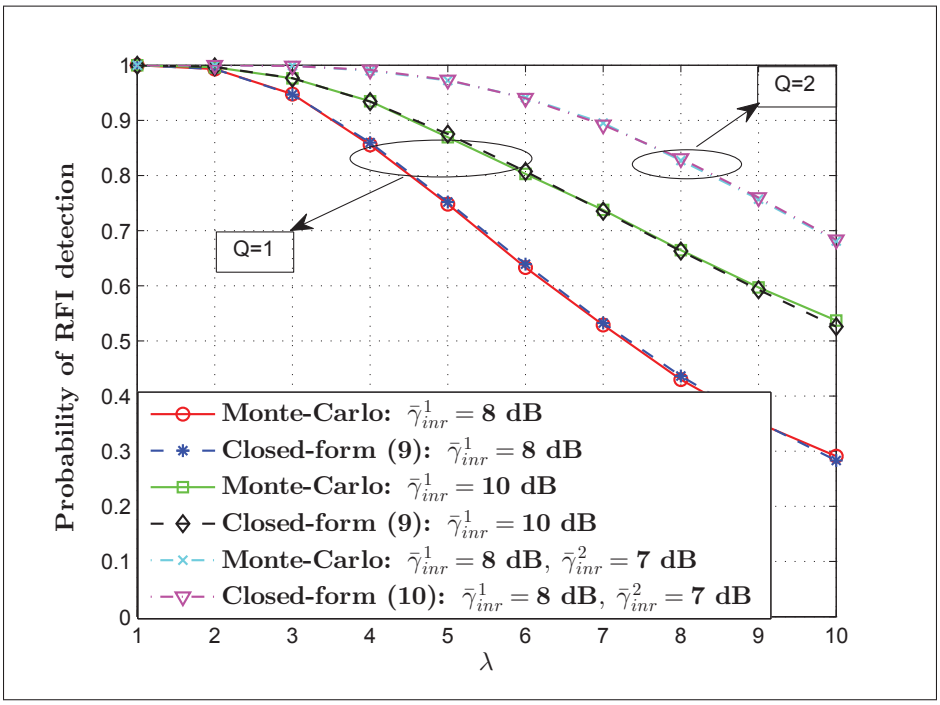

Figure 2.3 P_d versus λ: $\bar{\gamma}_{snr} = 0$ dB. Note that (9) and (10) stand for (2.9) and (2.10), respectively

Figs. 2.3 and 2.4, respectively, depict the P_d and P_f exhibited by PD. As demonstrated via Fig. 2.3, the numerical results of the exact expressions for P_d and the Monte-Carlo simulations are in a perfect overlap validating (2.9) and (2.10). In addition, Fig. 2.3 demonstrates that the detection performance of PD improves with the number of RFIs, as also shown in Lemma 1. Fig. 2.4 also corroborates an overlap between the numerical results of the exact expression for P_f and the Monte-Carlo simulations irrespective of $\bar{\gamma}_{snr}$. Hence, simulations also validate (2.12).

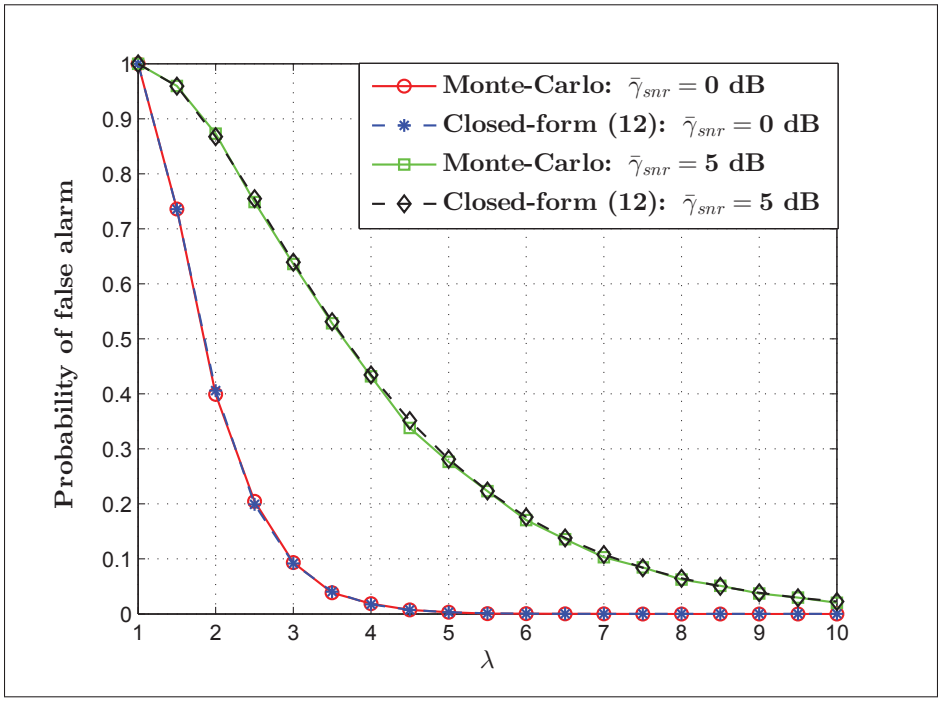

Figure 2.4 P_f versus λ. Note that (12) stands for (2.12)

Eventually, the complementary receiver operating characteristics (ROC) of PD is depicted via Fig. 2.5, where the probability of miss (P_m)—simulated as $P_m = 1 - P_d$—decreases as P_f increases and vice versa. Thus, such a natural trade-off is demonstrated while validating (2.9) and (2.12).

2.6 Conclusions

A computationally simple power-based broadband RFI detector is investigated. Contrary to the prior works, exact closed-form expressions for the probabilities of RFI detection and of false alarm are derived and validated through simulations. Simulations also corroborate that PD outperforms KD. Toward an efficient mitigation of broadband RFI(s), this paper finds applications in radio frequency operating systems that may suffer from broadband RFI(s). Moreover, this paper inspires further research toward an interference-aware SNR estimation.

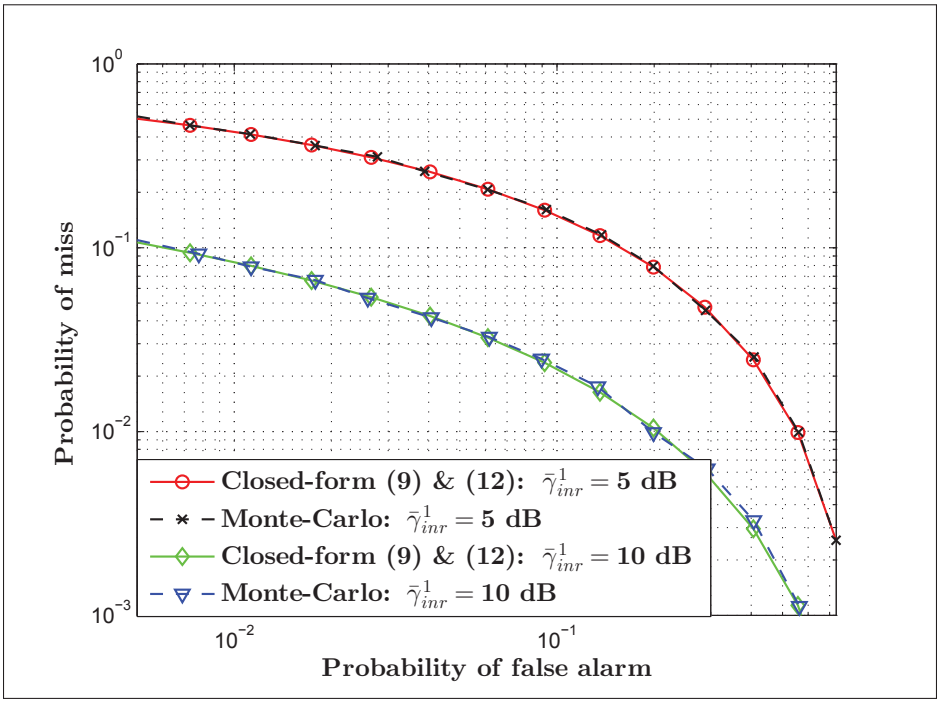

Figure 2.5 Complementary ROC: $\bar{\gamma}_{snr} = 0$ dB and 5×10^4 realizations. Note that (9) and (12) stand for (2.9) and (2.12), respectively

Acknowledgments

The authors acknowledge the funding provided by AVIO-601 Project; the Editor and the anonymous reviewers for helping them improve this manuscript significantly.

CHAPTER 3

PERFORMANCE ANALYSIS OF ENERGY-BASED RFI DETECTOR

Tilahun M. Getu[1,2], Wessam Ajib[2], and René Jr. Landry[1]

[1] Department of Electrical Engineering, École de Technologie Supérieure,
1100 Notre-Dame West, Montréal, Québec, Canada H3C 1K3
[2] Department of Computer Sciences, Université du Québec à Montréal,
201 Av. President-Kennedy, Montréal, Québec, Canada H2X 3Y7

This article was published in *IEEE Transactions on Wireless Communications* as of October 2018 (Getu *et al.*, 2018b).

"I am not discouraged, because every wrong attempt discarded is another step forward."—Thomas Edison

Abstract—As radio frequency interference (RFI) affects many systems operating radio frequencies, RFI detection is essential for excising such RFI efficiently. For this reason, here we investigate an energy-based RFI detector for wireless communication systems suffering from RFI. For this detector, its average probability of RFI detection is studied and approximated, and asymptotic closed-form expressions are derived. Besides, an exact closed-form expression for its average probability of false alarm is derived. Monte-Carlo simulations validate the derived analytical expressions and corroborate that the investigated energy detector (ED) outperforms a kurtosis detector (KD)—even under the scenario that KD intercepts the received signal for a longer interval—and a generalized likelihood ratio test (GLRT) detector. At last, the performance of ED is also assessed using real-world RFI contaminated data.

Index Terms—RFI detection and excision, energy detection, performance analysis, GLRT detector, real-world data.

3.1 Introduction

Radio frequency interference (RFI) can arise from either intentional or unintentional interferers; for example, out-of-band emissions by nearby transmitters and harmonics, jamming,

spoofing, and meaconing (Getu *et al.*, 2017, 2016, 2015b; Misra *et al.*, 2009; Jeffs *et al.*, 2005; Kaplan & Hegarty, 2006). As a result, RFI is becoming increasingly common in microwave radiometry (Misra *et al.*, 2009), radio astronomy (Jeffs *et al.*, 2005), and satellite communications (Borio *et al.*, 2008). For instance, global navigation satellite system (GNSS) and very small aperture terminal (VSAT) are increasingly suffering from RFI. In this respect, it is attested by (Newtec and IRG, Sep. 2013) that 93% of the satellite industry suffer from interference. Moreover, RFI occurs in ultra-wideband communication systems for narrowband interferers (Shi *et al.*, 2007); radar systems because of jammers (De Maio & Orlando, 2016); and cognitive radios for an imperfect spectrum sensing (Getu *et al.*, 2015a) and neighboring primary users emitting RFI (Boulogeorgos *et al.*, 2016b). Such primary users can constrain the spectrum sensing capability of an energy detector (Boulogeorgos *et al.*, 2016b).

The state-of-the-art encompasses several RFI detectors proposed for either microwave radiometry or GNSS applications. The RFI detection techniques based on kurtosis (Misra *et al.*, 2009; Ruf *et al.*, 2006), moment ratio (MR) (De Roo & Misra, 2010), fast Fourier transforms (Balaei & Dempster, 2009), spectrogram and discrete Wigner-Ville distribution (DWVD) (Borio *et al.*, 2008), and transformed-domain (Dovis *et al.*, 2012) are the main ones. However, these RFI detectors generally have limited applications and exhibit a lack of sufficient analytical performance characterizations with respect to (w.r.t.) a decision threshold.

In a mathematical context, while presuming a receiving reference antenna, the RFI detection problem can be posed as an adaptive radar detection problem tackled in (Ciuonzo *et al.*, 2016a,b, 2017; Aubry *et al.*, 2014) by exchanging the RFI and the signal of interest (SOI). As the RFI target vectors are generally unknown, nonetheless, the consideration of known left and right subspaces corresponding to the signal and/or interference makes the aforementioned detectors hardly realistic. For the same multi-antenna setting, the RFI detection problem can also be formulated in terms of the blind adaptation problems of (Scharf & McCloud, 2002) or the matched subspace detection problems of (Scharf & Friedlander, 1994); a source enumeration (Lu & Zoubir, 2015) problem of “two sources” versus “one source”; and a rank-1 signal detection problem (Ramírez *et al.*, 2011). Nevertheless, the blind adaptation techniques

of (Scharf & McCloud, 2002) require the knowledge of the subspaces spanned by the SOI and RFI and the matched subspace detectors of (Scharf & Friedlander, 1994) rely on the known subspaces spanned by the SOI and/or RFI; the two-step test of (Lu & Zoubir, 2015) cannot be adopted here, as the SOI and RFI are not necessarily Gaussian random processes; and (Ramírez *et al.*, 2011) can not be applied here for the multi-antenna SOI channel gains are not necessarily known and the underlying signals are not necessarily Gaussian random processes. Considering these reasons, further research toward a computationally simple and practically relevant RFI detector is worth pursuing.

In an energy detector (ED), on the other hand, energy detection is performed by comparing the incoming signal energy to a given threshold (Herath *et al.*, 2011). It was first used by Urkowitz (Urkowitz, 1967) for detecting unknown deterministic signals in white Gaussian noise. Recently, ED and its variants were deployed for the detection of unknown signals over fading channels (Herath *et al.*, 2011; Sofotasios *et al.*, 2016; Digham *et al.*, 2007), spectrum sensing in cognitive radio (Atapattu *et al.*, 2014; Gismalla & Alsusa, 2011; Gokceoglu *et al.*, 2014; Boulogeorgos *et al.*, 2016a), cooperative spectrum sensing in cognitive radio networks (Tavana *et al.*, 2017; Quan *et al.*, 2008), the design of ultra-wideband receivers (D'Amico *et al.*, 2007; Gishkori & Leus, 2013), and in an integrated information and energy receiver (Zhou *et al.*, 2013). Despite its widespread applications, the deployment and characterization of ED for RFI detection pose challenges. First, the distribution of the received signal when an RFI occurs is unknown for an unknown RFI distribution. Second, determining the average probability of RFI detection depends on the unknown distribution of the received signal which is directly affected by several random variables (RVs).

Accordingly, this paper investigates an energy-based RFI detector for wireless communication systems and assesses its applicability in the context of the Very Large Array (VLA) (NRAO, 2017) also by conducting real-world data based simulations. At first, the detector computes the received signal energy by exploiting the sampling theorem representation of bandlimited signals. Thereafter, it passes a decision about the RFI by comparing the computed energy with a decision threshold. Specifically, the main contributions of this paper are itemized below.

- We deploy the ED test statistic for the detection of RFI.
- Upon the reception of any kind of RFI, we show that the energy-based decision statistic admits the noncentral chi-square distribution with $2u$ degrees of freedom (DoF)—u being the time-bandwidth product—and a noncentrality parameter that depends on the signal-to-noise ratio (SNR), the interference-to-noise ratio (INR), the SOI, and the RFI.
- Approximated and asymptotic expressions are derived for the average probability of RFI detection. For the average probability of false alarm, an exact expression is derived.
- Simulations assess the performance of ED and validate the derived expressions.
- The performance of ED is also assessed using real-world RFI contaminated data.

Following this introduction, Sec. 3.2 describes the system model and the investigated detection. Sec. 3.3 details the performance analysis. Sec. 3.4 and Sec. 3.5 present the simulation results and the real-world data based simulations, respectively. Finally, the paper conclusions and outlooks are composed in Sec. 3.6.

Notation: Upper-case letters, italic letters, lower-case boldface letters, and upper-case boldface letters denote RVs, the values assigned to RVs, vectors, and matrices, respectively; $\triangleq$, $>>$, $\sim$, $\rightarrow$, and $n!$ denote equal by definition, much greater than, distributed as, approaches to, and n factorial, respectively; $*$, $\frac{\partial}{\partial x}$, $|$, $\mathrm{Re}\{\cdot\}$, $\mathscr{O}(\cdot)$, and χ^2 imply a discrete-time convolution, partial differentiation w.r.t. x, under, real part, the Landau notation, and chi-square, respectively; $\mathbb{E}\{\cdot\}$, $\Pr\{\cdot\}$, $U(\cdot)$, $I_n(\cdot)$, and $Q_u(\cdot,\cdot)$ stand for expectation, the probability of, the unit-step function defined via $U(y \geq 0) = 1$, the nth-order modified Bessel function of the first kind, and the uth-order generalized Marcum Q-function, respectively; and $\Gamma(\cdot)$, $\Gamma(\cdot,\cdot)$, $\mathscr{G}(\cdot,\cdot)$, $\mathscr{NA}(\cdot,\cdot)$, ${}_1F_1(\cdot;\cdot;\cdot)$, and $G_{\cdot,\cdot}^{\cdot,\cdot}(\cdot)$ implicate the gamma function, the (upper) incomplete gamma function, the gamma distribution, the Nakagami-m distribution, the special case of the generalized hypergeometric function (Gradshteyn & Ryzhik, 2007, eq. (9.14-1)), and the Meijer G-function (Gradshteyn & Ryzhik, 2007, eq. (9.301)), respectively.

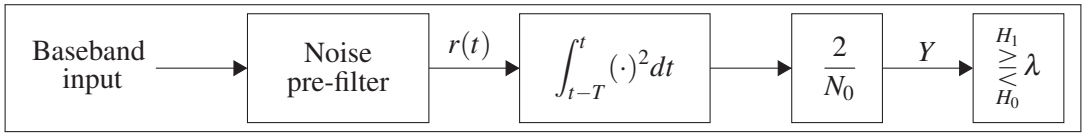

Figure 3.1 The investigated energy-based RFI detector

3.2 System Model and the Investigated Detection

3.2.1 System Model

We consider a received signal downconverted to its baseband equivalent. As shown in Fig. 3.1 that depicts the investigated ED, we assume that the baseband signal is filtered by the ideal noise pre-filter that has the bandwidth of the SOI. The presumed filter not only limits the noise bandwidth but also the bandwidth of RFI, if any (Urkowitz, 1967). To overcome aliasing, this paper assumes that the sampling operations obey the Nyquist sampling criterion (Oppenheim & Schafer, 2010). Since the Nakagami-*m* distribution offers the best fit to land-mobile, indoor-mobile multi-path propagation, and scintillating ionospheric radio links (Abdi *et al.*, 2003), (Simon & Alouini, 2005, p. 25), it is adopted by this paper to model the SOI and RFI fading channels. These narrowband channels are assumed to be flat fading channels since they have a good agreement with the experimental data (Loo, 1985; De Gaudenzi & Giannetti, 1998). Meanwhile, we assume that detection is performed only after the reception phase of pilot (preamble) symbols, if any.

The considered SOI can exhibit a one- or two-dimensional (2D) modulation schemes. For 2D schemes, ED can be integrated into the in-phase and/or quadrature component of a dedicated receiver (Proakis & Salehi, 2008). Specifically, we consider the SOI being the baseband equivalent of a deterministic passband signal—denoted by $\tilde{s}(t)$—given as $\tilde{s}(t) \in \left\{ s_k(t) = \mathrm{Re}\left\{ A_k p(t) e^{j2\pi f_c t} \right\} \right\}_{k=1}^{M}$ (Proakis & Salehi, 2008, eq. (3.2–45)) for $p(t)$, f_c, and M being a rectangular pulse of duration T_s, carrier frequency, and the modulation order, respectively; $A_k = 2k - 1 - M$, $A_k = e^{j\frac{2\pi}{M}(k-1)}$, and $A_k = A_k^I + jA_k^Q$ for M-ary pulse amplitude modulation

(PAM), M-ary phase shift keying (PSK), and M-ary quadrature amplitude modulation (QAM), respectively. To continue, a noise pre-filtered received baseband signal—denoted by $r(t)$—is expressed via a binary hypothesis test as

$$r(t) = \begin{cases} hs(t) + gv(t) + z(t) & : H_1 \\ hs(t) + z(t) & : H_0, \end{cases} \tag{3.1}$$

where H_0 and H_1 are hypotheses regarding the absence and presence of the RFI, respectively; $s(t)$ and $v(t)$ denote the aforementioned SOI and an RFI assumed unknown and deterministic, respectively; $h \sim \mathcal{NA}(m_1, \bar{h}_s)$ is the SOI channel gain for m_1 being the SOI fading severity parameter and $\bar{h}_s \triangleq \mathbb{E}\{h^2\}$; $g \sim \mathcal{NA}(m_2, \bar{g}_s)$ is the RFI channel gain for m_2 being the RFI fading severity parameter and $\bar{g}_s \triangleq \mathbb{E}\{g^2\}$; and $z(t)$ is a zero mean additive white Gaussian noise (AWGN) process with a known power spectral density of N_0 W/Hz. For analytical tractability, these assumptions are considered: m_1 and m_2 are integers; h and g are linearly independent.

3.2.2 The Investigated Detection

The investigated ED is diagrammed in Fig. 3.1, where the baseband input is, first, filtered by an ideal noise pre-filter. Second, squaring followed by a finite time integration produces the energy over T of the input signal (Urkowitz, 1967). Third, the energy is multiplied by $2/N_0$ to generate a decision variable Y. At Last, H_1 is detected when Y is greater than a decision threshold λ. Otherwise, H_0 is detected.

3.3 Performance Analysis

Hereinafter, the performance of the energy-based RFI detector is analyzed. In particular, approximated and asymptotic closed-form expressions are derived for the average probability of RFI detection. To do so, the probability density function (PDF) and the cumulative distribution function (CDF) of the ED test statistic are derived when an unknown RFI impinges on the receiver. Having employed the ED test statistic's PDF and CDF corresponding to the signal present hypothesis in the spectrum sensing (Atapattu *et al.*, 2014; Gismalla & Alsusa, 2011;

Gokceoglu *et al.*, 2014; Boulogeorgos *et al.*, 2016a) and unknown signal detection problems (Herath *et al.*, 2011; Sofotasios *et al.*, 2016; Digham *et al.*, 2007), the average probability of false alarm is also derived.

3.3.1 Distribution of the ED Test Statistic

From Fig. 3.1, the decision variable is equated as

$$Y \triangleq \frac{2}{N_0}\int_{t-T}^{t} r^2(t)dt. \tag{3.2}$$

Let $E_s = \int_{t-T}^{t} s^2(t)dt$ be the SOI energy; $\gamma_{snr} = h^2\frac{E_s}{N_0}$ be the SNR; and $f_{Y|H_0}(y)$ be the PDF of $Y|H_0$. Having been derived using the sampling theorem representation for bandlimited signals, $f_{Y|H_0}(y)$ admits the noncentral χ^2–distribution with $2u$ DoF and a noncentrality parameter $2\gamma_{snr}$ (Herath *et al.*, 2011; Urkowitz, 1967; Digham *et al.*, 2007). Thus,

$$f_{Y|H_0}(y) = \frac{1}{2}\big(y/2\gamma_{snr}\big)^{\frac{u-1}{2}} e^{-\frac{2\gamma_{snr}+y}{2}} I_{u-1}(\sqrt{2\gamma_{snr}y}). \tag{3.3}$$

The CDF under H_0—$F_{Y|H_0}(y) = \Pr\big\{Y \leq y|H_0\big\} = \int_{-\infty}^{y} f_{Y|H_0}(y)dy$—simplifies to

$$F_{Y|H_0}(y) = 1 - Q_u(\sqrt{2\gamma_{snr}}, \sqrt{y}). \tag{3.4}$$

Meanwhile, the distribution of $Y|H_1$ is characterized by the following theorem.

Theorem 2. Let $E_v = \int_{t-T}^{t} v^2(t)dt$ be the RFI energy. For any type of RFI, $Y|H_1$ admits the noncentral χ^2–distribution with $2u$ DoF and a noncentrality parameter ρ given by

$$\rho = 2(\gamma_{snr} + \gamma_{inr}) + \frac{2hg}{\sigma^2}\sum_{j=1}^{2u}\alpha_j\beta_j, \tag{3.5}$$

where W is the bandwidth of the SOI, $u = TW$, $\gamma_{inr} = g^2\frac{E_v}{N_0}$ defines the INR, $\alpha_j = s(j/2W)$, and $\beta_j = v(j/2W)$.

Proof. Please refer to Appendix 1 under APPENDIX III.

Employing Theorem 2, the PDF of $Y|H_1$ is given by $f_{Y|H_1}(y) = f_{Y|H_0}(y)\big|_{2\gamma_{snr}=\rho}$. Thus, the CDF of $Y|H_1$ is given by

$$F_{Y|H_1}(y) = \Pr\{Y \leq y|H_1\} = 1 - Q_u(\sqrt{\rho}, \sqrt{y}). \tag{3.6}$$

3.3.2 Average Probability of RFI Detection

The probability of detection $P_d = \Pr\{Y > \lambda|H_1\} = 1 - \Pr\{Y \leq \lambda|H_1\}$ simplifies via (3.6) as

$$P_d = 1 - F_{Y|H_1}(\lambda) = Q_u(\sqrt{\rho}, \sqrt{\lambda}). \tag{3.7}$$

Meanwhile, the P_d given by (3.7) satisfies the underneath theorem.

Theorem 3. Suppose P_s and P_v denote the SOI power and the RFI power, respectively. For the SOI and RFI, respectively, given by $s(t) = \sqrt{P_s}\sum_{n=-\infty}^{\infty} s_n p(t - nT_s)$ and $v(t) = \sqrt{P_v}\sum_{n=-\infty}^{\infty} v_n p(t - nT_s)$,

$$P_d \geq Q_u(\sqrt{2(\gamma_{snr} + \gamma_{inr})}, \sqrt{\lambda}), \tag{3.8}$$

if and only if (iff) $\sum_{j=1}^{2u} s_j v_j \geq 0$ and both signals experience non-deep fading channels.

Proof. Employing (3.5) in (3.7) and considering two cases—$\sum_{j=1}^{2u} s_j v_j = 0$ and $\sum_{j=1}^{2u} s_j v_j > 0$—via (Sun *et al.*, 2010, eq. (24)), the inequality in (3.8) follows. □

For the SOI and RFI as in Theorem 3, an approximated expression is derived in the sequel.

3.3.2.1 Approximated Expression

Note that the P_d given by (3.7) depends on the distribution of ρ which, in turn, depends on the joint distribution of several RVs. As detailed in Appendix 2 (under APPENDIX III), deriving

the PDF of ρ is either mathematically intractable or too complex. Consequently, we derive the approximated PDF of ρ which is stated below.

Theorem 4. Let $\Xi_{\eta_1\eta_2}^{m_1m_2}(i,k)$ be a weight defined in (Karagiannidis *et al.*, 2006a, eq. (A-5)); $\bar{\gamma}_{snr}$ be the average SNR; and $\bar{\gamma}_{inr}$ be the average INR. For $P_C(c_j) = \Pr\{s_j\}\Pr\{v_j\}$—$c_j = s_j v_j$, $(\eta_1,\eta_2) = \left(\frac{\bar{\gamma}_{snr}}{m_1}, \frac{\bar{\gamma}_{inr}}{m_2}\right) = \left(\frac{\bar{h}_s P_s \sum_{j=1}^{2u}\mathbb{E}\{s_j^2\}}{2m_1N_0W}, \frac{\bar{g}_s P_v \sum_{j=1}^{2u}\mathbb{E}\{v_j^2\}}{2m_2N_0W}\right)$, and

$$P_{Y_4}(r) = \underbrace{P_C(r) * P_C(r) * \cdots * P_C(r)}_{2u-1 \text{ fold discrete-time convolution}}, \quad r = \textstyle\sum_{j=1}^{2u} s_j v_j, \tag{3.9}$$

the approximated PDF of ρ is given by (3.10).

Proof. Please see Appendix 2 under APPENDIX III.

$$f_P(\rho) \approx \sum_{i=1}^{2}\sum_{k=1}^{m_i} \Xi_{\eta_1\eta_2}^{m_1m_2}(i,k)\left[\frac{\rho^{k-1}e^{-\frac{\rho}{2\eta_i}}P_{Y_4}(0)}{(2\eta_i)^k(k-1)!} + \sum_{r\in\mathscr{M}\setminus\{0\}} \frac{2P_{Y_4}(r)G_{0,2}^{2,0}\left(\frac{\rho^2}{4\eta_1\eta_2 r^2}\middle|\begin{matrix}-\\ m_1,m_2\end{matrix}\right)}{\rho(m_1-1)!(m_2-1)!}\right]U(\rho). \tag{3.10}$$

Remark 2. The right-hand side (RHS) of (3.10) is a valid PDF.

Proof. Please refer to Appendix 3 under APPENDIX III.

Using Theorem 4, the average probability of RFI detection—denoted by $\bar{P}_d$—can be approximated as

$$\bar{P}_d \approx \int_0^\infty P_d f_P(\rho) d\rho \approx \int_0^\infty Q_u(\sqrt{\rho},\sqrt{\lambda}) f_P(\rho) d\rho. \tag{3.11}$$

Meanwhile, the approximated expression is stated below.

Theorem 5. For $\prod_{m_1}^{m_2} = (m_1-1)!(m_2-1)!$, the approximated average probability of RFI detection is given by (3.12).

Proof. Please refer to Appendix 4 under APPENDIX III.

$$\bar{P}_d \approx 1 - e^{-\frac{\lambda}{2}} \sum_{n=u}^{\infty} \sum_{l=0}^{\infty} \sum_{i=1}^{2} \sum_{k=1}^{m_i} \frac{\lambda^{n+l} \Xi_{\eta_1\eta_2}^{m_1 m_2}(i,k)}{2^n l!(n+l)!} \left[\frac{P_{Y_4}(0)(l+k-1)!\eta_i^l}{2^l(1+\eta_i)^{l+k}(k-1)!} + \sum_{r \in \mathscr{M} \setminus \{0\}} \frac{P_{Y_4}(r)}{\sqrt{\pi}\prod_{m_1}^{m_2}} G_{2,2}^{2,2}\left(\frac{4}{\eta_1\eta_2 r^2} \middle|_{m_1,m_2}^{\frac{1-l}{2}, \frac{2-l}{2}} \right) \right]. \quad (3.12)$$

From (3.12), $\lim_{u\to\infty} \bar{P}_d \to 1$. Thus, the detection of RFI is certain on average when T gets larger. As $(\eta_1, \eta_2) \to (0, \infty)$, $(\bar{\gamma}_{snr}, \bar{\gamma}_{inr}) \to (0, \infty)$. Similarly, as $(\eta_1, \eta_2) \to (\infty, 0)$, $(\bar{\gamma}_{snr}, \bar{\gamma}_{inr}) \to (\infty, 0)$. Therefore, employing (Karagiannidis *et al.*, 2006a, eq. (A-5)) and (3.12), $\lim_{(\bar{\gamma}_{snr}, \bar{\gamma}_{inr}) \to (0,\infty)} \bar{P}_d = \lim_{(\bar{\gamma}_{snr}, \bar{\gamma}_{inr}) \to (\infty,0)} \bar{P}_d \to 1$, as $G_{2,2}^{2,2}(\cdot)$ approaches zero when $\frac{1}{\eta_1\eta_2}$ approaches ∞. This implies that ED detects RFI certainly whenever there is a big difference between the strength of the SOI and RFI.

3.3.2.2 Asymptotic Expression

The expression for $\bar{P}_d$ whenever $\gamma_{inr} >> \gamma_{snr}$ is derived subsequently. In this case, (3.5) simplifies to $\rho \approx 2\gamma_{inr}$ which is plugged into (3.7) to give

$$P_d \approx Q_u(\sqrt{2\gamma_{inr}}, \sqrt{\lambda}). \quad (3.13)$$

In (3.13), $\gamma_{inr} \sim \mathscr{G}(m_2, \bar{\gamma}_{inr})$ for $g \sim \mathscr{NA}(m_2, \bar{g}_s)$. Thus, $\bar{P}_d$ demands averaging over the gamma PDF $f_Y(\gamma_{inr}; m_2, \eta_2) = \frac{(\gamma_{inr})^{m_2-1}}{\eta_2^{m_2}\Gamma(m_2)} e^{-\frac{\gamma_{inr}}{\eta_2}} U(\gamma_{inr})$ (Karagiannidis *et al.*, 2006a, eq. (2)) which is employed in (3.11) to render

$$\bar{P}_d \approx \frac{m_2^{m_2}}{(\bar{\gamma}_{inr})^{m_2}\Gamma(m_2)} \int_0^{\infty} \frac{Q_u(\sqrt{2y}, \sqrt{\lambda}) y^{m_2} e^{-\frac{m_2 y}{\bar{\gamma}_{inr}}}}{y} dy \Big|_{y=\gamma_{inr}}. \quad (3.14)$$

Using (Simon & Alouini, 2005, eq. (4.63)), (3.14) simplifies to

$$\bar{P}_d \approx 1 - \frac{e^{-\frac{\lambda}{2}}}{\Gamma(m_2)} \left(\frac{m_2}{\bar{\gamma}_{inr}} \right)^{m_2} \sum_{n=u}^{\infty} \left(\lambda/2 \right)^{n/2} \times \int_0^{\infty} e^{-\left(1+\frac{m_2}{\bar{\gamma}_{inr}}\right)y} y^{m_2-1-n/2} I_n(\sqrt{2\lambda y}) dy \Big|_{y=\gamma_{inr}}. \quad (3.15)$$

Following (Herath *et al.*, 2011, eqs. (4) and (5)), the asymptotic average probability of RFI detection is given by

$$\bar{P}_d \approx 1 - e^{-\frac{\lambda}{2}} \kappa^{m_2} \sum_{n=u}^{\infty} (n!)^{-1} \left(\lambda/2 \right)^n {}_1F_1\left(m_2; n+1; \lambda\mu/2 \right), \quad (3.16)$$

where $\kappa = \frac{m_2}{\bar{\gamma}_{inr}+m_2}$ and $\mu = \frac{\bar{\gamma}_{inr}}{\bar{\gamma}_{inr}+m_2}$. From (3.16), $\lim_{\bar{\gamma}_{inr}\to\infty} \bar{P}_d \to 1$. Thus, as the RFI gets stronger, ED detects it with certainty.

Remark 3. Note that (3.16) coincides with the average probability of a deterministic signal detection over the Nakagami-*m* fading channel exhibited by ED (Herath *et al.*, 2011, eq. (5)).

It is to be noted that the aforementioned analyses also encompass the scenario that the SOI and RFI are non-overlapping after the initial filtering. In this scenario, the filtered RFI would have a bandwidth less than the bandwidth of the SOI. Consequently, the intercepted RFI energy becomes smaller by the virtue of Parseval's theorem (Proakis & Salehi, 2008); so does the average INR. Therefore, this is similar to the overlapping case with a reduced average INR.

3.3.3 Average Probability of False Alarm

As the RFI absent hypothesis—in the RFI detection problem—is the signal present hypothesis in the spectrum sensing and unknown signal detection problems (Herath *et al.*, 2011; Sofotasios *et al.*, 2016; Digham *et al.*, 2007; Atapattu *et al.*, 2014; Gismalla & Alsusa, 2011; Gokceoglu *et al.*, 2014; Boulogeorgos *et al.*, 2016a), (3.3) and (3.4) can be used to derive the average probability of false alarm—denoted by $\bar{P}_f$—for a given λ. Using (3.4), the probability of false alarm $P_f = \Pr\{Y > \lambda | H_0\} = 1 - \Pr\{Y \leq \lambda | H_0\}$ becomes

$$P_f = 1 - F_{Y|H_0}(\lambda) = Q_u(\sqrt{2\gamma_{snr}}, \sqrt{\lambda}). \quad (3.17)$$

For a given h, P_f is given by (3.17). Thus, $\bar{P}_f$ is obtained by averaging (3.17) over $f_Y(\gamma_{snr};m_1,\eta_1) = f_Y(\gamma_{inr};m_2,\eta_2)\big|_{(\gamma_{inr},m_2,\eta_2)=(\gamma_{snr},m_1,\eta_1)}$. Doing so by following (3.14)-(3.16),

$$\bar{P}_f = 1 - e^{-\frac{\lambda}{2}}\tilde{\kappa}^{m_1}\sum_{n=u}^{\infty}(n!)^{-1}\left(\lambda/2\right)^n {}_1F_1\left(m_1;n+1;\lambda\tilde{\mu}/2\right), \tag{3.18}$$

where $\tilde{\kappa} = \frac{m_1}{\bar{\gamma}_{snr}+m_1}$ and $\tilde{\mu} = \frac{\bar{\gamma}_{snr}}{\bar{\gamma}_{snr}+m_1}$. Employing (3.18), $\lim_{\bar{\gamma}_{snr}\to\infty}\bar{P}_f \to 1$. Thus, as the SOI gets stronger, ED would exhibit the maximum false alarm rate (FAR) for it would confuse the SOI for the RFI.

Remark 4. For the matching of hypotheses, (3.18) is identical with the average probability of a deterministic signal detection over the Nakagami-*m* fading channel (Herath *et al.*, 2011, eq. (5)).

Summarizing the overall performance analysis, (3.12) implies that the average detection performance of ED depends on the relative strength of the SOI w.r.t. the RFI and vice versa. Since (3.12) is valid—by the virtue of Theorem 2—irrespective of the type of RFI, the aforementioned dependence is valid regardless of the type of RFI. Similarly, it is inferred from (3.18) that the exhibited average FAR increases with the average strength of the SOI. Most important, because only the signal energy matters; not its form, ED can be applied for the detection of any deterministic signal (Urkowitz, 1967, Sec. I). Therefore, once the received signal is downconverted to its baseband equivalent, ED can be applied in both satellite (see Fig. 3.2) and terrestrial (for instance, see (Proakis & Salehi, 2008, Figs. 5.1–1 and 5.1–2)) communications regardless of their difference in the pre-baseband signal processing. Talking about practical applicability, however, ED requires an accurate noise power estimator, as it relies on the knowledge of the noise power.

3.4 Simulation Results

Without loss of generality, ED is applied in the context of a VSAT communication system. For a VSAT receiver located in a rural area free from scattering, the reception of a binary PSK

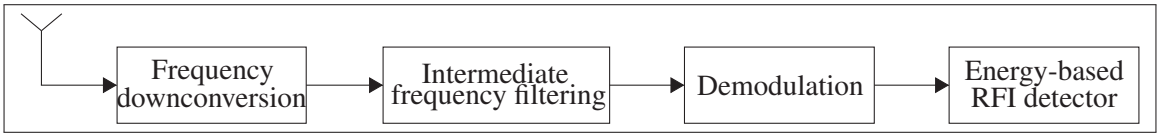

Figure 3.2 The simulated VSAT (Maral, 2003) scenario

(BPSK) modulated SOI transmitted by a regenerative geostationary earth orbit (GEO) satellite, a BPSK modulated RFI possibly emitted by a regenerative GEO satellite, and a line-of-sight reception are assumed. Moreover, the channel models and assumptions outlined in Sec. 3.2.1 are deployed.

Table 3.1 Simulation parameters unless otherwise mentioned

Parameters	Assigned value
(m_1, m_2)	$(2,2)$
(σ^2, P_s, P_v)	$(1\,\mathrm{W}, 10\,\mathrm{W}, 10\,\mathrm{W})$
No. of realizations	10^5

Table 3.2 Complexity comparison in terms of the number (No.) of multiplications and additions

Detectors	No. of multiplications	No. of additions
ED	$2u+1$	$2u-1$
KD	$12u+5$	$8u-4$

The simulated VSAT scenario is depicted in Fig. 3.2, where the received baseband signal after noise pre-filtering is modeled based on the GNSS received signal model in (Borio, 2008, eq. (2.2)). As seen in Fig. 3.2, ED can be cascaded to the VSAT receiver so as to detect RFI. Regarding the SOI and RFI propagation delays, perfect and identical estimates are assumed rendering a model consistent with (3.1). Having defined the average SNR and INR as in Theorem 4, simulations with parameters of Table 3.1—unless otherwise mentioned—are conducted.

Four results are given to assess the exhibited $\bar{P}_d$. First, a Monte-Carlo simulation named "simulation 1" is conducted via the binarization of (A III-4) w.r.t. λ—while employing (A III-8b)—followed by averaging. Second, (3.12) is implemented by approximating the infinite summations w.r.t. n and l through the first $50-u$ and 50 terms, respectively. Third, "simulation 2" is conducted by averaging (3.7). Fourth, (3.16) is implemented via the approximation of the infinite summation w.r.t. n by the first $50-u$ terms. Three results are presented to assess the exhibited $\bar{P}_f$. First, a Monte-Carlo simulation named "simulation 3" is conducted via the binarization of (A III-4) w.r.t. λ—while employing (A III-8b) and no RFI—followed by averaging. Second, (3.18) is implemented by approximating the infinite summation by the first $50-u$ terms. Third, a simulation named "simulation 4" is conducted by averaging (3.17).

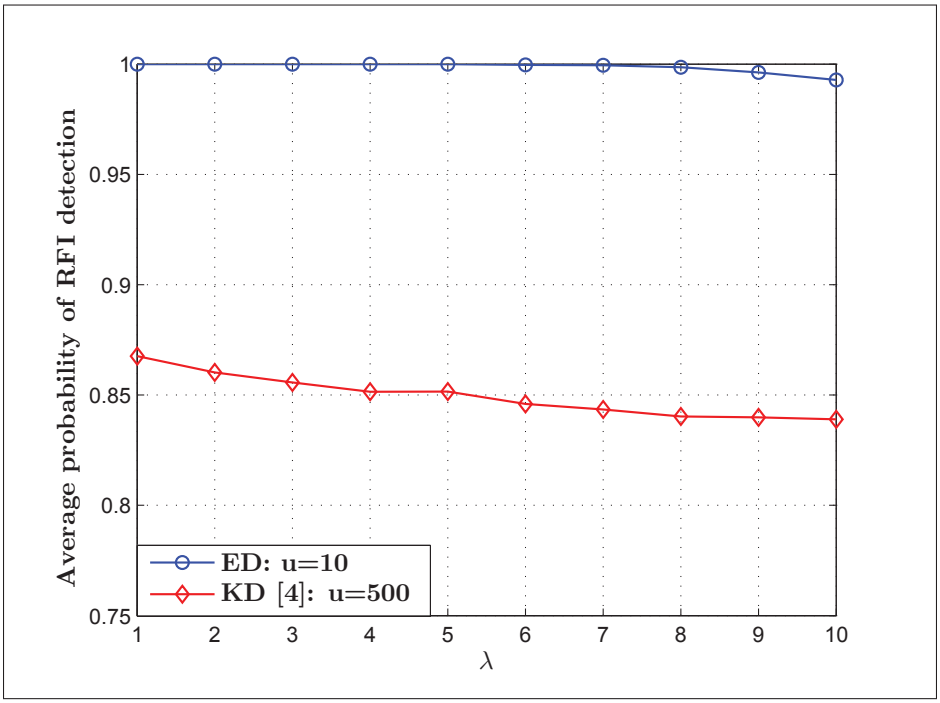

Figure 3.3 Comparison in $\bar{P}_d$: $(\bar{\gamma}_{snr}, \bar{\gamma}_{inr}) = (-5\text{ dB}, 5\text{ dB})$. Note that [4] represents (Misra *et al.*, 2009)

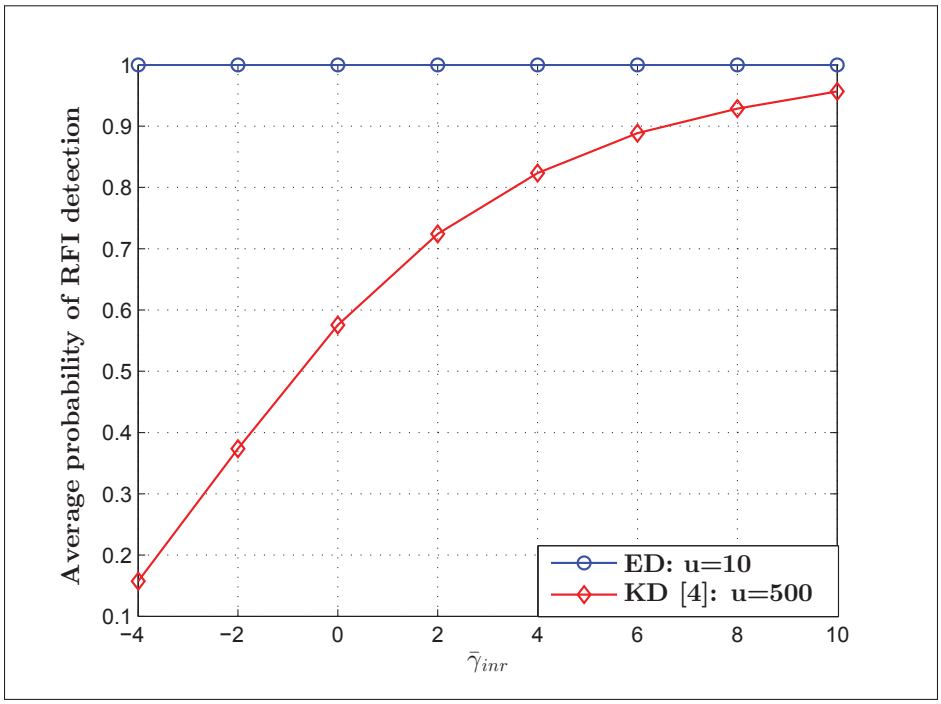

Figure 3.4 Comparison in $\bar{P}_d$: $(\bar{\gamma}_{snr}, \lambda) = (3 \text{ dB}, 2)$. Note that [4] represents (Misra *et al.*, 2009)

3.4.1 Performance Comparison with the State-of-the-art

Amongst the state-of-the-art algorithms (Misra *et al.*, 2009; Borio *et al.*, 2008; Ruf *et al.*, 2006; Balaei & Dempster, 2009; De Roo & Misra, 2010; Dovis *et al.*, 2012), we opt for a performance comparison with a kurtosis detector (KD). The choice is motivated by the fact that KD is a statistical algorithm—like ED—and the remaining ones are sub-optimal techniques that tend to exhibit some heuristics (cf. Appendix 5 under APPENDIX III). To continue, we assume a received baseband signal sampled at $T_s = 1/2W$ apart and conduct a Monte-Carlo simulation for KD (Misra *et al.*, 2009; Ruf *et al.*, 2006). Using this assumption which leads to (A III-8b), the kurtosis (κ) is computed through expectation-based operations in (Misra *et al.*, 2009, eqs. (1) and (2)). As computing expectation requires infinite samples, we update the RFI-free detection threshold stated in (Misra *et al.*, 2009) to our simulation setting. In this regard, we employ a threshold of $3 - \frac{1}{\bar{\gamma}_{inr} \ln(u^2/\lambda)} \leq \kappa \leq 3 + \frac{1}{\bar{\gamma}_{inr} \ln(u^2/\lambda)}$ for the detection of no RFI and perform averaging over 10^5 channel realizations.

Figs. 3.3 and 3.4 depict the $\bar{P}_d$ exhibited by ED and KD. Note that the performance of ED is simulated as per "simulation 1". Although ED intercepts the received signal for the $1/50$th duration of KD's, Fig. 3.3 corroborates that ED outperforms KD regardless of λ for a given $(\bar{\gamma}_{snr}, \bar{\gamma}_{inr})$. Fig. 3.4 also demonstrates that ED outperforms KD regardless of $\bar{\gamma}_{inr}$ for a given $(\bar{\gamma}_{snr}, \lambda)$. These superior performance gains are due to the fact that ED takes the energy of RFI into account to detect RFI unlike KD which relies merely on the kurtosis. Interestingly, such a gain is also guaranteed at a smaller computational complexity, as attested by Table 3.2 which tabulates the complexity comparison of ED and KD based on the test statistics in (A III-4) and (Misra *et al.*, 2009, eqs. (1) and (2)), respectively.

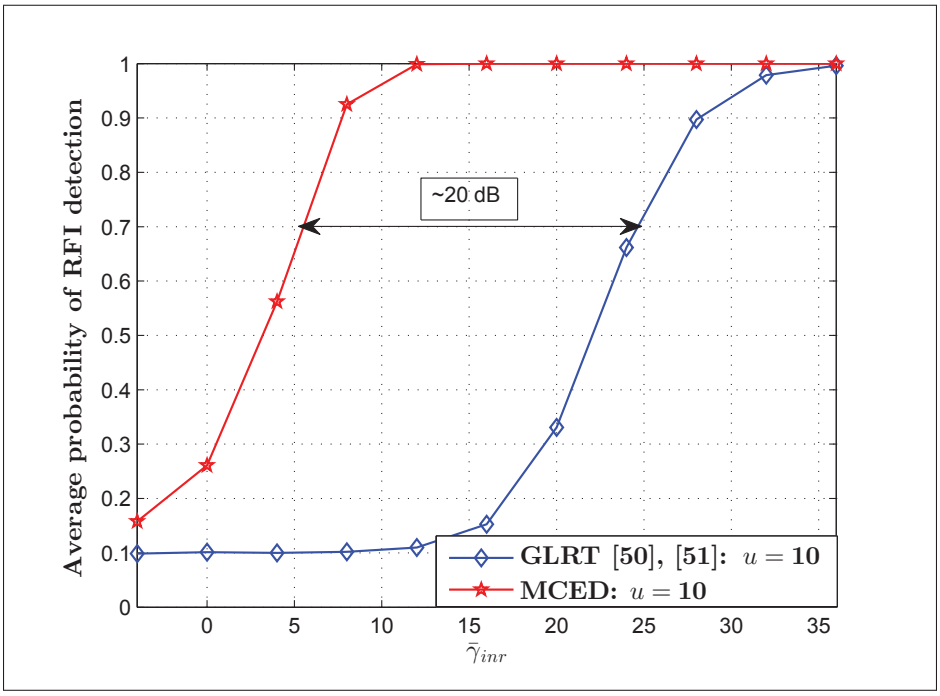

Figure 3.5 Comparison in $\bar{P}_d$: $(\bar{P}_f, \bar{\gamma}_{snr}) = (0.1, 0\,\text{dB})$ and $N_R = 5$. Note that [50] and [51] represent (Wang *et al.*, 2010) and (Taherpour *et al.*, 2010), respectively

3.4.2 Performance Comparison with GLRT

For a received baseband signal sampled at $T_s = 1/2W$ apart and a single-input multiple-output system, a generalized likelihood ratio test (GLRT) detector (Wang *et al.*, 2010; Taherpour *et al.*,

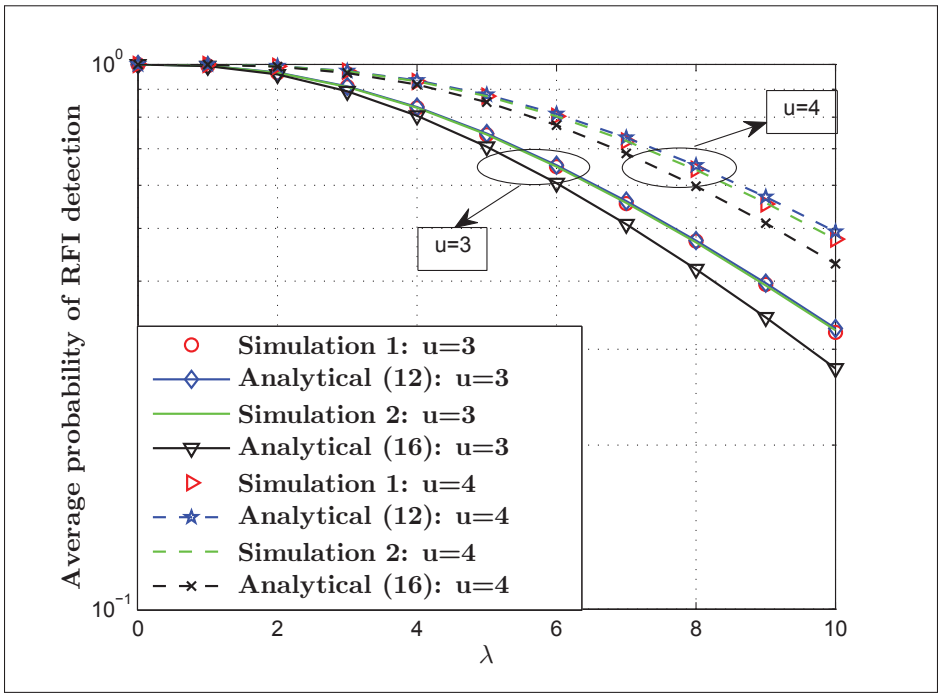

Figure 3.6 Comparison in $\bar{P}_d$: $(\bar{\gamma}_{snr}, \bar{\gamma}_{inr}) = (-5 \text{ dB}, 0 \text{ dB})$. Note that (12) and (16) stand for (3.12) and (3.16), respectively

2010)—a multi-antenna technique—is compared with the ED extended—similar to (Wang *et al.*, 2010, eq. (3))—to a multi-channel ED (MCED). In order to apply GLRT to the RFI detection problem at hand, we assume a perfect knowledge of the multi-antenna SOI channel gain $\boldsymbol{h}$ and project orthogonal to the SOI subspace using a projection matrix $\boldsymbol{P} = \boldsymbol{I}_{N_R} - \boldsymbol{h}(\boldsymbol{h}^H\boldsymbol{h})^{-1}\boldsymbol{h}^H$. Thereafter, we apply the GLRT statistic (Wang *et al.*, 2010, eq. (13)), (Taherpour *et al.*, 2010, eq. (39)) and conduct an RFI detection via comparison with a test threshold rendering the target average FAR of 0.1. To continue, MCED is simulated by applying ED per a receive antenna and adding the output of every ED. By doing so, the overall intercepted energy is compared with a test threshold resulting in the target average FAR of 0.1.

Having deployed the aforementioned simulation settings, the detection performance comparison of MCED and GLRT is depicted via Fig. 3.5. Although GLRT assumes a perfect knowledge of the multi-antenna SOI channel gains, MCED outperforms GLRT by around 20 dB. Although MCED assumes the knowledge of the noise power, such a significant performance

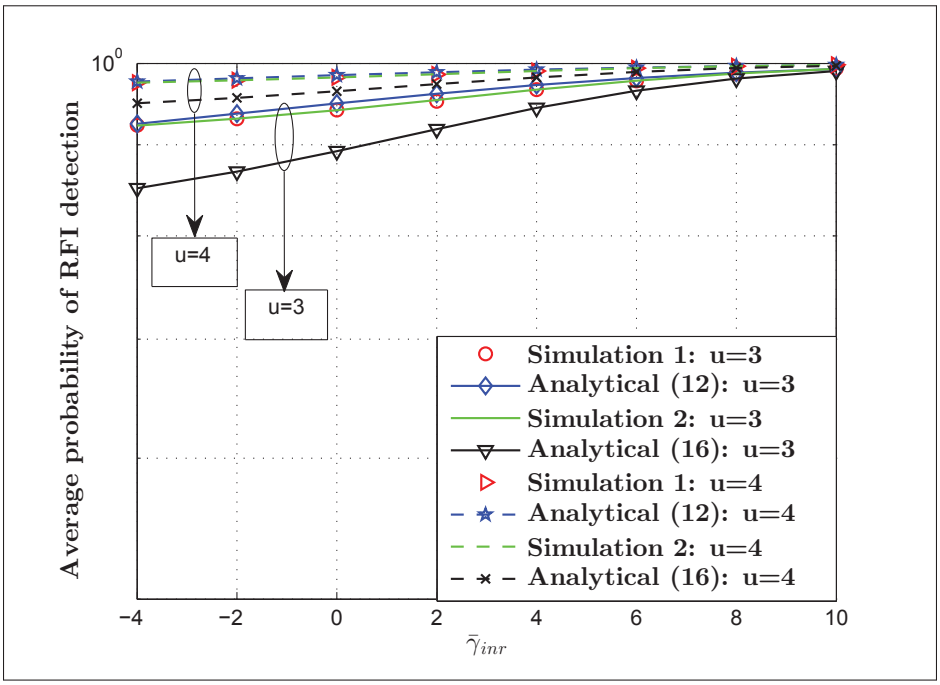

Figure 3.7 Comparison in $\bar{P}_d$: $(\bar{\gamma}_{snr}, \lambda) = (1 \text{ dB}, 3)$. Note that (12) and (16) stand for (3.12) and (3.16), respectively

gain interestingly comes with a low-computational complexity—see Table 3.2—unlike GLRT which first computes a singular value decomposition which is computationally complex—i.e., $\mathcal{O}\left(N_R^3\right)$ multiplications and additions (Zeng & Liang, 2009b)—for large-scale multi-antenna systems.

3.4.3 Validation of the Derived Analytical Expressions

Figs. 3.6 and 3.7 compare the $\bar{P}_d$ for different (λ, u) and $(\bar{\gamma}_{inr}, u)$, respectively. As shown, simulation 1, simulation 2, and (3.12) are in agreement. In addition, Figs. 3.6 and 3.7 reveal that the asymptotic curves suffer from a performance loss as λ gets larger for $(\bar{\gamma}_{snr}, \bar{\gamma}_{inr}, u) = (-5 \text{ dB}, 0 \text{ dB}, 3)$ and for small values of $\bar{\gamma}_{inr}$ estimated with $u = 3$, respectively. Meanwhile, Figs. 3.6 and 3.7 demonstrate that the performance of ED and the accuracy of (3.16) improve with u implying that a larger intercepted energy results in a better $\bar{P}_d$.

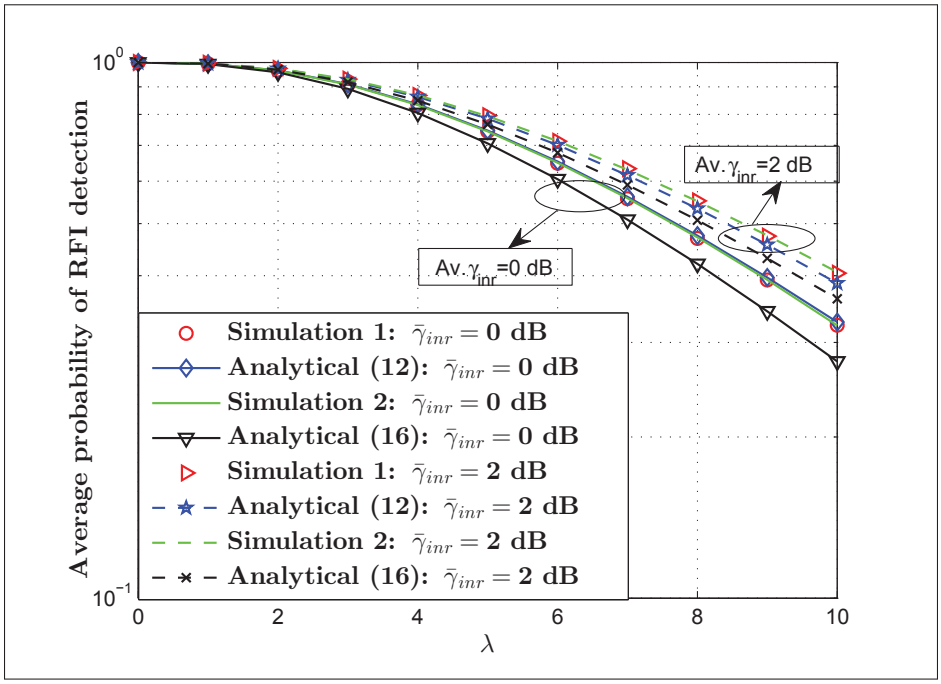

Figure 3.8 Comparison in $\bar{P}_d$: $(u, \bar{\gamma}_{snr}) = (3, -5 \text{ dB})$. Note that (12) and (16) stand for (3.12) and (3.16), respectively

Figs. 3.8 and 3.9 compare the $\bar{P}_d$ for different $(\lambda, \bar{\gamma}_{inr})$ and $(\bar{\gamma}_{snr}, \bar{\gamma}_{inr})$, respectively. As depicted, the increment of $\bar{\gamma}_{inr}$ results in a better $\bar{P}_d$. As $\bar{\gamma}_{inr}$ increases, it is observed in Fig. 3.8 that the asymptotic curve gets close to the approximated curve. Fig. 3.9 also corroborates that $\bar{P}_d$ improves not only with $\bar{\gamma}_{inr}$ but also with $\bar{\gamma}_{snr}$, as the increment in $\bar{\gamma}_{snr}$ (implicating the average SOI energy) is perceived by ED as the presence of an RFI rendering an increase in the intercepted energy.

Figs. 3.10-3.12 depict the exhibited $\bar{P}_f$. As it is evident from Figs. 3.10 and 3.12, the increment of u increases $\bar{P}_f$ since ED can be misled by the increment of the respective intercepted energy. Similarly, Figs. 3.11 and 3.12 display an increment in $\bar{P}_f$ when $\bar{\gamma}_{snr}$ increases for the same reason mentioned before. For the exhibited $\bar{P}_f$ which varies w.r.t. $\bar{\gamma}_{snr}$, these plots also corroborate that ED is not a constant FAR (CFAR) detector. Such a non-CFARness is directly related to the fact that ED is non-robust to noise uncertainty (Wang *et al.*, 2010; Huang & Chung,

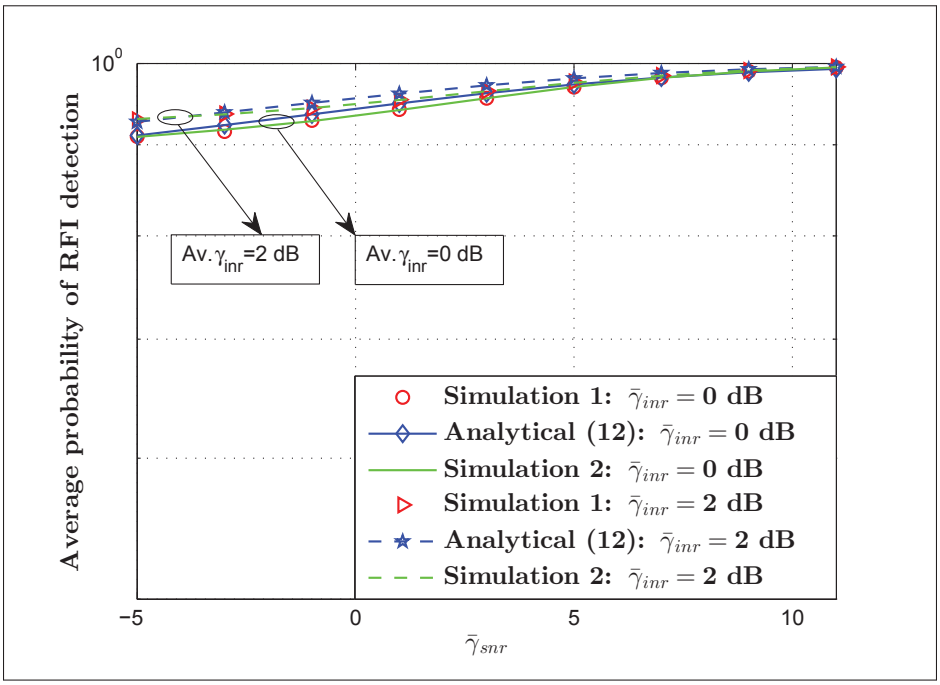

Figure 3.9 Comparison in $\bar{P}_d$: $(\lambda, u) = (3, 3)$. Note that (12) stands for (3.12)

2013a). Moreover, Figs. 3.10-3.12 showcase that simulation 3, simulation 4, and (3.18) are in an overlap.

3.4.4 Assessment of the Receiver Operating Characteristics

To assess the complementary receiver operating characteristics (CROC) (Digham *et al.*, 2007) of ED, Fig. 3.13 depicts the average probability of miss ($\bar{P}_m$)—simulated as $\bar{P}_m = 1 - \bar{P}_d$—versus $\bar{P}_f$. As displayed, the natural trade-off between $\bar{P}_m$ and $\bar{P}_f$ is corroborated; the CROC curves move inward when $\bar{\gamma}_{inr}$ increases; and the Monte-Carlo simulations validate (3.12) and (3.18).

3.5 Real-World Data Based Simulations

We assess the performance of ED using real-world RFI contaminated data received by one of the antennas of the VLA (NRAO, 2017). For this VLA data sampled at a sampling frequency

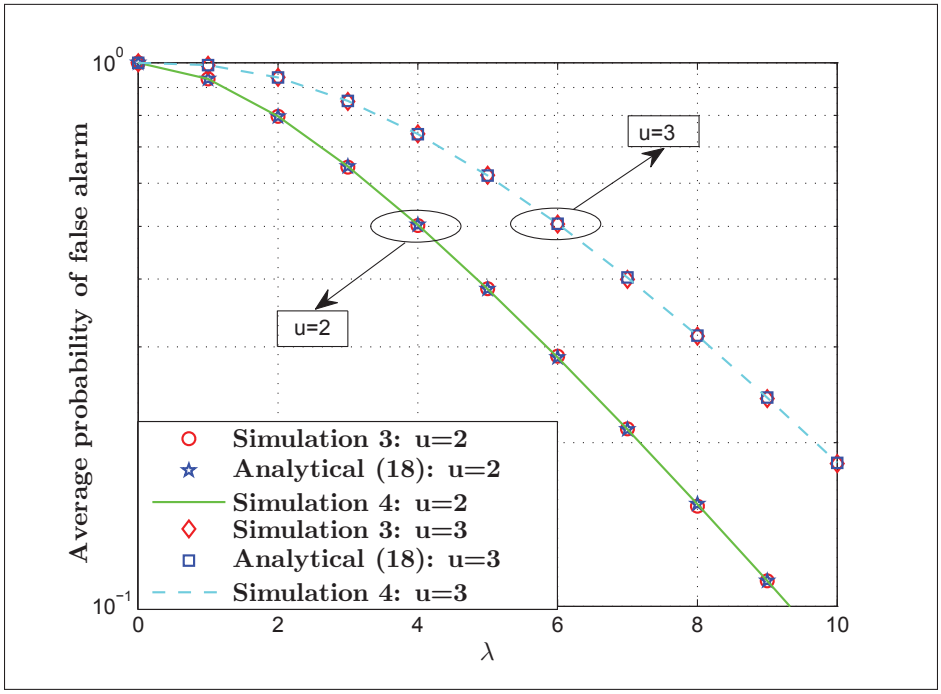

Figure 3.10 Comparison in $\bar{P}_f$: $\bar{\gamma}_{snr} = -4$ dB. Note that (18) stands for (3.18)

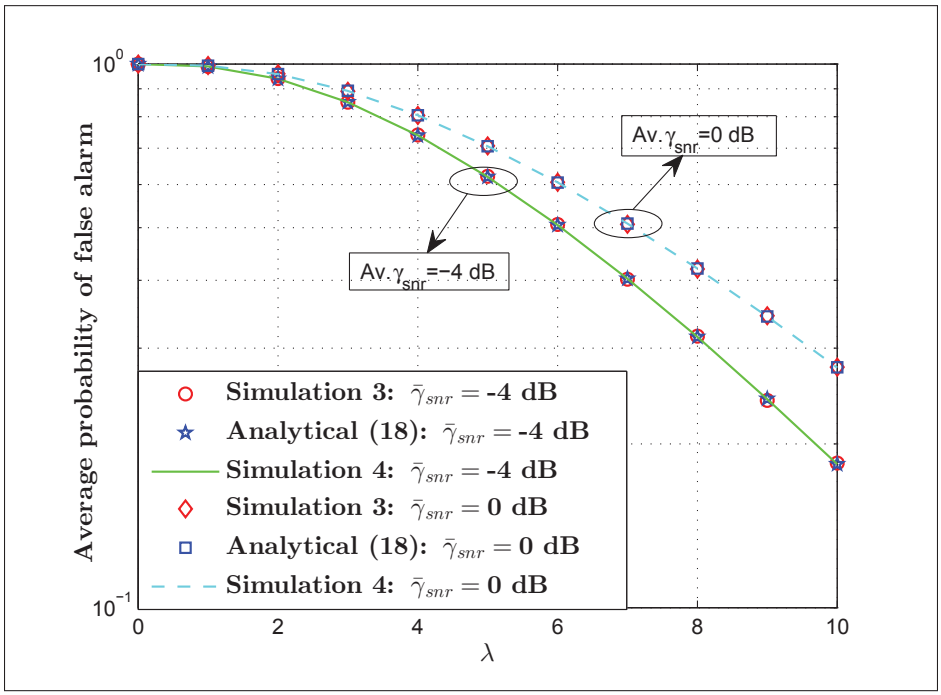

Figure 3.11 Comparison in $\bar{P}_f$: $u = 3$. Note that (18) stands for (3.18)

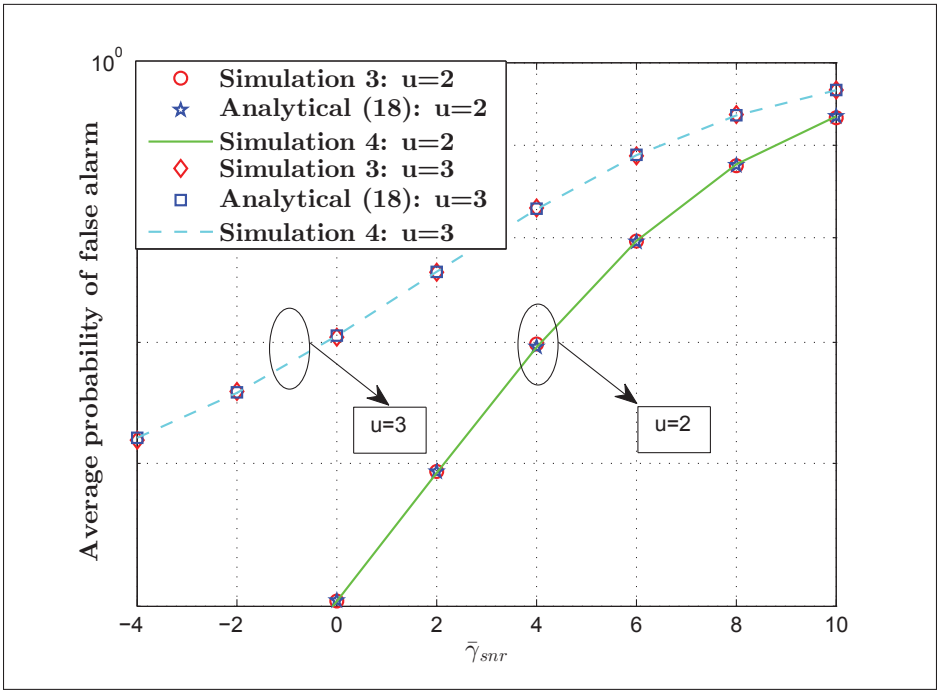

Figure 3.12 Comparison in $\bar{P}_f$: $\lambda = 5$. Note that (18) stands for (3.18)

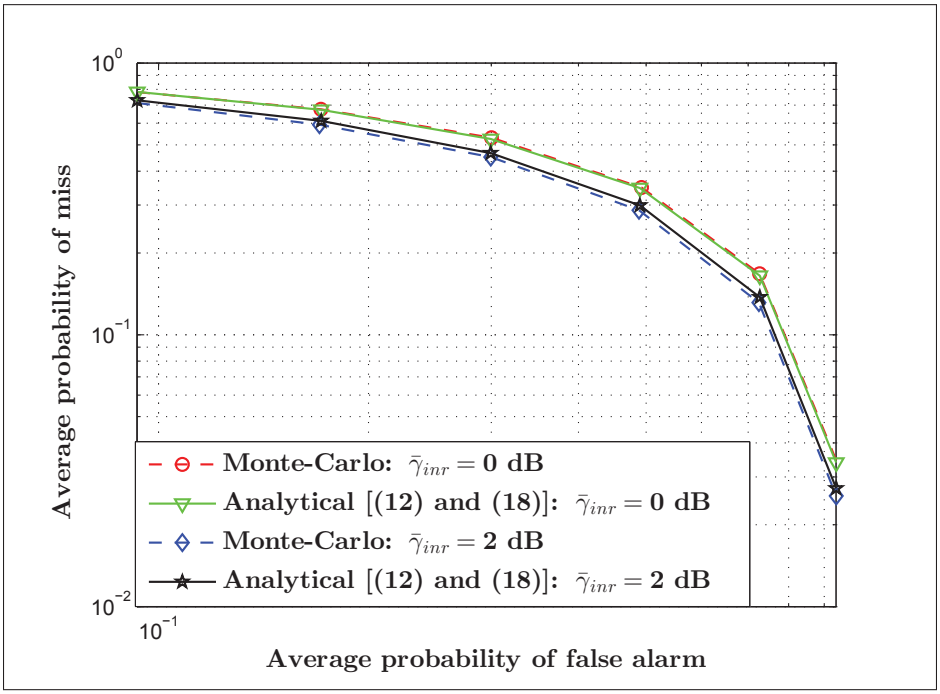

Figure 3.13 $\bar{P}_m$ versus $\bar{P}_f$: $(u, \bar{\gamma}_{snr}) = (3, -5 \text{ dB})$. Note that (12) and (18) stand for (3.12) and (3.18), respectively

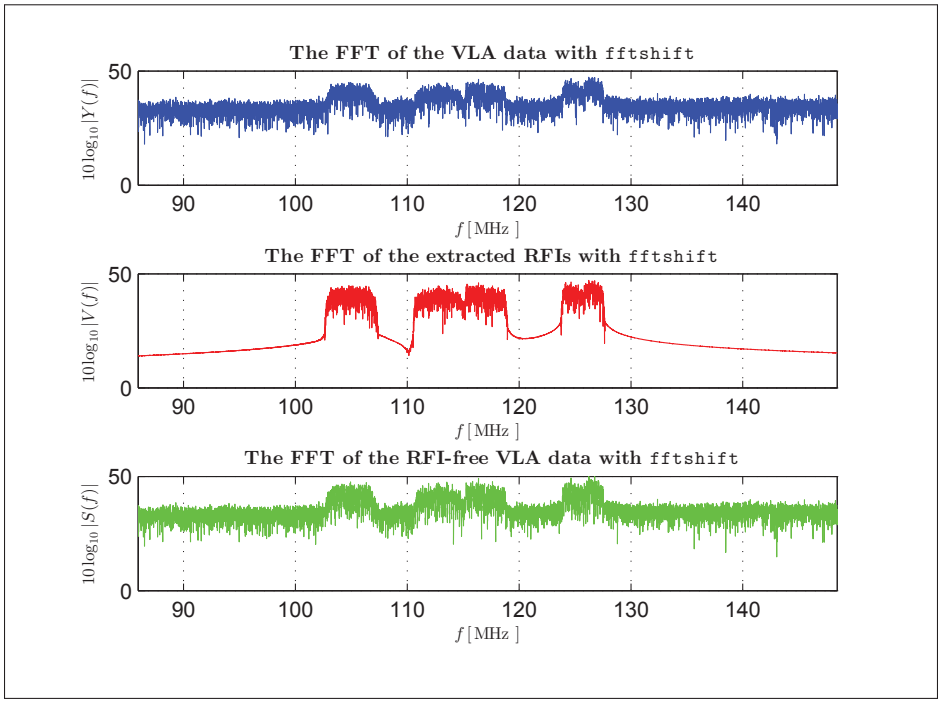

Figure 3.14 The extracted SOI and RFI

of 2048 MHz, (Getu *et al.*, 2017, Fig. 15) depicts its fast Fourier transforms (FFT) whose lower frequency component is diagrammed in (Getu *et al.*, 2017, Fig. 16).

3.5.1 Simulation Setup

As seen in (Getu *et al.*, 2017, Fig. 16), there are four impinging RFIs in four different subbands: 102.8-107.2 MHz, 110.7-115 MHz, 115.2-118.8 MHz, and 123.9-127.5 MHz. In order to simulate the performance of ED w.r.t. the specified average FAR, the respective decision threshold should be computed from the "signal+noise" hypothesis (H_0). To compute this decision threshold, the four impinging RFIs have to be filtered out and removed from the received signal. To extract the RFI-free signal, the four bandpass filters designed using the near-optimal *Kaiser windows* (Oppenheim & Schafer, 2010; Mitra, 2001) and reported through (Getu *et al.*, 2018d, Figs. 3 and 4) are deployed. Using these filters, the four RFIs are extracted and superimposed as manifested through their FFT plotted in Fig. 3.14. These superimposed RFIs—denoted by $\boldsymbol{v}$—are used as an RFI in the subsequent simulations. As depicted through an FFT operation

diagrammed in Fig. 3.14, the superimposed RFIs are then subtracted from the VLA data so as to obtain the RFI-free data which are, hereinafter, considered as the extracted SOI—denoted by $\boldsymbol{s}$.

To simulate the performance of ED for the ranges of average SNR and INR, the extracted SOI is contaminated by an AWGN of power σ^2. It is to be noted that the noise power is adjusted w.r.t. the average SNR and INR defined, respectively, as $\bar{\gamma}_{snr} = \|\boldsymbol{s}\|^2/N_t\sigma^2$ and $\bar{\gamma}_{inr} = \varphi\|\boldsymbol{v}\|^2/N_t\sigma^2$ for N_t being the number of samples in the VLA data and φ being a constant used to adjust the power of the extracted RFI w.r.t. the desired INR. To simulate the exhibited $\bar{P}_f$, the AWGN contaminated extracted SOI samples are employed as per (A III-4)—while employing no RFI—and compared with λ so as to pass a decision. On the other hand, the exhibited $\bar{P}_d$ is simulated by adding the extracted RFI—whose power was adjusted using $\sqrt{\varphi}$—to the extracted SOI contaminated by an AWGN. Thereafter, these samples are deployed in (A III-4) and compared with λ. Having repeated such comparisons $N_t/2u$ times followed by averaging, the respective Monte-Carlo simulation results are plotted.

3.5.2 Results

The exhibited $\bar{P}_d$ and $\bar{P}_f$ assessed using the VLA data are depicted in Figs. 3.15 and 3.16. As expected, Fig. 3.15 demonstrates that $\bar{P}_d$ improves with $\bar{\gamma}_{inr}$ and u. At the same time, the increment in u and hence the respective increment in the intercepted energy can mislead the detector and cause an undesired increment in $\bar{P}_f$, as demonstrated via Fig. 3.16.

3.6 Conclusions and Outlooks

3.6.1 Conclusions

As RFI is affecting many systems operating radio frequencies, it should be properly detected so as to be efficiently excised. In this respect, an energy-based RFI detector is investigated for wireless systems suffering from RFI. Having exploited the sampling theorem representation

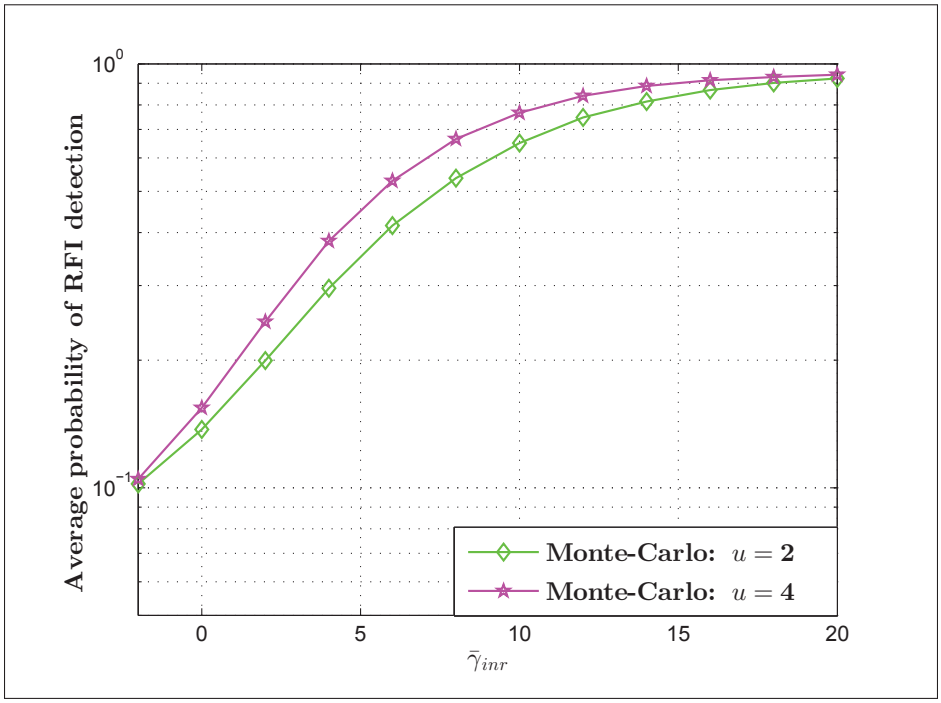

Figure 3.15 $\bar{P}_d$ using the VLA data: $(\bar{\gamma}_{snr}, \bar{P}_f) = (0\,\text{dB}, 0.1)$

of bandlimited signals, ED computes the intercepted energy which is employed to make a decision upon the RFI. In order to quantify the performance of ED, we derive novel closed-form expressions by determining the distribution of the received signal and the associated RVs whenever an RFI—which usually exhibits an unknown distribution—impinges on the receiving antenna. Assuming the Nakagami-*m* fading channels, approximated and asymptotic closed-form expressions are derived for the average probability of RFI detection, and an exact closed-form expression is derived for the average probability of false alarm. Simulations validate these expressions and corroborate that ED outperforms KD—even under the scenario that KD intercepts the received signal for a much longer interval—and a GLRT detector. Moreover, the performance of ED is also simulated and assessed using real-world RFI contaminated data.

3.6.2 Outlooks

Since the mixture of Gaussian (MoG) distribution exhibits a universal approximation property (Selim *et al.*, 2016), as it can be proved using the Wiener's theorem of approximation (Pla-

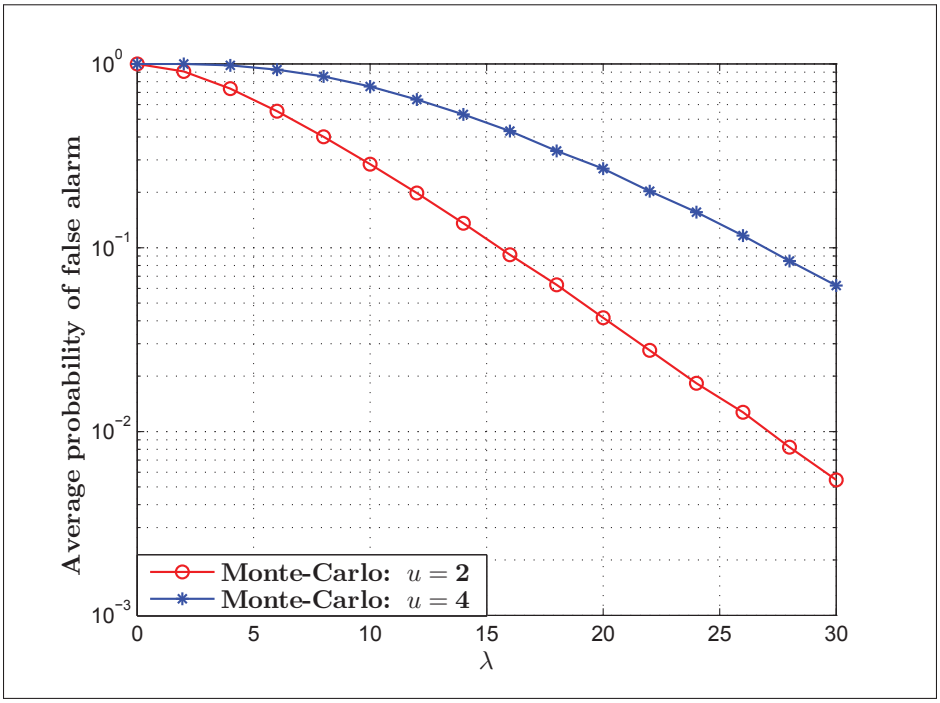

Figure 3.16 $\bar{P}_f$ using the VLA data: $\bar{\gamma}_{snr} = 0$ dB

taniotis & Hatzinakos, 2001), it can approximate any non-Gaussian distribution such as the Nakagami-*m* distribution. Hence, the MoG distribution has been deployed for channel modeling in wireless sensor networks (Salvo Rossi *et al.*, 2016, 2015b,a) and approximation of the envelope, and SNR distributions in several wireless fading channels (Selim *et al.*, 2016; Alhussein, 2015).

Following the MoG distribution's easiness in analytical tractability and high accuracy (Salvo Rossi *et al.*, 2016), we hereby approximate Nakagami-*m* distributed SOI channel's envelope with the MoG distribution. Bayesian information criterion (BIC) (Stoica & Selen, 2004; Selim *et al.*, 2016) is used to determine the number of mixture components C required for an approximation whose accuracy is assessed using the mean square error (MSE) between PDFs. To estimate parameters of the approximating MoG distribution, the expectation-maximization (EM) algorithm (Mengersen *et al.*, 2011, Ch. 1), (Bishop, 2006, Ch. 9) is deployed.

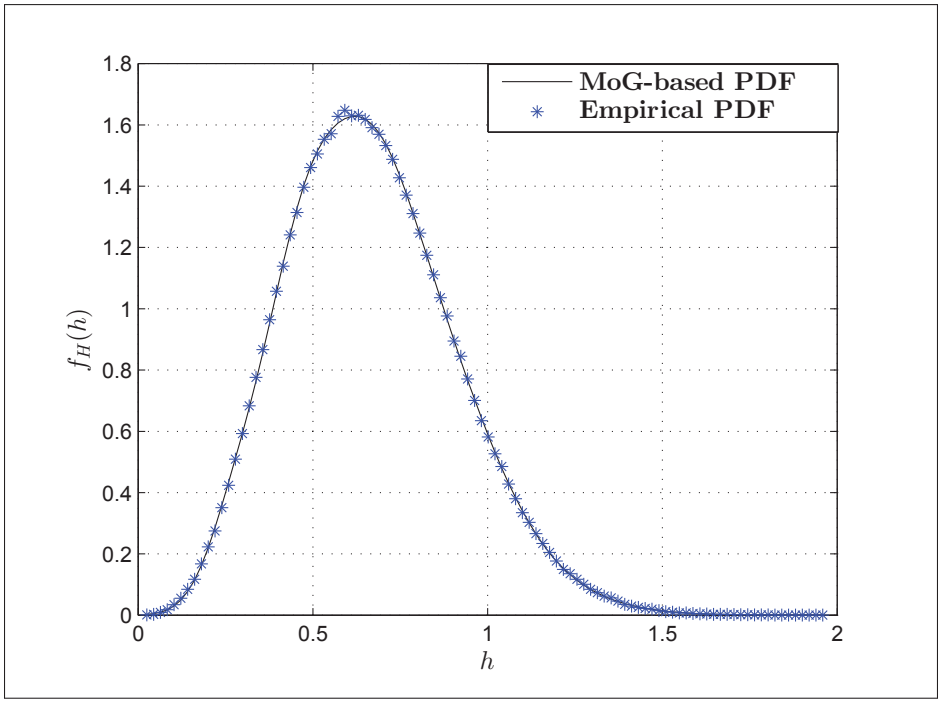

Figure 3.17 EM approximation: $(u, m_1, C, \sigma^2) = (2, 2, 6, 1\text{ W})$ and $(\bar{\gamma}_{snr}, P_s, N, \text{MSE}) = (0\text{ dB}, 1\text{ W}, 10^6, 3.9024 \times 10^{-5})$

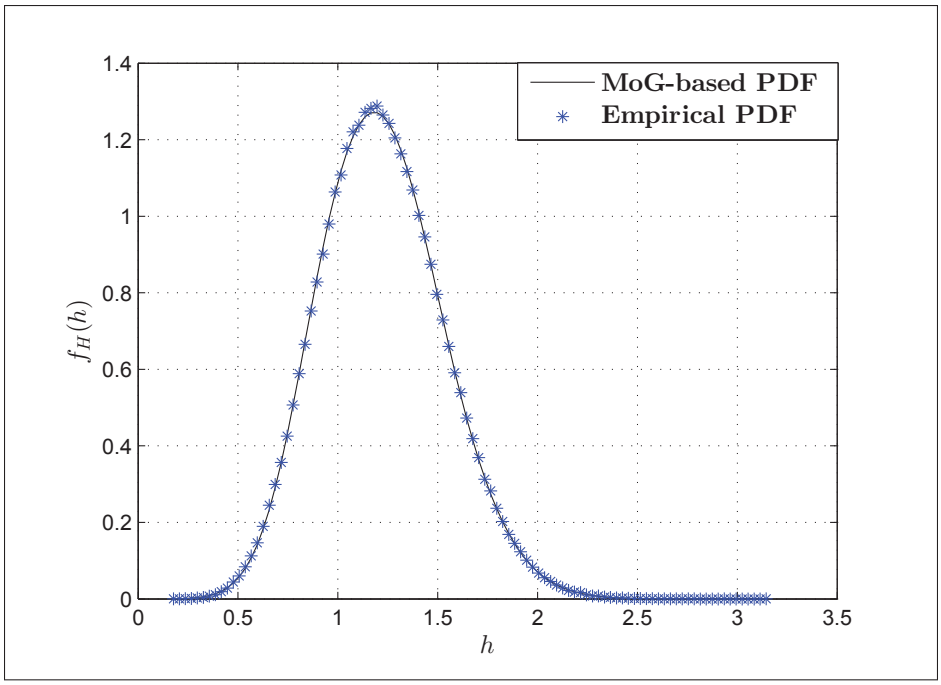

Figure 3.18 EM approximation: $(u, m_1, C, \sigma^2) = (2, 4, 6, 1\text{ W})$ and $(\bar{\gamma}_{snr}, P_s, N, \text{MSE}) = (5\text{ dB}, 1\text{ W}, 10^6, 2.7135 \times 10^{-5})$

To demonstrate the aforementioned universal approximation property using simulations, we adapt the MATLAB® code in (Alhussein, 2015, Appendix B) which implements a BIC assisted EM algorithm using N independent and identically distributed Nakagami-m random samples. For the reception of a BPSK modulated SOI over the Nakagami-m fading channel, the MoG-based PDF and the empirical PDF corresponding to the received signal's envelope are depicted in Figs. 3.17 and 3.18. As plotted, the MoG distribution approximates Nakagami-m distributed envelope with high accuracy. Accordingly, the performance analysis of an energy-based RFI detector using the MoG distributed fading channels has become our future undertaking.

Acknowledgments

The authors acknowledge the funding provided by AVIO-601 Project; Alan Erickson and Dr. Omar A. Yeste-Ojeda of the National Radio Astronomy Observatory for facilitating the RFI data; and the Editor and the anonymous reviewers for helping them improve the scope, clarity, and readability of this manuscript.

CHAPTER 4

EIGENVALUE-BASED RF INTERFERENCE DETECTOR FOR MULTI-ANTENNA WIRELESS COMMUNICATIONS

Tilahun M. Getu[1,2], Wessam Ajib[2], and René Jr. Landry[1]

[1] Department of Electrical Engineering, École de Technologie Supérieure,
1100 Notre-Dame West, Montréal, Québec, Canada H3C 1K3
[2] Department of Computer Sciences, Université du Québec à Montréal,
201 Av. President-Kennedy, Montréal, Québec, Canada H2X 3Y7

This article was revised and submitted to *Elsevier Signal Processing* as of March 2019
(Getu *et al.*, 2019, submitted).

"Mathematics is a language plus reasoning; it is like a language plus logic. Mathematics is a tool for reasoning."—Richard P. Feynman

Abstract—Radio frequency interference (RFI) is occurring in both satellite and terrestrial communication systems. In order to mitigate RFI efficiently, it has to be detected robustly. Toward this end, through the computation of an eigenvalue-based test statistic, an eigenvalue-based blind RFI detector is proposed for single-input multiple-output systems that may suffer from RFI. Valid for infinitely huge samples, performance closed-form expressions are derived through the derivation of the distribution of the equivalent test statistic and signified through simulations. For medium to large interference-to-noise ratio (INR) regimes and sample starved settings, simulations also corroborate that the proposed blind detector manifests a comparable detection performance with a generalized likelihood ratio test (GLRT) detector fed with the knowledge of the signal of interest (SOI) channel, and a matched subspace detector fed with the knowledge of the SOI and RFI channels. Such performance underscores the applicability of the proposed RFI detector for real-time applications.

Index Terms—RFI excision, RFI detection, eigenvalue detector, blind detector, GLRT detector, matched subspace detector.

4.1 Introduction

4.1.1 Related Works

Due to out-of-band emissions by nearby transmitters and harmonics, jammers, spoofers, and meaconers, radio frequency interference (RFI) is being increasingly common in microwave radiometry (Guner *et al.*, 2007), radio astronomy (RA) (van der Tol & van der Veen, 2005), and satellite communications (SatCom) (Nguyen *et al.*, 2015; Getu *et al.*, 2017). Regarding SatCom, 93% of the industrial applications suffer from interference—as reported in (Newtec and IRG, Sep. 2013)—and RFI is a potential threat to global navigation satellite system (Wildemeersch & Fortuny-Guasch, 2010). RFI also happens in cognitive radio systems for imperfect spectrum sensing (Getu *et al.*, 2015a) (as also analytically implicated through (Boulogeorgos *et al.*, 2016b)); ultra-wideband communications due to the prevalent narrowband interferers (Shi *et al.*, 2007); and radar because of the inevitable jammers (De Maio & Orlando, 2016). As such a widely occurring RFI must be first detected so as to be excised efficiently, researchers have paid attention, throughout the years, to the research sub-field of RFI detection.

In the aforementioned regard, the state-of-the-art encompasses a considerable number of RFI detectors. Mentioning the main ones, the RFI detector in asynchronous pulse blanking (Johnson & Ellingson, 2005), kurtosis detector (KD) (Misra *et al.*, 2009), fast Fourier transforms-based RFI detector (Balaei & Dempster, 2009), a precorrelation-based RFI detector (Borio *et al.*, 2008), and transformed-domain detectors (Dovis *et al.*, 2012). In general, these RFI detectors deployed frameworks that did not lead to analytical performance characterizations, which are often missing. On the other hand, the performance characterization of a given RFI detector is not a straightforward undertaking, as the distribution and parameters of the impinging RFI are generally unknown. Such a lack of knowledge makes the existing hypothesis testing frameworks (Kay, 1998; Scharf, 1991) hardly useful with regard to the aforementioned undertaking. Highlighting the latest research advancements pertaining to this research sub-field, meanwhile, a power-based broadband RFI detector and an energy-based RFI detector are investigated in (Getu *et al.*, 2018c) and (Getu *et al.*, 2018b), respectively. However, these RFI

detectors rely on the knowledge of the noise power and they are detectors proposed, mainly, for single-antenna systems. Thus, it is of an academic and practical significance to develop robust multi-antenna RFI detectors whose performance characterizations shall also be pursued.

Mathematically, the multi-antenna RFI detection problem can be related to the adaptive radar detection problem—considered in (Ciuonzo *et al.*, 2016a,b, 2017; Aubry *et al.*, 2014)—by exchanging the underlying RFI and the signal of interest (SOI) while presuming a receiving reference antenna. For the adaptive signal detection in homogeneous Gaussian disturbance and structured interference, (Ciuonzo *et al.*, 2016b) has derived several theoretically founded detectors which are proved to be the function of the maximal invariant statistic (MIS) corroborating their constant false alarm rate (CFAR) property. Following (De Maio & Orlando, 2016), (Ciuonzo *et al.*, 2017) exploits the principle of invariance to surmount the problem of adaptive vector subspace signal detection in a partially homogeneous Gaussian disturbance plus structured interference. In particular, (Ciuonzo *et al.*, 2017) derives an MIS which is shown to coincide with the adaptive normalized matched filter (Conte *et al.*, 1996) (adaptive coherence estimator (Scharf & McWhorter, 1996)) in a complementary subspace of the structured interference. Thereafter, several well-known test statistics are derived and shown to be statistically equivalent to the MIS. Similarly, (Aubry *et al.*, 2014) deals with the adaptive detection of point-like targets in a possibly heterogeneous environment. In a mathematical sense, some of the electronic counter-countermeasures (ECCM) techniques (Orlando, 2017; Bandiera *et al.*, 2010; Melvin & Scheer, 2013) are also related to the problem of multi-antenna RFI detection.

4.1.2 Motivation

Despite the mathematical resemblance, the detection techniques of (Ciuonzo *et al.*, 2016a,b, 2017; Aubry *et al.*, 2014) cannot be adopted as robust multi-antenna RFI detection techniques. The presumption of known left and right subspaces for the signal and interference makes the unifying framework of (Ciuonzo *et al.*, 2016b) hardly practical for multi-antenna RFI detection. Similarly, the assumptions that a target signature and a structured interference belong to known subspaces make (Ciuonzo *et al.*, 2017) unattractive for multi-antenna RFI detection.

Because of the assumption regarding a known subspace spanned by the interference steering vectors, (Aubry *et al.*, 2014) is also unattractive. Meanwhile, adapting the techniques of (Bandiera & Orlando, 2009) devised for a mismatched signal model is either challenging or complex, as the RFI target vectors are generally unknown and time-variant. Furthermore, as the impinging RFI may not be Gaussian and its distribution is generally unknown, adapting the ECCM related techniques—such as (Orlando, 2017), (Bandiera *et al.*, 2010), and (Melvin & Scheer, 2013, Ch. 12)—as robust multi-antenna RFI detection techniques would be hardly realistic.

Because it requires identifying the type of RFI which could be narrowband, broadband, continuous wave, or pulsed RFI (Nguyen *et al.*, 2015; Wildemeersch & Fortuny-Guasch, 2010), the development of a robust multi-antenna RFI detector is challenging. In this regard, an RFI detector should robustly detect any kind of RFI unlike KD which fails to detect Gaussian (near Gaussian) RFI(s) (Misra *et al.*, 2009). To be attractive for real-time applications, an RFI detector should not also rely on a large number of samples. Moreover, an RFI detector shall also be able to detect very weak RFI, as several such RFIs can make the communication (system) unreliable, especially in SatCom and RA which manifest a received signal whose strength is usually under the noise floor (van der Tol & van der Veen, 2005).

In another regard, eigenvalue-based detectors (Kortun *et al.*, 2012; Zeng & Liang, 2009b; Bianchi *et al.*, 2011) have been proposed for spectrum sensing in the context of cognitive radios. These detectors exhibit an attractive detection performance and their blindness makes them practically appealing. They do not also rely on the power spectral density of the noise unlike conventional energy detectors (Digham *et al.*, 2007; D'Amico *et al.*, 2007; Herath *et al.*, 2011; Boulogeorgos *et al.*, 2016a; Sofotasios *et al.*, 2013). Meanwhile, eigenvalues in the Karhunen-Loève transform domain were deployed to detect RFI, as detailed in (Maccone, 2010). Nonetheless, time-domain eigenvalue detection had not been investigated until recently. In line with this specific motivation, (Getu *et al.*, 2018, accepted) has disseminated a preliminary study regarding an eigenvalue-based multi-antenna RFI detection.

4.1.3 Contributions

Based on the lead of (Getu *et al.*, 2018, accepted), this article presents a full-fledged investigation on eigenvalue-based RFI detector and its performance analyses. As a consequence of the conducted investigation, the respective contributions are itemized beneath.

- For single-input multiple-output (SIMO) systems that may suffer from RFI, an eigenvalue-based RFI detector is studied and assessed.
- The distribution—valid for infinitely huge samples—of the equivalent test statistic is derived.
- Deploying the derived distribution, performance closed-form expressions—valid for infinitely large samples—regarding the probability of RFI detection and the probability of false alarm are derived.
- The performance of the investigated RFI detector is assessed through Monte-Carlo simulations which also signify the derived performance closed-form expressions.

Following this introduction, Sec. 4.2 describes the considered system model. Sec. 4.3 presents the problem formulation and the proposed detection followed by the performance analysis detailed in Sec. 4.4. Sec. 4.5 reports the simulation results succeeded by the paper conclusions and outlooks presented in Sec. 4.6.

4.1.4 Notation

Italic letters, lower-case boldface letters, and upper-case boldface letters denote scalars, vectors, and matrices, respectively; $\mathbb{C}^{N_R}$, $\mathbb{C}^{N\times M}$, and $\mathbb{H}^{N_R\times N_R}$ are the sets of N_R–dimensional vectors of complex numbers, of $N\times M$ complex matrices, and of $N_R\times N_R$ Hermitian matrices, respectively; $\rightarrow$, $\sim$, $|$, $\triangleq$, $\propto$, $(\cdot)^{-1}$, $(\cdot)^{T}$, and $(\cdot)^{H}$ denote approaches to, distributed as, conditioned on (under), equal by definition, statistically equivalent, inverse, transpose, and Hermitian, respectively; $\in$, $\equiv$, $>>$, $\rightarrow$, lim, $\boldsymbol{A}(:,i)$, $\boldsymbol{A}(:,i:j)$, and diag$(\cdot)$ implicate element of

(belongs to), is equivalent to, much greater than, approaches to, limit, the i-th column of $\boldsymbol{A}$, the columns of $\boldsymbol{A}$ between its i-th and j-th columns including its i-th and j-th columns, and diagonal (block diagonal) matrices, respectively; $(\cdot)^+$, $||\cdot||$, $\Pr\{\cdot\}$, $\mathbb{E}\{\cdot\}$, $\mathrm{tr}(\cdot)$, $\boldsymbol{I}_{N_R}$, and $\boldsymbol{0}_{N\times M}$ denote the Moore-Penrose inverse, Euclidean norm, the probability of, expectation, trace, an $N_R \times N_R$ identity matrix, and an $N \times M$ zero matrix, respectively; $\mathrm{Re}\{\cdot\}$, $\mathrm{Im}\{\cdot\}$, $\mathrm{Var}\{\cdot\}$, $\mathrm{Cov}\{\cdot,\cdot\}$, $\mathscr{N}_{N_R}(\cdot,\cdot)$, and $\mathscr{CN}_{N_R}(\boldsymbol{\mu},\boldsymbol{\Sigma})$ stand for real part, imaginary part, variance, covariance, the multivariate normal distribution of dimension N_R ($N_R \geq 2$), and the circularly symmetric complex multivariate normal distribution with mean $\boldsymbol{\mu} \in \mathbb{C}^{N_R}$ and covariance matrix $\boldsymbol{\Sigma} \in \mathbb{H}^{N_R\times N_R}$ ($N_R \geq 2$), respectively; χ^2_ν, $\chi'^2_\nu(\lambda)$, F_{ν_1,ν_2}, $F'_{\nu_1,\nu_2}(\lambda_1)$, and $F''_{\nu_1,\nu_2}(\lambda_1,\lambda_2)$ represent the central chi-square distribution with ν degrees of freedom (DoF), the noncentral chi-square distribution with ν DoF and noncentrality parameter (NCP) λ, the central F–distribution with (ν_1,ν_2) DoF, the singly noncentral F–distribution with (ν_1,ν_2) DoF and NCP λ_1, and the doubly noncentral F–distribution with (ν_1,ν_2) DoF and NCPs (λ_1,λ_2), respectively; and $F(\lambda;\nu_1,\nu_2)$, $F'(\lambda;\nu_1,\nu_2|\lambda_1)$, and $F''(\lambda;\nu_1,\nu_2|\lambda_1,\lambda_2)$ denote the cumulative distribution function (CDF) pertaining to F_{ν_1,ν_2}, the CDF pertaining to $F'_{\nu_1,\nu_2}(\lambda_1)$, and the CDF attributed to $F''_{\nu_1,\nu_2}(\lambda_1,\lambda_2)$, respectively, evaluated at λ.

4.2 System Model

First, we assume that the received passband signal is downconverted to its baseband equivalent and sampled at the Nyquist rate. In line with this assumption, we consider a SIMO system that may suffer from an RFI as depicted in Fig. 4.1. Along with the reception of the transmitted SOI, an RFI emitted by a nearby single-antenna source might also be received by the N_R antennas. For this scenario, the received multi-antenna signal contaminated by a noise and an impinging RFI is expressed as

$$\boldsymbol{y}[k] = \boldsymbol{h}s[k] + \boldsymbol{g}v[k] + \boldsymbol{z}[k] \in \mathbb{C}^{N_R}, \tag{4.1}$$

where $\boldsymbol{y}[k] \in \mathbb{C}^{N_R}$ is the k-th sample of the received multi-antenna signal; $\boldsymbol{h} = [h_1, h_2, \ldots, h_{N_R}]^T \in \mathbb{C}^{N_R}$ is the flat fading SOI channel gain vector assumed constant during the RFI detection

interval; $s[k]$ is the k-th unknown and deterministic symbol of the SOI; $\boldsymbol{g} = [g_1, g_2, \ldots, g_{N_R}]^T \in \mathbb{C}^{N_R}$ is the flat fading RFI channel gain vector assumed constant during the RFI detection interval; $v[k]$ is the k-th unknown and deterministic symbol of the RFI; and $\boldsymbol{z}[k] \sim \mathscr{CN}_{N_R}(\boldsymbol{0}, \sigma^2 \boldsymbol{I}_{N_R})$ is—with an unknown power of σ^2—a zero mean circularly symmetric complex additive white Gaussian noise (AWGN) vector, which manifests a spatially uncorrelated noise.

Inferring from (4.1), the RFI-free received multi-antenna signal is equated as

$$\boldsymbol{y}[k] = \boldsymbol{h}s[k] + \boldsymbol{z}[k] \in \mathbb{C}^{N_R}. \tag{4.2}$$

The remainder of this manuscript presumes that $\boldsymbol{h}$, $\boldsymbol{g}$, and $\boldsymbol{z}[k]$ are independent with each other.

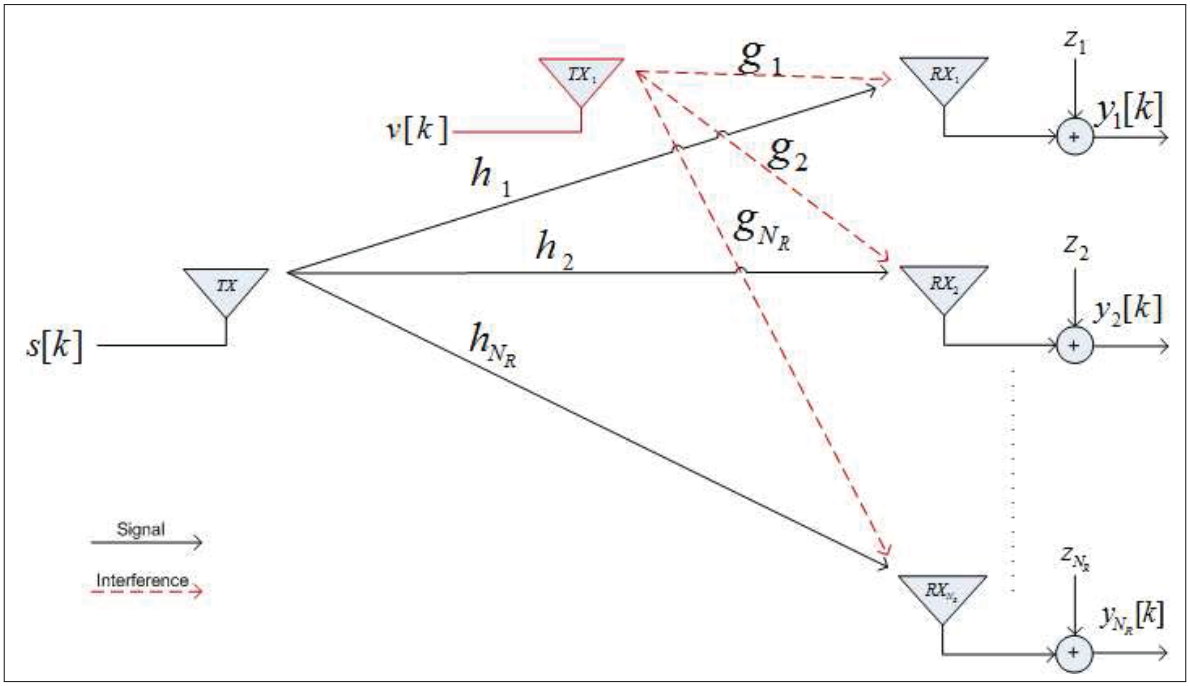

Figure 4.1 A baseband schematic of a SIMO system suffering from an RFI

4.3 Problem Formulation and Proposed Detection

4.3.1 Problem Formulation

A binary hypothesis test is formulated from (4.1) and (4.2) as

$$\boldsymbol{y}[k] = \begin{cases} \boldsymbol{h}s[k] + \boldsymbol{g}v[k] + \boldsymbol{z}[k] & : H_1 \\ \boldsymbol{h}s[k] + \boldsymbol{z}[k] & : H_0, \end{cases} \tag{4.3}$$

where $\{H_0, H_1\}$ are, respectively, hypotheses regarding the absence and presence of the RFI and $1 \leq k \leq N$ for N being the number of intercepted per-antenna samples. Stacking the observation vectors of N sampling intervals,

$$\boldsymbol{y} = \begin{cases} \boldsymbol{H}\boldsymbol{s} + \boldsymbol{G}\boldsymbol{v} + \boldsymbol{z} & : H_1 \\ \boldsymbol{H}\boldsymbol{s} + \boldsymbol{z} & : H_0, \end{cases} \tag{4.4}$$

where $\boldsymbol{y} = \left[\boldsymbol{y}^T[1], \boldsymbol{y}^T[2], \ldots, \boldsymbol{y}^T[N]\right]^T \in \mathbb{C}^{N_R N}$ is the stacked multi-antenna received signal samples, $\boldsymbol{H} = \text{diag}(\boldsymbol{h}, \boldsymbol{h}, \ldots, \boldsymbol{h}) \in \mathbb{C}^{N_R N \times N}$ is the SOI channel matrix, $\boldsymbol{G} = \text{diag}(\boldsymbol{g}, \boldsymbol{g}, \ldots, \boldsymbol{g}) \in \mathbb{C}^{N_R N \times N}$ is the RFI channel matrix, $\boldsymbol{s} = \left[s[1], s[2], \ldots, s[N]\right]^T \in \mathbb{C}^N$ is the stacked symbols of the SOI, $\boldsymbol{v} = \left[v[1], v[2], \ldots, v[N]\right]^T \in \mathbb{C}^N$ is the stacked RFI symbols, and $\boldsymbol{z} = \left[\boldsymbol{z}^T[1], \boldsymbol{z}^T[2], \ldots, \boldsymbol{z}^T[N]\right]^T \in \mathbb{C}^{N_R N} \sim \mathscr{CN}_{N_R N}(\boldsymbol{0}, \sigma^2 \boldsymbol{I}_{N_R N})$ is the stacked multi-antenna noise vector. If $\boldsymbol{H}$ and $\boldsymbol{G}$ were known in the matched subspace detection problem stated via (Scharf & Friedlander, 1994, eq. (2.4)), (4.4) and (Scharf & Friedlander, 1994, eq. (2.4)) would be equivalent problems for $\boldsymbol{S} = \boldsymbol{H}$, $\boldsymbol{\phi} = \boldsymbol{s}$; and $\mu = 1$, $\boldsymbol{H} = \boldsymbol{G}$, and $\boldsymbol{\theta} = \boldsymbol{v}$.[1]

The problem formulated in (4.4) can also be related to the adaptive radar signal detection problems of (Ciuonzo *et al.*, 2016a,b, 2017; Aubry *et al.*, 2014). However, adopting these techniques is challenging, since they rely on known subspace(s). The problem can also be posed as a source enumeration problem (Lu & Zoubir, 2015; Wax & Kailath, 1985; Stoica & Selen,

[1] Referring to (Scharf & Friedlander, 1994), please note that $\mu\boldsymbol{H}\boldsymbol{\theta}$ and $\boldsymbol{S}\boldsymbol{\phi}$ denote an information-bearing signal and an interference, respectively.

2004): “two sources” versus “one source”. Nonetheless, the technique of (Lu & Zoubir, 2015) cannot be adopted here, as $\{s[k], v[k]\}$ are not necessarily Gaussian random variables (RVs). Besides, the information criterion rules (Wax & Kailath, 1985; Stoica & Selen, 2004) are computationally complex, as they rely on the minimization of highly non-linear functions made of several maximum-likelihood estimates (Proakis & Salehi, 2008). For known $\boldsymbol{h}$ and Gaussian $\{s[k], v[k]\}$, it is worth mentioning that the problem can also be recast in terms of a unified generalized likelihood ratio test (GLRT) based spectrum sensing framework of (Axell & Larsson, 2011).

4.3.2 Proposed Detection

At first, the proposed eigenvalue-based RFI detector computes the sample covariance matrix (SCM) as

$$\hat{\boldsymbol{R}}_{yy} = \frac{1}{N}\sum_{k=1}^{N} \boldsymbol{y}[k]\boldsymbol{y}^H[k] = \frac{1}{N}\boldsymbol{Y}\boldsymbol{Y}^H \in \mathbb{H}^{N_R \times N_R}, \tag{4.5}$$

where $\boldsymbol{Y} = \big[\boldsymbol{y}[1], \boldsymbol{y}[2], \ldots, \boldsymbol{y}[N]\big] \in \mathbb{C}^{N_R \times N}$. Hereinafter, we assume that $N > N_R$ to ensure that all eigenvalues of the SCM are positive with probability one. Computing the singular value decomposition (SVD) of (4.5),

$$\hat{\boldsymbol{R}}_{yy} = \hat{\boldsymbol{U}}\hat{\boldsymbol{\Sigma}}\hat{\boldsymbol{V}}^H = [\hat{\boldsymbol{U}}_1 \;\; \hat{\boldsymbol{U}}_{2:N_R}]\hat{\boldsymbol{\Sigma}}\hat{\boldsymbol{V}}^H \overset{(a)}{=} \hat{\boldsymbol{U}}\hat{\boldsymbol{\Sigma}}\hat{\boldsymbol{U}}^H, \tag{4.6}$$

where $\hat{\boldsymbol{U}}_1 = \hat{\boldsymbol{U}}(:,1)$, $\hat{\boldsymbol{U}}_{2:N_R} = \hat{\boldsymbol{U}}(:,2:N_R)$, and $\hat{\boldsymbol{\Sigma}} = \mathrm{diag}\big(\hat{\sigma}_1, \hat{\sigma}_2, \ldots, \hat{\sigma}_{N_R}\big)$ for $\{\hat{\sigma}_i\}_{i=1}^{N_R}$ being the singular values—in decreasing order—of the SCM, and (a) emanates from the fact that an SCM is both a positive semi-definite and Hermitian matrix.

It shall be recalled that $\{\hat{\sigma}_i\}_{i=2}^{N_R}$ and $\{\hat{\sigma}_i\}_{i=3}^{N_R}$ are the noise eigenvalues under H_0 and H_1, respectively. Under H_1, if the interference-to-noise ratio (INR) is greater than the signal-to-noise ratio (SNR), $\hat{\sigma}_2$ is contributed by the signal and the noise; whereas $\hat{\sigma}_2$ is contributed by the interference and the noise provided that the SNR is greater than the INR. Employing this intuition, the

test statistic—that can flag the impinging RFI—is defined as

$$T \triangleq \frac{\hat{\sigma}_2}{\sum_{i=3}^{N_R} \hat{\sigma}_i}. \tag{4.7}$$

For λ being the decision threshold often set as per the desired false alarm rate (FAR), a decision rule follows as

$$T \underset{H_0}{\overset{H_1}{\gtrless}} \lambda. \tag{4.8}$$

Remark 5. Once the trace of the SCM is obtained, (4.7) can be computed via the first two dominant eigenvalues obtained efficiently using the *power method* (Golub & Van Loan, 2013, Chs. 7 and 8).

4.3.3 Equivalent Test Statistic

To derive an equivalent test statistic, we define a projection matrix $\hat{\boldsymbol{P}}_{2:N_R}$ and a projected SCM $\hat{\boldsymbol{R}}_{yy}^{(p)}$ as

$$\hat{\boldsymbol{P}}_{2:N_R} = \hat{\boldsymbol{U}}_{2:N_R}\hat{\boldsymbol{U}}_{2:N_R}^{+} \overset{(b)}{=} \hat{\boldsymbol{U}}_{2:N_R}\hat{\boldsymbol{U}}_{2:N_R}^{H} \tag{4.9a}$$

$$\hat{\boldsymbol{R}}_{yy}^{(p)} = \hat{\boldsymbol{P}}_{2:N_R}\hat{\boldsymbol{R}}_{yy}\hat{\boldsymbol{P}}_{2:N_R}^{H}, \tag{4.9b}$$

where (b) follows from the orthonormal columns of $\hat{\boldsymbol{U}}$. Computing the SVD of $\hat{\boldsymbol{R}}_{yy}^{(p)}$,

$$\hat{\boldsymbol{R}}_{yy}^{(p)} = \tilde{\boldsymbol{U}}\tilde{\boldsymbol{\Sigma}}\tilde{\boldsymbol{V}}^{H} = [\tilde{\boldsymbol{U}}_1 \;\; \tilde{\boldsymbol{U}}_{2:N_R}]\tilde{\boldsymbol{\Sigma}}\tilde{\boldsymbol{V}}^{H}, \tag{4.10}$$

where $\tilde{\boldsymbol{U}}_1 = \tilde{\boldsymbol{U}}(:,1)$, $\tilde{\boldsymbol{U}}_{2:N_R} = \tilde{\boldsymbol{U}}(:,2:N_R)$, and $\tilde{\boldsymbol{V}} = \tilde{\boldsymbol{U}}$. Substituting (4.6) and (4.9a) into (4.9b),

$$\hat{\boldsymbol{R}}_{yy}^{(p)} = \hat{\boldsymbol{U}}_{2:N_R}\hat{\boldsymbol{\Sigma}}_{2:N_R}\hat{\boldsymbol{U}}_{2:N_R}^{H}, \tag{4.11}$$

where $\hat{\boldsymbol{\Sigma}}_{2:N_R} = \mathrm{diag}(\hat{\sigma}_2, \hat{\sigma}_3, \ldots, \hat{\sigma}_{N_R})$. From (4.10) and (4.11), these relations can be concluded: $\tilde{\boldsymbol{U}} = \hat{\boldsymbol{U}}_{2:N_R} = \tilde{\boldsymbol{V}}$ and $\tilde{\boldsymbol{\Sigma}} = \hat{\boldsymbol{\Sigma}}_{2:N_R}$. A new projection matrix $\hat{\boldsymbol{P}}_2$ can then be computed using

$\tilde{\boldsymbol{U}}_1 = \hat{\boldsymbol{U}}_{2:N_R}(:,1) = \hat{\boldsymbol{U}}(:,2)$ as

$$\hat{\boldsymbol{P}}_2 = \hat{\boldsymbol{U}}_{2:N_R}(:,1)\hat{\boldsymbol{U}}^H_{2:N_R}(:,1) = \hat{\boldsymbol{U}}(:,2)\hat{\boldsymbol{U}}^H(:,2). \tag{4.12}$$

Realizing that $\mathrm{tr}(\hat{\boldsymbol{P}}_2\hat{\boldsymbol{R}}^{(p)}_{yy}) = \hat{\sigma}_2$ and $\mathrm{tr}\big((\boldsymbol{I}_{N_R} - \hat{\boldsymbol{P}}_2)\hat{\boldsymbol{R}}^{(p)}_{yy}\big) = \sum_{i=3}^{N_R}\hat{\sigma}_i$, the proposed test statistic can also be expressed as

$$T = \frac{\mathrm{tr}(\hat{\boldsymbol{P}}_2\hat{\boldsymbol{R}}^{(p)}_{yy})}{\mathrm{tr}\big((\boldsymbol{I}_{N_R} - \hat{\boldsymbol{P}}_2)\hat{\boldsymbol{R}}^{(p)}_{yy}\big)}. \tag{4.13}$$

Considering $(\nu_1, \nu_2) = \big(2N, 2N(N_R-2)\big)$ which are shown, in Appendix 1 (under APPENDIX IV), to be the DoF of the numerator and denominator of the right-hand side (RHS) of (4.13),

$$T \propto T_{\mathrm{eq}} = \frac{\nu_2}{\nu_1}\frac{\mathrm{tr}(\hat{\boldsymbol{P}}_2\hat{\boldsymbol{R}}^{(p)}_{yy})}{\mathrm{tr}\big((\boldsymbol{I}_{N_R} - \hat{\boldsymbol{P}}_2)\hat{\boldsymbol{R}}^{(p)}_{yy}\big)}. \tag{4.14}$$

Meanwhile, through the derivation of the distribution of T_{eq}, the performance analysis of the proposed detector is pursued subsequently.

4.4 Performance Analysis

The exact performance analysis of an eigenvalue-based detector is a complex undertaking. In this regard, the existing investigations resort to the asymptotic analysis of the underlying eigenvalue-based detectors (Zeng & Liang, 2009b; Bianchi *et al.*, 2011; Kritchman & Nadler, 2009; Nadakuditi & Edelman, 2008) by employing random matrix theory (Couillet & Debbah, 2011). While such analyses intuitively capture the asymptotic performance of the investigated detectors, it is demonstrated in (Kortun *et al.*, 2012) that their asymptotic threshold differs considerably from the exact value for finite sensors and samples. In (Kortun *et al.*, 2012), meanwhile, the probability density function (PDF) and CDF of the ratio of the largest eigenvalue to the trace of complex Wishart matrices were derived. Nevertheless, as we are not dealing with a noise only hypothesis and because we are operating a different test statistic, the exact

closed-form expressions of (Kortun *et al.*, 2012) cannot be adapted for our detection problem at hand.

Valid for any sample size N, obtaining exact closed-form expressions pertaining to the PDF and the CDF of the eigenvalue-based test statistic given by (4.7) is mathematically intractable. For our underlying hypotheses, specifically, the intractability tends to be significant since the type of the impinging RFI and its distribution are often unknown. Accordingly, through the derivation of the PDF of the equivalent test statistic defined in (4.14), performance characterizations—valid for infinitely large samples—are attempted subsequently.

4.4.1 The Distribution of T_{eq}

For infinitely huge samples, the distribution of T_{eq} is characterized below.

Theorem 6. Suppose $(\nu_1,\nu_2)=\big(2N,2N(N_R-2)\big)$; $\boldsymbol{h}\sim\mathscr{CN}_{N_R}(\boldsymbol{0},\boldsymbol{I}_{N_R})$ and $\boldsymbol{g}\sim\mathscr{CN}_{N_R}(\boldsymbol{0},\boldsymbol{I}_{N_R})$; $\mathbb{E}\{s^2[k]\}=P_s$ and $\mathbb{E}\{v^2[k]\}=P_v$ quantify the transmitted SOI and RFI powers, respectively; $\gamma_{snr}=\dfrac{\big|\big|\boldsymbol{Hs}\big|\big|^2}{NN_R\sigma^2}$ and $\gamma_{inr}=\dfrac{\big|\big|\boldsymbol{Gv}\big|\big|^2}{NN_R\sigma^2}$ be the SNR and INR, respectively; and $\hat{\boldsymbol{P}}_{3:N_R}=\hat{\boldsymbol{U}}(:,3:N_R)\hat{\boldsymbol{U}}^H(:,3:N_R)$. For $(\lambda_1^{H_1},\lambda_2^{H_1})=\frac{1}{\sigma^2}\sum_{k=1}^{N}\big(\big|\big|\hat{\boldsymbol{P}}_2(\boldsymbol{h}s[k]+\boldsymbol{g}v[k])\big|\big|^2,\big|\big|\hat{\boldsymbol{P}}_{3:N_R}(\boldsymbol{h}s[k]+\boldsymbol{g}v[k])\big|\big|^2\big)$ and $(\lambda_1^{H_0},\lambda_2^{H_0})=\frac{1}{\sigma^2}\sum_{k=1}^{N}\big(\big|\big|\hat{\boldsymbol{P}}_2\boldsymbol{h}s[k]\big|\big|^2,\big|\big|\hat{\boldsymbol{P}}_{3:N_R}\boldsymbol{h}s[k]\big|\big|^2\big)$, the distribution of T_{eq} is characterized as follows:

- if $(\gamma_{snr},\gamma_{inr})=(0,0)$, $\lim\limits_{N\to\infty}T_{\text{eq}}\sim F_{\nu_1,\nu_2}$;
- if $\gamma_{inr}=0$ and $\gamma_{snr}>0$, $\lim\limits_{N\to\infty}T_{\text{eq}}\sim F''_{\nu_1,\nu_2}(\lambda_1^{H_0},\lambda_2^{H_0})$; or
- if $\gamma_{inr}>0$ and $\gamma_{snr}>0$, $\lim\limits_{N\to\infty}T_{\text{eq}}\sim F''_{\nu_1,\nu_2}(\lambda_1^{H_1},\lambda_2^{H_1})$.

Proof. Please see Appendix 1 under APPENDIX IV.

When infinitely large samples are available, Theorem 6 attests that T_{eq} admits the central F–distribution whenever no SOI and RFI are received. Under H_0 and H_1, T_{eq} is characterized through the noncentral F–distribution with NCPs that, respectively, depend on the SNR, and

both the SNR and the INR provided that infinitely huge samples are available. If the received RFI and SOI are very weak, the effect of the NCPs would vanish rendering T_{eq} to admit the central F–distribution. As highlighted below for different values of N, meanwhile, the PDF of T_{eq} is assessed analytically and using simulations.

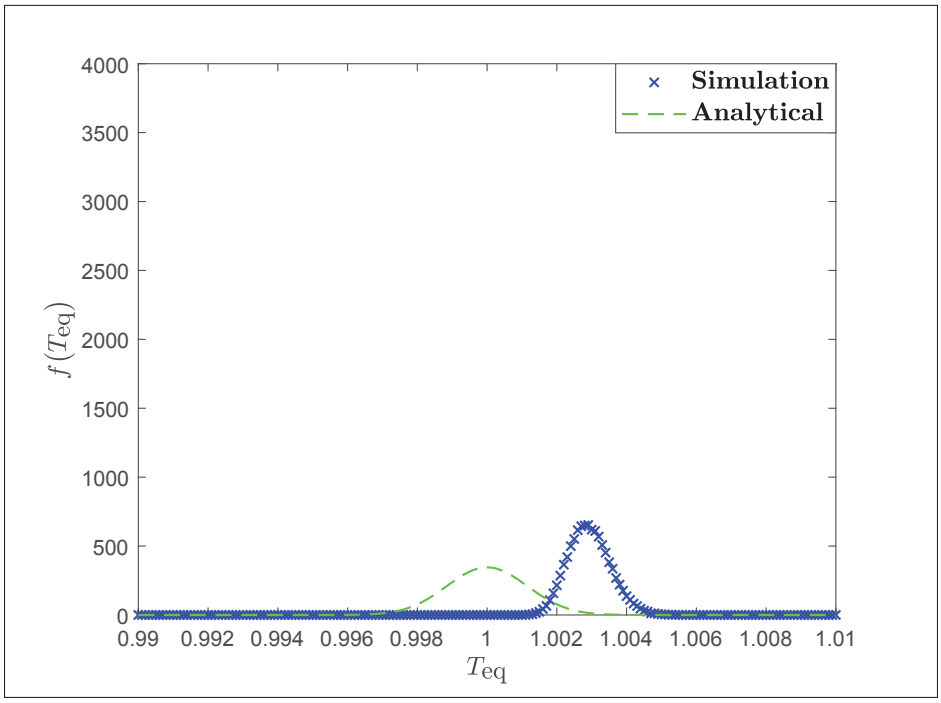

Figure 4.2 The PDF of T_{eq}: $N = 10^6$, $N_R = 5$, $\sigma = 1$ W, $(\gamma_{snr}, \gamma_{inr}) = (0,0)$, and 10^5 realizations

Employing a PDF estimation technique highlighted in (Kay, 2006, p. 20-21) and the MATLAB® function dubbed `fpdf`$(\cdot,\cdot,\cdot)$ scripted to compute the PDF of the central F–distribution analytically, the PDF of T_{eq} is depicted in Figs. 4.2 and 4.3. As seen in Fig. 4.2 for $N = 10^6$, the central F–distribution approximates the estimated PDF accurately except for $T_{\text{eq}} \in [0.996, 1.006]$. As N is increased to 10^7, the approximation through the central F–distribution becomes accurate except for the interval $T_{\text{eq}} \in [0.998, 1.002]$. Since increasing N is rendering in a better approximation, this is in line with the first case of Theorem 6.

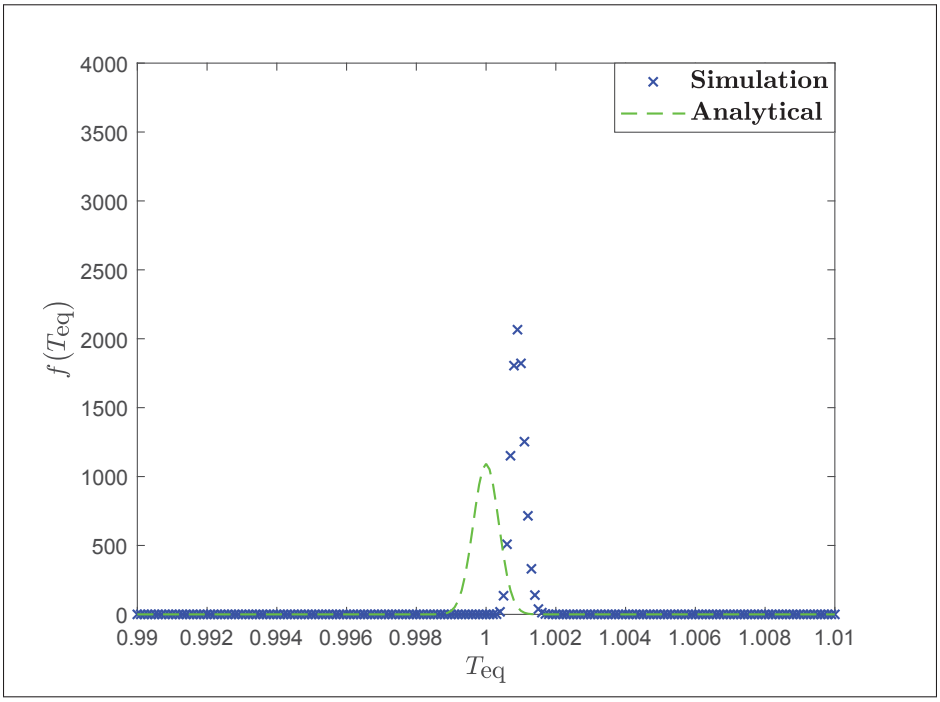

Figure 4.3 The PDF of T_{eq}: $N = 10^7$, $N_R = 5$, $\sigma = 1$ W, $(\gamma_{snr}, \gamma_{inr}) = (0,0)$, and 10^5 realizations

4.4.2 Performance Closed-Form Expressions

The probability of RFI detection and the probability of false alarm exhibited by the proposed detector are characterized beneath.

Proposition 1. For a given realization, let $P_d = \Pr\{T > \lambda | H_1\}$ and $P_f = \Pr\{T > \lambda | H_0\}$, respectively, define the probability of RFI detection and the probability of false alarm manifested by the proposed detector. When the preconditions of Theorem 6 are satisfied,

$$\lim_{N\to\infty} P_d = 1 - F''\left(\nu_2\lambda/\nu_1; \nu_1, \nu_2 | \lambda_1^{H_1}, \lambda_2^{H_1}\right) \tag{4.15}$$

$$\lim_{N\to\infty} P_f = 1 - F''\left(\nu_2\lambda/\nu_1; \nu_1, \nu_2 | \lambda_1^{H_0}, \lambda_2^{H_0}\right). \tag{4.16}$$

Proof. Please refer to Appendix 2 under APPENDIX IV.

Proposition 1 offers a generic characterization of the performance of the proposed detector. In addition, it inspires the underneath lemma which elucidates the performance of the proposed detector valid for the high SNR and INR regimes.

Lemma 2. Let $\lambda_{gv} = \frac{1}{\sigma^2}\sum_{k=1}^{N} \|\boldsymbol{g}v[k]\|^2$ and $\lambda_{hs} = \frac{1}{\sigma^2}\sum_{k=1}^{N} \|\boldsymbol{h}s[k]\|^2$. If the proposed detector is operating in the high SNR and INR regimes, and

- if $\gamma_{snr} >> \gamma_{inr}$,

$$\lim_{N\to\infty} P_d = 1 - F'\big(\nu_2\lambda/\nu_1; \nu_1, \nu_2|\lambda_{gv}\big); \tag{4.17}$$

- if $\gamma_{inr} >> \gamma_{snr}$,

$$\lim_{N\to\infty} P_d = 1 - F'\big(\nu_2\lambda/\nu_1; \nu_1, \nu_2|\lambda_{hs}\big). \tag{4.18}$$

Moreover, when the detector is operating in the high SNR regimes, then we obtain

$$\lim_{N\to\infty} P_f = 1 - F\big(\nu_2\lambda/\nu_1; \nu_1, \nu_2\big). \tag{4.19}$$

Proof. Please refer to Appendix 3 under APPENDIX IV.

Meanwhile, since the function that computes the CDF of the doubly noncentral F–distribution is unavailable in MATLAB®, we resort to its approximation via the central F–distribution. To do so, the noncentral χ^2–distributions—that constitute the noncentral F–distribution—are approximated by the central χ^2–distributions that lead to the central F–distribution (Johnson *et al.*, 1995). Using (Johnson *et al.*, 1995, eq. (30.54)), in this regard,

$$F''_{\nu_1,\nu_2}(\lambda_1,\lambda_2) \approx \frac{1+\lambda_1\nu_1^{-1}}{1+\lambda_2\nu_2^{-1}} F_{\nu,\nu'}, \tag{4.20}$$

where $\nu = (\nu_1+\lambda_1)^2(\nu_1+2\lambda_1)^{-1}$ and $\nu' = (\nu_2+\lambda_2)^2(\nu_2+2\lambda_2)^{-1}$. Using (4.20) and the CDF relation in (Bertsekas & Tsitsiklis, 2008, p. 206),

$$F''\big(\nu_2\lambda/\nu_1; \nu_1, \nu_2|\lambda_1^{H_1}, \lambda_2^{H_1}\big) \approx F\big(\lambda_{2,1}^{H_1}; \beta_1^{H_1}, \beta_2^{H_1}\big), \tag{4.21}$$

where $\lambda_{2,1}^{H_1} = \frac{1+\lambda_2^{H_1}\nu_2^{-1}}{1+\lambda_1^{H_1}\nu_1^{-1}}\left(\frac{\nu_2\lambda}{\nu_1}\right)$, $\beta_1^{H_1} = (\nu_1+\lambda_1^{H_1})^2(\nu_1+2\lambda_1^{H_1})^{-1}$, and $\beta_2^{H_1} = (\nu_2+\lambda_2^{H_1})^2(\nu_2+2\lambda_2^{H_1})^{-1}$. Similarly, adopting the aforementioned approximations also leads to the relation

$$F''\left(\nu_2\lambda/\nu_1;\nu_1,\nu_2|\lambda_1^{H_0},\lambda_2^{H_0}\right) \approx F\left(\lambda_{2,1}^{H_0};\beta_1^{H_0},\beta_2^{H_0}\right), \tag{4.22}$$

where $\lambda_{2,1}^{H_0} = \frac{1+\lambda_2^{H_0}\nu_2^{-1}}{1+\lambda_1^{H_0}\nu_1^{-1}}\left(\frac{\nu_2\lambda}{\nu_1}\right)$, $\beta_1^{H_0} = (\nu_1+\lambda_1^{H_0})^2(\nu_1+2\lambda_1^{H_0})^{-1}$, and $\beta_2^{H_0} = (\nu_2+\lambda_2^{H_0})^2(\nu_2+2\lambda_2^{H_0})^{-1}$. It is to be noted that (4.21) and (4.22) can be used for an approximated numerical assessment. In addition, (4.20) implies that the approximation through the central F–distribution becomes more accurate as $(\lambda_1,\lambda_2) \to (0,0)$.

4.5 Simulation Results

Evaluated for a SIMO system, this section reports the simulation results regarding the performance of the proposed RFI detector, matched subspace detector (MSD) (Scharf & Friedlander, 1994), and multi-antenna detectors (Huang & Chung, 2013a; Taherpour *et al.*, 2010; Wang *et al.*, 2010). Unless otherwise mentioned, the conducted simulations employ the parameters of Table 4.1.

Table 4.1 Simulation parameters if unmentioned

Parameters	Assigned value
N_R	5
γ_{snr}	0 dB
P_s	10 W
No. of realizations	10^5

Without loss of generality and similar to (Ramírez *et al.*, 2010; Getu *et al.*, 2018a), the independently distributed complex channel gains pertaining to the SOI and RFI—unless stated differently—are modeled by a Rayleigh fading as in Theorem 6. Unless otherwise mentioned and without loss of generality, we consider a quadrature phase shift keying (QPSK) modulated SOI and RFI, i.e, $s[k] = \sqrt{P_s/2}\left[s_k^I + js_k^Q\right]$ and $v[k] = \sqrt{P_v/2}\left[v_k^I + jv_k^Q\right]$ for $\{s_k^I, s_k^Q\} \in \{-1,1\}\times\{-1,1\}$ and $\{v_k^I, v_k^Q\} \in \{-1,1\}\times\{-1,1\}$.

The subsequent Monte-Carlo simulations of the proposed detector deploy the test statistic equated in (4.7) and the decision rule expressed in (4.8). These simulations consider the SNR and INR definitions stated in Theorem 6. Having adjusted the power of the received SOI and the received RFI, respectively, as per the SNR and INR definitions stated in Theorem 6, the Monte-Carlo simulations regarding exhibited P_d—by any considered detector—assume the reception of H_1 per a realization and average over the number of assumed realizations. Along with the simulation of P_d, the probability of miss-detection (P_m) exhibited by any considered detector is simulated as $P_m = 1 - P_d$. On the other hand, the simulations concerning the FAR—manifested by any detector—assumes a per-realization reception of H_0, whose SOI component is adjusted as per the SNR definition stated in Theorem 6, and average over the number of presumed realizations. Meanwhile, fixed for the detection performance assessment of the considered detectors, the decision thresholds rendering the desired FARs are obtained via Monte-Carlo simulations that average over 10^6 independent realizations under H_0. Regarding the proposed eigenvalue-based RFI detector, hereinafter, performance comparison with MSD; performance comparison with multi-antenna detectors; validation of the derived closed-form expressions; and assessment of the manifested FAR and complementary receiver operating characteristics (CROC) are reported.

4.5.1 Performance Comparison with MSD

To compare the proposed detector and an MSD (Scharf & Friedlander, 1994) which assumes real-valued signals, we emulate the transmission of a binary phase shift keying (BPSK) modulated SOI and BPSK modulated RFI over real-valued Rayleigh fading channels, i.e., $\boldsymbol{h} \sim \mathscr{N}_{N_R}(\mathbf{0}, \boldsymbol{I}_{N_R})$ and $\boldsymbol{g} \sim \mathscr{N}_{N_R}(\mathbf{0}, \boldsymbol{I}_{N_R})$. With respect to the desired FAR of 0.01, we detect the presence of RFI using the proposed detector and the MSD derived for a subspace signal detection in subspace interference and noise of unknown level (Scharf & Friedlander, 1994, Sec. VIII). For a given realization, the performance of MSD is assessed via the P_D expression given by (Scharf & Friedlander, 1994, eq. (8.10)) and its respective FAR threshold is obtained via the P_{FA} expression, also, equated in (Scharf & Friedlander, 1994, eq. (8.10)). As

the NCP (Scharf & Friedlander, 1994, eq. (8.7)) that comprises the closed-form detection expression (Scharf & Friedlander, 1994, eq. (8.10)) varies for every realization, we average the per-realization detection performance of MSD over 10^5 realizations. Similarly, the detection performance of the proposed RFI detector is assessed through Monte-Carlo simulations that also average over 10^5 realizations. Whereas for the respective P_m simulations, averaging over 10^6 realizations is considered.

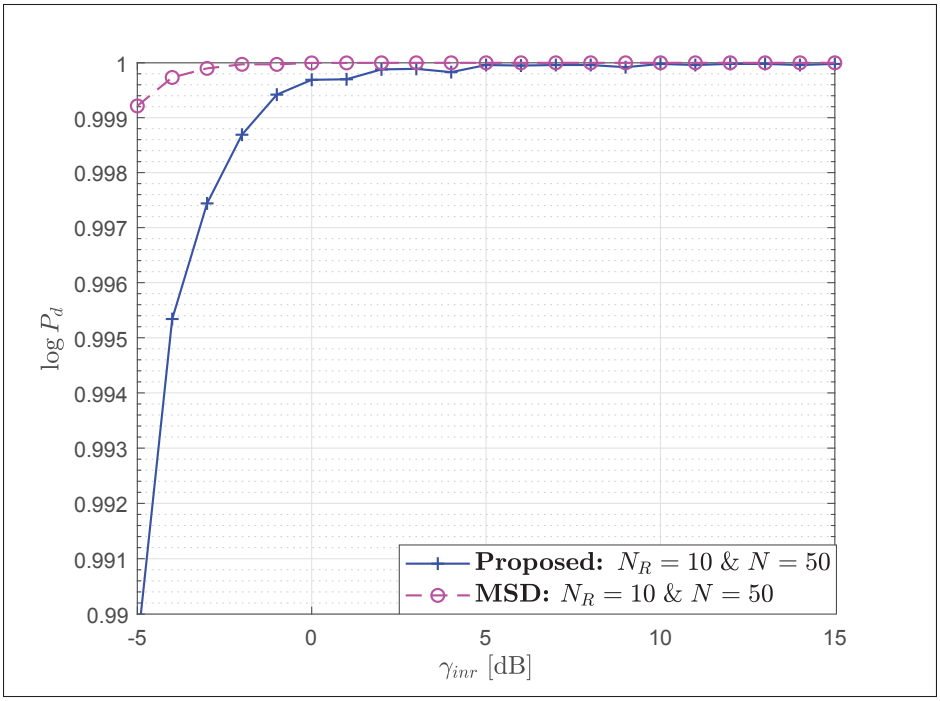

Figure 4.4 P_d versus γ_{inr}: $P_f = 0.01$

With respect to the aforementioned simulation settings, Figs. 4.4 and 4.5, respectively, depict the P_d and P_m exhibited by the proposed RFI detector and MSD. As seen in Fig. 4.4 for $\gamma_{inr} \geq 5$ dB, the proposed RFI detector has a comparable detection performance with MSD fed with the knowledge of $\boldsymbol{H}$ and $\boldsymbol{G}$ though the proposed detector is a blind one. Concerning Fig. 4.5, even though it is outperformed—in the low INR regimes—by MSD fed with the knowledge of $\boldsymbol{H}$ and $\boldsymbol{G}$, the proposed blind detector also enjoys a considerably small P_m, especially in the high INR regimes, manifested even for a sample starved setting as small as $N = 50$.

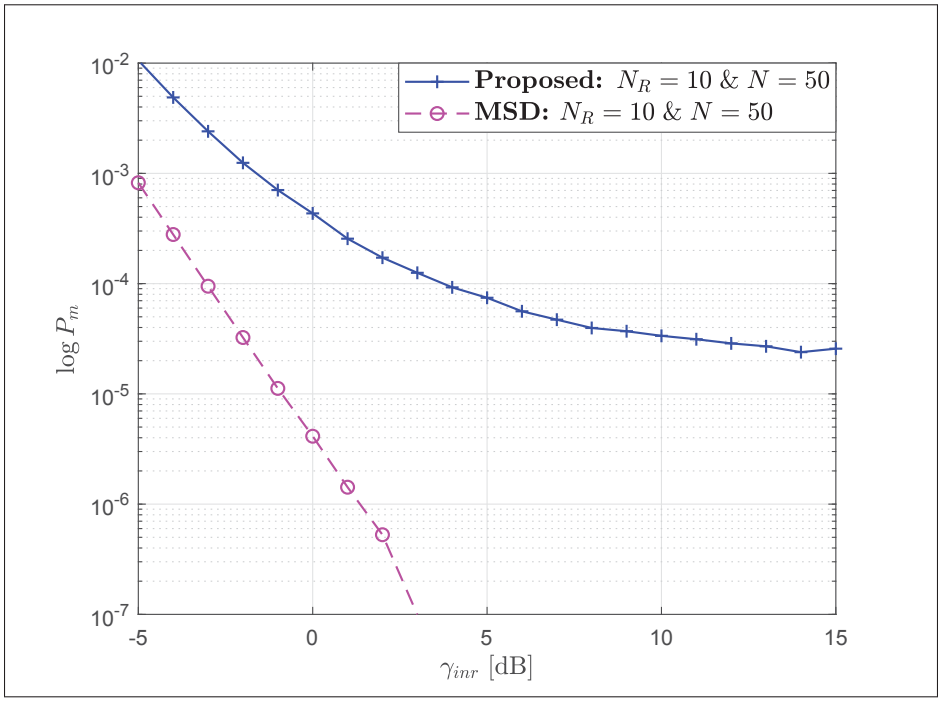

Figure 4.5 P_m versus γ_{inr}: $P_f = 0.01$ and 10^7 channel realizations

4.5.2 Performance Comparison with Multi-Antenna Detectors

We compare the performance of the proposed eigenvalue detector with multi-antenna detectors (Huang & Chung, 2013a; Taherpour *et al.*, 2010; Wang *et al.*, 2010) proposed for spectrum sensing in the context of cognitive radios (Axell *et al.*, 2012). To simulate the RFI detection performance of these detectors (Huang & Chung, 2013a; Taherpour *et al.*, 2010; Wang *et al.*, 2010), we first assume the availability of the knowledge of $\boldsymbol{h}$ and execute projection orthogonal to the SOI subspace using a projection matrix $\boldsymbol{P} = \boldsymbol{I}_{N_R} - \boldsymbol{h}(\boldsymbol{h}^H\boldsymbol{h})^{-1}\boldsymbol{h}^H$. Thereafter, along with the proposed blind detector, we simulate the F–test based detector (Huang & Chung, 2013a, eqs. (4) and (5)), blind GLRT (Taherpour *et al.*, 2010, eq. (39)), multi-channel energy detection (MCED) (Wang *et al.*, 2010, eq. (2)), and multi-channel energy detection with noise uncertainty (MCED-U) (Wang *et al.*, 2010, eq. (3)).

To simulate the detection performance of the F–test based detector (Huang & Chung, 2013a), the test statistic in (Huang & Chung, 2013a, eq. (5)) is computed via a projection matrix

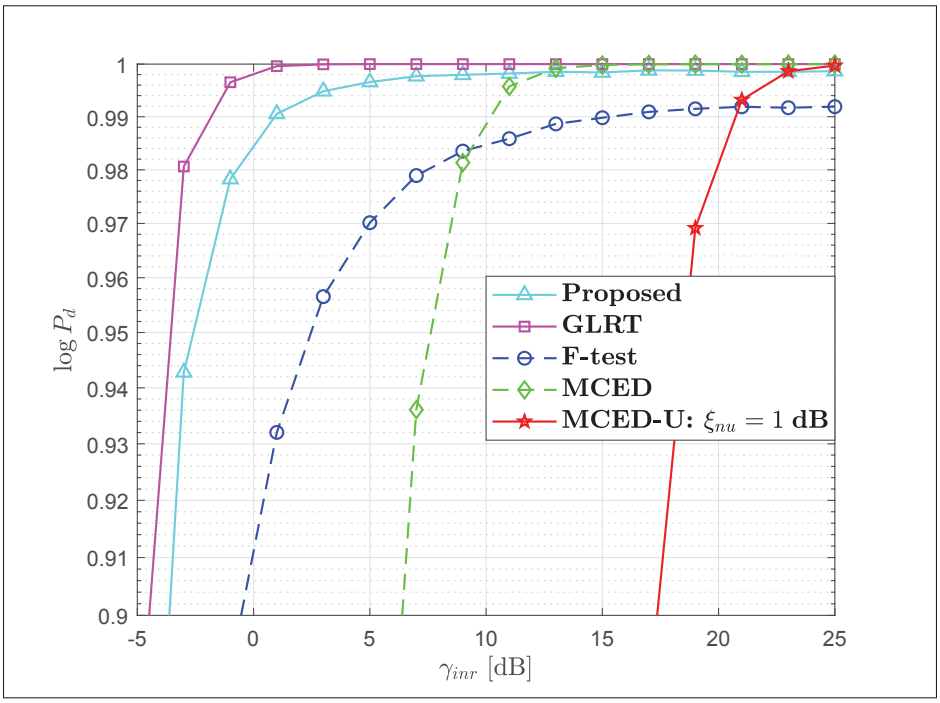

Figure 4.6 P_d versus γ_{inr}: $N = 50$ and $P_f = 0.01$

$\boldsymbol{P}' = \boldsymbol{I}_{N_R} - \boldsymbol{g}(\boldsymbol{g}^H\boldsymbol{g})^{-1}\boldsymbol{g}^H$, by also assuming the knowledge of $\boldsymbol{g}$, after projecting orthogonal to the SOI using $\boldsymbol{P}$. Having projected orthogonal to the SOI subspace, blind GLRT is simulated via (Taherpour *et al.*, 2010, eq. (39)). Note that such a GLRT statistic was also reported in (Wang *et al.*, 2010, eq. (13)). After also projecting orthogonal to the SOI subspace, MCED and MCED-U are, respectively, simulated via (Wang *et al.*, 2010, eq. (2)) and (Wang *et al.*, 2010, eq. (3)). To simulate the detection performance of MCED-U, we employ a constant noise uncertainty factor $\xi_{nu} = 10\log_{10}\eta_{nu}$ which is valid when the observation time is short (Wang *et al.*, 2010). Following the lead of (Tugnait, 2012), we assume that MCED-U overestimates σ^2 by a factor of uncertainty denoted by η_{nu}, i.e., $\hat{\sigma}^2 = \eta_{nu}\sigma^2$, and compute its respective threshold rendering the considered desired FAR. Nevertheless, the detection performance of MCED-U is simulated using data with the exact noise variance σ^2.

Observing at Fig. 4.6, the proposed blind RFI detector has a comparable detection performance with a GLRT fed with a perfect estimate of the SOI channel for the medium to high INR regimes. For the small INR regimes, the proposed detector outperforms the F-test detector

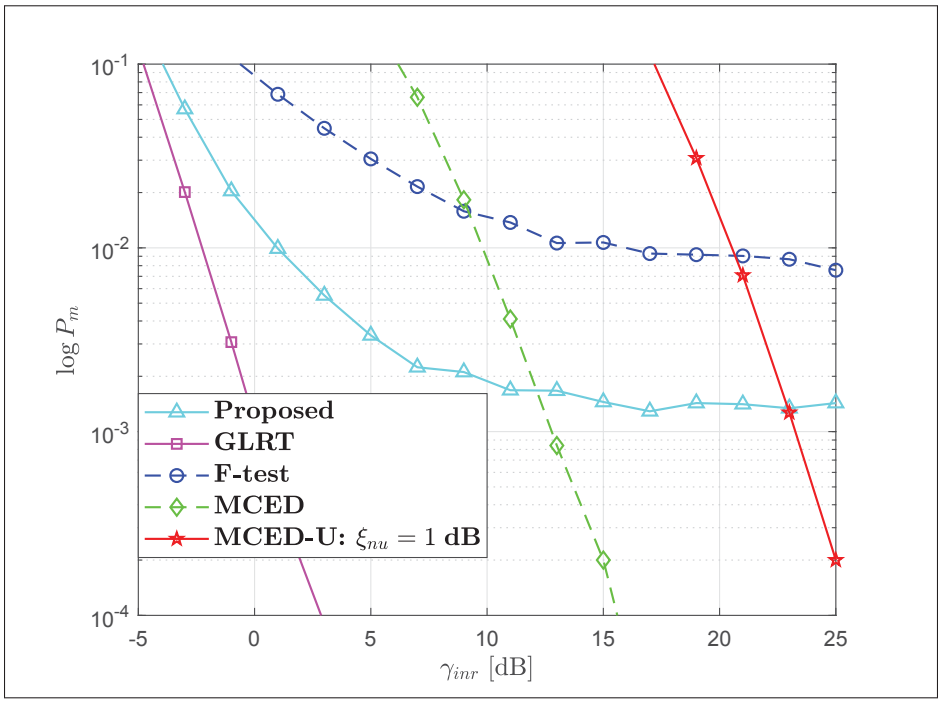

Figure 4.7 P_m versus γ_{inr}: $N = 50$ and $P_f = 0.01$

(Huang & Chung, 2013a, eqs. (4) and (5)), MCED (Wang *et al.*, 2010, eq. (2)), and MCED-U (Wang *et al.*, 2010, eq. (3)) with $\xi_{nu} = 1$ dB though the latter detectors are fed with the knowledge of the SOI channel. Such a performance manifested for a sample starved setting—as few as $N = 50$—implicates the applicability of the proposed blind detector for real-time detection of weak RFI(s) which usually occurs in SatCom and RA.

In order to offer further insight, we simulate the P_m versus γ_{inr} performance curves as depicted in Fig. 4.7. For the small INR regimes, the proposed blind detector manifests a comparable miss-detection performance with GLRT fed with the knowledge of the SOI channel. As the strength of the received RFI increases, MCED and MCED-U fed with both the knowledge of the SOI channel and the noise power—as ED requires the knowledge of the noise power—outperforms the proposed RFI detector. It is visible in Fig. 4.7 that the performance gains of MCED and MCED-U are evident with a significantly small P_m for a given INR. Summarizing the observations, however, from practicality and real-time processing perspectives, the

proposed blind detector is attractive as manifested through its detection and miss-detection performance for both the small and the high INR regimes.

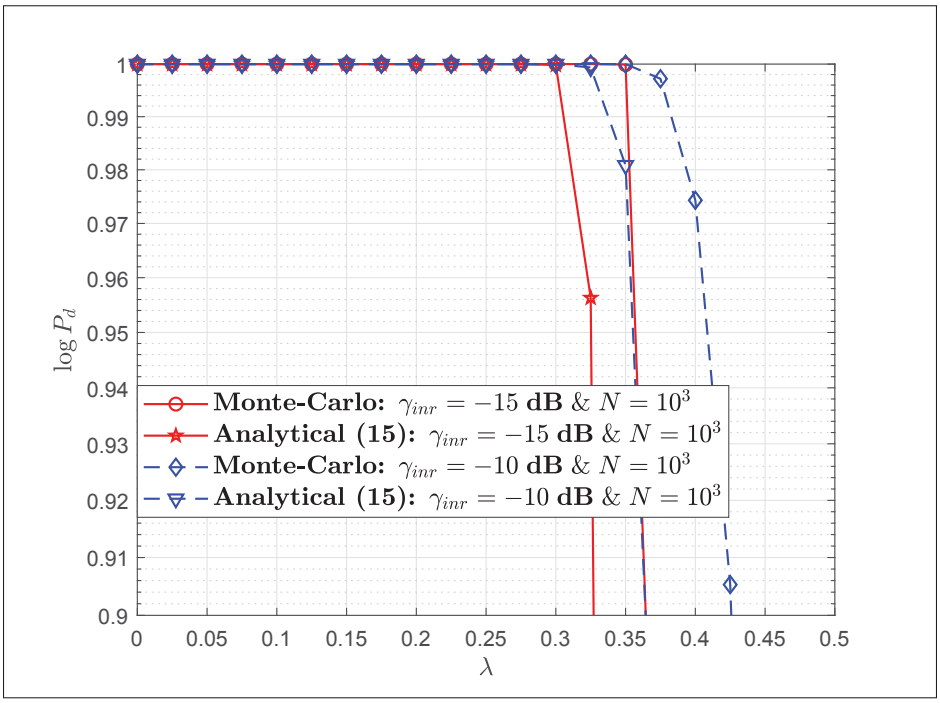

Figure 4.8 P_d versus λ: 10^4 realizations

4.5.3 Validation of the Derived Closed-Form Expressions

Hereinafter, the accuracy of the derived performance closed-form expressions—given by (4.15) and (4.16)—is assessed. Since there is no any, in its latest edition, MATLAB® function that implements the CDF of the doubly noncentral F–distribution, we evaluate (4.15) and (4.16) numerically using (4.21) and (4.22), respectively. As the NCPs—stated in Theorem 6—characterizing (4.15) and (4.16) depend on RVs that vary per a realization, the numerical evaluations of (4.15) and (4.16) are, thus, averaged over the considered number of realizations. With these simulation settings, Figs. 4.8 and 4.9 showcase the accuracy of (4.15); whereas Figs. 4.10 and 4.11 demonstrate how accurate (4.16) is.

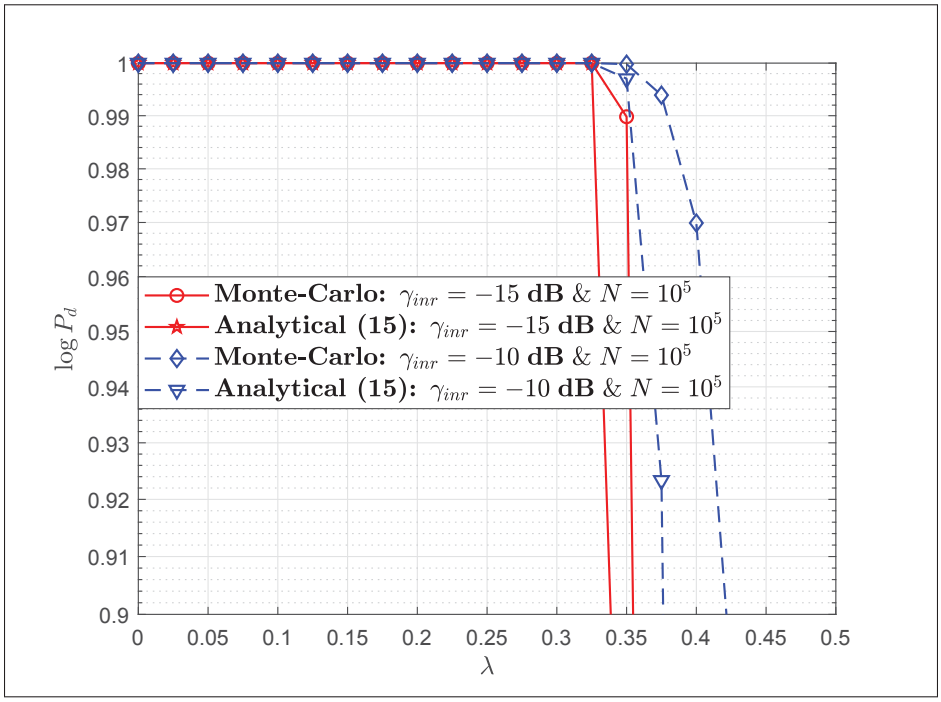

Figure 4.9 P_d versus λ: 10^4 realizations

Figs. 4.8 and 4.9 corroborate that the accuracy of (4.15) increases as N gets larger. On the other hand, Fig. 4.9 implicates that the accuracy of (4.15) also depends on the magnitude of the INR. Specifically, when the INR increases, it is observed in Fig. 4.8 that the accuracy of (4.15) gets worse, which is a manifestation of the approximation in (4.20) getting poorer as $(\lambda_1^{H_1}, \lambda_2^{H_1})$ gets larger.

Figs. 4.10 and 4.11 assess the FAR exhibited by the proposed detector and the accuracy of (4.16). As seen in these plots and in line with Proposition 1, the accuracy of (4.16), with respect to the Monte-Carlo simulations, increases as N gets larger and larger.

4.5.4 Assessment of the Manifested FAR and CROC

The impact of the number of received signal samples on the manifested FAR is assessed through Fig. 4.12. As depicted, the probability of false alarm becomes infinitesimally small as N gets larger. It is also demonstrated that the CFAR constraint is not satisfied in the fi-

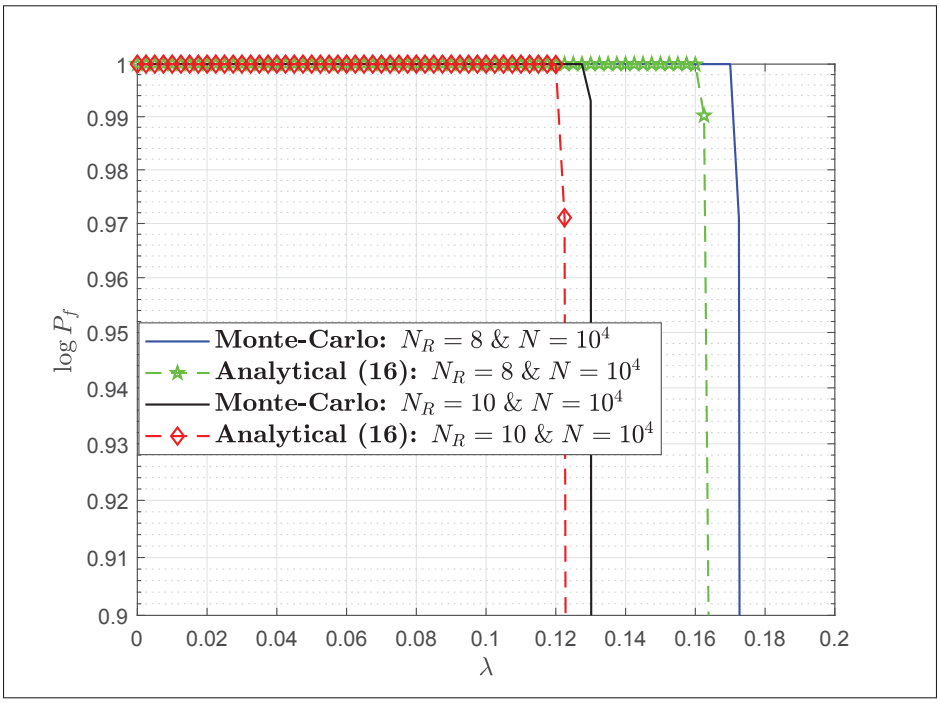

Figure 4.10 P_f versus λ: $\gamma_{snr} = -4$ dB and 10^3 realizations

nite length regime if the threshold is set using asymptotic false alarm probability—like GLRT (Taherpour *et al.*, 2010; Wang *et al.*, 2010). As originally addressed by (Scharf & Lytle, 1971), the proposed detector also exhibits difficulties to satisfy the FAR constraint exactly like complex detectors.

At last, the simulation assessments are culminated by the assessment of the CROC exhibited by the proposed RFI detector. In order to depict the underlying CROC, the P_m versus P_f curves are depicted for different N_R and γ_{inr} that comprise Fig. 4.13. As corroborated via Fig. 4.13, since the increment in INR or N_R provides an improvement in an RFI detection and hence a smaller likelihood of missing the impinging RFI, the CROC curves shift inward with respect to γ_{inr} and N_R. In addition, Fig. 4.13 demonstrates the natural trade-off between P_m and P_f.

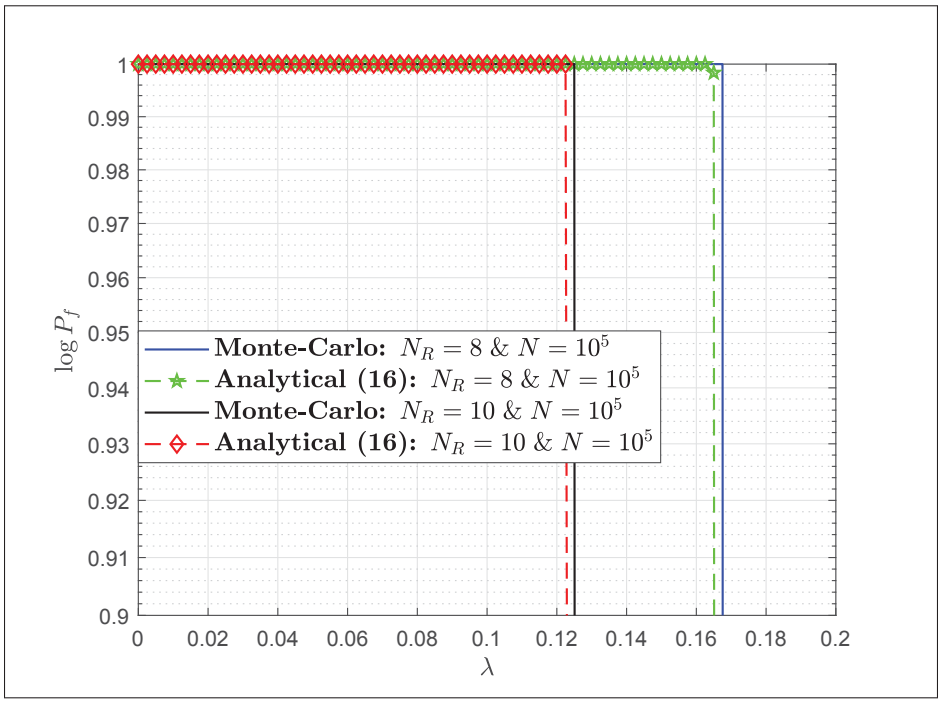

Figure 4.11 P_f versus λ: $\gamma_{snr} = -4$ dB and 10^3 realizations

4.6 Conclusions and Outlooks

4.6.1 Conclusions

An eigenvalue-based blind RFI detector is proposed and studied for SIMO systems that may suffer from RFI. Through the derivation of the distribution of the equivalent test statistic, performance closed-form expressions of the probability of RFI detection and probability of false alarm are derived for infinitely large samples. Meanwhile, the accuracy of the derived closed-form expressions is demonstrated through Monte-Carlo simulations. For sample starved settings and medium to large INR regimes, the conducted simulations also corroborate that the proposed detector exhibits a comparable detection performance with a GLRT detector fed with the knowledge of the SOI channel, and an MSD fed with the knowledge of the SOI and RFI channels. Such a performance reveals the attractiveness of the proposed RFI detector for real-time applications.

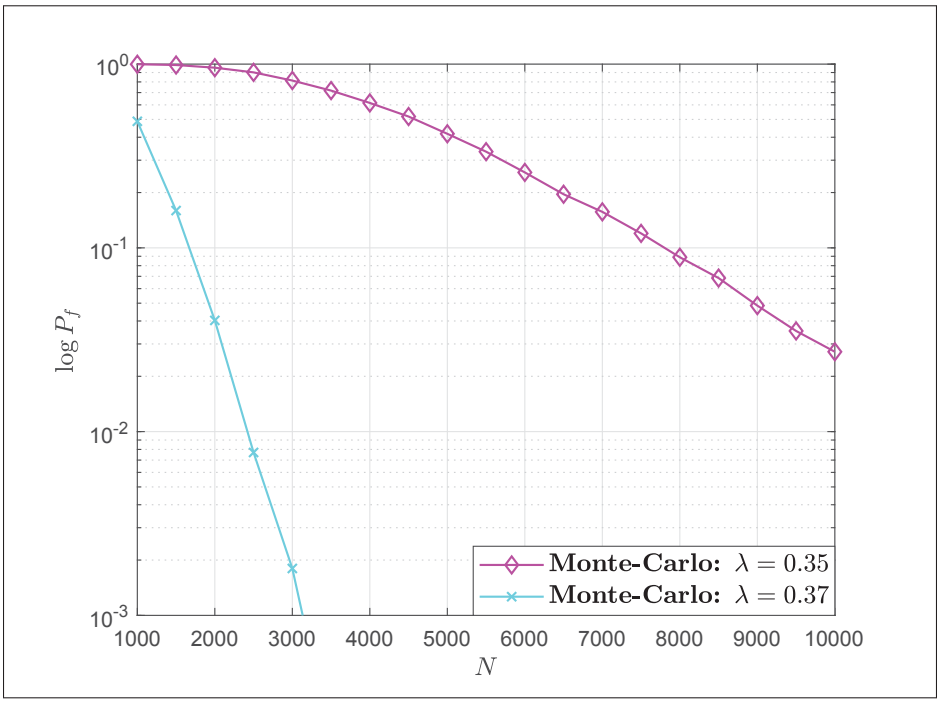

Figure 4.12 Impact of N on P_f: 10^4 realizations

4.6.2 Outlooks

If the values of $\boldsymbol{h}$ are known and $\{s[k], v[k]\}$ are Gaussian RVs, the underlying RFI detection problem can also be reformulated as the detection of rank-1 signals, which is a special case of the hypothesis test in (Ramírez *et al.*, 2011, eq. (3)). With respect to (Ramírez *et al.*, 2011) which considers the detection of rank-R ($R \geq 1$) signals with uncalibrated multiple antennas, the proposed eigenvalue detector can also be extended to the detection of rank-R ($R > 1$) RFI(s). To practically realize such an extension, the channel order of the SOI and the RFI(s) are required and hence source enumeration techniques (Lu & Zoubir, 2015; Stoica & Selen, 2004; Nadakuditi & Edelman, 2008) would be, preliminarily, needed. In addition to the aforementioned extension, the extension of the proposed RFI detector to the multiple-input multiple-output (MIMO) and massive MIMO systems (Müller *et al.*, 2014; Yin *et al.*, 2016)—that might also consider a rank-R ($R > 1$) RFI(s)—is worth addressing. Moreover, accounting for the inevitable calibration uncertainties of the N_R antenna frontends similar to (Tugnait, 2012; Ramírez *et al.*, 2011; Leshem & van der Veen, 2001), consideration of *inde-*

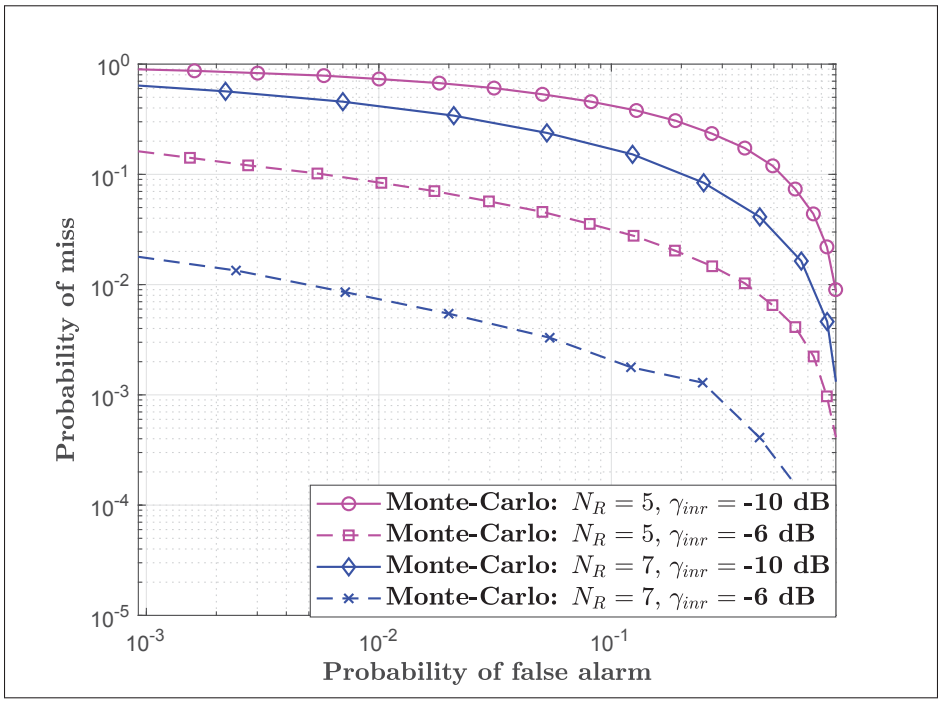

Figure 4.13 Complementary ROC: $N = 100$

pendent and non-identically distributed (i.ni.d.) noise samples is also worth investigating for SIMO, MIMO, and massive MIMO systems.

Acknowledgments

The authors acknowledge the funding provided by AVIO-601 Project sponsored by the Natural Sciences and Engineering Research Council of Canada (NSERC). The authors also acknowledge the anonymous technical reviewers and the Editor whose criticisms and insights have contributed toward the improvement of this manuscript's quality, scope, and accuracy.

CHAPTER 5

LINEAR AND MULTI-LINEAR RFI DETECTORS FOR MULTI-ANTENNA WIRELESS COMMUNICATIONS

Tilahun M. Getu[1,2], Wessam Ajib[2], and René Jr. Landry[1]

[1] Department of Electrical Engineering, École de Technologie Supérieure,
1100 Notre-Dame West, Montréal, Québec, Canada H3C 1K3
[2] Department of Computer Sciences, Université du Québec à Montréal,
201 Av. President-Kennedy, Montréal, Québec, Canada H2X 3Y7

This article was submitted to *IEEE Transactions on Wireless Communications* as of November 2018 (Getu *et al.*, 2018, submitted).

"The function of education is to teach one to think intensively and to think critically. Intelligence plus character - that is the goal of true education."—Martin Luther King, Jr.

Abstract—Radio frequency interference (RFI) is affecting various radio frequency operating systems. In practical wireless channels, RFI can be received through a multi-path fading channel. In such a scenario, robust detection of RFI can be challenging since the signal of interest can also be received through a multi-path fading channel. Hence, while introducing a tensor-based hypothesis testing framework, this paper proposes matrix- and tensor-based multi-antenna RFI detection techniques for an RFI that might be received through a multi-path fading channel. To characterize the performance of the proposed detectors, performance analyses that led to insightful asymptotic characterizations have been pursued. Simulations assess the performance of the proposed detectors and validate the derived asymptotic characterizations.

Index Terms—RFI detection, matrix-based detector, tensor-based detector, tensor-based hypothesis testing.

5.1 Introduction

5.1.1 Related Works

Radio frequency interference (RFI) is caused by intentional interferers—such as jammers, spoofers, and meaconers—and unintentional interferers—for instance, nearby transmitters and harmonics manifesting out-of-band emissions. Because of these interferers, RFI is becoming common in many radio frequency (RF) operating systems as diverse as microwave radiometry, radio astronomy, satellite communications, ultra-wideband communications, radar, and cognitive radios (van der Tol & van der Veen, 2005; Getu *et al.*, 2015b; Misra *et al.*, 2009; Borio *et al.*, 2008; Getu *et al.*, 2017; Ciuonzo *et al.*, 2016a; Bandiera & Orlando, 2009; Getu *et al.*, 2016; Boulogeorgos *et al.*, 2016b). To detect a widely occurring RFI that is also affecting 93% of the satellite industry (Newtec and IRG, Sep. 2013), the state-of-the-art encompasses several RFI detection techniques: for example, statistical (Misra *et al.*, 2009; Ruf *et al.*, 2006; De Roo & Misra, 2010; Balaei & Dempster, 2009; Getu *et al.*, 2018c,b) and transformed domain-based (Dovis *et al.*, 2012; Borio *et al.*, 2008) techniques.

Despite the considered assumptions regarding the type of the signal of interest (SOI), the type of RFI, the SOI channel, and/or the RFI channel, the multi-antenna RFI detection problem can be posed as an adaptive radar detection problem tackled in (Ciuonzo *et al.*, 2016a,b, 2017; Aubry *et al.*, 2014); the blind adaptation problems of (Scharf & McCloud, 2002) or the matched subspace detection problems of (Scharf & Friedlander, 1994); and the source enumeration problem of (Lu & Zoubir, 2015). However, an RFI can be emitted by different sources at different times and the assumption on the type of RFI cannot render a robust RFI detection. In addition, as transmitted signals usually traverse through a multi-path fading channel in practice (Simon & Alouini, 2005; Proakis & Salehi, 2008), RFI detectors can be sensitive to the errors pertaining to the inevitably inaccurate estimation of the SOI and RFI channels. As a result, further research toward a robust RFI detection would be of importance.

5.1.2 Motivation

Despite the fact that an RFI can traverse through a multi-path fading channel, robust detection techniques that are specifically designed for such an RFI has not been addressed to date. In such a setting, RFI detection can be challenging, as both the RFI channel and the SOI channel can be frequency selective which is a manifestation of a multi-path fading channel often encountered in practice (Simon & Alouini, 2005; Proakis & Salehi, 2008).

Concerning the detection of an RFI received through a multi-path fading channel, one of the viable research strategies would be the robust estimation of the subspace spanned by the received RFI. In this regard, the RFI detection problem boils down to the accurate estimation of the RFI parameter such as RFI subspace. Regarding a parameter estimation such as the RFI subspace estimation, the recent advancements in tensor-based signal processing (Haardt *et al.*, 2008; Roemer & Haardt, 2010; Roemer *et al.*, 2014; Getu *et al.*, 2017, 2018d) have revealed that tensor-based parameter estimators outperform their matrix-based counterparts. In line with these advancements, tensors have been investigated for several applications such as parameter/channel estimation (Haardt *et al.*, 2008; Song *et al.*, 2010a; Roemer & Haardt, 2010; Roemer *et al.*, 2014; Getu *et al.*, 2015a), single- and multi-interferer RFI excision (Getu *et al.*, 2015b, 2016, 2017, 2018d), source enumeration (da Costa *et al.*, 2011), blind recovery of signals and blind identification of mixtures (Lim & Comon, 2014), brain-source imaging (Becker *et al.*, 2014, 2015), and time-varying graph topology identification as well as tracking of dynamic networks (Shen *et al.*, 2017; Giannakis *et al.*, 2018). In spite of such broad applications, improved parameter estimation, and significant advancements in tensor-based signal processing, it is to be noted that tensors have not been employed for the detection of an RFI(s).

5.1.3 Contributions

Regarding the aforementioned motivation, this paper introduces a tensor-based hypothesis testing framework which can find several applications in communication systems and signal processing. This framework is introduced with respect to a tensor-based multi-antenna detection—

along with the matrix-based detection—of RFI received over a multi-path fading channel. In a nutshell, the contributions of this paper are itemized beneath.

- We introduce a tensor-based hypothesis testing framework whose application is tailored for the multi-antenna detection of RFI.
- For a reception through a multi-path fading channel and single-input multiple-output (SIMO) systems, we propose a matrix-based RFI detector (MB-RD) and a tensor-based RFI detector (TB-RD).
- The asymptotic performance of the proposed detectors is analytically characterized and assessed via Monte-Carlo simulations.

Following this introduction, Sec. 5.2 describes the considered system model. Sec. 5.3 presents the matrix-based detection and the MB-RD algorithm. Sec. 5.4 details the tensor-based detection which leads to the TB-RD algorithm. Sec. 5.5 follows with the performance analyses of TB-RD along with its performance comparison with MB-RD. Sec. 5.6 reports the corresponding simulation results and conclusions are drawn in Sec. 5.7.

5.1.4 Notation

Scalars, vectors, matrices, and tensors are denoted by italic letters, lower-case boldface letters, upper-case boldface letters, and boldface calligraphic letters, respectively; $\mathbb{C}^{N_R W}$, $\mathbb{C}^{N_R W \times r}$, and $\mathbb{H}^{N_R W \times N_R W}$ represent the sets of $N_R W$–dimensional vectors of complex numbers, of $N_R W \times r$ complex matrices, and of $N_R W \times N_R W$ Hermitian matrices, respectively; $\sim$, lim, $\propto$, $\triangleq$, $\boldsymbol{A}(:,i)$, and $\boldsymbol{A}(:,i:j)$ mean distributed as, limit, statistically equivalent, equal by definition, the i-th column of $\boldsymbol{A}$, and the columns of $\boldsymbol{A}$ between its i-th and j-th columns including its i-th and j-th columns, respectively; $\mathbf{0}_{M\times N}$, $\mathrm{diag}(\cdot)$, $(\cdot)^T$, $(\cdot)^H$, and $(\cdot)^+$ stand for an $M \times N$ zero matrix, diagonal (block diagonal) matrix, transpose, Hermitian, and the Moore-Penrose inverse, respectively; $\to$, $\min(\cdot,\cdot)$, $\max(\cdot,\cdot)$, $\Pr\{\cdot\}$, $\mathrm{tr}(\cdot)$, and $\mathscr{CN}_{N_R W}(\boldsymbol{\mu},\boldsymbol{\Sigma})$ denote approaches to, minimum, maximum, the probability of, trace, and the circularly symmetric complex multivariate normal distribution with mean $\boldsymbol{\mu} \in \mathbb{C}^{N_R W \times 1}$ and covariance matrix $\boldsymbol{\Sigma} \in \mathbb{H}^{N_R W \times N_R W}$—

$W \geq 1$ ($N_R W \geq 2$), respectively; and $>>$, $(\cdot)^{-1}$, $\otimes$, and $\boldsymbol{I}_W \left(\boldsymbol{I}_{N_R W}\right)$ implicate much greater than, inverse, Kronecker product, and a $W \times W \left(N_R W \times N_R W\right)$ identity matrix, respectively.

The tensor $\mathscr{Y} \in \mathbb{C}^{I_1 \times I_2 \times \ldots \times I_R}$ is an R-way array of size I_r along its r-th mode. The r-mode unfolding of $\mathscr{Y}$ is denoted by $[\mathscr{Y}]_{(r)} \in \mathbb{C}^{I_r \times I_{r+1} \ldots I_R I_1 \ldots I_{r-1}}$ and defined to be consistent with (Haardt *et al.*, 2008). The r-mode product of $\mathscr{Y}$ and $\boldsymbol{U}_r \in \mathbb{C}^{J_r \times I_r}$ is denoted as $\mathscr{X} = \mathscr{Y} \times_r \boldsymbol{U}_r$ and defined through $[\mathscr{X}]_{(r)} = \boldsymbol{U}_r [\mathscr{Y}]_{(r)}$ (Haardt *et al.*, 2008; Getu *et al.*, 2017). The r-mode product of $\mathscr{Y}$ and a tensor $\mathscr{C} \in \mathbb{C}^{J_1 \times J_2 \times \ldots \times J_r \times \ldots \times J_R}$ is denoted by and defined through (Vasilescu & Terzopoulos, 2007; Getu *et al.*, 2017)

$$\mathscr{D} = \mathscr{Y} \times_r \mathscr{C} \Leftrightarrow [\mathscr{D}]_{(r)} = [\mathscr{C}]_r [\mathscr{Y}]_{(r)}, \tag{5.1}$$

where $\mathscr{D} \in \mathbb{C}^{I_1 \times \ldots \times I_{r-1} \times J_r \times I_{r+1} \ldots \times I_R}$ and $I_r = J_1 J_2 \ldots J_{r-1} J_{r+1} \ldots J_R$. Applying (5.1) recursively, the r-mode product among three tensors $\mathscr{Y}$, $\mathscr{C}$, and $\mathscr{A} \in \mathbb{C}^{K_1 \times K_2 \times \ldots \times K_r \times \ldots \times K_R}$ is denoted by and defined through

$$\mathscr{D} = \mathscr{Y} \times_r \mathscr{C} \times_r \mathscr{A} \Leftrightarrow [\mathscr{D}]_{(r)} = [\mathscr{A}]_r [\mathscr{C}]_r [\mathscr{Y}]_{(r)}, \tag{5.2}$$

where $J_r = K_1 K_2 \ldots K_{r-1} K_{r+1} \ldots K_R$, $I_r = J_1 J_2 \ldots J_{r-1} J_{r+1} \ldots J_R$, and $\mathscr{D} \in \mathbb{C}^{I_1 \times \ldots \times I_{r-1} \times K_r \times I_{r+1} \ldots \times I_R}$.

For the set of N subsequent time snapshots in a measurement tensor $\mathscr{Y} \in \mathbb{C}^{I_1 \times I_2 \times \ldots \times I_R \times N}$, the sample covariance tensor (SCT) $\hat{\mathscr{R}}_{yy} \in \mathbb{C}^{I_1 \times I_2 \times \ldots \times I_R \times I_1 I_2 \ldots I_R}$ is defined as

$$\hat{\mathscr{R}}_{yy} \triangleq \frac{1}{N} \left[\mathscr{Y} \times_{R+1} \mathscr{Y}^H \right], \tag{5.3}$$

where $\mathscr{Y}^H$ is the Hermitian of a tensor $\mathscr{Y}$ defined with respect to (w.r.t.) its $(R+1)$-mode unfolding as $\left[\mathscr{Y}^H\right]_{(R+1)} = \left([\mathscr{Y}]_{(R+1)}\right)^H$. At last, the addition and subtraction between two comformable tensors $\mathscr{X}$ and $\mathscr{Y}$ are denoted by and defined through

$$\mathscr{X} \pm \mathscr{Y} \Leftrightarrow [\mathscr{X} \pm \mathscr{Y}]_{(r)} = [\mathscr{X}]_{(r)} \pm [\mathscr{Y}]_{(r)}. \tag{5.4}$$

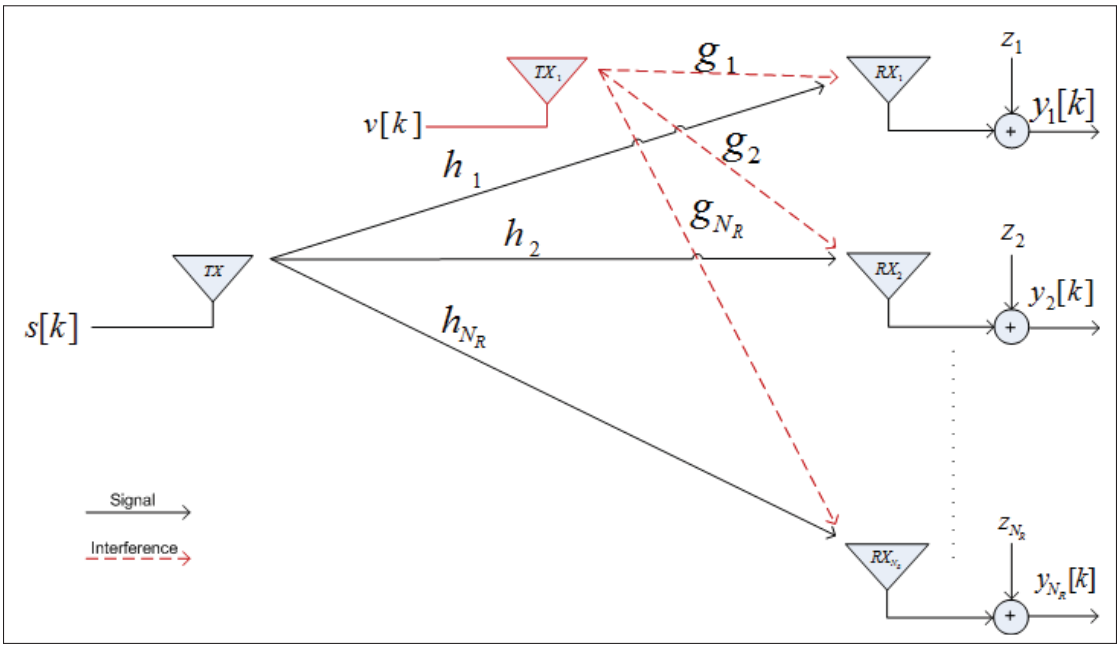

Figure 5.1 A baseband schematic depicting the l-th multi-path component of a SIMO system suffering from RFI

5.2 System Model

Consider a SIMO system over a multi-path fading channel that may also suffer from an RFI as depicted in Fig. 5.1. An SOI is transmitted by a single-antenna transmitter whose traversing channel—w.r.t. the N_R receive antennas—is modeled by a finite-duration impulse response filter (FIR) with $L+1$ taps. An RFI emitted by a nearby single-antenna transmitter that might have also been received by the N_R antennas is considered. The corresponding RFI channel is modeled by an FIR filter with L_1+1 taps. Meanwhile, we need to detect if an RFI impinges on the SIMO reception of the SOI.

Concerning the aforementioned scenario, the RFI detection problem can be posed as a binary hypothesis test given by

$$\boldsymbol{y}[k] = \begin{cases} \sum_{l=0}^{L} \boldsymbol{h}_l s[k-l] + \sum_{l=0}^{L_1} \boldsymbol{g}_l v[k-l] + \boldsymbol{z}[k] & : H_1 \\ \sum_{l=0}^{L} \boldsymbol{h}_l s[k-l] + \boldsymbol{z}[k] & : H_0, \end{cases} \tag{5.5}$$

where H_0 and H_1 are hypotheses on the RFI absence and presence, respectively; $\boldsymbol{y}[k] \in \mathbb{C}^{N_R}$ is the k-th sample multi-antenna received signal vector; $s[k]$ is the k-th unknown and deterministic symbol of the SOI; $v[k]$ is the k-th unknown and deterministic symbol of the RFI; $\boldsymbol{h}_l = [h_{1l}, h_{2l}, \ldots, h_{N_R l}]^T \in \mathbb{C}^{N_R}$ is the SOI channel gain vector for the l-th multi-path component; $\boldsymbol{g}_l = [g_{1l}, g_{2l}, \ldots, g_{N_R l}]^T \in \mathbb{C}^{N_R}$ is the RFI channel gain vector for the l-th multi-path component; and $\boldsymbol{z}[k] \sim \mathscr{CN}_{N_R}(\boldsymbol{0}, \sigma^2 \boldsymbol{I}_{N_R})$ is a zero mean circularly symmetric complex additive white Gaussian noise (AWGN) for σ^2 being the unknown noise power. Moreover, we assume that $\boldsymbol{h}_l$, $\boldsymbol{g}_l$, and $\boldsymbol{z}[k]$ are independent with each other.

5.3 Matrix-Based RFI Detection

5.3.1 Problem Formulation

Adopting the preliminary processing of (Getu *et al.*, 2015b) and (Getu *et al.*, 2017), we stack the observations of the N_R antennas and W data windows into a highly structured vector w.r.t. the m-th short-term interval (STI). Doing so by employing (5.5),

$$\boldsymbol{y}_m = \begin{cases} \boldsymbol{H}\boldsymbol{s}_m + \boldsymbol{G}\boldsymbol{v}_m + \boldsymbol{z}_m & : H_1 \\ \boldsymbol{H}\boldsymbol{s}_m + \boldsymbol{z}_m & : H_0, \end{cases} \tag{5.6}$$

where $\boldsymbol{y}_m \in \mathbb{C}^{N_R W}$, $\boldsymbol{s}_m = \big[s[mW], s[mW-1], \ldots, s[mW-W-L+1]\big]^T \in \mathbb{C}^{(W+L)}$, $\boldsymbol{v}_m = \big[v[mW], v[mW-1], \ldots, v[mW-W-L_1+1]\big]^T \in \mathbb{C}^{(W+L_1)}$, $\boldsymbol{H} \in \mathbb{C}^{N_R W \times (W+L)}$ is the SOI filtering matrix defined through (Song *et al.*, 2010a, eqs. (3) and (5)), and $\boldsymbol{z}_m \sim \mathscr{CN}_{N_R W}(\boldsymbol{0}, \sigma^2 \boldsymbol{I}_{N_R W})$ is the stacked multi-antenna noise vector. Moreover, $\boldsymbol{G} \in \mathbb{C}^{N_R W \times (W+L_1)}$ is the RFI filtering matrix structured as

$$\boldsymbol{G} = \Big[\boldsymbol{G}_1^T, \boldsymbol{G}_2^T, \ldots, \boldsymbol{G}_{N_R}^T\Big]^T, \tag{5.7}$$

where $\boldsymbol{G}_j \in \mathbb{C}^{W\times(W+L_1)}$ is a banded Toeplitz matrix, made of the j-th antenna's RFI impulse response $\boldsymbol{g}_j \overset{\triangle}{=} \left[g_{j0},\ldots,g_{jL_1}\right]^T$, given by

$$\boldsymbol{G}_j = \begin{bmatrix} g_{j0} & \cdots & g_{jL_1} & 0 & \cdots & \cdots & 0 \\ 0 & g_{j0} & \cdots & g_{jL_1} & 0 & \cdots & 0 \\ \vdots & \vdots & \vdots & \vdots & \vdots & \vdots & \vdots \\ 0 & \cdots & \cdots & 0 & g_{j0} & \cdots & g_{jL_1} \end{bmatrix}. \tag{5.8}$$

The horizontal concatenation of N STIs leads to a binary hypothesis test given by

$$\boldsymbol{Y} = \begin{cases} \boldsymbol{HS}+\boldsymbol{GV}+\boldsymbol{Z} & : H_1 \\ \boldsymbol{HS}+\boldsymbol{Z} & : H_0, \end{cases} \tag{5.9}$$

where $\boldsymbol{Y} = [\boldsymbol{y}_1,\boldsymbol{y}_2,\ldots,\boldsymbol{y}_N] \in \mathbb{C}^{N_RW\times N}$, $\boldsymbol{S} = [\boldsymbol{s}_1,\boldsymbol{s}_2,\ldots,\boldsymbol{s}_N] \in \mathbb{C}^{(W+L)\times N}$, $\boldsymbol{V} = [\boldsymbol{v}_1,\boldsymbol{v}_2,\ldots,\boldsymbol{v}_N] \in \mathbb{C}^{(W+L_1)\times N}$, and $\boldsymbol{Z} = [\boldsymbol{z}_1,\boldsymbol{z}_2,\ldots,\boldsymbol{z}_N] \in \mathbb{C}^{N_RW\times N}$. Based on the hypothesis testing stated through (5.9), the proposed MB-RD is discussed beneath.

5.3.2 Proposed Detection

Using (5.6), the sample covariance matrix (SCM) is computed as

$$\hat{\boldsymbol{R}}_{yy} = \frac{1}{N}\sum_{m=1}^{N} \boldsymbol{y}_m\boldsymbol{y}_m^H = \frac{1}{N}\boldsymbol{Y}\boldsymbol{Y}^H \in \mathbb{H}^{N_RW\times N_RW}. \tag{5.10}$$

In order to proceed further, we consider these assumptions: i) the SCM has full rank, i.e., $N \geq \max(W+L, W+L_1)$; (ii) $\boldsymbol{H}$ and $\boldsymbol{G}$ have full column rank, i.e., $N_RW \geq \max(W+L, W+L_1)$; and (iii) the window length is greater than both the SOI and RFI channel orders, i.e., $W > \max(L, L_1)$. Having employed these assumptions, MB-RD comprises the signal processing described subsequently.

First, the singular value decomposition (SVD) of $\boldsymbol{Y}$ is computed as

$$\boldsymbol{Y} = \tilde{\boldsymbol{U}}\tilde{\boldsymbol{\Sigma}}\tilde{\boldsymbol{V}}^H, \tag{5.11}$$

where $r = W + L$ and $\tilde{\boldsymbol{\Sigma}} = \text{diag}(\tilde{\boldsymbol{\Sigma}}_{1:r}, \tilde{\boldsymbol{\Sigma}}_{r+1:N_RW})$ for $\tilde{\boldsymbol{\Sigma}}_{1:r} = \text{diag}(\tilde{\sigma}_1, \tilde{\sigma}_2, \ldots, \tilde{\sigma}_r)$ and $\tilde{\boldsymbol{\Sigma}}_{r+1:N_RW} = \text{diag}(\tilde{\sigma}_{r+1}, \tilde{\sigma}_{r+2}, \ldots, \tilde{\sigma}_{N_RW})$. Using (5.11), the SVD of the SCM—equated as $\hat{\boldsymbol{R}}_{yy} = \hat{\boldsymbol{U}}\hat{\boldsymbol{\Sigma}}\hat{\boldsymbol{V}}^H$—is expressed as

$$\hat{\boldsymbol{R}}_{yy} = \tilde{\boldsymbol{U}}\left(\frac{\tilde{\boldsymbol{\Sigma}}^2}{N}\right)\tilde{\boldsymbol{U}}^H = \overbrace{[\hat{\boldsymbol{U}}_{1:r} \;\; \hat{\boldsymbol{U}}_{r+1:N_RW}]}^{\hat{\boldsymbol{U}}}\hat{\boldsymbol{\Sigma}}\hat{\boldsymbol{V}}^H, \tag{5.12}$$

where $\hat{\boldsymbol{U}} = \tilde{\boldsymbol{U}} = \hat{\boldsymbol{V}}, \hat{\boldsymbol{\Sigma}} = \tilde{\boldsymbol{\Sigma}}^2/N, \hat{\boldsymbol{U}}_{1:r} = \hat{\boldsymbol{U}}(:, 1:r) \in \mathbb{C}^{N_RW \times r}$ and $\hat{\boldsymbol{U}}_{r+1:N_RW} = \hat{\boldsymbol{U}}(:, r+1:N_RW) \in \mathbb{C}^{N_RW \times (N_RW - r)}$ are the subspaces spanned by the eigenvectors corresponding to the largest r eigenvalues and the smallest $N_RW - r$ eigenvalues, respectively, and $\hat{\boldsymbol{\Sigma}} = \text{diag}(\hat{\boldsymbol{\Sigma}}_{1:r}, \hat{\boldsymbol{\Sigma}}_{r+1:N_RW})$ for $\hat{\boldsymbol{\Sigma}}_{1:r} = \text{diag}(\hat{\sigma}_1, \hat{\sigma}_2, \ldots, \hat{\sigma}_r)$, $\hat{\boldsymbol{\Sigma}}_{r+1:N_RW} = \text{diag}(\hat{\sigma}_{r+1}, \hat{\sigma}_{r+2}, \ldots, \hat{\sigma}_{N_RW})$, and $\hat{\sigma}_1 > \hat{\sigma}_2 > \ldots > \hat{\sigma}_{N_RW}$. It shall be noted that $\boldsymbol{Y}$ and $\hat{\boldsymbol{R}}_{yy}$ span identical column space.

A projection matrix $\hat{\boldsymbol{P}}_{nd}$ which projects the received signal vector orthogonally onto the subspace spanned by the singular vectors corresponding to the r largest singular values is then computed from $\hat{\boldsymbol{U}}_{1:r}$ as

$$\hat{\boldsymbol{P}}_{nd} = \boldsymbol{I}_{N_RW} - \hat{\boldsymbol{U}}_{1:r}\hat{\boldsymbol{U}}^+_{1:r} = \hat{\boldsymbol{U}}_{r+1:N_RW}\hat{\boldsymbol{U}}^+_{r+1:N_RW}. \tag{5.13}$$

As $\hat{\boldsymbol{U}}_{1:r}$ offers orthonormal columns, $\hat{\boldsymbol{U}}^H_{1:r}\hat{\boldsymbol{U}}_{1:r} = \boldsymbol{I}_r$ and hence $\hat{\boldsymbol{U}}^+_{1:r} = (\hat{\boldsymbol{U}}^H_{1:r}\hat{\boldsymbol{U}}_{1:r})^{-1}\hat{\boldsymbol{U}}^H_{1:r} = \hat{\boldsymbol{U}}^H_{1:r}$. Thus, $\hat{\boldsymbol{P}}_{nd} = \boldsymbol{I}_{N_RW} - \hat{\boldsymbol{U}}_{1:r}\hat{\boldsymbol{U}}^H_{1:r}$ can be used instead for the sake of low computational burden. Using (5.13), the SCM projected orthogonal onto the subspace spanned by the singular vectors corresponding to the r largest singular values is obtained as

$$\hat{\boldsymbol{R}}^{(p)}_{yy} = \frac{1}{N}\sum_{m=1}^{N}\hat{\boldsymbol{P}}_{nd}\boldsymbol{y}_m(\hat{\boldsymbol{P}}_{nd}\boldsymbol{y}_m)^H = \hat{\boldsymbol{P}}_{nd}\hat{\boldsymbol{R}}_{yy}\hat{\boldsymbol{P}}^H_{nd}. \tag{5.14}$$

Computing the SVD of (5.14),

$$\hat{\boldsymbol{R}}_{yy}^{(p)} = \tilde{\hat{\boldsymbol{U}}}\tilde{\hat{\boldsymbol{\Sigma}}}\tilde{\hat{\boldsymbol{V}}}^H = [\tilde{\hat{\boldsymbol{U}}}_{1:r_1}\ \tilde{\hat{\boldsymbol{U}}}_{r_1+1:N_RW}]\tilde{\hat{\boldsymbol{\Sigma}}}\tilde{\hat{\boldsymbol{V}}}^H, \tag{5.15}$$

where $r_1 = W + L_1$, $\tilde{\hat{\boldsymbol{U}}}_{1:r_1} = \tilde{\hat{\boldsymbol{U}}}(:, 1:r_1) \in \mathbb{C}^{N_RW \times r_1}$ is the subspace spanned by the singular vectors corresponding to the largest r_1 singular values of $\hat{\boldsymbol{R}}_{yy}^{(p)}$, $\tilde{\hat{\boldsymbol{U}}}_{r_1+1:N_RW} = \tilde{\hat{\boldsymbol{U}}}(:, r_1+1:N_RW)$, and $\tilde{\hat{\boldsymbol{\Sigma}}} = \mathrm{diag}(\tilde{\hat{\boldsymbol{\Sigma}}}_{1:r_1}, \tilde{\hat{\boldsymbol{\Sigma}}}_{r_1+1:N_RW})$ for $\tilde{\hat{\boldsymbol{\Sigma}}}_{1:r_1} = \mathrm{diag}(\tilde{\hat{\sigma}}_1, \tilde{\hat{\sigma}}_2, \ldots, \tilde{\hat{\sigma}}_{r_1})$, $\tilde{\hat{\boldsymbol{\Sigma}}}_{r_1+1:N_RW} = \mathrm{diag}(\tilde{\hat{\sigma}}_{r_1+1}, \tilde{\hat{\sigma}}_{r_1+2}, \ldots, \tilde{\hat{\sigma}}_{N_RW})$, and $\tilde{\hat{\sigma}}_1 > \tilde{\hat{\sigma}}_2 > \ldots > \tilde{\hat{\sigma}}_{N_RW}$. Using $\tilde{\hat{\boldsymbol{U}}}_{1:r_1}$, a projection matrix $\hat{\boldsymbol{P}}_d$ is obtained as

$$\hat{\boldsymbol{P}}_d = \tilde{\hat{\boldsymbol{U}}}_{1:r_1}\tilde{\hat{\boldsymbol{U}}}_{1:r_1}^{+} = \tilde{\hat{\boldsymbol{U}}}_{1:r_1}\tilde{\hat{\boldsymbol{U}}}_{1:r_1}^{H}. \tag{5.16}$$

Having performed the aforementioned computations, it is now time to define the MB-RD test statistic which is able to discriminate the RFI presence instance from the RFI absence instance. To motivate the MB-RD test statistic, it shall be realized that (5.15) comprises a subspace spanned by the non-dominant $N_RW - r$ singular vectors computed using (5.12). Concerning this subspace, projection onto the subspace spanned by the r_1 dominant singular vectors is performed via (5.16). Employing (5.14) and (5.16), the MB-RD test statistic is formulated as

$$T^{\mathrm{MB}} \triangleq \frac{\nu_2}{\nu_1} \frac{\mathrm{tr}\big(\hat{\boldsymbol{P}}_d \hat{\boldsymbol{R}}_{yy}^{(p)}\big)}{\mathrm{tr}\big((\boldsymbol{I}_{N_RW} - \hat{\boldsymbol{P}}_d)\hat{\boldsymbol{R}}_{yy}^{(p)}\big)}, \tag{5.17}$$

where $\big(\nu_1, \nu_2\big) = \big(2Nr_1, 2N(N_RW - r_1)\big)$ are the degrees of freedom of the numerator and denominator, respectively. By using (5.17), a decision rule is then formulated as

$$T^{\mathrm{MB}} \underset{H_0}{\overset{H_1}{\gtrless}} \lambda, \tag{5.18}$$

where λ is a decision threshold. Whenever $T^{\mathrm{MB}} > \lambda$, H_1 is detected, as also implied by the linearity between the received signal samples and the joint CSI of the SOI and RFI. Otherwise, H_0 is detected. Meanwhile, MB-RD algorithm is summarized in Algorithm 5.1.

Algorithm 5.1 MB-RD Algorithm

Input: $\{\boldsymbol{y}_m\}_{m=1}^{N}$, λ, r, r_1, ν_1, and ν_2
Output: H_1 or H_0
Compute $\hat{\boldsymbol{R}}_{yy}$ and its SVD using (5.10) and (5.12)
Compute $\hat{\boldsymbol{P}}_{nd}$ using (5.13)
Compute $\hat{\boldsymbol{R}}_{yy}^{(p)}$ and its SVD using (5.14) and (5.15)
Compute $\hat{\boldsymbol{P}}_{d}$ using (5.16)
Compute T^{MB} using (5.17)
if $T^{\mathrm{MB}} > \lambda$, *detect* H_1
else, *detect* H_0

5.3.3 Equivalent Test Statistic

While recalling the Hermitianness and positive semi-definiteness of the SCM, i.e., $\hat{\boldsymbol{U}} = \hat{\boldsymbol{V}}$, deploying (5.12) and (5.13) in (5.14)

$$\hat{\boldsymbol{R}}_{yy}^{(p)} = \hat{\boldsymbol{U}}_{r+1:N_RW}\hat{\boldsymbol{\Sigma}}_{r+1:N_RW}\hat{\boldsymbol{U}}_{r+1:N_RW}^{H}. \tag{5.19}$$

From the positive semi-definiteness and Hermitianness of $\hat{\boldsymbol{R}}_{yy}^{(p)}$, $\tilde{\hat{\boldsymbol{U}}} = \tilde{\hat{\boldsymbol{V}}}$. Thus, (5.15) leads to

$$\hat{\boldsymbol{R}}_{yy}^{(p)} = [\tilde{\hat{\boldsymbol{U}}}_{1:r_1}\ \tilde{\hat{\boldsymbol{U}}}_{r_1+1:N_RW}]\tilde{\hat{\boldsymbol{\Sigma}}}[\tilde{\hat{\boldsymbol{U}}}_{1:r_1}\ \tilde{\hat{\boldsymbol{U}}}_{r_1+1:N_RW}]^{H}. \tag{5.20}$$

Equating (5.19) and (5.20),

$$\tilde{\hat{\boldsymbol{U}}}_{1:r_1} = \hat{\boldsymbol{U}}_{r+1:N_RW}(:, 1:r_1) \tag{5.21a}$$

$$\tilde{\hat{\boldsymbol{\Sigma}}} = \mathrm{diag}\big(\tilde{\hat{\boldsymbol{\Sigma}}}_{1:r_1},\ \tilde{\hat{\boldsymbol{\Sigma}}}_{r_1+1:N_RW}\big) = \hat{\boldsymbol{\Sigma}}_{r+1:N_RW} \tag{5.21b}$$

$$\tilde{\hat{\boldsymbol{U}}}_{r_1+1:N_RW} = \hat{\boldsymbol{U}}_{r+1:N_RW}(:, r_1+1:d), \tag{5.21c}$$

where $d = N_RW - r$. From (5.21c), an additional assumption can be inferred, i.e., $N_RW - r \geq r_1 + 1$ or equivalently, $N_RW \geq r + r_1 + 1 = 2W + L + L_1 + 1$.

To continue, substituting (5.21a) into (5.16),

$$\hat{\boldsymbol{P}}_d = \hat{\boldsymbol{U}}_{r+1:N_RW}(:,1:r_1)\hat{\boldsymbol{U}}^H_{r+1:N_RW}(:,1:r_1). \tag{5.22}$$

While deploying (5.21a)-(5.21c), substituting (5.20) and (5.22) into (5.17) leads to the equivalence in (5.23).

$$T^{\text{MB}} \propto \frac{\text{tr}\Big(\hat{\boldsymbol{U}}_{r+1:N_RW}(:,1:r_1)\hat{\boldsymbol{\Sigma}}_{r+1:N_RW}(1:r_1,1:r_1)\hat{\boldsymbol{U}}^H_{r+1:N_RW}(:,1:r_1)\Big)}{\text{tr}\Big(\hat{\boldsymbol{U}}_{r+1:N_RW}(:,r_1+1:d)\hat{\boldsymbol{\Sigma}}_{r+1:N_RW}(r_1+1:d,r_1+1:d)\hat{\boldsymbol{U}}^H_{r+1:N_RW}(:,r_1+1:d)\Big)}. \tag{5.23}$$

Applying the property of trace and the orthonormal property of $\hat{\boldsymbol{U}}$, (5.23) simplifies to

$$T^{\text{MB}} \propto \frac{\sum_{i=r+1}^{r+r_1}\hat{\sigma}_i}{\sum_{i=r+r_1+1}^{N_RW}\hat{\sigma}_i}. \tag{5.24}$$

To minimize computational complexity, it is worth noting that MB-RD can be implemented through (5.24).

5.4 Tensor-Based RFI Detection

5.4.1 Problem Formulation

To pursue a tensor-based formulation of the problem in (5.9), we assume that the received multi-antenna signal samples are arranged in a tensor $\mathscr{Y}$ diagrammed in Fig. 5.2—similar to the arrangement of (Getu *et al.*, 2015b). To continue, should $\left[\mathscr{Y}\right]^T_{(3)}$ be equal to $\boldsymbol{Y}$ expressed in (5.9), the multi-linear equivalent of (5.9) is given by

$$\mathscr{Y} = \begin{cases} \mathscr{H} \times_3 \boldsymbol{S}^T + \mathscr{G} \times_3 \boldsymbol{V}^T + \mathscr{Z} & : H_1 \\ \mathscr{H} \times_3 \boldsymbol{S}^T + \mathscr{Z} & : H_0, \end{cases} \tag{5.25}$$

where $\mathscr{H}$, $\mathscr{G}$, and $\mathscr{Z}$ are the SOI filtering tensor, the RFI filtering tensor, and the noise tensor, respectively. Note that $\mathscr{H}$ and $\mathscr{G}$ are, respectively, constructed by aligning the banded Toeplitz matrices $\left\{\boldsymbol{H}_j\right\}_{j=1}^{N_R}$ and $\left\{\boldsymbol{G}_j\right\}_{j=1}^{N_R}$ as in Fig. 5.2, i.e., $\left[\mathscr{H}\right]_{(3)}^T = \boldsymbol{H}$ and $\left[\mathscr{G}\right]_{(3)}^T = \boldsymbol{G}$.

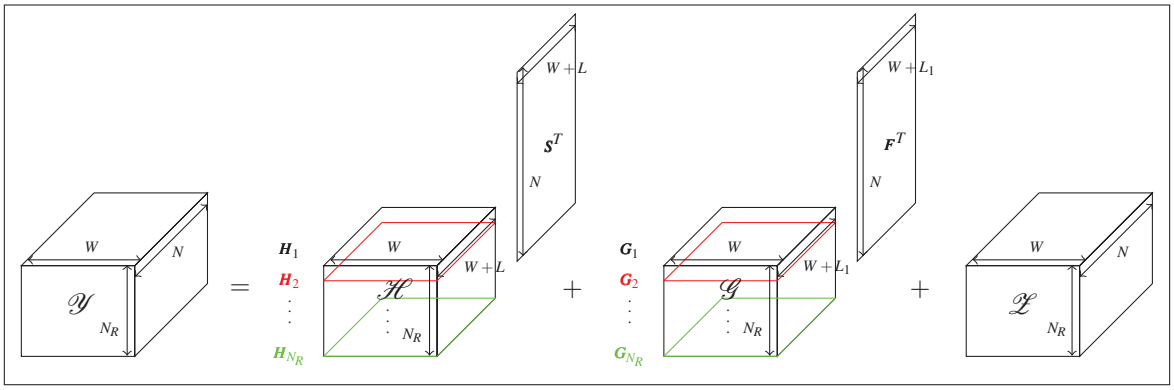

Figure 5.2 A multi-linear formulation from (5.9) under H_1 (Getu *et al.*, 2015b)

In the subsequent algorithm development, we adopted the assumptions of Sec. 5.3.2 and Sec. 5.3.3. To define an equivalent tensor for the matrix $\boldsymbol{Y}_p = \hat{\boldsymbol{P}}_{nd}\boldsymbol{Y}$, we define a projection tensor $\hat{\mathscr{P}}^{[nd]}$ via its 3-mode unfolding as

$$\left[\hat{\mathscr{P}}^{[nd]}\right]_{(3)}^T = \hat{\boldsymbol{P}}_{nd}. \tag{5.26}$$

Using $\hat{\mathscr{P}}^{[nd]}$, a tensor whose 3-mode unfolding transpose spans the subspace spanned by the singular vectors that correspond to the non-largest $N_RW - r$ singular values—computed in (5.12)—is defined as

$$\mathscr{Y}_p = \hat{\mathscr{P}}^{[nd]} \times_3 \mathscr{Y}. \tag{5.27}$$

Employing the definition in (5.1) and the equality in (5.26),

$$\left[\mathscr{Y}_p\right]_{(3)}^T = \left[\hat{\mathscr{P}}^{[nd]}\right]_{(3)}^T \left[\mathscr{Y}\right]_{(3)}^T = \left[\hat{\mathscr{P}}^{[nd]}\right]_{(3)}^T \boldsymbol{Y} = \hat{\boldsymbol{P}}_{nd}\boldsymbol{Y}. \tag{5.28}$$

Deploying (5.27), the respective SCT is computed as

$$\hat{\mathscr{R}}_{yy}^{(p)} = \frac{1}{N}\left[\mathscr{Y}_p \times_3 \mathscr{Y}_p^H\right]. \tag{5.29}$$

To obtain the subspace spanned by the eigenvectors corresponding to the dominant eigenvalues of $\left[\mathscr{Y}_p\right]_{(3)}^T$ which is also spanned by the eigenvectors corresponding to the dominant eigenvalues of $\left[\hat{\mathscr{R}}_{yy}^{(p)}\right]_{(3)}^T$, the truncated higher-order SVD (HOSVD) of (5.27) is given by (Roemer *et al.*, 2014; Getu *et al.*, 2017)

$$\mathscr{Y}_p \approx \tilde{\tilde{\mathscr{S}}}^{[1:r_1]} \times_1 \tilde{\tilde{\boldsymbol{U}}}_1^{[1:r_1]} \times_2 \tilde{\tilde{\boldsymbol{U}}}_2^{[1:r_1]} \times_3 \tilde{\tilde{\boldsymbol{U}}}_3^{[1:r_1]}, \tag{5.30}$$

where $\tilde{\tilde{\mathscr{S}}}^{[1:r_1]} \in \mathbb{C}^{\tilde{r}_1 \times \tilde{r}_2 \times \tilde{r}_3}$ is the truncated core tensor—$\tilde{r}_1 = \min\big(N_R,\ L_1+1\big)$, $\tilde{r}_2 = \min(W,\ NN_R)$, and $\tilde{r}_3 = \min\big(N,\ r_1\big)$—and $\tilde{\tilde{\boldsymbol{U}}}_n^{[1:r_1]} \in \mathbb{C}^{\tilde{f}_n \times \tilde{r}_n}$ is a unitary matrix of the dominant singular vectors of $[\mathscr{Y}_p]_{(n)}$, $n \in \{1,2,3\}$ and $[\tilde{f}_1, \tilde{f}_2, \tilde{f}_3] = [N_R, W, N]$ (Getu *et al.*, 2017, 2015b). Thus, since $N \geq r_1$, $\tilde{r}_2 = W$ and $\tilde{r}_3 = r_1$.

The respective tensor-based (TB) estimator for the subspace spanned by the r_1 singular vectors corresponding to the r_1 largest singular values—obtained in (5.15)—is defined as (Roemer *et al.*, 2014, eq. (17))

$$\tilde{\tilde{\mathscr{U}}}^{[1:r_1]} = \tilde{\tilde{\mathscr{S}}}^{[1:r_1]} \times_1 \tilde{\tilde{\boldsymbol{U}}}_1^{[1:r_1]} \times_2 \tilde{\tilde{\boldsymbol{U}}}_2^{[1:r_1]} \times_3 \tilde{\tilde{\boldsymbol{\Sigma}}}_{1:r_1}^{-1}, \tag{5.31}$$

where $\tilde{\tilde{\boldsymbol{\Sigma}}}_{1:r_1} = \tilde{\boldsymbol{\Sigma}}_{r+1:N_RW}(1:r_1, 1:r_1)$ is a normalization factor which has no impact on the subspace estimation accuracy (Roemer *et al.*, 2014). Underneath, being the result of the simplification of (5.31), the relationship between TB and matrix-based (MB) subspace estimators is stated.

Proposition 2. For $\tilde{\tilde{\boldsymbol{T}}}_c = \tilde{\tilde{\boldsymbol{U}}}_c^{[1:r_1]} \tilde{\tilde{\boldsymbol{U}}}_c^{[1:r_1]^H}$ and $c \in \big\{1,2\big\}$, the TB and MB subspace estimators are related as

$$\left[\tilde{\tilde{\mathscr{U}}}^{[1:r_1]}\right]_{(3)}^T = \big(\tilde{\tilde{\boldsymbol{T}}}_1 \otimes \tilde{\tilde{\boldsymbol{T}}}_2\big)\tilde{\tilde{\boldsymbol{U}}}_{1:r_1}. \tag{5.32}$$

Proof. Following the lines of (Roemer *et al.*, 2014, Appendix A), Proposition 2 can be proved for $R = 2$ by replacing $\left[\hat{\mathscr{U}}^{[s]}; \left[\mathscr{X}\right]_{(3)}^{T}; \hat{\mathbf{\Sigma}}_s\right]$ with $\left[\tilde{\tilde{\mathscr{U}}}^{[1:r_1]}; \left[\mathscr{Y}_p\right]_{(3)}^{T}; \tilde{\tilde{\mathbf{\Sigma}}}_{1:r_1}\right]$. A similar proof is also reported in (Getu *et al.*, 2015a, Appendix A). □

5.4.2 Proposed Detection

Note that TB and MB subspace estimators offer identical performance for $N_R \leq (L_1+1)$. When $N_R > (L_1+1)$, the TB estimator stated via (5.32) offers an improved estimate for the noise is better filtered in its three modes rendering an improved noise suppression, unlike the MB subspace estimator (Haardt *et al.*, 2008, Appendix I). This better filtering is achieved through the Kronecker projection matrix—$\tilde{\tilde{\boldsymbol{T}}}_1 \otimes \tilde{\tilde{\boldsymbol{T}}}_2$—which would characterize a tensor $\hat{\tilde{\mathscr{P}}}_{1,2}$ as

$$\left[\tilde{\tilde{\mathscr{P}}}_{1,2}\right]_{(3)}^{T} = \tilde{\tilde{\boldsymbol{T}}}_1 \otimes \tilde{\tilde{\boldsymbol{T}}}_2 = \tilde{\tilde{\boldsymbol{T}}}_1 \otimes \boldsymbol{I}_W, \tag{5.33}$$

where $\tilde{\tilde{\boldsymbol{T}}}_2 = \tilde{\tilde{\boldsymbol{U}}}_2^{[1:r_1]} \tilde{\tilde{\boldsymbol{U}}}_2^{[1:r_1]^H} = \boldsymbol{I}_W$ for $\tilde{r}_2 = W$ all the time. To leverage the aforementioned performance enhancement, we define a projection tensor $\tilde{\tilde{\mathscr{P}}}^{[d]} \in \mathbb{C}^{N_R \times W \times N_R W}$ defined via

$$\left[\tilde{\tilde{\mathscr{P}}}^{[d]}\right]_{(3)}^{T} = \left(\tilde{\tilde{\boldsymbol{T}}}_1 \otimes \boldsymbol{I}_W\right) \tilde{\tilde{\boldsymbol{U}}}_{1:r_1} \tilde{\tilde{\boldsymbol{U}}}_{1:r_1}^{H}. \tag{5.34}$$

We are now ready to define the TB-RD test statistic. Using (5.29) and (5.34), the TB-RD test statistic is defined as

$$T^{\mathrm{TB}} \triangleq \frac{\nu_2}{\nu_1} \frac{\mathrm{tr}\left(\left[\tilde{\tilde{\mathscr{P}}}^{[d]} \times_3 \hat{\mathscr{R}}_{yy}^{(p)}\right]_{(3)}^{T}\right)}{\mathrm{tr}\left(\left[\left(\tilde{\tilde{\mathscr{P}}}_{1,2} - \tilde{\tilde{\mathscr{P}}}^{[d]}\right) \times_3 \hat{\mathscr{R}}_{yy}^{(p)}\right]_{(3)}^{T}\right)}. \tag{5.35}$$

The corresponding decision rule is then given by

$$T^{\mathrm{TB}} \underset{H_0}{\overset{H_1}{\gtrless}} \lambda. \tag{5.36}$$

Regarding (5.36), TB-RD decides in favor of H_1 provided that $T^{\mathrm{TB}} > \lambda$. Otherwise, it detects H_0. Meanwhile, TB-RD algorithm is summarized in Algorithm 5.2.

Algorithm 5.2 TB-RD Algorithm

Input: $\{\boldsymbol{y}_m\}_{m=1}^{N}$, λ, r, r_1, ν_1, and ν_2
Output: H_1 or H_0
Compute $\hat{\mathscr{R}}_{yy}^{(p)}$ using (5.28) and (5.29)
Compute $\tilde{\tilde{\mathscr{P}}}_{1,2}$ using (5.33)
Compute $\tilde{\tilde{\mathscr{P}}}^{[d]}$ using (5.34)
Compute T^{TB} using (5.35)
if $T^{\mathrm{TB}} > \lambda$, *detect* H_1
else, *detect* H_0

In order to get further intuition about TB-RD, (5.35) is simplified and its result is stated in the underneath lemma.

Lemma 3. The TB-RD statistic given by (5.35) simplifies to (5.37) and (5.38).

$$T^{\mathrm{TB}} = \frac{\nu_2}{\nu_1} \frac{\mathrm{tr}\Big(\big[\tilde{\tilde{\mathscr{P}}}^{[d]}\big]_{(3)}^{T} \hat{\boldsymbol{R}}_{yy}^{(p)} \Big)}{\mathrm{tr}\Big(\big(\big[\tilde{\tilde{\mathscr{P}}}_{1,2}\big]_{(3)}^{T} - \big[\tilde{\tilde{\mathscr{P}}}^{[d]}\big]_{(3)}^{T} \big) \hat{\boldsymbol{R}}_{yy}^{(p)} \Big)}. \tag{5.37}$$

$$T^{\mathrm{TB}} \propto \frac{\mathrm{tr}\Big((\hat{\tilde{\boldsymbol{T}}}_1 \otimes \boldsymbol{I}_W) \hat{\boldsymbol{U}}_{r+1:N_R W}(:, 1:r_1) \hat{\boldsymbol{\Sigma}}_{r+1:N_R W}(1:r_1, 1:r_1) \hat{\boldsymbol{U}}_{r+1:N_R W}^{H}(:, 1:r_1) \Big)}{\mathrm{tr}\Big((\hat{\tilde{\boldsymbol{T}}}_1 \otimes \boldsymbol{I}_W) \hat{\boldsymbol{U}}_{r+1:N_R W}(:, r_1+1:d) \hat{\boldsymbol{\Sigma}}_{r+1:N_R W}(r_1+1:d, r_1+1:d) \hat{\boldsymbol{U}}_{r+1:N_R W}^{H}(:, r_1+1:d) \Big)}. \tag{5.38}$$

Proof. Please refer to Appendix 1 under APPENDIX V.

Note that (5.38) can be deployed to implement the low-complexity version of TB-RD.

5.5 Performance Analyses

In this section, the performance analyses of TB-RD and MB-RD are pursued. As the performance of TB-RD and MB-RD, respectively, depends solely on (5.35) and (5.17), the respective distributions are needed so as to derive the exact performance expressions. However, such distributions tend to be mathematically intractable, especially for the test statistics accommodating an impinging RFI with unknown distribution and highly time-variant channel. To overcome such a possible intractability, we analyze the probability of RFI detection exhibited by TB-RD and MB-RD for high signal-to-noise ratio (SNR) and interference-to-noise ratio (INR) regimes. In other words, the corresponding detection performance is analyzed when the perturbations get infinitesimally small. Moreover, the detection performance of TB-RD and MB-RD is analytically compared for different scenarios.

5.5.1 Performance Analyses for the High SNR and INR Regimes

The high SNR and INR regimes are the manifestations of infinitesimally small perturbations. For such perturbations, the first-order perturbation analysis is often a tool which is deployed to assess the asymptotic performance of subspace-based algorithms (Ciuonzo *et al.*, 2015; Roemer *et al.*, 2014; Liu *et al.*, 2008). As TB-RD and MB-RD are also subspace-based algorithms, the first-order perturbation analysis can also be employed so as to characterize their asymptotic performance, especially for the high SNR and INR regimes. In the subsequent analyses, to continue, quantization error is neglected so as to facilitate mathematical tractability.

To highlight the first-order perturbation analysis, we begin with the noiseless version $\tilde{\boldsymbol{Y}} = \left[\tilde{\boldsymbol{y}}_1, \tilde{\boldsymbol{y}}_2, \ldots, \tilde{\boldsymbol{y}}_N\right]$ whose SVD is computed as

$$\tilde{\boldsymbol{Y}} = \boldsymbol{U}\boldsymbol{\Sigma}\boldsymbol{V}^H, \tag{5.39}$$

where $\boldsymbol{U} = [\boldsymbol{U}_{1:\tilde{r}} \ \boldsymbol{U}_{\tilde{r}+1:N_RW}]$, for $\tilde{r} = r + r_1 = 2W + L + L_1$, $\boldsymbol{U}_{1:\tilde{r}} = \boldsymbol{U}(:, 1:\tilde{r}) \in \mathbb{C}^{N_RW \times \tilde{r}}$ denotes the true subspace jointly spanned by the SOI and the RFI (if any), $\boldsymbol{U}_{\tilde{r}+1:N_RW} = \boldsymbol{U}(:, \tilde{r}+1 : N_RW) \in \mathbb{C}^{N_RW \times (N_RW - \tilde{r})}$ represents the true noise subspace, and $\boldsymbol{\Sigma} = \text{diag}(\boldsymbol{\Sigma}_{1:r}, \boldsymbol{\Sigma}_{r+1:N_RW})$ for

$\boldsymbol{\Sigma}_{1:r} = \text{diag}(\sigma_1, \sigma_2, \ldots, \sigma_r)$, $\boldsymbol{\Sigma}_{r+1:N_RW} = \text{diag}(\sigma_{r+1}, \sigma_{r+2}, \ldots, \sigma_{\tilde{r}}, 0, 0, \ldots, 0)$, and $\sigma_1 \geq \sigma_2 \geq \ldots \geq \sigma_{\tilde{r}}$. Note that $\boldsymbol{U}_{1:r} = \boldsymbol{U}(:, 1:r)$ and $\boldsymbol{U}_{r+1:N_RW} = \boldsymbol{U}(:, r+1:N_RW)$ are the true subspace spanned by the r strongest signal and the true subspace jointly spanned by the remaining signals and noise, respectively. When an AWGN contaminates each $\tilde{\boldsymbol{y}}_k$, $\boldsymbol{Y}$ is decomposed as in (5.11) for $\tilde{\boldsymbol{U}} = [\tilde{\boldsymbol{U}}_{1:\tilde{r}} \;\; \tilde{\boldsymbol{U}}_{\tilde{r}+1:N_RW}] = [\hat{\boldsymbol{U}}_{1:\tilde{r}} \;\; \hat{\boldsymbol{U}}_{\tilde{r}+1:N_RW}]$ and the corresponding parameters in (5.39) are replaced by their respective estimates.

Comparing (5.39) and (5.11) via (Ciuonzo *et al.*, 2015, eqs. (18) and (20)) and noting that $\tilde{\boldsymbol{U}} = \hat{\boldsymbol{U}}$,

$$\hat{\boldsymbol{U}}_{1:\tilde{r}} = \boldsymbol{U}_{1:\tilde{r}} + \Delta\boldsymbol{U}_{1:\tilde{r}} \tag{5.40a}$$

$$\hat{\boldsymbol{U}}_{\tilde{r}+1:N_RW} = \boldsymbol{U}_{\tilde{r}+1:N_RW} + \Delta\boldsymbol{U}_{\tilde{r}+1:N_RW}, \tag{5.40b}$$

where $\Delta\boldsymbol{U}_{1:\tilde{r}} = \boldsymbol{U}_{\tilde{r}+1:N_RW}\boldsymbol{U}^H_{\tilde{r}+1:N_RW}\boldsymbol{Z}\boldsymbol{V}_{1:\tilde{r}}\boldsymbol{\Sigma}^{-1}_{1:\tilde{r}}$, for $\boldsymbol{V}_{1:\tilde{r}} = \boldsymbol{V}(:, 1:\tilde{r})$ and $\boldsymbol{\Sigma}_{1:\tilde{r}} = \boldsymbol{\Sigma}(1:\tilde{r}, 1:\tilde{r})$, is the perturbations in the joint SOI and RFI subspace, and $\Delta\boldsymbol{U}_{\tilde{r}+1:N_RW} = -\boldsymbol{U}_{1:\tilde{r}}\boldsymbol{\Sigma}^{-1}_{1:\tilde{r}}\boldsymbol{V}^H_{1:\tilde{r}}\boldsymbol{Z}^H\boldsymbol{U}_{\tilde{r}+1:N_RW}$ is the perturbations in the noise subspace. Similarly,

$$\hat{\boldsymbol{U}}_{r+1:N_RW} = \boldsymbol{U}_{r+1:N_RW} + \Delta\boldsymbol{U}_{r+1:N_RW}, \tag{5.41}$$

where $\Delta\boldsymbol{U}_{r+1:N_RW} = [\Delta\boldsymbol{U}_{1:\tilde{r}}(:, r+1:\tilde{r}), \Delta\boldsymbol{U}_{\tilde{r}+1:N_RW}]$ is the perturbations in the joint subspace of the second r_1 strongest signals and noise. Observing (5.40a) and (5.40b), both $\Delta\boldsymbol{U}_{1:\tilde{r}}$ and $\Delta\boldsymbol{U}_{\tilde{r}+1:N_RW}$ approach $\boldsymbol{0}$ as $\boldsymbol{Z} \to \boldsymbol{0}$. In other words, $\Delta\boldsymbol{U}_{r+1:N_RW} \to \boldsymbol{0}$ as $\boldsymbol{Z} \to \boldsymbol{0}$. With these analyses, the subsequent characterizations follow.

Theorem 7. Suppose $P_d = \Pr\{T^{\text{TB}} > \lambda | H_1\}$ be the probability of RFI detection exhibited by TB-RD. For $\lambda < \infty$ and $\boldsymbol{0}$ denoting $\boldsymbol{0}_{N_RW \times (N_RW - r)}$, $\lim_{\Delta\boldsymbol{U}_{r+1:N_RW} \to \boldsymbol{0}} P_d = 1$.

Proof. Please refer to Appendix 2 under APPENDIX V.

Theorem 7 implicates that TB-RD perfectly detects an RFI whenever the perturbations become infinitesimally small—correspondingly, when the SNR and INR are very high. Besides, it inspires the underneath corollary.

Corollary 1. Suppose the probability of RFI detection manifested by MB-RD is given by $P_d^{\text{mat}} = \Pr\{T^{\text{MB}} > \lambda | H_1\}$. For $\lambda < \infty$, $\lim_{\Delta \boldsymbol{U}_{r+1:N_R W} \to \boldsymbol{0}} P_d^{\text{mat}} = 1$.

Proof. From (5.23) and (5.38), $T^{\text{MB}} = T^{\text{TB}}\Big|_{\tilde{\hat{\boldsymbol{T}}}_1 \otimes \boldsymbol{I}_W = \boldsymbol{I}_{N_R W}}$. Thus, replacing $\tilde{\hat{\boldsymbol{T}}}_1 \otimes \boldsymbol{I}_W$ by $\boldsymbol{I}_{N_R W}$ and following the lines of Appendix 2 (under APPENDIX V), the result follows immediately. □

5.5.2 Comparison Between TB-RD and MB-RD

A comparison between the detection performance of MB-RD and TB-RD is stated beneath.

Theorem 8. For P_d and P_d^{mat} that are, respectively, exhibited by TB-RD and MB-RD,

- if $N_R \leq (L_1 + 1)$, $P_d = P_d^{\text{mat}}$;
- if the received SOI or RFI, respectively, corresponds to the very high SNR and INR regimes, $P_d = P_d^{\text{mat}}$; and
- if $N_R >> (L_1 + 1)$, $N_R W >> r + r_1$, and the exhibited SNR as well as INR are very low—i.e., $(\gamma_{snr},\ \gamma_{inr}) \to (0,\ 0)$, $P_d >> P_d^{\text{mat}}$.

Proof. Please see Appendix 3 under APPENDIX V.

It can be concluded from Theorem 8 that TB-RD offers no benefit in terms of performance improvement whenever $N_R \leq (L_1 + 1)$ which is in line with the fact that TB subspace estimators offer no improvement w.r.t. their MB counterparts for $N_R \leq (L_1 + 1)$. For $N_R >> (L_1 + 1)$ and $N_R W >> r + r_1$, the TB subspace estimator offers significant performance improvement for the low SNR and INR regimes, and sample starved settings. Such a performance improvement gets significant when the number of receive antennas increases. Leveraging this improvement, TB-RD renders a significant performance improvement for the low INR and SNR regimes

whenever $N_R >> (L_1+1)$ and $N_R W >> r+r_1$. For the high SNR and INR regimes, both the TB and MB subspace estimators offer parameter estimates with high accuracy. Accordingly, the improvement in detection performance provided by TB-RD vanishes and both detectors manifest identical asymptotic performance, as characterized in Theorem 7 and Corollary 1.

Table 5.1 Simulation parameters unless otherwise mentioned

Parameters	Assigned value
(L, L_1, P_s)	$(1, 1, 10\,\mathrm{W})$
(N_R, γ_{snr})	$(10, 0\,\mathrm{dB})$
(W, N)	$(10, 24)$
Number of realizations	10^5

5.6 Simulation Results

This section assesses the performance of MB-RD and TB-RD using Monte-Carlo simulations. Unless otherwise mentioned, these simulations use the parameters of Table 5.1. For a reception through a multi-path fading channel, the simulations consider the reception of a quadrature phase shift keying (QPSK) modulated SOI which might be interfered also by a QPSK modulated RFI. Specifically, for $\{s_k^I, s_k^Q\} \in \{-1,1\} \times \{-1,1\}$ and $\{v_k^I, v_k^Q\} \in \{-1,1\} \times \{-1,1\}$, we simulate the SOI and RFI as $s[k] = \sqrt{P_s/2}\big[s_k^I + j s_k^Q\big]$ and $v[k] = \sqrt{P_v/2}\big[v_k^I + j v_k^Q\big]$ for P_s and P_v being the transmitted power of the SOI and RFI, respectively. Similar to (Getu *et al.*, 2018a) and without loss of generality, the SOI and RFI multi-path fading channels are modeled by a zero mean complex AWGN with unit variance, i.e., $\big[\{\boldsymbol{h}_l\}_{l=0}^{L}, \{\boldsymbol{g}_l\}_{l=0}^{L_1}\big] \sim \mathscr{CN}_{N_R}(\boldsymbol{0}, \boldsymbol{I}_{N_R})$. Moreover, the SNR and INR are defined—w.r.t. an STI—as $\gamma_{snr} = \dfrac{\big|\big|\boldsymbol{H}\boldsymbol{s}_m\big|\big|^2}{N_R W \sigma^2}$ and $\gamma_{inr} = \dfrac{\big|\big|\boldsymbol{G}\boldsymbol{v}_m\big|\big|^2}{N_R W \sigma^2}$, respectively.

MB-RD is simulated by comparing (5.17) with a decision threshold. Implemented on the basis of Algorithm 5.2, TB-RD is simulated by comparing (5.37) with a decision threshold. While computing (5.37), the corresponding *matricization* and *tensorization* operations are performed using *Tensorlab* (Sorber *et al.*, Jan. 2014). Throughout this section, the decision threshold ren-

dering a false alarm rate (FAR) of 0.1 is obtained via Monte-Carlo simulations which average over 10^5 independent channel realizations. To simulate the P_d exhibited by different detectors, we assume the reception of an SOI and an RFI over multi-path fading channels, as modeled above, and their contamination by a complex AWGN. Whereas the simulation of P_f manifested by different detectors is conducted by assuming the reception of the SOI contaminated by a complex AWGN.

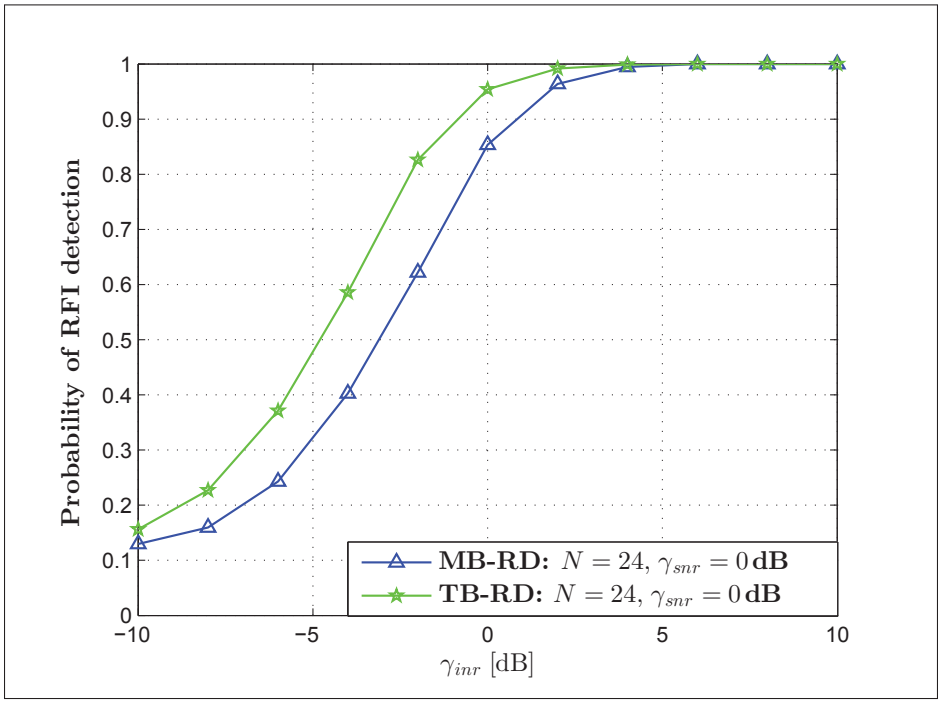

Figure 5.3 P_d versus γ_{inr}: $P_f = 0.1$ and 10^4 realizations

5.6.1 TB-RD versus MB-RD

Regarding the exhibited P_d, Figs. 5.3-5.5 showcase the performance comparison between TB-RD and MB-RD. As seen in these plots, TB-RD visibly improves MB-RD, especially in the detection of a weak RFI. The performance improvement is attributed to the fact that TB-RD deploys a TB subspace estimator which filters the noise in three modes rendering an improved noise suppression than its MB counterpart provided that $N_R > L_1 + 1$.

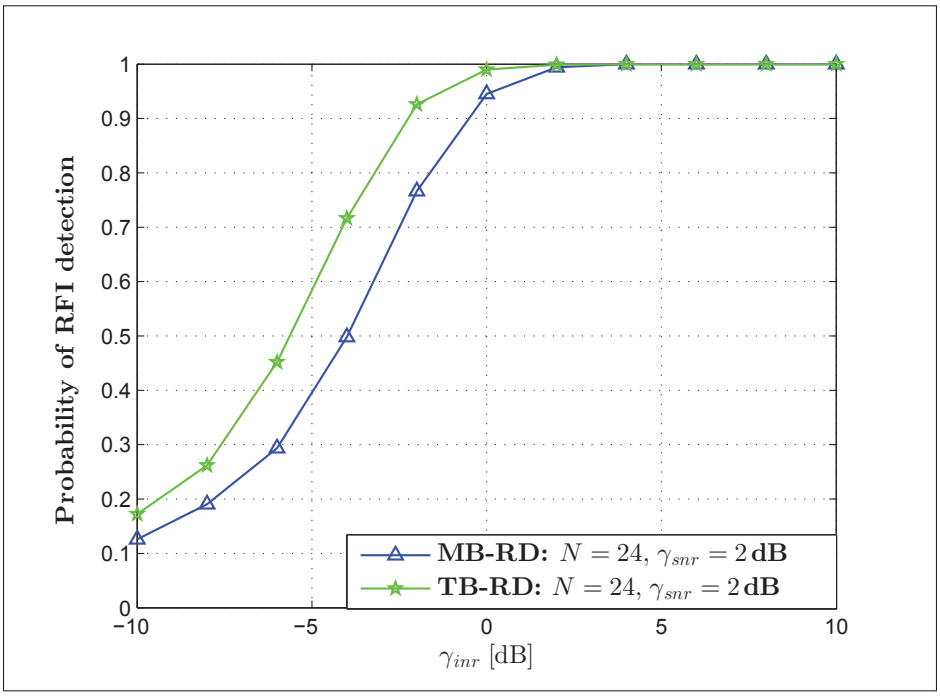

Figure 5.4 P_d versus γ_{inr}: $P_f = 0.1$ and 10^4 realizations

Comparing Figs. 5.3 and 5.4, it is demonstrated that the performance of TB-RD improves w.r.t. γ_{snr}. This improvement is because of the fact that the quality of the RFI subspace estimation increases with the increment of γ_{snr} which, in turn, implicates the better excision of the SOI executed through the first projection matrix. Moreover, Figs. 5.3-5.5 demonstrate that the RFI detection performance of TB-RD and MB-RD increases w.r.t. N_R since the increment in N_R improves the quality of the RFI subspace estimates and the tensor-based subspace estimator improves its matrix-based counterpart, respectively. Thus, it is corroborated via the aforementioned plots that TB-RD significantly improves MB-RD, especially for the low INR regimes. Such an improved detection of a weak RFI over multi-path fading channel is an important phenomenon in mobile satellite communication systems (Arapoglou *et al.*, 2011; Maral & Bousquet, 2009). For high INR regimes, Figs. 5.3-5.5 corroborate that MB-RD and TB-RD exhibit an identical performance—validating the second case of Theorem 8 proved in Appendix 3 (under APPENDIX V).

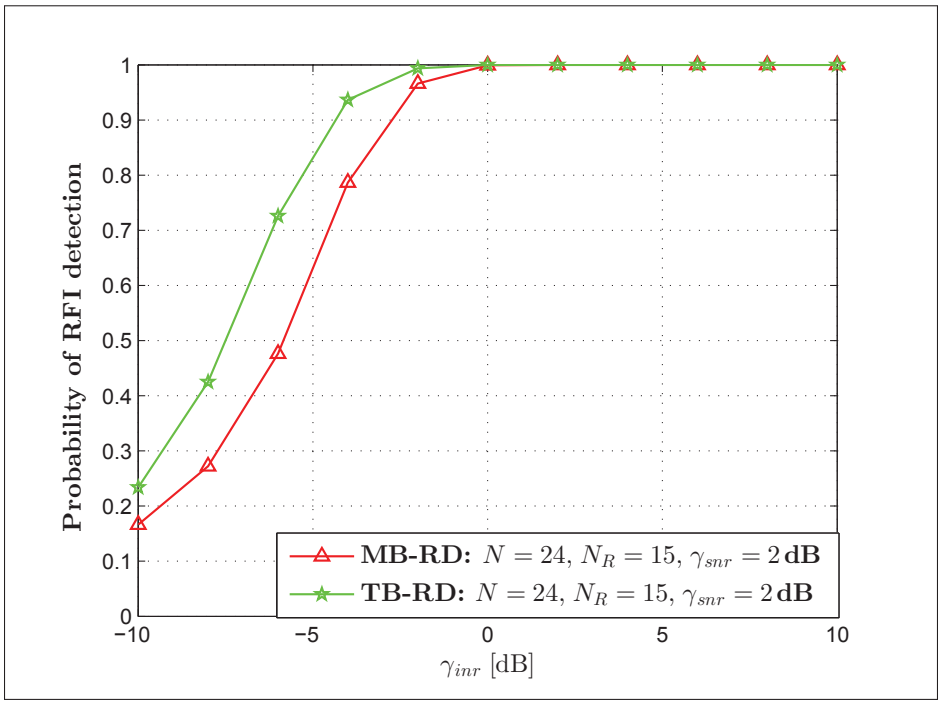

Figure 5.5 P_d versus γ_{inr}: $P_f = 0.1$ and 10^4 realizations

5.6.2 Comparison with a Multi-Antenna Detector

Generalized likelihood ratio test (GLRT) is a popular multi-antenna blind detection technique (Wang *et al.*, 2010; Taherpour *et al.*, 2010). To deploy it for an RFI detection and compare it with the proposed TB-RD, we, first, assume the availability of $\boldsymbol{H}$ and project the received signal toward the subspace orthogonal to the SOI subspace using the projection matrix $\boldsymbol{P} = \boldsymbol{I}_{N_R W} - \boldsymbol{H}(\boldsymbol{H}^H\boldsymbol{H})^{-1}\boldsymbol{H}^H$. Second, we compute the projected SCM using the projected received signal. Third, we compute the singular values of the projected SCM—which is both a Hermitian and positive semi-definite matrix—that are also the eigenvalues of the SCM, as the SVD and the EVD of a Hermitian matrix are identical. Fourth, using the computed eigenvalues, the blind GLRT statistic (Wang *et al.*, 2010, eq. (13)), (Taherpour *et al.*, 2010, eq. (39)) is computed and compared with a test threshold resulting in the desired FAR of 0.1.

Employing the aforementioned simulation setup for GLRT and the described simulation setup of TB-RD, Fig. 5.6 depicts the RFI detection performance comparison of GLRT and TB-

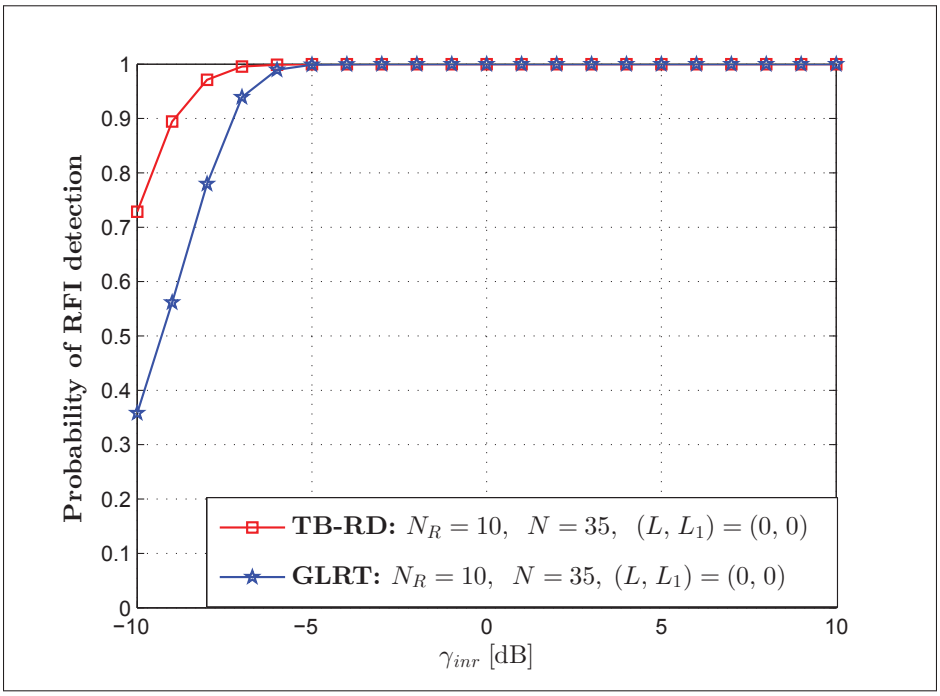

Figure 5.6 P_d versus γ_{inr}: $\gamma_{snr} = 0$ dB, $P_f = 0.1$, and 10^4 realizations

RD. As observed for $\gamma_{inr} \in \{-10, -7\}$ dB, TB-RD outperforms GLRT even though GLRT assumes the perfect knowledge of $\boldsymbol{H}$. Hence, regarding the detection of a weak RFI, TB-RD also manifests an appealing detection performance which is important for an RFI excision in radio astronomy and satellite communications, where the received line-of-sight signal often happens to be under the noise floor (van der Tol & van der Veen, 2005).

5.6.3 FAR and Complementary Receiver Operating Characteristics (CROC) Curves

5.6.3.1 FAR Curves

The FAR exhibited by MB-RD is depicted through Figs. 5.7 and 5.8. As seen, the FAR manifested by MB-RD increases with γ_{snr}—regardless of the number of receive antennas—for the increment in SNR is going to put the detector at a more ambiguity concerning the reception

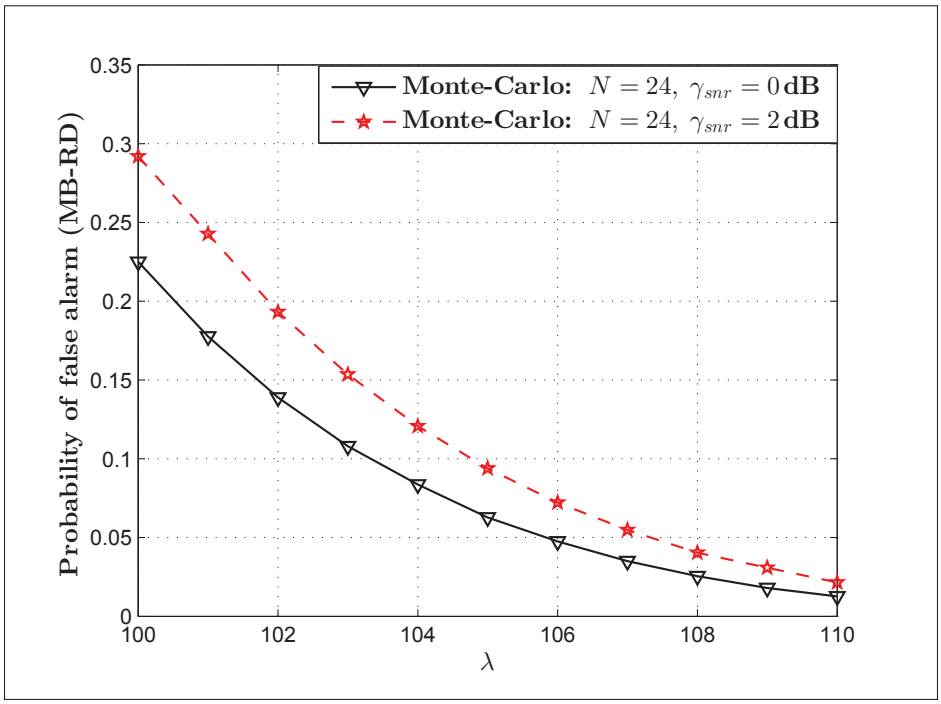

Figure 5.7 P_f versus λ manifested by MB-RD

of an RFI. Moreover, w.r.t. a given λ, the FAR exhibited by MB-RD also increases with N_R, as larger N_R results in a larger value of the MB-RD test statistic.

Similarly, Figs. 5.9 and 5.10 showcase the FAR exhibited by TB-RD. Like MB-RD, the FAR manifested by TB-RD increases with γ_{snr} irrespective of the number of receive antennas. This undesirable increment is because of the fact that the increment in SNR evokes more ambiguity to TB-RD so that the additional SOI energy would be miss-detected as the reception of an RFI. The value of the TB-RD test statistic in (5.37) increases with N_R rendering an increment in the exhibited FAR w.r.t. a given λ and an increase in N_R. At last, because Figs. 5.7-5.10 demonstrate a different FAR for a different SNR, neither MB-RD nor TB-RD is a constant FAR (CFAR) detector w.r.t. γ_{snr}.

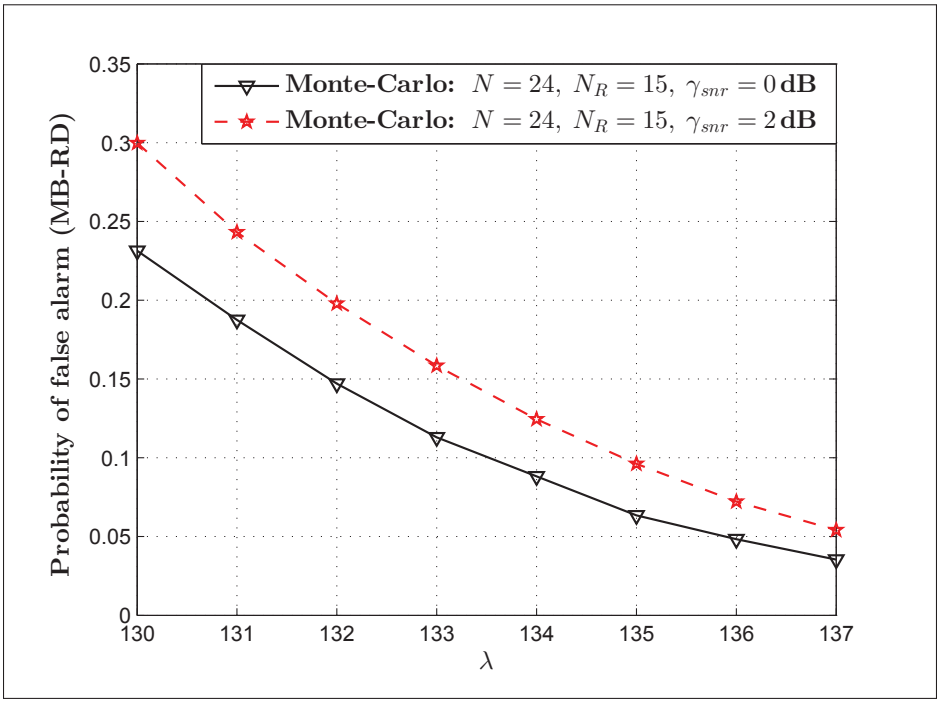

Figure 5.8 P_f versus λ manifested by MB-RD

5.6.3.2 CROC Curves

The CROC exhibited by MB-RD and TB-RD is showcased by Fig. 5.11, where a plot regarding the probability of miss (P_m)—simulated as $P_m = 1 - P_d$—versus P_f is depicted. As seen in Fig. 5.11, TB-RD exhibits a smaller P_m—for a given P_f—than MB-RD for $N_R \in \{5, 10\}$. As N_R increases from 5 to 10, it is also visible in Fig. 5.11 that the P_m exhibited by TB-RD is much smaller than the P_m exhibited by MB-RD. In other words, for $N_R = 10$, the P_d exhibited by TB-RD is much greater than the P_d exhibited by MB-RD. Accordingly, the third case of Theorem 8 is corroborated. Furthermore, the natural trade-off between P_m and P_f is demonstrated via Fig. 5.11.

5.7 Conclusions

RFI is occurring in various RF operating systems as diverse as radio astronomy, microwave radiometry, satellite communications, cognitive radios, ultra-wideband communications, and

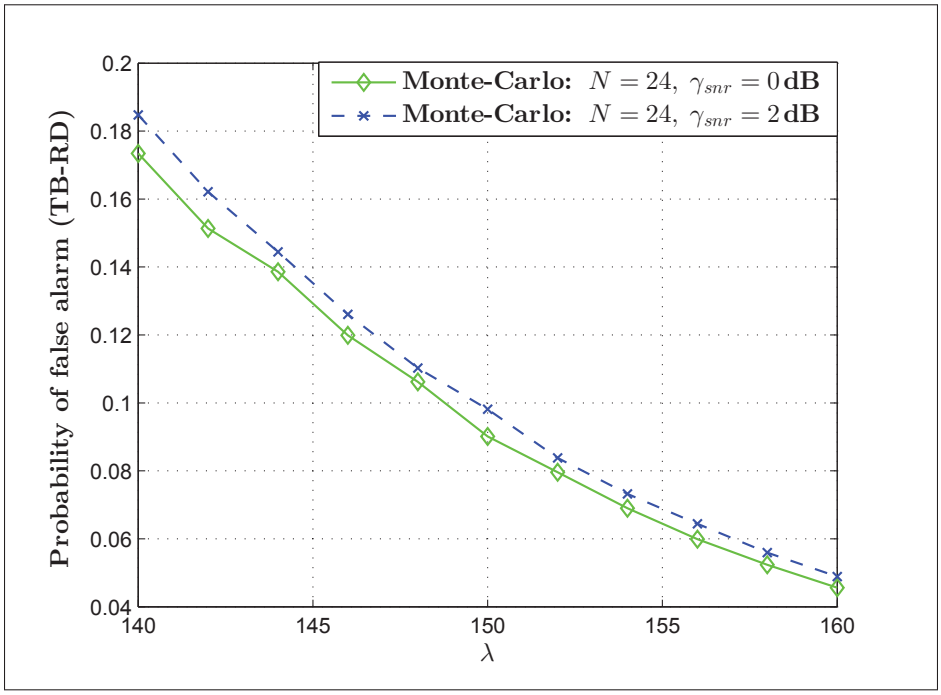

Figure 5.9 P_f versus λ exhibited by TB-RD

radar. The efficient excision of an RFI relies on an RFI detector which should also have a robust RFI detection capability for the detection of an RFI that might also be received through a multi-path fading channel. Toward this end, having been inspired by the recent advancements in tensor-based signal processing, this paper introduces the tensor-based RFI detection framework to the research sub-field of RFI detection. In particular, this paper proposes matrix- and tensor-based RFI detection algorithms for multi-antenna communications through a multi-path fading channel. For the proposed algorithms, insightful asymptotic performance analyses—that characterize the asymptotic behavior of the proposed detectors—have been reported. Simulations showcase the performance of the proposed detectors and validate the derived asymptotic characterizations of the proposed detectors.

Acknowledgment

The authors acknowledge the funding provided by AVIO-601 Project.

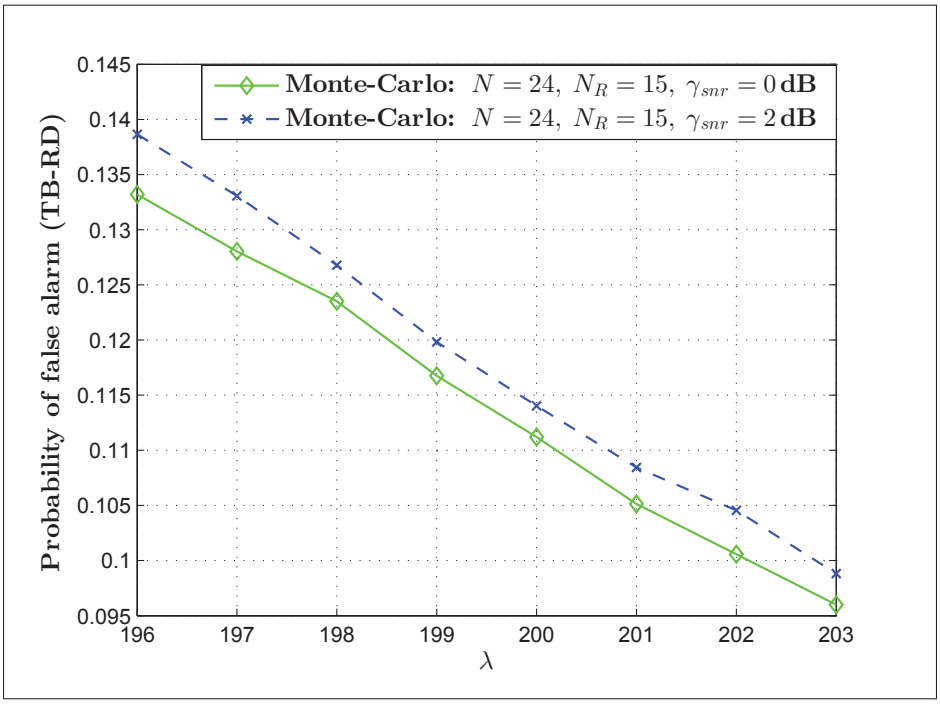

Figure 5.10 P_f versus λ exhibited by TB-RD

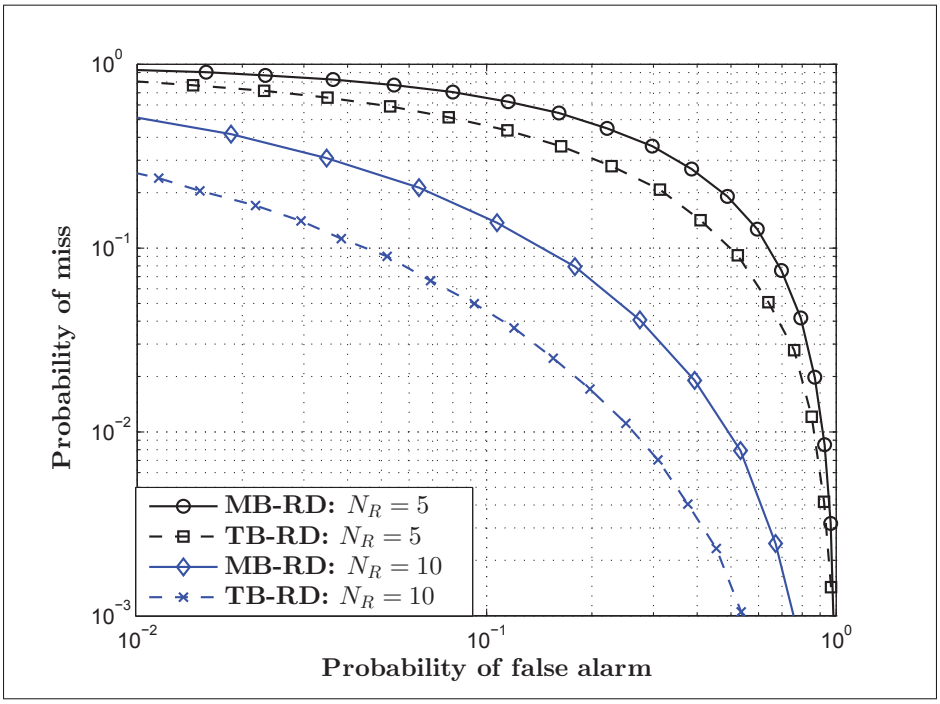

Figure 5.11 CROC: $(\gamma_{snr}, \gamma_{inr}) = (0\,\mathrm{dB}, 0\,\mathrm{dB})$

Part III

Advanced RFI Excision

CHAPTER 6

TENSOR-BASED EFFICIENT MULTI-INTERFERER RFI EXCISION ALGORITHMS FOR SIMO SYSTEMS

Tilahun M. Getu[1,2], Wessam Ajib[2], and Omar A. Yeste-Ojeda[3]

[1] Department of Electrical Engineering, École de Technologie Supérieure,
1100 Notre-Dame West, Montréal, Québec, Canada H3C 1K3
[2] Department of Computer Sciences, Université du Québec à Montréal,
201 Av. President-Kennedy, Montréal, Québec, Canada H2X 3Y7
[3] National Radio Astronomy Observatory, Charlottesville, VA 22902, USA

This article was published in *IEEE Transactions on Communications* as of July 2017
(Getu *et al.*, 2017).

"If you dream it, you can do it."—Walt Disney

Abstract—Radio frequency interference (RFI) is causing performance loss in microwave radiometry, radio astronomy, and satellite communications. As the number of interferers increases, the performance loss gets more severe and RFI excision becomes more difficult. In this regard, this paper introduces the multi-linear algebra framework to the multi-interferer RFI (MI-RFI) excision research by proposing a multi-linear subspace estimation and projection (MLSEP) algorithm for single-input multiple-output (SIMO) systems suffering from MI-RFI. Having employed smoothed observation windows, a smoothed MLSEP (s-MLSEP) algorithm, which enhances MLSEP, is also proposed. MLSEP and s-MLSEP require the knowledge of the number of interferers and their respective channel order. Accordingly, a novel smoothed matrix-based joint number of interferers and channel order enumerator is proposed. Performance analyses corroborate that both MLSEP and s-MLSEP can excise all interferers when the perturbations get infinitesimally small. For such perturbations, the analyses also attest that s-MLSEP exhibits a faster convergence to a zero excision error than MLSEP which, in turn, converges faster than a subspace projection algorithm. Despite its slight complexity, simulations and performance assessment on real-world data demonstrate that MLSEP outperforms

projection-based RFI excision algorithms. Simulations also corroborate that s-MLSEP outperforms MLSEP as the smoothing factor gets smaller.

Index Terms—RFI excision, multi-linear subspace estimation, multi-linear projection, joint enumeration, perturbation analysis.

6.1 Introduction

Radio frequency interference (RFI) is generally caused by out-of-band emissions by nearby transmitters and harmonics, jammers, spoofers, and meaconers. For these emitters, RFI is being prevalent in radio astronomy (van der Tol & van der Veen, 2005; Jeffs *et al.*, 2005), microwave radiometry (Guner *et al.*, 2007; Misra *et al.*, 2009), and global navigation satellite systems (GNSS) (Borio *et al.*, 2008). Moreover, RFI is evident in cognitive radio systems for imperfect spectrum sensing (Getu *et al.*, 2015a). Accordingly, the inevitable detection and excision of RFI have inspired the development of spectral (Guner *et al.*, 2007), temporal (Johnson & Ellingson, 2005), spectral-temporal (Borio *et al.*, 2008), transformed domain-based (Dovis *et al.*, 2012), statistical (Ruf *et al.*, 2006; Arribas *et al.*, 2013a,b), and spatial filtering-based (van der Tol & van der Veen, 2005; Jeffs *et al.*, 2005) RFI detection and excision algorithms.

Spectral detection and excision algorithms such as cross-frequency blanking (Guner *et al.*, 2007) and the mitigation algorithm in (Chen *et al.*, 2010) are proposed for microwave radiometry applications. These algorithms typically deploy fast Fourier transforms (FFT) and reconstructed interference, respectively, to mitigate RFI. Nevertheless, cross-frequency blanking requires detection thresholds that, if set incorrectly, can degrade performance and (Chen *et al.*, 2010) is not suitable for wideband RFI mitigation. To continue to the temporal algorithms, the popular asynchronous pulse blanking blanks the portion where the amplitude of the signal exceeds a threshold with respect to (w.r.t.) the noise. However, its performance suffers from the exploited heuristic threshold.

In many cases, an interfering signal may appear for a limited time and present a variable behavior in frequency (Dovis *et al.*, 2012). In such cases, a time-frequency representation such as a spectrogram or Gabor expansion can make the RFI easier to identify and remove (Borio *et al.*, 2008). In (Dovis *et al.*, 2012), the RFI is estimated in the time-frequency domain and then subtracted from the signal. Similarly, transformed domain-based algorithms employing Wavelet and Karhunen−Loève transform, and bordered autocorrelation method are detailed in (Dovis *et al.*, 2012) and (Maccone, 2010), respectively. However, the algorithms in (Dovis *et al.*, 2012) are computationally complex and (Maccone, 2010) is not capable of unambiguously detecting wideband signals, as reported in (Szumski, 2010).

Despite their benefits, both time-frequency and transformed-domain based algorithms suffer from computational complexity and hence one may resort to statistical algorithms such as kurtosis detection (Ruf *et al.*, 2006). Kurtosis detection, which is compared with pulse detection algorithm in (Misra *et al.*, 2009), assumes non-Gaussian RFI. On the other hand, statistical approaches which assume RFI with unknown statistics are proposed in (Arribas *et al.*, 2013a) and (Arribas *et al.*, 2013b). In (Arribas *et al.*, 2013a), the Neyman-Pearson detection theory and the generalized likelihood ratio test are deployed to obtain a new GNSS detection algorithm. Nonetheless, statistical detection and excision algorithms suffer from a computational complexity resulting from non-linear operations.

The previously highlighted approaches are not only computationally complex but also prone to RFI misdetection. At last, the signal processing practitioner may opt for spatial filtering techniques such as subspace projection (SP) (van der Tol & van der Veen, 2005) and cross subspace projection (CSP) (Jeffs *et al.*, 2005). SP and CSP rely on the eigenvalue decomposition (EVD) of the space-time autocorrelation matrix and the singular value decomposition (SVD) of the space-time crosscorrelation matrix, respectively. These algorithms are the state-of-the-art for excising RFI emitted by a relatively stationary interferer, especially for radio astronomy applications. Moreover, oblique projection beamforming (Hellbourg *et al.*, 2012) is proposed for cyclostationary RFI mitigation. Recently, a polynomial-augmented subspace projection (Lan-

don *et al.*, 2012) addressed low interference-to-noise ratio (INR), relatively rapid interference motion, and correlated noise scenarios.

Recent advances have corroborated that tensor-based parameter estimators which deploy truncated higher-order SVD (HOSVD) have outperformed their matrix-based counterparts (Roemer, 2012; Roemer *et al.*, 2014). Meanwhile, the congestion of licensed spectrum in both satellite and terrestrial communications calls for efficient signal processing algorithms that render efficient RFI excision. However, there is a lack of tensor-based efficient algorithms for the excision of multi-interferer RFI (MI-RFI). Hence, this paper tackles this issue via the enumerated contributions.

- The multi-linear subspace estimation and projection (MLSEP) algorithm is proposed for efficient MI-RFI excision in single-input multiple-output (SIMO) systems.
- We study smoothed observation windows to enhance the performance of MLSEP at the expense of computational complexity.
- **S**moothed **m**atrix-**b**ased **jo**int **n**umber of **i**nterferers and **c**hannel **o**rder **e**numerator (SMB-JoNICOE) is proposed.
- Novel asymptotic performance and convergence analyses are presented for MLSEP, smoothed MLSEP (s-MLSEP), and SP.
- The complexity analysis of MLSEP, s-MLSEP, SP, and CSP is presented.

Following this introduction, Section 6.2 presents the notation and system model. Section 6.3 details the MLSEP followed by Section 6.4 which presents the s-MLSEP. Section 6.5 then presents SMB-JoNICOE followed by performance and complexity analyses of Section 6.6. Thereafter, simulation results and performance assessment on real-world data are reported in Section 6.7 and Section 6.8, respectively. Finally, conclusions are drawn in Section 6.9.

6.2 Notation and System Model

6.2.1 Notation

Throughout the paper, scalars, vectors, matrices, and tensors are denoted by italic letters, lowercase boldface letters, uppercase boldface letters, and boldface calligraphic letters, respectively. The notation $\sim$, $\equiv$, $(:,i)$, $[\cdot,\cdot]$, $||\cdot||_F$, $(\cdot)^T$, $(\cdot)^H$, $\boldsymbol{I}_R$, $\boldsymbol{0}_{M\times N}$, $\mathscr{O}_t$, $\otimes$, $(\cdot)^{-1}$, $(\cdot)^+$, and $(\cdot)^{+r}$ imply distributed as, equivalence, the i-th column of a matrix, horizontal concatenation, Frobenius norm, transposition, Hermitian transposition, an $R\times R$ identity matrix, an $M\times N$ zero matrix, a zero tensor, Kronecker product, inverse, Moore-Penrose inverse, and the r-mode pseudoinverse of a tensor, respectively. Moreover, $\mathrm{vec}(\cdot)$, $\mathrm{unvec}(\cdot)$, $\mathrm{diag}(\cdot)$, $\min(\cdot,\cdot)$, $\max(\cdot,\cdot)$, $\lim$, $\mathbb{E}\{\cdot\}$, $\mathscr{CN}(\cdot,\cdot)$, and $U(\cdot)$ denote vectorization, unvectorization, diagonal matrix, minimum, maximum, limit, expectation, complex (multivariate) normal distribution, and unit step function, respectively.

The tensor $\mathscr{A}\in\mathbb{C}^{I_1\times I_2\times\ldots\times I_R}$ is an R-way array of size I_r along the r-th mode which is consistent with (Lathauwer *et al.*, 2000). The r-mode unfolding of $\mathscr{A}$ is denoted by $[\mathscr{A}]_{(r)}\in\mathbb{C}^{I_r\times I_{r+1}\ldots I_R I_1\ldots I_{r-1}}$ and defined as in (Lathauwer *et al.*, 2000) and (Haardt *et al.*, 2008). Moreover, the r-rank of $\mathscr{A}$ is defined as the rank of $[\mathscr{A}]_{(r)}$. The r-mode product of $\mathscr{A}$ and $\boldsymbol{U}_r\in\mathbb{C}^{J_r\times I_r}$ is denoted as $\mathscr{B}=\mathscr{A}\times_r\boldsymbol{U}_r$ and defined through $[\mathscr{B}]_{(r)}=\boldsymbol{U}_r[\mathscr{A}]_{(r)}$ (Haardt *et al.*, 2008).

Similarly, the r-mode product of $\mathscr{A}$ and a tensor $\mathscr{C}\in\mathbb{C}^{J_1\times J_2\times\ldots\times J_r\times\ldots\times J_R}$ is denoted by $\mathscr{D}=\mathscr{A}\times_r\mathscr{C}\in\mathbb{C}^{I_1\times\ldots\times I_{r-1}\times J_r\times I_{r+1}\times\ldots\times I_R}$ and defined through $[\mathscr{D}]_{(r)}=[\mathscr{C}]_r[\mathscr{A}]_{(r)}$ for $I_r=J_1J_2\ldots J_{r-1}$ $J_{r+1}\ldots J_R$ (Vasilescu & Terzopoulos, 2007). Accordingly, the r-mode identity tensor $\mathscr{I}_r\in\mathbb{C}^{J_1\times J_2\times\ldots\times J_r\times\ldots\times J_R}$ as well as the r-mode pseudoinverse tensor $\mathscr{A}^{+r}$ are both defined to satisfy (Vasilescu & Terzopoulos, 2007)

$$\left(\mathscr{A}\times_r\mathscr{A}^{+r}\right)\times_r\mathscr{A}=\mathscr{A}\ \text{ and }\ \mathscr{I}_r\times_r\mathscr{A}=\mathscr{A}, \tag{6.1}$$

where $[\mathscr{A}^{+r}]_{(r)}=[\mathscr{A}]_{(r)}^{+}$, $[\mathscr{I}]_{(r)}=\boldsymbol{I}_{J_r(\equiv J_{r+1}\ldots J_RJ_1\ldots J_{r-1})}$, $J_r=J_{r+1}\ldots J_RJ_1\ldots J_{r-1}$, and $J_r=I_{r+1}\ldots I_RI_1\ldots I_{r-1}$.

At last, `diag`$(\cdot)$, `min`$(\cdot)$, `length`$(\cdot)$, and `zeros`$(\cdot,\cdot)$ are the MATLAB® functions.

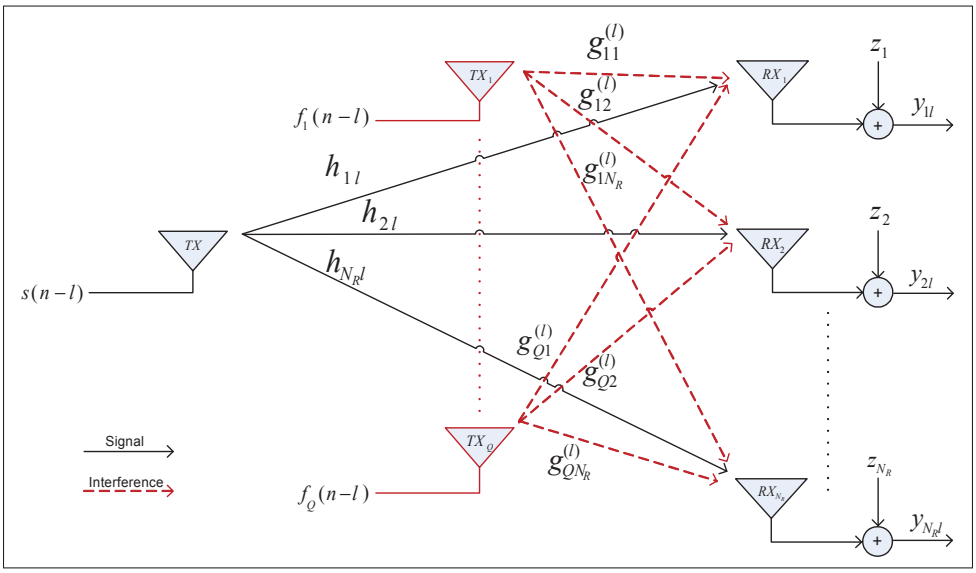

Figure 6.1 A baseband schematic depicting the l-th multi-path component of a SIMO system suffering from interference emitted by Q interferers

6.2.2 System Model

We consider a SIMO system with N_R receive antennas suffering from severe MI-RFI emitted by Q independent single-antenna interferers as shown in Fig. 6.1. The signal of interest (SOI) channel between the transmitter and each receive antenna pair is modeled as a finite-duration impulse response (FIR) filter with $L+1$ taps. The SOI channel is assumed to be time-invariant for a long-term interval (LTI). Similarly, the RFI channel between the i-th RFI transmitter and each receive antenna pair is modeled as an FIR filter with L_i+1 taps. Meanwhile, the MI-RFI channel is assumed to have a coherence time of $N_{\mathrm{SOI}}+1$ times the coherence time of the SOI—N_{SOI} being an arbitrary constant. The received baseband signal at time n is then given by

$$\boldsymbol{y}(n) = \sum_{l=0}^{L} \boldsymbol{h}_l s(n-l) + \sum_{i=1}^{Q} \sum_{l=0}^{L_i} \boldsymbol{g}_i^{(l)} f_i(n-l) + \boldsymbol{z}(n), \tag{6.2}$$

where $\{\boldsymbol{h}_l, \boldsymbol{g}_i^{(l)}\} \in \mathbb{C}^{N_R}$ are, respectively, the coefficients of the channel impulse responses corresponding to the l-th SOI and the i-th RFI's l-th channel taps, $s(n)$ denotes the unknown and deterministic symbol emitted by the SOI transmitter at time n, $f_i(n)$ is the sampled i-th broadband RFI which is usually modeled as a zero mean circularly symmetric complex additive white Gaussian noise (AWGN), and $\boldsymbol{z}(n) \sim \mathscr{CN}(\boldsymbol{0}, \sigma^2 \boldsymbol{I}_{N_R})$ is a sampled circularly symmetric complex AWGN. Furthermore, we assume that the Q Gaussian RFIs and the AWGN are independent.

6.3 MLSEP

MLSEP for MI-RFI excision comprises two phases. In the first phase, no SOI is transmitted for a duration of one LTI—similar to (Subbaram & Abend, 1993)—in order to estimate the projection tensor. One LTI is made of N short-term intervals (STIs). An STI has a duration of WT_s, where T_s denotes the symbol duration. During each STI, W samples from every N_R antennas are stacked. The horizontal concatenation of N stacked STIs forms a matrix. The multi-linear equivalent of such a matrix is deployed to estimate the MI-RFI subspace tensor using truncated HOSVD. Thereafter, the multi-linear projector is derived from the estimated MI-RFI subspace tensor.

In the second phase, an SOI is transmitted from the second LTI onwards for N_{SOI} LTIs and a per LTI MI-RFI excision is executed.

6.3.1 Problem Setup

Stacking the observation vectors of the N_R receive antennas and W data windows into one highly structured vector of size $N_R W \times 1$ w.r.t. the m-th STI gives

$$\boldsymbol{y}_m = \boldsymbol{H}\boldsymbol{s}_m + \sum_{i=1}^{Q} \boldsymbol{G}_i \boldsymbol{f}_{im} + \boldsymbol{z}_m \in \mathbb{C}^{N_R W}, \tag{6.3}$$

where $\boldsymbol{s}_m = \big[s\big(mW\big),\ldots,s\big(mW-W-L+1\big)\big]^T \in \mathbb{C}^{(W+L)}$, $\boldsymbol{f}_{im} = \big[f_i\big(mW\big),\ldots,f_i\big(mW-W-L_i+1\big)\big]^T \in \mathbb{C}^{(W+L_i)}$, and $\boldsymbol{z}_m$ are the sampled SOI, i-th RFI, and a zero mean AWGN, respectively. $\boldsymbol{H} \in \mathbb{C}^{N_R W\times(W+L)}$ is the SOI filtering matrix defined through (Song *et al.*, 2010a, eqs. (3) & (5)). $\boldsymbol{G}_i = \big[\boldsymbol{G}_{i1}^T,\ldots,\boldsymbol{G}_{iN_R}^T\big]^T \in \mathbb{C}^{N_R W\times(W+L_i)}$ is the i-th RFI filtering matrix for $\boldsymbol{G}_{ij} \in \mathbb{C}^{W\times(W+L_i)}$ being a banded Toeplitz matrix associated with the i-th RFI and the j-th receive antenna's impulse response $\boldsymbol{g}_{ij}$. $\boldsymbol{g}_{ij}$ is defined as $\boldsymbol{g}_{ij} \triangleq \big[g_{ij}^0,\ldots,g_{ij}^{L_i}\big]^T = \big[g_{ij}(t_0),\ldots,g_{ij}(t_0+L_iT_s)\big]^T$, where t_0 is the time-of-arrival, and

$$\boldsymbol{G}_{ij} = \begin{bmatrix} g_{ij}^0 & \ldots & g_{ij}^{L_i} & 0 & \ldots & \ldots & 0 \\ 0 & g_{ij}^0 & \ldots & g_{ij}^{L_i} & 0 & \ldots & 0 \\ \vdots & \vdots & \vdots & \vdots & \vdots & \vdots & \vdots \\ 0 & \ldots & \ldots & 0 & g_{ij}^0 & \ldots & g_{ij}^{L_i} \end{bmatrix}. \tag{6.4}$$

Meanwhile, expressing the summation in (6.3) as a matrix product gives

$$\boldsymbol{y}_m = \boldsymbol{H}\boldsymbol{s}_m + \boldsymbol{G}\boldsymbol{f}_m + \boldsymbol{z}_m \in \mathbb{C}^{N_R W}, \tag{6.5}$$

where $\boldsymbol{G} = [\boldsymbol{G}_1,\boldsymbol{G}_2,\ldots,\boldsymbol{G}_Q] \in \mathbb{C}^{N_R W\times\sum_{i=1}^{Q}(W+L_i)}$ represents the MI-RFI filtering matrix and $\boldsymbol{f}_m = \big[\boldsymbol{f}_{1m}^T,\ldots,\boldsymbol{f}_{Qm}^T\big]^T \in \mathbb{C}^{\sum_{i=1}^{Q}(W+L_i)}$ denotes the MI-RFI vector. The horizontal concatenation of (6.5) then renders

$$\boldsymbol{Y} = \boldsymbol{H}\boldsymbol{S} + \boldsymbol{G}\boldsymbol{F} + \boldsymbol{Z} \in \mathbb{C}^{N_R W\times N}, \tag{6.6}$$

where $\boldsymbol{S} = [\boldsymbol{s}_1,\ldots,\boldsymbol{s}_N]$, $\boldsymbol{F} = \big[\boldsymbol{F}_1^T,\ldots,\boldsymbol{F}_Q^T\big]^T$ for $\boldsymbol{F}_i = [\boldsymbol{f}_{i1},\ldots,\boldsymbol{f}_{iN}] \in \mathbb{C}^{(W+L_i)\times N}$, and $\boldsymbol{Z} = [\boldsymbol{z}_1,\ldots,\boldsymbol{z}_N]$. In the first LTI, no SOI is transmitted and the received signal becomes

$$\boldsymbol{Y}_I = \boldsymbol{G}\boldsymbol{F} + \boldsymbol{Z}. \tag{6.7}$$

In (6.7), $\boldsymbol{GF}$ and $\boldsymbol{G}$ span identical column space (Strang, 2003). However, the AWGN perturbs the singular vectors that span the MI-RFI subspace. The estimated MI-RFI subspace denoted

by $\hat{\boldsymbol{U}}_I \in \mathbb{C}^{N_R W \times \sum_{i=1}^{Q}(W+L_i)}$, for $N_R W \geq \sum_{i=1}^{Q}(W+L_i)$, can be obtained from the SVD of (6.7) as

$$\boldsymbol{Y}_I = \hat{\boldsymbol{U}}\hat{\boldsymbol{\Sigma}}\hat{\boldsymbol{V}}^H = [\hat{\boldsymbol{U}}_I \;\; \hat{\boldsymbol{U}}_n] \begin{bmatrix} \hat{\boldsymbol{\Sigma}}_I & \boldsymbol{0}_{r\times(N-r)} \\ \boldsymbol{0}_{d\times r} & \hat{\boldsymbol{\Sigma}}_n \end{bmatrix} [\hat{\boldsymbol{V}}_I \;\; \hat{\boldsymbol{V}}_n]^H, \tag{6.8}$$

where $r = \sum_{i=1}^{Q}(W+L_i)$, $d = N_R W - r$, $\hat{\boldsymbol{\Sigma}}_I = \mathrm{diag}(\hat{\sigma}_1, \ldots, \hat{\sigma}_r)$, and $\hat{\boldsymbol{\Sigma}}_n = \mathrm{diag}(\hat{\sigma}_{r+1}, \ldots, \hat{\sigma}_{N_R W})$.

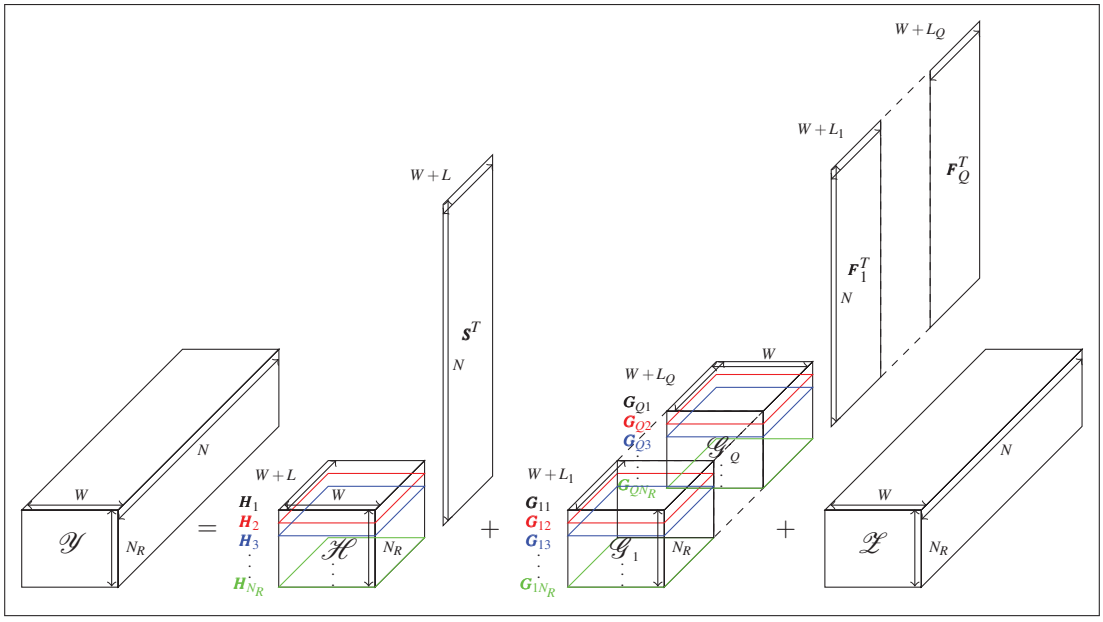

Figure 6.2 Multi-linear formulation from (6.6)

6.3.2 Problem Formulation

If we obtain W samples from all antennas positioned vertically while presuming that the temporal dimension moves horizontally, we will get an $N_R \times W$ matrix of samples per STI. During an LTI, we will then have N such matrices. Should we align the number of STIs in the third dimension, a three-way tensor of $N_R \times W \times N$ samples has resulted during an LTI. This arrangement maintains the inherent structure of the measurement data and inspires $\mathscr{Y} \in \mathbb{C}^{N_R \times W \times N}$ to model the received signal similar to (Song *et al.*, 2010a). Should $\left[\mathscr{Y}\right]_{(3)}^{T}$ be equal to $\boldsymbol{Y}$ in (6.6),

the multi-linear equivalent of (6.6) becomes

$$\mathscr{Y} = \mathscr{H} \times_3 \boldsymbol{S}^T + \mathscr{G} \times_3 \boldsymbol{F}^T + \mathscr{Z}, \tag{6.9}$$

where $\mathscr{H} \in \mathbb{C}^{N_R \times W \times (W+L)}$, $\mathscr{G} \in \mathbb{C}^{N_R \times W \times r}$, and $\mathscr{Z}$ are the SOI filtering tensor, the MI-RFI filtering tensor, and the noise tensor, respectively. $\mathscr{H}$ and $\mathscr{G}$ are constructed by aligning the banded Toeplitz matrices $\boldsymbol{H}_j$ and $\boldsymbol{G}_{ij}$ as in Fig. 6.2, i.e., $[\mathscr{H}]^T_{(3)} = \boldsymbol{H}$ and $[\mathscr{G}]^T_{(3)} = \boldsymbol{G}$. To ensure the identifiability of the SOI and the MI-RFI subspaces (Getu *et al.*, 2015b), $\boldsymbol{S}$, $\boldsymbol{F}$, $[\mathscr{H}]_{(3)}$, and $[\mathscr{G}]_{(3)}$ are assumed to have a full row rank and $W > \max(L, L_i)$. More precisely, $N \geq (W+L)$, $N \geq r$, $N_R W \geq W + L$, and $N_R W \geq r$.

6.3.2.1 MI-RFI Subspace Estimation

The subspace estimation is performed similarly to (Song *et al.*, 2010a). In the first LTI, no SOI transmission occurs and hence the truncated HOSVD of the received signal $\mathscr{Y}_I = \mathscr{G} \times_3 \boldsymbol{F}^T + \mathscr{Z}$ would be (Roemer *et al.*, 2014, eq. (16))

$$\mathscr{Y}_I \approx \hat{\mathscr{S}}^{[I]} \times_1 \hat{\boldsymbol{U}}_1^{[I]} \times_2 \hat{\boldsymbol{U}}_2^{[I]} \times_3 \hat{\boldsymbol{U}}_3^{[I]}, \tag{6.10}$$

where $\hat{\mathscr{S}}^{[I]} \in \mathbb{C}^{r_1 \times r_2 \times r_3}$ is the truncated core tensor and $\hat{\boldsymbol{U}}_n^{[I]} \in \mathbb{C}^{d_n \times r_n}$ is a unitary matrix of the dominant singular vectors of $[\mathscr{Y}_I]_{(n)}$—$n \in \{1,2,3\}$ and $[d_1, d_2, d_3] = [N_R, W, N]$ (Roemer *et al.*, 2014). Similar to the considerations of (Getu *et al.*, 2015b), $r_1 = \min\big(N_R,\ \sum_{i=1}^{Q}(L_i+1)\big)$, $r_2 = \min(W,\ NN_R)$, and $r_3 = \min\big(N,\ r\big)$. Accordingly, $r_2 = W$ and $r_3 = r$, since $N \geq r$. From (6.10), the estimated MI-RFI subspace tensor $\hat{\mathscr{U}}^{[I]} \in \mathbb{C}^{N_R \times W \times r}$ is defined as (Roemer *et al.*, 2014)

$$\hat{\mathscr{U}}^{[I]} = \hat{\mathscr{S}}^{[I]} \times_1 \hat{\boldsymbol{U}}_1^{[I]} \times_2 \hat{\boldsymbol{U}}_2^{[I]} \times_3 \hat{\boldsymbol{\Sigma}}_I^{-1}. \tag{6.11}$$

Here it is worth mentioning that the normalization factor $\hat{\boldsymbol{\Sigma}}_I^{-1}$—included for the sake of mathematical analysis—has no impact on the MI-RFI subspace estimation accuracy. The columns of $\left[\hat{\mathscr{U}}^{[I]}\right]^T_{(3)} \in \mathbb{C}^{N_R W \times r_3}$ span the estimated MI-RFI subspace and inspire the underneath theorem.

Theorem 9. The tensor-based MI-RFI subspace estimator $\left[\hat{\mathscr{U}}^{[I]}\right]^{T}_{(3)}$ and the matrix-based MI-RFI subspace estimator $\hat{\boldsymbol{U}}_I$ are related by

$$\left[\hat{\mathscr{U}}^{[I]}\right]^{T}_{(3)} = \left(\hat{\boldsymbol{T}}_1 \otimes \hat{\boldsymbol{T}}_2\right)\hat{\boldsymbol{U}}_I, \tag{6.12}$$

where $\hat{\boldsymbol{T}}_c = \hat{\boldsymbol{U}}_c^{[I]}\hat{\boldsymbol{U}}_c^{[I]^H}$, $c \in \{1,2\}$.

Proof. Following (Roemer *et al.*, 2014, Theorem 1), Theorem 9 can be proved for $R = 2$. □

If $N_R \leq \sum_{i=1}^{Q}(L_i+1)$, $r_1 = \min\left(N_R,\ \sum_{i=1}^{Q}(L_i+1)\right) = N_R$, $\hat{\boldsymbol{T}}_1 = \boldsymbol{I}_{N_R}$, and $\hat{\boldsymbol{T}}_2 = \boldsymbol{I}_W$, for $r_2 = W$. As a result, $\hat{\boldsymbol{T}}_1 \otimes \hat{\boldsymbol{T}}_2 = \boldsymbol{I}_{N_R W}$ renders identical estimates for the tensor- and the matrix-based MI-RFI estimators. If $N_R > \sum_{i=1}^{Q}(L_i+1)$, $r_1 = \min\left(N_R,\ \sum_{i=1}^{Q}(L_i+1)\right) = Q + \sum_{i=1}^{Q} L_i$. In this case, $\hat{\mathscr{U}}^{[I]}$ filters out the noise in its three different modes rendering an improved noise suppression, unlike $\hat{\boldsymbol{U}}_I$ (Haardt *et al.*, 2008, Appendix I). Accordingly, the tensor-based estimator offers a better estimate than its matrix-based counterpart.

6.3.2.2 Multi-Linear Projection

For a perfect $\hat{\mathscr{U}}^{[I]}$, the multi-linear projector is stated below.

Theorem 10. For a perfect $\hat{\mathscr{U}}^{[I]}$, the multi-linear projector $\mathscr{P} \in \mathbb{C}^{N_R \times W \times N_R W}$ which results in a perfect excision of the MI-RFI is given by

$$\mathscr{P} = \mathscr{I}_3 - \hat{\mathscr{U}}^{[I]} \times_3 \left(\hat{\mathscr{U}}^{[I]}\right)^{+3}, \tag{6.13}$$

where $\mathscr{I}_3 \in \mathbb{C}^{N_R \times W \times N_R W}$ is the 3-mode identity tensor, $\left(\hat{\mathscr{U}}^{[I]}\right)^{+3}$ is the 3-mode pseudoinverse tensor, $\left[\mathscr{I}_3\right]_{(3)} = \boldsymbol{I}_{N_R W}$, and $\left[\left(\hat{\mathscr{U}}^{[I]}\right)^{+3}\right]_{(3)} = \left[\hat{\mathscr{U}}^{[I]}\right]^{+}_{(3)}$.

Proof. cf. Appendix 1 under APPENDIX VI.

However, $\hat{\mathscr{U}}^{[I]}$ is imperfect and a perfect excision is impossible. To measure the resulting excision error, we make use of a performance parameter named root mean square excision error (RMSEE) which quantizes the root mean square MI-RFI excision error for an LTI as

$$\text{RMSEE} = \sqrt{\mathbb{E}\left\{ \left\| \left[\mathscr{P} \times_3 \mathscr{G} \right]_{(3)}^T \right\|_F^2 \right\}}. \tag{6.14}$$

We note that (6.14) is inspired by the fact that $\left\| \left[\mathscr{P} \times_3 \mathscr{G} \right]_{(3)}^T \right\|_F = 0$ under perfect excision.

The MLSEP routines which require the assumptions given at Section 6.3.2 are highlighted in Algorithm 6.1. Once the MI-RFI excision is conducted for N_{SOI} LTIs, the overall algorithm will be repeated for the subsequent MI-RFI excisions.

Algorithm 6.1 MLSEP Algorithm

Input: $\boldsymbol{Y}_I, \boldsymbol{Y}, N_R, W, N, Q, \{L_i\}_{i=1}^Q, N_{\text{SOI}}$
Output: RFI excised $\boldsymbol{Y}$

$r = \sum_{i=1}^Q (W + L_i)$, $r_1 = \min\left(N_R, \sum_{i=1}^Q (L_i + 1)\right)$, $r_2 = W$, $n = 1$
$\mathscr{Y}_I$ =the tensorization of $\left[\mathscr{Y}_I\right]_{(3)} = \boldsymbol{Y}_I^T$
Computation of $\hat{\mathscr{U}}^{[I]}$ using (6.12)
Computation of $\mathscr{P}$ using (6.13)
repeat
    $\mathscr{Y}$ =the tensorization of $\left[\mathscr{Y}\right]_{(3)} = \boldsymbol{Y}^T$
    return $\left[\mathscr{P} \times_3 \mathscr{Y}\right]_{(3)}^T$
    $n \leftarrow n + 1$
until $n \leq N_{\text{SOI}}$;

6.4 s-MLSEP

Smoothed observation windows are deployed to improve the performance of the proposed channel estimation algorithm in (Song *et al.*, 2010a). The improvement is for smoothed observation windows result in an improved estimate of the signal subspace. Similarly, we exploit smoothed observation windows exhibiting a smoothing factor η which denotes the number of

new samples in the next observed data window (Song *et al.*, 2010a). Consequently, we propose the s-MLSEP algorithm.

6.4.1 Problem Setup

If η new samples are included in the subsequent STIs, the observation windows will overlap for $1 \leq \eta < W$. To propose s-MLSEP, such overlapping windows are deployed for every antenna as in (Song *et al.*, 2010a, Fig. 6). For $1 \leq \eta < W$ and N^s overlapping windows, the smoothed version of (6.6) becomes

$$\boldsymbol{Y}^s = \boldsymbol{H}\boldsymbol{S}^s + \boldsymbol{G}\boldsymbol{F}^s + \boldsymbol{Z}^s \in \mathbb{C}^{N_R W \times N^s}, \tag{6.15}$$

where $\boldsymbol{S}^s = \left[\boldsymbol{s}_1^s, \ldots, \boldsymbol{s}_{N^s}^s\right]$ for $\boldsymbol{s}_m^s = \left[s\big(W+(m-1)\eta\big), \ldots, s\big(W+(m-1)\eta - W - L + 1\big)\right]^T \in \mathbb{C}^{(W+L)}$, $\boldsymbol{F}^s = [\boldsymbol{F}_{1s}^T, \ldots, \boldsymbol{F}_{Qs}^T]^T$ for $\boldsymbol{F}_{is} = [\boldsymbol{f}_{i1}^s, \ldots, \boldsymbol{f}_{iN^s}^s]$ and $\boldsymbol{f}_{im}^s = \big[f_i\big(W+(m-1)\eta\big), \ldots, f_i\big(W+(m-1)\eta - W - L_i + 1\big)\big]^T \in \mathbb{C}^{(W+L_i)}$, and $\boldsymbol{Z}^s$ is the smoothed AWGN.

Likewise, no SOI is transmitted in the first LTI. Thus, the smoothed received signal becomes

$$\boldsymbol{Y}_I^s = \boldsymbol{G}\boldsymbol{F}^s + \boldsymbol{Z}^s = \hat{\boldsymbol{U}}^s \hat{\boldsymbol{\Sigma}}^s \hat{\boldsymbol{V}}^{s^H}, \tag{6.16}$$

where $\hat{\boldsymbol{U}}^s = [\hat{\boldsymbol{U}}_I^s \ \hat{\boldsymbol{U}}_n^s]$ is the smoothed version of $\hat{\boldsymbol{U}}$, $\hat{\boldsymbol{U}}_I^s \in \mathbb{C}^{N_R W \times r}$ is the estimated smoothed MI-RFI subspace for $N_R W \geq r$, $\hat{\boldsymbol{V}}^s = [\hat{\boldsymbol{V}}_I^s \ \hat{\boldsymbol{V}}_n^s]$ is the smoothed equivalent of $\hat{\boldsymbol{V}}$, and $\hat{\boldsymbol{\Sigma}}^s = \operatorname{diag}\big(\hat{\boldsymbol{\Sigma}}_I^s, \hat{\boldsymbol{\Sigma}}_n^s\big)$ is the smoothed equivalent of $\hat{\boldsymbol{\Sigma}}$.

6.4.2 Problem Formulation

Similar to the formulation of Section 6.3.2, the multi-linear equivalent of (6.15) is

$$\mathscr{Y}^s = \mathscr{H} \times_3 \boldsymbol{S}^{sT} + \mathscr{G} \times_3 \boldsymbol{F}^{sT} + \mathscr{Z}^s \in \mathbb{C}^{N_R \times W \times N^s}. \tag{6.17}$$

The assumptions of Section 6.3.2 are then adopted to ensure the identifiability of subspaces.

6.4.2.1 Smoothed MI-RFI Subspace Estimation

In the first LTI, the truncated HOSVD of the received signal tensor $\mathscr{Y}_I^s = \mathscr{G} \times_3 \boldsymbol{F}^{sT} + \mathscr{Z}^s$ can be given as

$$\mathscr{Y}_I^s \approx \hat{\mathscr{S}}^{s[I]} \times_1 \hat{\boldsymbol{U}}_1^{s[I]} \times_2 \hat{\boldsymbol{U}}_2^{s[I]} \times_3 \hat{\boldsymbol{U}}_3^{s[I]}, \tag{6.18}$$

where $\hat{\mathscr{S}}^{s[I]} \in \mathbb{C}^{r_1^s \times r_2^s \times r_3^s}$ is the truncated core tensor and $\hat{\boldsymbol{U}}_n^{s[I]} \in \mathbb{C}^{d_n \times r_n^s}$ is a unitary matrix of the dominant singular vectors of $[\mathscr{Y}_I^s]_{(n)}$—$n \in \{1,2,3\}$ and $[d_1,d_2,d_3] = [N_R, W, N^s]$. Similar to (Getu *et al.*, 2015b), $r_1^s = \min\big(N_R,\ \sum_{i=1}^{Q}(L_i+1)\big)$, $r_2^s = W$, and $r_3^s = r$ for $N^s \geq r$. The estimated smoothed MI-RFI subspace tensor $\hat{\mathscr{U}}^{s[I]} \in \mathbb{C}^{N_R \times W \times r}$ is then defined as (Roemer *et al.*, 2014)

$$\hat{\mathscr{U}}^{s[I]} = \hat{\mathscr{S}}^{s[I]} \times_1 \hat{\boldsymbol{U}}_1^{s[I]} \times_2 \hat{\boldsymbol{U}}_2^{s[I]} \times_3 \hat{\boldsymbol{\Sigma}}_I^{s-1}. \tag{6.19}$$

Similar to Theorem 9, the smoothed tensor-based MI-RFI subspace estimator $\left[\hat{\mathscr{U}}^{s[I]}\right]_{(3)}^T \in \mathbb{C}^{N_R W \times r_3^s}$ and the smoothed matrix-based MI-RFI subspace estimator $\hat{\boldsymbol{U}}_I^s$ are related by

$$\left[\hat{\mathscr{U}}^{s[I]}\right]_{(3)}^T = \big(\hat{\boldsymbol{T}}_1^s \otimes \hat{\boldsymbol{T}}_2^s\big)\hat{\boldsymbol{U}}_I^s, \tag{6.20}$$

where $\hat{\boldsymbol{T}}_c^s = \hat{\boldsymbol{U}}_c^{s[I]}\hat{\boldsymbol{U}}_c^{s[I]^H}$, $c \in \{1,2\}$. Like the tensor-based MI-RFI subspace estimator, the smoothed version offers a better estimate than its smoothed matrix-based counterpart whenever $N_R > \sum_{i=1}^{Q}(L_i+1)$. Otherwise, both provide identical estimates.

6.4.2.2 Smoothed Multi-Linear Projection

By extending Theorem 10 for a perfect $\hat{\mathscr{U}}^{s[I]}$, the smoothed multi-linear projector $\mathscr{P}^s \in \mathbb{C}^{N_R \times W \times N_R W}$ that renders a perfect excision is given by

$$\mathscr{P}^s = \mathscr{I}_3 - \hat{\mathscr{U}}^{s[I]} \times_3 \left(\hat{\mathscr{U}}^{s[I]}\right)^{+3}, \tag{6.21}$$

where $\left[\mathscr{I}_3\right]_{(3)} = \boldsymbol{I}_{N_R W}$ and $\left[\left(\hat{\mathscr{U}}^{s[I]}\right)^{+3}\right]_{(3)} = \left[\hat{\mathscr{U}}^{s[I]}\right]^{+}_{(3)}$.

Nonetheless, $\hat{\mathscr{U}}^{s[I]}$ cannot be perfect and the resulting RMSEE is quantified by

$$\text{s-RMSEE} = \sqrt{\mathbb{E}\left\{\left\|\left[\mathscr{P}^{s} \times_3 \mathscr{G}\right]^{T}_{(3)}\right\|^2_F\right\}}. \tag{6.22}$$

Deploying smoothed equivalents in Algorithm 6.1, s-MLSEP routines can easily be adapted.

6.5 SMB-JoNICOE

To execute MLSEP and s-MLSEP as per Algorithm 6.1, r and r_1 should be initialized. As a result, both the number of interferers and their respective channel order are required. Although source enumeration (Lu & Zoubir, 2015) and channel order estimation (Vía *et al.*, 2006) are old problems, joint estimation of the number of interferers and their respective channel order has not been addressed. Meanwhile, the algorithm proposed in (Kotoulas *et al.*, 2006) estimates the number of sources of a multiple-input multiple-output system via the number of subsystems that attain each channel order. However, it can't identify the respective channel order of each source and is complex in terms of the number of required SVDs.

Accordingly, we propose SMB-JoNICOE which employs the eigenvalues (EVs) of the smoothed sample covariance matrix (s-SCM). SMB-JoNICOE merely deploys a single SVD and estimates both the number of interferers and their respective channel order during the first LTI. To do so, it executes iterative eigenvalue difference test and iterative eigenvalue comparison test with adaptive thresholds.

6.5.1 Problem Formulation

The population covariance matrix (PCM) is obtained by transmitting no SOI in the first LTI as (Lu & Zoubir, 2015, eq. (2))

$$\boldsymbol{R}_{y^s y^s} = \mathbb{E}\{\boldsymbol{y}_m^s \boldsymbol{y}_m^{s^H}\} = \boldsymbol{G}\boldsymbol{R}_{f^s f^s}\boldsymbol{G}^H + \sigma^2 \boldsymbol{I}_{N_R W}, \tag{6.23}$$

where $\boldsymbol{y}_m^s$ is the smoothed version of $\boldsymbol{y}_m$ and $\boldsymbol{R}_{f^s f^s} = \mathbb{E}\{\boldsymbol{f}_m^s \boldsymbol{f}_m^{s^H}\}$ is the smoothed MI-RFI PCM given by

$$\boldsymbol{R}_{f^s f^s} = \operatorname{diag}\Big(\underbrace{\sigma_1^2,\ldots,\sigma_1^2}_{W+L_1 \text{ terms}},\underbrace{\sigma_2^2,\ldots,\sigma_2^2}_{W+L_2 \text{ terms}},\ldots,\underbrace{\sigma_Q^2,\ldots,\sigma_Q^2}_{W+L_Q \text{ terms}}\Big), \tag{6.24}$$

where σ_i^2 is the power of the i-th broadband RFI and it is assumed that $\sigma_1 \geq \sigma_2 \geq \ldots \geq \sigma_Q$. Employing (6.24) into (6.23), the first $W + L_1$ EVs are likely to be close to each other, so do the second $W + L_2$ EVs, and so on. From theses numbers, we can estimate $\{L_i\}_{i=1}^{Q}$ and Q. However, we can't obtain the PCM, as infinite samples are required, and we resort to the estimation of the s-SCM obtained as (Lu & Zoubir, 2015, eq. (5))

$$\hat{\boldsymbol{R}}_{y^s y^s} = \frac{1}{N^s}\boldsymbol{Y}_I^s \boldsymbol{Y}_I^{s^H} = \frac{1}{N^s}\hat{\boldsymbol{U}}^s \hat{\boldsymbol{\Sigma}}^s \hat{\boldsymbol{\Sigma}}^{s^H} \hat{\boldsymbol{U}}^{s^H} = \hat{\boldsymbol{U}}^s \hat{\boldsymbol{\Lambda}}^s \hat{\boldsymbol{U}}^{s^H}, \tag{6.25}$$

where $\hat{\boldsymbol{\Lambda}}^s = \hat{\boldsymbol{\Sigma}}^s \hat{\boldsymbol{\Sigma}}^{s^H}/N^s$, $l_1 > l_2 > \ldots > l_r > \ldots > l_{N_R W}$ are the distinct EVs of the s-SCM—when $N \geq N_R W$—and $N_R W - r$ of them are contributed by the AWGN. Using these EVs, the noise EVs and the EVs of each interferer can be identified for the joint enumeration. Toward this end, the SMB-JoNICOE algorithm is devised.

6.5.2 SMB-JoNICOE Algorithm

Detailed in Algorithm 6.2, this algorithm computes the SVD of $\boldsymbol{Y}_I^s$ to obtain a vector $\tilde{\boldsymbol{\Lambda}}$ that comprises the EVs of $\boldsymbol{Y}_I^s$ (lines 1-2). Having employed $\tilde{\boldsymbol{\Lambda}}$, SMB-JoNICOE executes iterative eigenvalue difference test which subtracts the minimum eigenvalue (EV) $l_{\min}$ from a given EV so as to determine the noise EVs (lines 5-7). When the aforementioned test generates a value

Algorithm 6.2 SMB-JoNICOE Algorithm

Input: $\boldsymbol{Y}_I, N_R, W, N$
Output: $\{\hat{L}(\hat{Q}-i)\}_{i=0}^{\hat{Q}-1}, \hat{Q}$
1 Set values for Δ, ξ; decomposition of $\boldsymbol{Y}_I^s$ as in (6.16)
2 $\tilde{\boldsymbol{\Lambda}} = \mathtt{diag}\left(\hat{\boldsymbol{\Sigma}}^s \hat{\boldsymbol{\Sigma}}^{s^H}\right)/N^s$; $l_{\min} = \mathtt{min}\left(\tilde{\boldsymbol{\Lambda}}\right)$
3 **repeat**
4 $\quad \Delta \leftarrow \xi\Delta$; $k = \mathtt{length}(\tilde{\boldsymbol{\Lambda}})$
5 $\quad$ **repeat**
6 $\quad\quad \hat{r} \leftarrow k$; $k \leftarrow k-1$
7 $\quad$ **until** $\tilde{\boldsymbol{\Lambda}}(k) - l_{\min} \geq l_{\min}\Delta$;
8 $\quad m \leftarrow k-W$; $c \leftarrow 0$
9 $\quad$ **repeat**
10 $\quad\quad$ **if** $\hat{r}+c > \mathtt{length}(\tilde{\boldsymbol{\Lambda}})$, *then* **break**
11 $\quad\quad l_{\text{th}} \leftarrow \tilde{\boldsymbol{\Lambda}}(\hat{r}+c)$; $\hat{Q} \leftarrow 0$; $\hat{L} \leftarrow \mathtt{zeros}(1,100)$; $k \leftarrow \hat{r}-1$; $m \leftarrow k-W$
12 $\quad\quad$ **repeat**
13 $\quad\quad\quad \hat{l} = 0$
14 $\quad\quad\quad$ **repeat**
15 $\quad\quad\quad\quad \hat{l} \leftarrow \hat{l}+1$; $k \leftarrow k-1$
16 $\quad\quad\quad$ **until** $\tilde{\boldsymbol{\Lambda}}(k) \geq \tilde{\boldsymbol{\Lambda}}(m) + l_{\text{th}}$ & $k \geq 1$;
17 $\quad\quad\quad \hat{Q} \leftarrow \hat{Q}+1$
18 $\quad\quad\quad$ **if** $\hat{l}-W \geq W$, *then* **break**
19 $\quad\quad\quad \hat{L}(\hat{Q}) = \hat{l}-W$; $m \leftarrow m-W-\hat{L}(\hat{Q})$
20 $\quad\quad$ **until** $m < 1$;
21 $\quad\quad$ **if** $m < 0$, *then* **break**
22 $\quad\quad c \leftarrow c+1$
23 $\quad$ **until** $m < 0$;
24 $\quad$ **if** $m < 0$, *then* **break**
25 $\quad \xi \leftarrow \xi+1$
26 **until** $\xi\Delta \geq 2$;
27 **return** $\hat{L}(\hat{Q}), \hat{L}(\hat{Q}-1), \ldots, \hat{L}(2), \hat{L}(1), \hat{Q}$

greater than the product of the initialized threshold Δ and $l_{\min}$ (line 7), the algorithm would preliminarily identify the noise EVs. Hereinafter, it considers the remaining EVs as the MI-RFI EVs and conducts iterative eigenvalue comparison test so as to render a joint enumeration. In this regard, the algorithm employs the EV that is immediately greater than the largest estimated noise EV as a preliminary comparison threshold l_{th} (line 11 for $c = 0$).

SMB-JoNICOE commences an iterative eigenvalue comparison test by comparing the MI-RFI EVs with an adaptive threshold. The adaptive threshold is preliminarily set to l_{th} plus the value

of the W-th largest EV w.r.t. the smallest MI-RFI EV (lines 11 and 16 for $c = 0$). Then, the channel order of the first interferer would be estimated and the eigenvalue comparison test would resume for the remaining interferes (lines 12-20 for $c = 0$) provided that each estimated channel order is less than W (line 18). If not, the loop would break and go for the smaller comparison threshold by resetting all the estimated channel orders (lines 10-11 for $c > 0$). By the virtue of our assumptions, line 18 ensures that the estimated channel orders are less than W. If the loop doesn't break, the number of interferers will be estimated whenever there is a viable channel order estimate for every interferer (lines 17 and 27). Whenever the iterative eigenvalue comparison test resumes by descending W plus the estimated channel order values through $\tilde{\mathbf{\Lambda}}$ (line 19), SMB-JoNICOE will make sure that the last largest EV under test is the closest to the maximum EV (lines 21-24).

When iterative eigenvalue difference and iterative eigenvalue comparison tests satisfy all the loop controls, the algorithm returns the number of interferers and their respective channel order (line 27).

6.6 Performance and Complexity Analyses

This section presents the asymptotic performance and complexity analysis of MLSEP and s-MLSEP, and the asymptotic convergence analysis of SP, MLSEP, and s-MLSEP.

6.6.1 Asymptotic Performance Analysis

This performance analysis makes use of the first-order perturbation analysis detailed in (Li *et al.*, 1993). To facilitate mathematical tractability, quantization error is neglected. Besides, the contribution of the MI-RFI subspace to the perturbation of the singular vectors that span the MI-RFI subspace is discarded unlike (Liu *et al.*, 2008), since MLSEP relies on the overall MI-RFI subspace rather than on individual basis vectors.

To motivate perturbation analysis, we begin with $\boldsymbol{Y}_0 = \boldsymbol{GF}$ decomposed as

$$\boldsymbol{Y}_0 = [\boldsymbol{U}_I \, \boldsymbol{U}_n] \begin{bmatrix} \boldsymbol{\Sigma}_I & \boldsymbol{0}_{r\times(N-r)} \\ \boldsymbol{0}_{d\times r} & \boldsymbol{0}_{d\times(N-r)} \end{bmatrix} [\boldsymbol{V}_I \, \boldsymbol{V}_n]^H. \tag{6.26}$$

Comparing (6.8) and (6.26), and exploiting the first-order perturbation expansion (Roemer *et al.*, 2014, eq. (20)), it is possible to deduce that

$$\hat{\boldsymbol{U}}_I = \boldsymbol{U}_I + \Delta\boldsymbol{U}_I, \; \Delta\boldsymbol{U}_I = \boldsymbol{U}_n \boldsymbol{U}_n^H \boldsymbol{Z} \boldsymbol{V}_I \boldsymbol{\Sigma}_I^{-1}, \tag{6.27}$$

where $\Delta\boldsymbol{U}_I$ is the perturbations in the singular vectors that span the MI-RFI subspace. For $N_R \leq \sum_{i=1}^{Q}(L_i+1)$, $\hat{\boldsymbol{T}}_1 = \hat{\boldsymbol{U}}_1^{[I]} \hat{\boldsymbol{U}}_1^{[I]^H} = \boldsymbol{I}_{N_R}$ and

$$\left[\hat{\mathscr{U}}^{[I]}\right]_{(3)}^{T} = \left(\boldsymbol{I}_{N_R} \otimes \boldsymbol{I}_W\right) \hat{\boldsymbol{U}}_I = \boldsymbol{I}_{N_R W} \hat{\boldsymbol{U}}_I = \hat{\boldsymbol{U}}_I. \tag{6.28}$$

Inserting (6.27) into (6.28) then gives

$$\left[\hat{\mathscr{U}}^{[I]}\right]_{(3)}^{T} = \boldsymbol{U}_I + \left[\Delta\hat{\mathscr{U}}^{[I]}\right]_{(3)}^{T} = \boldsymbol{U}_I + \Delta\boldsymbol{U}_I. \tag{6.29}$$

When $N_R > \sum_{i=1}^{Q}(L_i+1)$, $\hat{\boldsymbol{T}}_1 \neq \boldsymbol{I}_{N_R}$ and (6.12) is simplified to

$$\left[\hat{\mathscr{U}}^{[I]}\right]_{(3)}^{T} = \left(\hat{\boldsymbol{U}}_1^{[I]} \hat{\boldsymbol{U}}_1^{[I]^H} \otimes \boldsymbol{I}_W\right) \hat{\boldsymbol{U}}_I. \tag{6.30}$$

Following the perturbation analysis extended to the HOSVD-based subspace estimate in (Roemer *et al.*, 2014)

$$\hat{\boldsymbol{U}}_1^{[I]} = \boldsymbol{U}_1^{[I]} + \Delta\boldsymbol{U}_1^{[I]}, \tag{6.31}$$

where $\Delta\boldsymbol{U}_1^{[I]} = \boldsymbol{U}_1^{[n]} \boldsymbol{U}_1^{[n]^H} \left[\mathscr{Z}\right]_{(1)} \boldsymbol{V}_1^{[I]} \boldsymbol{\Sigma}_1^{[I]^{-1}}$ (Roemer *et al.*, 2014, eq. (23)). Substituting (6.31) and (6.27) into (6.30), and omitting second-order terms afterward give (6.32).

Having exploited these analyses, the underneath theorem follows.

$$\left[\hat{\mathscr{U}}^{[I]}\right]_{(3)}^{T} = \boldsymbol{U}_I + \left[\Delta\hat{\mathscr{U}}^{[I]}\right]_{(3)}^{T}, \left[\Delta\hat{\mathscr{U}}^{[I]}\right]_{(3)}^{T} = \Delta\boldsymbol{U}_I + \left(\boldsymbol{U}_1^{[I]}\Delta\boldsymbol{U}_1^{[I]^H} \otimes \boldsymbol{I}_W\right)\boldsymbol{U}_I + \left(\Delta\boldsymbol{U}_1^{[I]}\boldsymbol{U}_1^{[I]^H} \otimes \boldsymbol{I}_W\right)\boldsymbol{U}_I. \tag{6.32}$$

Theorem 11. RMSEE exhibited by MLSEP satisfies the condition

$$\lim_{\Delta\boldsymbol{U}_I \to \boldsymbol{0}} \text{RMSEE} = 0. \tag{6.33}$$

Proof. cf. Appendix 2 under APPENDIX VI.

Theorem 11 has important implications though it is an asymptotic result. First, it implies that the RMSEE $= 0$ axis is a tight lower bound at high INR. Second, it implies that MLSEP can excise all interferers when the perturbations get infinitesimally small. Using the smoothed versions of (6.28) and (6.32) in (6.22), and following Appendix 2 (under APPENDIX VI) render

$$\lim_{\Delta\boldsymbol{U}_I^s \to \boldsymbol{0}} \text{s-RMSEE} = 0, \tag{6.34}$$

where $\Delta\boldsymbol{U}_I^s$ is the smoothed version of $\Delta\boldsymbol{U}_I$. Accordingly, s-MLSEP can also excise all interferers when the perturbations get infinitesimally small.

6.6.2 Asymptotic Convergence Analysis

Using the aforementioned analyses, the asymptotic convergence of SP and MLSEP is characterized beneath.

Theorem 12. When $N_R > \sum_{i=1}^{Q}(L_i + 1)$, $\lim_{\Delta\boldsymbol{U}_I \to \boldsymbol{0}}$ RMSEE converges to 0 for MLSEP faster than for SP.

Proof. cf. Appendix 3 under APPENDIX VI.

Adopting similar derivations, Corollary 2 has resulted.

Corollary 2. Whenever $1 \leq \eta < W$, $\lim_{\Delta \boldsymbol{U}_I^s \to \boldsymbol{0}}$ s-RMSEE converges to 0 faster than $\lim_{\Delta \boldsymbol{U}_I \to \boldsymbol{0}}$ RMSEE.

Proof. cf. Appendix 4 under APPENDIX VI.

Table 6.1 Comparison of the number of multiplications of an MI-RFI excision using different algorithms and N_R^a auxiliary antennas

Algorithms	No. of required multiplications
SP (van der Tol & van der Veen, 2005)	$N_R^2 r_2^2 \left[2N + N_R r_2 + (1+k_t) r_3\right]$
CSP (Jeffs *et al.*, 2005)	$N_R N_R^a r_2^2 \left[2N + k_t r_3 + \frac{N_R N}{N_R^a} - \frac{N_R r_3}{N_R^a} + N_R r_2\right]$
MLSEP	$k_t r_2 N_R N \left(r_1 + r_2 + r_3\right) + N_R^2 r_2^2 (1 + r_3 + N)$ $+ N_R r_2 r_3 (2r_3 + \frac{r_3^2}{N_R r_2} + N_R r_2) + N_R^2 r_1 + r_2^3$
s-MLSEP ($\eta = 1$)	$k_t r_2 N_R N^s \left(r_1 + r_2 + r_3\right) + N_R^2 r_2^2 (1 + r_3 + N^s)$ $+ N_R r_2 r_3 (2r_3 + \frac{r_3^2}{N_R r_2} + N_R r_2) + N_R^2 r_1 + r_2^3$

Table 6.2 Sample comparison of the number of multiplications of an MI-RFI excision using different algorithms and N_R^a auxiliary antennas

Algorithms	No. of multiplications for $N_R = 8$, $N_R^a = 6$, $k_t = 10$, $N = 60$ $r_1 = 4$, $r_2 = 5$, and $r_3 = 18$
SP (van der Tol & van der Veen, 2005)	572800
CSP (Jeffs *et al.*, 2005)	475200
MLSEP	835333
s-MLSEP ($\eta = 1$)	3761733

6.6.3 Complexity Analyses

In the sequel, the complexity of MLSEP, s-MLSEP, SP, and CSP is analyzed by assuming the knowledge of r_1, r_2, and r_3. In this analysis, orthogonal iteration (Golub & Van Loan, 2013)—being an efficient SVD implementation—is exploited to implement SVD and EVD, i.e., the EVD of $\boldsymbol{A}$ is analyzed as the SVD of $\boldsymbol{A}^2$.

For an $M \times N$ matrix $\boldsymbol{A}$ truncated to rank r, computation of its SVD demands $k_t MNr$ multiplications for k_t being a constant that depends on the design of the algorithm (Haardt *et al.*, 2008). Besides, MNK multiplications are carried out during the multiplication of $\boldsymbol{A}$ and an $N \times K$ matrix $\boldsymbol{B}$. Meanwhile, MLSEP requires the efficient implementation of three SVDs and additional multiplications as per (6.12). On top of that, extra multiplications are required for the computation of the projection tensor given by (6.13) and the eventual MI-RFI excision. In the computation of (6.13), the inverse operation is assumed to be implemented via a Gauss-Jordan elimination.

Having resorted to the aforementioned computations, the complexity analysis of MLSEP, SP (van der Tol & van der Veen, 2005), and CSP (Jeffs *et al.*, 2005) is tabulated in Tables 6.1 and 6.2. Besides, the complexity of s-MLSEP is tabulated for a given η and hence $N^s = N_{\text{tot}}/\eta - W/\eta + 1$, for N_{tot} being the number of observed symbols per LTI. According to Tables 6.1 and 6.2, MLSEP and s-MLSEP entail a slightly higher complexity. However, significant performance gain is leveraged by employing them, as demonstrated in Section 6.7.

Table 6.3 Simulation parameters unless otherwise mentioned

Simulation parameters	Assigned value
(L, L_1, L_2, L_3)	$(1,1,1,1)$
(Δ, β, ξ)	$(0.05, 0.5, 1)$
Pre-excision SINR	0 dB
t_0	$0.1T_s$
(N_R^a, N_{SOI})	$(6, 200$ LTIs$)$
No. of channel realizations	1000

6.7 Simulation Results

The performance of the MI-RFI subspace estimators, SMB-JoNICOE, MLSEP, and s-MLSEP is assessed via simulations which deploy the succeeding setup and simulation parameters of Table 6.3, unless otherwise mentioned.

During the first LTI and subsequent 200 LTIs, Q zero mean circularly symmetric complex white Gaussian signals—as a broadband MI-RFI—and Gray-coded 4-QAM symbols—as an SOI—contaminated by Q zero mean circularly symmetric complex white Gaussian signals are, respectively, transmitted over multi-path fading channels. To simulate the SOI and the i-th RFI multi-path fading channels, $(L+1)$- and (L_i+1)-ray multi-path continuous-time channels are constructed synchronously using the raised cosine pulse shaping filter $p_{rc}(t,\beta)$ exhibiting a roll-off factor β as $h_j(t) = \sum_{l=0}^{L} h_j^l p_{rc}(t - lT_s, \beta)$ and $g_{ij}(t) = \sum_{l=0}^{L_i} g_{ij}^l p_{rc}(t - lT_s, \beta)$, for $\{h_j^l, g_{ij}^l\} \sim \mathscr{CN}(0,1)$, respectively (Song *et al.*, 2010a). For $\boldsymbol{H}$ and $\{\boldsymbol{G}_i\}_{i=1}^{Q}$ normalized to a Frobenius norm of $\sqrt{W}$, signal-to-interference-plus-noise ratio (SINR) in dB denoted as $\gamma_{sinr}(\boldsymbol{P})$ for a projection matrix $\boldsymbol{P}$ and INR [dB] denoted as γ_{inr} are, respectively, defined for Q interferers with identical power as

$$\gamma_{sinr}(\boldsymbol{P}) = 10\log_{10} \frac{\mathbb{E}\{\|\boldsymbol{PHS}\|_F^2\}}{\mathbb{E}\{\|\boldsymbol{PGF}\|_F^2\} + \mathbb{E}\{\|\boldsymbol{PZ}\|_F^2\}} \tag{6.35a}$$

$$\gamma_{inr} = 10\log_{10} \frac{\mathbb{E}\left\{\|\boldsymbol{GF}\|_F^2\right\}}{\mathbb{E}\left\{\|\boldsymbol{Z}\|_F^2\right\}}. \tag{6.35b}$$

Average SINR gain [dB] is defined as $\frac{1}{N_{\mathrm{SOI}}} \sum_{n=1}^{N_{\mathrm{SOI}}} \left(\gamma_{sinr}(\boldsymbol{P}) - \gamma_{sinr}(\boldsymbol{I}_{N_R W})\right)$. To assess the performance of the MI-RFI subspace estimators, root mean square error (RMSE) is defined through a per column subspace estimation error as in (Liu *et al.*, 2008) and (Roemer *et al.*, 2009). Specifically,

$$\mathrm{RMSE} = \sqrt{\mathbb{E}\{\|\Delta\boldsymbol{U}\|_F^2\}}, \tag{6.36}$$

where $\Delta\boldsymbol{U}(:,k) = \hat{\boldsymbol{U}}(:,k) \dfrac{\hat{\boldsymbol{U}}^H(:,k)\boldsymbol{U}(:,k)}{|\hat{\boldsymbol{U}}^H(:,k)\boldsymbol{U}(:,k)|} - \boldsymbol{U}(:,k)$ and $\boldsymbol{U}$ is the true estimate. Similarly, the performance of SMB-JoNICOE is assessed via joint RMSE (J-RMSE) defined in (6.37), for $\Delta Q = \hat{Q} - Q$, $\Delta L_i = \hat{L}(i) - L_i$, and $U(\cdot)$ being a unit step function.

Implementation of Algorithm 6.1 simulates MLSEP whose average RMSEE is assessed by averaging (6.14) over 200 LTIs. Having deployed the equivalent smoothed matrices and tensors, s-MLSEP is simulated by adapting the aforementioned definitions and Algorithm 6.1. There-

$$\text{J-RMSE} = \sqrt{U(-\Delta Q)\mathbb{E}\Big\{\sum_{i=1}^{\hat{Q}}(\Delta L_i)^2 + (\Delta Q)^2\Big\} + U(\Delta Q)\mathbb{E}\Big\{\sum_{i=1}^{Q}(\Delta L_i)^2 + (\Delta Q)^2\Big\}}. \quad (6.37)$$

after, its average RMSEE is assessed by averaging (6.22) over 200 LTIs. Meanwhile, *Tensorlab* (Sorber *et al.*, Jan. 2014) is deployed for our *matricization* and *tensorization* operations, and all the performance assessments are reported subsequently.

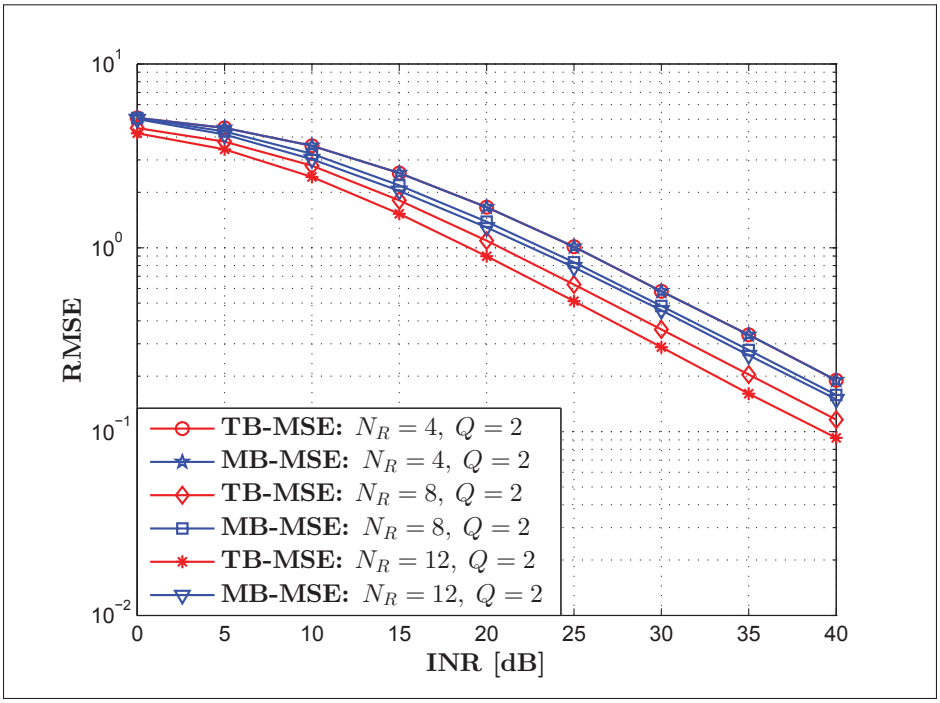

Figure 6.3 RMSE for TB-MSE and MB-MSE: $N_{\text{tot}} = 160$, $W = 8$, $N = 20$, and $(\sigma_1, \sigma_2) = (1, 1)$ W

6.7.1 Performance Assessment of the MI-RFI Subspace Estimators

Monte-Carlo simulations for the tensor-based MI-RFI subspace estimator (TB-MSE) and the matrix-based MI-RFI subspace estimator (MB-MSE) are conducted by employing $\left[\hat{\mathscr{U}}^{[I]}\right]^T_{(3)}$ and $\hat{\boldsymbol{U}}_I$, respectively, in (6.36) and deploying the aforementioned simulation setup. As corroborated by Fig. 6.3, TB-MSE and MB-MSE have identical RMSE performance when $N_R \leq$

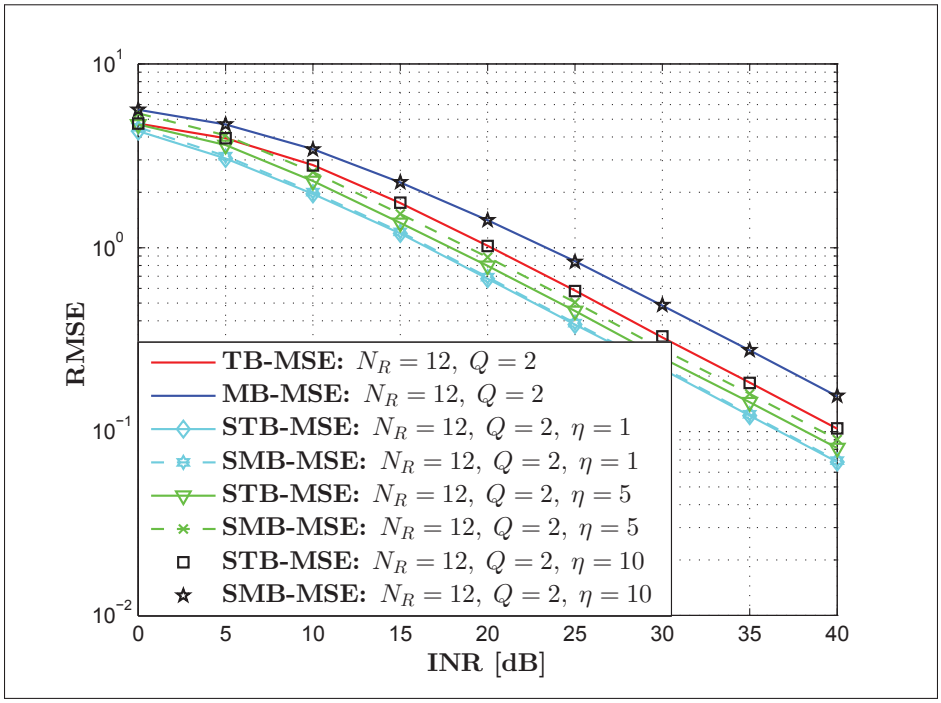

Figure 6.4 RMSE for TB-MSE, MB-MSE, STB-MSE, and SMB-MSE: $N_{\text{tot}} = 250$, $W = 10$, and $(\sigma_1, \sigma_2) = (1, 1)$ W

$\sum_{i=1}^{Q}(L_i + 1)$. Otherwise, TB-MSE outperforms MB-MSE, especially as N_R gets larger, for $\hat{\mathscr{U}}^{[I]}$ renders an improved noise suppression by filtering the noise in three different modes.

Similarly, Monte-Carlo simulations for the smoothed tensor-based MI-RFI subspace estimator (STB-MSE) and the smoothed matrix-based MI-RFI subspace estimator (SMB-MSE) are performed as per the aforementioned simulation setup while employing $\left[\hat{\mathscr{U}}^{s[I]}\right]^{T}_{(3)}$ and $\hat{\boldsymbol{U}}_I^s$, respectively, in (6.36). As demonstrated by Fig. 6.4, STB-MSE significantly improves SMB-MSE, especially for smaller values of η. As expected, STB-MSE and SMB-MSE, respectively, improve TB-MSE and MB-MSE whenever $\eta < W$. The smaller estimation errors are attributed to the smoothing which provides more observation windows. For $\eta = W$, STB-MSE and SMB-MSE overlap with TB-MSE and MB-MSE, respectively.

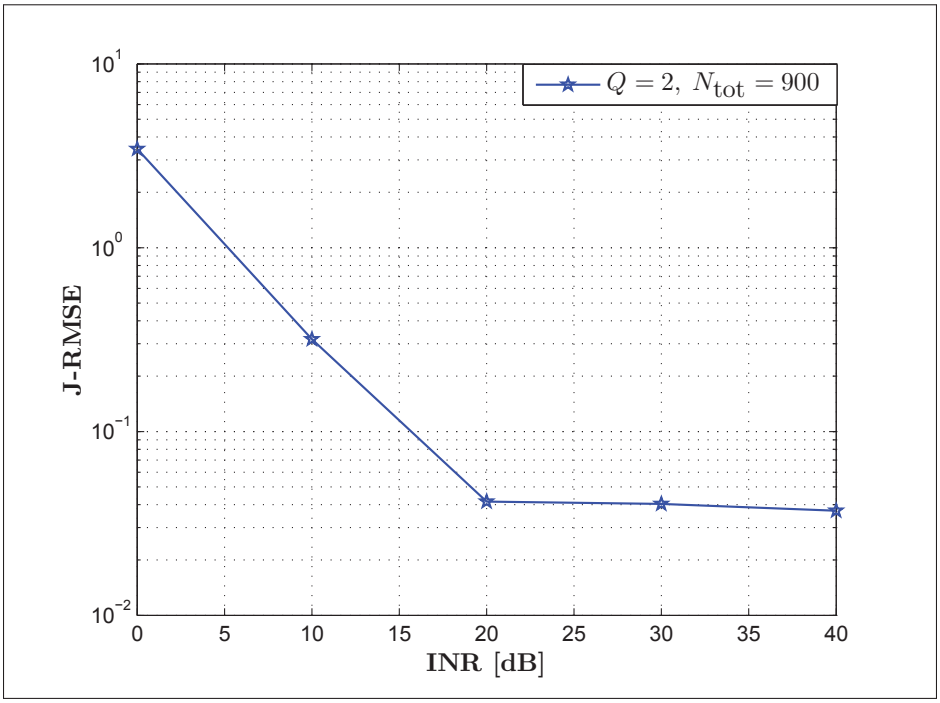

Figure 6.5 J-RMSE for SMB-JoNICOE over 5000 iterations:
$W = N_R = 8$, $\eta = 1$, and $(\sigma_1, \sigma_2) = (1, 1)$ W

6.7.2 Performance Assessment of SMB-JoNICOE

Having deployed the aforementioned simulation setup and (6.37), the J-RMSE performance of SMB-JoNICOE is simulated through Algorithm 6.2. As demonstrated by Figs. 6.5 & 6.6, J-RMSE for SMB-JoNICOE decreases as the INR increases. It is evident that an MI-RFI with stronger power will have a better joint estimate of the number of interferers and their respective channel order. It is also evident from Fig. 6.6 that J-RMSE gets smaller, as Q gets smaller. For an N_{tot} which is not large enough, increasing the INR won't help too much after some level of INR—as depicted in Figs. 6.5 & 6.6.

6.7.3 Performance Assessment of MLSEP

By deploying the aforementioned simulation setup, the average RMSEE performance of MLSEP is simulated along with the respective performances of SP and CSP. Having taken the EVD of

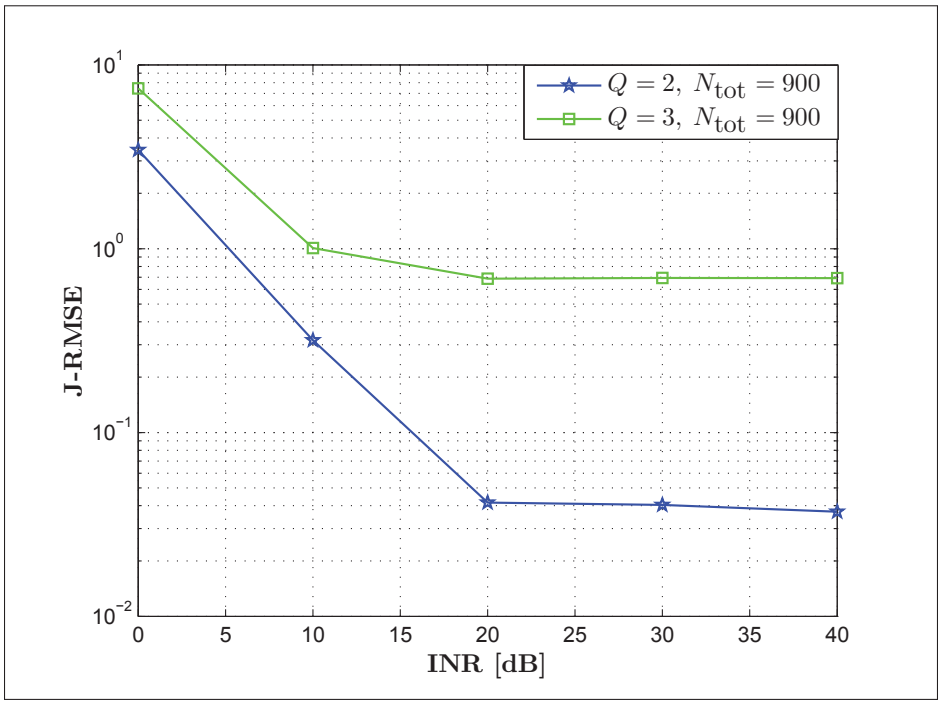

Figure 6.6 J-RMSE for SMB-JoNICOE over 5000 iterations: $W = N_R = 8$, $\eta = 1$, and $(\sigma_1, \sigma_2, \sigma_3) = (1, 1, 1)$ W

the space-time correlation matrix made of (6.3), the dominant eigenvectors are used for the simulation of SP. On the other hand, (6.3) and its equivalent received via N_R^a low-gain auxiliary antennas make the space-time crosscorrelation matrix whose SVD is exploited for the simulation of CSP. Low-gain auxiliary antennas exhibit large sidelobes where interference is observed at. Hence, any received weak interference would get strong. To simulate this phenomenon, we deploy an α factor which renders high INR. Meanwhile, average RMSEE exhibited by SP and CSP is simulated by averaging the matrix version of (6.14) over 200 LTIs.

6.7.3.1 Performance for Perfect $\{L_i\}_{i=1}^{Q}$ and Q

Fig. 6.7 demonstrates that MLSEP provides an INR gain of at least 5 dB, for $\gamma_{inr} \geq 10$ dB and $Q = 2$. This visible gain is attributed to the employed TB-MSE. Similarly, Fig. 6.8 demonstrates a better average SINR gain for MLSEP which is also attributed to the TB-MSE. Mean-

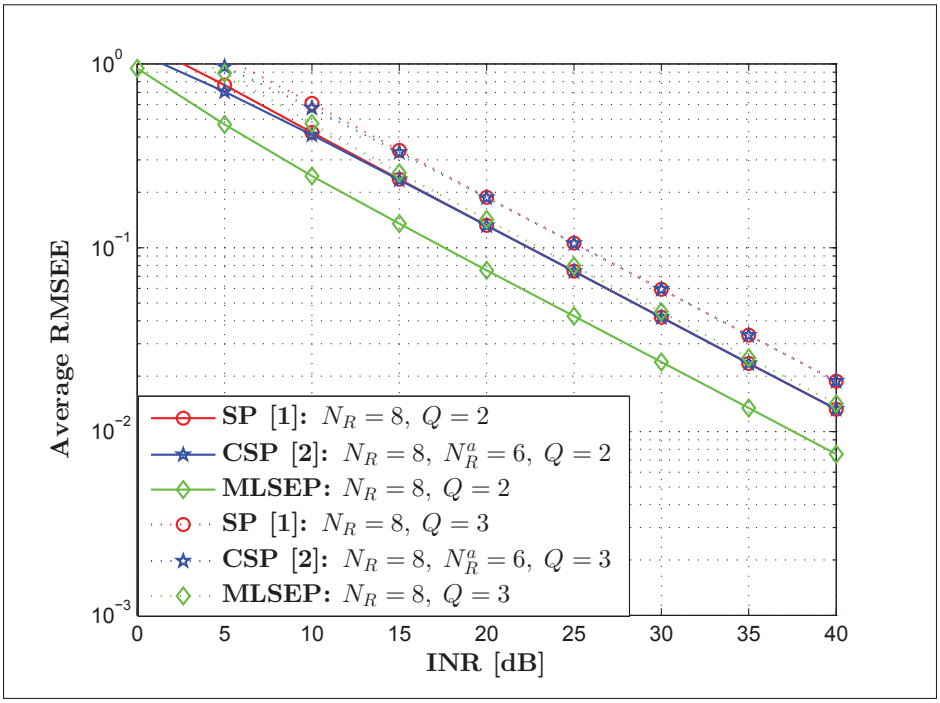

Figure 6.7 Average RMSEE for an MI-RFI excision using SP, CSP, and MLSEP: $N_{\text{tot}} = 300$, $W = 5$, $N = 60$, and $\alpha = 100$. Note that [1] and [2] represent (van der Tol & van der Veen, 2005) and (Jeffs *et al.*, 2005), respectively

while, it is evident from Fig. 6.8 that MLSEP performs close to the perfect excision algorithm which assumes a perfect knowledge of the MI-RFI channel.

6.7.3.2 Performance with SMB-JoNICOE

As it is also observed in Figs. 6.9 & 6.10, MLSEP simulated with estimates produced by SMB-JoNICOE improves SP and CSP. As the INR increases, MLSEP with SMB-JoNICOE performs very close to the genie-aided MLSEP which requires the knowledge of $\{L_i\}_{i=1}^{Q}$ and Q. This happens for SMB-JoNICOE produces estimates with high accuracy whenever the INR is high.

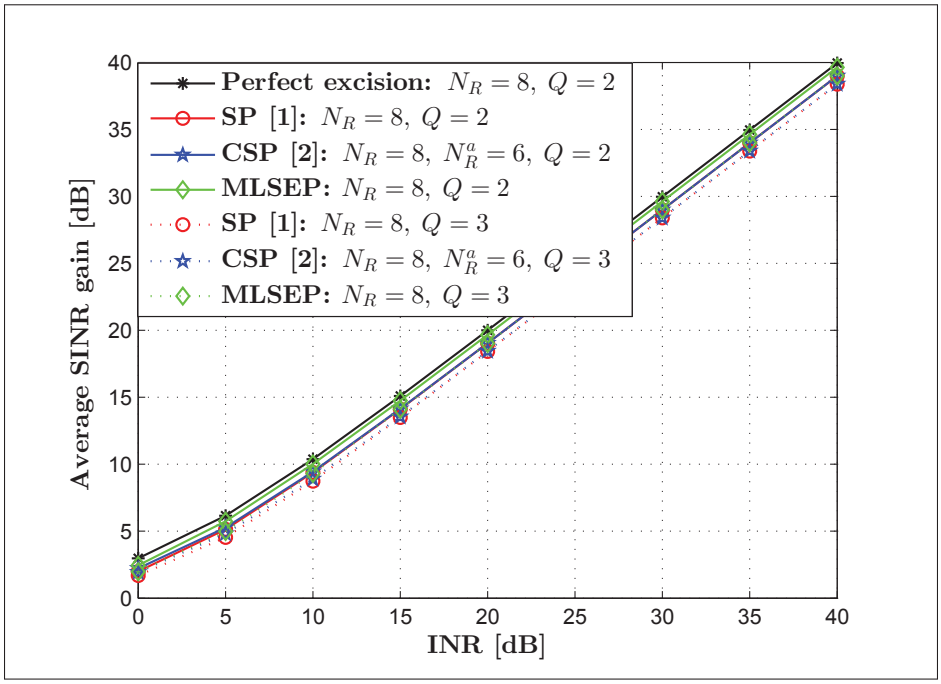

Figure 6.8 Average SINR gain of MI-RFI excision using SP, CSP, and MLSEP: $N_{\text{tot}} = 300$, $W = 5$, $N = 60$, and $\alpha = 100$. Note that [1] and [2] represent (van der Tol & van der Veen, 2005) and (Jeffs *et al.*, 2005), respectively

6.7.4 Performance Assessment of s-MLSEP

6.7.4.1 Performance for Perfect $\{L_i\}_{i=1}^{Q}$ and Q

Having employed the aforementioned setup, the average RMSEE and average SINR gain performances of s-MLSEP are plotted in Figs. 6.11 & 6.12, respectively. As it is evident from Fig. 6.11, s-MLSEP significantly improves MLSEP, as the smoothing factor gets smaller, despite an increase in computation time. The significant improvement is attributed to the STB-MSE which also renders an improvement in the average SINR gain depicted in Fig. 6.12.

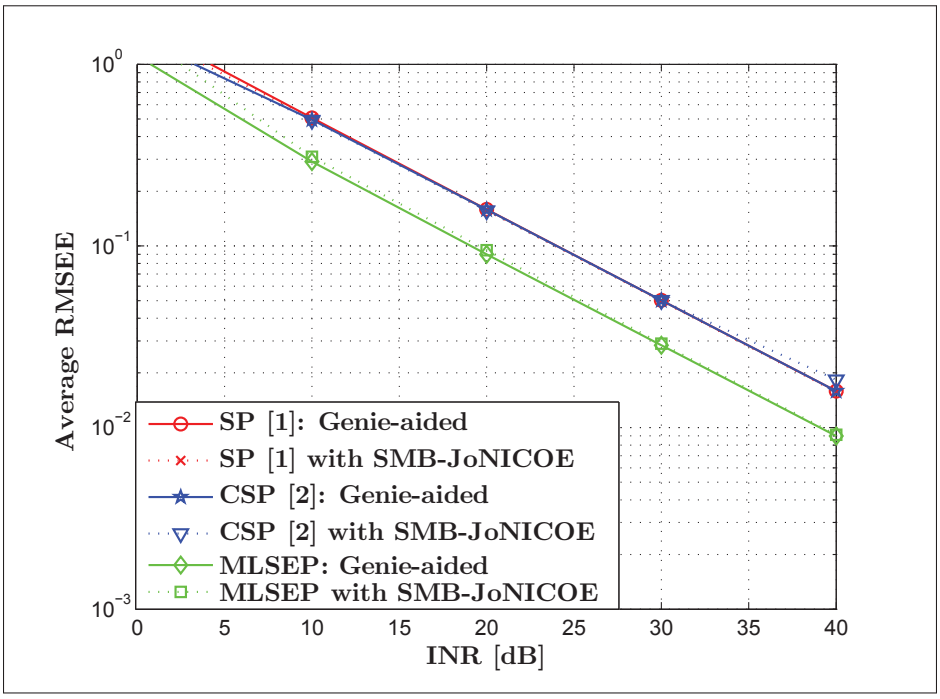

Figure 6.9 Average RMSEE for an MI-RFI excision using MLSEP: $N_{\text{tot}} = 800$ and $W = N_R = 8$. Note that [1] and [2] represent (van der Tol & van der Veen, 2005) and (Jeffs *et al.*, 2005), respectively

6.7.4.2 Performance with SMB-JoNICOE

For a similar reason to the ideal scenario discussed above, s-MLSEP simulated with estimates of SMB-JoNICOE improves MLSEP simulated with SMB-JoNICOE—as demonstrated by Figs. 6.13 & 6.14. Moreover, at high INR, s-MLSEP with SMB-JoNICOE performs very close to the genie-aided s-MLSEP which requires the knowledge of $\{L_i\}_{i=1}^{Q}$ and Q, since SMB-JoNICOE offers more precise estimates at high INR.

6.8 Performance Assessment on Real-World Data

To assess the MI-RFI excision on real-world data, we acquired real-time RFI contaminated analog-to-digital converter (ADC) data sampled at 2048 MHz. The ADC data were received by one of the antennas of the very large array (VLA) observatory (NRAO, 2017) and their

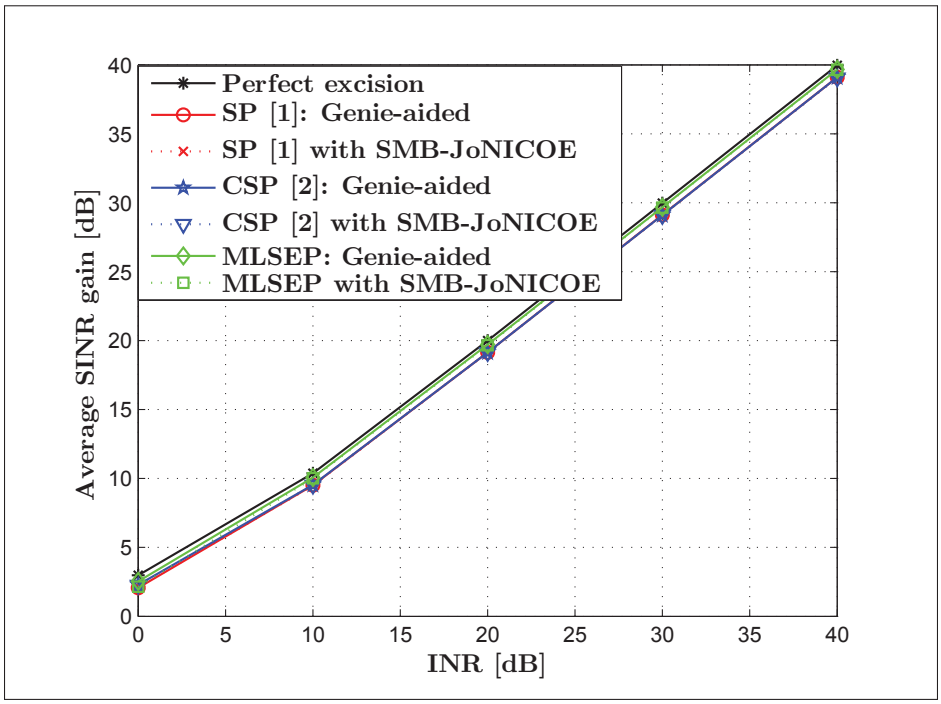

Figure 6.10 Average SINR gain of MI-RFI excision using MLSEP: $N_{\text{tot}} = 800$, $W = N_R = 8$, and $\eta = 1$. Note that [1] and [2] represent (van der Tol & van der Veen, 2005) and (Jeffs *et al.*, 2005), respectively

FFT is plotted in Figs. 6.15 & 6.16, where $f = 0$ Hz corresponds to a sky frequency of 3988 MHz and $10\log_{10}|Y(f)|$ indicates the magnitude of the FFT in dB. As seen in Fig. 6.16, there are four impinging RFIs from 102.8 MHz to 127.5 MHz. These frequencies plus the aforementioned sky frequency implies that the RFIs are caused by satellites transmitting in the downlink of a C band (Maral & Bousquet, 2009, Table 1.3). Meanwhile, it is assumed that the aforementioned RFIs are received upon a line-of-sight propagation, i.e., $\{L_i\}_{i=1}^{4} = 0$, because of the high directivity of the VLA antennas (NRAO, 2017) at this frequency and the received MI-RFI power.

In order to perform the performance assessment, first, the four RFIs are extracted using Kaiser window bandpass filters (Oppenheim & Schafer, 2010) and superimposed to generate the MI-RFI for the first antenna. Second, the VLA data and the MI-RFI received at the remaining $(N_R - 1)$ antennas are generated by considering a uniform linear array incurring one-symbol

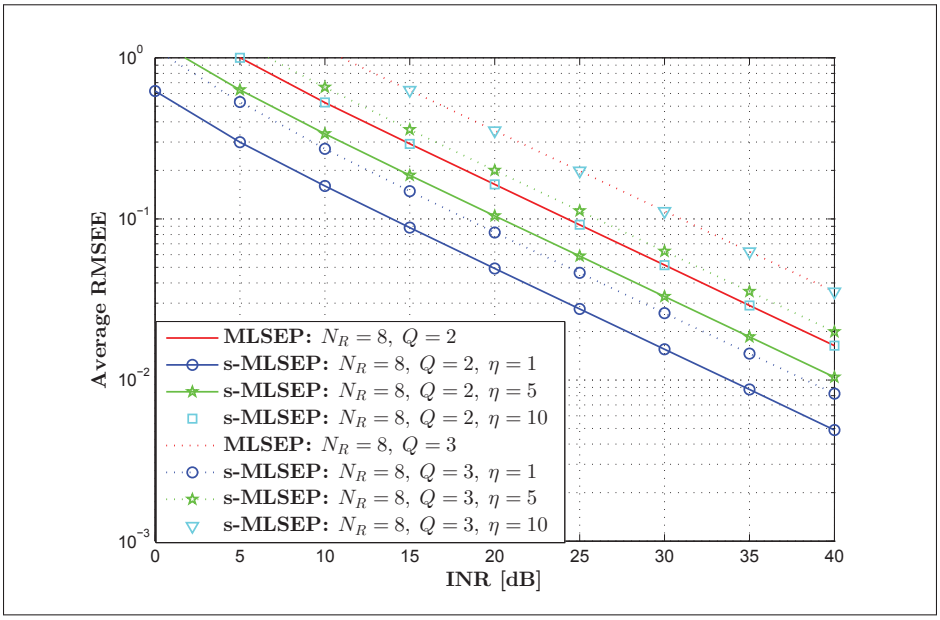

Figure 6.11 Average RMSEE for an MI-RFI excision using MLSEP and s-MLSEP: $N_{\text{tot}} = 600$, $W = 10$, and $N = 60$

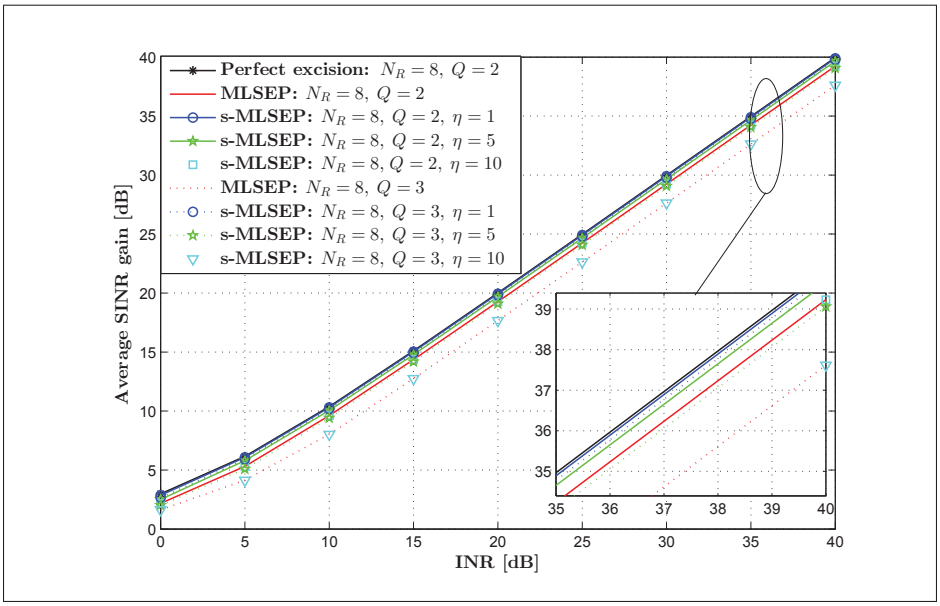

Figure 6.12 Average SINR gain of MI-RFI excision using MLSEP and s-MLSEP with $N_{\text{tot}} = 600$, $W = 10$, and $N = 60$

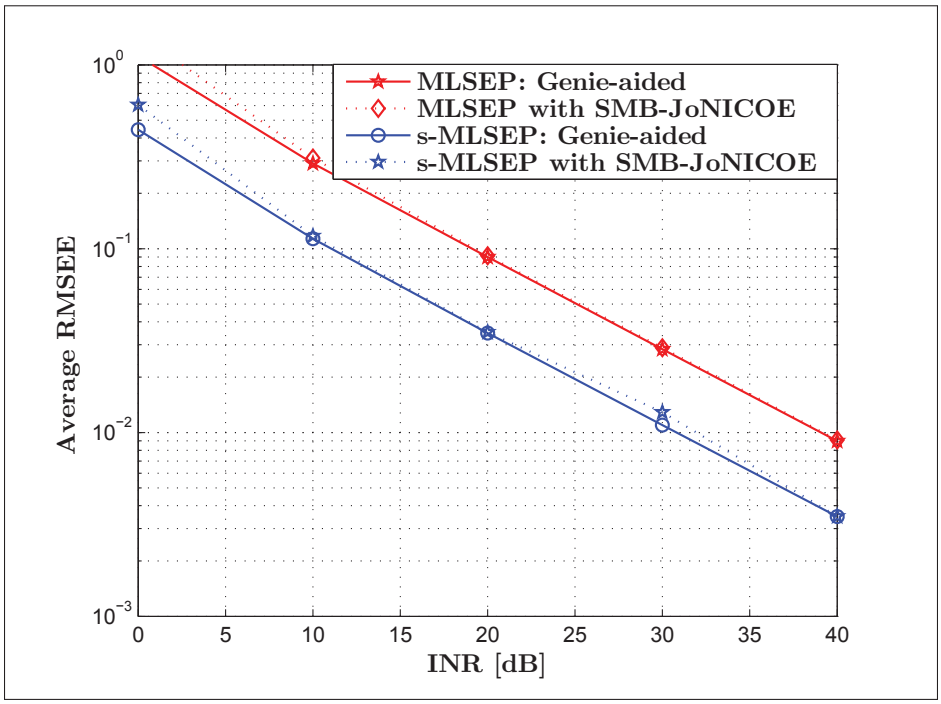

Figure 6.13 Average RMSEE performance of MLSEP and s-MLSEP: $N_{\text{tot}} = 800$, $W = N_R = 8$, and $\eta = 1$

delay between neighboring antennas. Next, a per LTI spatial filtering and MI-RFI excision are executed using MLSEP, SP, and CSP, for $[N_{\text{tot}}, \gamma_{inr}, N_R, N_R^a, W] = [800, 20\text{ dB}, 10, 6, 5]$.

The results of the MI-RFI excision using MLSEP, SP, and CSP are demonstrated in Figs. 6.17 & 6.18. Fig. 6.17 corroborates that the average residual MI-RFI power after MLSEP excision is almost one-fourth of the average residual MI-RFI power after SP or CSP excision, since the received power is proportional to the squared amplitude. Meanwhile, Fig. 6.18 showcases an almost flat spectrum rendered by MLSEP along with the non-flat spectra of SP and CSP. This implies the efficacy of MI-RFI excision using MLSEP, as also demonstrated by an approximately 10 dB excision of the MI-RFI spectrum. Moreover, Fig. 6.19 depicts the FFT of the spatially filtered VLA data using MLSEP, SP, and CSP. It shows that both SP and CSP render an almost flat spectrum from 0 MHz to 130 MHz, unlike the spectrum of the VLA data. On the contrary, the spectrum of the VLA data after the MI-RFI spatial filtering by MLSEP

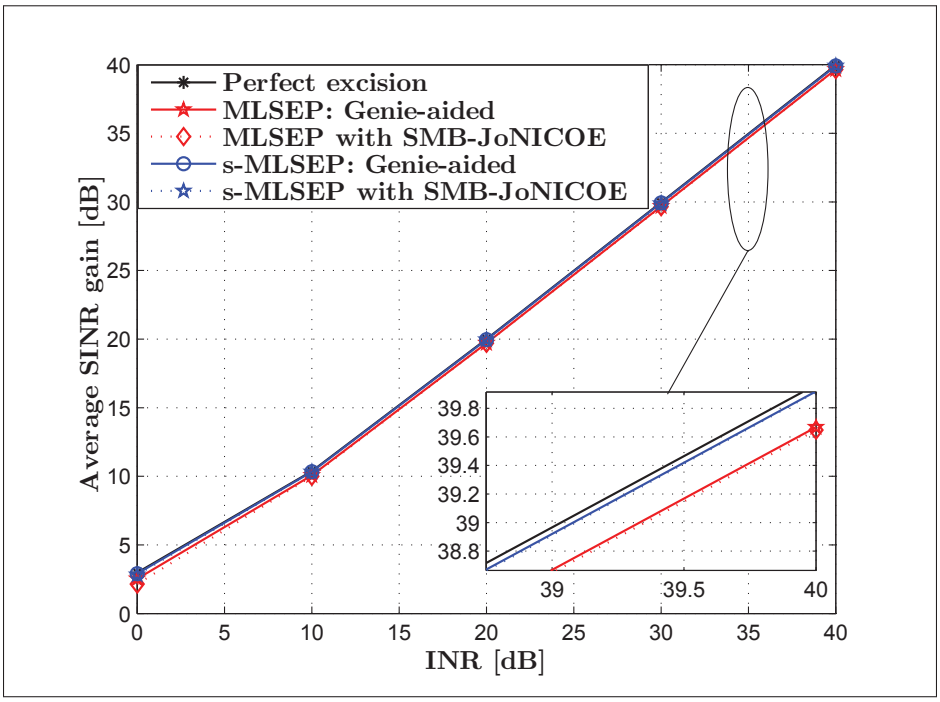

Figure 6.14 Average SINR gain performance of MLSEP and s-MLSEP: $N_{\text{tot}} = 800$, $W = N_R = 8$, and $\eta = 1$

produces a spectrum in the 0 MHz-130 MHz whose envelope almost follows that of the SOI, while efficiently excising the MI-RFI.

6.9 Conclusions

This paper introduces the multi-linear algebra framework to the MI-RFI excision research. To do so, TB-MSE, which provides a significant improvement in the estimation of the MI-RFI subspace whenever $N_R > \sum_{i=1}^{Q}(L_i+1)$, is deployed for the estimation of the MI-RFI subspace. Thereafter, the multi-linear projector that renders perfect excision of the MI-RFI, for the perfectly estimated MI-RFI subspace tensor, is derived. However, perfect estimate of the MI-RFI subspace tensor cannot be obtained and a performance parameter named RMSEE, which quantizes the root mean square MI-RFI excision error, is used. The aforementioned multi-linear estimation and projection produce MLSEP. Meanwhile, smoothed observation windows are exploited to propose s-MLSEP which enhances MLSEP at the expense of computation time.

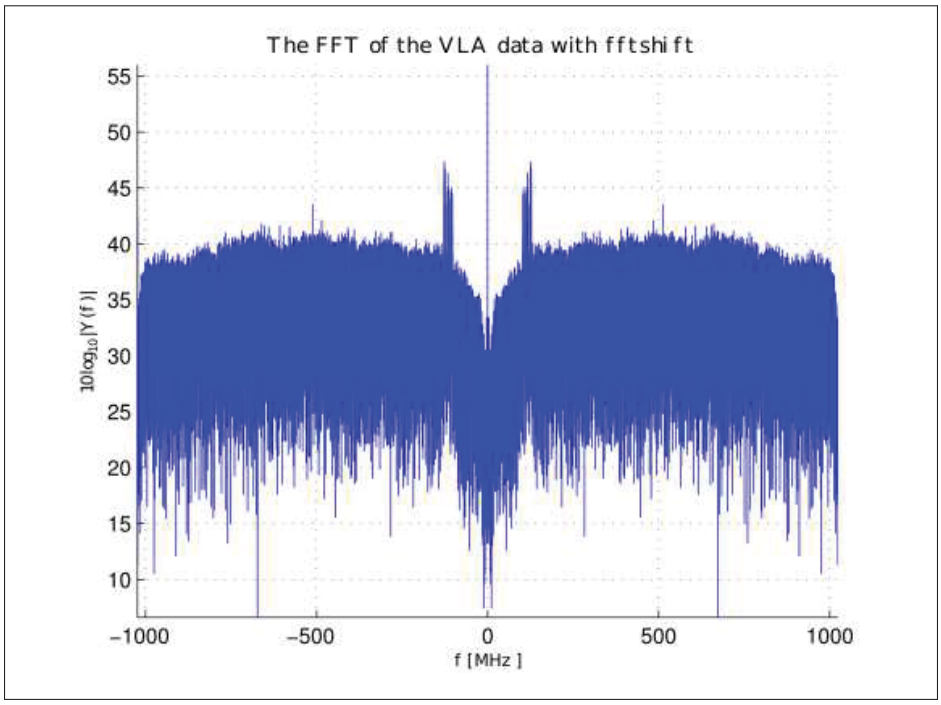

Figure 6.15 The absolute value of the FFT of the VLA data

As MLSEP and s-MLSEP require the knowledge of the number of interferers and their respective channel order, a novel SMB-JoNICOE, which jointly enumerates the number of interferers and their respective channel order, is proposed. Performance analyses which employ the first-order perturbation analysis corroborate that both MLSEP and s-MLSEP can excise all interferers when the perturbations get infinitesimally small. For such perturbations, the analyses also attest that s-MLSEP exhibits a faster convergence to a zero excision error than MLSEP which, in turn, converges faster than SP. Furthermore, the complexity of MLSEP and s-MLSEP is analyzed. Despite its complexity, Monte-Carlo simulations have corroborated that MLSEP significantly improves the state-of-the-art projection-based algorithms. Moreover, smoothing improves MLSEP at the price of computation time. At last, performance assessment on the real-world data also corroborates that MLSEP outperforms the state-of-the-art projection-based RFI excision algorithms.

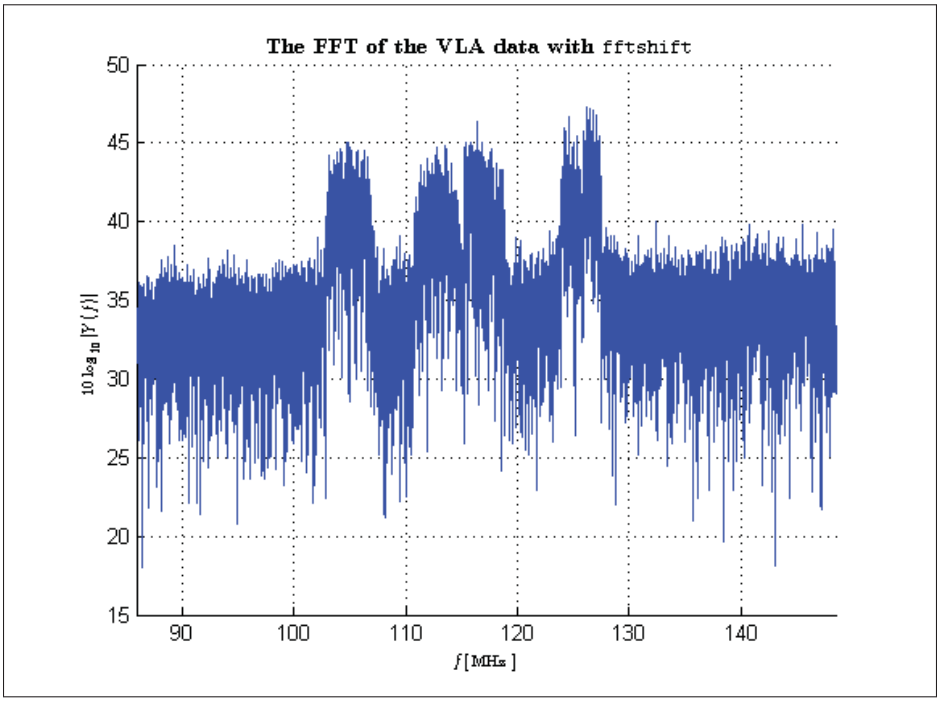

Figure 6.16 The lower frequency component

Acknowledgments

The authors acknowledge AVIO-601 project for the provided funding and Alan Erickson of the National Radio Astronomy Observatory for facilitating the RFI data.

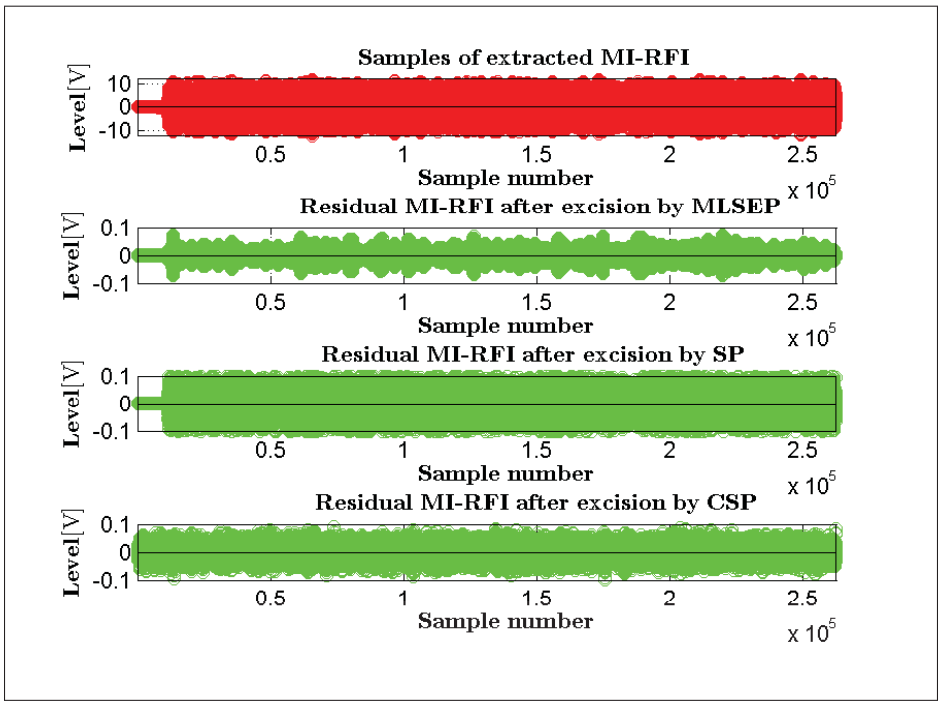

Figure 6.17 Real-world MI-RFI excision

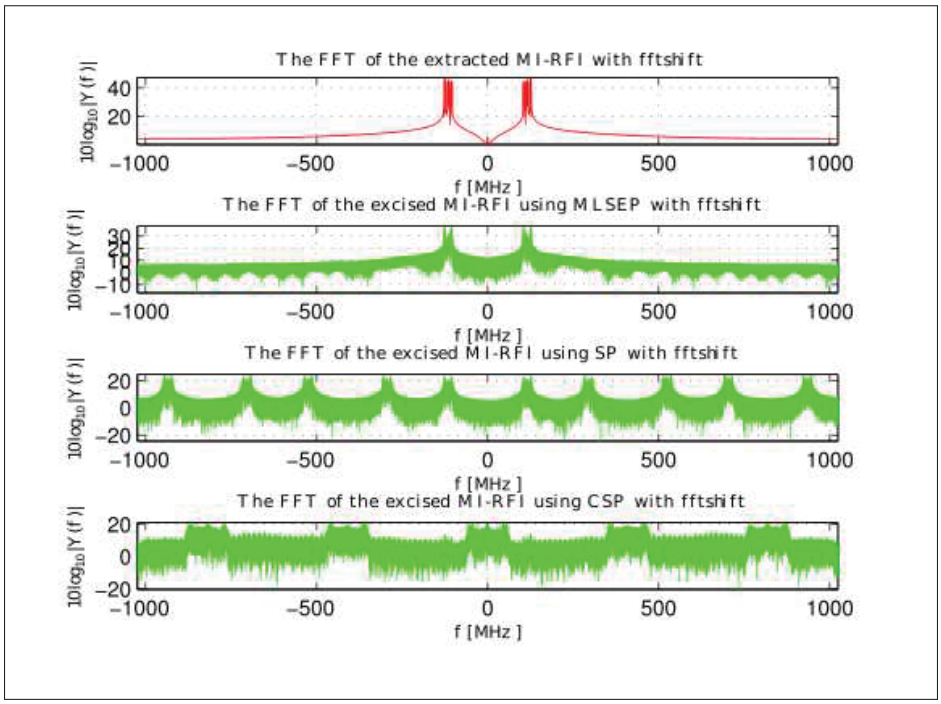

Figure 6.18 The FFT of a real-world MI-RFI excision

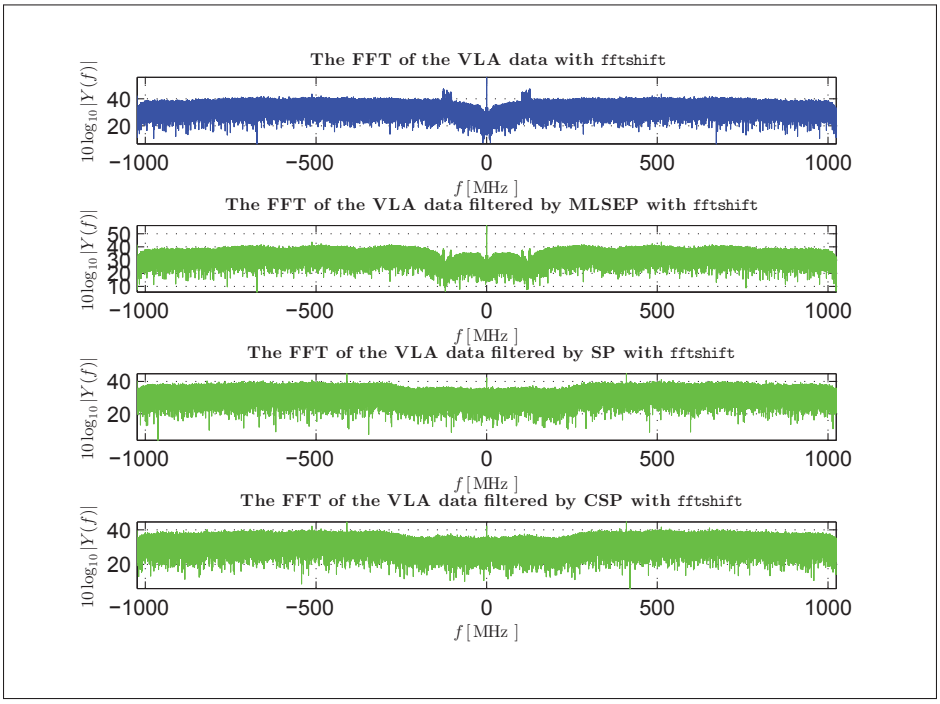

Figure 6.19 The FFT of the spatially filtered VLA data

Part IV

Advanced Spectrum Sensing

CHAPTER 7

SIMPLE F–TEST BASED SPECTRUM SENSING TECHNIQUES FOR MULTI-ANTENNA COGNITIVE RADIOS

Tilahun M. Getu[1,2], Wessam Ajib[2], and René Jr. Landry[1]

[1] Department of Electrical Engineering, École de Technologie Supérieure,
1100 Notre-Dame West, Montréal, Québec, Canada H3C 1K3
[2] Department of Computer Sciences, Université du Québec à Montréal,
201 Av. President-Kennedy, Montréal, Québec, Canada H2X 3Y7

This article was published in *IEEE Transactions on Communications* as of November 2018 (Getu *et al.*, 2018a).

"Everything is interesting if you go into it deeply enough."—Richard P. Feynman

Abstract—An F–test detector with a simple analytical false alarm threshold expression is considered an alternative to the blind detectors which exhibit complicated analytical expressions. However, the existing F–test requires the channel state information (CSI) as prior knowledge and is known to be sensitive to CSI estimation errors. In this paper, we present and evaluate simple F–test based spectrum sensing techniques that do not require the knowledge of CSI for multi-antenna cognitive radios. Exact and asymptotic analytical performance closed-form expressions are derived for the presented detectors. Simulations assess the performance of the presented detectors and validate the derived closed-form expressions. For an additive noise exhibiting the same variance across multiple-antenna frontends, simulations also corroborate that the presented detectors are constant false alarm rate (CFAR) detectors which are also robust against noise uncertainty.

Index Terms—Cognitive radio, spectrum sensing, channel state information, F–test, CFAR detectors.

7.1 Introduction

Cognitive radio (CR) is a promising technology to alleviate the problem of spectrum scarcity which is getting aggravated by an ever-increasing demand for higher data rates. To realize such a radio, licensed spectrum sharing techniques such as *spectrum underlay* and *spectrum overlay* have been proposed (Zhao & Sadler, 2007; Wang & Liu, 2011). In spectrum underlay, a secondary user (SU) is allowed to transmit on the licensed band of a primary user (PU) while respecting a PU's interference threshold (Wang & Liu, 2011). In spectrum overlay, SUs rather transmit after locating idle frequency bands, licensed to PUs, till a primary transmission is conducted on them (Wang & Liu, 2011; Haykin, 2005). Such an idle frequency band detection is called spectrum sensing and hence fundamental to CR based communication systems. As per the bandwidth of the signal to be detected, spectrum sensing techniques can be *narrowband* or *wideband* (Sharma *et al.*, 2015; Bogale *et al.*, 2015; Sun *et al.*, 2013; Jayaweera, 2014). Depending on the adopted sampling rate, the wideband techniques can be Nyquist based (Ali & Hamouda, 2017; Sun *et al.*, 2013) or sub-Nyquist based (Donoho, 2006; Venkataramani & Bresler, 2000). The Nyquist based wideband sensing techniques are based on either fast Fourier transforms (Quan *et al.*, 2009), Wavelets (Tian & Giannakis, 2006), or filterbanks (Farhang-Boroujeny, 2008). The sub-Nyquist ones deploy either compressive sampling (Donoho, 2006) or multi-coset sampling (Venkataramani & Bresler, 2000).

Delving into narrowband sensing, several narrowband spectrum sensing techniques have been proposed to date (Wang & Liu, 2011; Axell *et al.*, 2012; Haykin *et al.*, 2009; Ali & Hamouda, 2017; Sharma *et al.*, 2015). The conventional ones are energy detection (ED) (Jayaweera, 2014; Digham *et al.*, 2007; Sofotasios *et al.*, 2013), matched filtering (Poor, 1994), feature-based detection (Gardner, 1988), polarization detection (Guo *et al.*, 2016), sample covariance matrix (SCM) based algorithms (Kortun *et al.*, 2012; Zeng & Liang, 2009b,a; Bianchi *et al.*, 2011), moment ratio detection (Bogale & Vandendorpe, 2013a), and max-min detection (Bogale & Vandendorpe, 2014, 2013b). Nevertheless, ED relies on the known power spectral density of the noise and exhibits a high sensitivity to noise uncertainty (Wang & Liu, 2011; Axell *et al.*, 2012) leading to a poor performance at low signal-to-noise ratio (SNR) regardless

of the number of intercepted samples, as demonstrated via the *SNR walls* (Tandra & Sahai, 2008); matched filters suffer from intrinsic computational complexity; particular features need to be introduced to deploy feature detectors in OFDM-based communications (Wang & Liu, 2011); polarization detectors are computationally complex and sensitive to estimation errors (Guo *et al.*, 2016); SCM-based techniques suffer from performance loss under sample-starved settings—despite their blindness—and their asymptotic threshold differs considerably from the exact value for finite sensors and samples (Kortun *et al.*, 2012); moment ratio detection is computationally complex and relies on the asymptotic Gaussian distribution; and max-min detector suffers from huge computational complexity.

Apart from the highlighted conventional algorithms, some other algorithms such as Bartlett estimate-based energy detection (Gismalla & Alsusa, 2012), a frequency domain eigenvalue-based spectrum sensing algorithms (Yousif *et al.*, 2016), subband energy-based spectrum sensing algorithm (Dikmese *et al.*, 2016), energy detection spectrum sensing under RF imperfections and with multiple PUs (Boulogeorgos *et al.*, 2016a,b), and robust estimator-correlator and robust generalized likelihood detectors (Patel *et al.*, 2016) have been proposed. However, all these important contributions are less attractive for practical CR applications since they rely on the complex Gaussian distributed primary signal. On the other hand, unlike most of the aforementioned multi-antenna techniques which presume an *independent and identically distributed* (i.i.d.) noise samples, calibration uncertainties in the different antenna frontends are inevitable rendering *independent and non-identically distributed* (i.ni.d.) noise samples. Such a scenario was considered in (Leshem & van der Veen, 2001; Tugnait, 2012; Ramírez *et al.*, 2011): by assuming a Gaussian distributed received signal, a Hadamard ratio detector (HRD) was derived in (Leshem & van der Veen, 2001); a spectrum sensing technique which deploys asymptotic analysis of the discrete Fourier transform of the received multi-antenna signal—whose time domain version is an HRD—is proposed in (Tugnait, 2012); and (Ramírez *et al.*, 2011) devised a generalized likelihood ratio test (GLRT) based technique by proposing an efficient alternating minimization algorithm to compute its statistic.

Recently, the F–test based spectrum sensing technique was proposed in (Huang & Chung, 2013a,b) and corroborated to be superior over an energy detector, a maximum-minimum eigenvalue (MME) detector, and a GLRT detector, especially at low SNR. While exhibiting a moderate computational complexity, this detector is also robust against noise uncertainty and independent of noise power. However, it requires prior knowledge of the channel state information (CSI) between the primary transmitter and secondary receiver. Hence, it is susceptible to CSI estimation errors.

Inspired by the performance of the F–test detector of (Huang & Chung, 2013a), this paper presents modified versions of (Huang & Chung, 2013a) that do not require the knowledge of CSI nor the noise power. For these F–test based techniques, this paper studies and evaluates their performance analytically. Specifically, the respective contributions of this paper are itemized below.

- Along with its performance analyses, a detector named F–test via singular value decomposition (FT-v-SVD) is presented for a single-input multiple-output (SIMO) CR network operating over flat fading channels.
- Apart from its performance analyses, a detector dubbed generalized FT-v-SVD (g-FT-v-SVD) is presented for a multi-antenna spectrum sensing over frequency selective channels.
- The g-FT-v-SVD detector is generalized to accommodate a spectrum sensing over a multiple-input multiple-output (MIMO) CR network.
- For both i.i.d. and i.ni.d. noise samples, the performance of the presented detectors is assessed through Monte-Carlo simulations which also validate the derived analytical expressions.

Following this introduction, Sec. 7.2 presents the notation and system model. Sec. 7.3 details FT-v-SVD whose performance analyses are reported in Sec. 7.4. Sec. 7.5 details g-FT-v-SVD and its performance analyses. Sec. 7.6 provides a computational complexity analysis of different detectors. Sec. 7.7 reports the simulation results that inspire the paper conclusions drawn in Sec. 7.8.

7.2 Notation and System Model

7.2.1 Notation

Scalars, vectors, and matrices are denoted by italic letters, lower-case boldface letters, and upper-case boldface letters, respectively; $\sim$, $n!$, $\propto$, $\lceil\cdot\rceil$, $\equiv$, $\leftarrow$, and $\rightarrow$ mean distributed as, n factorial, statistically equivalent, the ceiling function, is equivalent to, assignment, and approaches to, respectively; lim, $\max\{\cdot,\cdot\}$, $||\cdot||$, $(\cdot)^T$, $(\cdot)^H$, $(\cdot)^{-1}$, and $(\cdot)^+$ imply limit, maximum, the Euclidean norm, transpose, Hermitian, inverse, and the Moore-Penrose inverse, respectively; $\mathbb{C}^M$, $\mathbb{C}^{M\times N}$, and $\mathbb{H}^{M\times M}$ denote the sets of M–dimensional vectors of complex numbers, of $M\times N$ complex matrices, and of $M\times M$ Hermitian matrices, respectively; $\text{diag}(\cdot)$, $\boldsymbol{A}(i,j)$, $\boldsymbol{A}(:,j)$, $\boldsymbol{A}(:,i:j)$, $\boldsymbol{I}_{N_R}\left(\boldsymbol{I}_{N_RW}\right)$, and $\mathbf{0}_{M\times N}$ denote a diagonal matrix, the (i,j)-th element of $\boldsymbol{A}$, the j-th column of $\boldsymbol{A}$, the columns of $\boldsymbol{A}$ between its i-th and j-th columns including its i-th and j-th columns, an $N_R\times N_R$ $\left(N_RW\times N_RW\right)$ identity matrix, and an $M\times N$ zero matrix, respectively; $\mathscr{O}(\cdot)$, $\Pr\{\cdot\}$, $\mathbb{E}\{\cdot\}$, $\text{tr}(\cdot)$, and $\mathscr{CN}_M(\boldsymbol{\mu},\boldsymbol{\Sigma})$ represent the Landau notation, the probability of, expectation, trace, and the circularly symmetric complex multivariate normal distribution with mean $\boldsymbol{\mu}\in\mathbb{C}^M$ and covariance matrix $\boldsymbol{\Sigma}\in\mathbb{H}^{M\times M}$ ($M\geq 2$), respectively; χ^2, F_{ν_1,ν_2}, $F'_{\nu_1,\nu_2}(\lambda_1)$, and $F''_{\nu_1,\nu_2}(\lambda_1,\lambda_2)$ denote chi-square, the central F–distribution with (ν_1,ν_2) degrees of freedom (DoF), the singly noncentral F–distribution with (ν_1,ν_2) DoF and a noncentrality parameter (NCP) of λ_1, and the doubly noncentral F–distribution with (ν_1,ν_2) DoF and NCPs of (λ_1,λ_2), respectively; and $F(\lambda;\nu_1,\nu_2)$, $F^{-1}(\lambda;\nu_1,\nu_2)$, $F'(\lambda;\nu_1,\nu_2|\lambda_1)$, and $F''(\lambda;\nu_1,\nu_2|\lambda_1,\lambda_2)$ denote the cumulative distribution function (CDF) of F_{ν_1,ν_2}, the inverse CDF of F_{ν_1,ν_2}, the CDF of $F'_{\nu_1,\nu_2}(\lambda_1)$, and the CDF of $F''_{\nu_1,\nu_2}(\lambda_1,\lambda_2)$, respectively, evaluated at λ.

7.2.2 System Model

Consider a CR communication system made of a primary transmitter and a secondary receiver with N_R antennas. First, the primary transmitter is assumed to have one antenna for simplicity; but a generalization regarding a multi-antenna primary transmitter is given in Sec. 7.5.4. For

an opportunistic transmission, the SU senses the licensed band through a frequency selective channel modeled as a finite-duration impulse response filter with $L+1$ taps. Toward this end, a binary hypothesis test is formulated on a primary signal detection as

$$\boldsymbol{y}[k] = \begin{cases} \sum_{l=0}^{L} \boldsymbol{h}_l s[k-l] + \boldsymbol{z}[k] & : H_1 \\ \boldsymbol{z}[k] & : H_0, \end{cases} \tag{7.1}$$

where H_0 and H_1 are, respectively, hypotheses regarding the idleness and activeness of a PU, $\boldsymbol{y}[k] \in \mathbb{C}^{N_R}$ is the k-th sample received signal vector, $\boldsymbol{z}[k] \sim \mathscr{CN}_{N_R}(\boldsymbol{0}, \boldsymbol{\Sigma})$ is a zero mean circularly symmetric complex additive white Gaussian noise (AWGN) with $\boldsymbol{\Sigma} \in \mathbb{H}^{N_R \times N_R}$, $\boldsymbol{h}_l = [h_{1l}, h_{2l}, \ldots, h_{N_R l}]^T \in \mathbb{C}^{N_R}$ is the l-th multi-path fading component's CSI vector assumed constant during the primary signal interception, and $s[k]$ is the k-th unknown and deterministic primary symbol.

For i.i.d. noise samples with power σ^2, $\boldsymbol{\Sigma} = \sigma^2 \boldsymbol{I}_{N_R}$ is considered. For i.ni.d. noise samples, we suppose $\boldsymbol{\Sigma} = \sigma^2 \boldsymbol{I}_{N_R} + \sigma^2 \boldsymbol{E}$, where $\boldsymbol{E} = \text{diag}(\varepsilon_1, \varepsilon_2, \ldots, \varepsilon_{N_R})$, $\varepsilon_i > 0$ and $1 \leq i \leq N_R$, is an error matrix accommodating the respective calibration uncertainties on the N_R antenna frontends. For flat fading channels, moreover, we consider $L = 0$ and $\boldsymbol{h}_0 = \boldsymbol{h}$.

7.3 FT-v-SVD: Algorithm

The FT-v-SVD algorithm is detailed for a reception over flat fading channels under i.i.d. noise samples. We also derive equivalent test statistics and discuss the effect of i.ni.d. noise samples on the performance of FT-v-SVD.

7.3.1 The Formulated F–Test

In the presented spectrum sensing technique, the SCM $\hat{\boldsymbol{R}}_{yy} \in \mathbb{C}^{N_R \times N_R}$ is, first, computed using (7.1) as

$$\hat{\boldsymbol{R}}_{yy} = \frac{1}{N} \sum_{k=1}^{N} \boldsymbol{y}[k] \boldsymbol{y}^H[k] = \frac{1}{N} \boldsymbol{Y} \boldsymbol{Y}^H, \tag{7.2}$$

where N is the number of intercepted per-antenna samples and $\boldsymbol{Y} = \big[\boldsymbol{y}[1], \boldsymbol{y}[2], \ldots, \boldsymbol{y}[N]\big] \in \mathbb{C}^{N_R \times N}$. Second, the SVD of the SCM is computed by using (7.2) as

$$\hat{\boldsymbol{R}}_{yy} = \hat{\boldsymbol{U}}\hat{\boldsymbol{\Sigma}}\hat{\boldsymbol{V}}^H = [\hat{\boldsymbol{U}}_s\ \hat{\boldsymbol{U}}_n]\hat{\boldsymbol{\Sigma}}\hat{\boldsymbol{V}}^H, \tag{7.3}$$

where $\hat{\boldsymbol{\Sigma}} = \text{diag}(\hat{\sigma}_1, \hat{\sigma}_2, \ldots, \hat{\sigma}_{N_R})$, for $\hat{\sigma}_1 \geq \hat{\sigma}_2 \ldots \geq \hat{\sigma}_{N_R}$ being the singular values, $\hat{\boldsymbol{U}}_s = \hat{\boldsymbol{U}}(:, 1) \in \mathbb{C}^{N_R}$ is the estimated subspace spanned by the singular vector corresponding to the largest singular value, and $\hat{\boldsymbol{U}}_n = \hat{\boldsymbol{U}}(:, 2 : N_R) \in \mathbb{C}^{N_R \times (N_R - 1)}$. Third, a projection matrix $\hat{\boldsymbol{P}}_s \in \mathbb{C}^{N_R \times N_R}$ is computed from $\hat{\boldsymbol{U}}_s$ as

$$\hat{\boldsymbol{P}}_s = \hat{\boldsymbol{U}}_s\hat{\boldsymbol{U}}_s^+ = \hat{\boldsymbol{U}}_s\hat{\boldsymbol{U}}_s^H, \tag{7.4}$$

where $\boldsymbol{U}_s^H\boldsymbol{U}_s = 1$ is exploited in $\boldsymbol{U}_s^+ = (\boldsymbol{U}_s^H\boldsymbol{U}_s)^{-1}\boldsymbol{U}_s^H$, as $\hat{\boldsymbol{U}}_s$ is an orthonormal vector.

Fourth, a decision statistic T which is based on the F–test is formed to verify the existence of a linear relationship between the received signal samples and the received primary signal. Following (Huang & Chung, 2013a, eq. (5)) and using (7.4), the FT-v-SVD test statistic and the corresponding decision rule are formulated as

$$T \triangleq \frac{\nu_2}{\nu_1} \frac{\text{tr}(\hat{\boldsymbol{P}}_s\hat{\boldsymbol{R}}_{yy})}{\text{tr}\big((\boldsymbol{I}_{N_R} - \hat{\boldsymbol{P}}_s)\hat{\boldsymbol{R}}_{yy}\big)} \underset{H_0}{\overset{H_1}{\gtrless}} \lambda, \tag{7.5}$$

where λ is the decision threshold and $(\nu_1, \nu_2) = \big(2N, 2N(N_R - 1)\big)$ are the DoF of the numerator and denominator, respectively.

Remark 6. Unlike (Huang & Chung, 2013a, eq. (5)), (7.5) is independent of the knowledge of the CSI between the primary transmitter and the secondary receiver.

7.3.2 Equivalent Test Statistics

This subsection derives test statistics that are statistically equivalent with the formulated F–test statistic. Substituting (7.2) and (7.4) into (7.5) renders

$$T \overset{(a)}{=} (N_R - 1)\frac{\mathrm{tr}(\hat{\sigma}_1 \hat{\boldsymbol{U}}_s \hat{\boldsymbol{V}}_s^H)}{\mathrm{tr}\big(\hat{\boldsymbol{U}}_n \hat{\boldsymbol{\Sigma}}_n \hat{\boldsymbol{V}}_n^H\big)}, \tag{7.6}$$

where (a) follows from the fact that $\hat{\boldsymbol{U}}_s \hat{\boldsymbol{U}}_s^H \hat{\boldsymbol{U}}_s = \hat{\boldsymbol{U}}_s$ and $\hat{\boldsymbol{U}}_s^H \hat{\boldsymbol{U}}_n = \boldsymbol{0}_{1\times(N_R-1)}$ for the columns and rows of $\hat{\boldsymbol{U}}$ are orthonormal (Horn & Johnson, 2013, Thm. 2.1.4). Because the SCM is a Hermitian as well as a positive semi-definite matrix, its eigenvalue decomposition and SVD are identical. Hence, $\hat{\boldsymbol{U}} = \hat{\boldsymbol{V}}$, $\hat{\boldsymbol{U}}_s = \hat{\boldsymbol{V}}_s$, and $\hat{\boldsymbol{U}}_n = \hat{\boldsymbol{V}}_n$. As a result,

$$T = (N_R - 1)\left[\frac{\hat{\sigma}_1 \mathrm{tr}(\hat{\boldsymbol{U}}_s \hat{\boldsymbol{U}}_s^H)}{\mathrm{tr}\big(\hat{\boldsymbol{U}}_n \hat{\boldsymbol{\Sigma}}_n \hat{\boldsymbol{U}}_n^H\big)} \overset{(b)}{=} \frac{\hat{\sigma}_1 \mathrm{tr}(\hat{\boldsymbol{U}}_s \hat{\boldsymbol{U}}_s^H)}{\mathrm{tr}\big(\hat{\boldsymbol{U}}_n^H \hat{\boldsymbol{U}}_n \hat{\boldsymbol{\Sigma}}_n\big)}\right], \tag{7.7}$$

where (b) follows for $\mathrm{tr}(\boldsymbol{AB}) = \mathrm{tr}(\boldsymbol{BA})$ (Magnus & Neudecker, 2007). From the orthonormal property of $\hat{\boldsymbol{U}}$, $\mathrm{tr}\big(\hat{\boldsymbol{U}}_s \hat{\boldsymbol{U}}_s^H\big) = ||\hat{\boldsymbol{U}}_s||^2 = 1$ and $\hat{\boldsymbol{U}}_n^H \hat{\boldsymbol{U}}_n = \boldsymbol{I}_{(N_R-1)}$. Accordingly, $\mathrm{tr}\big(\hat{\boldsymbol{U}}_n^H \hat{\boldsymbol{U}}_n \hat{\boldsymbol{\Sigma}}_n\big) = \mathrm{tr}\big(\hat{\boldsymbol{\Sigma}}_n\big) = \sum_{i=2}^{N_R} \hat{\sigma}_i$ and

$$T = (N_R - 1)\frac{\hat{\sigma}_1}{\sum_{i=2}^{N_R} \hat{\sigma}_i} \propto \frac{\hat{\sigma}_1}{\sum_{i=2}^{N_R} \hat{\sigma}_i}. \tag{7.8}$$

Remark 7. To reduce the computational complexity of the FT-v-SVD algorithm, it can also be implemented via (7.8) as an eigenvalue detector.

As $\sum_{i=2}^{N_R} \hat{\sigma}_i = \sum_{i=1}^{N_R} \hat{\sigma}_i - \hat{\sigma}_1$, the test statistic can also be further simplified to

$$T \propto \frac{\hat{\sigma}_1}{\sum_{i=1}^{N_R} \hat{\sigma}_i - \hat{\sigma}_1} = \frac{\hat{\sigma}_1 / \sum_{i=1}^{N_R} \hat{\sigma}_i}{1 - \hat{\sigma}_1 / \sum_{i=1}^{N_R} \hat{\sigma}_i} = \frac{y}{1-y}, \tag{7.9}$$

where $y = \hat{\sigma}_1 / \sum_{i=1}^{N_R} \hat{\sigma}_i$ and $1/N_R \leq y \leq 1$ (Wang *et al.*, 2010, Appendix II). Note that (7.9) increases monotonically over $y \in (1/N_R, 1)$. Consequently, the test statistic simplifies to

$$T \propto \frac{\hat{\sigma}_1}{\sum_{i=1}^{N_R} \hat{\sigma}_i}. \tag{7.10}$$

Remark 8. As the singular values and the eigenvalues of the SCM are identical, (7.10) and the blind GLRT statistic (Wang *et al.*, 2010, eq. (13)), (Taherpour *et al.*, 2010, eq. (39)) are identical.

7.3.3 Impact of i.ni.d. Noise Samples on FT-v-SVD

As the F–test is derived from a likelihood ratio test under i.i.d. noise samples (Seber, 2003, Ch. 4), this detector implicitly exploits the assumption that the noises in the different antenna frontends are i.i.d.. Nonetheless, calibration uncertainties are unavoidable rendering noises with unequal variance in the different antenna frontends (Leshem & van der Veen, 2001; Ramírez *et al.*, 2011). As elucidated in Sec. 7.4.3, i.ni.d. noise samples incur performance loss, especially for low to medium SNRs.

7.4 Performance Analyses of FT-v-SVD

7.4.1 Exact Performance Analyses: i.i.d. Noise Samples

For H_1, plugging (7.1) into (7.2) and, in turn, into (7.5) give

$$T|H_1 = \frac{\nu_2}{\nu_1}\frac{\hat{F}_1|H_1}{\hat{F}_2|H_1}, \tag{7.11}$$

where $\hat{F}_1|H_1 = \sum_{k=1}^{N}\big(\boldsymbol{h}s[k]+\boldsymbol{z}[k]\big)^H\hat{\boldsymbol{P}}_s\big(\boldsymbol{h}s[k]+\boldsymbol{z}[k]\big)$, $\hat{F}_2|H_1 = \sum_{k=1}^{N}\big(\boldsymbol{h}s[k]+\boldsymbol{z}[k]\big)^H\big(\boldsymbol{I}_{N_R}-\hat{\boldsymbol{P}}_s\big)\big(\boldsymbol{h}s[k]+\boldsymbol{z}[k]\big)$, and $\boldsymbol{z}[k] \sim \mathscr{CN}_{N_R}(\boldsymbol{0},\sigma^2\boldsymbol{I}_{N_R})$. As $T|H_1$ is the ratio of two independent and scaled non-central χ^2–distributed random variables (RVs), $T|H_1 \sim F''_{\nu_1,\nu_2}(\lambda_1^{H_1},\lambda_2^{H_1})$ (Johnson *et al.*, 1995, Ch. 30) for $\big(\lambda_1^{H_1},\lambda_2^{H_1}\big) = \frac{2}{\sigma^2}\sum_{k=1}^{N}\big(\big|\big|\hat{\boldsymbol{P}}_s\boldsymbol{h}s[k]\big|\big|^2,\big|\big|\big(\boldsymbol{I}_{N_R}-\hat{\boldsymbol{P}}_s\big)\boldsymbol{h}s[k]\big|\big|^2\big)$.

Similarly, the test statistic under H_0 becomes

$$T|H_0 = \frac{\nu_2}{\nu_1}\frac{\hat{F}_1|H_0}{\hat{F}_2|H_0}, \tag{7.12}$$

where $\hat{F}_1|H_0 = \sum_{k=1}^{N} \boldsymbol{z}^H[k]\hat{\boldsymbol{P}}_s\boldsymbol{z}[k]$ and $\hat{F}_2|H_0 = \sum_{k=1}^{N} \boldsymbol{z}^H[k](\boldsymbol{I}_{N_R} - \hat{\boldsymbol{P}}_s)\boldsymbol{z}[k]$. The right-hand side of (7.12) is a ratio of two independent and scaled χ^2–distributed RVs. Thus, $T|H_0 \sim F_{\nu_1,\nu_2}$ (Johnson *et al.*, 1995, Ch. 27). Hereinafter, the exact expressions for the probability of detection—denoted by P_d—and the probability of false alarm—denoted by P_f—are derived.

7.4.1.1 The Probability of False Alarm and Test Threshold

The exact $P_f = \Pr\{T > \lambda|H_0\} = \Pr\{T|H_0 > \lambda\}$ exhibited by FT-v-SVD is obtained as

$$P_f = 1 - \Pr\{T|H_0 \leq \lambda\} = 1 - F(\lambda; \nu_1, \nu_2). \tag{7.13}$$

For a given λ, ν_1, and ν_2, the false alarm rate (FAR) of FT-v-SVD, regardless of the noise power, is given by (7.13). Accordingly, FT-v-SVD is a constant false alarm rate (CFAR) detector under i.i.d. noise samples. From (7.13), meanwhile, the test threshold rendering a target $P_f = \alpha$ is given by $\lambda = F^{-1}(1-\alpha; \nu_1, \nu_2)$.

7.4.1.2 The Probability of Detection

The exact P_d for a given λ is computed as

$$P_d = \Pr\{T > \lambda|H_1\} = \Pr\{T|H_1 > \lambda\} = 1 - \Pr\{T|H_1 \leq \lambda\}. \tag{7.14}$$

Since $T|H_1 \sim F''_{\nu_1,\nu_2}(\lambda_1^{H_1}, \lambda_2^{H_1})$, (7.14) simplifies to

$$P_d = 1 - F''(\lambda; \nu_1, \nu_2|\lambda_1^{H_1}, \lambda_2^{H_1}). \tag{7.15}$$

As the function that computes $F''_{\nu_1,\nu_2}(\lambda_1, \lambda_2)$ is unavailable in a well-known software such as MATLAB®, we approximate $F''_{\nu_1,\nu_2}(\lambda_1, \lambda_2)$ by F_{ν_1,ν_2} through the approximation of the non-central χ^2–distributions by the central χ^2–distributions (Johnson *et al.*, 1995). Therefore, em-

ploying (Johnson *et al.*, 1995, eq. (30.54)),

$$F''_{\nu_1,\nu_2}(\lambda_1,\lambda_2) \approx \frac{1+\lambda_1\nu_1^{-1}}{1+\lambda_2\nu_2^{-1}} F_{\nu,\nu'}, \tag{7.16}$$

where $\nu = (\nu_1+\lambda_1)^2(\nu_1+2\lambda_1)^{-1}$ and $\nu' = (\nu_2+\lambda_2)^2(\nu_2+2\lambda_2)^{-1}$. Using the CDF relationship (Bertsekas & Tsitsiklis, 2008, p. 206),

$$F''\big(\lambda;\nu_1,\nu_2\big|\lambda_1^{H_1},\lambda_2^{H_1}\big) \approx F\big(\lambda';\beta_1^{H_1},\beta_2^{H_1}\big), \tag{7.17}$$

where $\lambda' = \big(1+\lambda_2^{H_1}\nu_2^{-1}\big)\lambda/\big(1+\lambda_1^{H_1}\nu_1^{-1}\big)$, $\beta_1^{H_1} = (\nu_1+\lambda_1^{H_1})^2(\nu_1+2\lambda_1^{H_1})^{-1}$ and $\beta_2^{H_1} = (\nu_2+\lambda_2^{H_1})^2(\nu_2+2\lambda_2^{H_1})^{-1}$. Note that (7.17) can be used for numerical assessments.

7.4.2 Asymptotic Performance Analyses: i.i.d. Noise Samples

The subsequent asymptotic performance analyses make use of the first-order perturbation analysis and the estimation theory of a population covariance matrix (PCM). The first-order perturbation analysis is mainly used as a performance analysis tool for subspace-based algorithms (Ciuonzo *et al.*, 2015; Roemer *et al.*, 2014; Liu *et al.*, 2008). Accordingly, it is deployed here to assess the asymptotic performance of FT-v-SVD. To facilitate mathematical tractability, quantization error is assumed negligible.

To motivate the first-order perturbation analysis under H_1, the noiseless SCM is defined as $\boldsymbol{R}_{yy}^{(n)} = \frac{1}{N}\sum_{k=1}^{N}\boldsymbol{y}[k]\boldsymbol{y}^H[k]\Big|_{\{\boldsymbol{z}[k]\}_{k=1}^{N}=0}$ and decomposed as

$$\boldsymbol{R}_{yy}^{(n)} = \boldsymbol{U}\boldsymbol{\Sigma}\boldsymbol{V}^H = [\boldsymbol{U}_s\,\boldsymbol{U}_n]\boldsymbol{\Sigma}[\boldsymbol{V}_s\,\boldsymbol{V}_n]^H, \tag{7.18}$$

where $\boldsymbol{\Sigma} = \mathrm{diag}(\sigma_1,0,\ldots,0)$, for $\boldsymbol{\Sigma}_s = \sigma_1$, $\boldsymbol{U}_s = \boldsymbol{U}(:,1)$ is the perfectly estimated primary signal subspace, and $\boldsymbol{U}_n = \boldsymbol{U}(:,2:N_R)$. Comparing (7.3) and (7.18) via the first-order perturbation analysis (Ciuonzo *et al.*, 2015, eqs. (18) and (20)),

$$\hat{\boldsymbol{U}}_s = \boldsymbol{U}_s + \Delta\boldsymbol{U}_s;\ \hat{\boldsymbol{U}}_n = \boldsymbol{U}_n + \Delta\boldsymbol{U}_n, \tag{7.19}$$

where $\Delta \boldsymbol{U}_s = \boldsymbol{U}_n \boldsymbol{U}_n^H \boldsymbol{Z} \boldsymbol{V}_s \boldsymbol{\Sigma}_s^{-1}$ is the perturbations in the primary signal subspace whereas $\Delta \boldsymbol{U}_n = -\boldsymbol{U}_s \boldsymbol{\Sigma}_s^{-1} \boldsymbol{V}_s^H \boldsymbol{Z}^H \boldsymbol{U}_n$ is the perturbations in the noise subspace for $\boldsymbol{Z} = N^{-1} \sum_{k=1}^{N} \big(\boldsymbol{h} s[k] \boldsymbol{z}^H[k] + \boldsymbol{z}[k] s^H[k] \boldsymbol{h}^H + \boldsymbol{z}[k] \boldsymbol{z}^H[k] \big)$—$\boldsymbol{z}[k] \sim \mathscr{CN}_{N_R}(\boldsymbol{0}, \sigma^2 \boldsymbol{I}_{N_R})$.

Using (7.19), the projection matrix is also given by

$$\hat{\boldsymbol{P}}_s = (\boldsymbol{U}_s + \Delta \boldsymbol{U}_s)(\boldsymbol{U}_s + \Delta \boldsymbol{U}_s)^{+}. \tag{7.20}$$

By utilizing (7.19) and (7.20) in (7.3) and (7.5), the asymptotic P_d and P_f are characterized subsequently.

7.4.2.1 Asymptotic Probability of Detection

The asymptotic P_d exhibited by FT-v-SVD is characterized beneath.

Proposition 3. For $\lambda < \infty$ and $\boldsymbol{0}$ implying $\boldsymbol{0}_{N_R \times 1}$, $\lim\limits_{\Delta \boldsymbol{U}_s \to \boldsymbol{0}} P_d = 1$.

Proof. Please refer to Appendix 1 under APPENDIX VII.

Proposition 3 corroborates that FT-v-SVD detects a primary signal perfectly when the perturbations get infinitesimally small. In other words, this detector is certain in detecting an active PU, as the respective SNR gets larger.

For infinitely large sample size, the estimation theory of a PCM asserts that the SCM perfectly approximates the PCM. To this end, the asymptotic P_d—with respect to (w.r.t.) N—is characterized by the following proposition.

Proposition 4.

$$\lim_{N \to \infty} P_d = 1 - F'(\lambda; \nu_1, \nu_2 | \lambda^{H_1}), \tag{7.21}$$

where $\lambda^{H_1} = \lim\limits_{N \to \infty} \dfrac{2}{\sigma^2} \sum\limits_{k=1}^{N} \big|\big| \boldsymbol{h} s[k] \big|\big|^2$. If $\lambda > (N_R - 1) \bar{\gamma}_{snr}^{\infty}$ for $\bar{\gamma}_{snr}^{\infty} = \lim\limits_{N \to \infty} \dfrac{1}{N} \sum\limits_{k=1}^{N} \dfrac{\big|\big| \boldsymbol{h} s[k] \big|\big|^2}{N_R \sigma^2}$ being the average SNR over an infinite duration, then $\lim\limits_{N \to \infty} P_d = 0$.

Proof. Please refer to Appendix 2 under APPENDIX VII.

7.4.2.2 Asymptotic Probability of False Alarm

Similarly, the estimation theory of a PCM is deployed to characterize the exhibited asymptotic P_f stated beneath.

Lemma 4. If $\lambda > 0$, $\lim_{N\to\infty} P_f = 0$.

Proof. Please see Appendix 3 under APPENDIX VII.

Remark 9. As $N \to \infty$, FT-v-SVD exhibits a null probability of false alarm.

7.4.3 Asymptotic Performance Analyses: i.ni.d. Noise Samples

Proposition 5. If P_d^{iid} and P_d^{inid}, respectively, denote the probability of detection under i.i.d. and i.ni.d. noise samples, $\lim_{N\to\infty} P_d^{\text{iid}} > \lim_{N\to\infty} P_d^{\text{inid}}$ whenever $\sigma^2\text{tr}\big(\boldsymbol{E}\big) > 0$. If $\sigma^2\text{tr}\big(\boldsymbol{E}\big) = 0$, on the other hand, $\lim_{N\to\infty} P_d^{\text{iid}} = \lim_{N\to\infty} P_d^{\text{inid}}$.

Proof. Please see Appendix 4 under APPENDIX VII.

Note that the i.i.d. and i.ni.d. cases render the same performance whenever $\sigma^2\text{tr}\big(\boldsymbol{E}\big) = 0$. In case of calibration errors, $\sigma^2\text{tr}\big(\boldsymbol{E}\big) = 0$ if and only if $\sigma^2 = 0$. Accordingly, both i.i.d. and i.ni.d. cases exhibit identical performance at high SNR which approximately implicates a zero noise covariance matrix.

7.5 g-FT-v-SVD: Algorithms and Performance Analyses

7.5.1 Detector for SIMO Systems

From (7.1), stacking the observations of the secondary antennas into a highly structured vector w.r.t. the m-th short-term interval (STI) made of W symbol durations gives (Getu *et al.*, 2017;

Song *et al.*, 2010a)

$$\boldsymbol{y}_m = \begin{cases} \boldsymbol{H}\boldsymbol{s}_m + \boldsymbol{z}_m & : H_1 \\ \boldsymbol{z}_m & : H_0, \end{cases} \tag{7.22}$$

where $\boldsymbol{y}_m \in \mathbb{C}^{N_R W}$, $\boldsymbol{s}_m = \big[s[mW], s[mW-1], \ldots, s[mW-W-L+1]\big]^T \in \mathbb{C}^{(W+L)}$, and $\boldsymbol{z}_m \sim \mathscr{CN}_{N_R W}(\boldsymbol{0}, \sigma^2 \boldsymbol{I}_{N_R W})$. Meanwhile, $\boldsymbol{H} = \Big[\boldsymbol{H}_1^T, \boldsymbol{H}_2^T, \ldots, \boldsymbol{H}_{N_R}^T\Big]^T \in \mathbb{C}^{N_R W \times (W+L)}$ is the secondary filtering matrix for $\boldsymbol{H}_j \in \mathbb{C}^{W \times (W+L)}$ being a banded Toeplitz matrix—made of the j-th antenna's impulse response $\boldsymbol{h}_j \triangleq \big[h_{j0}, \ldots, h_{jL}\big]^T$—defined as in (Song *et al.*, 2010a, eq. (5)) for $h_{ji} = h_i^{(j)}$, $i \in \{0, 1, \ldots, L\}$.

The SCM $\tilde{\tilde{\boldsymbol{R}}}_{yy} \in \mathbb{C}^{N_R W \times N_R W}$ and its SVD can then be computed as

$$\tilde{\tilde{\boldsymbol{R}}}_{yy} = \frac{1}{\tilde{N}} \sum_{m=1}^{\tilde{N}} \boldsymbol{y}_m \boldsymbol{y}_m^H = \frac{1}{\tilde{N}} \tilde{\boldsymbol{Y}} \tilde{\boldsymbol{Y}}^H \tag{7.23a}$$

$$= \tilde{\boldsymbol{U}} \tilde{\tilde{\boldsymbol{\Sigma}}} \tilde{\boldsymbol{V}}^H = [\tilde{\boldsymbol{U}}_s \; \tilde{\boldsymbol{U}}_n] \tilde{\tilde{\boldsymbol{\Sigma}}} \tilde{\boldsymbol{V}}^H, \tag{7.23b}$$

where $\tilde{N}$ denotes the number of intercepted STIs, $\tilde{\boldsymbol{Y}} = [\boldsymbol{y}_1, \boldsymbol{y}_2, \ldots, \boldsymbol{y}_{\tilde{N}}] \in \mathbb{C}^{N_R W \times \tilde{N}}$, $\tilde{\tilde{\boldsymbol{U}}}_s = \tilde{\tilde{\boldsymbol{U}}}(:, 1:r) \in \mathbb{C}^{N_R W \times r}$ is the estimated subspace spanned by the eigenvectors corresponding to the largest $r = W + L$ eigenvalues, $\tilde{\tilde{\boldsymbol{U}}}_n = \tilde{\tilde{\boldsymbol{U}}}(:, r+1 : N_R W) \in \mathbb{C}^{N_R W \times (N_R W - r)}$, and $\tilde{\tilde{\boldsymbol{\Sigma}}} = \mathrm{diag}(\tilde{\tilde{\sigma}}_1, \tilde{\tilde{\sigma}}_2, \ldots, \tilde{\tilde{\sigma}}_{N_R W})$ for $\big\{\tilde{\tilde{\sigma}}_i\big\}_{i=1}^{N_R W}$ being the singular values. Note that $\tilde{\tilde{\boldsymbol{U}}}_s$ is a primary signal subspace estimator under H_1. To identify the primary signal subspace under H_1, we make the following assumptions: the SCM is full rank, i.e., $\tilde{N} \geq (W + L)$ (Getu *et al.*, 2017); $\boldsymbol{H}$ has a full column rank, i.e., $N_R W \geq (W + L)$; and the window length is greater than the secondary channel order, i.e., $W > L$. The corresponding projection matrix $\tilde{\tilde{\boldsymbol{P}}}_s \in \mathbb{C}^{N_R W \times N_R W}$ is then defined as

$$\tilde{\tilde{\boldsymbol{P}}}_s = \tilde{\tilde{\boldsymbol{U}}}_s \tilde{\tilde{\boldsymbol{U}}}_s^+ = \tilde{\tilde{\boldsymbol{U}}}_s \tilde{\tilde{\boldsymbol{U}}}_s^H. \tag{7.24}$$

Using (7.23a) and (7.24), the g-FT-v-SVD test statistic and decision rule are formulated as

$$\tilde{T} \triangleq \frac{\tilde{\nu}_2}{\tilde{\nu}_1} \frac{\mathrm{tr}(\tilde{\tilde{\boldsymbol{P}}}_s \tilde{\tilde{\boldsymbol{R}}}_{yy})}{\mathrm{tr}\big((\boldsymbol{I}_{N_R W} - \tilde{\tilde{\boldsymbol{P}}}_s) \tilde{\tilde{\boldsymbol{R}}}_{yy}\big)} \underset{H_0}{\overset{H_1}{\gtrless}} \tilde{\lambda}, \tag{7.25}$$

where $(\tilde{\nu}_1, \tilde{\nu}_2) = \big(2\tilde{N}r, 2\tilde{N}(N_R W - r)\big)$ are the respective DoF and $\tilde{\lambda}$ is the decision threshold. Substituting (7.23b) and (7.24) into (7.25), and adopting the simplifications of (7.6)–(7.8),

$$\tilde{T} = \frac{N_R W - r}{r} \frac{\sum_{i=1}^{r} \tilde{\tilde{\sigma}}_i}{\sum_{i=r+1}^{N_R W} \tilde{\tilde{\sigma}}_i} \propto \frac{\sum_{i=1}^{r} \tilde{\tilde{\sigma}}_i}{\sum_{i=r+1}^{N_R W} \tilde{\tilde{\sigma}}_i}. \tag{7.26}$$

Following the highlighted processing, the g-FT-v-SVD algorithm is summarized in Algorithm 7.1.

Algorithm 7.1 g-FT-v-SVD Algorithm

Input: $\{\boldsymbol{y}_m\}_{m=1}^{\tilde{N}}$, $\tilde{\lambda}$, $\tilde{\nu}_1$, and $\tilde{\nu}_2$
Output: H_1 or H_0
1 Stack the observations through (7.22) and obtain $\boldsymbol{y}_m$
2 Compute $\tilde{\tilde{\boldsymbol{R}}}_{yy}$ and $\tilde{\tilde{\boldsymbol{U}}}_s$ using (7.23a) and (7.23b), respectively
3 Compute $\tilde{\tilde{\boldsymbol{P}}}_s$ using (7.24)
4 Compute $\tilde{T}$ using (7.25)
5 **if** $\tilde{T} > \tilde{\lambda}$, H_1 *is true*
6 **else**, H_0 *is true*

7.5.2 Performance Analyses

Based on the performance analyses of FT-v-SVD, g-FT-v-SVD is analyzed below.

Theorem 13. The exact $P_d = \Pr\{\tilde{T} > \tilde{\lambda}|H_1\} = \Pr\{\tilde{T}|H_1 > \tilde{\lambda}\}$ and $P_f = \Pr\{\tilde{T} > \tilde{\lambda}|H_0\} = \Pr\{\tilde{T}|H_0 > \tilde{\lambda}\}$ exhibited by g-FT-v-SVD are given by

$$P_d = 1 - F''\big(\tilde{\lambda}; \tilde{\nu}_1, \tilde{\nu}_2 \big| \tilde{\lambda}_1^{H_1}, \tilde{\lambda}_2^{H_1}\big) \tag{7.27a}$$

$$P_f = 1 - F\big(\tilde{\lambda}; \tilde{\nu}_1, \tilde{\nu}_2\big), \tag{7.27b}$$

where $\tilde{\lambda}_1^{H_1} = \frac{2}{\sigma^2} \sum_{m=1}^{\tilde{N}} ||\tilde{\tilde{\boldsymbol{P}}}_s \boldsymbol{H} \boldsymbol{s}_m||^2$ and $\tilde{\lambda}_2^{H_1} = \frac{2}{\sigma^2} \sum_{m=1}^{\tilde{N}} ||(\boldsymbol{I}_{N_R W} - \tilde{\tilde{\boldsymbol{P}}}_s) \boldsymbol{H} \boldsymbol{s}_m||^2$.

Proof. Following (7.11) and (7.15), replacing (7.22) under H_1 into (7.23a) and, in turn, into (7.25) render (7.27a). Following (7.12) and (7.13), adopting the same substitutions gives (7.27b). □

Regardless of the power of the contaminating AWGN, the FAR manifested by g-FT-v-SVD is given by (7.27b). Hence, g-FT-v-SVD is also a CFAR detector under i.i.d. noise samples. From (7.27b), the target threshold rendering a target $P_f = \tilde{\alpha}$ is obtained as $\tilde{\lambda} = F^{-1}\left(1-\tilde{\alpha};\tilde{\nu}_1,\tilde{\nu}_2\right)$. Meanwhile, the asymptotic behavior of g-FT-v-SVD is characterized beneath.

Proposition 6. For $\mathbf{0}$ denoting $\mathbf{0}_{N_R W\times r}$, the asymptotic P_d and P_f exhibited by g-FT-v-SVD are characterized through

$$\lim_{\Delta\tilde{\boldsymbol{U}}_s\to\mathbf{0}} P_d = 1 \tag{7.28a}$$

$$\lim_{\tilde{N}\to\infty} P_d = 1 - F'(\tilde{\lambda};\tilde{\nu}_1,\tilde{\nu}_2|\tilde{\lambda}^{H_1}) \tag{7.28b}$$

$$\lim_{\tilde{N}\to\infty} P_f = 0, \tag{7.28c}$$

where $\tilde{\lambda}^{H_1} = \lim\limits_{\tilde{N}\to\infty} \dfrac{2}{\sigma^2}\displaystyle\sum_{m=1}^{\tilde{N}} \left|\left|\boldsymbol{H}\boldsymbol{s}_m\right|\right|^2$, $\Delta\tilde{\boldsymbol{U}}_s$ is the perturbations in the primary signal subspace estimator $\tilde{\hat{\boldsymbol{U}}}_s$, and $\tilde{\lambda} > 0$.

Proof. The relationship in (7.28a) follows from the substitution of (ν_1,ν_2,T) by $(\tilde{\nu}_1,\tilde{\nu}_2,\tilde{T})$, $\left[\boldsymbol{I}_{N_R},\Delta\boldsymbol{U}_s\right]$ by $\left[\boldsymbol{I}_{N_R W},\Delta\tilde{\boldsymbol{U}}_s\right]$, and $\left[\hat{\boldsymbol{U}},\hat{\boldsymbol{\Sigma}},\hat{\boldsymbol{V}}\right]$ by $\left[\tilde{\hat{\boldsymbol{U}}},\tilde{\hat{\boldsymbol{\Sigma}}},\tilde{\hat{\boldsymbol{V}}}\right]$ in Appendix 1 (under APPENDIX VII). On top of the aforementioned replacement, replacing $\left[\boldsymbol{U},\boldsymbol{\Sigma},\boldsymbol{V}\right]$ by $\left[\tilde{\boldsymbol{U}},\tilde{\boldsymbol{\Sigma}},\tilde{\boldsymbol{V}}\right]$—for $\tilde{\boldsymbol{U}}$, $\tilde{\boldsymbol{\Sigma}}$, and $\tilde{\boldsymbol{V}}$ being the true estimates—and following Appendix 2 (under APPENDIX VII) render (7.28b). At last, using $\tilde{T}|H_0$ in place of $T|H_0$ and following Appendix 3 (under APPENDIX VII) result in (7.28c) whenever $\tilde{\lambda} > 0$. □

Remark 10. For $(L,W) = (0,1)$, the g-FT-v-SVD algorithm becomes the FT-v-SVD algorithm.

7.5.3 Impact of i.ni.d. Noise Samples

Similar to FT-v-SVD, g-FT-v-SVD assumes receiver frontends experiencing i.i.d. noise samples only. Practically, calibration uncertainties rendering i.ni.d. noise samples occur on the receiver frontends. As a result, g-FT-v-SVD—like FT-v-SVD—incurs a performance loss under i.ni.d. noise samples. Consequently, Proposition 5 is also valid for g-FT-v-SVD when $\boldsymbol{E}$ is replaced by $\tilde{\boldsymbol{E}}$ given by $\tilde{\boldsymbol{E}} = \operatorname{diag}\big(\underbrace{\tilde{\varepsilon}_1, \tilde{\varepsilon}_1, \ldots, \tilde{\varepsilon}_1}_{W \text{ times}}, \ldots, \underbrace{\tilde{\varepsilon}_{N_R}, \tilde{\varepsilon}_{N_R}, \ldots, \tilde{\varepsilon}_{N_R}}_{W \text{ times}}\big)$, $\tilde{\varepsilon}_i > 0$, $1 \leq i \leq N_R$.

7.5.4 Generalization to a MIMO CR Network

It is probable that a PU has a primary transmitter with N_T antennas and an SU equipped with N_R antennas senses the licensed spectrum for an opportunistic spectrum access. In this scenario, we have a MIMO CR network and the generalization of g-FT-v-SVD—hereinafter referred to as the MIMO CR g-FT-v-SVD—is presented subsequently.

Based on the system model in (Song *et al.*, 2013, Sec. II-A), the k-th received and sampled baseband signal $\boldsymbol{y}[k] \in \mathbb{C}^{N_R}$ is expressed via a binary hypothesis test given by

$$\boldsymbol{y}[k] = \begin{cases} \sum_{l=0}^{L} \boldsymbol{H}_l \boldsymbol{s}[k-l] + \boldsymbol{z}[k] & : H_1 \\ \boldsymbol{z}[k] & : H_0, \end{cases} \tag{7.29}$$

where $\boldsymbol{s}[k] = \big[s_1[k], s_2[k], \ldots, s_{N_T}[k]\big]^T \in \mathbb{C}^{N_T}$ denotes the k-th symbol vector transmitted through the N_T transmit antennas—$s_j[k]$ being the k-th unknown and deterministic primary symbol emitted by the j-th primary antenna—and $\boldsymbol{H}_l \in \mathbb{C}^{N_R \times N_T}$ comprises the MIMO channel impulse responses corresponding to the l-th multi-path fading component.

Similar to Sec. 7.5.1, stacking the observations of the secondary antennas into a highly structured vector w.r.t. the m-th STI gives

$$\tilde{\boldsymbol{y}}_m = \begin{cases} \boldsymbol{H}_T \tilde{\boldsymbol{s}}_m + \boldsymbol{z}_m & : H_1 \\ \boldsymbol{z}_m & : H_0, \end{cases} \tag{7.30}$$

where $\tilde{\boldsymbol{y}}_m \in \mathbb{C}^{N_R W}$, $\tilde{\boldsymbol{s}}_m = \left[\boldsymbol{s}_{1m}^T, \boldsymbol{s}_{2m}^T, \ldots, \boldsymbol{s}_{N_T m}^T\right]^T \in \mathbb{C}^{N_T(W+L)}$ for $\boldsymbol{s}_{jm} = \left[s_j[mW], s_j[mW-1], \ldots, s_j[mW-W-L+1]\right]^T \in \mathbb{C}^{(W+L)}$ (Song *et al.*, 2013), and $\boldsymbol{H}_T \in \mathbb{C}^{N_R W \times N_T(W+L)}$ is the MIMO filtering matrix made of banded Toeplitz matrices and defined through (Song *et al.*, 2013, eqs. (3)-(5)).

Using (7.30), the corresponding SCM $\tilde{\tilde{\boldsymbol{R}}}_{yy} \in \mathbb{C}^{N_R W \times N_R W}$ is computed as

$$\tilde{\tilde{\boldsymbol{R}}}_{yy} = \frac{1}{\tilde{\tilde{N}}} \sum_{m=1}^{\tilde{\tilde{N}}} \tilde{\boldsymbol{y}}_m \tilde{\boldsymbol{y}}_m^H = \frac{1}{\tilde{\tilde{N}}} \tilde{\tilde{\boldsymbol{Y}}} \tilde{\tilde{\boldsymbol{Y}}}^H, \tag{7.31}$$

where $\tilde{\tilde{N}}$ is the number of STIs and $\tilde{\tilde{\boldsymbol{Y}}} = [\tilde{\boldsymbol{y}}_1, \tilde{\boldsymbol{y}}_2, \ldots, \tilde{\boldsymbol{y}}_{\tilde{\tilde{N}}}]$. From (7.30), the PCM under H_1 becomes (Song *et al.*, 2013, eq. (6))

$$\tilde{\boldsymbol{R}}_{yy} = \mathbb{E}\{\tilde{\boldsymbol{y}}_m \tilde{\boldsymbol{y}}_m^H\} = \boldsymbol{H}_T \boldsymbol{R}_{\tilde{s}\tilde{s}} \boldsymbol{H}_T^H + \sigma^2 \boldsymbol{I}_{N_R W}, \tag{7.32}$$

where $\boldsymbol{R}_{\tilde{s}\tilde{s}} = \mathbb{E}\{\tilde{\boldsymbol{s}}_m \tilde{\boldsymbol{s}}_m^H\} \in \mathbb{C}^{\tilde{\tilde{r}} \times \tilde{\tilde{r}}}$, for $\tilde{\tilde{r}} = N_T(W+L)$, denotes the primary data correlation matrix which indicates an $N_R W \times \tilde{\tilde{r}}$ dimensional primary signal subspace. Applying SVD to (7.31),

$$\tilde{\tilde{\boldsymbol{R}}}_{yy} = \tilde{\tilde{\boldsymbol{U}}} \tilde{\tilde{\boldsymbol{\Sigma}}} \tilde{\tilde{\boldsymbol{V}}}^H = [\tilde{\tilde{\boldsymbol{U}}}_s \; \tilde{\tilde{\boldsymbol{U}}}_n] \tilde{\tilde{\boldsymbol{\Sigma}}} \tilde{\tilde{\boldsymbol{V}}}^H, \tag{7.33}$$

where $\tilde{\tilde{\boldsymbol{\Sigma}}} = \operatorname{diag}\left(\tilde{\tilde{\sigma}}_1, \tilde{\tilde{\sigma}}_2, \ldots, \tilde{\tilde{\sigma}}_{N_R W}\right)$, for $\tilde{\tilde{\sigma}}_i$ being the i-th singular value, $\tilde{\tilde{\boldsymbol{U}}}_s = \tilde{\tilde{\boldsymbol{U}}}(:, 1:\tilde{\tilde{r}}) \in \mathbb{C}^{N_R W \times \tilde{\tilde{r}}}$ denotes the estimated subspace spanned by the eigenvectors corresponding to the largest $\tilde{\tilde{r}}$ eigenvalues, and $\tilde{\tilde{\boldsymbol{U}}}_n = \tilde{\tilde{\boldsymbol{U}}}(:, \tilde{\tilde{r}}+1 : N_R W)$. To identify the primary signal subspace under H_1, meanwhile, we make these assumptions (Song *et al.*, 2013): $N_T < N_R$, $\tilde{\tilde{N}} \geq N_T(W+L)$, $N_R W \geq N_T(W+L)$, and $W > L$.

Using (7.31) and a projection matrix $\tilde{\tilde{\boldsymbol{P}}}_s \in \mathbb{C}^{N_R W \times N_R W}$ defined as $\tilde{\tilde{\boldsymbol{P}}}_s = \tilde{\tilde{\boldsymbol{U}}}_s \tilde{\tilde{\boldsymbol{U}}}_s^H$, the MIMO CR g-FT-v-SVD test statistic and decision rule are formulated as

$$\tilde{\tilde{T}} \triangleq \frac{\tilde{\tilde{\nu}}_2}{\tilde{\tilde{\nu}}_1} \frac{\mathrm{tr}(\tilde{\tilde{\boldsymbol{P}}}_s \tilde{\tilde{\boldsymbol{R}}}_{yy})}{\mathrm{tr}\big((\boldsymbol{I}_{N_R W} - \tilde{\tilde{\boldsymbol{P}}}_s)\tilde{\tilde{\boldsymbol{R}}}_{yy}\big)} \underset{H_0}{\overset{H_1}{\gtrless}} \tilde{\tilde{\lambda}}, \tag{7.34}$$

where $(\tilde{\tilde{\nu}}_1, \tilde{\tilde{\nu}}_2) = \big(2\tilde{\tilde{N}}\tilde{\tilde{r}}, 2\tilde{\tilde{N}}(N_R W - \tilde{\tilde{r}})\big)$ are the DoF and $\tilde{\tilde{\lambda}}$ is the decision threshold.

Remark 11. As the g-FT-v-SVD algorithm is an FT-v-SVD algorithm for $L = 0$ and $W = 1$, the FT-v-SVD algorithm can similarly be generalized to a MIMO CR network.

7.6 Computational Complexity Analysis

Based on (Huang & Chung, 2013a, Table I), the computational complexity analysis of the $F-$test (FT) detector (Huang & Chung, 2013a), a multi-channel energy detector (MCED) (Wang *et al.*, 2010), a blind GLRT detector (Taherpour *et al.*, 2010; Wang *et al.*, 2010), an MME detector (Zeng & Liang, 2009b), an FT-v-SVD, and a g-FT-v-SVD is tabulated in Tables 7.1 and 7.2. To minimize complexity, the complexity of FT-v-SVD and g-FT-v-SVD is, respectively, analyzed through the equivalent statistics in (7.8) and (7.26). Computing (7.8) requires computing an SCM and its SVD which require $NN_R(N_R+1)/2$, for even N, and $\mathscr{O}\big(N_R^3\big)$ complex multiplications and additions (Huang & Chung, 2013a; Zeng & Liang, 2009b), respectively. Similarly, computing (7.26) requires $\tilde{N}N_R W(N_R W+1)/2$ and $\mathscr{O}(N_R^3 W^3)$ complex multiplications and additions.

As a SIMO system with N_R antennas can be modeled via a single-antenna system oversampled at an oversampling factor $M = N_R$ (Zeng & Liang, 2009b, Sec. II), the computational complexity of max-min detector (Bogale & Vandendorpe, 2014, 2013b) is analyzed w.r.t. the complex multiplications and additions carried out in (Bogale & Vandendorpe, 2014, eqs. (5)-(14)). Detailing the overall analysis: the computation of $\boldsymbol{A}$ and $\boldsymbol{B}$ of (Bogale & Vandendorpe, 2014, eq. (5)) requires $N_R(N_R+1)\lceil N/2 \rceil$ multiplications each and $N_R(N_R+1)\lceil N/2 \rceil$ additions each; the SVD in (Bogale & Vandendorpe, 2014, eq. (8)) requires $\mathscr{O}\big(N_R^3\big)$ multiplications and $\mathscr{O}\big(N_R^3\big)$

Table 7.1 Computational complexity (in multiplication) analysis of different detectors

Detectors	Complex multiplications
MCED (Wang *et al.*, 2010)	$N_R N$
FT (Huang & Chung, 2013a)	$N_R(N_R+1)(1+\lceil N/2\rceil)$
Blind GLRT (Taherpour *et al.*, 2010; Wang *et al.*, 2010) $\big($MME (Zeng & Liang, 2009b)$\big)$	$N_R(N_R+1)\lceil N/2\rceil+\mathscr{O}\big(N_R^3\big)$
FT-v-SVD	$N_R(N_R+1)\lceil N/2\rceil+\mathscr{O}\big(N_R^3\big)$
g-FT-v-SVD	$N_RW(N_RW+1)\lceil \tilde{N}/2\rceil+\mathscr{O}\big(N_R^3W^3\big)$
max-min (Bogale & Vandendorpe, 2014, 2013b)	$(6N_R^2+NN_R)(N_R+1)+4N_R+2\mathscr{O}\big(N_R^3\big)$

Table 7.2 Computational complexity (in addition) analysis of different detectors

Detectors	Complex additions
MCED (Wang *et al.*, 2010)	$(N_R-1)(N-1)$
FT (Huang & Chung, 2013a)	$N_R(N_R+1)\lceil (N-1)/2\rceil+2(N_R-1)$
Blind GLRT (Taherpour *et al.*, 2010; Wang *et al.*, 2010) $\big($MME (Zeng & Liang, 2009b)$\big)$	$N_R(N_R+1)\lceil N/2\rceil+\mathscr{O}\big(N_R^3\big)$
FT-v-SVD	$N_R(N_R+1)\lceil N/2\rceil+\mathscr{O}\big(N_R^3\big)$
g-FT-v-SVD	$N_RW(N_RW+1)\lceil \tilde{N}/2\rceil+\mathscr{O}\big(N_R^3W^3\big)$
max-min (Bogale & Vandendorpe, 2014, 2013b)	$(N_R+1)(NN_R+4N_R-4)$ $+3N_R(N_R-1)(2N_R+1)+2\mathscr{O}\big(N_R^3\big)$

additions; the computation of $\tilde{\boldsymbol{A}}$, beneath (Bogale & Vandendorpe, 2014, eq. (13)), requires $4N_R^3$ multiplications and $4N_R^2(N_R-1)+N_R(N_R-1)$ additions; the SVD of $\tilde{\boldsymbol{A}}$ requires $\mathscr{O}\big(N_R^3\big)$ multiplications and $\mathscr{O}\big(N_R^3\big)$ additions; the computation of $\boldsymbol{\alpha}_{min}$ as well as $\boldsymbol{\alpha}_{max}$—employed in (Bogale & Vandendorpe, 2014, eqs. (6) and (7))—requires $N_R^3+N_R^2$ multiplications each and $N_R^2(N_R-1)+N_R(N_R-1)$ additions each; and the computation (via (Bogale & Vandendorpe, 2014, eq. (5))) of the numerator and denominator of (Bogale & Vandendorpe, 2014, eq. (14)) requires $2N_R(N_R+1)$ multiplications each and $2(N_R-1)(N_R+1)$ additions each. Summing up the overall computations, the complexity of max-min detector reported in Tables 7.1 and 7.2 is obtained.

An FT-v-SVD has similar complexity with that of GLRT and MME, and an FT exhibits the least computational complexity at the cost of the availability of perfect CSI. As per Tables 7.1 and 7.2, the multiplication and addition complexities of FT-v-SVD and g-FT-v-SVD are in the order of $\mathscr{O}\big(\max\{NN_R^2/2, N_R^3\}\big)$ and $\mathscr{O}\big(\max\{\tilde{N}N_R^2W^2/2, N_R^3W^3\}\big)$, respectively. Accordingly, the direct implementation of the presented algorithms are attractive for small-scale multi-antenna systems, as they exhibit a computational burden for high N_R and N or $\tilde{N}$.

Remark 12. By employing the trace of the SCM and the *power method*—which computes the maximum eigenvalue without computing the SVD (Golub & Van Loan, 2013)—so as to implement (7.8), the computational burden of FT-v-SVD can be alleviated for large-scale multi-antenna systems.

7.7 Simulation Results

Unless otherwise mentioned, this section provides Monte-Carlo simulations and/or analytical performance assessments of FT-v-SVD, g-FT-v-SVD, and MIMO CR g-FT-v-SVD by using the simulation parameters of Table 7.3. The performance of these detectors is exhaustively assessed also via a comparison with the state-of-the-art detectors.

Table 7.3 Simulation parameters unless otherwise mentioned

Simulation parameters	Assigned value
(N_R, W, L)	$(5, 3, 1)$
$(P_s, \tilde{N}, \tilde{\tilde{N}})$	$(10\ \text{W}, 100, 100)$
(Number of realizations, N)	$(10^3, 10^3)$

The subsequently reported results are conducted for SIMO systems unless they are explicitly accompanied by a pair (N_T, N_R) which implicates the MIMO CR network considered in Sec. 7.5.4. Unless it is explicitly stated as "a transmission over an AWGN channel", the reported detection plots are simulated for fading channels. To simulate the detection plots for a SIMO CR system over a frequency flat fading, a frequency selective fading, and an AWGN channels, we consider a quadrature phase shift keying (QPSK) modulated primary signal, i.e, $s[k] =$

$\sqrt{P_s/2}\left[s_k^I + js_k^Q\right]$ for P_s being the transmitted primary power and $\{s_k^I, s_k^Q\} \in \{-1,1\} \times \{-1,1\}$. For a MIMO CR network, we also consider QPSK symbols that are transmitted via the N_T antennas, i.e., $s_j[k] = \sqrt{P_s/2}\left[s_{kj}^I + js_{kj}^Q\right]$, $\{s_{kj}^I, s_{kj}^Q\} \in \{-1,1\} \times \{-1,1\}$ and $1 \leq j \leq N_T$.

Without loss of generality and similar to (Ramírez *et al.*, 2010), we assume that $\left\{\boldsymbol{h}_l\right\}_{l=0}^{L} \sim \mathscr{CN}_{N_R}(\boldsymbol{0}, \boldsymbol{I}_{N_R})$. Similarly, we assume that the elements of $\boldsymbol{H}_l$ exhibit the Gaussian distribution with zero mean and unit variance, i.e., $\boldsymbol{H}_l(i,j) \sim \mathscr{CN}_1(0,1)$, $0 \leq l \leq L$, $1 \leq i \leq N_R$, and $1 \leq j \leq N_T$. For the target FAR of 0.1, the corresponding FT-v-SVD decision threshold λ, the corresponding g-FT-v-SVD decision threshold $\tilde{\lambda}$, and the corresponding MIMO CR g-FT-v-SVD decision threshold $\tilde{\tilde{\lambda}}$ are obtained via the implementation—under H_0—of the test statistics in (7.5), (7.25), and (7.34), respectively, followed by averaging over 10^6 realizations. By defining the SNR as $\gamma_{snr} = \left|\left|\boldsymbol{h}s[k]\right|\right|^2 / \sum_{i=1}^{N_R}(1+\varepsilon_i)\sigma^2$, FT-v-SVD is simulated via (7.5); g-FT-v-SVD is simulated through (7.25) for an SNR defined as $\gamma_{snr} = \left|\left|\boldsymbol{H}\boldsymbol{s}_m\right|\right|^2 / \sum_{i=1}^{N_R W}(1+\tilde{\varepsilon}_i)\sigma^2$; and the MIMO CR g-FT-v-SVD is simulated via (7.34) for an SNR defined as $\gamma_{snr} = \left|\left|\boldsymbol{H}_T\tilde{\boldsymbol{s}}_m\right|\right|^2 / N_R W\sigma^2$. Moreover, the false alarm plots are simulated by considering the samples of an AWGN of power σ^2 as an input.

Regarding the performance assessment of FT-v-SVD with i.ni.d. noise samples and $N_R = 5$, $\boldsymbol{E} = \text{diag}\big(0.2, 0.1, 0.4, 0.1, 0.2\big)$ is considered. To simulate the performance of g-FT-v-SVD with i.ni.d. noise samples, we consider $N_R = 5$, $W = 3$, and $\tilde{\boldsymbol{E}} = \text{diag}\big(\boldsymbol{e}_1, \boldsymbol{e}_2, \boldsymbol{e}_3, \boldsymbol{e}_4, \boldsymbol{e}_5\big)$, where $\boldsymbol{e}_1 = \boldsymbol{e}_5 = [0.4, 0.4, 0.4]$, $\boldsymbol{e}_2 = \boldsymbol{e}_4 = [0.2, 0.2, 0.2]$, and $\boldsymbol{e}_3 = [0.8, 0.8, 0.8]$. For simulations under i.ni.d. noise samples, $\boldsymbol{E}$ and $\tilde{\boldsymbol{E}}$ are assumed constant and known to the FT-v-SVD and g-FT-v-SVD receivers, respectively. Unless stated explicitly, the simulations are conducted with i.i.d. noise samples. To simulate the effect of noise uncertainty, we assume—like (Tugnait, 2012)—that all detectors overestimate σ^2 by a factor of uncertainty denoted by η_{nu}, i.e., $\hat{\sigma}^2 = \eta_{nu}\sigma^2$, and compute the respective thresholds but the tests—of Sec. 7.7.3—are simulated using data with exact noise variance σ^2. For the usual assumption that the noise is stationary and ergodic, we deploy a constant noise uncertainty factor $\xi = 10\log_{10}\eta_{nu}$ that is usually valid when the observation time is short (Wang *et al.*, 2010).

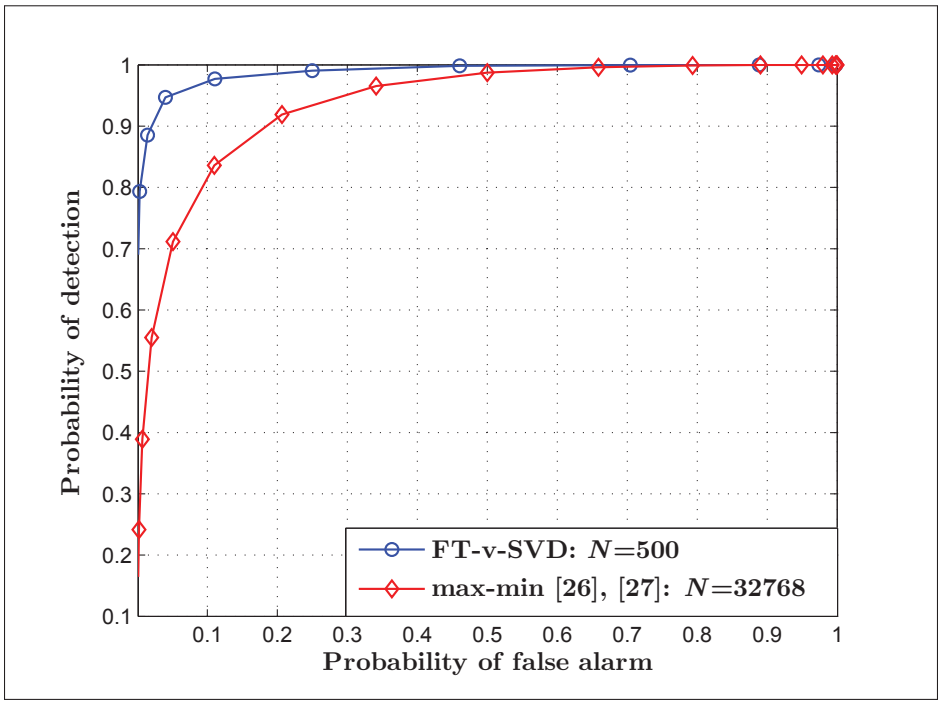

Figure 7.1 ROC for a transmission over an AWGN channel: $M = N_R = 8$ and $\gamma_{snr} = -14$ dB. Note that [26] and [27] represent (Bogale & Vandendorpe, 2014) and (Bogale & Vandendorpe, 2013b), respectively

7.7.1 Performance Assessment of FT-v-SVD

7.7.1.1 Performance Comparison with the State-of-the-art

We compare the max-min detector (Bogale & Vandendorpe, 2014, 2013b) applied to a system oversampled at $M = 8$ with the FT-v-SVD detector applied to a SIMO system with $N_R = 8$. To do so, the max-min algorithm is simulated for a synchronous receiver scenario via (Bogale & Vandendorpe, 2014, eqs. (22) and (23)) using the parameters of (Bogale & Vandendorpe, 2013b, Table II) estimated for a transmitter which employs a square root raised cosine filter. Having employed the same filter and assumed a perfect synchronization, the performance of FT-v-SVD is simulated through Monte-Carlo simulations averaged over 10^4 realizations. As seen in Fig. 7.1 which depicts the receiver operating characteristics (ROC) for a transmission over an AWGN channel, FT-v-SVD outperforms the max-min detector though the max-min

detector intercepts the received signal for a much longer time, i.e., $N = 2^{15}$ (32768) versus 500. It is worth noting that such an improvement is evident with a much lesser computational complexity, as analyzed in Tables 7.1 and 7.2.

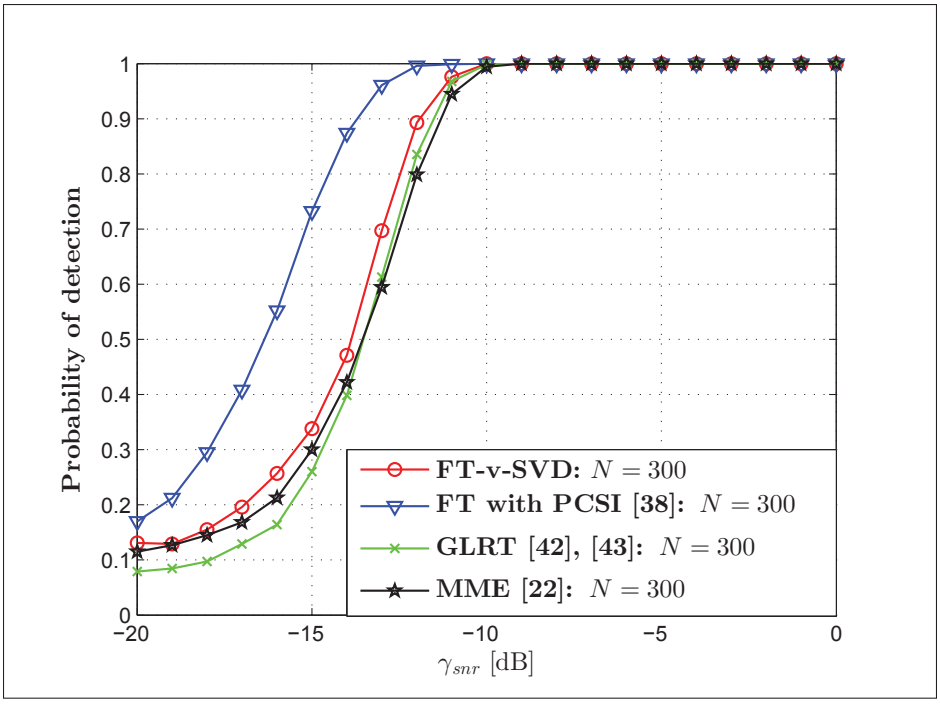

Figure 7.2 P_d versus γ_{snr}: $P_f = 0.1$ and 10^4 realizations. Note that [22], [38], [42], and [43] represent (Zeng & Liang, 2009b), (Huang & Chung, 2013a), (Taherpour *et al.*, 2010), and (Wang *et al.*, 2010), respectively

For the detection of a primary signal manifesting a very low SNR, Fig. 7.2 demonstrates that FT-v-SVD outperforms both MME (Zeng & Liang, 2009b) and GLRT (Taherpour *et al.*, 2010; Wang *et al.*, 2010). Moreover, it is corroborated by the same plot that FT-v-SVD—being a blind detector—performs as good as FT (Huang & Chung, 2013a) fed with a perfect CSI (PCSI) for $\gamma_{snr} \geq -10$ dB.

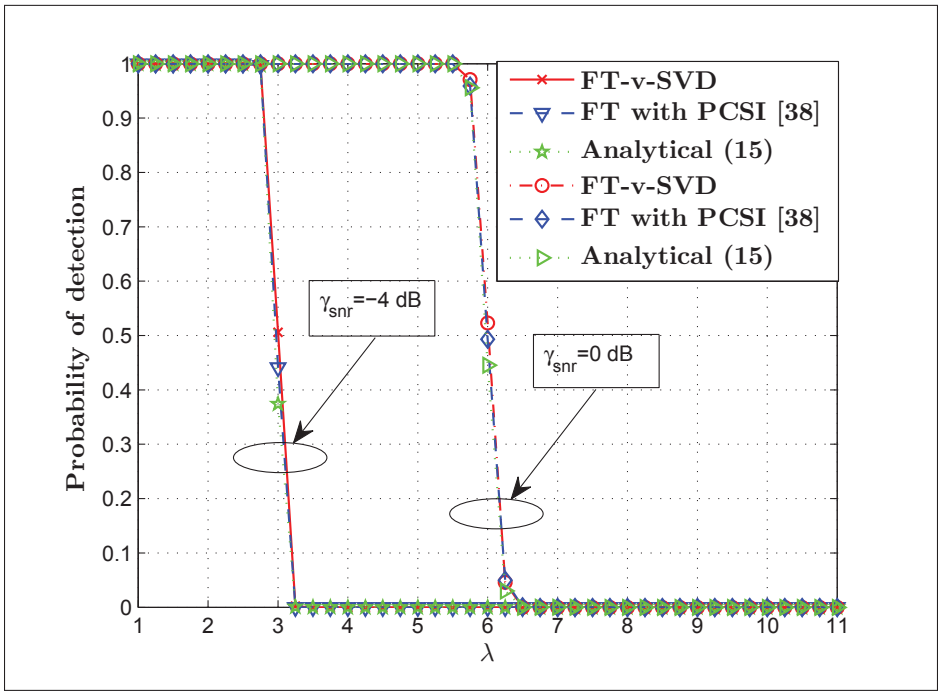

Figure 7.3 P_d versus λ. Note that [38] represents (Huang & Chung, 2013a) and (15) stands for (7.15)

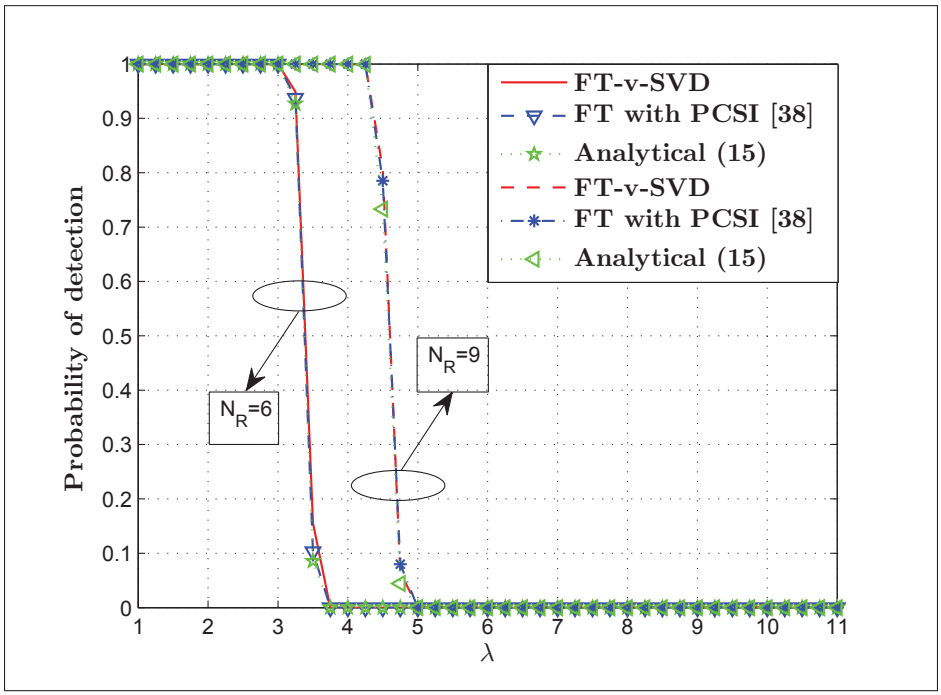

Figure 7.4 P_d versus λ: $\gamma_{snr} = -4$ dB. Note that [38] represents (Huang & Chung, 2013a) and (15) stands for (7.15)

7.7.1.2 Validation of the Closed-Form Detection Expressions

As observed in Fig. 7.3, FT-v-SVD which is a blind detector performs as good as the one in (Huang & Chung, 2013a) fed with PCSI regardless of the SNR. As λ increases, the detection performance of FT-v-SVD falls like FT with PCSI, as both become susceptible to more ambiguity. Fig. 7.4 displays the P_d versus λ plot w.r.t. a different number of secondary antennas. As before, FT-v-SVD and FT with PCSI manifest identical performance regardless of N_R. Besides, their detection performance improves with the increment of N_R. Meanwhile, Figs. 7.3 and 7.4 validate (7.15) which was plotted via the approximation in (7.17).

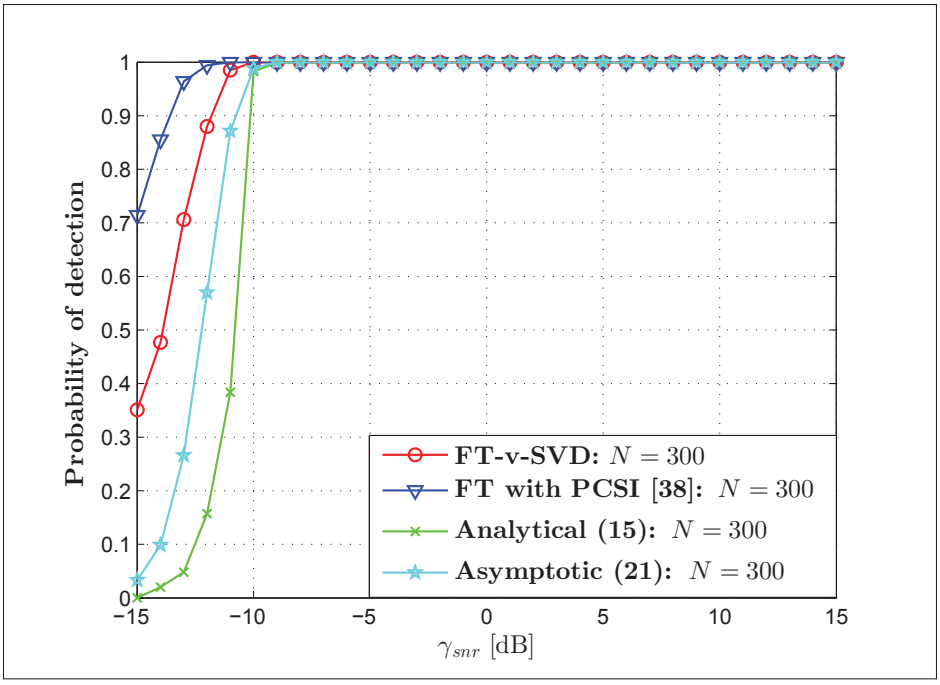

Figure 7.5 P_d versus γ_{snr}: $P_f = 0.1$. Note that [38] represents (Huang & Chung, 2013a); (15) and (21) stand for (7.15) and (7.21), respectively

As observed in Fig. 7.5, FT with PCSI performs better than FT-v-SVD, especially for a very low SNR and $N = 300$. This is evident because of the primary signal subspace estimates being poor whenever the SNR is very small, especially for a sample size as small as $N = 300$. For $\gamma_{snr} \geq -10$ dB, FT-v-SVD performs as good as FT fed with PCSI though the former is a

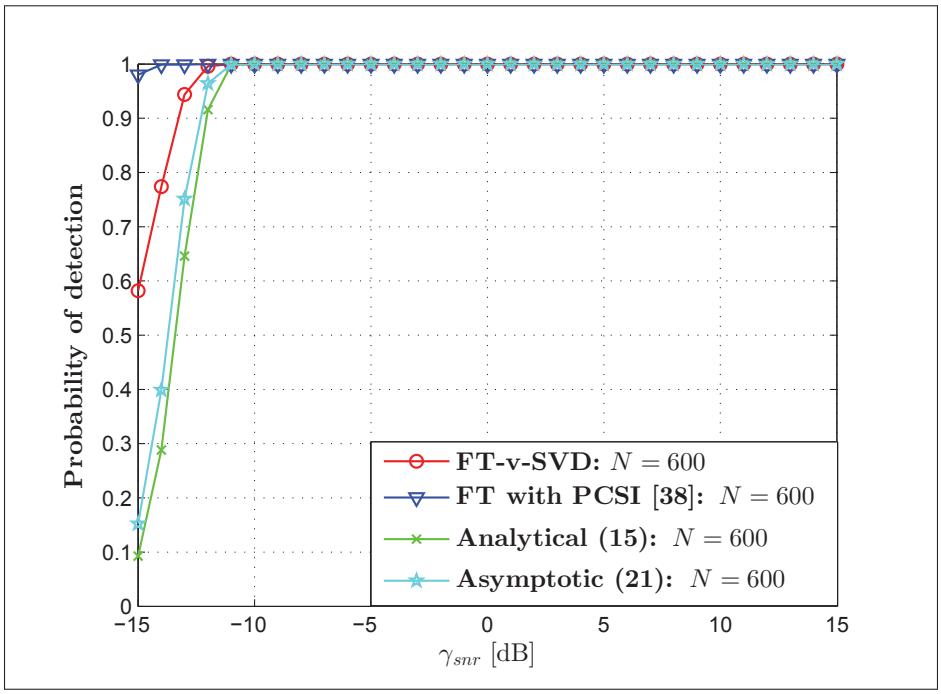

Figure 7.6 P_d versus γ_{snr}: $P_f = 0.1$. Note that [38] represents (Huang & Chung, 2013a); (15) and (21) stand for (7.15) and (7.21), respectively

blind detector. As the primary signal can be in a deep fade of the secondary receiver and hence manifesting a low SNR at the secondary antennas (Cabric, 2008), such a detection performance is important, especially for real-time and fast sensing applications. As N increases from 300 to 600, Fig. 7.6 demonstrates that the performance of FT-v-SVD approaches that of FT's even at very low SNR. This phenomenon implies that the blind detector—FT-v-SVD—performs as good as, regardless of the SNR, the detector fed with PCSI when N gets larger. For weak to moderately weak SNR, Figs. 7.5 and 7.6 validate the accuracy of the exact and asymptotic expressions given by (7.15) and (7.21), respectively. For $\gamma_{snr} \leq -10$ dB, the numerical results of these expressions deviate from the Monte-Carlo simulation results, especially for $N = 300$. This implies that (7.17) which was deployed to depict the numerical results of (7.15) renders a poor approximation. On the other hand, as N increases from 300 to 600, the accuracy of the asymptotic expression increases, regardless of the SNR, implying its validity as N gets larger.

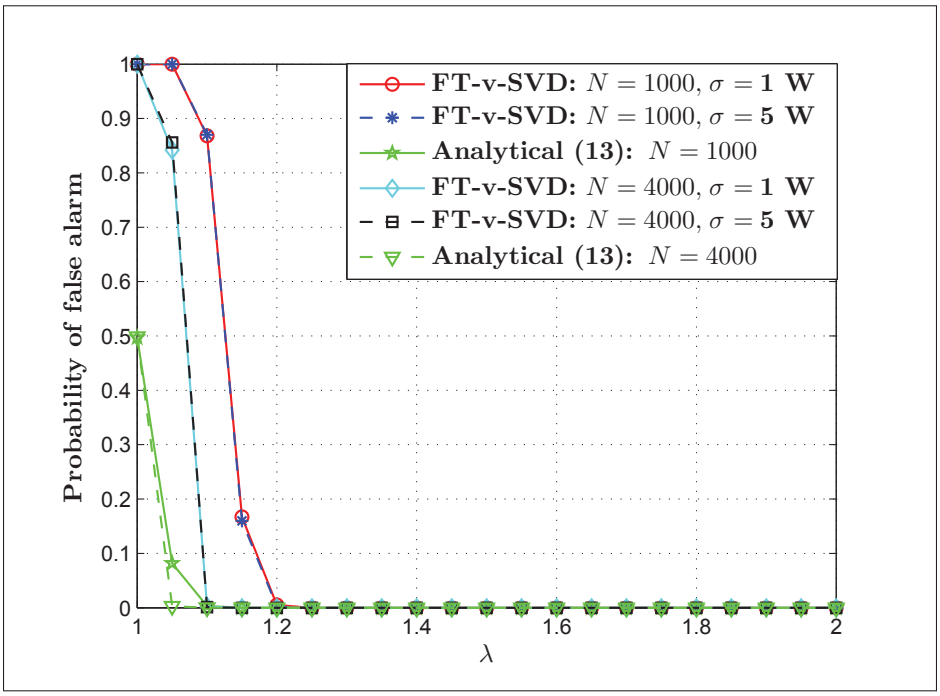

Figure 7.7 P_f versus λ. Note that (13) stands for (7.13)

7.7.1.3 The FAR and Complementary ROC Curves

Fig. 7.7 depicts the P_f versus λ plot exhibited by FT-v-SVD for $N \in \{1000, 4000\}$. As depicted, FT-v-SVD exhibits an identical P_f for $\sigma \in \{1, 5\}$ W for $N \in \{1000, 4000\}$. Accordingly, FT-v-SVD is a CFAR detector under i.i.d. noise samples, as also implied by (7.13). In addition, it is visible that the analytical and simulation results are overlapping for $\lambda \geq 1.2$ and $\lambda \geq 1.1$ at $N = 1000$ and $N = 4000$, respectively. For $\lambda < 1.1$ and $\lambda < 1.2$, there is a deviation between the analytical results and the Monte-Carlo simulation results, especially for $N = 1000$. As N increases from 1000 to 4000, the analytical and the Monte-Carlo simulation results become very close to each other. Meanwhile, increasing N renders a shift in the P_f plot to the $P_f = 0$ line indicating the validity of Lemma 4.

Fig. 7.8 depicts the complementary ROC manifested by FT-v-SVD and FT. As evident from Fig. 7.8, in comparison with FT-v-SVD, FT with PCSI offers a slightly smaller probability of missed detection (P_m)—simulated as $P_m = 1 - P_d$—for a given P_f. Exhibited by FT-v-SVD,

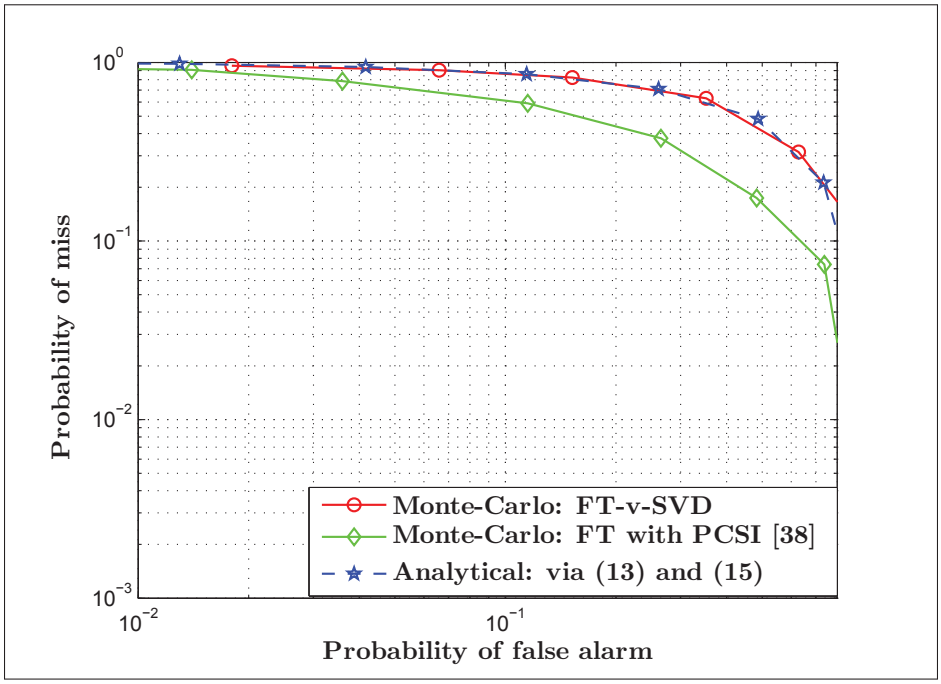

Figure 7.8 P_m versus P_f: $N = 50$ and $\gamma_{snr} = -15$ dB. Note that [38] represents (Huang & Chung, 2013a); (13) and (15) stand for (7.13) and (7.15), respectively

this performance loss is due to a slightly smaller P_d rendered by FT-v-SVD, especially for N as small as 50. Hence, this is a little price to pay by FT-v-SVD when compared with FT fed with PCSI. Moreover, Fig. 7.8 validates (7.15)—plotted via (7.17)—and (7.13).

7.7.1.4 Performance Assessment under i.i.d. and i.ni.d. Noise Samples

Figs. 7.9 and 7.10 display the P_d versus γ_{snr} plot for FT-v-SVD, FT with PCSI, and the time domain detector (Tugnait, 2012, eq. (25))—also known as an HRD (Leshem & van der Veen, 2001, eq. (3))—at the desired FAR of 0.1. Having observed Figs. 7.9 and 7.10, the following conclusions can be made: as the magnitude of the calibration uncertainties increases, FT—under i.ni.d. noise samples—suffers a performance loss even if it has a PCSI; for the small to high SNR regimes and small calibration uncertainties, FT-v-SVD performs as good as HRD; as the magnitude of calibration uncertainties increases, FT-v-SVD—under i.ni.d. noise samples—also suffers a performance loss for it is formulated using the F–test that is the result of a like-

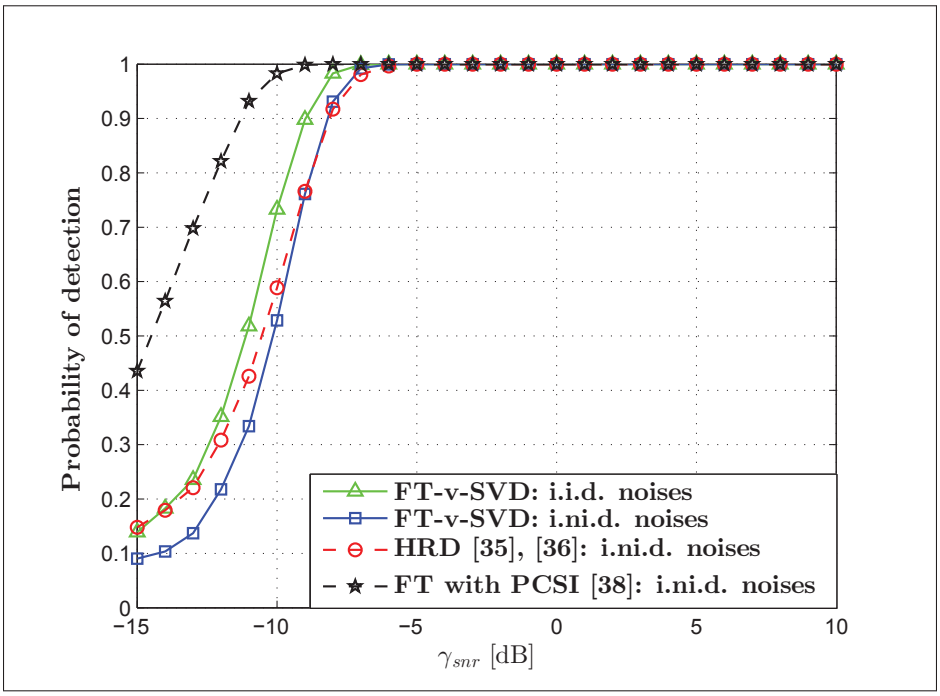

Figure 7.9 P_d versus γ_{snr}: $P_f = 0.1$, $N = 100$, and 10^4 channel realizations. Note that [35], [36], and [38] represent (Leshem & van der Veen, 2001), (Tugnait, 2012), and (Huang & Chung, 2013a), respectively

lihood ratio under i.i.d. noise samples (Seber, 2003, Ch. 4); and an HRD (Leshem & van der Veen, 2001, eq. (3)), (Tugnait, 2012, eq. (25))—derived under the assumption of i.ni.d. noise samples—exhibits no performance loss regardless of the magnitude of the calibration uncertainties. As a summary, Figs. 7.9 and 7.10 demonstrate that the detectors derived for i.i.d. noise samples suffer a performance loss at low SNR under i.ni.d. noise samples unlike the detectors derived using the assumption of i.ni.d. noise samples. Moreover, as seen in Figs. 7.9 and 7.10, both the i.i.d. and i.ni.d. cases exhibit identical performance at high SNR—the validation of Proposition 5.

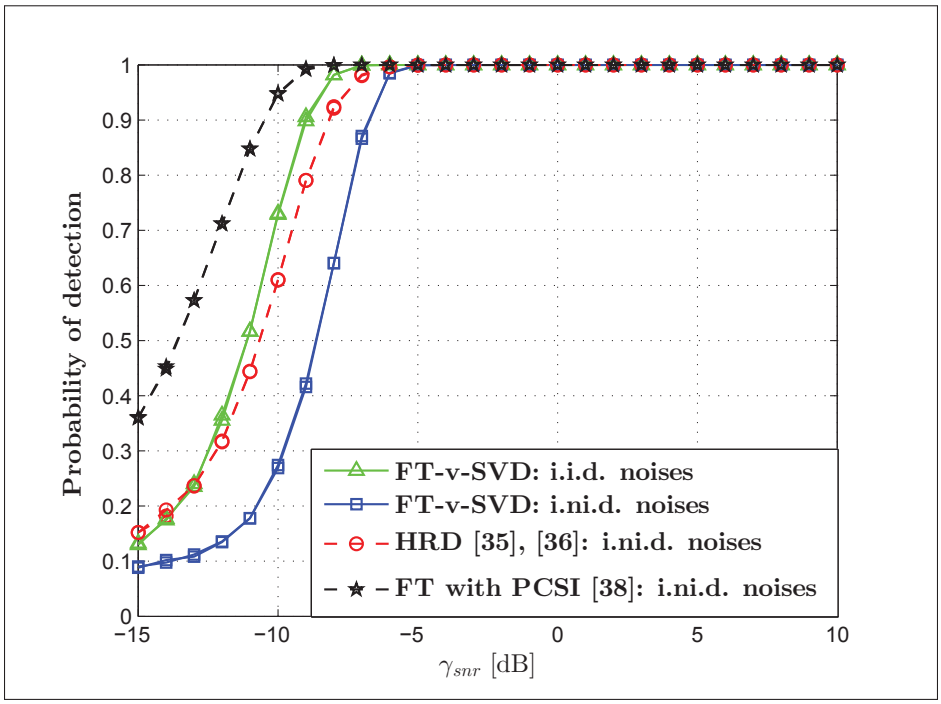

Figure 7.10 P_d versus γ_{snr}: $P_f = 0.1$, $N = 100$, $\boldsymbol{E} \leftarrow 3\boldsymbol{E}$, and 10^4 channel realizations. Note that [35], [36], and [38] represent (Leshem & van der Veen, 2001), (Tugnait, 2012), and (Huang & Chung, 2013a), respectively

7.7.2 Performance Assessment of g-FT-v-SVD

7.7.2.1 Assessment of Detection Performance

Fig. 7.11 displays the results of the Monte-Carlo simulation and the expression in (7.27a) that was plotted via the approximation in (7.17). As demonstrated, the P_d exhibited by g-FT-v-SVD improves with N_R and the Monte-Carlo results validate the accuracy of (7.27a).

Fig. 7.12 implicates that g-FT-v-SVD performs better with i.i.d. noise samples than with i.ni.d. noise samples—corroborating Proposition 5. For i.i.d. noise samples, the detection performance of g-FT-v-SVD is better with $L = 1$ than with $L = 2$, as the increment in channel order renders in a poor subspace estimation accuracy for the primary signal subspace. At the desired FAR of 0.1, the detection probability exhibited by g-FT-v-SVD approaches one even

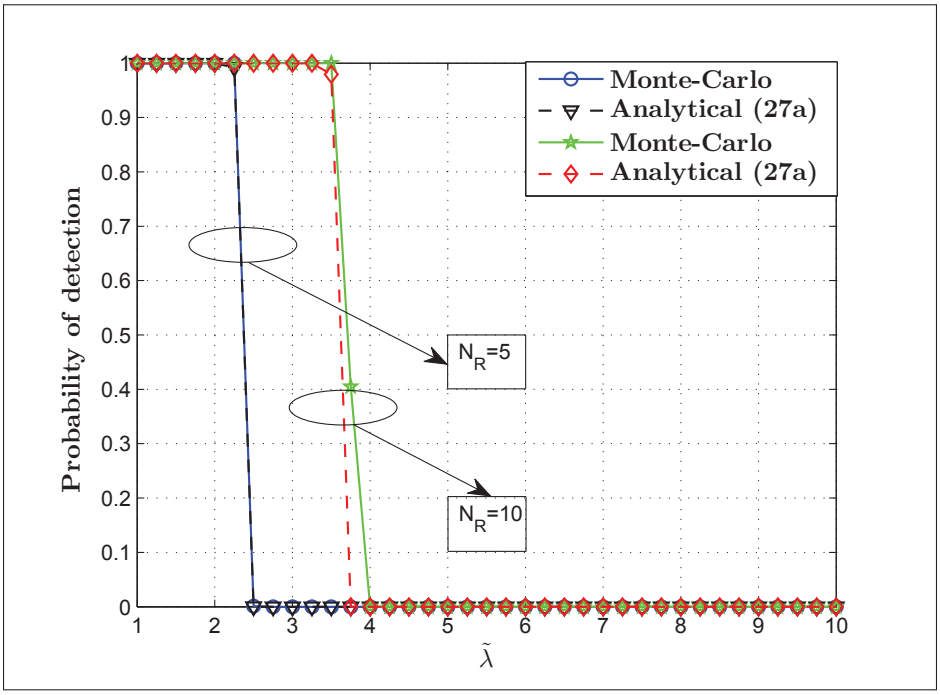

Figure 7.11 P_d versus $\tilde{\lambda}$: $\tilde{N} = 1000$, $W = 4$, $L = 2$, and $\gamma_{snr} = -4$ dB. Note that (27a) stands for (7.27a)

for an SNR as small as -5 dB. For the high SNR regimes, a detection probability of one is observed—validating (7.28a). Meanwhile, Fig. 7.13 corroborates the improvement w.r.t. N_R of the g-FT-v-SVD's detection performance.

Via Fig. 7.14, the impact of frequency selectivity on the detection performance of g-FT-v-SVD is assessed. As it is seen, g-FT-v-SVD suffers from the increment of L which implies the poor performance of the detector when the severity of frequency selective fading increases. In other words, the increment in L indicates the enlarging primary signal subspace—estimated via (7.23b). Consequently, a bigger subspace would be estimated with a lesser accuracy rendering the aforementioned poor performance whenever L increases.

7.7.2.2 Assessment of the FAR and Complementary ROC

The probability of false alarm exhibited by g-FT-v-SVD is depicted by Figs. 7.15-7.18. For both i.i.d. and i.ni.d. noise samples, and $L \in \{1,2\}$, g-FT-v-SVD exhibits an identical FAR for

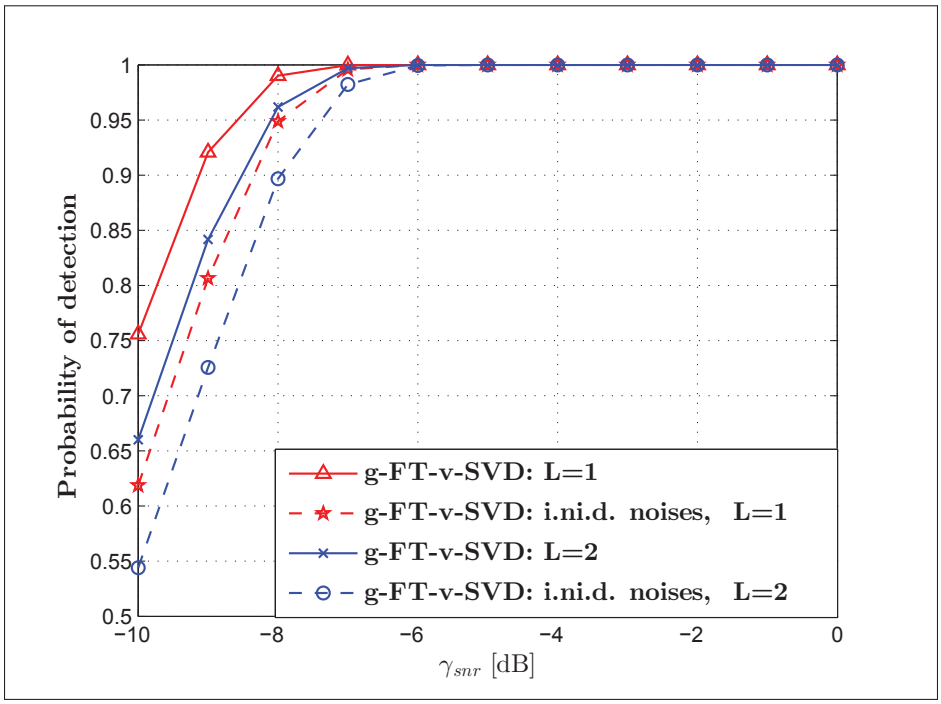

Figure 7.12 P_d versus γ_{snr}: $P_f = 0.1$ and 10^5 realizations

$\sigma \in \{1,5\}$ W. These phenomena corroborate that g-FT-v-SVD is a CFAR detector under i.i.d. noise samples, as also implied by (7.27b), and i.ni.d. noise samples. Practically, however, the CFAR property lacks when the noises are i.ni.d., as the elements of $\tilde{\boldsymbol{E}}$ are unknown and can vary since they can be RVs. Besides, Figs. 7.15 and 7.16 attest that the FAR increases w.r.t. L under i.i.d. as well as i.ni.d. noise samples, as increasing L makes the subspace estimation less accurate.

Regarding the FAR exhibited by g-FT-v-SVD, Figs. 7.17 and 7.18 display the respective simulation and analytical results. The plots essentially corroborate that both results overlap with each other for $\tilde{\lambda} \geq 1.3$ and $\tilde{\lambda} \geq 1.15$ for $\tilde{N} \in \{1000, 3000\}$ and $\tilde{N} \in \{3000, 6000\}$, respectively. It is also visible in Figs. 7.17 and 7.18 that the Monte-Carlo simulation gets very close to the plot of the closed-form in (7.27b), as $\tilde{N}$ is increased from 3000 to 6000. As $\tilde{N}$ gets larger and larger, the SCM perfectly estimates the PCM, especially when $N \to \infty$ ($\equiv \tilde{N} \to \infty$)—cf. Appendix 2 (under APPENDIX VII). Under this perfect estimation scenario, the g-FT-v-SVD test statistic in (7.25) would become the ratio of two independent χ^2–distributed RVs, with $(\tilde{\nu}_1, \tilde{\nu}_2)$

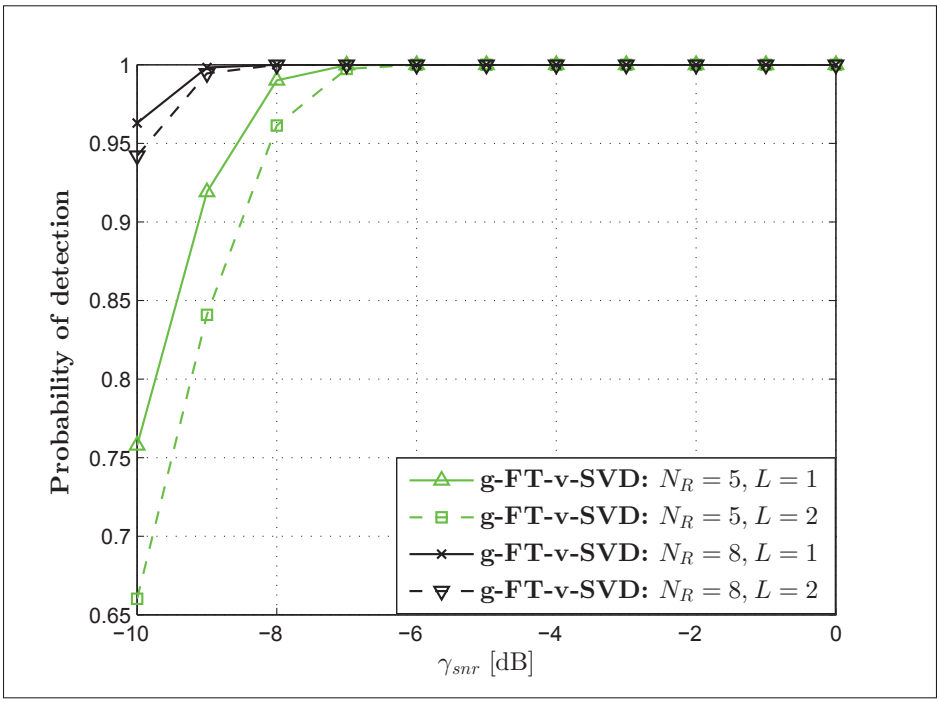

Figure 7.13 P_d versus γ_{snr}: $P_f = 0.1$ and 10^5 realizations

DoF, multiplied by $\tilde{\nu}_2/\tilde{\nu}_1$. Thus, this ratio is precisely distributed as $F_{\tilde{\nu}_1,\tilde{\nu}_2}$ when $\tilde{N}$ gets very large rendering the aforementioned improvement in the accuracy of (7.27b). Moreover, as $\tilde{N}$ is increased from 3000 to 6000, the simulation results get closer to the analytical results which are also getting closer to the $P_f = 0$ line—validating (7.28c).

The complementary ROC exhibited by g-FT-v-SVD is displayed via Fig. 7.19. This figure features the P_m versus P_f plot, where P_m is also simulated as $P_m = 1 - P_d$. As displayed, both the simulation and the analytical results overlap with each other. This validates the closed-form expressions of (7.27a)—plotted via the approximation in (7.17)—and (7.27b). Moreover, the natural trade-off between P_m and P_f is evident.

7.7.2.3 Performance Assessment in a MIMO CR Network

Figs. 7.20 and 7.21 depict the probabilities of detection and of false alarm exhibited by the MIMO CR g-FT-v-SVD, respectively. W.r.t. the desired FAR of 0.1, Fig. 7.20 showcases

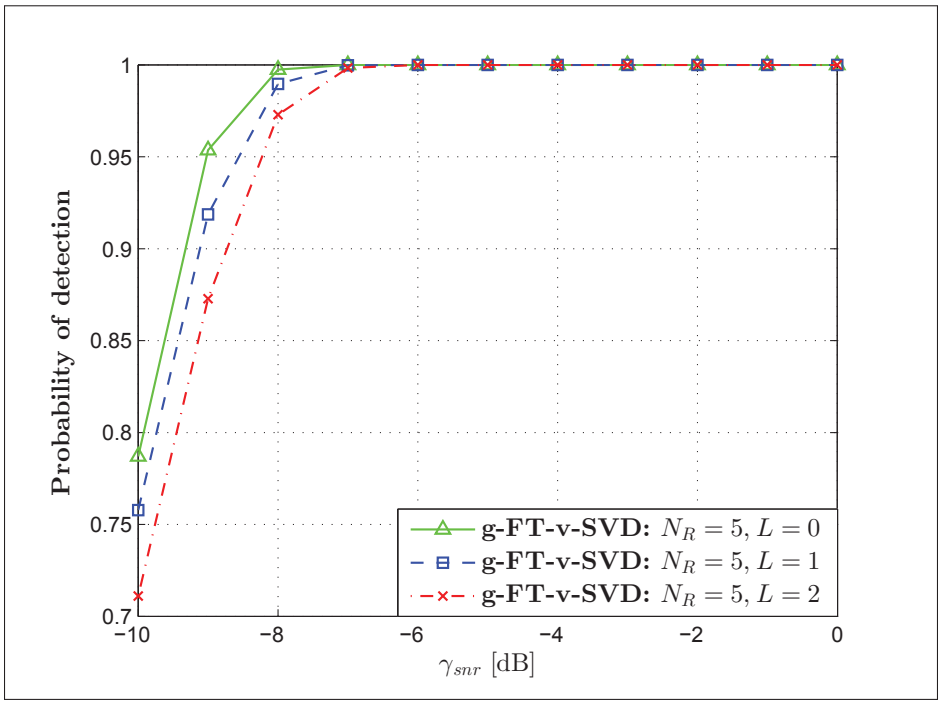

Figure 7.14 P_d versus γ_{snr}: $P_f = 0.1$ and 10^5 realizations

the detection performance of the MIMO CR g-FT-v-SVD for different values of N_T. As it is seen, the P_d exhibited by the MIMO CR g-FT-v-SVD decreases with the increment of N_T. Such a performance loss is attributed to the fact that a large N_T results in a large primary signal subspace—estimated via (7.33)—which is naturally estimated poorly. In other words, the observed performance loss can also be explained via an increase in interference emitted by the neighboring transmitting antennas whenever N_T increases. Such a phenomenon, similarly, affects the false alarm performance of the MIMO CR g-FT-v-SVD which increases w.r.t. N_T, as demonstrated in Fig. 7.21.

7.7.3 Performance Assessment of Detectors Under Noise Uncertainty

The impact of noise uncertainty on FT-v-SVD, g-FT-SVD, and MCED is showcased via Figs. 7.22 and 7.23. As it is evident from these plots, both FT-v-SVD and g-FT-SVD exhibit an identical ROC regardless of the values of the noise uncertainty. Hence, they are robust to noise uncertainty. On the contrary, as the noise uncertainty increases from 0.75 to 1 dB, it is demon-

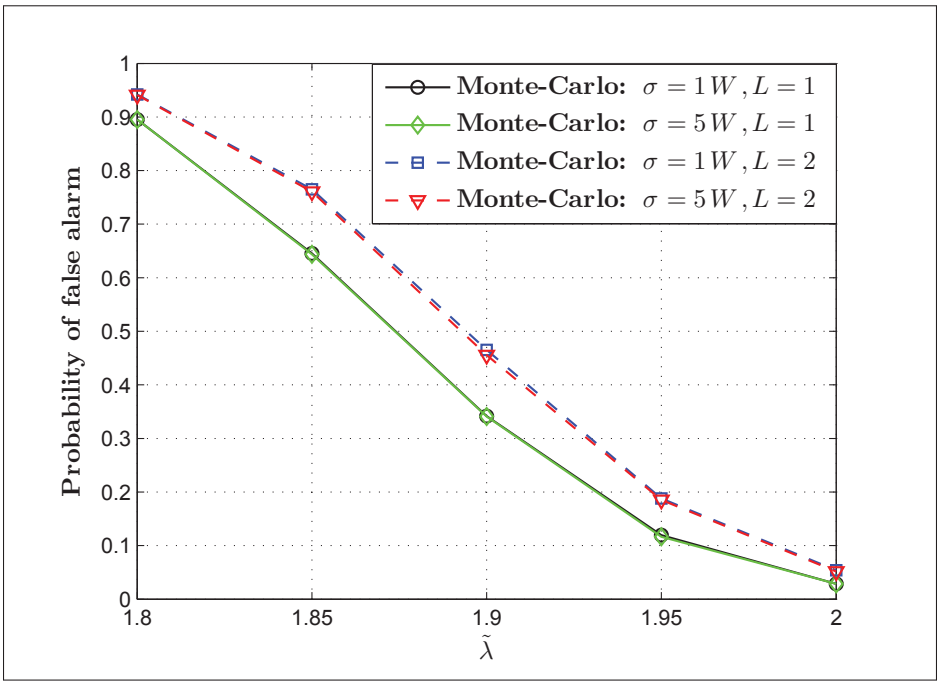

Figure 7.15 P_f versus $\tilde{\lambda}$ for g-FT-v-SVD: 10^4 realizations

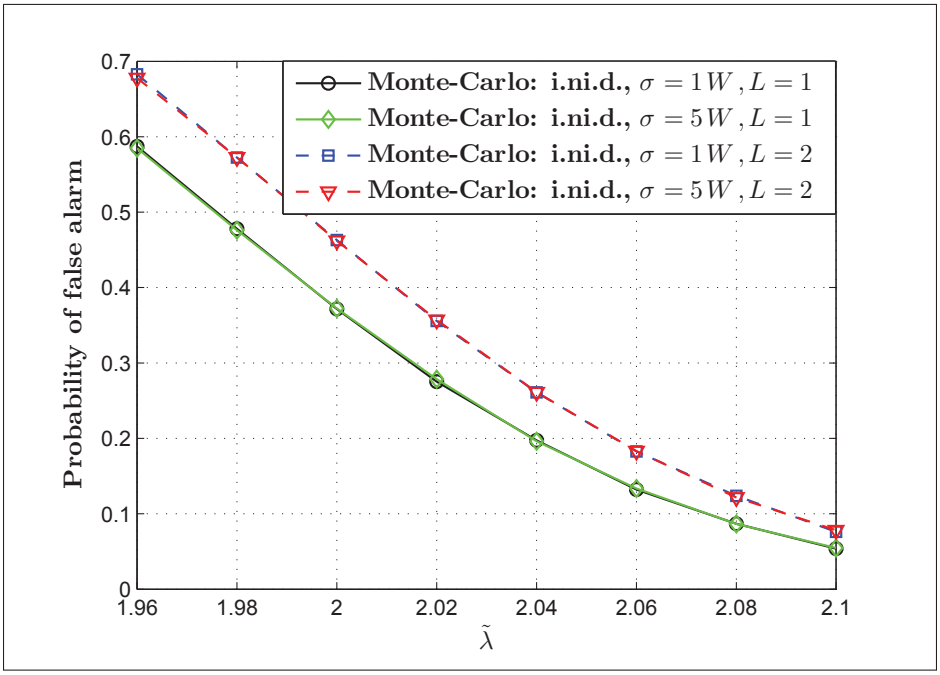

Figure 7.16 P_f versus $\tilde{\lambda}$ for g-FT-v-SVD: 10^5 realizations

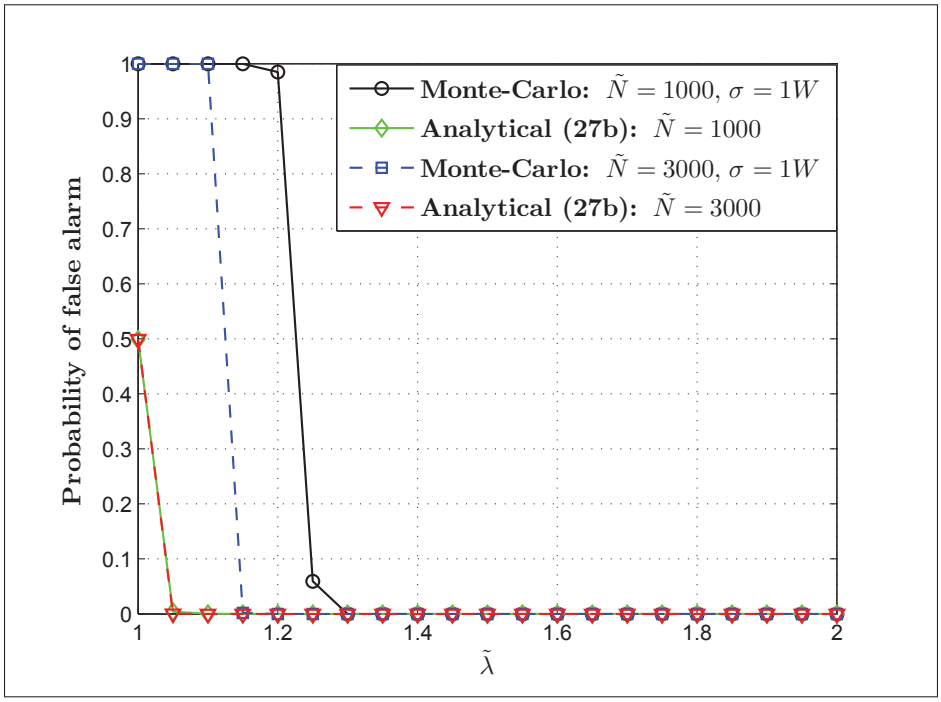

Figure 7.17 P_f versus $\tilde{\lambda}$ for g-FT-v-SVD: 10^4 realizations. Note that (27b) stands for (7.27b)

strated in Figs. 7.22 and 7.23 that MCED incurs a significant performance loss implicating its well-known non-robustness to noise uncertainty.

7.8 Conclusions

CR based communication systems help to overcome the discrepancy between spectrum under-utilization and spectrum scarcity. Such systems employing a spectrum overlay access scheme become efficient and reliable whenever spectrum holes are efficiently and robustly detected. In this respect, efficient and robust spectrum sensing shall not rely on the presumed noise power nor the primary signal characteristics. Such sensing shall be blind, independent of the knowledge of any CSI, and computationally simple—unlike some of the state-of-the-art spectrum sensing techniques which rely on several estimated parameters.

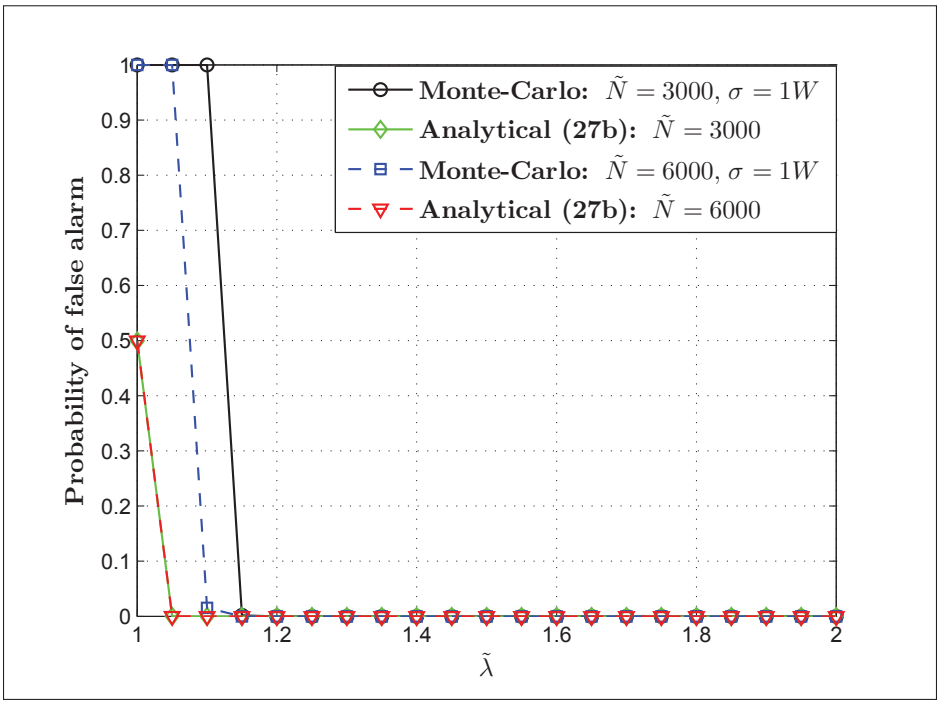

Figure 7.18 P_f versus $\tilde{\lambda}$ for g-FT-v-SVD: 10^4 realizations. Note that (27b) stands for (7.27b)

Accordingly, simple F–test based spectrum sensing techniques named FT-v-SVD and g-FT-v-SVD are presented for a spectrum sensing over a frequency flat and a frequency selective fading channels, respectively. For these detectors presented for SIMO systems, exact and asymptotic performance analyses are provided and validated. Along with the aforementioned detectors presented for SIMO systems, this paper also generalizes the g-FT-v-SVD detector for a MIMO CR network. Moreover, simulations assess the performance of the presented detectors under contaminating i.i.d. and i.ni.d. noise samples. As per the conducted simulations with i.i.d. noise samples, FT-v-SVD and g-FT-v-SVD are corroborated to be CFAR detectors which are also robust against noise uncertainty.

Acknowledgments

The authors acknowledge AVIO-601 Project for the provided funding and the anonymous reviewers for helping them improve the quality of this manuscript.

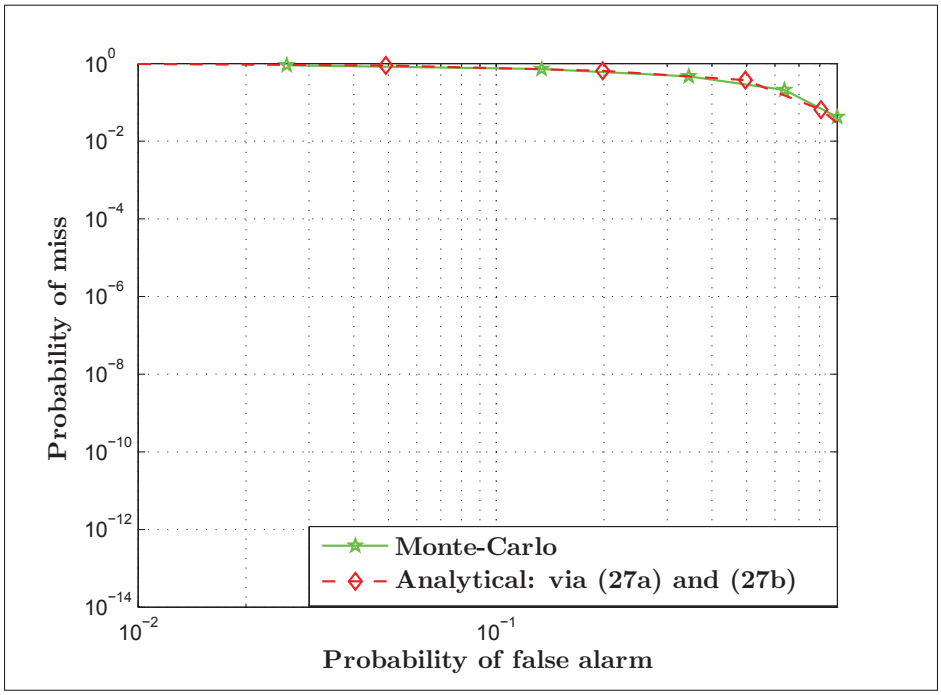

Figure 7.19 The complementary ROC for g-FT-v-SVD: $\gamma_{snr} = -15$ dB. Note that (27a) and (27b) stand for (7.27a) and (7.27b), respectively

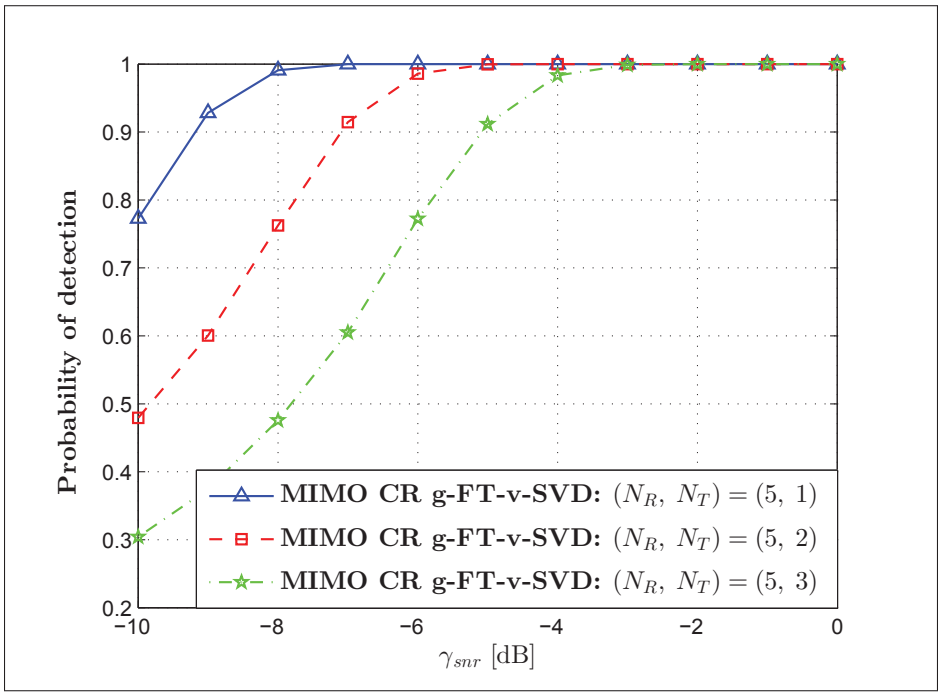

Figure 7.20 P_d versus γ_{snr}: $P_f = 0.1$ and 10^4 realizations

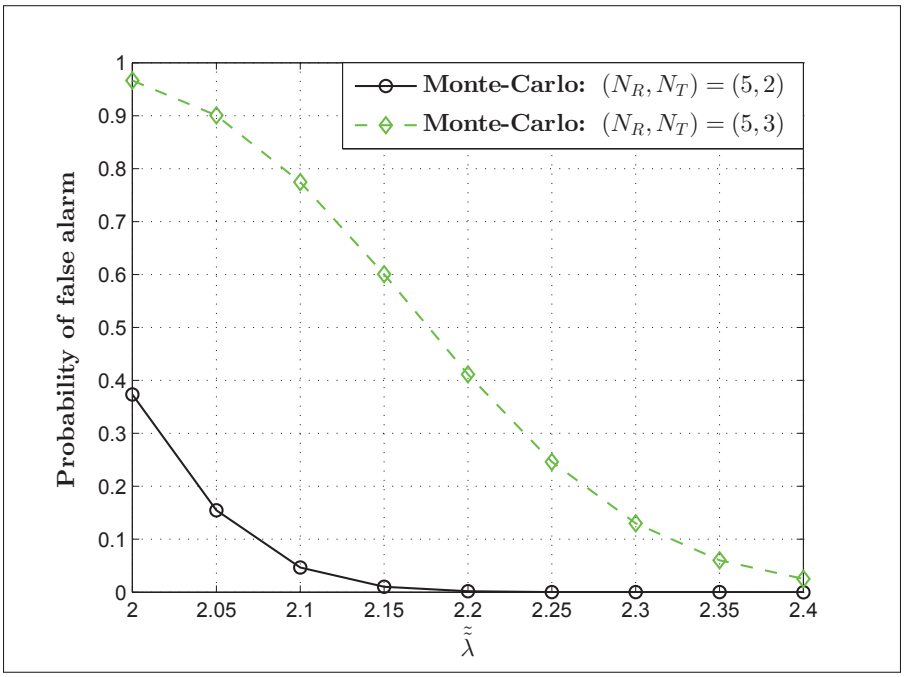

Figure 7.21 P_f versus $\tilde{\tilde{\lambda}}$ exhibited by the MIMO CR g-FT-v-SVD: 10^6 realizations

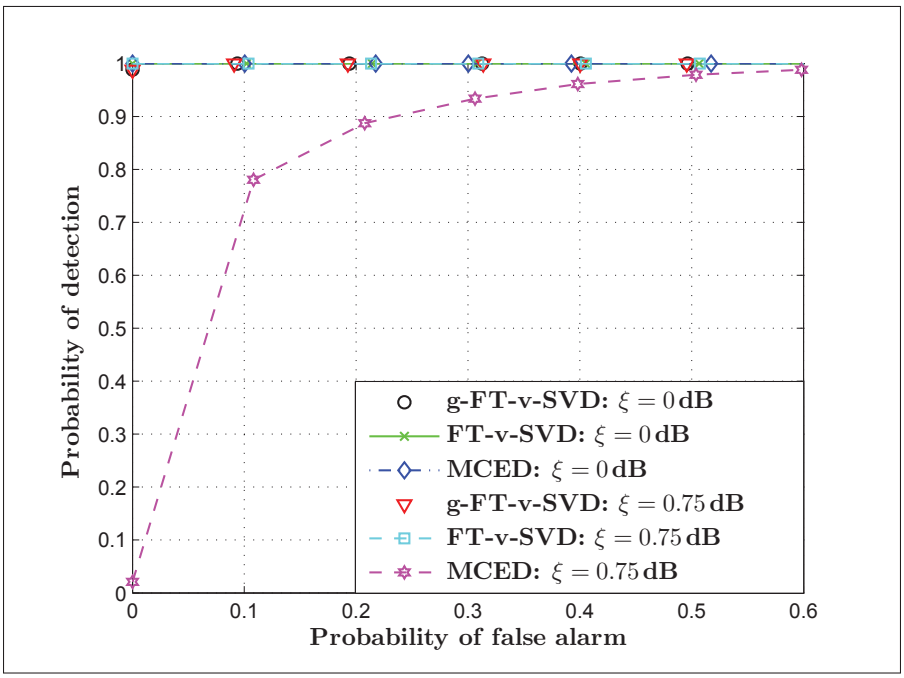

Figure 7.22 P_d versus P_f: $\left(N(\equiv \tilde{N}W), \gamma_{snr}\right) = (300, -6\,\mathrm{dB})$, and 10^5 realizations

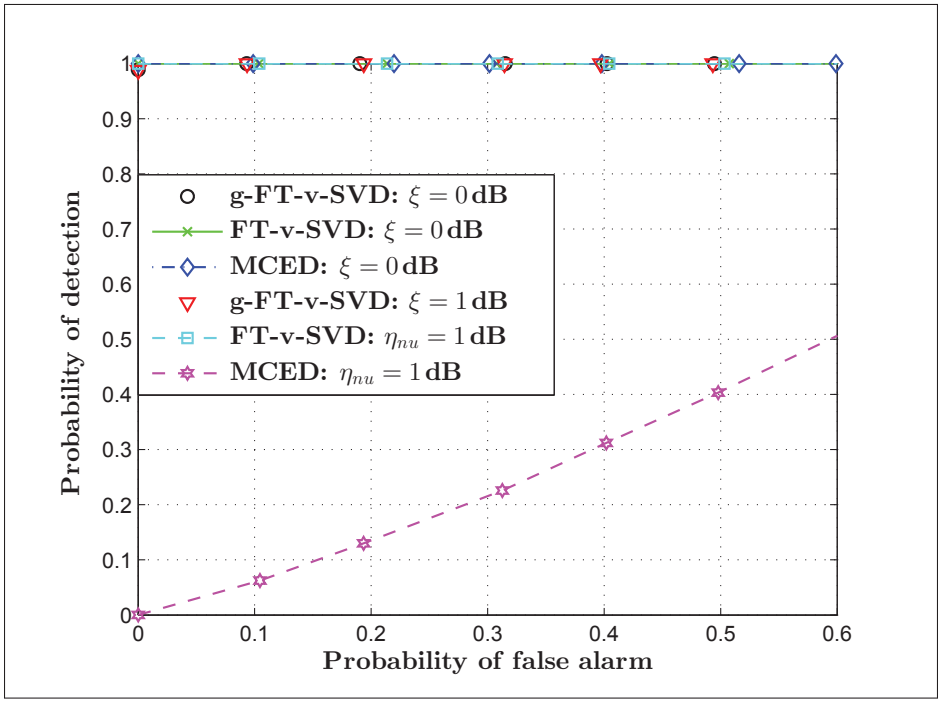

Figure 7.23 P_d versus P_f: $\left(N(\equiv \tilde{N}W), \gamma_{snr}\right) = (300, -6\,\mathrm{dB})$, and 10^5 realizations

Part V

Miscellaneous

CHAPTER 8

DISCUSSION OF THE RESULTS

"Imagination will often carry us to worlds that never were. But without it we go nowhere."—Carl Sagan

This chapter briefly discusses the overall results of this dissertation along with their implications and contributions to the respective research fields.

8.1 Discussion of the Results Reported in Part II

Recalling the objectives of this dissertation outlined in Section 1.4.1, the first goal of this dissertation has been the investigation and development of robust radio frequency interference (RFI) detection algorithms for satellite and terrestrial communications. After a thorough understanding of the state-of-the-art algorithms and their respective limitations, we have developed ideas that led to the investigation and development of robust RFI detection algorithms. To realize these ideas, we have employed the research methodology detailed in Section 1.4.2. Subsequently, the results of Chapters 2-5 along with their implications are discussed.

In Chapter 2, we have investigated a computationally simple power detector (PD) for the detection of broadband RFI(s). For the probabilities of RFI detection and of false alarm exhibited by this detector, exact closed-form expressions are derived and validated through simulations. Simulations also demonstrate that PD outperforms kurtosis detector (KD) (Misra *et al.*, 2009; Ruf *et al.*, 2006) that has failed to detect Gaussian (near-Gaussian) RFI. Despite such a superior performance of the investigated PD, the investigated PD requires an accurate estimate of the noise power and an average signal-to-noise ratio (SNR) which are needed to set a decision threshold as per the desired false alarm rate (FAR). To perform such estimations, the employed signal processing technique should be broadband RFI-aware, as RFI(s) can impinge on the received signal at any time. Accordingly, the results of Chapter 2 have inspired interference-

aware estimation techniques and such techniques are also key for realizing a communication paradigm dubbed *interference-aware wireless communications*.

Chapter 3 detailed the performance analysis of energy detector (ED) investigated for the detection of an RFI received through the Nakagami-*m* fading channel along with the signal of interest (SOI) also received via the same channel. Having exploited the sampling theorem representation of bandlimited signals, ED computes the intercepted received signal energy which is, in turn, deployed to make a decision upon the presence of the RFI. By deriving the distribution of the ED test statistic valid regardless of the type of the impinging RFI, novel approximated and asymptotic closed-form expressions are derived for the probability of RFI detection manifested by ED. A closed-form expression is also derived for the exhibited probability of false alarm. These derived closed-form expressions are validated by Monte-Carlo simulations. The simulations also demonstrate that the investigated ED outperforms both KD and a generalized likelihood ratio test (GLRT) detector. Regarding real-world data based simulations conducted using real-world RFI contaminated data received by one of the antennas of the Very Large Array (VLA) (NRAO, 2017) observatory, simulations further assess the performance of the investigated ED.

Once the received signal is downconverted to its baseband equivalent, it is worthwhile noting that ED can be applied in both satellite and terrestrial communications, regardless of their difference in the pre-baseband signal processing. In spite of such broad applicability and its appealing simplicity, ED notably relies on the knowledge of the noise power. Consequently, the realistic implementation of ED as an RFI detector needs an accurate noise power estimator and such an estimator should be an interference-aware estimator, as an RFI(s) can impinge on the received signal at any time. Moreover, as summarized and demonstrated in the outlooks section of Chapter 3, the mixture of Gaussian (MoG) distribution perfectly approximates Nakagami-*m* distributed BPSK modulated SOI. Interestingly, the MoG distribution offers such a high accuracy on top of its analytical tractability. As a result, the performance analysis of an energy-based RFI detector using the MoG distributed fading channels would be an important extension to the work reported in the same chapter.

As the first work on a multi-antenna RFI detection, Chapter 4 reports an eigenvalue-based robust multi-antenna RFI detection algorithm. The reported eigenvalue detector (EvD) is proposed for multi-antenna wireless communications, especially for single-input multiple-output (SIMO) systems that may suffer from a multi-antenna RFI. By deriving the distribution—valid for infinitely huge samples—of the equivalent test statistic, performance closed-form expressions, valid for infinitely large samples, regarding the probability of RFI detection and the probability of false alarm are derived. The derived closed-form expressions are corroborated by using Monte-Carlo simulations. For medium to large interference-to-noise ratio (INR) regimes and sample starved settings, simulations also corroborate that EvD manifests a comparable detection performance with a GLRT detector fed with the knowledge of the SOI channel, and a matched subspace detector fed with the knowledge of the SOI and RFI channels. Nonetheless, a single-antenna transmitter assumed by the considered SIMO system is not necessarily the case for the transmitters of the fourth generation (4G) and the fifth generation (5G) era, as they are usually equipped with a number of antennas for the sake of array gain, spatial diversity gain, spatial multiplexing gain, and interference reduction (Biglieri *et al.*, 2007). Accordingly, the proposed EvD shall be extended to accommodate multiple-input multiple-output (MIMO) and massive MIMO systems. Furthermore, accounting for the inevitable calibration uncertainties of the N_R antenna frontends similar to (Tugnait, 2012; Ramírez *et al.*, 2011; Leshem & van der Veen, 2001), consideration of *independent and non-identically distributed* (i.ni.d.) noise samples is also worth addressing for SIMO, MIMO, and massive MIMO systems.

Inspired by the results reported in Chapter 4 and Chapter 6—regarding a multi-interferer RFI (MI-RFI) excision, robust matrix- and tensor-based multi-antenna RFI detection techniques are proposed and reported in Chapter 5. Motivated by the fact that multi-path fading channels are usually manifested in practical wireless communication channels, the proposed techniques are, in particular, applicable for a multi-antenna RFI detection over a multi-path fading channel. To continue, we have addressed the issue of RFI detection over wireless multi-path fading channels; we have introduced a tensor-based hypothesis testing framework whose application is tailored for the detection of RFI; for reception through a multi-path fading channel and SIMO

systems, we propose a matrix-based RFI detector (MB-RD) and a tensor-based RFI detector (TB-RD); and the asymptotic performance of the proposed detectors is characterized analytically and assessed via Monte-Carlo simulations. The simulations validate the derived performance characterizations and notably demonstrate that TB-RD outperforms GLRT even though GLRT assumes the availability of the perfect knowledge of the SOI channel. Accounting for their inherent signal processing schemes, MB-RD and TB-RD assume that both the SOI and RFI fading channels remain constant for a long-term interval. On the contrary, some practical wireless channels manifest highly time-variant multi-path fading channel. Consequently, the extension of the proposed techniques to accommodate highly time-variant channel scenarios is of importance. Moreover, as highlighted in the previous paragraphs, MIMO and massive MIMO multi-antenna systems are preferable to SIMO systems. Thus, the extensions of MB-RD and TB-RD to account for MIMO and massive MIMO multi-antenna systems are worth addressing.

8.2 Discussion of the Results Reported in Part III

As outlined in Section 1.4.1, the second objective of this dissertation has been the investigation and development of efficient RFI excision algorithms for satellite and terrestrial communications. Following the methodology highlighted in Section 1.4.2, this dissertation has introduced the multi-linear (tensor) algebra framework to the RFI excision research sub-field. As detailed in Chapter 6, two novel tensor-based efficient RFI excision algorithms have been proposed. Inspired by their inherent signal processing schemes, these algorithms are named as the multi-linear subspace estimation and projection (MLSEP) algorithm and the smoothed MLSEP (s-MLSEP) algorithm. As demonstrated in Chapter 6, MLSEP outperforms the state-of-the-art projection based algorithms namely subspace projection (SP) (van der Tol & van der Veen, 2005) and cross subspace projection (CSP) (Jeffs *et al.*, 2005). With respect to the root mean square excision error (RMSEE) and the average signal-to-interference-plus-noise ratio (SINR) gain performance metrics, MLSEP outperforms both SP and CSP, especially whenever $N_R > \sum_{i=1}^{Q}(L_i+1)$—$L_i+1$ being the number of channel taps of the i-th interferer and Q being

the number of interferers. Such a performance gain is also demonstrated via simulations that employ a simulation setting that the number of interferers and their respective channel order are estimated by the smoothed matrix-based joint number of interferers and channel order enumerator (SMB-JoNICOE)—an algorithm also reported in Chapter 6. Simulations also corroborate that s-MLSEP enhances MLSEP at the expense of computation time.

Apart from the aforementioned simulations, performance assessment using real-world data received by one of the antennas of the VLA also corroborates that MLSEP outperforms both SP and CSP. Such a performance gain has also been further validated by a theorem which states—for $\Delta\boldsymbol{U}_I$ being the perturbations in the MI-RFI subspace—that $\lim_{\Delta\boldsymbol{U}_I \to \mathbf{0}}$ RMSEE converges to 0 for MLSEP faster than for SP provided that $N_R > \sum_{i=1}^{Q}(L_i + 1)$. As discussed and presented in Chapter 6, the significant performance gains of MLSEP and s-MLSEP over SP and CSP are attributed to the fact that the deployed tensor-based subspace estimators outperform their matrix-based counterparts. However, for N_{SOI} being an arbitrary constant, the tensor-based subspace estimator employs the assumption that the MI-RFI channel is assumed to have a coherence time of $N_{\text{SOI}} + 1$ times the coherence time of the SOI. As a result, such an assumption would restrict the applicability of the proposed tensor-based algorithms to, mainly, the quasi-stationary MI-RFI scenario(s). Despite the fact that the multi-linear algebra framework was introduced to the RFI excision research sub-field, further research which shall make the tensor framework applicable for a time-variant MI-RFI scenario(s) is needed. Accordingly, both MLSEP and s-MLSEP would serve as foundational multi-linear algorithms that shall be extended to incorporate the inherently time-variant nature of the MI-RFI channel.

8.3 Discussion of the Results Reported in Part IV

As a third objective, this dissertation has also aimed at the investigation and development of advanced low-complexity spectrum sensing techniques. Having conducted detailed research survey on the numerous state-of-the-art spectrum sensing techniques, we have identified an idealistic assumption on the existing F–test detector reported in (Huang & Chung, 2013a) though it was corroborated—via simulations—to be superior over an energy detector, a maximum-

minimum eigenvalue (MME) detector, and a GLRT detector, especially at low SNRs. While exhibiting a moderate computational complexity, the reported detector of (Huang & Chung, 2013a) is also robust against a noise power uncertainty and independent of the knowledge of the noise power. With respect to the aforementioned limitation, we have developed ideas that overcome the limitations of (Huang & Chung, 2013a) and also extended the F–test framework so that it would incorporate the multi-path fading channel scenario which is evident in practical wireless communication channels. Beneath, the results of Chapter 7 and their respective implications are discussed.

Having been motivated by the performance of the F–test detector of (Huang & Chung, 2013a) and its low computational complexity, Chapter 7 presents simple F–test based spectrum sensing techniques that do not require the knowledge of any channel state information (CSI). Specifically, along with its performance analyses, a detector named F–test via singular value decomposition (FT-v-SVD) is presented for SIMO cognitive radio (CR) networks operating over flat fading channels; apart from its performance analyses, a detector dubbed generalized FT-v-SVD (g-FT-v-SVD) is presented for a multi-antenna spectrum sensing over frequency selective channels; and the g-FT-v-SVD detector is generalized to accommodate a spectrum sensing over the MIMO CR networks. Meanwhile, the performance of the presented detectors is assessed through Monte-Carlo simulations which also validate the derived analytical expressions. Despite a computational complexity analysis that reveals that the presented blind F–test based detectors exhibit a low computational complexity and an attractive detection performance, the considered SIMO and MIMO systems are not necessarily the case for systems of the 5G era. Therefore, the extension of the presented detectors so as to accommodate the scenarios of massive MIMO systems shall be addressed.

CONCLUSION AND RECOMMENDATIONS

"Intellectual growth should commence at birth and cease only at death."—Albert Einstein

For intentional and unintentional man-made interference, radio frequency interference (RFI) is becoming increasingly common in various radio frequency operating systems as diverse as microwave radiometry, radio astronomy, satellite communications, ultra-wideband communications, radar, and cognitive radio. If left unmitigated, such RFI can result in a severe system performance loss. Toward an efficient RFI mitigation, the state-of-the-art encompasses several RFI detection and excision algorithms. However, amongst their limitations, these algorithms exhibit considerable computational complexity and they eventually render inefficient RFI excision. On the other hand, as an enabler of cognitive radio (CR), numerous spectrum sensing techniques have been proposed to date. On the contrary, among their limitations, some of the state-of-the-art spectrum sensing techniques rely either on the presumed characteristics of the primary signal(s) or the availability of the channel state information (CSI). Motivated by these limitations, this Ph.D. dissertation has investigated and presented advanced signal processing techniques regarding RFI detection, RFI mitigation, and spectrum sensing.

With respect to RFI detection and its first objective, this dissertation has investigated and presented five RFI detectors: a power detector proposed for the detection of broadband RFI(s); an energy detector investigated for RFI detection in wireless communication systems; a blind eigenvalue-based detector proposed for single-input multiple-output (SIMO) systems that may suffer from RFI; and matrix- and tensor-based RFI detectors proposed for a robust detection of RFI received through a multi-path fading channel featuring SIMO systems. For these RFI detectors, this dissertation has presented detailed performance analyses that are corroborated by Monte-Carlo simulations. Simulations also assess the performance of the aforementioned RFI detectors in comparison with some of the state-of-the-art RFI detectors.

Once RFI is robustly detected, the next step is its efficient excision. Toward this end and the realization of its second objective, this dissertation has investigated and presented a multi-linear subspace estimation and projection (MLSEP) algorithm and a smoothed MLSEP (s-MLSEP) algorithm proposed for the MI-RFI excision in SIMO systems that suffer from MI-RFI. Performance analyses corroborate that both MLSEP and s-MLSEP can excise all interferers when the perturbations get infinitesimally small. For such perturbations, the analyses also attest that s-MLSEP exhibit a faster convergence to a zero excision error than MLSEP which, in turn, converges faster than a subspace projection algorithm. Monte-Carlo simulations and simulations conducted using real-world RFI contaminated data have corroborated the performance of the proposed multi-linear RFI excision algorithms. Although at the expense of computation time, the simulations have also demonstrated that s-MLSEP outperforms MLSEP as the smoothing factor gets smaller.

Concerning its third objective, this dissertation has investigated and presented simple F–test based spectrum sensing techniques that do not require the knowledge of CSI for multi-antenna CRs. Applicable for different multi-antenna systems, the investigated blind F–test detectors are derived for both frequency flat and frequency selective primary-to-secondary channels. Exact and asymptotic analytical performance closed-form expressions are derived for the presented detectors. Simulations assess the performance of the presented detectors and validate the derived closed-form expressions. For an additive noise exhibiting the same variance across multiple-antenna frontends, simulations also corroborate that the presented detectors are constant false alarm rate detectors which are robust against noise uncertainty.

Finally, to outline the recommendations of this dissertation, the aforementioned investigations inspire new research from both specialist and generalist points of view. From specialist points of view, this dissertation inspires research—but not limited to—on tensor-based RFI excision techniques for highly time-variant wireless environments; linear and multi-linear multi-antenna

RFI detection techniques applicable also for highly time-variant wireless environments; efficient spectrum sensing in highly time-variant primary-to-secondary wireless channel environments; machine learning (deep learning) enabled RFI detection; and RFI detection using bootstrap techniques (Zoubir & Robert Iskander, 2007; Zoubir & Iskander, 2004). On another regard, this dissertation also inspires extensive research that can be conducted from generalist points of view. In particular, this dissertation motivates research toward *interference-resistant* wireless communications—for instance, interference-resistant terrestrial communications and interference-resistant satellite communications; interference-resistant optical communications; interference-resistant molecular (nano) communications (Nakano *et al.*, 2013; Farsad *et al.*, 2016); interference-resistant mobile molecular communications (Nakano *et al.*, 2017); an interference-resistant biomedical signal processing; and interference-resistant robotic communications and control.

APPENDIX I

APPENDICES OF CHAPTER 1

1. List of Journal Papers [J]

- [J6] T. M. Getu, W. Ajib, and R. Jr. Landry, "Linear and Multi-Linear RFI Detectors for Multi-Antenna Wireless Communications," *IEEE Trans. Wireless Commun.*, submitted, Nov. 2018.
- [J5] T. M. Getu, W. Ajib, and R. Jr. Landry, "Eigenvalue-Based RF Interference Detector for Multi-Antenna Wireless Communications," *Elsevier Signal Process.*, submitted, Mar. 2019.
- [J4] T. M. Getu, W. Ajib, and R. Jr. Landry, "Power-Based Broadband RF Interference Detector for Wireless Communication Systems," *IEEE Wireless Commun. Lett.*, vol. 7, no. 6, pp. 1002-1005, Dec. 2018.
- [J3] T. M. Getu, W. Ajib, and R. Jr. Landry, "Simple F–Test Based Spectrum Sensing Techniques for Multi-Antenna Cognitive Radios," *IEEE Trans. Commun.*, vol. 66, no. 11, pp. 5081-5096, Nov. 2018.
- [J2] T. M. Getu, W. Ajib, and R. Jr. Landry, "Performance Analysis of Energy-Based RFI Detector," *IEEE Trans. Wireless Commun.*, vol. 17, no. 10, pp. 6601-6616, Oct. 2018.
- [J1] T. M. Getu, W. Ajib, and O. A. Yeste-Ojeda, "Tensor-Based Efficient Multi-Interferer RFI Excision Algorithms for SIMO Systems," *IEEE Trans. Commun.*, vol. 65, no. 7, pp. 3037-3052, Jul. 2017.

2. List of Conference Papers [C]

- [C12] T. M. Getu, W. Ajib, and R. Jr. Landry, "INR Walls: Fundamental Limits in RFI Detection," in *Proc. IEEE Int. Conf. on Commun. (IEEE ICC 2019)*, Shanghai, China, 20-24 May 2019, submitted.
- [C11] T. M. Getu, W. Ajib, and R. Jr. Landry, "Performance Analysis of Energy-Based RF Interference Detector," in *Proc. IEEE Wireless Commun. and Netw. Conf. (IEEE WCNC 2019)*, Marrakech, Morocco, 15-18 April 2019, submitted.
- [C10] T. M. Getu, W. Ajib, and R. Jr. Landry, "Power-Based Continuous Wave RFI Detector for RF Operating Systems," in *Proc. IEEE Global Conf. on Signal and Inform. Process. (IEEE GlobalSIP 2018)*, Anaheim, CA, USA, 26–29 Nov. 2018.
- [C9] T. M. Getu, W. Ajib, and R. Jr. Landry, "A Simple F–Test Based Spectrum Sensing Technique for MIMO Cognitive Radio Networks," in *Proc. Int. Conf. on Wireless and Mobile Comput., Netw. and Commun. (WiMob 2018)*, Limassol, Cyprus, 15-17 Oct. 2018, pp. 1-8.
- [C8] T. M. Getu, W. Ajib, and R. Jr. Landry, "Energy-Based RFI Detection: Theory and Results," in *Proc. Int. Workshop on Sel. Topics in Wireless and Mobile Comput. (STWiMob 2018)*, Limassol, Cyprus, 15-17 Oct. 2018, pp. 161-168.
- [C7] T. M. Getu, W. Ajib, and R. Jr. Landry, "An Eigenvalue-Based Multi-Antenna RFI Detection Algorithm," in *Proc. IEEE Veh. Technol. Conf. (VTC2018-Fall)*, Chicago, IL, USA, 27-30 Aug. 2018.
- [C6] T. M. Getu, W. Ajib, and R. Jr. Landry, "A Simple F–Test Based Multi-Antenna Spectrum Sensing Technique," in *Proc. IEEE Veh. Technol. Conf. (VTC2018-Fall)*, Chicago, IL, USA, 27-30 Aug. 2018.
- [C5] T. M. Getu, W. Ajib, O. A. Yeste-Ojeda, and R. Jr. Landry, "Tensor-Based Efficient Multi-Interferer RFI Excision: Results Using Real-World Data," in *Proc. Int. Conf. on Comput., Netw. and Commun. (ICNC 2018)*, Maui, HI, USA, 5-8 Mar. 2018, pp. 917-921.

- [C4] T. M. Getu, W. Ajib, and R. Jr. Landry, "Matrix-Based Joint Interference and Channel Order Enumerators for SIMO Systems Suffering From RFI," in *Proc. Int. Conf. on Comput., Netw. and Commun. (ICNC 2018) CNC Workshop*, Maui, HI, USA, 5-8 Mar. 2018, pp. 305-309.
- [C3] T. M. Getu, W. Ajib, and R. Jr. Landry, "Oversampling-Based Algorithm for Efficient RF Interference Excision in SIMO Systems," in *Proc. IEEE Global Conf. on Signal and Inform. Process. (IEEE GlobalSIP 2016)*, Greater Washington, DC, USA, 7-9 Dec. 2016, pp. 1423-1427.
- [C2] T. M. Getu, W. Ajib, and O. A. Yeste-Ojeda, "Multi-Linear Subspace Estimation and Projection for Efficient RFI Excision in SIMO Systems," in *Proc. IEEE Global Conf. on Signal and Inform. Process. (IEEE GlobalSIP 2015)*, Orlando, FL, USA, 14-16 Dec. 2015, pp. 1397-1401.
- [C1] T. M. Getu, W. Ajib, and O. A. Yeste-Ojeda, "Efficient Semi-Blind Channel Estimators for SIMO Systems Suffering From Broadband RFI," in *Proc. IEEE Int. Conf. on Ubiquitous Wireless Broadband (IEEE ICUWB 2015)*, Montreal, QC, Canada, 4-7 Oct. 2015, pp. 1-5.

3. Highlight of Contributions

During the course of this Ph.D. dissertation, we have made contributions to the research sub-fields of RFI detection, RFI excision, spectrum sensing, source enumeration, and channel estimation. Specifically:

- [J6], [J5], [J4], and [J2] are our journal contributions regarding RFI detection on top of [C12], [C11], [C10], [C8], and [C7] which are our conference contributions to the same research sub-field;
- [J1] is our main contribution concerning RFI excision along with the respective conference contributions through [C5], [C3], and [C2];
- with respect to spectrum sensing, we have made journal contributions through [J3] as well as conference contributions in terms of [C9] and [C6];
- concerning source enumeration (model order selection), we have made a contribution through [C4]; and
- we have made a contribution in channel estimation in terms of [C1].

APPENDIX II

APPENDICES OF CHAPTER 2

1. Proof of Theorem 1

For independent $\{v_j[n]\}_{j=1}^{Q}$, h, $\{g_j\}_{j=1}^{Q}$, and $z[n]$,

$$Y|H_1 = \mathbb{E}\{\big(\overbrace{hs[n]+\textstyle\sum_{j=1}^{Q} g_j v_j[n]}^{\tilde{r}[n]}+z[n]\big)^2\} \tag{A II-1a}$$

$$= \mathbb{E}\{\tilde{r}^2[n]\}+2\mathbb{E}\{\tilde{r}[n]\}\mathbb{E}\{z[n]\}+\sigma^2 \tag{A II-1b}$$

$$\overset{(a)}{=} \mathbb{E}\{(hs[n]+\textstyle\sum_{j=1}^{Q} g_j v_j[n])^2\}+\sigma^2, \tag{A II-1c}$$

where (a) follows for $\mathbb{E}\{z[n]\}=0$.

For the considered independence, $\mathbb{E}\{s[n]v_j[n]\}=\mathbb{E}\{v_i[n]v_j[n]\}=0$, $i\neq j$. Thus,

$$Y|H_1 = \mathbb{E}\{h^2 s^2[n]\}+\textstyle\sum_{j=1}^{Q}\mathbb{E}\{g_j^2 v_j^2[n]\}+\sigma^2 \tag{A II-2a}$$

$$= \bar{h}_s\mathbb{E}\{s^2[n]\}+\textstyle\sum_{j=1}^{Q}\bar{g}_{j,s}\mathbb{E}\{v_j^2[n]\}+\sigma^2. \tag{A II-2b}$$

From Sec. 2.2.1 , $\mathbb{E}\{v_j^2[n]\}=P_j\mathbb{E}\{v_{j,l}^2\}=P_j$ and $\mathbb{E}\{s^2[n]\}=P\mathbb{E}\{s_n^2\}$. As a result,

$$Y|H_1 = \bar{h}_s P\mathbb{E}\{s_n^2\}+\textstyle\sum_{j=1}^{Q}\bar{g}_{j,s}P_j+\sigma^2 \tag{A II-3a}$$

$$\overset{(b)}{=} \sigma^2\big(\bar{\gamma}_{snr}+\textstyle\sum_{j=1}^{Q}\bar{\gamma}_{inr}^{j}+1\big), \tag{A II-3b}$$

where (b) follows from (2.5).

Under H_0, $\{v_j[n]\}_{j=1}^{Q}=0$. Accordingly,

$$Y|H_0 = \mathbb{E}\{(hs[n]+\textstyle\sum_{j=1}^{Q} g_j v_j[n]+z[n])^2\}\big|_{\{\bar{\gamma}_{inr}^{j}\}_{j=1}^{Q}=0}. \tag{A II-4}$$

Deploying (A II-1a)—via its equivalent given by (A II-3b)—in (A II-4),

$$Y|H_0 = \sigma^2\left(\bar{\gamma}_{snr} + \sum_{j=1}^{Q} \bar{\gamma}_{inr}^{j} + 1\right)\Big|_{\{\bar{\gamma}_{inr}^{j}\}_{j=1}^{Q}=0} = \sigma^2\left(\bar{\gamma}_{snr} + 1\right). \tag{A II-5}$$

Finally, combining (A II-3b) and (A II-5) leads to (2.4). □

APPENDIX III

APPENDICES OF CHAPTER 3

1. Proof of Theorem 2

For a baseband input of bandwidth W, we note that $2u$ terms are sufficient to approximate its energy in a finite duration sample of a bandlimited process (Urkowitz, 1967, Appendix). For a lowpass (baseband) process, the values are obtained by sampling the process at $1/2W$ times apart. Having relied on the aforementioned approximation which is the result of the Karhunen−Loève transform, terms of H_1 in (3.1) are represented as (Urkowitz, 1967, eqs. (11) and (12))

$$\big(hs(t), gv(t), z(t)\big) = \sum_{j=1}^{2u} \big(h\alpha_j, g\beta_j, \xi_j\big)\,\mathrm{sinc}(2Wt-j), \tag{A III-1}$$

where $\xi_j = z(j/2W)$ and $\mathrm{sinc}(x) = \sin(\pi x)/\pi x$. It is to be noted that the type of RFI in (A III-1) is irrelevant for the approximation and each ξ_j is a Gaussian RV with a zero mean and variance of $\sigma^2 = N_0 W$.

Deploying (A III-1) in (3.1),

$$r(t)|H_1 = \sum_{j=1}^{2u} \big(h\alpha_j + g\beta_j + \xi_j\big)\ \mathrm{sinc}(2Wt-j). \tag{A III-2}$$

Substituting (A III-2) into (3.2) results in

$$Y|H_1 = \frac{2}{N_0}\sum_{j=1}^{2u}\sum_{i=1}^{2u}\big(h\alpha_j + g\beta_j + \xi_j\big)\big(h\alpha_i + g\beta_i + \xi_i\big) \times \underbrace{\int_{t-T}^{t} \mathrm{sinc}(2Wt-j)\ \mathrm{sinc}(2Wt-i)dt}_{=\frac{1}{2W},\ \text{if } j=i;\ =0,\ \text{if } j\neq i.}. \tag{A III-3}$$

Employing the orthogonality of sinc functions (Urkowitz, 1967, eq. (5)) and recalling that $\sigma^2 = N_0 W$,

$$Y|H_1 = \sum_{j=1}^{2u} \left(h\alpha_j/\sigma + g\beta_j/\sigma + \xi_j/\sigma\right)^2. \tag{A III-4}$$

As every ξ_j is a Gaussian RV with a zero mean and variance of σ^2, ξ_j/σ is a Gaussian RV with a zero mean and variance of 1. Thus, $Y|H_1$ in (A III-4) admits the noncentral χ^2–distribution with $2u$ DoF and a noncentrality parameter given by

$$\rho = \sum_{j=1}^{2u} \left(h\alpha_j/\sigma + g\beta_j/\sigma\right)^2. \tag{A III-5}$$

Expanding (A III-5) and substituting $\sigma^2 = N_0 W$ yields

$$\rho = 2\frac{h^2}{N_0}\left(\frac{1}{2W}\sum_{j=1}^{2u}\alpha_j^2\right) + 2\frac{g^2}{N_0}\left(\frac{1}{2W}\sum_{j=1}^{2u}\beta_j^2\right) + 2\sum_{j=1}^{2u}\left(\frac{h\alpha_j}{\sigma}\right)\left(\frac{g\beta_j}{\sigma}\right). \tag{A III-6}$$

Following the stated suppositions that $E_s = \int_{t-T}^{t} s^2(t)dt$ and $E_v = \int_{t-T}^{t} v^2(t)dt$,

$$(E_s, E_v) = \underbrace{\sum_{j=1}^{2u}\sum_{i=1}^{2u}(\alpha_j\alpha_i, \beta_j\beta_i)\overbrace{\int_{t-T}^{t}\mathrm{sinc}(2Wt-j)\mathrm{sinc}(2Wt-i)dt}^{=\frac{1}{2W},\ \text{if } j=i;\ =0,\ \text{if } j\neq i.}}_{=\frac{1}{2W}\sum_{j=1}^{2u}(\alpha_j^2,\beta_j^2)}. \tag{A III-7}$$

At last, plugging (A III-7) into (A III-6) and realizing that $(\gamma_{snr}, \gamma_{inr}) = (h^2E_s/N_0, g^2E_v/N_0)$ lead to (3.5). □

2. Proof of Theorem 4

Recalling that $(\alpha_j, \beta_j) = \big(s(j/2W), v(j/2W)\big)$ and using the SOI, and RFI representations as in Theorem 3,

$$(\alpha_j, \beta_j) = \sum_{n=-\infty}^{\infty} \big(\sqrt{P_s}s_n, \sqrt{P_v}v_n\big)p(j/2W - nT_s) \tag{A III-8a}$$

$$= \big(\sqrt{P_s}s_j, \sqrt{P_v}v_j\big), \tag{A III-8b}$$

where $p(j/2W - nT_s) = 1$ iff $j = n$ is exploited, as $p(t)$ is a rectangular pulse of duration T_s. Substituting (A III-8b) into (A III-7) results in

$$\big(E_s, \bar{E}_s\big) = \frac{P_s}{2W} \sum_{j=1}^{2u} \big(s_j^2, \mathbb{E}\{s_j^2\}\big) \tag{A III-9a}$$

$$\big(E_v, \bar{E}_v\big) = \frac{P_v}{2W} \sum_{j=1}^{2u} \big(v_j^2, \mathbb{E}\{v_j^2\}\big), \tag{A III-9b}$$

where $\bar{E}_s$ and $\bar{E}_v$ are the average SOI energy and the average RFI energy, respectively.

Substituting (A III-8b) into (3.5) gives

$$\rho = 2Z, \tag{A III-10}$$

where

$$Z = \gamma_{snr} + \gamma_{inr} + \frac{hg\sqrt{P_s P_v}}{\sigma^2} \sum_{j=1}^{2u} s_j v_j. \tag{A III-11}$$

Accordingly, the PDF of ρ can be obtained from the PDF of Z. If we suppose

$$Y_1 = \gamma_{snr}, \;\; Y_2 = \gamma_{inr} \tag{A III-12a}$$

$$Y = Y_1 + Y_2 \tag{A III-12b}$$

$$Y_3 = \frac{hg\sqrt{P_s P_v}}{\sigma^2}, \;\; Y_4 = \sum_{j=1}^{2u} s_j v_j \tag{A III-12c}$$

$$X = Y_3 Y_4, \tag{A III-12d}$$

then

$$Z = Y + X. \tag{A III-13}$$

Prior to diving to the PDF derivation, we note that Z becomes a mixed RV whenever the discrete RV Y_4 becomes non-zero. More precisely,

$$Z = \begin{cases} Y, & \text{if } Y_4 = 0, \\ X + Y, & \text{if } Y_4 \neq 0. \end{cases} \tag{A III-14}$$

To derive the PDF $f_Z(z)$, we resort to the derivation of the CDF of Z, i.e., $F_Z(z)$, by deploying the total probability theorem (Bertsekas & Tsitsiklis, 2008, p. 28) and applying differentiation afterward. Note that $F_Z(z) = \Pr\{Z \leq z\}$. Applying the total probability theorem through (A III-14) gives

$$F_Z(z) = \Pr\{Y \leq z\} P_{Y_4}(0) + \sum_{\substack{r: \\ r \neq 0}} \Pr\big\{Z \leq x + y | Y_4 = r\big\} P_{Y_4}(r) \tag{A III-15}$$

$$F_Z(z) = F_Y(z) P_{Y_4}(0) + \sum_{\substack{r: \\ r \neq 0}} F_{Z|Y_4=r}(x + y | Y_4 = r) P_{Y_4}(r), \tag{A III-16}$$

Differentiating (A III-16) w.r.t. z then gives

$$f_Z(z) = f_Y(z) P_{Y_4}(0) + \sum_{\substack{r: \\ r \neq 0}} f_{Z|Y_4=r}(x + y | Y_4 = r) P_{Y_4}(r). \tag{A III-17}$$

To continue, we are going to pursue the derivation of the probability mass function (PMF) of Y_4. Should we let $c_j = s_j v_j$, $1 \leq j \leq 2u$, then for the independence of s_j and v_j (Bertsekas & Tsitsiklis, 2008; Gallager, 2013),

$$P_C(c_j) = \Pr\{s_j\}\Pr\{v_j\}. \tag{A III-18}$$

Meanwhile, Y_4 becomes the sum of $2u$ RVs, $\{c_j\}_{j=1}^{2u}$, and its PMF can be recursively determined as the PMF of $A_n = A_{n-1} + c_n$ for $A_0 = 0$. To continue (Bertsekas & Tsitsiklis, 2008, p. 213),

$$P_{A_2}(r) = \Pr\{A_2 = r\} = \Pr\{c_1 + c_2 = r\} \tag{A III-19a}$$

$$= \sum_{n=-\infty}^{\infty} P_C(n) P_C(r-n) = P_C(r) * P_C(r). \tag{A III-19b}$$

Similarly,

$$P_{A_3}(r) = \Pr\{A_2 + c_3 = r\} = \sum_{n=-\infty}^{\infty} P_{A_2}(n) P_C(r-n) \tag{A III-20a}$$

$$= P_{A_2}(r) * P_C(r) \tag{A III-20b}$$

$$= P_C(r) * P_C(r) * P_C(r). \tag{A III-20c}$$

Pursuing the recursive analysis further eventually gives

$$P_{Y_4}(r) = P_{A_{2u}}(r) = \underbrace{P_C(r) * P_C(r) * \cdots * P_C(r)}_{2u-1 \text{ fold discrete-time convolution}}, \tag{A III-21}$$

where $r = \sum_{j=1}^{2u} s_j v_j$.

Should we presume that all the possible values of r belong to a set $\mathscr{M}$, then $\mathscr{M} = \mathscr{M}^- \cup \{0\} \cup \mathscr{M}^+$ for $\mathscr{M}^-$ and $\mathscr{M}^+$ being the set of all possible negative and positive values of r,

respectively. Accordingly,

$$f_Z(z) = f_Y(z)P_{Y_4}(0) + \sum_{r^- \in \mathscr{M}^-} f_{Z|Y_4}(x+y|Y_4 = r^-)P_{Y_4}(r^-) + \sum_{r^+ \in \mathscr{M}^+} f_{Z|Y_4}(x+y|Y_4 = r^+)P_{Y_4}(r^+). \quad \text{(A III-22)}$$

If $r > 0$, $x > 0$, and $x < 0$ when $r < 0$—cf. (A III-12d). Hence, determining the PDF of Z for both conditions depends on the PDF of X and Y. However, these RVs depend on the transmitted SOI and RFI, the SOI channel, and the RFI channel. Accordingly, X and Y are dependent RVs rendering the derivation of the exact PDF of Z either mathematically intractable or too complex. To the best of our knowledge, such a PDF hasn't been derived to date.

To overcome the aforementioned intractability, we approximate the resulting PDF for $r > 0$ by the PDF of the sum of two independent RVs. Relying on (Bertsekas & Tsitsiklis, 2008, p. 214),

$$f_{Z|Y_4}(x+y|Y_4 = r^+) \approx \int_{-\infty}^{\infty} f_{X|Y_4}(x|Y_4 = r^+) f_Y(z-x)dx. \quad \text{(A III-23)}$$

Similarly, the PDF for $r < 0$ is approximated by the PDF of the difference of two independent RVs. Thus, relying on (Bertsekas & Tsitsiklis, 2008, p. 216),

$$f_{Z|Y_4}(x+y|Y_4 = r^-) \approx \int_{-\infty}^{\infty} f_Y(x) f_{X|Y_4}(x-z|Y_4 = r^-)dx. \quad \text{(A III-24)}$$

Substituting (A III-23) and (A III-24) into (A III-22) results in

$$f_Z(z) \approx f_Y(z)P_{Y_4}(0) + \sum_{r^+ \in \mathscr{M}^+} P_{Y_4}(r^+) \int_{-\infty}^{\infty} f_{X|Y_4}(x|Y_4 = r^+) f_Y(z-x)dx + \sum_{r^- \in \mathscr{M}^-} P_{Y_4}(r^-) \int_{-\infty}^{\infty} f_Y(x) f_{X|Y_4}(x-z|Y_4 = r^-)dx. \quad \text{(A III-25)}$$

Henceforth, the PDFs $f_Y(y)$, $f_{X|Y_4}(x|Y_4 = r^-)$, and $f_{X|Y_4}(x|Y_4 = r^+)$ are derived. From the considered Nakagami-m fading channels, h^2 and g^2 are gamma distributed (Trigui *et al.*, 2009). Accordingly, $Y_1 \sim \mathscr{G}(m_1, \Omega_1)$ and $Y_2 \sim \mathscr{G}(m_2, \Omega_2)$ for $\Omega_1 = \bar{\gamma}_{snr} = \frac{\bar{h}_s \bar{E}_s}{N_0} = \frac{\bar{h}_s P_s \sum_{j=1}^{2u} \mathbb{E}\{s_j^2\}}{2N_0 W}$ and

$\Omega_2 = \bar{\gamma}_{inr} = \frac{\bar{g}_s \bar{E}_v}{N_0} = \frac{\bar{g}_s P_v \sum_{j=1}^{2u} \mathbb{E}\{v_j^2\}}{2N_0 W}$. For the integerness of m_1 and m_2, Y_1 and Y_2 exhibit the Erlang distribution expressed via its PDF as (Karagiannidis *et al.*, 2006a, eq. (2))

$$f_{Y_l}(y; m_l, \eta_l) = \frac{y^{m_l - 1}}{\eta_l^{m_l}(m_l - 1)!} e^{-\frac{y}{\eta_l}} U(y), \tag{A III-26}$$

where $1 \leq l \leq 2$, $\eta_1 = \frac{\bar{\gamma}_{snr}}{m_1}$, and $\eta_2 = \frac{\bar{\gamma}_{inr}}{m_2}$. The PDF of Y, which is the sum of two mutually independent Erlang distributed RVs, is then given by (Karagiannidis *et al.*, 2006a, eq. (6))

$$f_Y(y) = \sum_{i=1}^{2} \sum_{k=1}^{m_i} \Xi_{\eta_1 \eta_2}^{m_1 m_2}(i,k) f_{Y_i}(y; k, \eta_i), \tag{A III-27}$$

where the weight $\Xi_{\eta_1 \eta_2}^{m_1 m_2}(i,k)$ is as defined in (Karagiannidis *et al.*, 2006a, eq. (A-5)). Using (A III-26) and (A III-27),

$$f_Y(z) = \sum_{i=1}^{2} \sum_{k=1}^{m_i} \Xi_{\eta_1 \eta_2}^{m_1 m_2}(i,k) \frac{z^{k-1}}{\eta_i^k (k-1)!} e^{-\frac{z}{\eta_i}} U(z). \tag{A III-28}$$

Meanwhile, the PDF of Y_3 can be recognized as the distribution of the product of two independent Nakagami-m distributed RVs $\frac{h\sqrt{P_s}}{\sigma}$ and $\frac{g\sqrt{P_v}}{\sigma}$ with local mean received powers of $\tilde{\Omega}_1 = \frac{\bar{h}_s P_s}{\sigma^2}$ and $\tilde{\Omega}_2 = \frac{\bar{g}_s P_v}{\sigma^2}$, respectively. Employing (Karagiannidis *et al.*, 2007, eq. (4)) for $N = 2$, the PDF of Y_3 becomes

$$f_{Y_3}(y) = \frac{2y^{-1}}{\prod_{j=1}^{2}(m_j - 1)!} G_{0,2}^{2,0}\left(y^2 \prod_{j=1}^{2} \left(\frac{m_j}{\tilde{\Omega}_j} \right) \Bigg|_{m_1, m_2}^{-} \right). \tag{A III-29}$$

Recognizing that $\tilde{\Omega}_1$ and $\tilde{\Omega}_2$ are, respectively, the ratio of the average SOI power and the average RFI power to the noise power, $\tilde{\Omega}_1 = \bar{\gamma}_{snr}$ and $\tilde{\Omega}_2 = \bar{\gamma}_{inr}$. In addition, the PDF in (A III-29) is a non-negative function (Karagiannidis *et al.*, 2006b). Hence, it can be further expressed as

$$f_{Y_3}(y) = \frac{2y^{-1}}{(m_1 - 1)!(m_2 - 1)!} G_{0,2}^{2,0}\left(\frac{y^2}{\eta_1 \eta_2} \Bigg|_{m_1, m_2}^{-} \right) U(y). \tag{A III-30}$$

Once $f_{Y_3}(y)$ and $P_{Y_4}(r)$ are obtained, $f_{X|Y_4}(x|Y_4 = r^-)$ and $f_{X|Y_4}(x|Y_4 = r^+)$ can be derived by using the total probability theorem (Bertsekas & Tsitsiklis, 2008, p. 28) for $r < 0$ and $r > 0$, respectively. To derive these PDFs, we resort to the derivation of the CDF of X and apply derivative afterward. Employing the definition of CDF (Bertsekas & Tsitsiklis, 2008, p. 148),

$$F_{X|Y_4}(x|Y_4 = r^+) = \Pr\{Y_3 r \leq x\} = F_{Y_3}(x/r). \tag{A III-31}$$

Differentiating (A III-31) w.r.t. x yields

$$f_{X|Y_4}(x|Y_4 = r^+) = f_{Y_3}(x/r)/r. \tag{A III-32}$$

Similarly, for $r < 0$ ($|r| = -r$),

$$F_{X|Y_4}(x|Y_4 = r^-) = \Pr\{-Y_3|r| \leq x\} \tag{A III-33a}$$

$$= \Pr\big\{-Y_3 \leq x/|r|\big\} = F_{-Y_3}(x/|r|). \tag{A III-33b}$$

Differentiating (A III-33b) w.r.t. x results in

$$f_{X|Y_4}(x|Y_4 = r^-) = f_{-Y_3}(x/|r|)/|r| \tag{A III-34a}$$

$$\overset{(a)}{=} \frac{1}{|-1|} f_{Y_3}(x/-|r|)/|r| = \frac{f_{Y_3}(x/r)}{|r|}, \tag{A III-34b}$$

where (a) follows from the PDF relation (Bertsekas & Tsitsiklis, 2008, p. 205) for $-Y_3 = -1 \times Y_3$. Utilizing (A III-32) and (A III-34b) in (A III-25),

$$f_Z(z) \approx f_Y(z) P_{Y_4}(0) + \sum_{r \in \mathscr{M}^+} \frac{P_{Y_4}(r)}{r} \int_{-\infty}^{\infty} f_{Y_3}(x/r) f_Y(z-x) dx + \sum_{r \in \mathscr{M}^-} \frac{P_{Y_4}(r)}{|r|} \int_{-\infty}^{\infty} f_Y(x) f_{Y_3}((x-z)/r) dx. \tag{A III-35}$$

From (A III-28), $f_Y(z-x)$ is a non-negative function with a support, w.r.t. x, of $[0, z]$ whenever $r > 0$. From (A III-30), $f_{Y_3}((x-z)/r)$ is also a non-negative function with a support, w.r.t. x,

of $[-z,0]$. As a result,

$$f_Z(z) \approx f_Y(z)P_{Y_4}(0) + \sum_{r\in\mathscr{M}^+} \frac{P_{Y_4}(r)}{r} \int_0^z f_{Y_3}(x/r) f_Y(z-x)dx + \sum_{r\in\mathscr{M}^-} \frac{P_{Y_4}(r)}{|r|} \int_{-z}^0 f_Y(x) f_{Y_3}((x-z)/r)dx. \quad \text{(A III-36)}$$

Meanwhile, substituting (A III-26) into (A III-27) produces the expression

$$f_Y(y) = \sum_{i=1}^{2} \sum_{k=1}^{m_i} \Xi_{\eta_1\eta_2}^{m_1 m_2}(i,k) \frac{y^{k-1}}{\eta_i^k (k-1)!} e^{-\frac{y}{\eta_i}} U(y). \quad \text{(A III-37)}$$

Substituting (A III-37) into (A III-36) results in (A III-38).

$$f_Z(z) \approx f_Y(z)P_{Y_4}(0) + \sum_{r\in\mathscr{M}^+} \sum_{i=1}^{2} \sum_{k=1}^{m_i} \frac{P_{Y_4}(r)\Xi_{\eta_1\eta_2}^{m_1 m_2}(i,k)}{r} \underbrace{\int_0^z f_{Y_3}(x/r) \frac{(z-x)^{k-1} e^{-\frac{z-x}{\eta_i}}}{\eta_i^k (k-1)!} dx}_{I_1} + \sum_{r\in\mathscr{M}^-} \sum_{i=1}^{2} \sum_{k=1}^{m_i} \frac{P_{Y_4}(r)\Xi_{\eta_1\eta_2}^{m_1 m_2}(i,k)}{|r|} \underbrace{\int_{-z}^0 \frac{x^{k-1} e^{-\frac{x}{\eta_i}}}{\eta_i^k (k-1)!} f_{Y_3}((x-z)/r)dx}_{I_2}. \quad \text{(A III-38)}$$

As $f_{Y_3}(y)$ in (A III-30) is a product of a power function and the Meijer G-function (Gradshteyn & Ryzhik, 2007, eq. (9.301)), I_1 and I_2—of (A III-38)—are convolutions between the gamma distribution, and the product of a power function and the Meijer G-function. To the best of our knowledge, the solutions of these integrals have never been reported in any mathematical book nor website. Thus, we offer the solutions, as detailed in the underneath lemma.

Lemma 5.

$$I_1 = \int_0^z f_{Y_3}(x/r) \frac{(z-x)^{k-1} e^{-\frac{z-x}{\eta_i}}}{\eta_i^k (k-1)!} dx = f_{Y_3}(z/r) \quad \text{(A III-39a)}$$

$$I_2 = \int_{-z}^0 \frac{x^{k-1} e^{-\frac{x}{\eta_i}}}{\eta_i^k (k-1)!} f_{Y_3}((x-z)/r)dx = f_{Y_3}(z/|r|). \quad \text{(A III-39b)}$$

Proof. To solve the aforementioned integrals, we start by recapping the partial differentiation of the (upper) incomplete gamma function (Wolfram Research Inc., Jan. 2002, eq. (06.06.20.0003.01)). Thus,

$$\frac{\partial \Gamma(a,z)}{\partial z} = -e^{-z} z^{a-1}. \tag{A III-40}$$

Using (A III-40) and the chain rule of differentiation,

$$\frac{\partial \Gamma(k,(z-x)/\eta_i)}{\partial x} = e^{-\frac{z-x}{\eta_i}} \frac{(z-x)^{k-1}}{\eta_i^k}. \tag{A III-41}$$

Deploying (A III-41) in (A III-39a) gives

$$I_1 = \int_0^z \frac{\partial \Gamma(k,(z-x)/\eta_i)}{\partial x} \frac{f_{Y_3}(x/r)}{(k-1)!} dx. \tag{A III-42}$$

Employing the definition in (Woods, 1934, eq. (1), p. 66), it can be inferred that

$$\frac{\partial \Gamma(k,(z-x)/\eta_i)}{\partial x} = \lim_{\Delta x \to 0} \frac{\Gamma\left(k, \frac{z-x+\Delta x)}{\eta_i}\right) - \Gamma\left(k, \frac{z-x}{\eta_i}\right)}{\Delta x}. \tag{A III-43}$$

Substituting (A III-43) into (A III-42) and exchanging the limit and integral operations result in

$$I_1 = \lim_{\Delta x \to 0} \frac{1}{\Delta x} \left[\int_0^z \Gamma(k,(z+\Delta x-x)/\eta_i) \frac{f_{Y_3}(x/r)}{(k-1)!} dx - \int_0^z \Gamma(k,(z-x)/\eta_i) \frac{f_{Y_3}(x/r)}{(k-1)!} dx \right]. \tag{A III-44}$$

To surmount the $z+\Delta x$ term in (A III-44), (A III-44) can be written as

$$I_1 = \lim_{\Delta x \to 0} \frac{1}{\Delta x} \left[\int_{\Delta x}^{z+\Delta x} \Gamma(k,(z-x)/\eta_i) \frac{f_{Y_3}(x/r)}{(k-1)!} dx - \int_0^z \Gamma(k,(z-x)/\eta_i) \frac{f_{Y_3}(x/r)}{(k-1)!} dx \right]. \tag{A III-45}$$

As Δx is very close to zero, (A III-45) can be simplified to

$$I_1 = \lim_{\Delta x \to 0} \frac{1}{\Delta x} \left[\int_0^{z+\Delta x} \frac{\Gamma(k,(z-x)/\eta_i)}{(k-1)!} f_{Y_3}(x/r)dx - \int_0^{z} \frac{\Gamma(k,(z-x)/\eta_i)}{(k-1)!} f_{Y_3}(x/r)dx \right]. \quad \text{(A III-46)}$$

Considering the integrals in (A III-46) as a two-variable function of the integration limits and deploying the aforementioned definition of a partial derivative, (A III-46) is the partial derivative of the integral w.r.t. z. Thus,

$$I_1 = \frac{\partial}{\partial z} \int_0^{z} \frac{\Gamma(k,(z-x)/\eta_i)}{(k-1)!} f_{Y_3}(x/r)dx. \quad \text{(A III-47)}$$

It is straightforward to observe that the derivative of the integral is its integrand. Following (Woods, 1934, eq. (1), p. 141),

$$I_1 = \left. \frac{\Gamma\left(k, \frac{z-x}{\eta_i}\right) f_{Y_3}(x/r)}{(k-1)!} \right|_{x=z} = \frac{\Gamma(k,0) f_{Y_3}(z/r)}{(k-1)!}. \quad \text{(A III-48)}$$

Recalling that $\Gamma(k,0) = \Gamma(k) = (k-1)!$ for k is an integer,

$$I_1 = f_{Y_3}(z/r). \quad \text{(A III-49)}$$

To continue, letting $t = x - z$ ($x = t + z$), $dt = dx$ and

$$I_2 = \int_{-2z}^{-z} \frac{(t+z)^{k-1}}{\eta_i^k (k-1)!} e^{-\frac{t+z}{\eta_i}} f_{Y_3}(t/r)dt \quad \text{(A III-50a)}$$

$$= -\int_{-2z}^{-z} \frac{(t+z)^{k-1}}{\eta_i^k (k-1)!} e^{-\frac{t+z}{\eta_i}} f_{Y_3}(t/r)dt. \quad \text{(A III-50b)}$$

Employing (A III-40),

$$\frac{\partial \Gamma(k,(t+z)/\eta_i)}{\partial t} = -e^{-\frac{t+z}{\eta_i}} \left(\frac{t+z}{\eta_i} \right)^{k-1} \times \frac{1}{\eta_i}. \quad \text{(A III-51)}$$

Substituting (A III-51) into (A III-50b) and adopting identical procedures as in (A III-43)-(A III-46) render

$$I_2 = -\int_{-2z}^{-z} \frac{\partial \Gamma(k,(t+z)/\eta_i)}{\partial t} \frac{f_{Y_3}\left(\frac{t}{r}\right)}{(k-1)!} dt \tag{A III-52a}$$

$$= -\frac{\partial}{\partial(-z)} \int_{-2z}^{-z} \frac{\Gamma(k,(t+z)/\eta_i)}{(k-1)!} f_{Y_3}\left(\frac{t}{r}\right) dt \tag{A III-52b}$$

$$= -\frac{\partial}{\partial(-z)} \int_{-2z}^{-z} \frac{\Gamma(k,(t-(-z))/\eta_i)}{(k-1)!} f_{Y_3}\left(\frac{t}{r}\right) dt \tag{A III-52c}$$

$$= \left[\frac{\partial}{\partial c} \int_{2c}^{c} \frac{\Gamma(k,(t-c)/\eta_i)}{(k-1)!} f_{Y_3}\left(\frac{t}{r}\right) dt\right]_{c=-z} \tag{A III-52d}$$

$$= \left[\frac{\Gamma(k,(t-c)/\eta_i)}{(k-1)!} f_{Y_3}\left(\frac{t}{r}\right)\Big|_{t=c}\right]_{c=-z} \tag{A III-52e}$$

$$= \left[\frac{\Gamma(k,0)}{(k-1)!} f_{Y_3}\left(\frac{c}{r}\right)\right]_{c=-z} = f_{Y_3}(z/|r|). \tag{A III-52f}$$

□

Using Lemma 5, (A III-30), and realizing that $U(z/r) = U(z)$ for $r > 0$,

$$I_1 = \frac{2r}{z(m_1-1)!(m_2-1)!} G_{0,2}^{2,0}\left(\frac{z^2}{\eta_1\eta_2 r^2}\Big|_{m_1,m_2}^{-}\right) U(z) \tag{A III-53a}$$

$$I_2 = \frac{2|r|}{z(m_1-1)!(m_2-1)!} G_{0,2}^{2,0}\left(\frac{z^2}{\eta_1\eta_2 r^2}\Big|_{m_1,m_2}^{-}\right) U(z). \tag{A III-53b}$$

Substituting (A III-28), (A III-53a), and (A III-53b) into (A III-38) results in (A III-54).

$$f_Z(z) \approx \sum_{i=1}^{2}\sum_{k=1}^{m_i} \Xi_{\eta_1\eta_2}^{m_1 m_2}(i,k)\left[\frac{z^{k-1}e^{-\frac{z}{\eta_i}} P_{Y_4}(0)}{\eta_i^k (k-1)!} + \sum_{r\in\mathscr{M}\setminus\{0\}} \frac{2P_{Y_4}(r) G_{0,2}^{2,0}\left(\frac{z^2}{\eta_1\eta_2 r^2}\Big|_{m_1,m_2}^{-}\right)}{z(m_1-1)!(m_2-1)!}\right] U(z). \tag{A III-54}$$

The PDF of ρ, $f_P(\rho)$, can now be inferred from $f_Z(z)$ given by (A III-54). From (A III-10), $\rho = 2Z$. As a result (Bertsekas & Tsitsiklis, 2008, p. 205),

$$f_P(\rho) = \frac{1}{2} f_Z(\rho/2). \tag{A III-55}$$

Finally, substituting (A III-54) into (A III-55) and realizing that $U(\rho/2) = U(\rho)$ result in (3.10). □

3. Proof of Remark 2

From (A III-5), we note that ρ is non-negative. Hence, the RHS of (3.10)—denoted by $\tilde{f}_P(\rho)$—is non-negative for all ρ since $U(\rho) = 0$ for $\rho < 0$. Meanwhile, $\tilde{f}_P(\rho)$ will be a valid PDF iff $\int_0^\infty \tilde{f}_P(\rho) d\rho = 1$. Deploying (3.10),

$$\int_0^\infty \tilde{f}_P(\rho) d\rho = \sum_{i=1}^{2} \sum_{k=1}^{m_i} \frac{\Xi_{\eta_1\eta_2}^{m_1 m_2}(i,k) P_{Y_4}(0)}{(2\eta_i)^k (k-1)!} \times \int_0^\infty \rho^{k-1} e^{-\frac{\rho}{2\eta_i}} d\rho + \sum_{r \in \mathscr{M} \setminus \{0\}} \sum_{i=1}^{2} \sum_{k=1}^{m_i} P_{Y_4}(r) \times \frac{\Xi_{\eta_1\eta_2}^{m_1 m_2}(i,k)}{(m_1-1)!(m_2-1)!} \underbrace{\int_0^\infty \frac{2}{\rho} G_{0,2}^{2,0}\left(\frac{\rho^2}{4\eta_1\eta_2 r^2} \middle|_{m_1,m_2}^{-} \right) d\rho}_{I(\rho)}. \tag{A III-56}$$

With the aid of (Gradshteyn & Ryzhik, 2007, eq. (3.381.3)) and for integer k,

$$\int_0^\infty \rho^{k-1} e^{-\frac{\rho}{2\eta_i}} d\rho = (2\eta_i)^k \Gamma(k,0) = (2\eta_i)^k (k-1)!. \tag{A III-57}$$

Letting $t = \rho^2$, $dt = 2\rho d\rho$, $d\rho = \frac{dt}{2\rho}$, and

$$I(\rho) = \int_0^\infty \frac{1}{t} G_{0,2}^{2,0}\left(\frac{t}{4\eta_1\eta_2 r^2} \middle|_{m_1,m_2}^{-} \right) dt \tag{A III-58a}$$

$$\overset{(a)}{=} \Gamma(m_1)\Gamma(m_2) \overset{(b)}{=} (m_1-1)!(m_2-1)!, \tag{A III-58b}$$

where (a) follows through the aid of (Adamchik & Marichev, 1990, eq. (24)) and (b) follows for the integerness of $\{m_i\}_{i=1}^2$.

Substituting (A III-57) and (A III-58b) into (A III-56) results in

$$\int_0^{\infty} \tilde{f}_P(\rho)d\rho = \sum_{i=1}^{2}\sum_{k=1}^{m_i} \Xi_{\eta_1\eta_2}^{m_1 m_2}(i,k) \times \left[P_{Y_4}(0) + \sum_{r\in\mathscr{M}\setminus\{0\}} P_{Y_4}(r)\right]. \tag{A III-59}$$

From a valid gamma distribution-based PDF defined in (A III-27), $\Xi_{\eta_1\eta_2}^{m_1 m_2}(i,k)$ satisfies the constraint: $\sum_{i=1}^{2}\sum_{k=1}^{m_i} \Xi_{\eta_1\eta_2}^{m_1 m_2}(i,k) = 1$. As a result,

$$\int_0^{\infty} \tilde{f}_P(\rho)d\rho = \sum_{r\in\mathscr{M}} P_{Y_4}(r) \overset{(c)}{=} 1, \tag{A III-60}$$

where (c) follows for the sum of a PMF over its support is 1 (Bertsekas & Tsitsiklis, 2008, p. 75). Therefore, the RHS of $f_P(\rho)$ is a valid PDF. □

4. Proof of Theorem 5

Deploying (Simon & Alouini, 2005, eq. (4.63)) in (3.11) and employing $\int_0^{\infty} f_P(\rho)d\rho = \int_0^{\infty} \tilde{f}_P(\rho)d\rho = 1$,

$$\bar{P}_d \approx 1 - e^{-\frac{\lambda}{2}} \sum_{n=u}^{\infty} \lambda^{\frac{n}{2}} \int_0^{\infty} e^{-\frac{\rho}{2}} \rho^{-\frac{n}{2}} I_n(\sqrt{\rho\lambda}) f_P(\rho)d\rho. \tag{A III-61}$$

Supposing $t = \sqrt{\rho\lambda}$, $\rho = t^2/\lambda$, $d\rho = \frac{2t}{\lambda}dt$, and

$$\bar{P}_d \approx 1 - 2e^{-\frac{\lambda}{2}} \sum_{n=u}^{\infty} \lambda^{n-1} \int_0^{\infty} e^{-\frac{t^2}{2\lambda}} t^{-n+1} I_n(t) f_P\left(\frac{t^2}{\lambda}\right)dt. \tag{A III-62}$$

Substituting the series representation of $I_n(t)$ (Jeffrey & Dai, 2008, eq. (17.7.1.1-3)) into (A III-62) and simplifying,

$$\bar{P}_d \approx 1 - \sum_{n=u}^{\infty}\sum_{l=0}^{\infty} \frac{2e^{-\frac{\lambda}{2}}\lambda^{n-1}}{2^{n+2l} l!(n+l)!} \int_0^{\infty} t^{2l+1} e^{-\frac{t^2}{2\lambda}} f_P\left(\frac{t^2}{\lambda}\right)dt. \tag{A III-63}$$

Substituting (3.10) into (A III-63) results in (A III-64).

$$\bar{P}_d \approx 1-2e^{-\frac{\lambda}{2}}\sum_{n=u}^{\infty}\sum_{l=0}^{\infty}\sum_{i=1}^{2}\sum_{k=1}^{m_i}\frac{\lambda^n \Xi_{\eta_1\eta_2}^{m_1m_2}(i,k)}{2^{n+2l}l!(n+l)!}\Bigg[\frac{P_{Y_4}(0)}{(2\lambda\eta_i)^k(k-1)!}\underbrace{\int_0^{\infty}t^{2l+2k-1}e^{-\frac{t^2(1+\eta_i)}{2\eta_i\lambda}}dt}_{I_3}$$
$$+\frac{2}{(m_1-1)!(m_2-1)!}\sum_{r\in\mathscr{M}\setminus\{0\}}P_{Y_4}(r)\underbrace{\int_0^{\infty}t^{2l-1}e^{-\frac{t^2}{2\lambda}}G_{0,2}^{2,0}\left(\frac{t^4}{4\eta_1\eta_2\lambda^2r^2}\Bigg|_{m_1,m_2}^{-}\right)dt}_{I_4}\Bigg]. \quad \text{(A III-64)}$$

To simplify (A III-64), we let $v=t^2$. Consequently, $dv=2tdt$, $\frac{dv}{2v^{1/2}}=dt$, and

$$I_3=\frac{1}{2}\int_0^{\infty}v^{l+k-1}e^{-\frac{v(1+\eta_i)}{2\eta_i\lambda}}dv \quad \text{(A III-65a)}$$
$$\overset{(d)}{=}\frac{\Gamma(l+k,0)}{2}\left(\frac{2\eta_i\lambda}{1+\eta_i}\right)^{l+k} \quad \text{(A III-65b)}$$
$$=\frac{(l+k-1)!}{2}\left(\frac{2\eta_i\lambda}{1+\eta_i}\right)^{l+k}, \quad \text{(A III-65c)}$$

where (d) follows with the aid of (Gradshteyn & Ryzhik, 2007, eq. (3.381.3)). Recalling $v=t^2$, $dv=2tdt$ and $\frac{dv}{2v^{1/2}}=dt$,

$$I_4=\frac{1}{2}\int_0^{\infty}v^{l-1}e^{-\frac{v}{2\lambda}}G_{0,2}^{2,0}\left(\frac{v^2}{4\eta_1\eta_2\lambda^2r^2}\Bigg|_{m_1,m_2}^{-}\right)dv \quad \text{(A III-66a)}$$
$$\overset{(e)}{=}\frac{2^{2l}\lambda^l}{4\sqrt{\pi}}G_{2,2}^{2,2}\left(\frac{4}{\eta_1\eta_2r^2}\Bigg|_{m_1,m_2}^{\frac{1-l}{2},\frac{2-l}{2}}\right), \quad \text{(A III-66b)}$$

where (e) follows with the aid of (Wolfram Research Inc., Feb. 2007, eq. (07.34.21.0088.01)). Eventually, substituting (A III-65c) and (A III-66b) into (A III-64) and rearranging render (3.12). □

5. Remarks on the State-of-the-art RFI Detectors

The MR detector of (De Roo & Misra, 2010) relies on a huge number of samples to invoke the Gaussian approximation which signifies its sub-optimality in sample starved settings. The authors of (Balaei & Dempster, 2009) assume the GPS signal to be a real, bandpass, zero mean, and wide-sense stationary Gaussian process (see (Balaei & Dempster, 2009, Sec. III)); a hardly practical assumption which underscores the sub-optimality of the technique. By neglecting the impact of the GNSS signal, it appears in (Borio *et al.*, 2008, Appendix A) that the spectrogram test statistic in the absence of interference exhibits the central χ^2–distribution—employed to derive the FAR expression—which implicates a sub-optimality whenever the SNR is greater than zero. The distribution of the DWVD test statistic in the absence of RFI is approximated via the Gaussian distribution rendering a sub-optimal detection scheme proposed also by the authors of (Borio *et al.*, 2008). Finally, since the transformed-domain techniques (Dovis *et al.*, 2012; Musumeci & Dovis, 2012) didn't exploit any explicit test statistic so as to detect an RFI, they tend to be heuristic and hence sub-optimal techniques.

APPENDIX IV

APPENDICES OF CHAPTER 4

1. Proof of Theorem 6

Recalling the equivalent test statistic given by (4.14),

$$T_{\text{eq}} = \frac{\nu_2}{\nu_1} \frac{\text{tr}(\hat{\boldsymbol{P}}_2 \hat{\boldsymbol{R}}_{yy}^{(p)})}{\text{tr}\big((\boldsymbol{I}_{N_R} - \hat{\boldsymbol{P}}_2)\hat{\boldsymbol{R}}_{yy}^{(p)}\big)}. \tag{A IV-1}$$

Substituting (4.9b) into (A IV-1) and exploiting $\text{tr}(\boldsymbol{AB}) = \text{tr}(\boldsymbol{BA})$ (Magnus & Neudecker, 2007),

$$T_{\text{eq}} = \frac{\nu_2}{\nu_1} \frac{\text{tr}(\hat{\boldsymbol{P}}_2 \hat{\boldsymbol{P}}_{2:N_R} \hat{\boldsymbol{R}}_{yy} \hat{\boldsymbol{P}}_{2:N_R}^H)}{\text{tr}\big((\boldsymbol{I}_{N_R} - \hat{\boldsymbol{P}}_2)\hat{\boldsymbol{P}}_{2:N_R} \hat{\boldsymbol{R}}_{yy} \hat{\boldsymbol{P}}_{2:N_R}^H\big)} \tag{A IV-2a}$$

$$= \frac{\nu_2}{\nu_1} \frac{\text{tr}(\hat{\boldsymbol{P}}_{2:N_R}^H \hat{\boldsymbol{P}}_2 \hat{\boldsymbol{P}}_{2:N_R} \hat{\boldsymbol{R}}_{yy})}{\text{tr}\big((\boldsymbol{I}_{N_R} - \hat{\boldsymbol{P}}_2)\hat{\boldsymbol{P}}_{2:N_R} \hat{\boldsymbol{R}}_{yy} \hat{\boldsymbol{P}}_{2:N_R}^H\big)} \tag{A IV-2b}$$

$$= \frac{\nu_2}{\nu_1} \frac{\text{tr}(\hat{\boldsymbol{P}}_{2:N_R}^H \hat{\boldsymbol{P}}_2 \hat{\boldsymbol{P}}_{2:N_R} \hat{\boldsymbol{R}}_{yy})}{\text{tr}\big(\hat{\boldsymbol{P}}_{2:N_R}^H (\boldsymbol{I}_{N_R} - \hat{\boldsymbol{P}}_2)\hat{\boldsymbol{P}}_{2:N_R} \hat{\boldsymbol{R}}_{yy}\big)}. \tag{A IV-2c}$$

To continue, we hereinafter simplify the arguments of the numerator and denominator of the RHS of (A IV-2c). Employing (4.9a) and (4.12), and the fact that the projection matrices $\hat{\boldsymbol{P}}_2$ and $\hat{\boldsymbol{P}}_{2:N_R}$ are Hermitian—$\hat{\boldsymbol{P}}_2 = \hat{\boldsymbol{P}}_2^H$ and $\hat{\boldsymbol{P}}_{2:N_R} = \hat{\boldsymbol{P}}_{2:N_R}^H$—and idempotent—$\hat{\boldsymbol{P}}_2\hat{\boldsymbol{P}}_2 = \hat{\boldsymbol{P}}_2$ and $\hat{\boldsymbol{P}}_{2:N_R}\hat{\boldsymbol{P}}_{2:N_R} = \hat{\boldsymbol{P}}_{2:N_R}$ (Strang, 2003),

$$\hat{\boldsymbol{P}}_{2:N_R}^H \hat{\boldsymbol{P}}_2 \hat{\boldsymbol{P}}_{2:N_R} = \hat{\boldsymbol{U}}_{2:N_R} \hat{\boldsymbol{U}}_{2:N_R}^H \big[\hat{\boldsymbol{U}}_{2:N_R}(:,1)\hat{\boldsymbol{U}}_{2:N_R}^H(:,1)\big] \hat{\boldsymbol{U}}_{2:N_R} \hat{\boldsymbol{U}}_{2:N_R}^H \tag{A IV-3a}$$

$$\overset{(a)}{=} \hat{\boldsymbol{U}}_{2:N_R} \big[1 \;\; \boldsymbol{0}_{1\times(N_R-2)}\big]^H \big[1 \;\; \boldsymbol{0}_{1\times(N_R-2)}\big] \hat{\boldsymbol{U}}_{2:N_R}^H \tag{A IV-3b}$$

$$\overset{(b)}{=} \hat{\boldsymbol{U}}_{2:N_R}(:,1)\hat{\boldsymbol{U}}_{2:N_R}^H(:,1) = \hat{\boldsymbol{U}}(:,2)\hat{\boldsymbol{U}}^H(:,2) = \hat{\boldsymbol{P}}_2, \tag{A IV-3c}$$

where (a) and (b) follow from the orthonormal columns of $\hat{\boldsymbol{U}}$. By the same fashion, employing (A IV-3c), (4.9a), and (4.12):

$$\hat{\boldsymbol{P}}_{2:N_R}^H(\boldsymbol{I}_{N_R}-\hat{\boldsymbol{P}}_2)\hat{\boldsymbol{P}}_{2:N_R} = \hat{\boldsymbol{P}}_{2:N_R}^H\hat{\boldsymbol{P}}_{2:N_R} - \hat{\boldsymbol{P}}_{2:N_R}^H\hat{\boldsymbol{P}}_2\hat{\boldsymbol{P}}_{2:N_R} \tag{A IV-4a}$$

$$= \hat{\boldsymbol{P}}_{2:N_R} - \hat{\boldsymbol{P}}_2 \tag{A IV-4b}$$

$$= \hat{\boldsymbol{U}}_{2:N_R}\hat{\boldsymbol{U}}_{2:N_R}^H - \hat{\boldsymbol{U}}_{2:N_R}(:,1)\hat{\boldsymbol{U}}_{2:N_R}^H(:,1) \tag{A IV-4c}$$

$$\overset{(c)}{=} \left[\boldsymbol{I}_{N_R} - \hat{\boldsymbol{U}}(:,1)\hat{\boldsymbol{U}}^H(:,1)\right] - \hat{\boldsymbol{U}}(:,2)\hat{\boldsymbol{U}}^H(:,2) \tag{A IV-4d}$$

$$\overset{(d)}{=} \boldsymbol{I}_{N_R} - \hat{\boldsymbol{U}}(:,1:2)\hat{\boldsymbol{U}}^H(:,1:2) \tag{A IV-4e}$$

$$= \hat{\boldsymbol{U}}(:,3:N_R)\hat{\boldsymbol{U}}^H(:,3:N_R) = \hat{\boldsymbol{P}}_{3:N_R}, \tag{A IV-4f}$$

where (c) is because of the orthonormal columns of $\hat{\boldsymbol{U}}$ leading to the relationship that $\hat{\boldsymbol{U}}(:,1)\hat{\boldsymbol{U}}^H(:,1)+\hat{\boldsymbol{U}}(:,2:N_R)\hat{\boldsymbol{U}}^H(:,2:N_R) = \boldsymbol{I}_{N_R}$ and (4.12); (d) follows by noticing that $\hat{\boldsymbol{U}}(:,1:2) = \left[\hat{\boldsymbol{U}}(:,1)\ \ \hat{\boldsymbol{U}}(:,2)\right]$.

Following the aforementioned simplifications, substituting (A IV-3c) and (A IV-4f) into (A IV-2c),

$$T_{\text{eq}} = \frac{\text{tr}(\hat{\boldsymbol{P}}_2\hat{\boldsymbol{R}}_{yy})/\nu_1\sigma^2}{\text{tr}\left(\hat{\boldsymbol{P}}_{3:N_R}\hat{\boldsymbol{R}}_{yy}\right)/\nu_2\sigma^2}, \tag{A IV-5}$$

where division by σ^2 is accommodated into the numerator and denominator, as it brings no difference to the underlying statistic. Meanwhile, substituting (4.5) into (A IV-5) and applying the properties of trace (Magnus & Neudecker, 2007, p. 11) recursively,

$$T_{\text{eq}} = \frac{\text{tr}\left(\hat{\boldsymbol{P}}_2\sum_{k=1}^{N}\boldsymbol{y}[k]\boldsymbol{y}^H[k]\right)/\nu_1\sigma^2}{\text{tr}\left(\hat{\boldsymbol{P}}_{3:N_R}\sum_{k=1}^{N}\boldsymbol{y}[k]\boldsymbol{y}^H[k]\right)/\nu_2\sigma^2} = \frac{\text{tr}\left(\sum_{k=1}^{N}\hat{\boldsymbol{P}}_2\boldsymbol{y}[k]\boldsymbol{y}^H[k]\right)/\nu_1\sigma^2}{\text{tr}\left(\sum_{k=1}^{N}\hat{\boldsymbol{P}}_{3:N_R}\boldsymbol{y}[k]\boldsymbol{y}^H[k]\right)/\nu_2\sigma^2}. \tag{A IV-6}$$

Moreover,

$$T_{\text{eq}} = \frac{\sum_{k=1}^{N} \text{tr}\Big(\hat{\boldsymbol{P}}_2 \boldsymbol{y}[k]\boldsymbol{y}^H[k]\Big)/\nu_1\sigma^2}{\sum_{k=1}^{N} \text{tr}\Big(\hat{\boldsymbol{P}}_{3:N_R} \boldsymbol{y}[k]\boldsymbol{y}^H[k]\Big)/\nu_2\sigma^2} = \frac{\sum_{k=1}^{N} \text{tr}\Big(\boldsymbol{y}^H[k]\hat{\boldsymbol{P}}_2 \boldsymbol{y}[k]\Big)/\nu_1\sigma^2}{\sum_{k=1}^{N} \text{tr}\Big(\boldsymbol{y}^H[k]\hat{\boldsymbol{P}}_{3:N_R} \boldsymbol{y}[k]\Big)/\nu_2\sigma^2} \tag{A IV-7a}$$

$$\overset{(e)}{=} \frac{\sum_{k=1}^{N} \boldsymbol{y}^H[k]\hat{\boldsymbol{P}}_2 \boldsymbol{y}[k]/\nu_1\sigma^2}{\sum_{k=1}^{N} \boldsymbol{y}^H[k]\hat{\boldsymbol{P}}_{3:N_R} \boldsymbol{y}[k]/\nu_2\sigma^2} \overset{(f)}{=} \frac{\sum_{k=1}^{N} \boldsymbol{y}^H[k]\hat{\boldsymbol{U}}(:,2)\hat{\boldsymbol{U}}^H(:,2)\boldsymbol{y}[k]/\nu_1\sigma^2}{\sum_{k=1}^{N} \boldsymbol{y}^H[k]\hat{\boldsymbol{U}}(:,3:N_R)\hat{\boldsymbol{U}}^H(:,3:N_R)\boldsymbol{y}[k]/\nu_2\sigma^2}, \tag{A IV-7b}$$

where (e) follows from the fact that the trace of a 1×1 matrix is itself and (f) follows from (A IV-3c) and (A IV-4f). To continue, let

$$a_k = \sigma^{-1}\hat{\boldsymbol{U}}^H(:,2)\boldsymbol{y}[k] \in \mathbb{C} \tag{A IV-8a}$$

$$\boldsymbol{b}_k = \sigma^{-1}\hat{\boldsymbol{U}}^H(:,3:N_R)\boldsymbol{y}[k] \in \mathbb{C}^{(N_R-2)}. \tag{A IV-8b}$$

Plugging (A IV-8a) and (A IV-8b) into the RHS of (A IV-7b) then leads to

$$T_{\text{eq}} = \frac{\frac{1}{\nu_1}\sum_{k=1}^{N} a_k^H a_k}{\frac{1}{\nu_2}\sum_{k=1}^{N} \boldsymbol{b}_k^H \boldsymbol{b}_k} \tag{A IV-9a}$$

$$= \frac{\frac{1}{\nu_1}\sum_{k=1}^{N} a_k^H a_k}{\frac{1}{\nu_2}\sum_{k=1}^{N}\sum_{j=1}^{N_R-2} \boldsymbol{b}_k^H[j]\boldsymbol{b}_k[j]}, \tag{A IV-9b}$$

where $\boldsymbol{b}_k[j] = \sigma^{-1}\hat{\boldsymbol{U}}^H(:,2+j)\boldsymbol{y}[k]$. By exploiting (A IV-9b) for infinitely huge samples, it is now time to determine the distribution of T_{eq} for the underneath three cases.

Case 1. $(\gamma_{snr},\gamma_{inr}) = (0,0)$: this condition implies that neither the SOI nor the RFI is received by the receiving antennas. For this scenario, $a_k = \sigma^{-1}\hat{\boldsymbol{U}}^H(:,2)\boldsymbol{z}[k]$ and $\boldsymbol{b}_k = \sigma^{-1}\hat{\boldsymbol{U}}^H(:,3:N_R)\boldsymbol{z}[k]$. Employing the properties of mean and variance (Seber, 2003; Gallager, 2013; Papoulis & Pillai, 2002), as $\boldsymbol{z}[k] \sim \mathscr{CN}_{N_R}(\boldsymbol{0},\sigma^2\boldsymbol{I}_{N_R})$, $\mathbb{E}\{a_k\} = \sigma^{-1}\mathbb{E}\{\hat{\boldsymbol{U}}^H(:,2)\boldsymbol{z}[k]\} = \sigma^{-1}\hat{\boldsymbol{U}}^H(:,2)\boldsymbol{0}_{N_R\times 1} = 0$; $\text{Var}\{a_k\} = \frac{1}{\sigma^2}\hat{\boldsymbol{U}}^H(:,2)\sigma^2\hat{\boldsymbol{U}}(:,2) = \hat{\boldsymbol{U}}^H(:,2)\hat{\boldsymbol{U}}(:,2) = 1$. Hence, $a_k \sim \mathscr{CN}_1(0,1)$.

Deploying the properties of mean and variance (Seber, 2003; Gallager, 2013; Papoulis & Pillai, 2002), similarly, $\boldsymbol{b}_k \sim \mathscr{CN}_{(N_R-2)}(\mathbf{0}, \boldsymbol{I}_{(N_R-2)})$.

Since $a_k \sim \mathscr{CN}_1(0,1)$, $\mathrm{Re}\{a_k\} \sim \mathscr{N}_1(0,1)$ $\left(\equiv \left[\mathrm{Re}\{a_k\}\right]^2 \sim \chi_1^2 \right)$, $\mathrm{Im}\{a_k\} \sim \mathscr{N}_1(0,1)$ $\left(\equiv \left[\mathrm{Im}\{a_k\}\right]^2 \sim \chi_1^2 \right)$, and it shall be recalled that $a_k^H a_k = \left[\mathrm{Re}\{a_k\}\right]^2 + \left[\mathrm{Im}\{a_k\}\right]^2$. As a result, for the independence of the constituent terms, $a_k^H a_k \sim \chi_2^2$ and hence $\sum_{k=1}^{N} a_k^H a_k \sim \chi_{2N}^2$. Hence, the numerator of T_{eq} is made of the sum of $2N$ chi-square distributed independent RVs (each with a DoF of 1) and hence it has a degree of freedom of $2N = \nu_1$. Consequently, $\sum_{k=1}^{N} a_k^H a_k \sim \chi_{\nu_1}^2$. To continue, as each element of $\boldsymbol{b}_k$ is independently drawn from the complex normal distribution of zero mean and unit variance, $\mathrm{Re}\{\boldsymbol{b}_k[j]\} \sim \mathscr{N}_1(0,1)$ $\left(\equiv \left[\mathrm{Re}\{\boldsymbol{b}_k[j]\}\right]^2 \sim \chi_1^2 \right)$, $1 \le j \le (N_R-2)$ and $1 \le k \le N$; $\mathrm{Im}\{\boldsymbol{b}_k[j]\} \sim \mathscr{N}_1(0,1)$ $\left(\equiv \left[\mathrm{Im}\{\boldsymbol{b}_k[j]\}\right]^2 \sim \chi_1^2 \right)$, $1 \le j \le (N_R-2)$ and $1 \le k \le N$; it shall be recalled, once again, that $\boldsymbol{b}_k^H[j]\boldsymbol{b}_k[j] = \left[\mathrm{Re}\{\boldsymbol{b}_k[j]\}\right]^2 + \left[\mathrm{Im}\{\boldsymbol{b}_k[j]\}\right]^2$, $1 \le j \le (N_R-2)$ and $1 \le k \le N$; and all the constituent terms are independent of each other (Seber, 2003, Ch. 2). As a result, for $1 \le j \le (N_R-2)$ and $1 \le k \le N$, $\boldsymbol{b}_k^H[j]\boldsymbol{b}_k[j] \sim \chi_2^2$, $\sum_{j=1}^{N_R-2} \boldsymbol{b}_k^H[j]\boldsymbol{b}_k[j] \sim \chi_{2(N_R-2)}^2$, and $\sum_{k=1}^{N}\sum_{j=1}^{N_R-2} \boldsymbol{b}_k^H[j]\boldsymbol{b}_k[j] \sim \chi_{2N(N_R-2)}^2$. Note that the denominator of T_{eq} is made of the sum of $2N(N_R-2)$ chi-square distributed independent RVs (each with a DoF of 1) and hence it exhibits a DoF of $2N(N_R-2) = \nu_2$. In other words, $\sum_{k=1}^{N}\sum_{j=1}^{N_R-2} \boldsymbol{b}_k^H[j]\boldsymbol{b}_k[j] \sim \chi_{\nu_2}^2$.

Employing the above analyses in (A IV-9b),

$$T_{\mathrm{eq}} \sim \frac{\chi_{\nu_1}^2/\nu_1}{\chi_{\nu_2}^2/\nu_2}. \tag{A IV-10}$$

Attempting at a further standardized characterization, (A IV-10) implicates that the central F–distribution can characterize the distribution of T_{eq} provided that an independence precondition is satisfied. In this regard, if the distribution of T_{eq} is to be expressed in terms of the central F–distribution, it should be attested that $\chi_{\nu_1}^2$ and $\chi_{\nu_2}^2$ are independent RVs (Johnson *et al.*, 1995, p. 322). In other words, the constituent Gaussian RVs of the numerator and denominator of (A IV-9b) should be independent (as discussed before, it shall be recalled that all the constituent Gaussian RVs of the numerator are independent with each other; all the corresponding

Gaussian RVs of the denominator are also independent.). Should the sought independence be true, it would suffice to show that $a_k = \sigma^{-1}\hat{\boldsymbol{U}}^H(:,2)\boldsymbol{y}[k]$ and $\boldsymbol{b}_k = \sigma^{-1}\hat{\boldsymbol{U}}^H(:,3:N_R)\boldsymbol{y}[k]$ are independent.

According to (Seber, 2003, Theorem 2.5, p. 25), a_k and $\boldsymbol{b}_k$ would be independent if and only if $\mathrm{Cov}\{a_k,\boldsymbol{b}_k\} = \boldsymbol{0}_{1\times(N_R-2)}$. To check if this is true or not, we deploy the definition of covariance stated in (Seber, 2003, Theorem 1.2, p. 6) for real RVs. Thus, adapting the definition to our scenario (as we are dealing with complex RVs) while recalling that $\mathbb{E}\{a_k\} = 0$ and $\mathbb{E}\{\boldsymbol{b}_k\} = \boldsymbol{0}_{(N_R-2)\times 1}$,

$$\mathrm{Cov}\{a_k,\boldsymbol{b}_k\} = \mathbb{E}\Big\{\big(a_k - \mathbb{E}\{a_k\}\big)\big(\boldsymbol{b}_k - \mathbb{E}\{\boldsymbol{b}_k\}\big)^H\Big\} \tag{A IV-11a}$$

$$= \mathbb{E}\Big\{a_k\boldsymbol{b}_k^H\Big\} = \frac{1}{\sigma^2}\hat{\boldsymbol{U}}^H(:,2)\mathbb{E}\Big\{\boldsymbol{y}[k]\boldsymbol{y}^H[k]\Big\}\hat{\boldsymbol{U}}(:,3:N_R) \tag{A IV-11b}$$

$$\overset{(g)}{=} \frac{1}{\sigma^2}\hat{\boldsymbol{U}}^H(:,2)\mathbb{E}\Big\{\boldsymbol{z}[k]\boldsymbol{z}^H[k]\Big\}\hat{\boldsymbol{U}}(:,3:N_R), \tag{A IV-11c}$$

where (g) is the result of the aforementioned preconditions that $(\gamma_{snr},\gamma_{inr}) = (0,0)$. When infinitely large samples are available, $\mathbb{E}\Big\{\boldsymbol{z}[k]\boldsymbol{z}^H[k]\Big\} = \lim\limits_{N\to\infty}\dfrac{1}{N}\sum\limits_{k=1}^{N}\boldsymbol{z}[k]\boldsymbol{z}^H[k] = \sigma^2\boldsymbol{I}_{N_R}$. Therefore, exploiting the inherent property concerning the orthonormal columns of $\hat{\boldsymbol{U}}$,

$$\lim_{N\to\infty}\mathrm{Cov}\{a_k,\boldsymbol{b}_k\} = \hat{\boldsymbol{U}}^H(:,2)\hat{\boldsymbol{U}}(:,3:N_R) = \boldsymbol{0}_{1\times(N_R-2)}. \tag{A IV-12}$$

Under an infinitely huge sample setting and $(\gamma_{snr},\gamma_{inr}) = (0,0)$, hence, a_k and $\boldsymbol{b}_k$ are independent—making $\chi^2_{\nu_1}$ and $\chi^2_{\nu_2}$ independent. Consequently, for the scenario under consideration and the availability of infinite samples, (A IV-10) would satisfy the definition of the central F–distribution (Johnson *et al.*, 1995, Ch. 27, p. 322) and hence

$$\lim_{N\to\infty} T_{\mathrm{eq}} \sim F_{\nu_1,\nu_2}. \tag{A IV-13}$$

■

Case 2. $\gamma_{inr} = 0$ and $\gamma_{snr} > 0$: for this scenario, H_0 is true and hence $\boldsymbol{y}[k] = \boldsymbol{h}s[k] + \boldsymbol{z}[k]$. Accordingly,

$$a_k = \sigma^{-1}\hat{\boldsymbol{U}}^H(:,2)\big(\boldsymbol{h}s[k] + \boldsymbol{z}[k]\big) \in \mathbb{C} \tag{A IV-14a}$$

$$\boldsymbol{b}_k = \sigma^{-1}\hat{\boldsymbol{U}}^H(:,3:N_R)\big(\boldsymbol{h}s[k] + \boldsymbol{z}[k]\big) \in \mathbb{C}^{(N_R-2)}. \tag{A IV-14b}$$

Employing the simplifications of Case 1,

$$\sum_{k=1}^{N} a_k^H a_k = \sum_{k=1}^{N} \big[\mathrm{Re}\{a_k\}\big]^2 + \big[\mathrm{Im}\{a_k\}\big]^2 \tag{A IV-15a}$$

$$= \sum_{k=1}^{N} \big[\mathrm{Re}\{\sigma^{-1}\hat{\boldsymbol{U}}^H(:,2)(\boldsymbol{h}s[k] + \boldsymbol{z}[k])\}\big]^2 + \big[\mathrm{Im}\{\sigma^{-1}\hat{\boldsymbol{U}}^H(:,2)(\boldsymbol{h}s[k] + \boldsymbol{z}[k])\}\big]^2. \tag{A IV-15b}$$

Expanding (A IV-15b) leads to

$$\sum_{k=1}^{N} a_k^H a_k = \sum_{k=1}^{N} \big[\mathrm{Re}\big\{\sigma^{-1}\hat{\boldsymbol{U}}^H(:,2)\boldsymbol{h}s[k]\big\} + \mathrm{Re}\{\sigma^{-1}\hat{\boldsymbol{U}}^H(:,2)\boldsymbol{z}[k]\}\big]^2 + \sum_{k=1}^{N} \big[\mathrm{Im}\{\sigma^{-1}\hat{\boldsymbol{U}}^H(:,2)\boldsymbol{h}s[k]\} + \mathrm{Im}\{\sigma^{-1}\hat{\boldsymbol{U}}^H(:,2)\boldsymbol{z}[k]\}\big]^2. \tag{A IV-16}$$

As both $\mathrm{Re}\{\sigma^{-1}\hat{\boldsymbol{U}}^H(:,2)\boldsymbol{z}[k]\}$ and $\mathrm{Im}\{\sigma^{-1}\hat{\boldsymbol{U}}^H(:,2)\boldsymbol{z}[k]\}$ manifest a distribution $\mathcal{N}_1(0,1)$, it can be concluded that $\sum_{k=1}^{N} a_k^H a_k \sim \chi'^2_{\nu_1}(\lambda_1^{H_0})$, where $\lambda_1^{H_0}$ is the NCP inferred from (A IV-16) and expressed as

$$\lambda_1^{H_0} = \frac{1}{\sigma^2}\sum_{k=1}^{N} \big[\mathrm{Re}\big\{\hat{\boldsymbol{U}}^H(:,2)\boldsymbol{h}s[k]\big\}\big]^2 + \frac{1}{\sigma^2}\sum_{k=1}^{N} \big[\mathrm{Im}\big\{\hat{\boldsymbol{U}}^H(:,2)\boldsymbol{h}s[k]\big\}\big]^2 \tag{A IV-17a}$$

$$= \frac{1}{\sigma^2}\sum_{k=1}^{N} \Big(\big[\mathrm{Re}\big\{\hat{\boldsymbol{U}}^H(:,2)\boldsymbol{h}s[k]\big\}\big]^2 + \big[\mathrm{Im}\big\{\hat{\boldsymbol{U}}^H(:,2)\boldsymbol{h}s[k]\big\}\big]^2\Big). \tag{A IV-17b}$$

Furthermore,

$$\lambda_1^{H_0} = \frac{1}{\sigma^2}\sum_{k=1}^{N}(\boldsymbol{h}s[k])^H\hat{\boldsymbol{U}}(:,2)\hat{\boldsymbol{U}}^H(:,2)\boldsymbol{h}s[k] = \frac{1}{\sigma^2}\sum_{k=1}^{N}(\boldsymbol{h}s[k])^H\underbrace{\hat{\boldsymbol{P}}_2}_{=\hat{\boldsymbol{P}}_2^H\hat{\boldsymbol{P}}_2}\boldsymbol{h}s[k] \tag{A IV-18a}$$

$$= \frac{1}{\sigma^2}\sum_{k=1}^{N}\left(\hat{\boldsymbol{P}}_2\boldsymbol{h}s[k]\right)^H\hat{\boldsymbol{P}}_2\boldsymbol{h}s[k] \tag{A IV-18b}$$

$$= \frac{1}{\sigma^2}\sum_{k=1}^{N}\left\|\hat{\boldsymbol{P}}_2\boldsymbol{h}s[k]\right\|^2. \tag{A IV-18c}$$

Similarly, realizing that $\boldsymbol{b}_k[j] = \sigma^{-1}\hat{\boldsymbol{U}}^H(:,2+j)(\boldsymbol{h}s[k]+\boldsymbol{z}[k])$,

$$\sum_{k=1}^{N}\sum_{j=1}^{N_R-2}\boldsymbol{b}_k^H[j]\boldsymbol{b}_k[j] = \sum_{k=1}^{N}\sum_{j=1}^{N_R-2}\left[\mathrm{Re}\{\boldsymbol{b}_k[j]\}\right]^2+\left[\mathrm{Im}\{\boldsymbol{b}_k[j]\}\right]^2. \tag{A IV-19}$$

Pursuing the simplification of (A IV-19) through expansion,

$$\sum_{k=1}^{N}\sum_{j=1}^{N_R-2}\boldsymbol{b}_k^H[j]\boldsymbol{b}_k[j] = \sum_{k=1}^{N}\sum_{j=1}^{N_R-2}\left[\mathrm{Re}\{\sigma^{-1}\hat{\boldsymbol{U}}^H(:,2+j)(\boldsymbol{h}s[k]+\boldsymbol{z}[k])\}\right]^2 + \sum_{k=1}^{N}\sum_{j=1}^{N_R-2}\left[\mathrm{Im}\{\sigma^{-1}\hat{\boldsymbol{U}}^H(:,2+j)(\boldsymbol{h}s[k]+\boldsymbol{z}[k])\}\right]^2 \tag{A IV-20}$$

$$\sum_{k=1}^{N}\sum_{j=1}^{N_R-2}\boldsymbol{b}_k^H[j]\boldsymbol{b}_k[j] = \sum_{k=1}^{N}\sum_{j=1}^{N_R-2}\left[\mathrm{Re}\{\sigma^{-1}\hat{\boldsymbol{U}}^H(:,2+j)\boldsymbol{h}s[k]+\sigma^{-1}\hat{\boldsymbol{U}}^H(:,2+j)\boldsymbol{z}[k]\}\right]^2 + \sum_{k=1}^{N}\sum_{j=1}^{N_R-2}\left[\mathrm{Im}\{\sigma^{-1}\hat{\boldsymbol{U}}^H(:,2+j)\boldsymbol{h}s[k]+\sigma^{-1}\hat{\boldsymbol{U}}^H(:,2+j)\boldsymbol{z}[k]\}\right]^2. \tag{A IV-21}$$

Realizing in (A IV-21) that $\mathrm{Re}\{\sigma^{-1}\hat{\boldsymbol{U}}^H(:,2+j)\boldsymbol{z}[k]\} \sim \mathcal{N}_1(0,1)$ and $\mathrm{Im}\{\sigma^{-1}\hat{\boldsymbol{U}}^H(:,2+j)\boldsymbol{z}[k]\} \sim \mathcal{N}_1(0,1)$, $\sum_{k=1}^{N}\sum_{j=1}^{N_R-2}\boldsymbol{b}_k^H[j]\boldsymbol{b}_k[j] \sim \chi'^2_{\nu_2}(\lambda_2^{H_0})$, where $\lambda_2^{H_0}$ is the NCP that is inferred from

(A IV-21) as

$$\lambda_2^{H_0} = \frac{1}{\sigma^2}\sum_{k=1}^{N}\sum_{j=1}^{N_R-2}\left[\mathrm{Re}\{\hat{\boldsymbol{U}}^H(:,2+j)\boldsymbol{h}s[k]\}\right]^2 + \frac{1}{\sigma^2}\sum_{k=1}^{N}\sum_{j=1}^{N_R-2}\left[\mathrm{Im}\{\hat{\boldsymbol{U}}^H(:,2+j)\boldsymbol{h}s[k]\}\right]^2 \tag{A IV-22a}$$

$$= \frac{1}{\sigma^2}\sum_{k=1}^{N}\sum_{j=1}^{N_R-2}(\boldsymbol{h}s[k])^H\hat{\boldsymbol{U}}(:,2+j)\hat{\boldsymbol{U}}^H(:,2+j)\boldsymbol{h}s[k] \tag{A IV-22b}$$

$$= \frac{1}{\sigma^2}\sum_{k=1}^{N}(\boldsymbol{h}s[k])^H\hat{\boldsymbol{U}}(:,3:N_R)\hat{\boldsymbol{U}}^H(:,3:N_R)\boldsymbol{h}s[k] = \frac{1}{\sigma^2}\sum_{k=1}^{N}(\boldsymbol{h}s[k])^H\overbrace{\hat{\boldsymbol{P}}_{3:N_R}^H\hat{\boldsymbol{P}}_{3:N_R}}^{=\hat{\boldsymbol{P}}_{3:N_R}}\boldsymbol{h}s[k] \tag{A IV-22c}$$

$$= \frac{1}{\sigma^2}\sum_{k=1}^{N}\left(\hat{\boldsymbol{P}}_{3:N_R}^H\boldsymbol{h}s[k]\right)^H\hat{\boldsymbol{P}}_{3:N_R}\boldsymbol{h}s[k] \tag{A IV-22d}$$

$$= \frac{1}{\sigma^2}\sum_{k=1}^{N}\left\|\hat{\boldsymbol{P}}_{3:N_R}\boldsymbol{h}s[k]\right\|^2. \tag{A IV-22e}$$

Employing the above-detailed simplifications in (A IV-9b),

$$T_{\mathrm{eq}} \sim \frac{\chi'^2_{\nu_1}(\lambda_1^{H_0})/\nu_1}{\chi'^2_{\nu_2}(\lambda_2^{H_0})/\nu_2}. \tag{A IV-23}$$

If (A IV-23) has to be simplified in terms of the noncentral F–distribution, $\chi'^2_{\nu_1}(\lambda_1^{H_0})$ and $\chi'^2_{\nu_2}(\lambda_2^{H_0})$ should be independent (Johnson *et al.*, 1995, Ch. 30, p. 480). In other words, a_k and $\boldsymbol{b}_k$—equated, respectively, in (A IV-14a) and (A IV-14b)—should be independent. Equivalently, $\mathrm{Cov}\{a_k,\boldsymbol{b}_k\} = \mathbb{E}\left\{\left(a_k-\mathbb{E}\{a_k\}\right)\left(\boldsymbol{b}_k-\mathbb{E}\{\boldsymbol{b}_k\}\right)^H\right\}$ becomes a zero vector provided that (A IV-23) should admit the noncentral F–distribution.

To continue with the computation of $\mathrm{Cov}\{a_k,\boldsymbol{b}_k\}$, meanwhile, using (A IV-14a) and (A IV-14b):

$$\mathbb{E}\{a_k\} = \sigma^{-1}\hat{\boldsymbol{U}}^H(:,2)\left(\mathbb{E}\{\boldsymbol{h}\}\mathbb{E}\{s[k]\}+\mathbb{E}\{\boldsymbol{z}[k]\}\right) \overset{(h)}{=} 0 \tag{A IV-24a}$$

$$\mathbb{E}\{\boldsymbol{b}_k\} = \sigma^{-1}\hat{\boldsymbol{U}}^H(:,3:N_R)\left(\mathbb{E}\{\boldsymbol{h}\}\mathbb{E}\{s[k]\}+\mathbb{E}\{\boldsymbol{z}[k]\}\right) \overset{(i)}{=} \boldsymbol{0}_{(N_R-2)\times 1}, \tag{A IV-24b}$$

where (h) and (i) follow for $\mathbb{E}\{\boldsymbol{h}\} = \mathbb{E}\{\boldsymbol{z}[k]\} = \mathbf{0}_{N_R\times 1}$—due to the presumed zero mean Gaussian distribution. Thus,

$$\mathrm{Cov}\{a_k, \boldsymbol{b}_k\} = \frac{1}{\sigma^2}\hat{\boldsymbol{U}}^H(:,2)\mathbb{E}\Big\{(\boldsymbol{h}s[k]+\boldsymbol{z}[k])(\boldsymbol{h}s[k]+\boldsymbol{z}[k])^H\Big\}\hat{\boldsymbol{U}}(:,3:N_R) \tag{A IV-25a}$$

$$\overset{(j)}{=} \frac{1}{\sigma^2}\hat{\boldsymbol{U}}^H(:,2)\Bigg(\mathbb{E}\{\boldsymbol{h}\boldsymbol{h}^H\}\underbrace{\mathbb{E}\{s^2[k]\}}_{=P_s}+\mathbb{E}\{\boldsymbol{z}[k]\boldsymbol{z}^H[k]\}\Bigg)\hat{\boldsymbol{U}}(:,3:N_R), \tag{A IV-25b}$$

where (j) follows for the independence of $\boldsymbol{h}$ and $\boldsymbol{z}[k]$, and the presumption that $\mathbb{E}\{\boldsymbol{h}\} = \mathbb{E}\{\boldsymbol{z}[k]\} = \mathbf{0}_{N_R\times 1}$. When infinite samples are available, $\mathbb{E}\{\boldsymbol{h}\boldsymbol{h}^H\} = \boldsymbol{I}_{N_R}$ and $\mathbb{E}\{\boldsymbol{z}[k]\boldsymbol{z}^H[k]\} = \sigma^2\boldsymbol{I}_{N_R}$. As a result,

$$\lim_{N\to\infty}\mathrm{Cov}\{a_k, \boldsymbol{b}_k\} = \frac{1}{\sigma^2}\hat{\boldsymbol{U}}^H(:,2)(P_s+\sigma^2)\boldsymbol{I}_{N_R}\hat{\boldsymbol{U}}(:,3:N_R) \tag{A IV-26a}$$

$$= \frac{P_s+\sigma^2}{\sigma^2}\hat{\boldsymbol{U}}^H(:,2)\hat{\boldsymbol{U}}(:,3:N_R) \overset{(k)}{=} \mathbf{0}_{1\times(N_R-2)}, \tag{A IV-26b}$$

where (k) follows because of the orthonormality constraint characterizing the columns of $\hat{\boldsymbol{U}}$. As a summary, for infinitely huge samples, $\boldsymbol{h} \sim \mathscr{CN}_{N_R}(\mathbf{0}, \boldsymbol{I}_{N_R})$, $\mathbb{E}\{s^2[k]\} = P_s$, and $\boldsymbol{z}[k] \sim \mathscr{CN}_{N_R}(\mathbf{0}, \sigma^2\boldsymbol{I}_{N_R})$, $\chi'^2_{\nu_1}(\lambda_1^{H_0})$ and $\chi'^2_{\nu_2}(\lambda_2^{H_0})$ are independent RVs making (A IV-23) satisfy the definition regarding the noncentral F–distribution (Johnson *et al.*, 1995, Ch. 30, p. 480) with (ν_1, ν_2) DoF and NCPs $(\lambda_1^{H_0}, \lambda_2^{H_0})$. Therefore, under the aforementioned conditions,

$$\lim_{N\to\infty} T_{\mathrm{eq}} \sim F''_{\nu_1,\nu_2}(\lambda_1^{H_0}, \lambda_2^{H_0}). \tag{A IV-27}$$

■

Case 3. $\gamma_{inr} > 0$ and $\gamma_{snr} > 0$: this case is exactly Case 2 subjected to a constraint of $\gamma_{inr} > 0$. With regard to such a constraint,

$$a_k = \frac{1}{\sigma}\hat{\boldsymbol{U}}^H(:,2)\big(\boldsymbol{h}s[k]+\boldsymbol{g}v[k]+\boldsymbol{z}[k]\big) \in \mathbb{C} \tag{A IV-28a}$$

$$\boldsymbol{b}_k = \frac{1}{\sigma}\hat{\boldsymbol{U}}^H(:,3:N_R)\big(\boldsymbol{h}s[k]+\boldsymbol{g}v[k]+\boldsymbol{z}[k]\big) \in \mathbb{C}^{(N_R-2)}. \tag{A IV-28b}$$

As seen in (A IV-28a) and(A IV-28b), a_k and $\boldsymbol{b}_k$ admit the same distribution except the shift, in the corresponding NCPs, by $\boldsymbol{g}v[k]$. Hence,

$$T_{\text{eq}} \sim \frac{\chi'^2_{\nu_1}(\lambda_1^{H_1})/\nu_1}{\chi'^2_{\nu_2}(\lambda_2^{H_1})/\nu_2}, \tag{A IV-29}$$

where $(\lambda_1^{H_1}, \lambda_2^{H_1}) = \frac{1}{\sigma^2}\sum_{k=1}^{N}\left(\left\|\hat{\boldsymbol{P}}_2(\boldsymbol{h}s[k]+\boldsymbol{g}v[k])\right\|^2, \left\|\hat{\boldsymbol{P}}_{3:N_R}(\boldsymbol{h}s[k]+\boldsymbol{g}v[k])\right\|^2\right)$. To express (A IV-29) in terms of the noncentral F–distribution, $\chi'^2_{\nu_1}(\lambda_1^{H_1})$ and $\chi'^2_{\nu_2}(\lambda_2^{H_1})$ are required to be independent, and hence $\text{Cov}\{a_k, \boldsymbol{b}_k\} = \mathbb{E}\left\{\left(a_k - \mathbb{E}\{a_k\}\right)\left(\boldsymbol{b}_k - \mathbb{E}\{\boldsymbol{b}_k\}\right)^H\right\}$ should be a zero row vector.

Employing (A IV-28a) and (A IV-28b), and following (A IV-24a)-(A IV-25b):

$$\text{Cov}\{a_k, \boldsymbol{b}_k\} = \frac{1}{\sigma^2}\hat{\boldsymbol{U}}^H(:,2)\left(\mathbb{E}\{\boldsymbol{h}\boldsymbol{h}^H\}\underbrace{\mathbb{E}\{s^2[k]\}}_{=P_s} + \mathbb{E}\{\boldsymbol{g}\boldsymbol{g}^H\}\underbrace{\mathbb{E}\{v^2[k]\}}_{=P_v} + \mathbb{E}\{\boldsymbol{z}[k]\boldsymbol{z}^H[k]\}\right)\hat{\boldsymbol{U}}(:,3:N_R) \tag{A IV-30a}$$

$$\overset{(l)}{=} \frac{P_s + P_v + \sigma^2}{\sigma^2}\hat{\boldsymbol{U}}^H(:,2) \times \boldsymbol{I}_{N_R} \times \hat{\boldsymbol{U}}(:,3:N_R) \overset{(m)}{=} \boldsymbol{0}_{1\times(N_R-2)}, \tag{A IV-30b}$$

where (l) follows because of the independence of $\boldsymbol{h}$, $\boldsymbol{g}$, and $\boldsymbol{z}[k]$, and the considered assumption that $\boldsymbol{h} \sim \mathscr{CN}_{N_R}(\boldsymbol{0}, \boldsymbol{I}_{N_R})$ and $\boldsymbol{g} \sim \mathscr{CN}_{N_R}(\boldsymbol{0}, \boldsymbol{I}_{N_R})$; and (m) follows from the orthonormal columns of $\hat{\boldsymbol{U}}$. Under these conditions—$\boldsymbol{h} \sim \mathscr{CN}_{N_R}(\boldsymbol{0}, \boldsymbol{I}_{N_R})$, $\boldsymbol{g} \sim \mathscr{CN}_{N_R}(\boldsymbol{0}, \boldsymbol{I}_{N_R})$, $\mathbb{E}\{s^2[k]\} = P_s$, $\mathbb{E}\{v^2[k]\} = P_v$, and $\boldsymbol{z}[k] \sim \mathscr{CN}_{N_R}(\boldsymbol{0}, \sigma^2\boldsymbol{I}_{N_R})$—and the availability of infinite samples, $\chi'^2_{\nu_1}(\lambda_1^{H_1})$ and $\chi'^2_{\nu_2}(\lambda_2^{H_1})$ would be independent RVs. Consequently, for the underlying case and the preconditions of Theorem 6, as per (Johnson *et al.*, 1995, Ch. 30, p. 480),

$$\lim_{N\to\infty} T_{\text{eq}} \sim F''_{\nu_1,\nu_2}(\lambda_1^{H_1}, \lambda_2^{H_1}). \tag{A IV-31}$$

■

Finally, accommodating Case 1, Case 2, and Case 3 leads to Theorem 6. □

2. Proof of Proposition 1

This proof begins with the derivation of the closed-form expression—valid under infinitely huge samples—of P_d. Thereafter, the corresponding closed-form expression of P_f is inferred.

Employing the definition in Proposition 1, (4.13), and (4.14):

$$P_d = \Pr\{T > \lambda | H_1\} = \Pr\left\{ \frac{\nu_1}{\nu_2} T_{\text{eq}} > \lambda \middle| H_1 \right\} = \Pr\left\{ T_{\text{eq}} > \frac{\nu_2 \lambda}{\nu_1} \middle| H_1 \right\} \tag{A IV-32a}$$

$$= 1 - \Pr\left\{ T_{\text{eq}} \leq \frac{\nu_2 \lambda}{\nu_1} \middle| H_1 \right\} = 1 - \Pr\left\{ T_{\text{eq}} | H_1 \leq \frac{\nu_2 \lambda}{\nu_1} \right\}. \tag{A IV-32b}$$

To simplify (A IV-32b), it shall be realized that $T_{\text{eq}}|H_1$ corresponds to the scenario that the corresponding SNR and INR being greater than zero, i.e., $T_{\text{eq}}|H_1 \equiv T_{\text{eq}}\Big|_{\gamma_{snr}>0 \ \& \ \gamma_{inr}>0}$. Consequently,

$$P_d = 1 - \Pr\left\{ T_{\text{eq}}\Big|_{\gamma_{snr}>0 \ \& \ \gamma_{inr}>0} \leq \frac{\nu_2 \lambda}{\nu_1} \right\} \tag{A IV-33a}$$

$$\lim_{N\to\infty} P_d \overset{(a)}{=} 1 - \Pr\left\{ \lim_{N\to\infty} T_{\text{eq}}\Big|_{\gamma_{snr}>0 \ \& \ \gamma_{inr}>0} \leq \frac{\nu_2 \lambda}{\nu_1} \right\}, \tag{A IV-33b}$$

where (a) follows through the exploitation of the properties of limit. Meanwhile, invoking the third "if condition" of Theorem 6,

$$\lim_{N\to\infty} P_d = 1 - \Pr\left\{ \underbrace{T_{\text{eq}}}_{\sim F''_{\nu_1,\nu_2}(\lambda_1^{H_1}, \lambda_2^{H_1})} \leq \frac{\nu_2 \lambda}{\nu_1} \right\}. \tag{A IV-34}$$

Therefore, the CDF of $F''_{\nu_1,\nu_2}(\lambda_1^{H_1}, \lambda_2^{H_1})$ can be deployed to simplify (A IV-34) to

$$P_d = 1 - F''\left(\nu_2 \lambda / \nu_1; \nu_1, \nu_2 | \lambda_1^{H_1}, \lambda_2^{H_1}\right). \tag{A IV-35}$$

Employing the definition $P_f = \Pr\{T > \lambda | H_0\}$, (4.13), and (4.14); and following (A IV-32a) through (A IV-32b),

$$P_f = 1 - \Pr\left\{ T_{\text{eq}} \leq \frac{\nu_2 \lambda}{\nu_1} \middle| H_0 \right\} = 1 - \Pr\left\{ T_{\text{eq}} | H_0 \leq \frac{\nu_2 \lambda}{\nu_1} \right\}. \tag{A IV-36}$$

Under H_0 (no RFI condition), $\gamma_{inr} = 0$ and $\gamma_{snr} > 0$. As a result, $T_{\text{eq}}|H_0 \equiv T_{\text{eq}}\Big|_{\gamma_{inr}=0 \ \& \ \gamma_{snr}>0}$ and hence

$$\lim_{N\to\infty} P_f \overset{(b)}{=} 1 - \Pr\left\{ \lim_{N\to\infty} T_{\text{eq}}\Big|_{\gamma_{inr}=0 \ \& \ \gamma_{snr}>0} \leq \frac{\nu_2 \lambda}{\nu_1} \right\} \tag{A IV-37a}$$

$$\overset{(c)}{=} 1 - \Pr\left\{ \underbrace{T_{\text{eq}}}_{\sim F''_{\nu_1,\nu_2}(\lambda_1^{H_0}, \lambda_2^{H_0})} \leq \frac{\nu_2 \lambda}{\nu_1} \right\}, \tag{A IV-37b}$$

where (b) follows directly from the properties of limit and (c) follows by utilizing the second "if condition" of Theorem 6. Meanwhile, deploying the CDF of $F''_{\nu_1,\nu_2}(\lambda_1^{H_0}, \lambda_2^{H_0})$ in (A IV-37b) leads to the expression

$$\lim_{N\to\infty} P_f = 1 - F''\left(\nu_2 \lambda / \nu_1; \nu_1, \nu_2 | \lambda_1^{H_0}, \lambda_2^{H_0}\right). \tag{A IV-38}$$

□

3. Proof of Lemma 2

First, please note that $\hat{\boldsymbol{P}}_2$ projects toward the subspace spanned by the singular vector corresponding to the second largest singular value; $\hat{\boldsymbol{P}}_{3:N_R}$ projects toward the subspace jointly spanned by the singular vectors corresponding to the remaining smallest singular values. To continue, as $N \to \infty$, the population covariance matrix (PCM) $\boldsymbol{R}_{yy} = \mathbb{E}\{\boldsymbol{y}[k]\boldsymbol{y}^H[k]\}$ would be perfectly estimated by the SCM $\hat{\boldsymbol{R}}_{yy}$. In this regard, the signal subspace (which is spanned by the SOI and/or the RFI) would be perfectly differentiated from the orthogonal noise subspace. For this scenario:

- if the proposed detector is operating in the high SNR and INR regimes, and $\gamma_{snr} >> \gamma_{inr}$, the first and the second largest singular values are contributed by the SOI and RFI, respectively. This is also corroborated by the fact that the contribution of the noise eigenvalues in the high SNR and INR regimes is close to zero, as the contaminating noise has a very weak power, i.e., $\hat{\boldsymbol{P}}_2\boldsymbol{h} = \boldsymbol{0}_{N_R\times 1}$, $\hat{\boldsymbol{P}}_2\boldsymbol{g} = \boldsymbol{g}$, and $\hat{\boldsymbol{P}}_{3:N_R}\boldsymbol{g} = \hat{\boldsymbol{P}}_{3:N_R}\boldsymbol{h} = \boldsymbol{0}_{N_R\times 1}$. From the suppositions of Theorem 6 and Lemma 2, thus,

$$(\lambda_1^{H_1}, \lambda_2^{H_1}) = \frac{1}{\sigma^2}\sum_{k=1}^{N}\left(\Big\|\overbrace{\hat{\boldsymbol{P}}_2\boldsymbol{h}}^{=\boldsymbol{0}_{N_R\times 1}}\boldsymbol{s}[k] + \overbrace{\hat{\boldsymbol{P}}_2\boldsymbol{g}}^{=\boldsymbol{g}}v[k]\Big\|^2, \Big\|\overbrace{\hat{\boldsymbol{P}}_{3:N_R}\boldsymbol{h}}^{=\boldsymbol{0}_{N_R\times 1}}\boldsymbol{s}[k] + \overbrace{\hat{\boldsymbol{P}}_{3:N_R}\boldsymbol{g}}^{=\boldsymbol{0}_{N_R\times 1}}v[k]\Big\|^2\right) \quad \text{(A IV-39a)}$$

$$= \frac{1}{\sigma^2}\sum_{k=1}^{N}\left(\big\|\boldsymbol{g}v[k]\big\|^2, 0\right) = (\lambda_{gv}, 0). \quad \text{(A IV-39b)}$$

Meanwhile, recalling that the singly noncentral F–distribution is the result of the doubly noncentral distribution with one of its NCPs being zero (Johnson *et al.*, 1995, Ch. 30, p. 480), the closed-form expression given by (4.17) follows from (4.15). ■

- if the proposed detector is operating in the high SNR and INR regimes, and $\gamma_{inr} >> \gamma_{snr}$, the first and the second largest singular values are contributed by the RFI and SOI, respectively, i.e., $\hat{\boldsymbol{P}}_2\boldsymbol{h} = \boldsymbol{h}$, $\hat{\boldsymbol{P}}_2\boldsymbol{g} = \boldsymbol{0}_{N_R\times 1}$, and $\hat{\boldsymbol{P}}_{3:N_R}\boldsymbol{g} = \hat{\boldsymbol{P}}_{3:N_R}\boldsymbol{h} = \boldsymbol{0}_{N_R\times 1}$. Hence,

$$(\lambda_1^{H_1}, \lambda_2^{H_1}) = \frac{1}{\sigma^2}\sum_{k=1}^{N}\left(\Big\|\overbrace{\hat{\boldsymbol{P}}_2\boldsymbol{h}}^{=\boldsymbol{h}}\boldsymbol{s}[k] + \overbrace{\hat{\boldsymbol{P}}_2\boldsymbol{g}}^{=\boldsymbol{0}_{N_R\times 1}}v[k]\Big\|^2, \Big\|\overbrace{\hat{\boldsymbol{P}}_{3:N_R}\boldsymbol{h}}^{=\boldsymbol{0}_{N_R\times 1}}\boldsymbol{s}[k] + \overbrace{\hat{\boldsymbol{P}}_{3:N_R}\boldsymbol{g}}^{=\boldsymbol{0}_{N_R\times 1}}v[k]\Big\|^2\right) \quad \text{(A IV-40a)}$$

$$= \frac{1}{\sigma^2}\sum_{k=1}^{N}\left(\big\|\boldsymbol{h}\boldsymbol{s}[k]\big\|^2, 0\right) = (\lambda_{hs}, 0). \quad \text{(A IV-40b)}$$

Similarly, deploying (A IV-40b) in (4.15), (4.18) becomes evident. ■

If the proposed RFI detector is operating in the high SNR regimes, on the other hand, the largest singular value is contributed entirely by the SOI and the rest of the eigenvalues are the noise eigenvalues of equal magnitude (especially, as $N \to \infty$), i.e., $\hat{\boldsymbol{P}}_2\boldsymbol{h} = \boldsymbol{0}_{N_R\times 1}$

and $\hat{\boldsymbol{P}}_{3:N_R}\boldsymbol{h} = \boldsymbol{0}_{N_R\times 1}$. Accordingly, evoking the supposition of Theorem 6,

$$(\lambda_1^{H_0}, \lambda_2^{H_0}) = \frac{1}{\sigma^2}\sum_{k=1}^{N}\Big(\big\| \underbrace{\hat{\boldsymbol{P}}_2\boldsymbol{h}}_{=\boldsymbol{0}_{N_R\times 1}} s[k]\big\|^2, \big\|\underbrace{\hat{\boldsymbol{P}}_{3:N_R}\boldsymbol{h}}_{=\boldsymbol{0}_{N_R\times 1}} s[k]\big\|^2\Big) \tag{A IV-41a}$$

$$= (0,0). \tag{A IV-41b}$$

Plugging (A IV-41b) into (4.16) and realizing that the central F–distribution is the non-central F–distribution with zero NCPs (Johnson *et al.*, 1995, Ch. 27, p. 322), (4.19) follows. ■

Eventually, accommodating the aforementioned scenarios leads to Lemma 2. □

APPENDIX V

APPENDICES OF CHAPTER 5

1. Proof of Lemma 3

Following the definitions in (5.1) and (5.4),

$$\left[\left(\tilde{\hat{\mathscr{P}}}_{1,2}-\tilde{\hat{\mathscr{P}}}^{[d]}\right)\times_3\hat{\mathscr{R}}_{yy}^{(p)}\right]_{(3)}^{T}=\left(\left[\tilde{\hat{\mathscr{P}}}_{1,2}\right]_{(3)}^{T}-\left[\tilde{\hat{\mathscr{P}}}^{[d]}\right]_{(3)}^{T}\right)\left[\hat{\mathscr{R}}_{yy}^{(p)}\right]_{(3)}^{T} \tag{A V-1a}$$

$$\left[\tilde{\hat{\mathscr{P}}}^{[d]}\times_3\hat{\mathscr{R}}_{yy}^{(p)}\right]_{(3)}^{T}=\left[\tilde{\hat{\mathscr{P}}}^{[d]}\right]_{(3)}^{T}\left[\hat{\mathscr{R}}_{yy}^{(p)}\right]_{(3)}^{T}. \tag{A V-1b}$$

Applying the definition in (5.1) to (5.29) and, in turn, utilizing (5.28) and (5.14),

$$\left[\hat{\mathscr{R}}_{yy}^{(p)}\right]_{(3)}^{T}=\frac{1}{N}\left[\mathscr{Y}_p\right]_{(3)}^{T}\left(\left[\mathscr{Y}_p\right]_{(3)}^{T}\right)^{H} \tag{A V-2a}$$

$$=\hat{\boldsymbol{P}}_{nd}\hat{\boldsymbol{R}}_{yy}\hat{\boldsymbol{P}}_{nd}^{H}=\hat{\boldsymbol{R}}_{yy}^{(p)}. \tag{A V-2b}$$

Substituting (A V-2b) into (A V-1a) and (A V-1b), and, in turn, into (5.35) gives (5.37).

To continue, employing (5.16) in (5.34),

$$\left[\tilde{\hat{\mathscr{P}}}^{[d]}\right]_{(3)}^{T}=\left(\tilde{\hat{\boldsymbol{T}}}_1\otimes\boldsymbol{I}_W\right)\hat{\boldsymbol{P}}_d. \tag{A V-3}$$

Exploiting (5.33) and (A V-3) in (5.37),

$$T^{\mathrm{TB}}=\frac{\nu_2}{\nu_1}\frac{\mathrm{tr}\left(\left(\tilde{\hat{\boldsymbol{T}}}_1\otimes\boldsymbol{I}_W\right)\hat{\boldsymbol{P}}_d\hat{\boldsymbol{R}}_{yy}^{(p)}\right)}{\mathrm{tr}\left(\left(\tilde{\hat{\boldsymbol{T}}}_1\otimes\boldsymbol{I}_W\right)\left(\boldsymbol{I}_{N_RW}-\hat{\boldsymbol{P}}_d\right)\hat{\boldsymbol{R}}_{yy}^{(p)}\right)}. \tag{A V-4}$$

Deploying (5.16) and (5.20) in (A V-4),

$$T^{\mathrm{TB}}=\frac{\nu_2}{\nu_1}\frac{\mathrm{tr}\left(\left(\tilde{\hat{\boldsymbol{T}}}_1\otimes\boldsymbol{I}_W\right)\tilde{\hat{\boldsymbol{U}}}_{1:r_1}\tilde{\hat{\boldsymbol{\Sigma}}}_{1:r_1}\tilde{\hat{\boldsymbol{U}}}_{1:r_1}^{H}\right)}{\mathrm{tr}\left(\left(\tilde{\hat{\boldsymbol{T}}}_1\otimes\boldsymbol{I}_W\right)\tilde{\hat{\boldsymbol{U}}}_{r_1+1:N_RW}\tilde{\hat{\boldsymbol{\Sigma}}}_{r_1+1:N_RW}\tilde{\hat{\boldsymbol{U}}}_{r_1+1:N_RW}^{H}\right)}. \tag{A V-5}$$

From (5.21b),

$$\tilde{\hat{\boldsymbol{\Sigma}}}_{1:r_1} = \hat{\boldsymbol{\Sigma}}_{r+1:N_R W}(1:r_1, 1:r_1) \tag{A V-6a}$$

$$\tilde{\hat{\boldsymbol{\Sigma}}}_{r_1+1:N_R W} = \hat{\boldsymbol{\Sigma}}_{r+1:N_R W}(r_1+1:d, r_1+1:d). \tag{A V-6b}$$

At last, substituting (5.21a), (5.21c), (A V-6a), and (A V-6b) into (A V-5) leads to (5.38). □

2. Proof of Theorem 7

Employing the stated definition, $\lim_{\Delta \boldsymbol{U}_{r+1:N_R W} \to \boldsymbol{0}} P_d = \Pr\{ \lim_{\Delta \boldsymbol{U}_{r+1:N_R W} \to \boldsymbol{0}} T^{\mathrm{TB}} > \lambda \,|H_1\}$. In other words, $\lim_{\Delta \boldsymbol{U}_{r+1:N_R W} \to \boldsymbol{0}} P_d = \Pr\{ \lim_{\Delta \boldsymbol{U}_{r+1:N_R W} \to \boldsymbol{0}} T^{\mathrm{TB}} | H_1 > \lambda\}$. While employing (5.21a)-(5.21c), applying limit and its properties to (5.38),

$$\lim_{\Delta \boldsymbol{U}_{r+1:N_R W} \to \boldsymbol{0}} P_d = \Pr\left\{ \frac{\mathrm{tr}(\hat{\boldsymbol{N}}_1)}{\mathrm{tr}(\hat{\boldsymbol{N}}_2)} \middle| H_1 > \tilde{\lambda} \right\}, \tag{A V-7}$$

where $\tilde{\lambda} = \nu_1 \lambda / \nu_2$ and

$$\hat{\boldsymbol{N}}_1 = \lim_{\Delta \boldsymbol{U}_{r+1:N_R W} \to \boldsymbol{0}} \left\{ (\tilde{\hat{\boldsymbol{T}}}_1 \otimes \boldsymbol{I}_W) \tilde{\boldsymbol{U}}_{1:r_1} \tilde{\hat{\boldsymbol{\Sigma}}}_{1:r_1} \tilde{\boldsymbol{U}}^H_{1:r_1} \right\} \tag{A V-8}$$

$$\hat{\boldsymbol{N}}_2 = \lim_{\Delta \boldsymbol{U}_{r+1:N_R W} \to \boldsymbol{0}} \left\{ (\tilde{\hat{\boldsymbol{T}}}_1 \otimes \boldsymbol{I}_W) \tilde{\boldsymbol{U}}_{r_1+1:N_R W} \tilde{\hat{\boldsymbol{\Sigma}}}_{r_1+1:N_R W} \tilde{\boldsymbol{U}}^H_{r_1+1:N_R W} \right\}. \tag{A V-9}$$

For $\left[\mathscr{Y}_p\right]_{(1)}$ decomposed as $\left[\mathscr{Y}_p\right]_{(1)} = \left[\tilde{\boldsymbol{U}}_1^{[1:r_1]} \; \tilde{\boldsymbol{U}}_1^{[n]}\right] \tilde{\hat{\boldsymbol{\Sigma}}}_1^{[i]} \left[\tilde{\boldsymbol{V}}_1^{[1:r_1]} \; \tilde{\boldsymbol{V}}_1^{[n]}\right]^H$ and $\tilde{\hat{\boldsymbol{\Sigma}}}_1^{[1:r_1]} = \tilde{\hat{\boldsymbol{\Sigma}}}_1^{[i]}(1:r_1, 1:r_1)$, the perturbation analysis extended to the HOSVD-based subspace estimate (Roemer *et al.*, 2014, Sec. III-B) leads to

$$\tilde{\hat{\boldsymbol{U}}}_1^{[1:r_1]} = \tilde{\boldsymbol{U}}_1^{[1:r_1]} + \Delta \tilde{\boldsymbol{U}}_1^{[1:r_1]}, \tag{A V-10}$$

where $\tilde{\boldsymbol{U}}_1^{[1:r_1]}$ denotes the true version of $\tilde{\hat{\boldsymbol{U}}}_1^{[1:r_1]}$ and $\Delta \tilde{\boldsymbol{U}}_1^{[1:r_1]} = \tilde{\boldsymbol{U}}_1^{[n]} \tilde{\boldsymbol{U}}_1^{[n]^H} \left[\tilde{\mathscr{Z}}\right]_{(1)} \tilde{\boldsymbol{V}}_1^{[1:r_1]} \tilde{\boldsymbol{\Sigma}}_1^{[1:r_1]^{-1}}$ (Roemer *et al.*, 2014, eq. (23)) for $\tilde{\boldsymbol{U}}_1^{[n]}$ and $\tilde{\boldsymbol{\Sigma}}_1^{[1:r_1]}$ being the true versions of $\tilde{\hat{\boldsymbol{U}}}_1^{[n]}$ and $\tilde{\hat{\boldsymbol{\Sigma}}}_1^{[1:r_1]}$,

respectively. Expanding (A V-8) and (A V-9) using the properties of limit, (5.21a)-(5.21c), and (A V-10), (A V-11) and (A V-12) follow.

$$\hat{\boldsymbol{N}}_1 = \lim_{\Delta \boldsymbol{U}_{r+1:N_R W} \to \boldsymbol{0}} \left(\tilde{\hat{\boldsymbol{T}}}_1 \otimes \boldsymbol{I}_W\right) \times \lim_{\Delta \boldsymbol{U}_{r+1:N_R W} \to \boldsymbol{0}} \hat{\boldsymbol{U}}_{r+1:N_R W}(:, 1:r_1) \times \lim_{\Delta \boldsymbol{U}_{r+1:N_R W} \to \boldsymbol{0}} \hat{\boldsymbol{\Sigma}}_{r+1:N_R W}(1:r_1, 1:r_1) \times \left[\lim_{\Delta \boldsymbol{U}_{r+1:N_R W} \to \boldsymbol{0}} \hat{\boldsymbol{U}}_{r+1:N_R W}(:, 1:r_1)\right]^H. \quad \text{(A V-11)}$$

$$\hat{\boldsymbol{N}}_2 = \lim_{\Delta \boldsymbol{U}_{r+1:N_R W} \to \boldsymbol{0}} (\tilde{\hat{\boldsymbol{T}}}_1 \otimes \boldsymbol{I}_W) \times \lim_{\Delta \boldsymbol{U}_{r+1:N_R W} \to \boldsymbol{0}} \hat{\boldsymbol{U}}_{r+1:N_R W}(:, r_1+1:N_R W - r) \times \lim_{\Delta \boldsymbol{U}_{r+1:N_R W} \to \boldsymbol{0}} \hat{\boldsymbol{\Sigma}}_{r+1:N_R W}(r_1+1:N_R W - r, r_1+1:N_R W - r) \times \left[\lim_{\Delta \boldsymbol{U}_{r+1:N_R W} \to \boldsymbol{0}} \hat{\boldsymbol{U}}_{r+1:N_R W}(:, r_1+1:N_R W - r)\right]^H. \quad \text{(A V-12)}$$

To simplify (A V-11) and (A V-12), we simplify the respective limits using the first-order perturbation analysis. Deploying (A V-10),

$$\lim_{\Delta \boldsymbol{U}_{r+1:N_R W} \to \boldsymbol{0}} \left\{(\tilde{\hat{\boldsymbol{T}}}_1 \otimes \boldsymbol{I}_W) = \left((\tilde{\boldsymbol{U}}_1^{[1:r_1]} + \Delta\tilde{\boldsymbol{U}}_1^{[1:r_1]})(\tilde{\boldsymbol{U}}_1^{[1:r_1]^H} + \Delta\tilde{\boldsymbol{U}}_1^{[1:r_1]^H}) \otimes \boldsymbol{I}_W\right)\right\} = \left(\tilde{\boldsymbol{U}}_1^{[1:r_1]}\tilde{\boldsymbol{U}}_1^{[1:r_1]^H} \otimes \boldsymbol{I}_W\right) = \boldsymbol{A}. \quad \text{(A V-13)}$$

From (5.41), (A V-14) and (A V-15) become evident.

$$\lim_{\Delta \boldsymbol{U}_{r+1:N_R W} \to \boldsymbol{0}} \left\{\hat{\boldsymbol{U}}_{r+1:N_R W}(:, 1:r_1) = \boldsymbol{U}_{r+1:N_R W}(:, 1:r_1) + \Delta\boldsymbol{U}_{r+1:N_R W}(:, 1:r_1)\right\} = \boldsymbol{U}_{r+1:N_R W}(:, 1:r_1). \quad \text{(A V-14)}$$

$$\lim_{\Delta \boldsymbol{U}_{r+1:N_R W} \to \mathbf{0}} \Big\{ \hat{\boldsymbol{U}}_{r+1:N_R W}(:, r_1+1 : N_R W - r) = \boldsymbol{U}_{r+1:N_R W}(:, r_1+1 : N_R W - r) + \Delta \boldsymbol{U}_{r+1:N_R W}(:, r_1+1 : N_R W - r) \Big\} = \boldsymbol{U}_{r+1:N_R W}(:, r_1+1 : N_R W - r). \quad \text{(A V-15)}$$

Realizing that (5.39) is valid when the perturbations go to zero,

$$\lim_{\Delta \boldsymbol{U}_{r+1:N_R W} \to \mathbf{0}} \hat{\boldsymbol{\Sigma}}_{r+1:N_R W}(1 : r_1, 1 : r_1) = \boldsymbol{\Sigma}_{1:r_1}, \quad \text{(A V-16)}$$

where $\boldsymbol{\Sigma}_{1:r_1} = \boldsymbol{\Sigma}_{r+1:N_R W}(1 : r_1, 1 : r_1)$. Besides, for $a = r_1 + 1$ and $b = N_R W - r$,

$$\lim_{\Delta \boldsymbol{U}_{r+1:N_R W} \to \mathbf{0}} \hat{\boldsymbol{\Sigma}}_{r+1:N_R W}(a : b, a : b) = \operatorname{diag}\big(0, 0, \ldots, 0\big). \quad \text{(A V-17)}$$

Deploying (A V-13), (A V-14), and (A V-16) in (A V-11),

$$\hat{\boldsymbol{N}}_1 = \boldsymbol{A}\boldsymbol{U}_{r+1:N_R W}(:, 1 : r_1)\boldsymbol{\Sigma}_{1:r_1}\boldsymbol{U}^H_{r+1:N_R W}(:, 1 : r_1). \quad \text{(A V-18)}$$

Similarly, employing (A V-13), (A V-15), and (A V-17) in (A V-12),

$$\hat{\boldsymbol{N}}_2 = \mathbf{0}_{N_R W \times N_R W}. \quad \text{(A V-19)}$$

Finally, substituting (A V-18) and (A V-19) into (A V-7) while employing the property of trace,

$$\lim_{\Delta \boldsymbol{U}_{r+1:N_R W} \to \mathbf{0}} P_d = \Pr\big\{ \operatorname{tr}\big(\hat{\boldsymbol{N}}_1\big)/0 = \infty > \tilde{\lambda} \big\} \quad \text{(A V-20)}$$

Thus, if $\lambda = \nu_2 \tilde{\lambda}/\nu_1 < \infty$, $\lim_{\Delta \boldsymbol{U}_{r+1:N_R W} \to \mathbf{0}} P_d = 1$. □

3. Proof of Theorem 8

To prove the theorem, three cases are shown subsequently.

Case 4. $N_R \leq (L_1+1)$—for this case, $\tilde{r}_1 = \min(N_R, L_1+1) = N_R$. Thus, $\tilde{\tilde{\boldsymbol{T}}}_1 = \boldsymbol{I}_{N_R}$. Employing this relation—$\boldsymbol{I}_{N_R} \otimes \boldsymbol{I}_W = \boldsymbol{I}_{N_R W}$—in (A V-4) and recalling (5.17),

$$T^{\mathrm{TB}} = \frac{\nu_2}{\nu_1} \frac{\mathrm{tr}(\hat{\boldsymbol{P}}_d \hat{\boldsymbol{R}}_{yy}^{(p)})}{\mathrm{tr}\big((\boldsymbol{I}_{N_R W} - \hat{\boldsymbol{P}}_d)\hat{\boldsymbol{R}}_{yy}^{(p)}\big)} = T^{\mathrm{MB}}. \tag{A V-21}$$

As a result, $P_d = P_d^{\mathrm{mat}}$. ■

Case 5. For the very high SNR and INR regimes—this scenario corresponds to the infinitesimally small perturbations which render very high SNR and INR values. Thus, the behavior of the test statistic in (A V-4) can be assessed when the perturbations go to zero. To continue, from (Getu *et al.*, 2017, eq. (63)),

$$\tilde{\tilde{\boldsymbol{T}}}_1 = \boldsymbol{I}_{N_R} - \tilde{\tilde{\boldsymbol{U}}}_1^{[n]} \tilde{\tilde{\boldsymbol{U}}}_1^{[n]^H}, \tag{A V-22}$$

where $\tilde{\tilde{\boldsymbol{U}}}_1^{[n]}$ provides an orthonormal basis for the noise subspace which is obtained through—as discussed in Appendix 2 (under APPENDIX V)—the SVD of $[\mathscr{Y}_p]_{(1)}$. For the very high SNR and INR regimes, the overall signal lies in the signal subspace. Hence, it is possible to argue that

$$\tilde{\tilde{\boldsymbol{T}}}_1 \approx \boldsymbol{I}_{N_R}. \tag{A V-23}$$

Employing (A V-23) in (A V-4),

$$T^{\mathrm{TB}} \approx \frac{\nu_2}{\nu_1} \frac{\mathrm{tr}\big(\hat{\boldsymbol{P}}_d \hat{\boldsymbol{R}}_{yy}^{(p)}\big)}{\mathrm{tr}\big((\boldsymbol{I}_{N_R W} - \hat{\boldsymbol{P}}_d)\hat{\boldsymbol{R}}_{yy}^{(p)}\big)} = T^{\mathrm{MB}}, \tag{A V-24}$$

where the estimated parameters are to be replaced by their true estimates. Thus, for the very high SNR and INR regimes, $P_d = P_d^{\mathrm{mat}}$. ■

Case 6. For the low SNR and INR regimes with the constraint: $N_R >> (L_1+1)$ and $N_R W >> r+r_1$—this scenario is going to be investigated by also using (A V-4). Realizing that a projection matrix $\tilde{\tilde{\boldsymbol{T}}}_1$ is Hermitian, i.e., $\tilde{\tilde{\boldsymbol{T}}}_1^H = \tilde{\tilde{\boldsymbol{T}}}_1$, and idempotent, i.e., $\tilde{\tilde{\boldsymbol{T}}}_1 \tilde{\tilde{\boldsymbol{T}}}_1 = \tilde{\tilde{\boldsymbol{T}}}_1$, the subsequent simplifications follow.

Let $F_1 = \mathrm{tr}\Big((\tilde{\tilde{\boldsymbol{T}}}_1 \otimes \boldsymbol{I}_W) \hat{\boldsymbol{P}}_d \hat{\boldsymbol{R}}_{yy}^{(p)} \Big)$ and $F_2 = \mathrm{tr}\Big((\tilde{\tilde{\boldsymbol{T}}}_1 \otimes \boldsymbol{I}_W) \hat{\boldsymbol{R}}_{yy}^{(p)} \Big)$. With these suppositions, it is inferred from (A V-4) that

$$T^{\mathrm{TB}} = \frac{\nu_2}{\nu_1} \frac{F_1}{F_2 - F_1}. \tag{A V-25}$$

Using the identity that $\mathrm{tr}(\boldsymbol{AB}) = \mathrm{tr}(\boldsymbol{BA})$ (Magnus & Neudecker, 2007, p. 11),

$$F_1 = \mathrm{tr}\Big(\hat{\boldsymbol{P}}_d \hat{\boldsymbol{R}}_{yy}^{(p)} (\tilde{\tilde{\boldsymbol{T}}}_1 \otimes \boldsymbol{I}_W) \Big) \tag{A V-26a}$$

$$F_2 = \mathrm{tr}\Big(\hat{\boldsymbol{R}}_{yy}^{(p)} (\tilde{\tilde{\boldsymbol{T}}}_1 \otimes \boldsymbol{I}_W) \Big). \tag{A V-26b}$$

Deploying (A V-22) in (A V-26a), the identity $(\boldsymbol{A}+\boldsymbol{B}) \otimes \boldsymbol{C} = \boldsymbol{A} \otimes \boldsymbol{C} + \boldsymbol{B} \otimes \boldsymbol{C}$ (Magnus & Neudecker, 2007, p. 32), and the identity $\mathrm{tr}(\boldsymbol{A}-\boldsymbol{B}) = \mathrm{tr}(\boldsymbol{A}) - \mathrm{tr}(\boldsymbol{B})$ (Magnus & Neudecker, 2007, p. 11), (A V-27) follows.

$$F_1 = \mathrm{tr}\big(\hat{\boldsymbol{P}}_d \hat{\boldsymbol{R}}_{yy}^{(p)} ((\boldsymbol{I}_{N_R} - \tilde{\boldsymbol{U}}_1^{[n]} \tilde{\boldsymbol{U}}_1^{[n]H}) \otimes \boldsymbol{I}_W) \big) = \mathrm{tr}\big(\hat{\boldsymbol{P}}_d \hat{\boldsymbol{R}}_{yy}^{(p)} \big) - \underbrace{\mathrm{tr}\big(\hat{\boldsymbol{P}}_d \hat{\boldsymbol{R}}_{yy}^{(p)} (\tilde{\boldsymbol{U}}_1^{[n]} \tilde{\boldsymbol{U}}_1^{[n]H} \otimes \boldsymbol{I}_W) \big)}_{F_{1,1}}$$

$$= \mathrm{tr}\big(\hat{\boldsymbol{P}}_d \hat{\boldsymbol{R}}_{yy}^{(p)} \big) - F_{1,1}. \tag{A V-27}$$

As $F_2 = F_1 \big|_{\hat{\boldsymbol{P}}_d = \boldsymbol{I}_{N_R W}}$, it is inferred from (A V-27) that

$$F_2 = \mathrm{tr}\big(\hat{\boldsymbol{R}}_{yy}^{(p)} \big) - F_{2,1}, \tag{A V-28}$$

where

$$F_{2,1} = F_{1,1} \big|_{\hat{\boldsymbol{P}}_d = \boldsymbol{I}_{N_R W}}. \tag{A V-29}$$

Substituting (A V-27) and (A V-28) into (A V-25),

$$T^{\mathrm{TB}} = \frac{\nu_2}{\nu_1} \frac{\mathrm{tr}\big(\hat{\boldsymbol{P}}_d \hat{\boldsymbol{R}}_{yy}^{(p)}\big) - F_{1,1}}{\mathrm{tr}\big((\boldsymbol{I}_{N_R W} - \hat{\boldsymbol{P}}_d)\hat{\boldsymbol{R}}_{yy}^{(p)}\big) - (F_{2,1} - F_{1,1})}. \tag{A V-30}$$

When $N_R >> (L_1+1)$ and $\big(\gamma_{snr},\ \gamma_{inr}\big) \rightarrow \big(0,\ 0\big)$, it can be visualized that the overall received signal lies on the noise subspace which is orthogonal to the signal subspace. Accordingly, it can be argued that $\tilde{\tilde{\boldsymbol{U}}}_1^{[n]} \tilde{\tilde{\boldsymbol{U}}}_1^{[n]^H} \approx \boldsymbol{I}_{N_R}$ which, in turn, implicates that

$$F_{1,1} \approx \mathrm{tr}\Big(\hat{\boldsymbol{P}}_d \hat{\boldsymbol{R}}_{yy}^{(p)} \boldsymbol{I}_{N_R W} = \hat{\boldsymbol{P}}_d \hat{\boldsymbol{R}}_{yy}^{(p)}\Big) = \sum_{i=r+1}^{r+r_1} \hat{\sigma}_i. \tag{A V-31}$$

From (A V-29) and (A V-31),

$$F_{2,1} \approx \mathrm{tr}\Big(\hat{\boldsymbol{R}}_{yy}^{(p)} \boldsymbol{I}_{N_R W} = \hat{\boldsymbol{R}}_{yy}^{(p)}\Big) = \sum_{i=r+1}^{N_R W} \hat{\sigma}_i. \tag{A V-32}$$

To continue, since an SCM is both a Hermitian and positive semi-definite matrix, it is to be noted that $\hat{\sigma}_i \approx \sigma^2 > 0,\ \forall\ i \geq r + r_1 + 1$, which is much stronger than the strength of the received SOI and RFI signals whenever $(\gamma_{snr}, \gamma_{inr}) \rightarrow (0,0)$. Using (A V-31) and (A V-32), (A V-30) simplifies to

$$T^{\mathrm{TB}} \approx \frac{\nu_2}{\nu_1} \frac{\mathrm{tr}\big(\hat{\boldsymbol{P}}_d \hat{\boldsymbol{R}}_{yy}^{(p)}\big) - \sum_{i=r+1}^{r+r_1} \hat{\sigma}_i}{\mathrm{tr}\big((\boldsymbol{I}_{N_R W} - \hat{\boldsymbol{P}}_d)\hat{\boldsymbol{R}}_{yy}^{(p)}\big) - \sum_{i=r+r_1+1}^{N_R W} \hat{\sigma}_i} \tag{A V-33a}$$

$$\overset{(a)}{>>} \frac{\nu_2}{\nu_1} \frac{\mathrm{tr}\big(\hat{\boldsymbol{P}}_d \hat{\boldsymbol{R}}_{yy}^{(p)}\big) - \sum_{i=r+1}^{r+r_1} \hat{\sigma}_i}{\mathrm{tr}\big((\boldsymbol{I}_{N_R W} - \hat{\boldsymbol{P}}_d)\hat{\boldsymbol{R}}_{yy}^{(p)}\big)} \tag{A V-33b}$$

$$\overset{(b)}{=} T^{\mathrm{MB}} - \frac{\nu_2}{\nu_1} \times \frac{\sum_{i=r+1}^{r+r_1} \hat{\sigma}_i}{\sum_{i=r+r_1+1}^{N_R W} \hat{\sigma}_i}, \tag{A V-33c}$$

where (a) follows for $\sum_{i=r+r_1+1}^{N_R W} \hat{\sigma}_i \approx (N_R W - r - r_1)\sigma^2 >> 0$ and (b) follows from (5.17).

To continue further, we analyze the behavior of $\frac{\sum_{i=r+1}^{r+r_1}\hat{\sigma}_i}{\sum_{i=r+r_1+1}^{N_RW}\hat{\sigma}_i}$ whenever $N_RW >> r+r_1$ and $\left(\gamma_{snr},\, \gamma_{inr}\right) \to \left(0,\, 0\right)$—the preliminary conditions. As both the SNR and INR get close to zero, $\sum_{i=r+1}^{r+r_1}\hat{\sigma}_i \approx r_1\sigma^2$, $\sum_{i=r+r_1+1}^{N_RW}\hat{\sigma}_i \approx (N_RW-r-r_1)\sigma^2$, and hence

$$\frac{\sum_{i=r+1}^{r+r_1}\hat{\sigma}_i}{\sum_{i=r+r_1+1}^{N_RW}\hat{\sigma}_i} \approx \frac{r_1\sigma^2}{\left(N_RW-(r+r_1)\right)\sigma^2} \overset{(c)}{\approx} \frac{r_1}{N_RW} \overset{(d)}{\approx} 0, \tag{A V-34}$$

where (c) follows for $N_RW >> r+r_1$ and (d) follows for the consideration that $N_RW >> r+r_1 > r_1$. Meanwhile, employing (A V-34) in (A V-33c) renders $T^{\mathrm{TB}} >> T^{\mathrm{MB}}$. Equivalently, $\Pr\left\{T^{\mathrm{TB}} > \lambda | H_1\right\} >> \Pr\left\{T^{\mathrm{MB}} > \lambda | H_1\right\}$. Correspondingly, $P_d >> P_d^{\mathrm{mat}}$. ■

Eventually, combining Case 4, Case 5, and Case 6, Theorem 8 follows. □

APPENDIX VI

APPENDICES OF CHAPTER 6

1. Proof of Theorem 10

For a perfect $\hat{\mathscr{U}}^{[I]}$, $\mathscr{P} \in \mathbb{C}^{N_R \times W \times N_R W}$ excises the MI-RFI in (6.9) if and only if (iff)

$$\mathscr{P} \times_3 \hat{\mathscr{U}}^{[I]} = \mathscr{P} \times_3 \mathscr{G} = \mathscr{O}_t = \hat{\mathscr{U}}^{[I]} - \hat{\mathscr{U}}^{[I]}, \tag{A VI-1}$$

where $\mathscr{O}_t \in \mathbb{C}^{N_R \times W \times r}$ is a zero tensor. Employing (6.1), $\left(\hat{\mathscr{U}}^{[I]} \times_3 \left(\hat{\mathscr{U}}^{[I]}\right)^{+3}\right) \times_3 \hat{\mathscr{U}}^{[I]} = \hat{\mathscr{U}}^{[I]}$ and $\mathscr{I}_3 \times_3 \hat{\mathscr{U}}^{[I]} = \hat{\mathscr{U}}^{[I]}$. Accordingly, perfect excision is possible iff

$$\mathscr{P} \times_3 \hat{\mathscr{U}}^{[I]} = \mathscr{I}_3 \times_3 \hat{\mathscr{U}}^{[I]} - \left(\hat{\mathscr{U}}^{[I]} \times_3 \left(\hat{\mathscr{U}}^{[I]}\right)^{+3}\right) \times_3 \hat{\mathscr{U}}^{[I]} = \mathscr{O}_t. \tag{A VI-2}$$

Applying the definition of the 3-mode product of two tensors (cf. Section 6.2.1) and the distributive property of matrix product to (A VI-2) give

$$\left[\mathscr{P} \times_3 \hat{\mathscr{U}}^{[I]}\right]_{(3)} = \left[\hat{\mathscr{U}}^{[I]}\right]_{(3)} \left(\left[\mathscr{I}_3\right]_{(3)} - \left[\hat{\mathscr{U}}^{[I]} \times_3 \left(\hat{\mathscr{U}}^{[I]}\right)^{+3}\right]_{(3)}\right). \tag{A VI-3}$$

Thereafter, the tensorization of (A VI-3) renders

$$\mathscr{P} \times_3 \hat{\mathscr{U}}^{[I]} = \left(\mathscr{I}_3 - \hat{\mathscr{U}}^{[I]} \times_3 \left(\hat{\mathscr{U}}^{[I]}\right)^{+3}\right) \times_3 \hat{\mathscr{U}}^{[I]}. \tag{A VI-4}$$

Finally, it is easily inferred from (A VI-4) that

$$\mathscr{P} = \mathscr{I}_3 - \hat{\mathscr{U}}^{[I]} \times_3 \left(\hat{\mathscr{U}}^{[I]}\right)^{+3}. \tag{A VI-5}$$

□

2. Proof of Theorem 11

Applying the definition of the r-mode product of two tensors (cf. Section 6.2.1) and transposition to (6.14) render

$$\text{RMSEE} = \sqrt{\mathbb{E}\left\{ \left\| [\mathscr{P}]^T_{(3)} [\mathscr{G}]^T_{(3)} \right\|_F^2 \right\}}. \tag{A VI-6}$$

From the MLSEP problem formulation, $[\mathscr{G}]^T_{(3)} = \boldsymbol{G}$—cf. Section 6.3.2. As a result,

$$\text{RMSEE} = \sqrt{\mathbb{E}\left\{ \left\| [\mathscr{P}]^T_{(3)} \boldsymbol{G} \right\|_F^2 \right\}}. \tag{A VI-7}$$

From (6.13) and the definition of the 3-mode unfolding—cf. Section 6.2.1,

$$\left[\mathscr{P}\right]^T_{(3)} = \boldsymbol{I}_{N_R W} - \left[\hat{\mathscr{U}}^{[I]}\right]^T_{(3)} \left(\left[\hat{\mathscr{U}}^{[I]}\right]^T_{(3)} \right)^+. \tag{A VI-8}$$

Using (6.29) or (6.32) in (A VI-8) and substituting it into (A VI-7) afterward lead to (A VI-9).

$$\text{RMSEE} = \sqrt{\mathbb{E}\left\{ \left\| \left(\boldsymbol{I}_{N_R W} - \left(\boldsymbol{U}_I + \left[\Delta\hat{\mathscr{U}}^{[I]}\right]^T_{(3)} \right) \left(\boldsymbol{U}_I + \left[\Delta\hat{\mathscr{U}}^{[I]}\right]^T_{(3)} \right)^+ \right) \boldsymbol{G} \right\|_F^2 \right\}}. \tag{A VI-9}$$

Applying limit and its respective properties to (A VI-9) gives (A VI-10).

$$\lim_{\Delta \boldsymbol{U}_I \to \boldsymbol{0}} \text{RMSEE} = \sqrt{\mathbb{E}\left\{ \left\| \left(\boldsymbol{I}_{N_R W} - \left(\boldsymbol{U}_I + \lim_{\Delta \boldsymbol{U}_I \to \boldsymbol{0}} \left[\Delta\hat{\mathscr{U}}^{[I]}\right]^T_{(3)} \right) \left(\boldsymbol{U}_I + \lim_{\Delta \boldsymbol{U}_I \to \boldsymbol{0}} \left[\Delta\hat{\mathscr{U}}^{[I]}\right]^T_{(3)} \right)^+ \right) \boldsymbol{G} \right\|_F^2 \right\}}. \tag{A VI-10}$$

To simplify (A VI-10), the underneath lemma is required.

Lemma 6.

$$\lim_{\Delta \boldsymbol{U}_I \to \boldsymbol{0}} \left[\Delta \hat{\mathscr{U}}^{[I]} \right]_{(3)}^{T} = \boldsymbol{0}. \tag{A VI-11}$$

Proof. The proof of (A VI-11) depends on N_R. Thus, two cases are shown in the sequel.

Case 7. $N_R \leq \sum_{i=1}^{Q} (L_i + 1)$

From the equality in (6.29), $\lim_{\Delta \boldsymbol{U}_I \to \boldsymbol{0}} \left[\Delta \hat{\mathscr{U}}^{[I]} \right]_{(3)}^{T} = \lim_{\Delta \boldsymbol{U}_I \to \boldsymbol{0}} \Delta \boldsymbol{U}_I = \boldsymbol{0}$. ■

Case 8. $N_R > \sum_{i=1}^{Q} (L_i + 1)$

Employing (6.32),

$$\lim_{\Delta \boldsymbol{U}_I \to \boldsymbol{0}} \left[\Delta \hat{\mathscr{U}}^{[I]} \right]_{(3)}^{T} = \lim_{\Delta \boldsymbol{U}_I \to \boldsymbol{0}} \Big\{ \Delta \boldsymbol{U}_I + \big(\boldsymbol{U}_1^{[I]} \Delta \boldsymbol{U}_1^{[I]^H} \otimes \boldsymbol{I}_W \big) \boldsymbol{U}_I + \big(\Delta \boldsymbol{U}_1^{[I]} \boldsymbol{U}_1^{[I]^H} \otimes \boldsymbol{I}_W \big) \boldsymbol{U}_I \Big\} \tag{A VI-12}$$

$$\lim_{\Delta \boldsymbol{U}_I \to \boldsymbol{0}} \left[\Delta \hat{\mathscr{U}}^{[I]} \right]_{(3)}^{T} = \Big(\boldsymbol{U}_1^{[I]} \times \Big(\lim_{\Delta \boldsymbol{U}_I \to \boldsymbol{0}} \Delta \boldsymbol{U}_1^{[I]} \Big)^H \otimes \boldsymbol{I}_W \Big) \boldsymbol{U}_I + \Big(\Big(\lim_{\Delta \boldsymbol{U}_I \to \boldsymbol{0}} \Delta \boldsymbol{U}_1^{[I]} \Big) \times \boldsymbol{U}_1^{[I]^H} \otimes \boldsymbol{I}_W \Big) \boldsymbol{U}_I. \tag{A VI-13}$$

To continue, the aforementioned limit should be computed. Utilizing (6.31) for $\Delta \boldsymbol{U}_1^{[I]}$,

$$\lim_{\Delta \boldsymbol{U}_I \to 0} \Delta \boldsymbol{U}_1^{[I]} = \lim_{\Delta \boldsymbol{U}_I \to 0} \overbrace{\boldsymbol{U}_1^{[n]} \boldsymbol{U}_1^{[n]^H}}^{\tilde{\boldsymbol{U}}_1^{[n]}} [\mathscr{Z}]_{(1)} \overbrace{\boldsymbol{V}_1^{[I]} \boldsymbol{\Sigma}_1^{[I]^{-1}}}^{\tilde{\boldsymbol{V}}_1^{[I]}} \tag{A VI-14a}$$

$$= \lim_{\Delta \boldsymbol{U}_I \to 0} \operatorname{unvec} \Big(\operatorname{vec} \big(\tilde{\boldsymbol{U}}_1^{[n]} [\mathscr{Z}]_{(1)} \tilde{\boldsymbol{V}}_1^{[I]} \big) \Big), \tag{A VI-14b}$$

where $\tilde{\boldsymbol{U}}_1^{[n]} = \boldsymbol{U}_1^{[n]}\boldsymbol{U}_1^{[n]^H}$ and $\tilde{\boldsymbol{V}}_1^{[I]} = \boldsymbol{V}_1^{[I]}\boldsymbol{\Sigma}_1^{[I]^{-1}}$. Applying the property of "vec"—referring to (Magnus & Neudecker, 2007, eq. (5), p. 35)—and limit to (A VI-14b),

$$\lim_{\Delta\boldsymbol{U}_I\to 0}\Delta\boldsymbol{U}_1^{[I]} = \text{unvec}\Big((\tilde{\boldsymbol{V}}_1^{[I]^T}\otimes\tilde{\boldsymbol{U}}_1^{[n]})\lim_{\Delta\boldsymbol{U}_I\to 0}\text{vec}\big([\mathscr{Z}]_{(1)}\big)\Big). \tag{A VI-15}$$

From (6.27), $\Delta\boldsymbol{U}_I\to 0$ as $\boldsymbol{Z}\to 0$. On the other hand, $\text{vec}\big([\mathscr{Z}]_{(1)}\big) = \boldsymbol{K}_{W\times N_RN}\text{vec}\big(\boldsymbol{Z}\big)$ (Roemer *et al.*, 2014, eq. (73)), for $\boldsymbol{K}_{W\times N_RN}\in\mathbb{R}^{N_RWN\times N_RWN}$ being the commutation matrix (Magnus & Neudecker, 2007). As a result,

$$\lim_{\Delta\boldsymbol{U}_I\to 0}\Delta\boldsymbol{U}_1^{[I]} = \text{unvec}\Big((\tilde{\boldsymbol{V}}_1^{[I]^T}\otimes\tilde{\boldsymbol{U}}_1^{[n]})\boldsymbol{K}_{W\times N_RN}\lim_{\boldsymbol{Z}\to 0}\text{vec}\big(\boldsymbol{Z}\big)\Big) = \boldsymbol{0}. \tag{A VI-16}$$

Substituting (A VI-16) into (A VI-13), $\lim_{\Delta\boldsymbol{U}_I\to\boldsymbol{0}}\Big[\Delta\hat{\mathscr{U}}^{[I]}\Big]_{(3)}^T = \boldsymbol{0}$. ■

Eventually, combining Case 7 and Case 8 results in

$$\lim_{\Delta\boldsymbol{U}_I\to\boldsymbol{0}}\Big[\Delta\hat{\mathscr{U}}^{[I]}\Big]_{(3)}^T = \boldsymbol{0}. \tag{A VI-17}$$

□

Deploying Lemma 6 in (A VI-10) results in

$$\lim_{\Delta\boldsymbol{U}_I\to\boldsymbol{0}}\text{RMSEE} = \sqrt{\mathbb{E}\Big\{\big\|\big(\boldsymbol{I}_{N_RW}-\boldsymbol{U}_I\boldsymbol{U}_I^{+}\big)\boldsymbol{G}\big\|_F^2\Big\}}. \tag{A VI-18}$$

To simplify (A VI-18), we use the following relation:

$$\boldsymbol{G} = \boldsymbol{G}\boldsymbol{I}_r = \boldsymbol{G}(\boldsymbol{F}\boldsymbol{F}^H)(\boldsymbol{F}\boldsymbol{F}^H)^{-1} = (\boldsymbol{G}\boldsymbol{F})\boldsymbol{F}^H(\boldsymbol{F}\boldsymbol{F}^H)^{-1}. \tag{A VI-19}$$

From (6.26), $\boldsymbol{GF} = \boldsymbol{U}_I \boldsymbol{\Sigma}_I \boldsymbol{V}_I^H$. Thus,

$$\boldsymbol{G} = (\boldsymbol{U}_I \boldsymbol{\Sigma}_I \boldsymbol{V}_I^H)\boldsymbol{F}^H(\boldsymbol{F}\boldsymbol{F}^H)^{-1} = \boldsymbol{U}_I \boldsymbol{\Sigma}_I \boldsymbol{V}_I^H \boldsymbol{F}^H(\boldsymbol{F}\boldsymbol{F}^H)^{-1}. \tag{A VI-20}$$

Substituting (A VI-20) into (A VI-18) renders

$$\lim_{\Delta \boldsymbol{U}_I \to \boldsymbol{0}} \text{RMSEE} = \sqrt{\mathbb{E}\Big\{ \big\| \big(\boldsymbol{U}_I - \boldsymbol{U}_I \boldsymbol{U}_I^+ \boldsymbol{U}_I\big) \boldsymbol{\Sigma}_I \boldsymbol{V}_I^H \boldsymbol{F}^H (\boldsymbol{F}\boldsymbol{F}^H)^{-1} \big\|_F^2 \Big\}}. \tag{A VI-21}$$

For $\boldsymbol{U}_I$ possesses linearly independent columns, $\boldsymbol{U}_I^+ = \big(\boldsymbol{U}_I{}^H \boldsymbol{U}_I\big)^{-1} \boldsymbol{U}_I{}^H$. Accordingly,

$$\boldsymbol{U}_I - \boldsymbol{U}_I \boldsymbol{U}_I^+ \boldsymbol{U}_I = \boldsymbol{U}_I - \boldsymbol{U}_I \underbrace{\big(\boldsymbol{U}_I{}^H \boldsymbol{U}_I\big)^{-1} \boldsymbol{U}_I{}^H \boldsymbol{U}_I}_{=\boldsymbol{I}_r} = \boldsymbol{0}. \tag{A VI-22}$$

Substituting (A VI-22) into (A VI-21), and taking Frobenius norm eventually result in

$$\lim_{\Delta \boldsymbol{U}_I \to \boldsymbol{0}} \text{RMSEE} = 0. \tag{A VI-23}$$

□

3. Proof of Theorem 12

Substituting $\boldsymbol{U}_I + \Big[\Delta \hat{\mathscr{U}}^{[I]}\Big]_{(3)}^T = \Big[\hat{\mathscr{U}}^{[I]}\Big]_{(3)}^T$ to (A VI-9) results in

$$\text{RMSEE} = \sqrt{\mathbb{E}\Big\{ \Big\| \Big[\boldsymbol{I}_{N_R W} - \Big[\hat{\mathscr{U}}^{[I]}\Big]_{(3)}^T \Big(\Big[\hat{\mathscr{U}}^{[I]}\Big]_{(3)}^T \Big)^+ \Big] \boldsymbol{G} \Big\|_F^2 \Big\}}. \tag{A VI-24}$$

Whenever $N_R > \sum_{i=1}^{Q} (L_i + 1)$—cf. (6.12),

$$\Big[\hat{\mathscr{U}}^{[I]}\Big]_{(3)}^T = \big(\hat{\boldsymbol{T}}_1 \otimes \hat{\boldsymbol{T}}_2\big)\hat{\boldsymbol{U}}_I = \big(\hat{\boldsymbol{T}}_1 \otimes \boldsymbol{I}_W\big)\hat{\boldsymbol{U}}_I. \tag{A VI-25}$$

Employing SVD, $\left[\mathscr{Y}_I\right]_{(1)} = \hat{\boldsymbol{U}}_1\hat{\boldsymbol{\Sigma}}_1\hat{\boldsymbol{V}}_1^H$, for $\hat{\boldsymbol{U}}_1 = \left[\hat{\boldsymbol{U}}_1^{[I]}\ \ \hat{\boldsymbol{U}}_1^{[n]}\right]$. As a result,

$$\hat{\boldsymbol{T}}_1 = \hat{\boldsymbol{U}}_1^{[I]}\hat{\boldsymbol{U}}_1^{[I]^H} = \boldsymbol{I}_{N_R} - \hat{\boldsymbol{U}}_1^{[n]}\hat{\boldsymbol{U}}_1^{[n]^H}. \tag{A VI-26}$$

Employing (A VI-26) in (A VI-25) by applying the distributive property of Kronecker product (Magnus & Neudecker, 2007) gives

$$\left[\hat{\mathscr{U}}^{[I]}\right]_{(3)}^T = \hat{\boldsymbol{U}}_I - \underbrace{\left(\hat{\boldsymbol{U}}_1^{[n]}\hat{\boldsymbol{U}}_1^{[n]^H} \otimes \boldsymbol{I}_W\right)}_{\boldsymbol{\Upsilon}}\hat{\boldsymbol{U}}_I \tag{A VI-27a}$$

$$= \hat{\boldsymbol{U}}_I - \boldsymbol{\Upsilon}\hat{\boldsymbol{U}}_I = \boldsymbol{U}_I + \Delta\boldsymbol{U}_I - \boldsymbol{C}(\boldsymbol{\Upsilon}), \tag{A VI-27b}$$

where (6.27) is utilized in (A VI-27b), $\boldsymbol{\Upsilon} = \left(\hat{\boldsymbol{U}}_1^{[n]}\hat{\boldsymbol{U}}_1^{[n]^H} \otimes \boldsymbol{I}_W\right)$, and $\boldsymbol{C}(\boldsymbol{\Upsilon}) = \boldsymbol{\Upsilon}\boldsymbol{U}_I + \boldsymbol{\Upsilon}\Delta\boldsymbol{U}_I$. Substituting (A VI-27b) into (A VI-24) results in (A VI-28).

$$\text{RMSEE} = \sqrt{\mathbb{E}\left\{\left\|\left[\boldsymbol{I}_{N_R W} - \left(\boldsymbol{U}_I + \Delta\boldsymbol{U}_I - \boldsymbol{C}(\boldsymbol{\Upsilon})\right)\left(\boldsymbol{U}_I + \Delta\boldsymbol{U}_I - \boldsymbol{C}(\boldsymbol{\Upsilon})\right)^+\right]\boldsymbol{G}\right\|_F^2\right\}}. \tag{A VI-28}$$

Employing (6.27) in the projection matrix $\boldsymbol{P} = \boldsymbol{I}_{N_R W} - \hat{\boldsymbol{U}}_I(\hat{\boldsymbol{U}}_I)^+$ gives the RMSEE for SP as

$$\text{sp-RMSEE} = \sqrt{\mathbb{E}\left\{\left\|\left[\boldsymbol{I}_{N_R W} - (\boldsymbol{U}_I + \Delta\boldsymbol{U}_I)(\boldsymbol{U}_I + \Delta\boldsymbol{U}_I)^+\right]\boldsymbol{G}\right\|_F^2\right\}}. \tag{A VI-29}$$

From (A VI-23) & (A VI-28), the convergence (CON) of $\lim_{\Delta\boldsymbol{U}_I \to \boldsymbol{0}}$ RMSEE to 0 depends on the CON of

$$\tilde{\boldsymbol{C}}(\Delta\boldsymbol{U}_I) = \Delta\boldsymbol{U}_I - \boldsymbol{C}(\boldsymbol{\Upsilon}) = \Delta\boldsymbol{U}_I - \left(\boldsymbol{\Upsilon}\boldsymbol{U}_I + \boldsymbol{\Upsilon}\Delta\boldsymbol{U}_I\right). \tag{A VI-30}$$

From (A VI-23) & (A VI-29), the CON of $\lim_{\Delta\boldsymbol{U}_I \to \boldsymbol{0}}$ sp-RMSEE to 0 depends on the CON of $\Delta\boldsymbol{U}_I$. Meanwhile,

$$\hat{\boldsymbol{U}}_1^{[n]} = \boldsymbol{U}_1^{[n]} + \Delta\boldsymbol{U}_1^{[n]}, \tag{A VI-31}$$

where $\Delta \boldsymbol{U}_1^{[n]} = -\boldsymbol{U}_1^{[I]} \boldsymbol{\Sigma}_1^{[I]^{-1}} \boldsymbol{V}_1^{[I]^H} [\mathscr{Z}]_{(1)}^H \boldsymbol{U}_1^{[n]} \in \mathbb{C}^{N_R \times (N_R - r_1)}$ (Li *et al.*, 1993, eqs. (7) & (11)) is the perturbations in the singular vectors that span the noise subspace.

Employing (A VI-31),

$$\boldsymbol{\Upsilon} = \left[\left(\boldsymbol{U}_1^{[n]} \boldsymbol{U}_1^{[n]^H} + \boldsymbol{U}_1^{[n]} \Delta \boldsymbol{U}_1^{[n]^H} \right) \otimes \boldsymbol{I}_W \right] + \left(\left(\Delta \boldsymbol{U}_1^{[n]} \boldsymbol{U}_1^{[n]^H} + \Delta \boldsymbol{U}_1^{[n]} \Delta \boldsymbol{U}_1^{[n]^H} \right) \otimes \boldsymbol{I}_W \right]. \quad \text{(A VI-32)}$$

Substituting (A VI-32) into (A VI-30), and discarding second- and third-order terms result in (A VI-33).

$$\tilde{\boldsymbol{C}}(\Delta \boldsymbol{U}_I) = \Delta \boldsymbol{U}_I - \left(\boldsymbol{U}_1^{[n]} \boldsymbol{U}_1^{[n]^H} \otimes \boldsymbol{I}_W \right) \boldsymbol{U}_I - \left(\boldsymbol{U}_1^{[n]} \Delta \boldsymbol{U}_1^{[n]^H} \otimes \boldsymbol{I}_W \right) \boldsymbol{U}_I - \left(\Delta \boldsymbol{U}_1^{[n]} \boldsymbol{U}_1^{[n]^H} \otimes \boldsymbol{I}_W \right) \boldsymbol{U}_I - \left(\boldsymbol{U}_1^{[n]} \boldsymbol{U}_1^{[n]^H} \otimes \boldsymbol{I}_W \right) \Delta \boldsymbol{U}_I. \quad \text{(A VI-33)}$$

Letting $\Theta = \boldsymbol{U}_1^{[I]} \boldsymbol{\Sigma}_1^{[I]^{-1}} \boldsymbol{V}_1^{[I]^H}$ and adopting the simplifications of (A VI-14a)–(A VI-16), $\lim_{\Delta \boldsymbol{U}_I \to 0} \Delta \boldsymbol{U}_1^{[n]} = \boldsymbol{0}$. Asymptotically, as $\boldsymbol{Z} \to \boldsymbol{0}$, $\left[\mathscr{Y}_I \right]_{(1)} = \boldsymbol{U}_1^{[I]} \boldsymbol{\Sigma}_1^{[I]} \boldsymbol{V}_1^{[I]^H}$. As a result, $\boldsymbol{U}_1^{[n]} \boldsymbol{U}_1^{[n]^H} \approx \boldsymbol{0}$ and

$$\tilde{\boldsymbol{C}}(\Delta \boldsymbol{U}_I) \approx \Delta \boldsymbol{U}_I - \left(\boldsymbol{U}_1^{[n]} \Delta \boldsymbol{U}_1^{[n]^H} \otimes \boldsymbol{I}_W \right) \boldsymbol{U}_I - \left(\Delta \boldsymbol{U}_1^{[n]} \boldsymbol{U}_1^{[n]^H} \otimes \boldsymbol{I}_W \right) \boldsymbol{U}_I. \quad \text{(A VI-34)}$$

To continue, the CON of $\Delta \boldsymbol{U}_I = \boldsymbol{U}_n \boldsymbol{U}_n^H \boldsymbol{Z} \boldsymbol{V}_I \boldsymbol{\Sigma}_I^{-1} \in \mathbb{C}^{N_R W \times r}$ to $\boldsymbol{0}$ depends on the CON of $\boldsymbol{Z}$ and $\boldsymbol{U}_n \boldsymbol{U}_n^H$. As each element of $\boldsymbol{U}_n \in \mathbb{C}^{N_R W \times (N_R W - r)}$ is close to zero, $\boldsymbol{U}_n \boldsymbol{U}_n^H$ converges to $(N_R W - r) \boldsymbol{Z} \boldsymbol{Z}^H$ as $\boldsymbol{Z} \to \boldsymbol{0}$, since $(N_R W - r)$ terms are being multiplied and summed per element. As a result, the order of convergence (OOC) of $\Delta \boldsymbol{U}_I$ is of $(N_R W - r) \boldsymbol{Z} \boldsymbol{Z}^H \boldsymbol{Z}$.

On the other hand, the CON of $\left(\Delta \boldsymbol{U}_1^{[n]} \boldsymbol{U}_1^{[n]^H} \otimes \boldsymbol{I}_W \right) \boldsymbol{U}_I$ to $\boldsymbol{0}$ depends on the CON of $[\mathscr{Z}]_{(1)}$ and $\boldsymbol{U}_1^{[n]} \boldsymbol{U}_1^{[n]^H}$, as $\Delta \boldsymbol{U}_1^{[n]} \boldsymbol{U}_1^{[n]^H} = -\boldsymbol{U}_1^{[I]} \boldsymbol{\Sigma}_1^{[I]^{-1}} \boldsymbol{V}_1^{[I]^H} [\mathscr{Z}]_{(1)}^H \boldsymbol{U}_1^{[n]} \boldsymbol{U}_1^{[n]^H}$. As $\Delta \boldsymbol{U}_I \to \boldsymbol{0}$ and hence $\boldsymbol{Z} \to \boldsymbol{0}$, $\boldsymbol{U}_1^{[n]} \boldsymbol{U}_1^{[n]^H} \to \boldsymbol{0}$ and $[\mathscr{Z}]_{(1)} \to \boldsymbol{0}$—cf. Lemma 6.

As each element of $\boldsymbol{U}_1^{[n]} \in \mathbb{C}^{N_R \times (N_R - r_1)}$ is close to 0, $\boldsymbol{U}_1^{[n]}\boldsymbol{U}_1^{[n]^H}$ converges to $(N_R - r_1)[\mathscr{Z}]_{(1)}[\mathscr{Z}]_{(1)}^H$ as $[\mathscr{Z}]_{(1)} \to \mathbf{0}$, since $(N_R - r_1)$ terms are being multiplied and summed per element. Hence, $\Delta\boldsymbol{U}_1^{[n]}\boldsymbol{U}_1^{[n]^H}$ exhibits an OOC of $(N_R - r_1)[\mathscr{Z}]_{(1)}^H[\mathscr{Z}]_{(1)}[\mathscr{Z}]_{(1)}^H$. To this end, the OOC of $\left(\Delta\boldsymbol{U}_1^{[n]}\boldsymbol{U}_1^{[n]^H} \otimes \boldsymbol{I}_W\right)\boldsymbol{U}_I$ is of $(N_R - r_1)\boldsymbol{Z}\boldsymbol{Z}^H\boldsymbol{Z}$ and hence $\frac{N_R - r_1}{N_R W - r}\Delta\boldsymbol{U}_I$, as $[\mathscr{Z}]_{(1)} \to \mathbf{0}$ when $\boldsymbol{Z} \to \mathbf{0}$.

Deploying a similar logic, the OOC of $\left(\boldsymbol{U}_1^{[n]}\Delta\boldsymbol{U}_1^{[n]^H} \otimes \boldsymbol{I}_W\right)\boldsymbol{U}_I$ is also of $\frac{N_R - r_1}{N_R W - r}\Delta\boldsymbol{U}_I$. Thus, $\boldsymbol{\mu}^{\text{MLSEP}}$ being the OOC of MLSEP becomes

$$\boldsymbol{\mu}^{\text{MLSEP}} = \Delta\boldsymbol{U}_I - 2\frac{N_R - r_1}{N_R W - r}\Delta\boldsymbol{U}_I. \tag{A VI-35}$$

Similarly, $\boldsymbol{\mu}^{\text{SP}}$ being the OOC of SP becomes

$$\boldsymbol{\mu}^{\text{SP}} = \Delta\boldsymbol{U}_I. \tag{A VI-36}$$

As $W > 1$, $\alpha_I = 2\frac{N_R - r_1}{N_R W - r} = \frac{2}{W}\frac{N_R W - W r_1}{N_R W - r} < 1$. Combining (A VI-35) and (A VI-36)

$$\boldsymbol{\mu}^{\text{MLSEP}} = \boldsymbol{\mu}^{\text{SP}} - \alpha_I\Delta\boldsymbol{U}_I, \tag{A VI-37}$$

Employing (A VI-37), $\boldsymbol{\mu}^{\text{MLSEP}}$ approaches $\mathbf{0}$ faster than $\boldsymbol{\mu}^{\text{SP}}$ whenever $\Delta\boldsymbol{U}_I \to \mathbf{0}$. Therefore, $\lim_{\Delta\boldsymbol{U}_I \to \mathbf{0}}$ RMSEE converges to 0 faster for MLSEP than for SP when $N_R > \sum_{i=1}^{Q}(L_i + 1)$. □

4. Proof of Corollary 2

Deploying (A VI-37) for $N_R > \sum_{i=1}^{Q}(L_i + 1)$, $\lim_{\Delta\boldsymbol{U}_I^s \to \mathbf{0}}$ s-RMSEE converges to zero with an OOC

$$\boldsymbol{\mu}^{\text{s-MLSEP}} = \Delta\boldsymbol{U}_I^s - \alpha_I\Delta\boldsymbol{U}_I^s. \tag{A VI-38}$$

Employing (6.8), the PCM and SCM are, respectively, obtained similar to (6.23) and (6.25) as

$$\boldsymbol{R}_{yy} = \mathbb{E}\{\boldsymbol{y}_m \boldsymbol{y}_m^H\} = \boldsymbol{U}\boldsymbol{\Sigma}\boldsymbol{\Sigma}^H\boldsymbol{U}^H \tag{A VI-39a}$$

$$\hat{\boldsymbol{R}}_{yy} = \frac{1}{N}\boldsymbol{Y}_I\boldsymbol{Y}_I^H = \frac{1}{N}\hat{\boldsymbol{U}}\hat{\boldsymbol{\Sigma}}\hat{\boldsymbol{\Sigma}}^H\hat{\boldsymbol{U}}^H. \tag{A VI-39b}$$

It is to be noted that the perfect MI-RFI subspace can be estimated via the PCM. When $1 \leq \eta < W$, $N^s > N$ and hence more samples result in a better estimate of the PCM. Employing (A VI-39a), (A VI-39b), (6.25), and (6.23), $\|\boldsymbol{R}_{y^s y^s} - \hat{\boldsymbol{R}}_{y^s y^s}\|_F < \|\boldsymbol{R}_{yy} - \hat{\boldsymbol{R}}_{yy}\|_F \Leftrightarrow \|\Delta\boldsymbol{U}_I^s\|_F < \|\Delta\boldsymbol{U}_I\|_F$. Hence, $\boldsymbol{\mu}^{\text{s-MLSEP}}$ approaches $\mathbf{0}$ faster than $\boldsymbol{\mu}^{\text{MLSEP}}$, as $\Delta\boldsymbol{U}_I^s$ approaches $\mathbf{0}$ faster than $\Delta\boldsymbol{U}_I$.

When $N_R \leq \sum_{i=1}^{Q}(L_i+1)$, (6.29) corroborates that $\boldsymbol{\mu}^{\text{MLSEP}} = \Delta\boldsymbol{U}_I$ and $\boldsymbol{\mu}^{\text{s-MLSEP}} = \Delta\boldsymbol{U}_I^s$. Likewise, $\boldsymbol{\mu}^{\text{s-MLSEP}}$ approaches $\mathbf{0}$ faster than $\boldsymbol{\mu}^{\text{MLSEP}}$ provided that $1 \leq \eta < W$.

Therefore, $\lim_{\Delta\boldsymbol{U}_I^s \to \mathbf{0}}$ s-RMSEE converges to 0 faster than $\lim_{\Delta\boldsymbol{U}_I \to \mathbf{0}}$ RMSEE whenever $1 \leq \eta < W$. $\square$

APPENDIX VII

APPENDICES OF CHAPTER 7

1. Proof of Proposition 3

Substituting (7.20) and (7.3) into (7.5) and, in turn, applying limit along with its properties render (A VII-1).

$$\lim_{\Delta \boldsymbol{U}_s \to \boldsymbol{0}} T|H_1 = \frac{\nu_2}{\nu_1} \frac{\operatorname{tr}\big((\boldsymbol{U}_s + \lim\limits_{\Delta \boldsymbol{U}_s \to \boldsymbol{0}} \Delta \boldsymbol{U}_s)(\boldsymbol{U}_s + \lim\limits_{\Delta \boldsymbol{U}_s \to \boldsymbol{0}} \Delta \boldsymbol{U}_s)^{+} [\boldsymbol{U}_s + \lim\limits_{\Delta \boldsymbol{U}_s \to \boldsymbol{0}} \Delta \boldsymbol{U}_s \;\; \boldsymbol{U}_n + \lim\limits_{\Delta \boldsymbol{U}_s \to \boldsymbol{0}} \Delta \boldsymbol{U}_n] \lim\limits_{\Delta \boldsymbol{U}_s \to \boldsymbol{0}} \hat{\boldsymbol{\Sigma}} \hat{\boldsymbol{V}}^H\big)}{\operatorname{tr}\big((\boldsymbol{I}_{N_R} - (\boldsymbol{U}_s + \lim\limits_{\Delta \boldsymbol{U}_s \to \boldsymbol{0}} \Delta \boldsymbol{U}_s)(\boldsymbol{U}_s + \lim\limits_{\Delta \boldsymbol{U}_s \to \boldsymbol{0}} \Delta \boldsymbol{U}_s)^{+}) [\boldsymbol{U}_s + \lim\limits_{\Delta \boldsymbol{U}_s \to \boldsymbol{0}} \Delta \boldsymbol{U}_s \;\; \boldsymbol{U}_n + \lim\limits_{\Delta \boldsymbol{U}_s \to \boldsymbol{0}} \Delta \boldsymbol{U}_n] \lim\limits_{\Delta \boldsymbol{U}_s \to \boldsymbol{0}} \hat{\boldsymbol{\Sigma}} \hat{\boldsymbol{V}}^H\big)}. \tag{A VII-1}$$

From (7.19), $\Delta \boldsymbol{U}_s \to \boldsymbol{0}$ as $\boldsymbol{Z} \to \boldsymbol{0}_{N_R \times N_R}$ $\big(\equiv \{\boldsymbol{z}[k]\}_{k=1}^{N} \to \boldsymbol{0}_{N_R \times 1} \big)$. As $\Delta \boldsymbol{U}_s \to \boldsymbol{0}$, hence, $\Delta \boldsymbol{U}_n \to \boldsymbol{0}_{N_R \times (N_R - 1)}$ for it also depends on $\boldsymbol{Z}$—cf. the note below (7.19). Consequently,

$$\lim_{\Delta \boldsymbol{U}_s \to \boldsymbol{0}} \Delta \boldsymbol{U}_s = \boldsymbol{0}_{N_R \times 1} \;\; \& \;\; \lim_{\Delta \boldsymbol{U}_s \to \boldsymbol{0}} \Delta \boldsymbol{U}_n = \boldsymbol{0}_{N_R \times (N_R - 1)}. \tag{A VII-2}$$

Utilizing (A VII-2) in (A VII-1) results in

$$\lim_{\Delta \boldsymbol{U}_s \to \boldsymbol{0}} T|H_1 = \frac{\nu_2}{\nu_1} \frac{\operatorname{tr}(\boldsymbol{U}_s \boldsymbol{U}_s^{+} [\boldsymbol{U}_s \; \boldsymbol{U}_n] \lim\limits_{\Delta \boldsymbol{U}_s \to \boldsymbol{0}} \hat{\boldsymbol{\Sigma}} \hat{\boldsymbol{V}}^H)}{\operatorname{tr}\big((\boldsymbol{I}_{N_R} - \boldsymbol{U}_s \boldsymbol{U}_s^{+})[\boldsymbol{U}_s \; \boldsymbol{U}_n] \lim\limits_{\Delta \boldsymbol{U}_s \to \boldsymbol{0}} \hat{\boldsymbol{\Sigma}} \hat{\boldsymbol{V}}^H\big)}. \tag{A VII-3}$$

Employing the product property of limit, $\lim\limits_{\Delta \boldsymbol{U}_s \to \boldsymbol{0}} \hat{\boldsymbol{\Sigma}} \hat{\boldsymbol{V}}^H = \lim\limits_{\Delta \boldsymbol{U}_s \to \boldsymbol{0}} \hat{\boldsymbol{\Sigma}} \times \lim\limits_{\Delta \boldsymbol{U}_s \to \boldsymbol{0}} \hat{\boldsymbol{V}}^H = \boldsymbol{\Sigma} \boldsymbol{V}^H$ since the estimates become perfect when the perturbations get infinitesimally small. Thus, recalling that

$\boldsymbol{U}_s^+ = (\boldsymbol{U}_s^H \boldsymbol{U}_s)^{-1} \boldsymbol{U}_s^H = \boldsymbol{U}_s^H,$

$$\lim_{\Delta \boldsymbol{U}_s \to \boldsymbol{0}} T|H_1 = \frac{\nu_2}{\nu_1} \frac{\mathrm{tr}(\boldsymbol{U}_s \boldsymbol{U}_s^H [\boldsymbol{U}_s \, \boldsymbol{U}_n] \boldsymbol{\Sigma} \boldsymbol{V}^H)}{\mathrm{tr}\big((\boldsymbol{I}_{N_R} - \boldsymbol{U}_s \boldsymbol{U}_s^H)[\boldsymbol{U}_s \, \boldsymbol{U}_n] \boldsymbol{\Sigma} \boldsymbol{V}^H\big)} \tag{A VII-4a}$$

$$\overset{(a)}{=} \frac{\nu_2}{\nu_1} \frac{\mathrm{tr}\big([\boldsymbol{U}_s \;\; \boldsymbol{0}_{N_R \times (N_R-1)}] \boldsymbol{\Sigma} \boldsymbol{V}^H\big)}{\mathrm{tr}\big([\boldsymbol{0}_{N_R \times 1} \;\; \boldsymbol{U}_n] \boldsymbol{\Sigma} \boldsymbol{V}^H\big)}, \tag{A VII-4b}$$

where (a) follows for $\boldsymbol{U}_s \boldsymbol{U}_s^H \boldsymbol{U}_s = \boldsymbol{U}_s$ and $\boldsymbol{U}_s^H \boldsymbol{U}_n = \boldsymbol{0}_{1 \times (N_R-1)}$. Substituting $\boldsymbol{\Sigma}$ and $\boldsymbol{V}$ defined in (7.18) into (A VII-4b) gives

$$\lim_{\Delta \boldsymbol{U}_s \to \boldsymbol{0}} T|H_1 = \frac{\nu_2}{\nu_1} \frac{\mathrm{tr}(\boldsymbol{U}_s \boldsymbol{\Sigma}_s \boldsymbol{V}_s^H)}{\mathrm{tr}\big(\boldsymbol{0}_{N_R \times N_R}\big)} = \infty. \tag{A VII-5}$$

From (7.14), $\lim\limits_{\Delta \boldsymbol{U}_s \to \boldsymbol{0}} P_d = \lim\limits_{\Delta \boldsymbol{U}_s \to \boldsymbol{0}} \Pr\{T|H_1 > \lambda\}$ and hence

$$\lim_{\Delta \boldsymbol{U}_s \to \boldsymbol{0}} P_d = \Pr\Big\{ \lim_{\Delta \boldsymbol{U}_s \to \boldsymbol{0}} T|H_1 > \lambda \Big\}. \tag{A VII-6}$$

For $\lambda < \infty$, thus, employing (A VII-5) in (A VII-6) results in

$$\lim_{\Delta \boldsymbol{U}_s \to \boldsymbol{0}} P_d = \Pr\{\infty > \lambda\} = 1. \tag{A VII-7}$$

□

2. Proof of Proposition 4

As $N \to \infty$, the PCM under H_1 and its SVD are given by $\boldsymbol{R}_{yy} = \mathbb{E}\big\{\boldsymbol{h} s[k] s^H[k] \boldsymbol{h}^H\big\} + \sigma^2 \boldsymbol{I}_{N_R}$ and

$$\boldsymbol{R}_{yy} = \boldsymbol{U} \boldsymbol{\Sigma} \boldsymbol{V}^H = [\boldsymbol{U}_s \, \boldsymbol{U}_n] \boldsymbol{\Sigma} [\boldsymbol{V}_s \, \boldsymbol{V}_n]^H, \tag{A VII-8}$$

where $\boldsymbol{U}_s = \boldsymbol{U}(:,1)$ is the true primary signal subspace, $\boldsymbol{U}_n = \boldsymbol{U}(:, 2 : N_R)$ is the true noise subspace, and $\boldsymbol{\Sigma} = \mathrm{diag}\big(\boldsymbol{\Sigma}_s, \boldsymbol{\Sigma}_n\big)$ for $\boldsymbol{\Sigma}_s = \sigma_1$, $\boldsymbol{\Sigma}_n = \mathrm{diag}\big(\sigma_2, \sigma_3, \ldots, \sigma_{N_R}\big)$, and $\sigma_1 \geq \sigma_2 \geq \ldots \geq \sigma_{N_R}$. As $N \to \infty$, the SOI and noise subspaces are perfectly estimated. Hence, we can infer that

$$\mathbb{E}\{\boldsymbol{h}s[k](\boldsymbol{h}s[k])^H\} = \boldsymbol{U}_s\boldsymbol{\Sigma}_s\boldsymbol{V}_s^H \tag{A VII-9a}$$

$$\sigma^2\boldsymbol{I}_{N_R} = \boldsymbol{U}_n\boldsymbol{\Sigma}_n\boldsymbol{V}_n^H. \tag{A VII-9b}$$

As $N \to \infty$, the SCM perfectly estimates the PCM, i.e., $\lim\limits_{N\to\infty} \hat{\boldsymbol{R}}_{yy} = \boldsymbol{R}_{yy}$. Hence,

$$\lim_{N\to\infty} \hat{\boldsymbol{P}}_s = \boldsymbol{P}_s = \boldsymbol{U}_s\boldsymbol{U}_s^{+} = \boldsymbol{U}_s\boldsymbol{U}_s^H. \tag{A VII-10}$$

From the decision rule,

$$\lim_{N\to\infty} P_d = \lim_{N\to\infty} \Pr\{T > \lambda | H_1\} = \lim_{N\to\infty} \Pr\{T | H_1 > \lambda\} \tag{A VII-11a}$$

$$= \Pr\Big\{ \lim_{N\to\infty} T | H_1 > \lambda \Big\}. \tag{A VII-11b}$$

Utilizing (7.5) and applying the properties of limit gives

$$\lim_{N\to\infty} T|H_1 = \frac{\nu_2}{\nu_1} \frac{\operatorname{tr}\big(\lim\limits_{N\to\infty} \hat{\boldsymbol{P}}_s \times \lim\limits_{N\to\infty} \hat{\boldsymbol{R}}_{yy} \big)}{\operatorname{tr}\big((\boldsymbol{I}_{N_R} - \lim\limits_{N\to\infty} \hat{\boldsymbol{P}}_s) \lim\limits_{N\to\infty} \hat{\boldsymbol{R}}_{yy} \big)} \tag{A VII-12a}$$

$$= \frac{\nu_2}{\nu_1} \frac{\operatorname{tr}\big(\boldsymbol{P}_s\boldsymbol{R}_{yy}\big)}{\operatorname{tr}\big((\boldsymbol{I}_{N_R} - \boldsymbol{P}_s)\boldsymbol{R}_{yy}\big)}. \tag{A VII-12b}$$

Expressing $\boldsymbol{R}_{yy}$ via infinite summation of products,

$$\lim_{N\to\infty} T|H_1 = \lim_{N\to\infty} \frac{\nu_2}{\nu_1} \frac{\sum_{k=1}^{N} \tilde{\boldsymbol{y}}^H[k]\boldsymbol{P}_s\tilde{\boldsymbol{y}}[k]}{\sum_{k=1}^{N} \tilde{\boldsymbol{y}}^H[k]\big(\boldsymbol{I}_{N_R} - \boldsymbol{P}_s\big)\tilde{\boldsymbol{y}}[k]}, \tag{A VII-13}$$

where $\tilde{\boldsymbol{y}}[k] = \boldsymbol{h}s[k] + \boldsymbol{z}[k]$.

Meanwhile, $\boldsymbol{P}_s$ and $\left(\boldsymbol{I}_{N_R}-\boldsymbol{P}_s\right)$ perfectly project toward the primary signal and noise subspaces, respectively. Accordingly, $\lim_{N\to\infty} T|H_1 \sim F'_{\nu_1,\nu_2}(\lambda^{H_1})$ for λ^{H_1} being an NCP defined as

$$\lambda^{H_1} = \lim_{N\to\infty} \frac{2}{\sigma^2}\left\{ \sum_{k=1}^{N} \left|\left|\boldsymbol{P}_s \boldsymbol{h}\boldsymbol{s}[k]\right|\right|^2 = \left|\left|\boldsymbol{h}\boldsymbol{s}[k]\right|\right|^2 \right\}. \tag{A VII-14}$$

Consequently,

$$\lim_{N\to\infty} P_d = \Pr\Big\{ \lim_{N\to\infty} T|H_1 > \lambda \Big\} \tag{A VII-15a}$$

$$= 1 - \Pr\Big\{ \lim_{N\to\infty} T|H_1 \le \lambda \Big\} \tag{A VII-15b}$$

$$= 1 - F'(\lambda; \nu_1, \nu_2|\lambda^{H_1}). \tag{A VII-15c}$$

To further characterize the asymptotic P_d, we simplify (A VII-13). Substituting (A VII-8) and (A VII-10) into (A VII-12b) results in

$$\lim_{N\to\infty} T|H_1 = \frac{\nu_2}{\nu_1} \frac{\mathrm{tr}\big(\boldsymbol{U}_s\boldsymbol{U}_s^H[\boldsymbol{U}_s\ \boldsymbol{U}_n]\boldsymbol{\Sigma}\boldsymbol{V}^H\big)}{\mathrm{tr}\big((\boldsymbol{I}_{N_R}-\boldsymbol{U}_s\boldsymbol{U}_s^H)[\boldsymbol{U}_s\ \boldsymbol{U}_n]\boldsymbol{\Sigma}\boldsymbol{V}^H\big)}. \tag{A VII-16}$$

Recalling that $\boldsymbol{U}_s\boldsymbol{U}_s^H\boldsymbol{U}_s = \boldsymbol{U}_s$ and $\boldsymbol{U}_s^H\boldsymbol{U}_n = \boldsymbol{0}_{1\times(N_R-1)}$, (A VII-16) simplifies to

$$\lim_{N\to\infty} T|H_1 = \frac{\nu_2}{\nu_1} \frac{\mathrm{tr}([\boldsymbol{U}_s\ \ \boldsymbol{0}_{N_R\times(N_R-1)}]\boldsymbol{\Sigma}\boldsymbol{V}^H)}{\mathrm{tr}\big([\boldsymbol{0}_{N_R\times 1}\ \ \boldsymbol{U}_n]\boldsymbol{\Sigma}\boldsymbol{V}^H\big)} \tag{A VII-17a}$$

$$= \frac{\nu_2}{\nu_1} \frac{\mathrm{tr}\big(\boldsymbol{U}_s\boldsymbol{\Sigma}_s\boldsymbol{V}_s^H\big)}{\mathrm{tr}\big(\boldsymbol{U}_n\boldsymbol{\Sigma}_n\boldsymbol{V}_n^H\big)} \tag{A VII-17b}$$

$$\overset{(b)}{=} \frac{\nu_2}{\nu_1} \frac{\mathbb{E}\{\mathrm{tr}\big(\boldsymbol{h}\boldsymbol{s}[k](\boldsymbol{h}\boldsymbol{s}[k])^H\big)\}}{\mathrm{tr}\big(\sigma^2\boldsymbol{I}_{N_R}\big)}, \tag{A VII-17c}$$

where (b) follows from (A VII-9a) and (A VII-9b).

Expressing expectation via the average of infinite summation of products gives

$$\lim_{N\to\infty} T|H_1 = (N_R-1)\bar{\gamma}_{snr}^{\infty}, \tag{A VII-18}$$

where $\bar{\gamma}_{snr}^{\infty} = \lim_{N\to\infty} \frac{1}{N} \sum_{k=1}^{N} \left|\left|\boldsymbol{h}s[k]\right|\right|^2 / N_R\sigma^2$ is the average SNR defined over an infinite duration. Hence,

$$\lim_{N\to\infty} P_d = \Pr\{\lim_{N\to\infty} T|H_1 > \lambda\} \tag{A VII-19a}$$

$$= \Pr\{(N_R - 1)\bar{\gamma}_{snr}^{\infty} > \lambda\}. \tag{A VII-19b}$$

Therefore, whenever $\lambda > (N_R - 1)\bar{\gamma}_{snr}^{\infty}$, $\lim_{N\to\infty} P_d = 0$. □

3. Proof of Lemma 4

By definition,

$$\lim_{N\to\infty} P_f = \lim_{N\to\infty} \Pr\{T > \lambda|H_0\} = \lim_{N\to\infty} \Pr\{T|H_0 > \lambda\} \tag{A VII-20a}$$

$$= \Pr\{\lim_{N\to\infty} T|H_0 > \lambda\}. \tag{A VII-20b}$$

From (7.1), $T|H_0 = T|H_1\big|_{\{s[k]\}_{k=1}^{N}=0}$. Thus,

$$\lim_{N\to\infty} T|H_0 = \lim_{N\to\infty} T|H_1\big|_{\{s[k]\}_{k=1}^{N}=0}. \tag{A VII-21}$$

Using (A VII-13) in (A VII-21) results in

$$\lim_{N\to\infty} T|H_0 = \lim_{N\to\infty} \frac{\nu_2}{\nu_1} \frac{F_1|H_0}{F_2|H_0}, \tag{A VII-22}$$

where $F_1|H_0 = \sum_{k=1}^{N} \boldsymbol{z}^H[k]\boldsymbol{P}_s\boldsymbol{z}[k]$ and $F_2|H_0 = \sum_{k=1}^{N} \boldsymbol{z}^H[k](\boldsymbol{I}_{N_R} - \boldsymbol{P}_s)\boldsymbol{z}[k]$. Consequently, it is evident that $\lim_{N\to\infty} T|H_0 \sim F_{\nu_1,\nu_2}$ and hence

$$\lim_{N\to\infty} P_f = 1 - F(\lambda; \nu_1, \nu_2). \tag{A VII-23}$$

To characterize P_f further, we deploy (A VII-18) in (A VII-21). Doing so results in

$$\lim_{N\to\infty} T|H_0 = 0. \tag{A VII-24}$$

Using (A VII-24) in (A VII-20b), $\lim_{N\to\infty} P_f = \Pr\big\{ \lim_{N\to\infty} T|H_0 > \lambda \big\} = \Pr\big\{0 > \lambda\big\}$. Therefore, if $\lambda > 0$, $\lim_{N\to\infty} P_f = 0$. □

4. Proof of Proposition 5

For the i.i.d. case, $\boldsymbol{R}_{yy} = \mathbb{E}\{\boldsymbol{h}s[k]s^H[k]\boldsymbol{h}^H\} + \sigma^2\boldsymbol{I}_{N_R}$ whenever $N \to \infty$. For the i.ni.d. case, $\boldsymbol{R}_{yy} = \mathbb{E}\{\boldsymbol{h}s[k]s^H[k]\boldsymbol{h}^H\} + \sigma^2\boldsymbol{I}_{N_R} + \sigma^2\boldsymbol{E}$ provided that $N \to \infty$. For perfectly estimated signal and noise subspaces, we can argue via (A VII-9a) and (A VII-9b)—for the i.ni.d. case—that

$$\mathbb{E}\big\{\boldsymbol{h}s[k](\boldsymbol{h}s[k])^H\big\} = \boldsymbol{U}_s\boldsymbol{\Sigma}_s\boldsymbol{V}_s^H \tag{A VII-25a}$$

$$\sigma^2\boldsymbol{I}_{N_R} + \sigma^2\boldsymbol{E} = \boldsymbol{U}_n\boldsymbol{\Sigma}_n\boldsymbol{V}_n^H. \tag{A VII-25b}$$

By definition, $\lim_{N\to\infty} P_d^{\text{inid}} = \lim_{N\to\infty} \Pr\big\{T^{\text{inid}} > \lambda|H_1\big\} = \lim_{N\to\infty} \Pr\big\{T^{\text{inid}}|H_1 > \lambda\big\}$. Thus,

$$\lim_{N\to\infty} P_d^{\text{inid}} = \Pr\big\{ \lim_{N\to\infty} T^{\text{inid}}|H_1 > \lambda \big\}. \tag{A VII-26}$$

Following the simplifications of (A VII-12a)-(A VII-17c),

$$\lim_{N\to\infty} T^{\text{inid}}|H_1 = \frac{\nu_2}{\nu_1}\frac{\text{tr}\big(\boldsymbol{U}_s\boldsymbol{\Sigma}_s\boldsymbol{V}_s^H\big)}{\text{tr}\big(\boldsymbol{U}_n\boldsymbol{\Sigma}_n\boldsymbol{V}_n^H\big)} \tag{A VII-27a}$$

$$\overset{(c)}{=} \frac{\nu_2}{\nu_1}\frac{\mathbb{E}\{\text{tr}\big(\boldsymbol{h}s[k](\boldsymbol{h}s[k])^H\big)\}}{\text{tr}\big(\sigma^2\boldsymbol{I}_{N_R} + \sigma^2\boldsymbol{E}\big)}, \tag{A VII-27b}$$

where (c) follows from (A VII-25a) and (A VII-25b). If $\text{tr}\big(\boldsymbol{E}\big) > 0$, it is evident from the comparison of (A VII-27b) and (A VII-17c)—derived for i.i.d. noise samples—that $\lim_{N\to\infty} T|H_1 >$

$\lim_{N\to\infty} T^{\text{inid}}|H_1$. Therefore, whenever $\sigma^2\text{tr}(\boldsymbol{E}) > 0$,

$$\Pr\Big\{\lim_{N\to\infty} T|H_1 > \lambda\Big\} > \Pr\Big\{\lim_{N\to\infty} T^{\text{inid}}|H_1 > \lambda\Big\}. \tag{A VII-28}$$

In other words, $\lim_{N\to\infty} P_d^{\text{iid}} > \lim_{N\to\infty} P_d^{\text{inid}}$ whenever $\sigma^2\text{tr}(\boldsymbol{E}) > 0$. When $\sigma^2\text{tr}(\boldsymbol{E}) = 0$, (A VII-28) turns into an equality relationship. Thus, $\lim_{N\to\infty} P_d^{\text{iid}} = \lim_{N\to\infty} P_d^{\text{inid}}$ provided that $\sigma^2\text{tr}(\boldsymbol{E}) = 0$. $\square$

BIBLIOGRAPHY

Abdi, A., Lau, W. C., Alouini, M. S. & Kaveh, M. (2003). A New Simple Model for Land Mobile Satellite Channels: First- and Second-Order Statistics. *IEEE Trans. Wireless Commun.*, 2(3), 519-528. doi: 10.1109/TWC.2003.811182.

Adamchik, V. S. & Marichev, O. I. (1990). The algorithm for calculating integrals of hypergeometric type functions and its realization in reduce system. *Proc. Int. Conf. Symbolic Algebraic Comput.*, pp. 212-224.

Alhussein, O. (2015). *Performance Analysis of Wireless Fading Channels: A Unified Approach*. (Master's thesis, School of Eng. Sci., Simon Fraser Univ., Burnaby, BC, Canada).

Ali, A. & Hamouda, W. (2017). Advances on Spectrum Sensing for Cognitive Radio Networks: Theory and Applications. *IEEE Commun. Surveys Tuts.*, 19(2), 1277-1304. doi: 10.1109/COMST.2016.2631080.

Arapoglou, P. D., Liolis, K., Bertinelli, M., Panagopoulos, A., Cottis, P. & Gaudenzi, R. D. (2011). MIMO over Satellite: A Review. *IEEE Commun. Surveys Tuts.*, 13(1), 27-51. doi: 10.1109/SURV.2011.033110.00072.

Arribas, J., Fernandez-Prades, C. & Closas, P. (2013a). Antenna Array Based GNSS Signal Acquisition for Interference Mitigation. *IEEE Trans. Aerosp. Electron. Syst.*, 49(1), 223-243.

Arribas, J., Fernandez-Prades, C. & Closas, P. (2013b). Multi-Antenna Techniques for Interference Mitigation in GNSS Signal Acquisition. *EURASIP J. Adv. Signal Process.*, 2013(1). doi: 10.1186/1687-6180-2013-143.

Atapattu, S., Tellambura, C. & Jiang, H. (2014). *Energy Detection for Spectrum Sensing in Cognitive Radio*. New York, NY, USA: Springer-Verlag.

Aubry, A., De Maio, A., Orlando, D. & Piezzo, M. (2014). Adaptive Detection of Point-Like Targets in the Presence of Homogeneous Clutter and Subspace Interference. *IEEE Signal Process. Lett.*, 21(7), 848-852. doi: 10.1109/LSP.2014.2309434.

AVIO-601. (2018). AVIO-601 Project: Interference Mitigation in Satellite Communications. Consulted at https://lassena.etsmtl.ca/IMG/pdf/-8.pdf.

Axell, E. & Larsson, E. G. (2011, May). A unified framework for GLRT-based spectrum sensing of signals with covariance matrices with known eigenvalue multiplicities. *Proc. IEEE Int. Conf. on Acoust., Speech and Signal Process. (IEEE ICASSP)*, pp. 2956-2959. doi: 10.1109/ICASSP.2011.5946277.

Axell, E., Leus, G., Larsson, E. G. & Poor, H. V. (2012). Spectrum Sensing for Cognitive Radio : State-of-the-Art and Recent Advances. *IEEE Signal Process. Mag.*, 29(3), 101-116. doi: 10.1109/MSP.2012.2183771.

Balaei, A. T. & Dempster, A. G. (2009). A Statistical Inference Technique for GPS Interference Detection. *IEEE Trans. Aerosp. Electron. Syst.*, 45(4), 1499-1511. doi: 10.1109/TAES.2009.5310313.

Balaei, A., Dempster, A. & Barnes, J. (2006, Apr.). A novel approach in detection and characterization of CW interference of GPS signal using receiver estimation of C/No. *IEEE/ION Position, Location, and Navigation Symp.*, pp. 1120-1126. doi: 10.1109/PLANS.2006.1650719.

Bandiera, F. & Orlando, D. (2009). Advanced Radar Detection Schemes under Mismatched Signal Models. *Synthesis Lectures Signal Process.*, 4(1), 1-105.

Bandiera, F., Farina, A., Orlando, D. & Ricci, G. (2010). Detection Algorithms to Discriminate Between Radar Targets and ECM Signals. *IEEE Trans. Signal Process.*, 58(12), 5984-5993. doi: 10.1109/TSP.2010.2077283.

Bauernfeind, R., Kramer, I., Beckmann, H., Eissfeller, B. & Vierroth, V. (2011, Jun.). In-Car jammer interference detection in automotive GNSS receivers and localization by means of vehicular communication. *IEEE Forum on Integrated and Sustainable Transportation System (FISTS)*, pp. 376-381. doi: 10.1109/FISTS.2011.5973616.

Bauza, J. M. T. (2012). *Radio Frequency Interference in Microwave Radiometry: Statistical Analysis and Study of Techniques for Detection and Mitigation*. (Ph.D. thesis, UPC, Barcelona Tech.).

Becker, H., Albera, L., Comon, P., Haardt, M., Birot, G., Wendling, F., Gavaret, M., Bénar, C. G. & Merlet, I. (2014). EEG Extended Source Localization: Tensor-Based vs. Conventional Methods. *NeuroImage*, 96, 143-157. doi: https://doi.org/10.1016/j.neuroimage.2014.03.043.

Becker, H., Albera, L., Comon, P., Gribonval, R., Wendling, F. & Merlet, I. (2015). Brain-Source Imaging: From Sparse to Tensor Models. *IEEE Signal Process. Mag.*, 32(6), 100-112. doi: 10.1109/MSP.2015.2413711.

Behrens, R. & Scharf, L. (1994). Signal Processing Applications of Oblique Projection Operators. *IEEE Trans. Signal Process.*, 42(6), 1413-1424. doi: 10.1109/78.286957.

Bertsekas, D. P. & Tsitsiklis, J. N. (2008). *Introduction to Probability* (ed. 2). Belmont, MA, USA: Athena Scientific.

Bianchi, P., Debbah, M., Maida, M. & Najim, J. (2011). Performance of Statistical Tests for Single-Source Detection Using Random Matrix Theory. *IEEE Trans. Inf. Theory*, 57(4), 2400-2419. doi: 10.1109/TIT.2011.2111710.

Biglieri, E., Calderbank, R., Constantinides, A., Goldsmith, A., Paulraj, A. & Poor, H. V. (2007). *MIMO Wireless Communications*. New York, NY, USA: Cambridge Univ. Press.

Bishop, C. M. (2006). *Pattern Recognition and Machine Learning*. New York, NY, USA: Springer-Verlag.

Bogale, T. E. & Vandendorpe, L. (2013a, Mar.). Moment based spectrum sensing algorithm for cognitive radio networks with noise variance uncertainty. *Proc. Annu. Conf. on Inform. Sci. and Syst. (CISS)*, pp. 1-5. doi: 10.1109/CISS.2013.6552277.

Bogale, T. E. & Vandendorpe, L. (2013b, Jul.). Linearly combined signal energy based spectrum sensing algorithm for cognitive radio networks with noise variance uncertainty. *Proc. Int. Conf. on Cognitive Radio Oriented Wireless Networks*, pp. 80-86. doi: 10.1109/CROWNCom.2013.6636798.

Bogale, T. E. & Vandendorpe, L. (2014). Max-Min SNR Signal Energy Based Spectrum Sensing Algorithms for Cognitive Radio Networks with Noise Variance Uncertainty. *IEEE Trans. Wireless Commun.*, 13(1), 280-290. doi: 10.1109/TWC.2013.122613.130406.

Bogale, T. E., Vandendorpe, L. & Le, L. B. (2015). Wide-Band Sensing and Optimization for Cognitive Radio Networks With Noise Variance Uncertainty. *IEEE Trans. Commun.*, 63(4), 1091-1105. doi: 10.1109/TCOMM.2015.2394390.

Borio, D., Camoriano, L., Savasta, S. & Presti, L. L. (2008). Time-Frequency Excision for GNSS Applications. *IEEE Syst. J.*, 2(1), 27-37. doi: 10.1109/JSYST.2007.914914.

Borio, D. (2008). *A Statistical Theory for GNSS Signal Acquisition*. (Ph.D. thesis, Dept. of Electron. and Telecommun., Polytechnic Univ. Turin, Turin, Italy).

Boulogeorgos, A. A. A., Chatzidiamantis, N. D. & Karagiannidis, G. K. (2016a). Energy Detection Spectrum Sensing Under RF Imperfections. *IEEE Trans. Commun.*, 64(7), 2754-2766. doi: 10.1109/TCOMM.2016.2561294.

Boulogeorgos, A. A. A., Chatzidiamantis, N. D. & Karagiannidis, G. K. (2016b). Spectrum Sensing With Multiple Primary Users Over Fading Channels. *IEEE Commun. Lett.*, 20(7), 1457-1460. doi: 10.1109/LCOMM.2016.2554545.

Cabric, D. (2008). Addressing Feasibility of Cognitive Radios. *IEEE Signal Process. Mag.*, 25(6), 85-93. doi: 10.1109/MSP.2008.929367.

Chen, G., Zhao, Z., Zhu, G., Huang, Y. & Li, T. (2010). HF Radio-Frequency Interference Mitigation. *IEEE Geosci. Remote Sens. Lett.*, 7(3), 479-482. doi: 10.1109/L-GRS.2009.2039340.

Ciuonzo, D., Romano, G. & Solimene, R. (2015). Performance Analysis of Time-Reversal MUSIC. *IEEE Trans. Signal Process.*, 63(10), 2650-2662. doi: 10.1109/TSP.2015.2417507.

Ciuonzo, D., De Maio, A. & Orlando, D. (2016a). A Unifying Framework for Adaptive Radar Detection in Homogeneous Plus Structured Interference—Part I: On the Maximal Invariant Statistic. *IEEE Trans. Signal Process.*, 64(11), 2894-2906. doi: 10.1109/TSP.2016.2519003.

Ciuonzo, D., Maio, A. D. & Orlando, D. (2016b). A Unifying Framework for Adaptive Radar Detection in Homogeneous Plus Structured Interference—Part II: Detectors Design. *IEEE Trans. Signal Process.*, 64(11), 2907-2919. doi: 10.1109/TSP.2016.2519005.

Ciuonzo, D., De Maio, A. & Orlando, D. (2017). On the Statistical Invariance for Adaptive Radar Detection in Partially Homogeneous Disturbance Plus Structured Interference. *IEEE Trans. Signal Process.*, 65(5), 1222-1234. doi: 10.1109/TSP.2016.2620115.

Conte, E., Lops, M. & Ricci, G. (1996). Adaptive Matched Filter Detection in Spherically Invariant Noise. *IEEE Signal Process. Lett.*, 3(8), 248-250. doi: 10.1109/97.511809.

Couillet, R. & Debbah, M. (2011). *Random Matrix Methods for Wireless Communications*. Cambridge, UK: Cambridge Univ. Press.

da Costa, J. P. C. L., Roemer, F., Haardt, M. & de Sousa, R. T. (2011). Multi-Dimensional Model Order Selection. *EURASIP J. on Advances in Signal Process.*, 2011(1), 1-13. doi: 10.1186/1687-6180-2011-26.

D'Amico, A. A., Mengali, U. & de Reyna, E. A. (2007). Energy-Detection UWB Receivers with Multiple Energy Measurements. *IEEE Trans. Wireless Commun.*, 6(7), 2652-2659. doi: 10.1109/TWC.2007.05974.

De Gaudenzi, R. & Giannetti, F. (1998). DS-CDMA Satellite Diversity Reception for Personal Satellite Communication: Satellite-to-Mobile Link Performance Analysis. *IEEE Trans. Veh. Technol.*, 47(2), 658-672. doi: 10.1109/25.669103.

De Maio, A. & Orlando, D. (2016). Adaptive Radar Detection of a Subspace Signal Embedded in Subspace Structured Plus Gaussian Interference via Invariance. *IEEE Trans. Signal Process.*, 64(8), 2156-2167. doi: 10.1109/TSP.2015.2507544.

De Roo, R. D. & Misra, S. (2010). A Moment Ratio RFI Detection Algorithm that Can Detect Pulsed Sinusoids of Any Duty Cycle. *IEEE Geosci. Remote Sens. Lett.*, 7(3), 606-610. doi: 10.1109/LGRS.2010.2043051.

De Roo, R. D., Misra, S. & Ruf, C. S. (2007). Sensitivity of the Kurtosis Statistic as a Detector of Pulsed Sinusoidal RFI. *IEEE Trans. Geosci. Remote Sens.*, 45(7), 1938-1946. doi: 10.1109/TGRS.2006.888101.

Digham, F. F., Alouini, M. S. & Simon, M. K. (2007). On the Energy Detection of Unknown Signals Over Fading Channels. *IEEE Trans. Commun.*, 55(1), 21-24. doi: 10.1109/T-COMM.2006.887483.

Dikmese, S., Sofotasios, P., Renfors, M. & Valkama, M. (2016). Subband Energy Based Reduced Complexity Spectrum Sensing under Noise Uncertainty and Frequency-Selective Spectral Characteristics. *IEEE Trans. Signal Process.*, 64(1), 131-145. doi: 10.1109/TSP.2015.2480048.

Donoho, D. L. (2006). Compressed Sensing. *IEEE Trans. Inf. Theory*, 52(4), 1289-1306. doi: 10.1109/TIT.2006.871582.

Dovis, F. & Musumeci, L. (2011, June). Use of Wavelet transforms for interference mitigation. *Int. Conf. on Localization and GNSS (ICL-GNSS)*, pp. 116-121. doi: 10.1109/ICL-GNSS.2011.5955275.

Dovis, F., Musumeci, L., Linty, N. & Pini, M. (2012). Recent Trends in Interference Mitigation and Spoofing Detection. *Int. J. of Embedded and Real-Time Commun. Syst.*, 3(3), 1-17.

Farhang-Boroujeny, B. (2008). Filter Bank Spectrum Sensing for Cognitive Radios. *IEEE Trans. Signal Process.*, 56(5), 1801-1811. doi: 10.1109/TSP.2007.911490.

Farsad, N., Yilmaz, H. B., Eckford, A., Chae, C. & Guo, W. (2016). A Comprehensive Survey of Recent Advancements in Molecular Communication. *IEEE Commun. Surveys Tut.*, 18(3), 1887-1919. doi: 10.1109/COMST.2016.2527741.

Gallager, R. G. (2013). *Stochastic Processes: Theory for Applications*. Cambridge, UK: Cambridge Univ. Press.

Gardner, W. A. (1988). Signal Interception: A Unifying Theoretical Framework for Feature Detection. *IEEE Trans. Commun.*, 36(8), 897-906. doi: 10.1109/26.3769.

Getu, T. M., Ajib, W. & Yeste-Ojeda, O. A. (2015a, Oct.). Efficient semi-blind channel estimators for SIMO systems suffering from broadband RFI. *Proc. IEEE Int. Conf. on Ubiquitous Wireless Broadband*.

Getu, T. M., Ajib, W. & R. Jr. Landry. (2016, 7-9 Dec.). Oversampling-based algorithm for efficient RF interference excision in SIMO systems. *Proc. IEEE Global Conf. on Signal and Inform. Process. (IEEE GlobalSIP)*, pp. 1423-1427.

Getu, T. M., Ajib, W. & Yeste-Ojeda, O. A. (2017). Tensor-Based Efficient Multi-Interferer RFI Excision Algorithms for SIMO Systems. *IEEE Trans. Commun.*, 65(7), 3037-3052. doi: 10.1109/TCOMM.2017.2694006.

Getu, T. M., Ajib, W. & Landry, R. (2018a). Simple F–Test-Based Spectrum Sensing Techniques for Multi-Antenna Cognitive Radios. *IEEE Trans. Commun.*, 66(11), 5081-5096. doi: 10.1109/TCOMM.2018.2846239.

Getu, T. M., Ajib, W. & R. Jr. Landry. (2018b). Performance Analysis of Energy-Based RFI Detector. *IEEE Trans. Wireless Commun.*, 17(10), 6601-6616. doi: 10.1109/TWC.2018.2861733.

Getu, T. M., Ajib, W. & R. Jr. Landry. (2018c). Power-Based Broadband RF Interference Detector for Wireless Communication Systems. *IEEE Wireless Commun. Lett.*, 7(6), 1002-1005. doi: 10.1109/LWC.2018.2845373.

Getu, T. M., Ajib, W., Yeste-Ojeda, O. A. & R. Jr. Landry. (2018d, 5-8 Mar.). Tensor-based efficient multi-interferer RFI excision algorithms: Results using real-world data. *Proc. Int. Conf. on Comput., Netw. and Commun. (ICNC 2018)*, pp. 917-921.

Getu, T. M., Ajib, W. & R. Jr. Landry. (2018, accepted, Aug.). An eigenvalue-based multi-antenna RFI detection algorithm. *Proc. IEEE Veh. Technol. Conf. (VTC2018-Fall)*.

Getu, T. M., Ajib, W. & R. Jr. Landry. (2018, submitted). Linear and Multi-Linear RFI Detectors for Multi-Antenna Wireless Communications. *IEEE Trans. Wireless Commun.*

Getu, T. M., Ajib, W. & R. Jr. Landry. (2019, submitted). Eigenvalue-Based RF Interference Detector for Multi-Antenna Wireless Communications. *Elsevier Signal Process.*

Getu, T. M. (Apr. 2018). WCL MATLAB® Files. Consulted at https://github.com/tiluxscho/WCL-Matlab-Files.

Getu, T. M., Ajib, W. & Yeste-Ojeda, O. A. (2015b, Dec.). Multi-linear subspace estimation and projection for efficient RFI excision in SIMO systems. *Proc. IEEE Global Conf. on Signal and Inform. Process. (IEEE GlobalSIP)*, pp. 1397-1401.

Giannakis, G. B. & Tsatsanis, M. K. (1994). Time-Domain Tests for Gaussianity and Time-Reversibility. *IEEE Trans. Signal Process.*, 42(12), 3460-3472. doi: 10.1109/78.340780.

Giannakis, G. B., Shen, Y. & Karanikolas, G. V. (2018). Topology Identification and Learning over Graphs: Accounting for Nonlinearities and Dynamics. *Proc. IEEE*, 106(5), 787-807. doi: 10.1109/JPROC.2018.2804318.

Gishkori, S. & Leus, G. (2013). Compressive Sampling Based Energy Detection of Ultra-Wideband Pulse Position Modulation. *IEEE Trans. Signal Process.*, 61(15), 3866-3879. doi: 10.1109/TSP.2013.2260747.

Gismalla, E. H. & Alsusa, E. (2012). On the Performance of Energy Detection Using Bartlett's Estimate for Spectrum Sensing in Cognitive Radio Systems. *IEEE Trans. Signal Process.*, 60(7), 3394-3404. doi: 10.1109/TSP.2012.2191544.

Gismalla, E. & Alsusa, E. (2011). Performance Analysis of the Periodogram-Based Energy Detector in Fading Channels. *IEEE Trans. Signal Process.*, 59(8), 3712-3721. doi: 10.1109/TSP.2011.2153849.

Giunta, G., Hao, C. & Orlando, D. (2018). Estimation of Rician K-Factor in the Presence of Nakagami-m Shadowing for the LoS Component. *IEEE Wireless Commun. Lett.*, 7(4), 550-553. doi: 10.1109/LWC.2018.2794447.

Gokceoglu, A., Dikmese, S., Valkama, M. & Renfors, M. (2014). Energy Detection under IQ Imbalance with Single- and Multi-Channel Direct-Conversion Receiver: Analysis and Mitigation. *IEEE J. Sel. Areas Commun.*, 32(3), 411-424. doi: 10.1109/JSAC.2014.1403001.

Goldsmith, A., Jafar, S. A., Maric, I. & Srinivasa, S. (2009). Breaking Spectrum Gridlock With Cognitive Radios: An Information Theoretic Perspective. *Proc. IEEE*, 97(5), 894-914. doi: 10.1109/JPROC.2009.2015717.

Golub, G. H. & Van Loan, C. F. (2013). *Matrix Computations* (ed. 4). Baltimore, MD, USA: The Johns Hopkins Univ. Press.

Gradshteyn, I. S. & Ryzhik, I. M. (2007). *Table of Integrals, Series, and Products* (ed. 7). Academic Press, Burlington, MA, USA.

Guner, B., Johnson, J. T. & Niamsuwan, N. (2007). Time and Frequency Blanking for Radio-Frequency Interference Mitigation in Microwave Radiometry. *IEEE Trans. Geosci. Remote Sens.*, 45(11), 3672-3679. doi: 10.1109/TGRS.2007.903680.

Guo, C., Chen, S. & Liu, F. (2016). Polarization-Based Spectrum Sensing Algorithms for Cognitive Radios: Upper and Practical Bounds and Experimental Assessment. *IEEE Trans. Veh. Technol.*, 65(10), 8072-8086. doi: 10.1109/TVT.2015.2501826.

Haardt, M., Roemer, F. & Del Galdo, G. (2008). Higher-Order SVD-Based Subspace Estimation to Improve the Parameter Estimation Accuracy in Multidimensional Harmonic Retrieval Problems. *IEEE Trans. Signal Process.*, 56(7), 3198-3213. doi: 10.1109/TSP.2008.917929.

Haykin, S., Thomson, D. J. & Reed, J. H. (2009). Spectrum Sensing for Cognitive Radio. *Proc. IEEE*, 97(5), 849-877. doi: 10.1109/JPROC.2009.2015711.

Haykin, S. (2005). Cognitive Radio: Brain-Empowered Wireless Communications. *IEEE J. Sel. Areas Commun.*, 23(2), 201-220. doi: 10.1109/JSAC.2004.839380.

Hellbourg, G., Weber, R., Capdessus, C. & Boonstra, A.-J. (2012, Aug.). Oblique projection beamforming for RFI mitigation in radio astronomy. *IEEE Statistical Signal Process. Workshop (SSP)*, pp. 93-96. doi: 10.1109/SSP.2012.6319860.

Heo, J., Ju, H., Park, S., Kim, E. & Hong, D. (2014). Simultaneous Sensing and Transmission in Cognitive Radio. *IEEE Trans. Wireless Commun.*, 13(4), 1948-1959. doi: 10.1109/TWC.2014.030614.130532.

Herath, S. P., Rajatheva, N. & Tellambura, C. (2011). Energy Detection of Unknown Signals in Fading and Diversity Reception. *IEEE Trans. Commun.*, 59(9), 2443-2453. doi: 10.1109/TCOMM.2011.071111.090349.

Horn, R. A. & Johnson, C. R. (2013). *Matrix Analysis* (ed. 2). New York, NY, USA: Cambridge Univ. Press.

Huang, Q. & Chung, P. J. (2013a). An F–Test Based Approach for Spectrum Sensing in Cognitive Radio. *IEEE Trans. Wireless Commun.*, 12(8), 4072-4079. doi: 10.1109/TWC.2013.071613.121633.

Huang, Q. & Chung, P. J. (2013b, Jun.). An F–test for multiple antenna spectrum sensing in cognitive radio. *Proc. IEEE Int. Conf. on Commun. (IEEE ICC)*, pp. 4677-4681. doi: 10.1109/ICC.2013.6655310.

Hussain, S. & Fernando, X. N. (2014). Performance Analysis of Relay-Based Cooperative Spectrum Sensing in Cognitive Radio Networks Over Non-Identical Nakagami-*m* Channels. *IEEE Trans. Commun.*, 62(8), 2733-2746. doi: 10.1109/TCOMM.2014.2338856.

Jayaweera, S. K. (2014). *Signal Processing for Cognitive Radios* (ed. 1). Hoboken, NJ, USA: Wiley.

Jeffrey, A. & Dai, H.-H. (2008). *Handbook of Mathematical Formulas and Integrals* (ed. 4). Cambridge, MA, USA: Academic Press.

Jeffs, B., Li, L. & Warnick, K. F. (2005). Auxiliary Antenna-Assisted Interference Mitigation for Radio Astronomy Arrays. *IEEE Trans. Signal Process.*, 53(2), 439-451. doi: 10.1109/TSP.2004.840787.

Johnson, J. T. & Ellingson, S. W. (2005). Examination of a Simple Pulse Blanking Technique for RFI Mitigation. *Radio Sci.*, 40(5), RS5S03.

Johnson, J. & Guner, B. (2007, Jul.). Cross frequency blanking for RFI mitigation: A C-band case study. *IEEE Int. Geoscience and Remote Sensing Symp. (IGARSS)*, pp. 2710-2713. doi: 10.1109/IGARSS.2007.4423402.

Johnson, N. L., Kotz, S. & Balakrishnan, N. (1995). *Continuous Univariate Distributions* (ed. 2). Hoboken, NJ, USA: Wiley.

Kaplan, E. D. & Hegarty, C. J. (Eds.). (2006). *Understanding GPS: Principles and Applications* (ed. 2). Norwood, MA, USA: Artech House.

Karagiannidis, G. K., Sagias, N. C. & Tsiftsis, T. A. (2006a). Closed-Form Statistics for the Sum of Squared Nakagami-*m* Variates and its Applications. *IEEE Trans. Commun.*, 54(8), 1353-1359. doi: 10.1109/TCOMM.2006.878812.

Karagiannidis, G. K., Tsiftsis, T. A. & Mallik, R. K. (2006b). Bounds for Multihop Relayed Communications in Nakagami-*m* Fading. *IEEE Trans. Commun.*, 54(1), 18-22. doi: 10.1109/TCOMM.2005.861679.

Karagiannidis, G. K., Sagias, N. C. & Mathiopoulos, P. T. (2007). $N*$Nakagami: A Novel Stochastic Model for Cascaded Fading Channels. *IEEE Trans. Commun.*, 55(8), 1453-1458. doi: 10.1109/TCOMM.2007.902497.

Kay, S. M. (1998). *Fundamentals of Statistical Signal Processing: Detection Theory, Vol. II*. Prentice-Hall, Englewood Cliffs, NJ.

Kay, S. M. (2006). *Intuitive Probability and Random Processes Using MATLAB®*. New York, NY, USA: Springer.

Kortun, A., Sellathurai, M., Ratnarajah, T. & Zhong, C. (2012). Distribution of the Ratio of the Largest Eigenvalue to the Trace of Complex Wishart Matrices. *IEEE Trans. Signal Process.*, 60(10), 5527-5532. doi: 10.1109/TSP.2012.2205922.

Kotoulas, D., Koukoulas, P. & Kalouptsidis, N. (2006). Subspace Projection Based Blind Channel Order Estimation of MIMO Systems. *IEEE Trans. Signal Process.*, 54(4), 1351-1363. doi: 10.1109/TSP.2005.863104.

Kritchman, S. & Nadler, B. (2009). Non-Parametric Detection of the Number of Signals: Hypothesis Testing and Random Matrix Theory. *IEEE Trans. Signal Process.*, 57(10), 3930-3941. doi: 10.1109/TSP.2009.2022897.

Kurz, L., Tasdemir, E., Bornkessel, D., Noll, T., Kappen, G., Antreich, F., Sgammini, M. & Meurer, M. (2012, Dec.). An architecture for an embedded antenna-array digital GNSS receiver using subspace-based methods for spatial filtering. *Proc. the 6th ESA Workshop on Satellite Navigation Technologies and European Workshop on GNSS Signals and Signal Process. (NAVITEC)*, pp. 1-8. doi: 10.1109/NAVITEC.2012.6423050.

Kurz, L., Tasdemir, E. & Noll, T. (2014, Dec.). JamCam: A camera-integrated GNSS receiver for spatial detection of radio frequency interference sources. *Proc. the 7th ESA Workshop on Satellite Navigation Technologies and European Workshop on GNSS Signals and Signal Processing (NAVITEC)*, pp. 1-8. doi: 10.1109/NAVITEC.2014.7045134.

Landon, J., Jeffs, B. & Warnick, K. F. (2012). Model-Based Subspace Projection Beamforming for Deep Interference Nulling. *IEEE Trans. Signal Process.*, 60(3), 1215-1228. doi: 10.1109/TSP.2011.2177825.

Lathauwer, L. D., Moor, B. D. & Vandewalle, J. (2000). A Multilinear Singular Value Decomposition. *SIAM J. Matrix Anal. Appl.*, 21, 1253-1278.

Leshem, A. & van der Veen, A. J. (2001). Multichannel Detection of Gaussian Signals with Uncalibrated Receivers. *IEEE Signal Process. Lett.*, 8(4), 120-122. doi: 10.1109/97.911477.

Li, F., Liu, H. & Vaccaro, R. (1993). Performance Analysis for DOA Estimation Algorithms: Unification, Simplification, and Observations. *IEEE Trans. Aerosp. Electron. Syst.*, 29(4), 1170-1184. doi: 10.1109/7.259520.

Lim, L.-H. & Comon, P. (2014). Blind Multilinear Identification. *IEEE Trans. Inf. Theory*, 60(2), 1260-1280.

Liu, J., Liu, X. & Ma, X. (2008). First-Order Perturbation Analysis of Singular Vectors in Singular Value Decomposition. *IEEE Trans. Signal Process.*, 56(7), 3044-3049. doi: 10.1109/TSP.2007.916137.

Loo, C. (1985). A Statistical Model for a Land Mobile Satellite Link. *IEEE Trans. Veh. Technol.*, 34(3), 122-127. doi: 10.1109/T-VT.1985.24048.

Lu, Z. & Zoubir, A. M. (2015). Source Enumeration in Array Processing Using a Two-Step Test. *IEEE Trans. Signal Process.*, 63(10), 2718-2727. doi: 10.1109/TSP.2015.2414894.

Maccone, C. (2010). The KLT (Karhunen-Loève Transform) to Extend SETI Searches to Broad-band and Extremely Feeble Signals. *Acta Astronautica*, 67(11-12), 1427-1439.

Magnus, J. R. & Neudecker, H. (2007). *Matrix Differential Calculus With Applications in Statistics and Econometrics* (ed. 3). Hoboken, NJ, USA: Wiley.

Maral, G. (2003). *VSAT Networks* (ed. 2). Hoboken, NJ, USA: Wiley.

Maral, G. & Bousquet, M. (2009). *Satellite Communications Systems: Systems, Techniques and Technology* (ed. 5). Hoboken, NJ, USA: Wiley.

Melvin, W. L. & Scheer, J. A. (Eds.). (2013). *Principles of Modern Radar: Advanced Techniques*. Edison, NJ, USA: SciTech.

Mengersen, K. L., Robert, C. P. & Titterington, D. M. (Eds.). (2011). *Mixtures: Estimation and Applications* (ed. 1). Hoboken, NJ, USA: Wiley.

Miridakis, N. I., Tsiftsis, T. A., Alexandropoulos, G. C. & Debbah, M. (2017). Simultaneous Spectrum Sensing and Data Reception for Cognitive Spatial Multiplexing Distributed Systems. *IEEE Trans. Wireless Commun.*, 16(5), 3313-3327. doi: 10.1109/TWC.2017.2681067.

Misra, S., Mohammed, P. N., Guner, B., Ruf, C. S., Piepmeier, J. R. & Johnson, J. T. (2009). Microwave Radiometer Radio-Frequency Interference Detection Algorithms: A Comparative Study. *IEEE Trans. Geosci. Remote Sens.*, 47(11), 3742-3754. doi: 10.1109/T-GRS.2009.2031104.

Misra, S. (2011). *Development of Radio Frequency Interference Detection Algorithms for Passive Remote Sensing*. (Ph.D. thesis, Univ. of Michigan).

Mitra, S. K. (2001). *Digital Signal Processing: A Computer-Based Approach* (ed. 2nd). New York, NY, USA: McGraw-Hill.

Motella, B. (2008). *Interference Monitoring for Global Navigation Satellite Systems*. (Ph.D. thesis, Dept. of Electron. and Telecommun., Polytechnic Univ. Turin, Turin, Italy).

Motella, B., Pini, M. & Dovis, F. (2007). Investigation on the Effect of Strong Out-of-band Signals on Global Navigation Satellite Systems Receivers. *Springer GPS Solutions*, 12(2), 77-86. doi: 10.1007/s10291-007-0085-5.

Müller, R. R., Cottatellucci, L. & Vehkaperä, M. (2014). Blind Pilot Decontamination. *IEEE J. Sel. Topics Signal Process.*, 8(5), 773-786. doi: 10.1109/JSTSP.2014.2310053.

Musumeci, L. & Dovis, F. (2012, Jun.). A comparison of transformed-domain techniques for pulsed interference removal on GNSS signals. *Proc. Int. Conf. on Localization and GNSS (ICL-GNSS)*, pp. 1-6.

Nadakuditi, R. R. & Edelman, A. (2008). Sample Eigenvalue Based Detection of High-Dimensional Signals in White Noise Using Relatively Few Samples. *IEEE Trans. Signal Process.*, 56(7), 2625-2638. doi: 10.1109/TSP.2008.917356.

Nakano, T., Okaie, Y., Kobayashi, S., Koujin, T., Chan, C., Hsu, Y., Obuchi, T., Hara, T., Hiraoka, Y. & Haraguchi, T. (2017). Performance Evaluation of Leader–Follower-Based Mobile Molecular Communication Networks for Target Detection Applications. *IEEE Trans. Commun.*, 65(2), 663-676. doi: 10.1109/TCOMM.2016.2628037.

Nakano, T., Eckford, A. W. & Haraguchi, T. (2013). *Molecular Communication*. Cambridge Univ. Press. doi: 10.1017/CBO9781139149693.

Newtec. (2018). Newtec Inc. Consulted at https://www.newtec.eu/.

Newtec and IRG. (Sep. 2013). 93% of the industry suffers from satellite interference. Consulted at http://www.newtec.eu/article/release/93-of-the-industry-suffers-from-satellite-interference.

Nguyen *et al.* (2015). *Radio Interference Modeling and Prediction for Satellite Operation Applications* (Tech. Rep.): Air Force Research Laboratory and The Catholic Univ. of America.

NRAO. (2017). Very Large Array of The National Radio Astronomy Observatory. Consulted at http://www.vla.nrao.edu/.

Oltrogge, D. & Rashid, H. (2012, Oct.). Effective strategies for satellite communications RFI mitigation. *Proc. the 1st IEEE AESS European Conf. on Satellite Telecommun. (ESTEL)*, pp. 1-7. doi: 10.1109/ESTEL.2012.6400106.

Oppenheim, A. V. & Schafer, R. W. (2010). *Discrete-Time Signal Processing* (ed. 3). Upple Saddle River, NJ, USA: Pearson Higher Edu.

Orlando, D. (2017). A Novel Noise Jamming Detection Algorithm for Radar Applications. *IEEE Signal Process. Lett.*, 24(2), 206-210. doi: 10.1109/LSP.2016.2645793.

Papoulis, A. & Pillai, S. U. (2002). *Probability, Random Variables, and Stochastic Processes* (ed. 4). New York, NY, USA: McGraw-Hili.

Patel, A., Biswas, S. & Jagannatham, A. K. (2016). Optimal GLRT-Based Robust Spectrum Sensing for MIMO Cognitive Radio Networks With CSI Uncertainty. *IEEE Trans. Signal Process.*, 64(6), 1621-1633. doi: 10.1109/TSP.2015.2500183.

Plataniotis, K. N. & Hatzinakos, D. (2001). Gaussian Mixtures and their Applications to Signal Processing. In Stergiopoulos, S. (Ed.), *Advanced Signal Processing Handbook* (ch. 3). Boca Raton, FL, USA: CRC Press.

Poor, H. V. (1994). *An Introduction to Signal Detection and Estimation*. New York, NY, USA: Springer-Verlag.

Proakis, J. G. & Manolakis, D. K. (2006). *Digital Signal Processing* (ed. 4). Upper Saddle River, NJ, USA: Prentice-Hall.

Proakis, J. G. & Salehi, M. (2008). *Digital Communications* (ed. 5). New York, NY, USA: McGraw-Hill.

Quan, Z., Cui, S. & Sayed, A. H. (2008). Optimal Linear Cooperation for Spectrum Sensing in Cognitive Radio Networks. *IEEE J. Sel. Topics Signal Process.*, 2(1), 28-40. doi: 10.1109/JSTSP.2007.914882.

Quan, Z., Cui, S., Sayed, A. H. & Poor, H. V. (2009). Optimal Multiband Joint Detection for Spectrum Sensing in Cognitive Radio Networks. *IEEE Trans. Signal Process.*, 57(3), 1128-1140. doi: 10.1109/TSP.2008.2008540.

Ramírez, D., Vía, J., Santamaría, I. & Scharf, L. L. (2010). Detection of Spatially Correlated Gaussian Time Series. *IEEE Trans. Signal Process.*, 58(10), 5006-5015. doi: 10.1109/TSP.2010.2053360.

Ramírez, D., Vazquez-Vilar, G., López-Valcarce, R., Vía, J. & Santamaría, I. (2011). Detection of Rank-*P* Signals in Cognitive Radio Networks With Uncalibrated Multiple Antennas. *IEEE Trans. Signal Process.*, 59(8), 3764-3774. doi: 10.1109/TSP.2011.2146779.

Richharia, M. (2014). *Mobile Satellite Communications: Principles and Trends* (ed. 2). West Sussex, UK: Wiley.

Roemer, F. (2012). *Advanced Algebraic Concepts for Efficient Multi-Channel Signal Processing*. (Ph.D. thesis, Fakultät Elektrotechnik Informationstechnik, Tech. Univ. Ilmenau, Ilmenau, Germany).

Roemer, F. & Haardt, M. (2010). Tensor-Based Channel Estimation and Iterative Refinements for Two-Way Relaying With Multiple Antennas and Spatial Reuse. *IEEE Trans. Signal Process.*, 58(11), 5720-5735. doi: 10.1109/TSP.2010.2062179.

Roemer, F., Becker, H., Haardt, M. & Weis, M. (2009, Dec.). Analytical performance evaluation for HOSVD-based parameter estimation schemes. *Proc. 3rd IEEE Int. Workshop on Comput. Adv. in Multi-Sensor Adapt. Process. (CAMSAP)*, pp. 77-80. doi: 10.1109/CAMSAP.2009.5413232.

Roemer, F., Haardt, M. & Del Galdo, G. (2014). Analytical Performance Assessment of Multi-Dimensional Matrix- and Tensor-Based ESPRIT-Type Algorithms. *IEEE Trans. Signal Process.*, 62(10), 2611-2625. doi: 10.1109/TSP.2014.2313530.

Ruf, C. S., Gross, S. M. & Misra, S. (2006). RFI Detection and Mitigation for Microwave Radiometry with an Agile Digital Detector. *IEEE Trans. Geosci. Remote Sens.*, 44(3), 694-706. doi: 10.1109/TGRS.2005.861411.

Salvo Rossi, P., Ciuonzo, D. & Ekman, T. (2015a). HMM-Based Decision Fusion in Wireless Sensor Networks With Noncoherent Multiple Access. *IEEE Commun. Lett.*, 19(5), 871-874. doi: 10.1109/LCOMM.2015.2413407.

Salvo Rossi, P., Ciuonzo, D., Kansanen, K. & Ekman, T. (2015b). On Energy Detection for MIMO Decision Fusion in Wireless Sensor Networks Over NLOS Fading. *IEEE Commun. Lett.*, 19(2), 303-306. doi: 10.1109/LCOMM.2014.2379714.

Salvo Rossi, P., Ciuonzo, D., Kansanen, K. & Ekman, T. (2016). Performance Analysis of Energy Detection for MIMO Decision Fusion in Wireless Sensor Networks Over Arbitrary Fading Channels. *IEEE Trans. Wireless Commun.*, 15(11), 7794-7806. doi: 10.1109/TWC.2016.2607703.

Sardarabadi, A. M., van der Veen, A. J. & Boonstra, A. J. (2016). Spatial Filtering of RF Interference in Radio Astronomy Using a Reference Antenna Array. *IEEE Trans. Signal Process.*, 64(2), 432-447. doi: 10.1109/TSP.2015.2483481.

Scharf, L. & Lytle, D. (1971). Signal Detection in Gaussian Noise of Unknown Level: An Invariance Application. *IEEE Trans. Inf. Theory*, 17(4), 404-411. doi: 10.1109/TIT.1971.1054668.

Scharf, L. L. & Friedlander, B. (1994). Matched Subspace Detectors. *IEEE Trans. Signal Process.*, 42(8), 2146-2157. doi: 10.1109/78.301849.

Scharf, L. L. & McCloud, M. L. (2002). Blind Adaptation of Zero Forcing Projections and Oblique Pseudo-Inverses for Subspace Detection and Estimation When Interference Dominates Noise. *IEEE Trans. Signal Process.*, 50(12), 2938-2946. doi: 10.1109/TSP.2002.805245.

Scharf, L. L. & McWhorter, L. T. (1996, Nov.). Adaptive Matched Subspace Detectors and Adaptive Coherence Estimators. *Proc. 30th Asilomar Conf. Signals, Syst., Comput.*, pp. 1114-1117. doi: 10.1109/ACSSC.1996.599116.

Scharf, L. L. (1991). *Statistical Signal Processing: Detection, Estimation, and Time Series Analysis*. Reading, MA, USA: Addison-Wesley.

Schonhoff, T. A. & Giordano, A. A. (2006). *Detection and Estimation Theory and Its Applications*. Upper Saddle River, NJ, USA: Prentice-Hall.

Seber, G. A. F. (2003). *Linear Regression Analysis* (ed. 2). Hoboken, NJ, USA: Wiley.

Selim, B., Alhussein, O., Muhaidat, S., Karagiannidis, G. K. & Liang, J. (2016). Modeling and Analysis of Wireless Channels via the Mixture of Gaussian Distribution. *IEEE Trans. Veh. Technol.*, 65(10), 8309-8321. doi: 10.1109/TVT.2015.2503351.

Sgammini, M., Antreich, F., Meurer, M., Kurz, L. & Noll, T. (2012, Sep.). Blind adaptive beamformer based on orthogonal projections for GNSS. *Proc. the 24th Annu. Int. Tech. Meeting of the Satellite Division of the Institute of Navigation (ION) - Global Satellite Navigation System (GNSS)*, pp. 1-8. doi: 10.1109/NAVITEC.2014.7045134.

Sharma, S. K., Bogale, T. E., Chatzinotas, S., Ottersten, B., Le, L. B. & Wang, X. (2015). Cognitive Radio Techniques Under Practical Imperfections: A Survey. *IEEE Commun. Surveys Tuts.*, 17(4), 1858-1884. doi: 10.1109/COMST.2015.2452414.

Shen, Y., Baingana, B. & Giannakis, G. B. (2017). Tensor Decompositions for Identifying Directed Graph Topologies and Tracking Dynamic Networks. *IEEE Trans. Signal Process.*, 65(14), 3675-3687. doi: 10.1109/TSP.2017.2698369.

Shi, K., Zhou, Y., Kelleci, B., Fischer, T. W., Serpedin, E. & l. Karsilayan, A. (2007). Impacts of Narrowband Interference on OFDM-UWB Receivers: Analysis and Mitigation. *IEEE Trans. Signal Process.*, 55(3), 1118-1128. doi: 10.1109/TSP.2006.887153.

SIG. (2018). Satcoms Innovation Group (SIG). Consulted at https://satig.space/.

Sigut, J., Demetrio, J., Moreno, L., Estevez, J., Aguilar, R. & Alayon, S. (2005). An Asymptotically Optimal Detector for Gaussianity Testing. *IEEE Trans. Signal Process.*, 53(11), 4186-4193. doi: 10.1109/TSP.2005.857042.

Simon, M. K. & Alouini, M.-S. (2005). *Digital Communication over Fading Channels* (ed. 2). Hoboken, NJ, USA: Wiley.

Sofotasios, P. C., Rebeiz, E., Zhang, L., Tsiftsis, T. A., Cabric, D. & Freear, S. (2013). Energy Detection Based Spectrum Sensing Over $\kappa-\mu$ and $\kappa-\mu$ Extreme Fading Channels. *IEEE Trans. Veh. Technol.*, 62(3), 1031-1040. doi: 10.1109/TVT.2012.2228680.

Sofotasios, P. C., Mohjazi, L., Muhaidat, S., Al-Qutayri, M. & Karagiannidis, G. K. (2016). Energy Detection of Unknown Signals Over Cascaded Fading Channels. *IEEE Antennas Wireless Propag. Lett.*, 15, 135-138. doi: 10.1109/LAWP.2015.2433212.

Song, B., Haardt, M. & Roemer, F. (2013, Aug.). A tensor-based subspace method for blind estimation of MIMO channels. *Proc. Int. Symp. on Wireless Commun. Syst. (ISWCS)*, pp. 1-5.

Song, B., Roemer, F. & Haardt, M. (2010a, Nov.). Blind estimation of SIMO channels using a tensor-based subspace method. *Proc. Asilomar Conf. on Signals, Syst. and Comput.*, pp. 8-12. doi: 10.1109/ACSSC.2010.5757455.

Song, S. H., Hamdi, K. & Letaief, K. B. (2010b). Spectrum Sensing with Active Cognitive Systems. *IEEE Trans. Wireless Commun.*, 9(6), 1849-1854. doi: 10.1109/TWC.2010.06.090924.

Sonnenschein, A. & Fishman, P. M. (1992). Radiometric Detection of Spread-Spectrum Signals in Noise of Uncertain Power. *IEEE Trans. Aerosp. Electron. Syst.*, 28(3), 654-660. doi: 10.1109/7.256287.

Sorber, L., Barel, M. V. & Lathauwer, L. D. (Jan. 2014). Tensorlab v2.0. Consulted at http://www.tensorlab.net/.

Stevenson, C. R., Chouinard, G., Lei, Z., Hu, W., Shellhammer, S. J. & Caldwell, W. (2009). IEEE 802.22: The First Cognitive Radio Wireless Regional Area Network Standard. *IEEE Commun. Mag.*, 47(1), 130-138. doi: 10.1109/MCOM.2009.4752688.

Stoica, P. & Selen, Y. (2004). Model-Order Selection: A Review of Information Criterion Rules. *IEEE Signal Process. Mag.*, 21(4), 36-47. doi: 10.1109/MSP.2004.1311138.

Strang, G. (2003). *Introduction to Linear Algebra* (ed. 3). Wellesley, MA, USA: Wellesley-Cambridge Press.

Subbaram, H. & Abend, K. (1993). Interference Suppression via Orthogonal Projections: A Performance Analysis. *IEEE Trans. Antennas Propag.*, 41(9), 1187-1194. doi: 10.1109/8.247744.

Sun, H., Nallanathan, A., Wang, C. X. & Chen, Y. (2013). Wideband Spectrum Sensing for Cognitive Radio Networks: A Survey. *IEEE Wireless Commun.*, 20(2), 74-81. doi: 10.1109/MWC.2013.6507397.

Sun, Y., Baricz, A. & Zhou, S. (2010). On the Monotonicity, Log-Concavity, and Tight Bounds of the Generalized Marcum and Nuttall Q-Functions. *IEEE Trans. Inf. Theory*, 56(3), 1166-1186. doi: 10.1109/TIT.2009.2039048.

Szumski, A. (2010). Finding the Interference: KLT (Karhunen-Loève Transform) as an Instrument to Detect Weak RF Signals. *Inside GNSS*, 67(3), 56 - 64.

Taherpour, A., Nasiri-Kenari, M. & Gazor, S. (2010). Multiple Antenna Spectrum Sensing in Cognitive Radios. *IEEE Trans. Wireless Commun.*, 9(2), 814-823. doi: 10.1109/TWC.2009.02.090385.

Tandra, R. & Sahai, A. (2008). SNR Walls for Signal Detection. *IEEE J. Sel. Topics Signal Process.*, 2(1), 4-17. doi: 10.1109/JSTSP.2007.914879.

Tani, A. & Fantacci, R. (2008). Performance Evaluation of a Precorrelation Interference Detection Algorithm for the GNSS Based on Nonparametrical Spectral Estimation. *IEEE Syst. J.*, 2(1), 20-26. doi: 10.1109/JSYST.2007.914772.

Tavana, M., Rahmati, A., Shah-Mansouri, V. & Maham, B. (2017). Cooperative Sensing With Joint Energy and Correlation Detection in Cognitive Radio Networks. *IEEE Commun. Lett.*, 21(1), 132-135. doi: 10.1109/LCOMM.2016.2613858.

Tian, Z. & Giannakis, G. B. (2006, Jun.). A Wavelet approach to wideband spectrum sensing for cognitive radios. *Proc. Int. Conf. Cogn. Radio Oriented Wireless Netw. Commun.*, pp. 1-5. doi: 10.1109/CROWNCOM.2006.363459.

Trigui, I., Laourine, A., Affes, S. & Stephenne, A. (2009). Performance Analysis of Mobile Radio Systems over Composite Fading/Shadowing Channels with Co-located Interference. *IEEE Trans. Wireless Commun.*, 8(7), 3448-3453. doi: 10.1109/TWC.2009.081250.

Tsakalaki, E., Alrabadi, O. N., Tatomirescu, A., de Carvalho, E. & Pedersen, G. F. (2014). Concurrent Communication and Sensing in Cognitive Radio Devices: Challenges and an Enabling Solution. *IEEE Trans. Antennas Propag.*, 62(3), 1125-1137. doi: 10.1109/TAP.2013.2280051.

Tugnait, J. K. (2012). On Multiple Antenna Spectrum Sensing Under Noise Variance Uncertainty and Flat Fading. *IEEE Trans. Signal Process.*, 60(4), 1823-1832. doi: 10.1109/TSP.2011.2180721.

Urkowitz, H. (1967). Energy Detection of Unknown Deterministic Signals. *Proc. IEEE*, 55(4), 523-531. doi: 10.1109/PROC.1967.5573.

van der Tol, S. & van der Veen, A. J. (2005). Performance Analysis of Spatial Filtering of RF Interference in Radio Astronomy. *IEEE Trans. Signal Process.*, 53(3), 896-910. doi: 10.1109/TSP.2004.842177.

Van Trees, H. L. (2002). *Optimum Array Processing: Part IV of Detection, Estimation, and Modulation Theory*. New York, NY, USA: Wiley.

Vasilescu, M. & Terzopoulos, D. (2007, Oct.). Multilinear projection for appearance-based recognition in the tensor framework. *Proc. IEEE Int. Conf. on Comput. Vision (IEEE ICCV)*, pp. 1-8. doi: 10.1109/ICCV.2007.4409067.

Venkataramani, R. & Bresler, Y. (2000). Perfect Reconstruction Formulas and Bounds on Aliasing Error in Sub-Nyquist Nonuniform Sampling of Multiband Signals. *IEEE Trans. Inf. Theory*, 46(6), 2173-2183. doi: 10.1109/18.868487.

Vía, J., Santamaría, I. & Pérez, J. (2006). Effective Channel Order Estimation Based on Combined Identification/Equalization. *IEEE Trans. Signal Process.*, 54(9), 3518-3526. doi: 10.1109/TSP.2006.879271.

Wang, B. & Liu, K. J. R. (2011). Advances in Cognitive Radio Networks: A Survey. *IEEE J. Sel. Topics Signal Process.*, 5(1), 5-23. doi: 10.1109/JSTSP.2010.2093210.

Wang, P., Fang, J., Han, N. & Li, H. (2010). Multiantenna-Assisted Spectrum Sensing for Cognitive Radio. *IEEE Trans. Veh. Technol.*, 59(4), 1791-1800. doi: 10.1109/TVT.2009.2037912.

Wax, M. & Kailath, T. (1985). Detection of Signals by Information Theoretic Criteria. *IEEE Trans. Acoust., Speech, Signal Process.*, 33(2), 387-392. doi: 10.1109/TASSP.1985.1164557.

Wildemeersch, M. & Fortuny-Guasch, J. (2010). *Radio Frequency Interference Impact Assessment on Global Navigation Satellite Systems* (Tech. Rep.): EC Joint Research Centre, Security Tech. Assessment Unit.

Wolfram Research Inc. (Feb. 2007). MeijerG. Consulted at http://functions.wolfram.com/HypergeometricFunctions/MeijerG/21/02/07/0005/.

Wolfram Research Inc. (Jan. 2002). Incomplete gamma function. Consulted at http://functions.wolfram.com/GammaBetaErf/Gamma2/20/01/02/0001/.

Woods, F. S. (1934). *Advanced Calculus (New ed.): A Course Arranged with Special Reference to the Needs of Students of Applied Mathematics*. Boston, MA, USA: Ginn and Company.

Yin, H., Cottatellucci, L., Gesbert, D., Müller, R. R. & He, G. (2016). Robust Pilot Decontamination Based on Joint Angle and Power Domain Discrimination. *IEEE Trans. Signal Process.*, 64(11), 2990-3003. doi: 10.1109/TSP.2016.2535204.

Ying, Y., Whitworth, T. & Sheridan, K. (2012, Oct.). GNSS interference detection with software defined radio. *Proc. the 1st IEEE AESS European Conf. on Satellite Telecommun. (ESTEL)*, pp. 1-6. doi: 10.1109/ESTEL.2012.6400121.

Yousif, E., Ratnarajah, T. & Sellathurai, M. (2016). A Frequency Domain Approach to Eigenvalue-Based Detection With Diversity Reception and Spectrum Estimation. *IEEE Trans. Signal Process.*, 64(1), 35-47. doi: 10.1109/TSP.2015.2474309.

Yuan, J. (1998). Tests of Gaussianity and Linearity for Random Fields Using Estimated Higher Order Spectra. *IEEE Trans. Signal Process.*, 46(1), 247-250. doi: 10.1109/78.651229.

Yucek, T. & Arslan, H. (2009). A Survey of Spectrum Sensing Algorithms for Cognitive Radio Applications. *IEEE Commun. Surveys Tuts.*, 11(1), 116-130. doi: 10.1109/SURV.2009.090109.

Zeng, Y. & Liang, Y. C. (2009a). Spectrum-Sensing Algorithms for Cognitive Radio Based on Statistical Covariances. *IEEE Trans. Veh. Technol.*, 58(4), 1804-1815. doi: 10.1109/TVT.2008.2005267.

Zeng, Y. & Liang, Y.-C. (2009b). Eigenvalue-Based Spectrum Sensing Algorithms for Cognitive Radio. *IEEE Trans. Commun.*, 57(6), 1784-1793. doi: 10.1109/T-COMM.2009.06.070402.

Zhao, Q. & Sadler, B. M. (2007). A Survey of Dynamic Spectrum Access. *IEEE Signal Process. Mag.*, 24(3), 79-89. doi: 10.1109/MSP.2007.361604.

Zhou, X., Zhang, R. & Ho, C. K. (2013). Wireless Information and Power Transfer: Architecture Design and Rate-Energy Tradeoff. *IEEE Trans. Commun.*, 61(11), 4754-4767. doi: 10.1109/TCOMM.2013.13.120855.

Zoubir, A. & Iskander, D. (2004). *Bootstrap Techniques for Signal Processing*. Cambridge Univ. Press.

Zoubir, A. & Robert Iskander, D. (2007). Bootstrap Methods and Applications. *IEEE Signal Process. Mag.*, 24(4), 10-19. doi: 10.1109/MSP.2007.4286560.